

IN AXIAL-FLOW TURBOMACHINES: VOLUME 2

AD-A199 697

MC FILE COPY
AGARD-AG-298 VOL.2

(2)

AGARD-AG-298 VOL.2

AGARD

ADVISORY GROUP FOR AEROSPACE RESEARCH & DEVELOPMENT

7 RUE ANCELLE 92200 NEUILLY SUR SEINE FRANCE

AGARDograph No.298

AGARD Manual

on

Aeroelasticity in Axial-Flow Turbomachines

Volume 2

Structural Dynamics and
Aeroelasticity

SEP 28 198



NORTH ATLANTIC TREATY ORGANIZATION

DISTRIBUTION AND AVAILABILITY
ON BACK COVER

This document has been approved
for public release and may be
distributed in unlimited quantities.

2

AGARD-AG-298
Volume 2

NORTH ATLANTIC TREATY ORGANIZATION
ADVISORY GROUP FOR AEROSPACE RESEARCH AND DEVELOPMENT
(ORGANISATION DU TRAITE DE L'ATLANTIQUE NORD)

AGARDograph No.298

AGARD MANUAL
on
AEROELASTICITY IN AXIAL-FLOW TURBOMACHINES
VOLUME 2
STRUCTURAL DYNAMICS AND AEROELASTICITY

Edited by

Max F. Platzer
Department of the Navy
Naval Postgraduate School
Monterey, CA 93943-5100, USA

and

Franklin O. Carta
United Technologies Research Center
East Hartford, CT 06108, USA

DTIC
COPY
INSPECTED
6

Accession For	
NTIS GRAAI	
DTIC TAB	
Unannounced	
Justification	
By	
Distribution/	
Availability Codes	
Dist	Avail and/or Special

A-1

This document has been approved
for public release and contains no
classification or handling requirements.

S DTIC
ELECTED
SEP 28 1988
D
E

This AGARDograph was prepared at the request of the Propulsion and Energetics Panel
and of the Structures and Materials Panel of AGARD.

88 9 27 112

THE MISSION OF AGARD

According to its Charter, the mission of AGARD is to bring together the leading personalities of the NATO nations in the fields of science and technology relating to aerospace for the following purposes:

- Recommending effective ways for the member nations to use their research and development capabilities for the common benefit of the NATO community;
- Providing scientific and technical advice and assistance to the Military Committee in the field of aerospace research and development (with particular regard to its military application);
- Continuously stimulating advances in the aerospace sciences relevant to strengthening the common defence posture;
- Improving the co-operation among member nations in aerospace research and development;
- Exchange of scientific and technical information;
- Providing assistance to member nations for the purpose of increasing their scientific and technical potential;
- Rendering scientific and technical assistance, as requested, to other NATO bodies and to member nations in connection with research and development problems in the aerospace field

The highest authority within AGARD is the National Delegates Board consisting of officially appointed senior representatives from each member nation. The mission of AGARD is carried out through the Panels which are composed of experts appointed by the National Delegates, the Consultant and Exchange Programme and the Aerospace Applications Studies Programme. The results of AGARD work are reported to the member nations and the NATO Authorities through the AGARD series of publications of which this is one.

Participation in AGARD activities is by invitation only and is normally limited to citizens of the NATO nations.

The content of this publication has been reproduced
directly from material supplied by AGARD or the authors.

Published June 1988

Copyright © AGARD 1988
All Rights Reserved

ISBN 92-835-0467-4

Printed by Specialised Printing Services Limited
40 Chigwell Lane, Loughton, Essex IG10 3TZ

PREFACE

The first volume of this Manual reviewed the state of the art of unsteady turbomachinery aerodynamics as required for the study of aeroelasticity in axial turbomachines. It is the objective of the present second volume to complete the review by presenting to state of the art of structural dynamics and of aeroelasticity.

As pointed out in the preface to the first volume, further engine performance improvements and the avoidance of expensive engine modifications required to overcome aerodynamic/aeroelastic stability problems will not depend only on the continued systematic research in unsteady turbomachinery aeroelasticity. Rather, the need to transfer highly specialised unsteady aerodynamic and aeroelastic information to the turbomachinery design community and the introduction of young engineers to these disciplines suggested the compilation of a "Manual on Aeroelasticity in Turbomachines", similar to the "AGARD Manual on Aeroelasticity" for the aeroelastic design of flight vehicles, due to the lack of any textbook or other comprehensive compendium on unsteady aerodynamics and aeroelasticity in turbomachines.

This conclusion was presented to and endorsed by the AGARD Propulsion and Energetics and Structures and Materials Panels, the U.S. Office of Naval Research, the Naval Air Systems Command, and the Air Force Office of Scientific Research. The support of these organizations is gratefully acknowledged. We are especially indebted to the late Dr Herbert J. Mueller, Research Administrator and Chief Scientist of the Naval Air Systems Command, for his encouragement and guidance during the initial phase of the project. Thanks are also due to Dr Gerhard Heiche and Mr George Derderian (Naval Air Systems Command), Dr Albert Wood (Office of Naval Research), Dr Anthony Amos (Air Force Office of Scientific Research) and Mr David Drane (AGARD) for their continuing interest and support.

In the present second volume, after an introduction and overview by Sisto, the structural dynamics characteristics and analysis methods applicable to single blades and whole bladed assemblies are reviewed. Ewins first presents a chapter on basic structural dynamics, followed by a chapter on individual blades, written together with R. Henry, and concludes with a chapter on bladed assemblies. This is followed by an exposition of the blade fatigue problem and its assessment methods, written by Armstrong. The problem of life time prediction is reviewed by Labourdette, who also summarizes ONERA's research in viscoplasticity and continuous damage mechanics. The remaining chapters are devoted to aeroelasticity. Carta first introduces the reader to the problem of blade-disk shroud aeroelastic coupling. Crawley then presents detailed aeroelastic formations and solutions for tuned and mistuned rotors. Special attention is given in this chapter to the effects of mistuning. The sophisticated instrumentation and test procedures required to perform a fan flutter test are reviewed in considerable detail by Stargardter. The effect of stagnation temperature and pressure on flutter is demonstrated by Jeffers, who presents flutter boundaries obtained in a heavily instrumented fan rig as well as in a full-scale engine. In the concluding chapter the currently available forced vibration and flutter design methodology is reviewed and put in perspective by Snyder and Burns.

The editors are deeply indebted to the authors for their willingness to contribute their time and energies to this project in spite of other pressing demands. Our thanks also go to the authors' employers for their support. Funding limitations made it necessary to limit the number of contributors. Nevertheless, we hope that a fairly comprehensive and balanced coverage of the field of turbomachinery unsteady aerodynamics and aeroelasticity was accomplished and that the two volumes on unsteady turbomachinery aerodynamics and on turbomachinery structural dynamics and aeroelasticity will be found useful as an introduction to this important special discipline and as a basis for future work.

Max F. Platzer and Franklin O. Carta, Editors

STRUCTURES AND MATERIALS PANEL

Chairman: Professor Paolo Santini
Dipartimento Aerospaziale
Università degli Studi di Roma
"La Sapienza"
Via Eudossiana, 16
00185 Roma — Italy

Deputy Chairman: Prof Dr-Ing. Hans Försching
Direktor der DFVLR Institut für Aeroelastik
Bunsenstrasse 10
D-3400 Göttingen — Germany

MEMBERS OF THE SUB COMMITTEE ON AEROELASTICITY

Chairman: Prof Dr-Ing Hans Försching
Direktor der DFVLR Institut für Aeroelastik
Bunsenstrasse 10
D-3400 Göttingen — Germany

SMP Members

Dr L.Chesta — IT	Mr R.F.O'Connell — US
Dr R.Freymann — LU	Prof. P.Santini — IT
Prof. V.Giavotto — IT	Mr C.W.Skingle — UK
Mr J.B.de Jonge — NL	Mr D.C.Thorby — UK
Dr J.J.Kacprzynski — CA	Prof. A.F.Tovar de Lemos — PO
Mr O.F.Maurer — US	Mr R.J.Zwaan — NL

PANEL EXECUTIVE

Mr Murray C.McConnell — UK

AGARD-OTAN
7, rue Ancelle
92200 Neuilly sur Seine
France
Tel: (1) 4738 5790 Telex: 610176

From USA and Canada
AGARD-NATO
Attn: SMP Executive
APO New York 09777

ABSTRACT

The first volume of this Manual reviewed the state of the art of unsteady turbomachinery aerodynamics as required for the study of aeroelasticity in axial turbomachines. This second volume aims to complete the review by presenting the state of the art of structural dynamics and of aeroelasticity.

The eleven chapters in this second volume give an overview of the subject and reviews of the structural dynamics characteristics and analysis methods applicable to single blades and bladed assemblies.

The blade fatigue problem and its assessment methods, and life-time-prediction are considered. Aeroelastic topics covered include: the problem of blade-disc shroud aeroelastic coupling, formulations and solutions for tuned and mistuned rotors, and instrumentation on test procedures to perform a fan flutter test. The effect of stagnation temperature and pressure on flutter is demonstrated and currently available forced vibration and flutter design methodology is reviewed.

RESUME

Le premier volume de ce manuel a examiné l'état actuel des connaissances dans le domaine de l'aérodynamique instationnaire des turbomachines en vue de l'étude de l'aéroélasticité dans les turbomachines axiales. Ce deuxième volume vient compléter cet examen, en présentant l'état actuel des connaissances dans les domaines de la dynamique des structures et de l'aéroélasticité.

Les onze chapitres du présent volume donnent un aperçu du sujet, avec un examen des caractéristiques de la dynamique des structures et des méthodes d'analyse applicables aux aubes simples et aux ensembles munis d'aubes. Le problème de la fatigue des aubes est examiné, ainsi que les méthodes d'estimation de la fatigue et de la durée de vie des aubes.

Parmi les questions aéroélastiques couvertes, nous signalerons, le problème du couplage aéroélastique de l'aube et le talon du disque, les formulations et les solutions en ce qui concerne les rotors accordés et désaccordés, et l'instrumentation nécessaire et les procédures à suivre pour la réalisation des essais de flottement des soufflantes. L'effet de la température et de la pression d'arrêt sur le flottement est démontré et la méthodologie de calcul de la vibration forcée et du flottement, employé à l'heure actuel, est passée en revue.

CONTENTS

	Page
PREFACE	iii
STRUCTURES AND MATERIALS PANEL	iv
ABSTRACT	v
XII. INTRODUCTION AND OVERVIEW F.Sisto, Stevens Institute of Technology	
Introduction	12-1
Overview	12-2
XIII. BASIC STRUCTURAL DYNAMICS D.J.Ewins, Imperial College of Science and Technology	
Introduction	13-1
Structural Dynamic Characteristics	13-1
Structural Dynamic Analysis Methods	13-4
Finite Element Modelling (by R.Henry)	13-8
Dynamic Analysis Methods for Structural Assemblies	13-11
XIV. STRUCTURAL DYNAMIC CHARACTERISTICS OF INDIVIDUAL BLADES D.J.Ewins, Imperial College of Science and Technology, and R.Henry, Institut National des Sciences Appliquées	
Introduction	14-1
Vibration Properties of Uniform Beams and Plates	14-2
Factors Which Influence the Vibration Properties of Blades	14-5
Analysis Methods for Practical Blades	14-15
XV. STRUCTURAL DYNAMIC CHARACTERISTICS OF BLADED ASSEMBLIES D.J.Ewins, Imperial College of Science and Technology	
Introduction	15-1
Structural Dynamics Models for Bladed Assemblies	15-2
Basic Structural Dynamic Properties — Natural Frequencies, Mode Shapes	15-5
Modal Properties for Various Bladed Assemblies	15-10
Dynamic Analysis for Practical Assemblies (by R.Henry)	15-15
Vibration Properties of Mistuned and Packeted Bladed Assemblies	15-21
Forced Vibration Response	15-31
XVI. FATIGUE AND ASSESSMENT METHODS OF BLADE VIBRATION E.K.Armstrong, Rolls-Royce plc	
Introduction	16-1
Character of Fatigue	16-1
Observations on Blade Fatigue	16-6
Factors Affecting Blade Amplitudes of Vibration	16-9
Methods of Assessment	16-12
Amplitude Ratio Method	16-13
Stress Level Method	16-20
Comparison of Methods	16-26
Steps of Assessment and Test Conditions	16-28
Conclusions	16-31
Appendix I	16-33
XVII. LIFE TIME PREDICTION: SYNTHESIS OF ONERA'S RESEARCH IN VISCOPLASTICITY AND CONTINUOUS DAMAGE MECHANICS. APPLIED TO ENGINE MATERIALS AND STRUCTURES R.Labourdette, ONERA	
Introduction	17-1
Behaviour of Macroscopic Volume Element	17-1
Damage Description	17-7
Structural Life Prediction at High Temperature Under Complex Loadings	17-12
Conclusions	17-15

	Page
XVIII. AEROELASTIC COUPLING – AN ELEMENTARY APPROACH	
F.O.Carta, United Technologies Research Center	
Introduction	18-1
Nomenclature	18-2
System Mode shapes	18-3
Analysis	18-4
Results	18-8
Parametric Variations	18-12
Conclusion	18-15
Appendices	18-15
XIX. AEROELASTIC FORMULATIONS FOR TURBOMACHINES AND PROPELLERS	
E.F.Crawley, Massachusetts Institute of Technology	
Introduction	19-1
Formulation and Solution of the Aeroelastic Problem	19-3
Formulation for Multiple Section Degrees of Freedom	19-7
Formulation for Multiple Spanwise Blade Modes	19-8
Solutions for Sinusoidal Temporal Representations	19-10
Explicit Time Dependent Formulation of Aerodynamic Forces	19-13
Trends in Aeroelastic Stability	19-15
Effects of Mistuning on Stability	19-18
Appendix A	19-23
Appendix B	19-24
XX. FAN FLUTTER TEST	
H.Stargardter, Pratt and Whitney Aircraft	
Introduction	20-1
Test Procedure for a Flutter Evaluation	20-1
Identification of Blade Vibration	20-2
Fan Flutter Test, A Case History	20-4
Summary	20-35
XXI. AEROELASTIC THERMAL EFFECTS	
J.D.Jeffers, III, Tampa, Florida	
Introduction	21-1
Historical Background	21-1
Follow-on Research	21-4
Concluding Remarks	21-6
XXII. FORCED VIBRATION AND FLUTTER DESIGN METHODOLOGY	
L.E.Snyder and D.W.Burns, General Motors Corporation	
Introduction	22-1
Characteristics of Flutter and Forced Vibration	22-1
Forced Vibration Design	22-3
Flutter Design	22-17
Addendum to Program Listing for Unsteady Two-Dimensional Linearized Subsonic Flow in Cascades, Volume I, Chapter 3, pages 3-34 to 3-30	A-1
ALPHABETICAL LISTING OF REFERENCES	R-1

INTRODUCTION AND OVERVIEW

by
F. SISTO
 Department of Mechanical Engineering
 Stevens Institute of Technology
 Hoboken, New Jersey 07030
 USA

INTRODUCTION

Background. With minor exceptions Chapters I through 11 contained in the earlier Volume I of this Manual have been devoted to an exposition of those types of unsteady aerodynamics required for the study of aeroelasticity in axial turbomachines. Referring once again to Collar's triangle of forces (see Chapter 1) it is clear that the present volume dealing with structural dynamics, or the third side of the triangle connecting the vertices labelled elastic forces and inertial forces, completes the mnemonic of the aeroelastic triangle.

Structural dynamics, independently of its role in aeroelasticity, has had a broad, vigorous development in the present century. This outgrowth of structural mechanics has been marked, after the earliest work by Euler, Bernoulli and Lagrange and the subsequent practical contribution of those such as Timoshenko and DenHartog, by the formalization of tensor notation, which is thought to be more compact and therefore more general. Perhaps the most recent and most useful development has been the adaptation of the matrix method to structural dynamics. With the necessary substructuring and/or discretization of complex structures, the matrix method has brought to bear the powerful mathematics of linear algebra and the matrix calculus to the field of structural dynamics. It is not surprising therefore, that for real system designs, (e.g., an elastic disk bladed with 4% tip thickness airfoils and provided with butting part-span shrouds) the matrix formulation of aeroelastic problems is not only useful, but increasingly needed. The widespread adoption of the finite element method (for fine-grain quantitative accuracy) coupled with modal analysis (for the development of robust computational and experimental methods) characterize the present state of structural dynamics. Vectorization of the equations for efficient program execution on super-computers is a reality and future application of parallel processors seems certain.

Volume II, the present volume, begins with three chapters devoted exclusively to subjects in structural dynamics. Sufficient fundamental information therefore is covered, with the completion of Chapters 13, 14, and 15, to support some of the special aeroelastic studies presented in the remainder of the volume. These topics range from fatigue and blade life prediction to aeroelastic coupling, mistuning effects, experimentation and thermal effects. The Manual concludes with the all-important implications for design.

Stress Prediction. Referring to the previous list of topics addressed in Chapters 16 through 22 (the last chapter

in Volume II) it is important to note the gap between flutter prediction and stress prediction. Although linear analysis of aerodynamically forced vibration will yield a vibration amplitude, given some specified law for mechanical damping, the same is not true for flutter, or self-excited aeroelastic instability. Only the boundary between stability and instability may be discriminated with linear theory. Thus the typical aeroelastic eigenvalue analysis will not yield a flutter stress prediction.

For the assessment of fatigue damage, or in general the severity of the flutter vibration, it is currently necessary to employ experimental means. A system with measured flutter behavior may be assessed for the accumulation of damage over a given operating cycle and redesigned to lower the damage level. Most likely, the redesign will attempt to eliminate flutter entirely. With forced vibration the reduction of stress by redesign is quite feasible if the cause has been properly diagnosed.

In the future, application of nonlinear analysis will improve the capability to predict blade stress during flutter. This capability is now in an embryonic state with the first results issuing from stall flutter theories employing nonlinear aerodynamics. The particular theories are those which effectively display a hysteretic dependence of aerodynamic forces and moments on blade displacement and velocity. In addition, there may be amplitude dependence of forces which is not linear in this displacement and velocity.

For single degree of freedom systems, thus employing a single modal coordinate, the flutter amplitude prediction effectively makes use of the aerodynamic work concept. In turn this is an expression of the more general principle of harmonic balance expounded in nonlinear mechanics. How this capability may effectively be expanded to multiple degrees of freedom, for particular formulations of the nonlinear aerodynamic forces, is currently an active area of analytical and computational investigation. Formulation of the explicit time dependence of the aerodynamic forces for arbitrary blade motions is a requirement first described in Chapter 19. For complex geometry, nonlinear structures and flows with sharp gradients, time domain solutions may be the solutions of choice. Simultaneous integration of unsteady aerodynamic and structural dynamic subprograms by time marching will be facilitated with modern computational developments and allow the realistic treatment of nonlinearity in both structure and fluid models. Flutter stress prediction will become increasingly possible as these developments materialize.

OVERVIEW

Fundamentals. In Chapter 13, entitled Basic Structural Dynamics, the underlying mechanism of blade vibration in axial turbomachines is reviewed briefly by David Ewins. The concepts of structural dynamics begin with the establishment of continuous and later discrete models. The distribution of inertial and elastic (or mass and stiffness) properties are described, and also damping, thus deriving a set of governing differential equations. This method of analysis concludes with solutions of these partial differential equations. In the case of the free vibration, the solution yields the modal properties: the eigenfunctions and the characteristic frequencies. The forced vibration solution yields the actual distribution of displacements (strain) and stresses for specified external excitations. It is not emphasized at this point that when the aerodynamic forces are linearly dependent only on blade displacements and velocities these forces may effectively be taken on the left hand side resulting in the statement of an aeroelastic eigenvalue problem.

Discrete system and continuous system analyses are summarized by Professor Ewins. The finite element model is summarized in a separate section by Dr. R. Henry who is also the co-author of Chapter 14 following. It is pointed out that the energy method of equation derivation presumed in Lagrange's Equation is capable of supplying the effects of centrifugal stiffening, centrifugal softening and gyroscopic.

This chapter concludes with a discussion of different methods of analyzing structural assemblies, including most generally the bladed disk assembly with interconnecting shrouds between adjacent blades. In particular the concept of substructuring is presented along with the use of modal coordinates for synthesizing the overall system equations. For example, the blades may be represented by a very few modal degrees of freedom for inclusion in an analysis of a bladed disk assembly. Brief summaries then follow the two methods of system coupling: modal coupling and frequency response coupling.

Beams and Plates. In Chapter 14 entitled Structural Dynamic Characteristics of Individual Blades, David Ewins and R. Henry continue with the exposition of single blades treated alternatively as beams or plates.

Beams, or beamlike blades, have deformation functionally dependent solely on the radial coordinate whereas with plate-like structures the deformation will also be dependent on the chordwise coordinate (i.e., the cross-section itself distorts). For beams the aspect ratio is greater than for plate-like structures and in both cases the thickness ratio is considerably less than unity, at the blade tips especially.

Initially, the vibration properties of uniform beams are described in terms of natural frequency and mode shape and as

affected by geometry, boundary conditions (end and shroud fixity), rotor rotation and centrifugal and Coriolis forces.

Tables are presented showing the natural frequencies and modes shapes for the gravest modes in flapwise bending, edge-wise bending, and torsional modes and for five different sets of end conditions. Second order effects due to rotatory inertia and shear deflection are elucidated for typical geometry and material properties.

Similar studies illustrating the effect of aspect ratio using plate theory are presented next for uniform geometry continuous plates. The modes are now best described in terms of the location of the nodal lines.

When the uniform beam is modified to include linear taper or linear twist significant changes in natural frequencies are observed, although the mode shapes are relatively unchanged for the tapered blade. With the twisted blades the modes become more complicated with flapwise and edgewise components of deformation appearing in the bending modes (i.e., flexural modes are coupled bending-bending). Similar conclusions apply to plate-type analysis of lower aspect ratio geometries.

Discussions of root flexibility, static deflection and rotor rotation follow. The limiting values of flexibility are discussed qualitatively, the chief conclusion being that at some point of lowered root rigidity it is necessary to consider the bladed-disc assembly (rather than the blade alone) to properly identify the modal properties of that system due to the coupling between blades afforded by the flexible disk.

Blade lean and pretwist in a centrifugal field and gas bending loads provide sources of "static" deformations about which vibrations may occur. The centrifugal effect also changes the blade effective stiffness, providing an increase for vibration normal to the plane of rotation and a small decrease for vibratory displacements in the plane of rotation. Professor Ewins notes that these effects must be taken into account in order to predict accurately the modal properties under operating conditions which, for a rotor blade, include the centrifugal effects attendant to rotation.

Noting that the finite element method is most flexible and now in wide use, a discussion of the beam-type elements and plate shell elements then follows. Short sections describe the ability of the FEM to formulate complex cross-section properties, root and platform flexibilities, shrouds, "static" loads (noted previously), Coriolis and centrifugal effect, and the temperature effect on modulus of elasticity.

The concluding section of this chapter is a description of the previous concepts as applied to three specific rotor configurations, by computation, and including some experimental verification. The first example is the analysis of a low pressure turbine blade using a straight, tapered,

twisted beam element and illustrating the effect of bending-bending-torsion coupling. Inertia coupling due to non-coincidence of section centroids and center of twist and the effect of rotation are demonstrated in a series of examples. A number of practical conclusions are drawn concerning the effects on natural frequency and mode shapes and the consequent need for using "refined" beam-type elements for aeroelastic studies.

The second example, the analysis of a fan blade using three node triangular plate elements, elucidates the untwist effect which, along with accurate centrifugal stiffening, requires an iterative solution procedure. Coriolis effects can be safely ignored for this particular problem of mode definition. This is not necessarily true for highly swept blades, or blades on a precessing rotor. In any event, the nonlinear iterative solution procedure, for example, using an updated Lagrangian formulation at each iteration, is recommended.

The third example is a high pressure turbine blade modelled with thick shell elements. Dynamic analysis shows that the rotation effect is weak for both frequency and mode shape for this "thick" blade. The change in frequency can be adequately estimated from the nonrotating case using the method of Rayleigh Quotients.

The final paragraphs of the chapter consist of practical recommendations for structural dynamic modelling of single blades based on the findings of the preceding studies and computations.

Blade-Disk Model. In Chapter 15, Structural Dynamics of Bladed Assemblies, the subject material of the previous two chapters is brought together by David Ewins for the treatment of practical systems. As in the previous two chapters there is also an important contribution by Dr. R. Henry in this chapter.

Initially, the configurations to be examined are described, ranging from unshrouded identical blades to packetted blades to blades that are not identical to each other. Disks are considered with various degrees of flexibility up to complete rigidity. In the remainder of the chapter the natural frequencies and mode shapes are presented for these various assemblies and the major controlling factors are described. The results of analyzing and computing a number of representative cases are presented qualitatively in the text and in the form of figures for more quantitative comparisons and tests.

Models which are evaluated by computation are generally at three distinct levels of abstraction: the lumped parameter model where full axisymmetry is assumed; the beam and plate models of blades with either axisymmetric, cyclically symmetric (i.e., rotationally periodic structure) or full blade-to-blade variation; and finally, the finite element model in which axisymmetry, or at best cyclic symmetry with substructuring must be assumed due to computing limitations.

The computed results reveal the typical feature (for each configuration) of 'single' and 'double' modes of which the latter is in the majority. Most of the assemblies' modes occur in these pairs with similar shapes and identical frequencies. This is consistent with the identification of these combined modes by the number of nodal diameters, n . The special nature of modes for $n = 0$ and $n = 1$ is discussed as is the general behavior as n becomes very large. With the beam, plate, and finite element models nodal circles may also appear. For an N -bladed disk, the maximum value for n is $1/2N$ ($(N-1)/2$ if N is odd) for the discrete lumped parameter model. However, for continuous disk or shroud models higher values of n are possible, but the blade or rim displacement for $n > N/2$ are indistinguishable from the mode with $N-n$ nodal diameters. This 'aliasing' property is very significant and may allow an infeeding of energy from aerodynamic sources at frequencies associated with n nodal diameters, but with $N-n$ nodal diameters being measured. This important feature is fully discussed and elucidated.

A number of configurations are analyzed, with an $N = 36$ bladed disk used to study parametrically the effects of disk stiffness, root flexibility, stagger, twist, shroud stiffness and shroud connection.

Dr. Henry presents the results of analyzing a specific turbine rotor using finite elements and assuming axisymmetry. The six lowest frequency modes are discussed as well as their variation with rotational speed. The important point is made that if cyclic symmetry must be assumed (e.g., due to a small N , and hence with blades which cannot be modelled as beams) then the mode shapes no longer display simple diameters and circles as nodal lines.

The important characteristics of mistuned assemblies is discussed next leading to the important characteristics of mode and frequency splitting. Each double mode with identical frequencies and mode shapes in the tuned state splits into distinct modes with close natural frequencies and modal shapes upon the introduction of mistuning. The very complex behavior of mistuned assemblies is discussed including the effects of regular versus random mistuning, the effect of damping (may introduce complex modes if the damping is non-proportional) and the effect of lashing the blades in packets. The subject of mistuning as applied to self-excited systems is returned to in Chapter 19.

The chapter closes with a discussion of force vibration assuming two types of forcing: single point harmonic excitation and engine-order excitation. It is emphasized that a resonance can be obtained only by excitation at the proper frequency and with an appropriate spatial distribution (i.e., the sign of the work done on the vibration will depend locally on the phase between the force and the displacement and will be zero at the nodes). The detailed character of the response of a number of computed cases is presented for both types of excitation. It is empha-

sized that the aliasing phenomenon appears most important; in the eng \rightarrow order case. An (N-n)th engine order excitation and an nth engine-order excitation will be equally effective in exciting modes with n diametral nodes and the vibration will occur at an N-n multiple of the rotational speed. The corresponding alias vibration where the nth engine order excites N-n nodal diameter modes is also demonstrated and discussed. This and other extremely complex behavior is presented for a number of computed cases. The chapter ends with a discussion and an estimate of the increase in forced response on the "worst", or "rogue", blade attributable to a particular degree of mistuning. This is a fitting conclusion for the third chapter on structural dynamics where the emphasis is on forcing, not necessarily or exclusively from aerodynamic sources. It should be emphasized, as introduced briefly in Chapter 1 and discussed more fully in Chapter 19, that the conclusions on the harmful effect of mistuning may be quite different in the case of self-excited aeroelastic instabilities.

Vibratory Blade Failure. Chapter 16, Fatigue and Assessment Methods of Blade Vibrations, by Keith Armstrong is a thorough treatise on the practical aspects of blade failure and its prevention. The initial sections of this chapter are taken up with many definitions related to metal fatigue and the character of the phenomenon.

Definition of alternating stress, the experimental means of testing metal samples and/or blades with a high number of stress reversals, the establishment thereby of S-N curves and the use of these data to construct the modified Goodman diagram are all thoroughly discussed. The qualitative nature of these diagrams is described, including the factors which affect them such as notch sensitivity, mean stress level, (due to static loading as well as residual stresses) the presence of defects and the propagation of fatigue cracks.

This leads to a discussion of fracture mechanics, particularly as applied to compressor/fan blades and turbine buckets. The effect of grain size, loading history (leading to Miner's hypothesis for the accumulation of damage) surface treatment, low cycle fatigue, fretting, erosion, corrosion, and data scatter are discussed. The need for fatigue testing is emphasized, the correspondence between sample or coupon testing versus blade testing is discussed and the methods of testing are described.

A discussion follows of the factors affecting amplitude of blade vibration, noting the previously discussed disparity between flutter and forced vibration insofar as amplitude determination is involved. The manner of stress measurement using strain gages is discussed and the practical diagnosis of vibration of both types in running compressors is presented by examples. This broad ranging mid-chapter exposition by Dr. Armstrong is one in which qualitative factors related to vane and blade vibration, its detection, and developmental steps for its amelioration are discussed in considerable detail.

The emphasis is on jet engine experience; flight conditions and installation characteristics enter the discussion frequently.

A detailed derivation is then given of the "amplitude ratio" method of forced vibration assessment. The application of the method is discussed, including correlations supplied from cantilever beam theory, different blade materials, fatigue capability, material damping, temperature, statistical scatter, and the evolution of design/development rules.

The "amplitude ratio" method is contrasted with the stress level method of assessing blade vibration and fatigue failures. This second method depends on a detailed knowledge of the vibratory and steady stresses and has become increasingly used as the finite element method of stress analysis has come into widespread use. The application of the method, and the special effects that can be handled (such as restraint of edge warping, centrifugal forces, etc.) is discussed at length and practical examples are presented.

The two methods are compared and the benefits of each are emphasized. Modern practice in a large organization will be to use an efficient blend of the two. The influence on design and an historical description, with many examples and practical observations, concludes this extremely useful chapter on the blade vibration aspects of jet engine design and operation. The successful developments of the past twenty years in the United Kingdom are described and explicated in the text of this chapter.

High Temperature Material Behavior. Chapter 17 has a long title, Lifetime Prediction: Synthesis of ONERA's Research in Viscoelasticity and Continuous Damage Mechanics Applied to Engine Materials and Structures. Contrasted with the title, this short chapter by R. Labourdette deals with the problems of high temperature turbine blades: creep and fatigue. While in the previous chapter temperature effects are recognized but not dealt with in great depth this is not so in the present chapter; temperature effects are paramount. The work is a joint effort of ONERA and SNECMA.

Adopting a tensor notation, viscoelasticity of high temperature materials is formulated in the general thermodynamic framework of irreversible processes. This branch of continuum mechanics is applied to the cyclic straining of the prototypical turbine blade beyond the elastic limit. Creep represents the response to loading over long periods of time, i.e., with a very low frequency of the loading cycle. For fatigue behavior the frequencies are much higher and the vibration thus defined is most appropriate to the province of dynamic aeroelasticity. The theory is also quite general and accounts for an interaction between creep and fatigue.

The model developed for general viscoelastic behavior of a metallic material is then applied to the generation of a new theory for damage accumulation. This theory of damage on the microscopic scale

leads to the all-important prediction of crack initiation which is the starting point for subsequent macroscopic treatment of crack propagation under cyclic straining. The theory, based on continuum damage mechanics, is expressed in a finite element program EVPCYCL developed by Dr. Labourdette at ONERA. The program algorithm integrates constitutive equations of the developed theory, and predicts the cycles to crack initiation for given loading and temperature histories. Comparison with experimental data shows that the viscoplasticity model is an accurate tool for prediction of crack initiation. The method is being extended to anisotropic materials (e.g., single crystal alloys) and more complex geometry. The appearance of these very useful new results is anticipated with interest for later editions of this Manual.

Systems Instability. Stemming from its central importance in the description of bladed-disk flutter, the coupled theory introduced by Franklin O. Carta (1967) has been summarized by him in Chapter 18, Aeroelastic Coupling - An Elementary Approach. The historical setting for the appearance of this type of flutter is outlined briefly, noting that the bending/torsion coupling is augmented by part-span shrouds typical of post-1950 turbofans. This coupling of the bladed-shrouded-disk is shown later to be critically destabilizing.

The equations of motion of the aeroelastic system, expressed in travelling wave form, are combined with unsteady aerodynamic terms and the solution for the flutter condition is discriminated by the method of aerodynamic work integrated over the blade span. The intrablade phase angle is fixed at 90 degrees by the structural coupling, and, with isolated airfoil aerodynamics, the flutter instability is shown to be most susceptible in the modes having an intermediate number (i.e., 3, 4, or 5) of diametral nodes with forward travelling waves. The greater the degree of bending/torsion coupling the greater the likelihood of coupled flutter instability. Parametric studies of shroud location confirm this trend and experiments with research compressors lend further support to those general conclusions.

This chapter concludes with a survey of many recent studies employing compressible cascade aerodynamics and tuned and alternatively mistuned rotors. In this section of the chapter Frank Carta shows that the importance of the interblade phase angle is uniminished in these system mode instabilities. In fact, the number of nodal diameters of a particular mode is a surrogate variable for the interblade phase angle; specifically $\sigma = 2\pi n/N$ where n is the number of nodal diameters and N is the number of blades in the row. This proxy relationship between n and σ is not emphasized elsewhere in Volume II, although the groundwork for the importance of σ in turbomachine aeroelasticity is laid down firmly in Volume I of this Manual.

Conclusions, drawn from this straightforward analysis of the fundamental aeroelastic problem of coupled systems, have wide validity with respect to the material

of most of the remaining chapters. The principal value of Chapter 18 is that it is a compact exposition of self-excited aeroelastic instability as it is actually encountered in axial turbomachines when dominated by strong structural coupling between blades. Succeeding chapters build on this exposition and may be contrasted and related to it for increased comprehension and relevance of the material in those chapters. In this sense Chapter 18 encapsulates the entire Manual by means of a cogent and historically significant example and its subsequent generalizations.

Mistuning Effects. In Chapter 19, Aeroelastic Formulation and Trends for Tuned and Mistuned Rotors, the general system approach to turbomachine aeroelasticity is expounded by Edward Crawley. The structural dynamic and aerodynamic models are combined in a consistent manner to yield an aeroelastic model. The results are discussed with major emphasis on stability discrimination (flutter). Explicit time domain aerodynamics is discussed for use in predicting forced vibration response. Considerable attention is given to the effects of mistuning and algorithms for optimization of this effect are presented and discussed.

Noting that the available model formulations are somewhat incomplete, particularly with respect to aerodynamic operators, the point is made that the time dependence can be expressed within the time domain or the frequency domain. The mathematical models are then developed beginning with the representative section having a single degree of freedom. A cascade of such blades is coupled only through the motion-dependent force influence of one blade on another. By making the assumption of sinusoidal time dependence with a fixed interblade phase angle, σ , the travelling wave modes of the aeroelastic eigenvalue problem are determined. It is pointed out that this model, initially chosen for the aerodynamics formulation, is not unique. It is adequate for tuned system SDOF analysis.

The aeroelastic eigenvalue problem can be, and is, reformulated in terms of individual blade coordinates. When this is done the aerodynamic influence coefficient matrix which results has a high degree of symmetry, depending on the degree of geometric uniformity*. Each element is obtained from a discrete Fourier transform of the complex force coefficient obtained from the conventional travelling wave formulation. In this second form (i.e., individual blade coordinates) the aeroelastic equation demonstrates that a given blade is strongly affected only by its most immediate neighbors.

A third alternative formulation is in terms of the standing waves, or twin orthogonal modes introduced earlier in Chapter 15 for the discussion of forced vibration. The aeroelastic eigenvalue problem expressed in this form allows the

*For complete uniformity the matrix is circulant, the properties of which were first exploited by Lane (1956).

use of experimentally determined standing wave structural modes.

These results are subsequently generalized for two degrees of freedom per blade, e.g., coupled bending/torsion, and then to multiple degrees of freedom. In broad terms this amounts to replacing single elements in the previous formulation by sub-matrices and sub-vectors. Furthermore, modal coordinates are usually adopted for the multiple degree of freedom model. The transformation of the blade aerodynamic forces is detailed in an appendix. In all these developments Professor Crawley makes numerous qualitative comments concerning the properties of the various matrices and describes underlying physical characteristics of the aeroelastic system.

Solution of the various problem formulations are then exemplified by expressing the aerodynamic forces in travelling-wave form (sinusoidal motion) and restricting the analysis to one or two degrees of freedom for a cascade of characteristic-section blades. Traditional methods, such as the V-g and p-k methods are then discussed for solution, and subject to special conditions such as the very large mass ratio of blade to air. I.e., the real part of the aeroelastic eigenvalue is very close to the natural frequency in vacuo. The character of the eigenvalue plots is discussed giving some insight as to how these may be expected to differ from fixed wing results. Naturally, the interblade phase angle is a key parameter.

For the first time in the Manual the need is described for obtaining the explicit time dependence of the aerodynamic forces for arbitrary blade motions. This form of the aerodynamic operators, for studying response to tip rubs or surge for example, is theoretically derivable by a complex inverse Fourier integral from the frequency domain expression. In practice this is accomplished by using the so-called Pade' approximation, whose derivation is outlined.

The analytical methods described up to this point are applied next to a short discussion of trends in aeroelastic stability of turbomachine rotors. Analyzing a simplified system, it is demonstrated that a necessary but not sufficient condition for aeroelastic stability is that the blades be self-damped; i.e., the effect of a blade's motion upon itself must be to contribute positive aerodynamic damping. The unsteady interactions amongst or between blades in the cascade are destabilizing for at least one possible interblade phase angle. This blade-to-blade destabilizing influence is reduced by mistuning, and is hence desirable. Mistuning, however, can never produce stability when the self-damping is negative. With nonzero structural damping blades of larger (blade to air) mass ratio are relatively more stable.

The effect of coupling is qualitatively discussed and it is noted that kinematic coupling (e.g., the presence of some bending displacements in a predominantly torsional natural mode) may be quite important in determining stability whereas

the dynamic coupling, e.g. through the aerodynamic reactions, is usually not strong enough to be of significance. The effect of loading is speculated as being a possible source of flutter near stall, and the stability trends with reduced velocity are discussed qualitatively, noting both structural and aerodynamic implications of the reduced frequency parameter.

The remainder of the chapter is concerned with mistuning for stability enhancement. Using a simplified example for a supersonic fan with structural (mass) mistuning and restricted to torsional motion, it is shown that optimal mistuning is more effective than alternate mistuning which might intuitively be chosen. The details of the optimal mistuning patterns are then discussed, where the optima have been obtained by minimizing a penalty function using nonlinear programming techniques detailed elsewhere.

Basically the optimum patterns are 'almost' alternate mistuning, i.e., with important exceptions on one or two blades. Practical considerations devolve upon the accuracy with which an intentional mistuning pattern can be effectuated due to errors in measurement, manufacture, or selective assembly. Based on consideration of this nature, alternate mistuning is more robust and may be the method of choice. The detailed analysis of mistuning patterns and their practicality in the manufacturing phase forms a fitting conclusion to this extremely important concept which is one of the dominant areas of practical application in turbomachinery aeroelasticity today. More research on mistuning may be expected to yield increasingly practical results.

Aeroelastic Research in Rotors. In Chapter 20, Fan Flutter Test, by Hans Stargardter, aeroelastic instability in a turbomachine is investigated experimentally. In this sense it epitomizes the purely experimental approach to the subject of the Manual.

Using an existing single stage fan research rig, a great deal of sophisticated instrumentation was installed for the measurement of steady and unsteady aerodynamic quantities as well as blade deflection and deformation. (Deformation measurements were limited to steady untwist and uncambering due to centrifugal effects.) In order to emphasize the range and complexity of the instrumentation, these systems are simply listed here; their frequency response, accuracy, and modes of operation are detailed in the text of the Chapter.

Instrumentation: Strain gages, laser beams and blade-mounted mirrors, semiconductor pressure transducers, hot film gages (probes and anemometers), time code generator and revolution counter, wedge probes, static taps and thermocouples. Most unique was the large number of small mirrors fixed to the rotor blades in a variety of radial and chordwise positions. By recording the position of reflected laser light beams it was possible to reduce the data to yield blade deflection, both steady and unsteady (i.e., mode

shapes) as well as static untwist and uncamber. The acquisition of reliable blade surface pressures and the reconstruction of passage pressure distribution near the housing are described. Of equal importance was the recording and electronic reduction of these data. Sophisticated enhancement and spectral processing of the periodic signals was employed, and analysis of the on-rotor data as a superposition of backward and forward rotating harmonic waves, allowed comparison and correlation with other data measured in absolute coordinates, i.e., relative to the fixed housing of the fan. Phasing was obtained using cross-spectral density techniques. These overall data reduction methods are unique. As noted throughout the Manual, the phasing of certain parameters along the cascade, e.g., the interblade phase angle, is of supreme importance in understanding and describing aeroelastic phenomena in turbomachines.

Using this powerful system for the acquisition of flutter-related data the experimental exploration of fan flutter led to some interesting results. The flutter region of the fan was mapped out. Aero-jynamic work computation led to the determination of modal aerodynamic damping values and are shown to be negative in flutter. The historic correlation of the flutter region in incidence versus reduced velocity coordinates, and as depicted somewhat humorously in Figure 2 of Chapter 1, is confirmed experimentally in the final figure of Chapter 20. A number of other observations are made concerning the steady pressure distribution, the passage Mach number distribution, the localization of instability influence near the leading edge and the roles of uncamber and untwist in flutter.

Perhaps the most important contribution of the Chapter is the detailed information concerning blade frequency, vibration amplitude, and interblade phase angle. For this type of flutter, identified as the subsonic/transonic flutter of region I in Figure 1 of Chapter 1, the frequencies of all blades are identical; there is a single flutter frequency, i.e., "frequency entrainment" has taken place. Thus the interblade phase angle between any two blades is well-defined and remains constant in time. However, the value of the interblade angle varies from passage to passage on the rotor and concomitantly, the vibration amplitudes vary from blade to blade (but not in time). This detailed experimental revelation of the flutter mode goes beyond the analytical or computational description of the flutter mode in a mistuned stage. Mistuning, as characterized by the assembled blade natural frequency distribution, is shown to correlate with the blade amplitude at flutter. Thus, it is suggested by Hans Stargardter, that the analysis of flutter in mistuned stages consider the following model: The blade amplitude pattern represents "a family of spatial harmonics described by the superposition of a number of rotating nodal diameter patterns, each characterized by a different number of nodal diameters with different but uniform amplitudes and different but uniform phase indexing, with each pattern rotating at a speed that results in the same flutter frequency w_A" In Chapter 20 these pat-

terns are identified by spectral processing of the experimental data. The guidance that this result provides for the theoretical computational aeroelastician is profound. It will be interesting to see in the future how this mutual stimulation of theory and experiment will help to define the most realistic and therefore most useful aeroelastic model for a row of turbomachine blades which are always mistuned to some extent.

Effects of Ambient Variables. In Chapter 21, Aeroelastic Thermal Effects, by James D. Jeffers, II, the effect on flutter of variable inlet stagnation temperature and pressure is reported. These experimentally derived results were obtained in a sequence of tests beginning with a heavily instrumented fan rig, progressing on to a full-scale engine program and concluding with a full parametric flutter mapping of the engine under NASA auspices.

The 3-stage fan rig, operated under standard sea level static inlet conditions demonstrated a first stage stall flutter boundary referred to a representative span, similar to Figure 2 of Chapter 1. The mode was predominantly with a 5 nodal diameter system mode, and classified in region Ia of Figure 1 in Chapter 1. The important conclusion that the operating line of the fan component would not penetrate the stall flutter region was a factor in clearing the engine for fabrication. Subsequently, simulated flight testing of the full engine which included high Mach number conditions at altitude, uncovered a flutter condition. However, the mode was predominantly above shroud torsion at a slightly higher frequency corresponding to the next higher natural mode. This important and unexpected result was then mapped in great detail using the high altitude facility at NASA Lewis.

In this program the imposition of higher inlet stagnation temperature, and to a lesser extent higher inlet stagnation pressure, were found to be destabilizing. Although the effect was quantitatively measured for the particular flight article of the test, no theoretical underlying explanation was offered. Flutter has multiple-parameter dependence and when there is a validated analytical theory, these dependencies are made explicit. However, the theory of unsteady stalled aerodynamics is still in a deficient state, particularly with respect to Mach number and Reynolds number dependence (see Chapter 8). Thus, the results, reported for the first time in Dr. Jeffers' chapter, are quantitatively useful as the basis for a semi-empirical model for unsteady stalled aerodynamics.

Perhaps of most importance was the experimental confirmation of the stall flutter mode as described in the previous chapter; the vibration at a single frequency in rotor-fixed coordinates is composed of a number of different nodal diameter mode shapes travelling in both forward and backward directions in these coordinates. As noted in the previous chapter, the blade-to-blade vibration amplitudes vary around the rotor circum-

ference as does the interblade phase angle. In essence, the present chapter demonstrated that the contribution of each complex mode to the overall aeroelastic mode is dependent as well upon inlet and engine operating conditions. A reliable stall flutter prediction system in a practical sense remains somewhat elusive.

Aeroelastic Design. The terminus of the Manual is Chapter 22, entitled Forced Vibration and Flutter Design Methodology, authored by Lynn Snyder and Donald Burns. The focus here is on summarizing what is known about aeroelasticity in axial turbomachines and bringing it to bear on the process of design. The procedure may be iterative in the sense that a candidate design which fails flutter or fatigue criteria is redesigned and then re-analyzed or re-tested. Whereas flutter is to be avoided entirely, the criterion for forced vibration is to limit the stresses to some fraction of the endurance limit. These two contrasting criteria have been noted previously in the Manual. Prediction is based on empirical correlation and semi-empiricism for certain phenomena while some types of flutter are assessed on a theoretical/analytical basis.

In order to limit forced vibration response at the design stage it is necessary to first identify the sources of excitation by constructing a Campbell diagram based on calculated natural modes and on noting potential mechanical and aerodynamic periodic forces. This is followed by an assessment of stresses as the intersections on the diagram in the running range. This assessment is based mostly on empirical correlation for each mechanism, e.g., rotor blade excitation in the torsional mode from upstream struts. The predicted stresses are then entered into a modified Goodman diagram for several high stress points on the blade, taking into account stress concentration factors, notch sensitivity, temperature distribution and scatter of fatigue data (a factor of safety amounting to three standard deviations typically is used). If a blade is found deficient in this assessment, or for that matter at a later stage in the course of subsequent experimentation, there are a number of corrective measures that can be taken in the redesign effort. These range from weakening the effective source of excitation, to changing the forcing and/or natural frequencies, to the introduction of increased mechanical damping. An example is given of the assessment of a particular turbine rotor row. This was found to have an adequate vibratory stress margin, and hence, redesign was not required.

In the discussion of flutter assessment, five different types of mechanisms are discussed by Dr. Snyder and Mr. Burns. These correspond roughly to the regions in Figure 1 of Chapter 1. Each of the five phenomena are discussed with respect to changes in five dominant flutter design parameters: reduced velocity, Mach number, steady loading, mode shape, and pressure or density level. In the last parameter the effect of temperature is subsumed in pressure and density through the perfect gas law and the effect of temperature is felt also in the Mach number through the acoustic velocity.

Each of the five types of flutter are then discussed: subsonic/transonic stall flutter, unstalled supersonic flutter, supersonic torsional flutter, choke flutter, and supersonic stall flutter. The characteristics with respect to unique frequency and interblade phase angle, mode shape and operative mechanism are discussed at length. Corrective actions that may be taken by the designer, such as lowering the reduced velocity for example, are presented in the concluding sections of the chapter. In a sense this final section of Chapter 22 of Volume II and of the entire Manual, is the most immediately useful to the operator or designer faced with self-excited aeroelastic instability in an axial turbomachine. Although the chapter is rife with practical explanation of vibration mechanisms and the means to ameliorate or eliminate the resulting fatigue damage, this is most particularly true of the final section. Although there is always need for further research, this final chapter indicates that much is known about aeroelastic problems in axial turbomachines and much can be done of a practical nature to eliminate its harmful aspects. It is always nice to close on an optimistic note.

Acknowledgements. The author is pleased to acknowledge the support of the Naval Air System Command, via the Naval Post-graduate School, for supporting these particular publishing efforts. More importantly, the editors and other contributors are to be congratulated for their application to a difficult assignment, under sometimes trying circumstances. The result has been a very valuable set of reference volumes that are now available to the aerospace research and development community. AGARD is also to be commended for its foresight in undertaking the project initially and for underwriting substantial production costs.

BASIC STRUCTURAL DYNAMICS

by

D. J. EWINS

Imperial College of Science and Technology
 Department of Mechanical Engineering
 Exhibition Road, London SW7 2BX

INTRODUCTION

We now turn our attention to the other major aspect of this work: namely, the structural dynamics effects which combine with the aero/fluid phenomena previously detailed in Volume I to constitute the complete aeroelastic problem. The objectives of this present chapter are to provide the necessary introduction for the following three chapters which deal with the purely structural dynamic aspects of blade and bladed assembly vibration. These chapters will in turn be followed by others describing methods which enable us to combine both the aero-and the structural dynamic characteristics, thereby describing the full aeroelastic phenomena. Throughout, we shall be examining the problem from the viewpoint of the analyst wishing to predict the magnitude and nature of blade vibration in order to assess the damage incurred by the blades as a result. Thus, we shall be concerned with two complementary aspects: the vibration properties of a blade or bladed assembly and its response characteristics. Of course, these are closely related but it is very important to establish at the outset that they are not one and the same thing.

In this chapter, we shall be introducing both the concepts applicable to the structural dynamics aspects and the properties of interest as well as summarizing the appropriate analysis methods which are available for deriving the required information in specific cases. As it is intended to provide a summary applicable to the most general cases, it will be necessarily concise and readers requiring a more exhaustive treatment are referred to a suitable text. On the other hand, readers already familiar with structural dynamic analysis methods might only need to consult later sections of this chapter. Subsequent chapters will assume familiarity with the contents of this one.

We shall begin by discussing the first task of the structural dynamicist - that of formulating a suitable mathematical model. This amounts to specifying the distribution of mass and stiffness and, if appropriate, the mechanical damping effects as well (although this is usually rather more difficult to do). A separate section deals with the now widespread use of finite element methods for this modelling task. Following this modelling stage, a set of equations of motion can be developed and then solved in different forms to determine the various characteristics required. The first of these is the undamped free vibration solution, yielding the fundamental vibration properties of natural frequencies and mode shapes for the basic structure (the 'modal properties'). Modified values for these data can be derived if damping

parameters are introduced to the model. The final analysis stage is that for a forced vibration response and this task requires the introduction of additional information in the shape of the forcing function. Here, it can be seen that the forced vibration response depends not only on the structure itself (as is the case for the modal properties) but also on the additional factors contained in the forcing or excitation function(s).

Finally, in the section "Dynamic Analysis Method for Structural Assemblies" we shall outline some of the special analysis methods which are especially appropriate for dealing with the particular structural forms common in bladed assemblies. It will be seen that in most such cases it is essential that all the blades in one row or stage be analyzed simultaneously in a single model and not treated independently as individual blades. This often results in rather large models, especially for those stages with many blades. Not only is this expensive but since the blades are generally (assumed to be) identical it is inefficient unless the multi-component and repeated symmetry characteristics of the assembly are exploited. Methods to achieve this are discussed in this concluding section.

STRUCTURAL DYNAMIC CHARACTERISTICSModelling

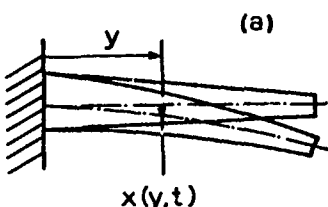
The first task in any vibration analysis is the definition of a suitable mathematical model upon which the required analysis can be based. In the present case, we seek to describe first the mass (or inertia) and stiffness properties of the structure in question, and then - if possible - to include some consideration of the mechanical damping effects. It is usually the case that the mass and stiffness effects can be much more readily represented than can those for the damping and so many dynamic analyses are performed including only these two primary structural elements. However, although it is true that the damping often has a relatively minor effect on the basic modal properties (which are determined ignoring damping), it must also be noted that it is of particular importance in determining vibration response levels, especially around resonance. Furthermore, it is found that one of the major contributions of the aerodynamic effects to blade vibration characteristics is in respect of the contribution to the damping levels. Thus, due consideration must be given in our studies of the structural dynamics to the consequences and methods of including damping in the models.

Although the analysis methods which follow are general, and apply to all types

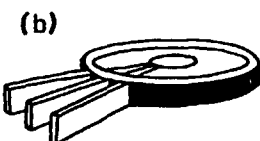
of structure, it is appropriate and helpful if we confine our interpretation and application of them to blade-and bladed assembly-like structures. (By bladed assembly, we refer to a bladed disk, or to a set of stator vanes attached to an annular casing, or to a group of blades interconnected by a shroud band, as shown in Figure 1.) Before presenting the formal analysis procedures in current usage, it should be noted that there are two fundamentally different approaches to the task of describing the dynamics of a structure. These approaches are embodied in the two types of model which will be referred to as 'Continuous' and 'Discrete'. Although the development of finite element methods has resulted in an emphasis on the latter type of modelling, both have a role to play and will be included in this review.

Continuous Models

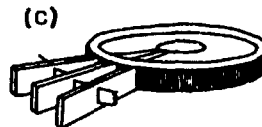
If we wish to describe the vibration behaviour of a beam-like structure such as that sketched in Figure 1(a), then it is clear that we need to be able to define the motion of all points of the structure at all times and thus that a variable function of the type $x(y,t)$ would form the basis of an analysis. If we extend this concept to a more complex configuration, such as the bladed disk in Figure 1(b), then the variable function would need to become $x(r,\theta,t)$. In this type of formulation, it is necessary to find expressions for the mass and stiffness distributions which are also continuous functions of position. These expressions are then used to determine inertial forces and stiffness forces (or kinetic energy and strain energy) which are combined to develop governing equations of motion for the system. As will be seen later, these are in the form of partial differential equations for which closed form analytic solutions are only available under special and rather restricting conditions. If these conditions - which generally demand much simpler and more uniform geometries than are used in practice - are not applicable, then approximate numerical solutions must be sought. Because of this limitation, and the non-optimal format of the equations thus generated for efficient numerical solution, the alternative procedure employing discrete models such as the finite element model is standard practice for most practical applications. Nevertheless, the continuous type of model does have advantages and is particularly useful for qualitative and comparative studies.



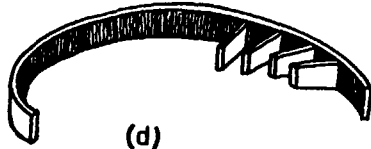
a) Single Blade



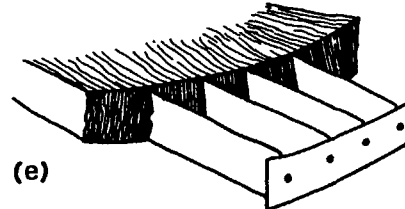
b) Unshrouded Bladed Disk



c) Shrouded Bladed Disk



d) Stator Row



e) Blade Packet

Figure 1. Basic Structural Configurations for Bladed Systems.

Discrete Models

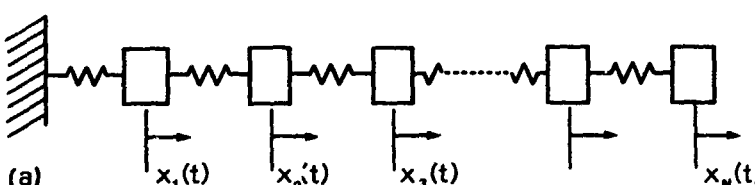
The basis of the discrete model is the separation of the inertia and stiffness (and damping) effects so that the model consists of a collection of separate components, each of which is either a mass or a spring (or a damper) - see Figure 2(a). This process necessarily reduces the continuum of the previous form to a finite set of discrete elements and so the variable function which is used to describe the motion of the system now consists of a finite set of individual parameters of the form $x_j(t)$, $j=1, N$, where N is the order of the discrete model and is its number of degrees of freedom. (Note that a continuous system thus has an infinite number of degrees of freedom.) Describing the various forces or energy terms in this case leads to a set of linear ordinary differential equations which can be conveniently formulated in matrix notation, thereby rendering them amenable to numerical solution.

The development of a discrete model for a given structure can be undertaken in various ways. In the limit, we can envisage the representation of each component of the structure by a large number of separate mass and spring elements following closely the geometry of the structure. This is, in effect, the finite element approach and results in a very large number of degrees of freedom and thus equations of motion - see Section "Finite Element Modelling". Alternatively, it is possible to devise rather more schematic models of much lower order which are capable of describing adequately the global behaviour of the model - i.e., its major mode shapes and their natural frequencies - but is not capable describing in detail what is happening in every part of the system. For

example, we shall later refer to a lumped mass-spring model for a bladed assembly in which each blade is represented by just one or two masses; clearly, this is too coarse a model to describe the deflection pattern across the whole blade but it is adequate to describe the relative displacement from one blade to the next in the assembly.

Damping

It is also appropriate to mention here the question of including damping effects in the model. In the present application, any damping effects which are provided by the aero - or fluid dynamic effects will be introduced separately and it is necessary to include here only those damping effects which are of a mechanical origin - material hysteresis, friction in joints, etc. Unfortunately, it is not possible to introduce these effects in an accurate way since almost all such mechanisms are non-linear and thus not easily accommodated in our equations of motion. Two types of damping model are used in an attempt to simulate the energy dissipating effects of the actual mechanisms which obtain, but neither is a 'correct' model. The first of these is the traditional viscous dashpot model, consisting of a damper element which generates a force proportional to the relative velocity across its ends. The second is known as the 'structural' or 'hydromechanic' damper model and is similar to the viscous one except that the damping rate is not constant (as is the case for viscous) but varies inversely with the frequency of vibration. This alternative model was developed as a result of the inability of viscous damping to represent correctly the observed phenomenon that energy dissipation mechanisms in most structures are vibration amplitude-dependent but not frequency-dependent.



a) Schematic Model

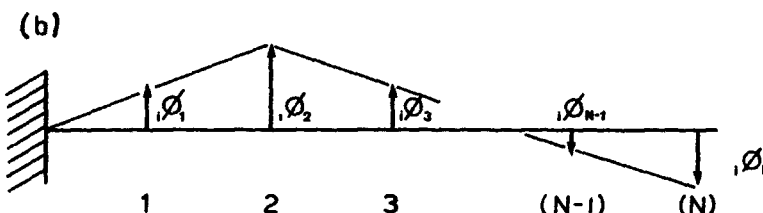


Figure 2. Discrete Model of Beam-Like Structure.

However, the drawback to the structural damping model is its presupposition that vibration is taking place at a prescribed frequency, or set of frequencies: a situation not strictly true for transient vibration. Having said that, use of one of these two models is almost essential if the equations of motion are to remain linear: more accurate descriptions of the damping effects (and, to some degree, the stiffness effects) would lead to a non-linear model, the added complexity of which is almost certainly not practicable in the present case.

Vibration Properties

Once the model has been established and used to generate a set of equations of motion, these are then analyzed for two types of solution. The first of these is the free-vibration solution, which yields the intrinsic modal properties possessed by the structure. Most important amongst these are the natural frequencies - those frequencies at which vibration will take place in the absence of any continuing excitation. Associated with each such natural frequency is a corresponding mode shape which describes how the displacement of the system varies from point to point across its geometry, see Figure 2(b). It is an important feature of these modal properties that free vibration can take place in any one of the 'normal' modes (natural frequency and mode shape combination) completely independently of all the other modes.

When the system is undamped, the modal properties are quite straightforward, and easy to interpret, but when damping is added, they become rather more complex. The natural 'frequency' itself becomes complex with both an oscillatory component (as for the undamped case) and a decay component, the latter being due entirely to the damping. The mode shapes can also become complex in that they describe not only the relative amplitudes of vibration for the different positions on the system but also introduce phase differences. This means that when vibrating in one such complex mode, each part of the system reaches its maximum displacement at a different instant to its neighbour. In a classical or undamped system normal mode, all parts reach their maximum excursion simultaneously.

Response Characteristics

While the modal properties are an essential part of the structural dynamic analysis of any system, they do not provide the whole picture and in order to complete the analysis it is generally necessary to undertake also the second type of solution; namely, that for forced-vibration response. At this stage in the analysis, it is necessary to introduce some additional information in the form of the excitation or forcing function (and it is just this fact that makes the response solution fundamentally different from the free-vibration analysis). This generally falls into one of two types - steady, or continuous, excitation and transient

excitation. It is the former which leads to the description of the resonance phenomenon which is the forced vibration manifestation of a natural frequency or mode of vibration. However, it is most important to establish that not all modes of vibration will necessarily exhibit a resonance under forced vibration conditions: the nature of the excitation function is just as important in determining resonance as are the modal properties of the system itself.

In the case of transient response calculations, interest is very often confined to what happens immediately after such an excitation has been applied. If the combined effect of all the damping elements is negative, then vibration will tend to grow uncontrollably once started by some transient disturbance: otherwise, it will tend to die away.

Summary

Thus, to summarize, the main features of a structural dynamic analysis are:

- the construction of a suitable mathematical model;
- the derivation of a set of governing equations of motion;
- the free vibration solution to yield the intrinsic modal properties of the structure; and
- the forced vibration solution to describe the actual displacements (and stresses, etc.) under some specified excitation conditions.

STRUCTURAL DYNAMIC ANALYSIS METHODS

Derivation of Equations of Motion for Discrete Systems

Having developed a discrete model for a given structure, the derivation of its equations of motion is a routine task. It should be noted at the outset that there is no unique set of such equations. First of all, the variables chosen to describe the system's behaviour (the coordinates) are themselves not unique, but even given a specific set of these variables, then we may develop an infinity of equally valid sets of equations of motion. The one thing all these different equation sets share is the solution.

A valid set of equations can be derived by one of two methods, based respectively on equilibrium and energy principles. In both cases, the starting point is to assume that the system is in a state of general motion, with displacements, velocities and accelerations in all its coordinates, x, \dot{x}, \ddot{x} . Following this assumption, it is possible to define all the forces which are acting upon each component of the model and by applying equilibrium conditions at all junctions between components, we can derive a set of governing equations - the equations of motion. In the case of free vibration,

with no externally applied forces, the equations contain only the system parameters and the (unknown) displacement variables of each component.

Alternatively, expressions for the instantaneous energy levels - kinetic, stored and dissipated - can be derived from the same starting point and by applying the principle of conservation of energy, a similar and equally valid set of equations can be derived.

In all cases, it is convenient to write the equations in matrix form and thus to describe the mass and stiffness properties of the system in terms of a mass matrix $[M]$ and a stiffness matrix $[K]$. A corresponding viscous damping matrix $[C]$, or structural damping matrix $[H]$ may be defined as well, if the damping effects are included. The general form of the equations of motion is then:

$$[M] \ddot{\{x\}} + [K] \dot{\{x\}} + [C] \{x\} + i[H] \{x\} = \{f(t)\} \quad (1)$$

Once again, it is important to note that these system matrices apply only when the coordinate set is $\{x\}$ and are not a unique description of the system's characteristics. The system matrices must exhibit certain properties and in many cases they will be symmetric matrices. Even if the equations as derived are not symmetric, they can often be rearranged so as to become symmetric. However, under conditions where gyroscopic inertia effects are present, or where certain hydrodynamic or aerodynamic effects apply, then some of the system matrices may be non-symmetric, with a consequent increase in the complexity of the ensuing analysis and properties. We shall concentrate here on the standard case where symmetry of the system matrices is obtained.

Free Vibration Solution for the Undamped System

The basic system properties can be derived from the equations of motion for the undamped system in the absence of any excitation. For this case, the equations of motion reduce to:

$$[M] \ddot{\{x\}} + [K] \dot{\{x\}} = \{0\} \quad (2)$$

and the method of solution is to assume that simple harmonic motion is possible of the form:

$$\{x(t)\} = \{x\} e^{i\omega t} \quad (3)$$

Substitution into the Equation (2) shows that this is indeed a valid solution to the equations, provided that the frequency is one of a finite set of specific values (ω_r) and, further, that the displacements of different parts of the system conform to a specific pattern. The specific values of frequency - the natural frequencies ω_r - are determined by solving the determinantal equation:

$$\det|[K] - \omega^2 [M]| = 0 \quad (4)$$

and the corresponding patterns, or mode shapes $\{\psi\}_r$, by solving the homogeneous equations:

$$([K] - \omega_r^2 [M]) \{\psi\}_r = \{0\} \quad (5)$$

(NOTE that this does not give a unique answer for the displacement amplitudes of the individual variables, $\{x\}$. Because the equations are homogeneous, only RELATIVE amplitudes are obtained and as a result it is appropriate to assign them a different parameter, $\{\phi\}$, which reflects this indeterminacy of scale.)

The mode shapes have important properties of orthogonality which, concisely stated, are:

$$\{\psi\}_r^T [M] \{\psi\}_s = 0: \omega_r \neq \omega_s \quad (5a)$$

and

$$\{\psi\}_r^T [K] \{\psi\}_s = 0: \omega_r \neq \omega_s \quad (5b)$$

These can be grouped into the simple matrix expressions:

$$\{\psi\}^T [M] \{\psi\} = [m_r] \quad (6)$$

$$\{\psi\}^T [K] \{\psi\} = [k_r]$$

where the individual elements m_r and k_r are referred to as the 'modal masses' and 'modal stiffnesses'. As mentioned earlier, the coordinates used are not the only variables which can be used to describe the system's behaviour. We could rewrite the equations of motion using a different set of coordinates, such as $\{p\}$ which are defined as

$$\{p\} = \{\psi\}^{-1} \{x\} \quad (7)$$

Substituting into (2) and premultiplying by $\{\psi\}^T$, leads to:

$$\{\psi\}^T [M] \{\psi\} \{p\} + \{\psi\}^T [K] \{\psi\} \{p\} = \{0\} \quad (8)$$

which reduces to:

$$[m_r] \{\ddot{p}\}_r + [k_r] \{p\}_r = \{0\} \quad (9a)$$

It is clear from this that each individual equation contained in the complete set takes on the simple form:

$$m_r \ddot{p}_r + k_r p_r = 0 \quad (9b)$$

leading directly to the solution that

$$\omega_r^2 = k_r/m_r$$

It may be seen that the values for m_r and k_r will vary according to the scaling used for the mode shapes, and so these parameters are not unique. However, their ratio - the square of the natural frequency - is unique. It is found convenient to scale the modes in a particular way known as mass-normalization. This requires simply the rescaling of all the elements in $\{\phi\}_r$ by $\sqrt{m_r}$ to give:

$$\{\phi\}_r = (m_r)^{-1/2} \{\psi\}_r \quad (10)$$

This leads to a more convenient form of the orthogonality statement in (6):

$$\begin{aligned} [\phi]^T [M] [\phi] &= [M] \\ [\phi]^T [K] [\phi] &= \omega_r^2 \end{aligned} \quad (11)$$

Free Vibration Solution for Damped Systems

When damping is added to the system, a similar type of result is obtained to that described above but each of the modal parameters becomes complex. The natural frequencies become complex so that the solution postulated in (2) takes the form:

$$\{x(t)\} = \{x\}e^{ast} = \{x\}e^{-at} e^{i\omega t} \quad (12)$$

indicating not only oscillation (at frequency ω) but also an exponential decay (rate = a). Thus, free vibration of a damped system also consists of a number of independent modes, each of which has this type of complex natural frequency.

Similarly, the mode shapes may become complex, indicating phase differences between one point and the next, in addition to the amplitude differences.

The exact form of the modal properties varies with the type of damping. For viscous damping, the analysis becomes rather lengthy but a set of natural frequencies and mode shapes are obtained in the form of complex conjugate pairs:

$$\begin{bmatrix} s_r & 0 \\ \vdots & \vdots \\ 0 & s_r \end{bmatrix}, \begin{bmatrix} \psi_r & \psi_r^* \\ \vdots & \vdots \\ \psi_r^* & s_r \psi_r \end{bmatrix} \quad (13)$$

If structural damping is used, the algebra is simpler although the mathematical rigour is less, and a set of complex natural frequencies and mode shapes are obtained:

$$[\lambda_r^2] : [\psi] \text{ (complex)} \quad (14)$$

where

$$\lambda_r^2 = \omega_r^2(1+in_r)$$

$$\{x(t)\} = A\{\phi\}_r e^{i\lambda_r t}$$

In practice, it is found that for systems with relatively light damping (the case for most applications to blade systems), the inclusion of damping has virtually no effect on the oscillatory component of the natural frequency and is only effective at introducing the decay rate. If the damping is 'proportional' - i.e., is distributed in a similar way to the mass and/or stiffness - then the modes of the damped system are not complex, and are in fact identical to those of the system without damping. However, it is particularly relevant to note here the conditions under which the mode shapes become noticeably complex, and thus differ significantly from the undamped system properties. This is found to happen when

the damping is relatively localized AND when the system has close natural frequencies. This last characteristic is of particular relevance here because axisymmetric bladed assemblies possess most of their modes in pairs with identical or very close natural frequencies. Such modes may thus be particularly prone to a high degree of complexity.

Forced Vibration Solution

Although we are likely to be concerned with response predictions for any type of excitation, we shall show that undertaking an analysis for the frequency response properties (response to individual point harmonic excitation forces) permits the extension to any more general excitation conditions. Thus, we shall concentrate on this particular form of response prediction.

The basic relationships are simply stated: if the excitation forces can be represented by the simple harmonic function

$$\{f(t)\} = \{f\}e^{i\omega t} \quad (15a)$$

then it may reasonably be assumed that the response will be similarly sinusoidal and have the form:

$$\{x(t)\} = \{x\}e^{i\omega t} \quad (15b)$$

These response and excitation functions are related by the frequency response function matrix $[H(\omega)]$ as follows:

$$\{x\}e^{i\omega t} = [H(\omega)] \{f\}e^{i\omega t} \quad (16)$$

Substituting (15) into the basic equation of motion (1), first for the un-damped case, gives:

$$[H(\omega)] = ([K] - \omega^2[M])^{-1} \quad (17)$$

which, while correct, is not very convenient for numerical application. It requires the inversion of a large matrix at each frequency of interest and does not readily permit the calculation of just one or two of the frequency response elements in the matrix. Following the simplifying effect of transforming the equations of motion by the mode shape matrix (Equations (8) and (9)), we find that if we premultiply both sides of Equation (17) by $[\phi]$, and introduce $[\phi][\phi]^{-1} = [I]$, then it may be replaced by

$$[H(\omega)] = [\phi] \{(\omega_r^2 - \omega^2)\}^{-1} [\phi]^T \quad (18a)$$

which is both easier to compute and considerably easier to interpret. Specifically, it is possible to extract just one element $H_{jk}(\omega)$ from the frequency response function matrix, which provides the (harmonic) response at point j per unit (harmonic) excitation at point k:

$$H_{jk}(\omega) = \frac{x_j}{f_k} = \sum_{r=1}^N \frac{r^{\psi_j} r^{\psi_k}}{\lambda_r^2 - \omega^2} \quad (19b)$$

If damping is added, the expression changes only slightly in form, becoming complex to reflect the additional influence. For structural damping, the matrix equation becomes

$$[H(\omega)] = [\phi] \{(\lambda_r^2 - \omega^2)\}^{-1} [\phi]^T \quad (19a)$$

and the individual element:

$$H_{jk}(\omega) = \sum_{r=1}^N \frac{r^{\psi_j} r^{\psi_k}}{\lambda_r^2 - \omega^2} \quad (19b)$$

For viscous damping, the expressions are:

$$[H(\omega)] = [\psi] \{ (i\omega - s_r) \}^{-1} [\psi]^T \quad (20a)$$

and

$$H_{jk}(\omega) = \sum_{r=1}^N \frac{r^{\psi_j} r^{\psi_k}}{(i\omega - s_r)} \quad (20b)$$

or

$$= \left(\sum_{r=1}^N \frac{r^{\psi_j} r^{\psi_k}}{i\omega - s_r} + \frac{r^{\psi_j*} r^{\psi_k*}}{i\omega - s_r*} \right) \quad (20c)$$

Where * denotes complex conjugate.

Lastly, it remains to demonstrate the applicability of these frequency responses to more general types of excitation than harmonic ones (even though these latter may constitute the majority of cases for bladed assemblies).

If the excitation is periodic, but not harmonic, then it can generally be described by a Fourier series:

$$f(t) = \sum_{n=-\infty}^{\infty} f_n e^{i\omega_n t}, \quad \omega_n = \frac{2\pi n}{T} \quad (21a)$$

as also can the resulting response:

$$x(t) = \sum_{n=-\infty}^{\infty} x_n e^{i\omega_n t} \quad (21b)$$

Each of the constituent components, f_n and x_n , are then related by the corresponding frequency response function:

$$x_n = H(\omega_n) f_n \quad (21c)$$

Those excitations which do not respond to this approach, such as transients, may be more amenable to a time domain analysis. This is typically stated as follows: the time history response $x(t)$ caused by a force $f(t)$ can be expressed by the integral equation:

$$x(t) = \int_{-\infty}^t f(t') h(t-t') dt' \quad (22)$$

where $h(t)$ is the unit impulse response function. This, in turn, may be shown to be related to the frequency response function via another Fourier transform:

$$h(t) = \frac{1}{2\pi} \int_{-\infty}^{\infty} H(\omega) e^{i\omega t} d\omega \quad (23)$$

Thus, the frequency responses provide all the necessary information to evaluate the forced response of a system to any type of excitation.

Continuous System Analysis

It was mentioned earlier that attempts to describe the dynamic behaviour of systems with continuously-distributed mass and stiffness resulted in partial differential equations which lacked convenient analytic solutions in the general case. We shall summarize one particular case here to illustrate the nature of the equations produced and to show some of the potential advantages of this type of approach: for a more detailed development of the analysis, reference should be made to a standard vibration text, such as Thompson (1981) or Bishop & Johnson (1960).

Consider the case of bending of a beam, such as that shown in Figure 1(a). If we study an element of the beam while it is undergoing free vibration (Figure 3), we find that the equation of equilibrium can be stated as:

$$\frac{\partial^2}{\partial y^2} (EI \frac{\partial^2 x}{\partial y^2}) + \rho A \frac{\partial^2 x}{\partial t^2} = 0 \quad (24)$$

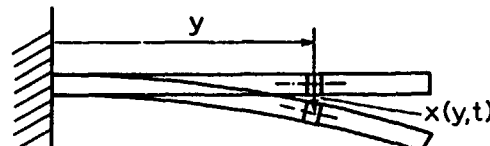


Figure 3. Continuous Model of Beam-Like Structure.

If we now assume simple harmonic motion, as before, but this time with the specific form $x(y,t) = \phi(y) \exp(i\omega t)$, the this equation becomes:

$$\frac{d^2}{dy^2} (EI\phi''(y)) - \rho A \omega^2 \phi(y) = 0 \quad (25)$$

Solution of this equation requires the specification of some boundary conditions and of the variation of the section properties along the length of the beam. The latter requirement means that the solution is difficult to obtain in a closed analytic form if the section properties vary along the beam, as is the case in most practical blades. However, for the cases which can be solved analytically (constant section properties), we find that our assumption of simple harmonic vibration was a valid solution, provided that a certain condition is satisfied. This condition varies with the boundary conditions, but is usually similar to the specific example shown below for the case of a cantilever beam of length L (clamped at one end, free at the other):

$$1 + \cos(\lambda L) \cosh(\lambda L) = 0; \quad . \quad (26)$$

$$\lambda^4 = \frac{\omega^2 \rho A}{EI}$$

Clearly, solving this equation leads to an infinity of roots, λ_r , or natural frequencies, ω_r , and each of these may be back-substituted to determine the corresponding mode shape, or $\phi_r(y)$, such as

$$\phi_r(y) = \left\{ \begin{array}{l} (\sin \lambda_r y - \sinh \lambda_r y) \\ + \frac{\cos \lambda_r L + \cosh \lambda_r L}{\sin \lambda_r L - \sinh \lambda_r L} (\cos \lambda_r y - \cosh \lambda_r y) \end{array} \right\} \quad (26)$$

for the cantilever example.

A forced vibration analysis may also be made using this type of model and leads to closed form expressions for individual frequency response functions. As an example, we quote the tip response function for the cantilever example:

$$H_{LL}(\omega) = \frac{\sin(\lambda L) \cosh(\lambda L) - \cos(\lambda L) \sinh(\lambda L)}{EI \lambda^3 (1 + \cos(\lambda L) \cosh(\lambda L))} \quad (27a)$$

This can also be presented in a series form:

$$H_{LL}(\omega) = \sum_{r=1}^{\infty} \frac{(4/A\rho L)}{\omega_r^2 - \omega^2} \quad (27b)$$

noting the infinite limit on the series. Similar analyses may be made for the torsional and axial vibration of beams and for two-dimensional bending of plates, resulting each time in partial differential equations of motion of various forms. The general solution takes a different form in each case, but there is a generic similarity between all of them.

FINITE ELEMENT MODELLING

(contributed by R. Henry,
Institut National des Sciences Appliquées)

So far, we have not explained how the basic modelling and derivation of the equations of motion is approached and it is now appropriate to address this task, using finite element methods.

The finite element method (FEM) is a powerful numerical procedure for solving the mathematical problems of engineering and physics and is particularly well suited for complex structures such as the bladed assemblies with which we are concerned here. The mathematical foundations of the finite element method are unquestionably an important area but are beyond the scope of this text, where the technique has to be considered simply as a tool for a specific practical engineering problem. In the following paragraphs, we present a brief review of the method as it would be applied to analyze a bladed assembly including, where appropriate, the effects of rotation - not easily accommodated in the preceding analyses. In the finite element method, considerations of energy are generally used in order to develop the equations of motion and so this section will concentrate on that process: once the equations are available, they may be used to study the structural dynamics as outlined in the preceding sections.

General Method for Analysis of Rotating Structures

The analysis of rotating structures has to take into account the centrifugal effects in addition to the inertia and stiffness terms which are applicable to all structures and, as a result, the potential and kinetic energies are a little more complicated to derive than for non-rotating structures. Assuming that the material is homogeneous, continuous, linearly elastic and undamped, a general procedure can be simply presented, as follows.

Expressions for the Strains and Stresses.
The strain vector (ϵ) related to the displacement (x) of a typical point is derived according to the type of structure (one-, two-, or three-dimensional). In matrix form, it reduces to:

$$\{\epsilon\} = \{\epsilon_L\} + \{\epsilon_{NL}\} \quad (28)$$

where $\{\epsilon_L\}$ is the linear classical strain vector and $\{\epsilon_{NL}\}$ a non-linear geometric strain vector representing the geometric coupling due to rotation. Assuming the validity of Hooke's law, the stress vector is:

$$\{\sigma\} = [D] \{\epsilon\} \quad (29)$$

Strain Energy: Analytical Form.

Integrating over the whole structure gives an expression for the total strain energy (U):

$$\begin{aligned} U &= \frac{1}{2} \int_{\tau} \{\epsilon\}^T \{\sigma\} d\tau \\ &= \frac{1}{2} \int_{\tau} \{\epsilon\}^T [D] \{\epsilon\} d\tau \end{aligned} \quad (30a)$$

and substituting (28) in (30) leads to:

$$\begin{aligned} U &= U_K (\epsilon_L, \epsilon_L) + U_G (\epsilon_L, \epsilon_{NL}) \\ &\quad + U_0 (\epsilon_{NL}, \epsilon_{NL}) \end{aligned} \quad (30b)$$

where U_K , U_G , and U_0 are, respectively, the classical linear elastic strain energy, the strain energy due to the geometric coupling (tension and bending); and a term of higher order that will be neglected.

Absolute Velocity. Writing the absolute velocity of a typical point M in a moving coordinate system (O) linked to the axis of rotation of the structure rotating at an angular velocity Ω , which gives:

$$\dot{v}_M = \frac{d}{dt}(\vec{OM}) + \vec{\Omega} \times \vec{OM} \quad (31)$$

and this can be expressed in term of the displacement (x) and velocity (\dot{x}).

Kinetic Energy: Analytical Form. Integrating over the whole component gives the kinetic energy of the structure:

$$T = \frac{1}{2} \int_{\tau} \rho v_M \cdot v_M d\tau \quad (32a)$$

(assuming a uniform mass density, ρ).

Substituting (31) into (32a) leads to:

$$\begin{aligned} T &= T_M(\dot{x}^2) + T_C(x, \dot{x}) \\ &\quad + T_S(x^2) + T_F(x) + T_0 \end{aligned} \quad (32b)$$

where T_M , T_C , T_S , and T_F are respectively the contributions to the kinetic energy from the inertia or mass effect, the coriolis effect, the supplementary centrifugal effect and the centrifugal forces effect respectively. T_0 is a constant term which cancels in later calculations.

In most practical cases, the complex geometry and non-classical boundary conditions of real structures require U and T to be evaluated using an approximate numerical method, such as the finite element method. Here, the structure is divided into simple elements of finite size (the finite elements) that are connected at certain points, called nodal points or 'nodes', which are generally (though not always) situated on the boundaries of the elements (Figure 4).

Discretisation. The magnitudes of the continuous variables (such as displacement (x)) at the nodes are denoted by a vector ($\{x_e\}$), whose components are called the nodal values or nodal degrees of freedom, and these are to be determined. The continuous displacement (x) is then approximated over each element by a polynomial expression [N] that is defined using the nodal values. A different polynomial is defined for each kind of element, but it must be selected in such a way that continuity is maintained along the element boundaries. The general form for the displacements of an element e , is given by:

$$\{x\} = [N] \{x_e\} \quad (33a)$$

and in the same way for the velocity:

$$\{\dot{x}\} = [N] \{\dot{x}_e\} \quad (33b)$$

and for the strains (28):

$$\{\epsilon\} = [B] \{x_e\} \quad (33c)$$

It must be noted that the matrix $[B]$ includes both the linear and the non-linear parts of the strain definition (Equation 28).

Finite Element Expression for the Potential Energy. Using equation (30a) for a typical element e and substituting (33c) leads to:

$$\begin{aligned} 2 U_e &= \{\epsilon_e\}^T [K_{Le}] \{x_e\} \\ &\quad + \{x_e\}^T [K_{Ge}] \{x_e\} \end{aligned} \quad (34)$$

where $[K_{Le}]$ is the element linear stiffness matrix and $[K_{Ge}]$ the element geometric stiffness matrix which is linked to the initial stress vector $\{\sigma_0\}$ due to the centrifugal forces.

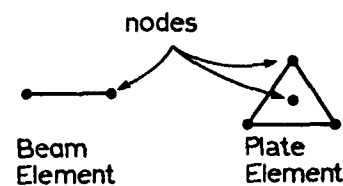


Figure 4. Basic Finite Elements.

Finite Element Expression for the Kinetic Energy. Substituting (33a) and (33b) into the general equation (32a) for an element e leads to:

(35)

$$2T_e = \{\ddot{x}_e\}^T [M_e] \{\dot{x}_e\} + 2\{\dot{x}_e\}^T [G_e] \{\dot{x}_e\} \\ + \{x_e\}^T [K_{se}] \{x_e\} + \{x_e\}^T \{F_{ce}(\Omega^2)\}$$

where $[M_e]$ is the mass matrix of the element e , $[G_e]$ the gyroscopic coriolis matrix, $[K_{se}]$ the supplementary stiffness due to rotation which is of the form $[\Omega^2 M_{se}]$ (where $[M_{se}]$ is called centrifugal mass), $\{F_{ce}(\Omega^2)\}$ is the vector of element nodal forces equivalent to the centrifugal volumic forces.

Assembly. If the structure is composed of n elements, and remembering that energies are scalar quantities, expressions for the potential and kinetic energies of the whole structure can be derived:

$$U = \sum_{e=1}^n U_e ; T = \sum_{e=1}^n T_e \quad (36)$$

The continuity of the nodal displacements $\{x_e\}$ at the connecting nodes is now prescribed, and so U and T are expressed in terms of independent degrees of freedom $\{x\}$, which are the unknowns of the problem.

Governing Equations of Motion. Applying Lagrange's equation:

$$\frac{d}{dt} \left(\frac{\partial T}{\partial \dot{x}_i} \right) - \left(\frac{\partial T}{\partial x_i} \right) + \left(\frac{\partial U}{\partial x_i} \right) = Q_i \quad (37)$$

to the expressions in (36) gives a set of equations of motion for the whole structure, including the effects of rotation. The general form of these equations is:

$$[M]\ddot{x} + [G]\dot{x} + [K_L + K_G(\sigma_0) - \Omega^2 M_G]x = \{F_c(\Omega^2) + F(t, \dot{x}, \ddot{x})\} \quad (38a)$$

Equation (38a) has the same general form as that quoted for discrete systems (see Equation 1) although here containing additional terms due to the rotation effects. It is important to note that the matrix $[G]$ is not a viscous damping matrix, but the so-called coriolis matrix which is antisymmetric and which represents the gyroscopic effects. As to the stiffness, some special terms are added allowing for the centrifugal stiffening, $[K_G]$, and the centrifugal softening due to the centrifugal mass effect, $[M_G]$. $\{F_c(\Omega^2)\}$ is the nodal equivalent force vector which is the discrete form of the

static centrifugal force distribution. F can be any other static or dynamic excitation force, such as the aerodynamic forces that will be detailed in other chapters. However, we shall concentrate here on the basic case where rotating structures such as blades or bladed disk assemblies are to be considered purely from a structural dynamics standpoint and where such additional excitation forces are not considered.

Static and Dynamic Solutions for Rotating Structures

The general form of Equation (38a) applies to all rotating structures, whatever is their physical shape. The finite element model is able to include and to combine unidimensional, two-or three-dimensional components.

Static Solution. It is of practical interest for the designer to know the stress distribution due to centrifugal forces. For this case, the equation of motion reduces to:

(38b)

$$[K_L + K_G(\sigma_0) - \Omega^2 M_G]\{x\}_S = \{F_c(\Omega^2)\}$$

where σ_0 is linked to $\{x\}_S$ via Hooke's law (29) and the strain-displacement relation (33c). Noting that (38b) is non-linear, since σ_0 is unknown a priori, the solution needs an iterative process, such as the Newton-Raphson method. In practice, just a few iterations (two or three) are sufficient to obtain good estimates for the centrifugal stresses in the finite elements (at the center of gravity, or at nodes) and the corresponding principal stresses ($\sigma_1, \sigma_2, \sigma_3$). A yield criterion such as von Mises can be used to determine whether the elastic limit (σ_E) has been reached:

$$\sigma_{VM} = \frac{1}{\sqrt{2}} \{(\sigma_1 - \sigma_2)^2 + (\sigma_2 - \sigma_3)^2 + (\sigma_3 - \sigma_1)^2\}^{1/2} < \sigma_E \quad (39)$$

Dynamic Solution. In order to construct a diagram which shows how the natural frequencies vary with speed of rotation (a Campbell diagram -the usual format for presenting the basic dynamic properties), these frequencies and their associated mode shapes have to be extracted assuming that the displacement vector $\{x\}$ is the superposition of the static displacements $\{x\}_S$ and the dynamic displacement $\{x\}_D$. In other words, the system is assumed to vibrate about the equilibrium position determined by the static solution, (38b). In this case, the governing equations for the dynamic analysis are derived from (38a) and (38b) and reduce to:

(38c)

$$[M]\ddot{x}_D + [G]\dot{x}_D + [K_L + K_G(\sigma_0) - \Omega^2 M_G]x_D = \{0\}$$

and the way to obtain the solution has been outlined in the section "Free Vibration Solution for Damped Systems."

If the Coriolis effects can be neglected - and this is usually so for radial or quasi radial blades - then $[G]$ is disregarded and (38c) reduces to:

$$(38d) \quad [M] \ddot{x}_d + [K_L + K_G(\omega_0) - \omega^2 M_G] x_d = \{0\}$$

which is the governing equation of motion for a classical undamped system. The motion is assumed to be simple harmonic and the method of solution has been detailed in section "Free Vibration Solution for the Undamped System." At this stage, it should be noted that the finite element approach may involve a very large number of degrees of freedom and, consequently, the extraction of the eigenvalues and eigenvectors can be a formidable task. In this case, instead of solving the determinantal equation (4), it is often more convenient to use special numerical methods such as the Sturm Sequences (Gupta, 1973) or the Simultaneous Iterative Method (Jennings & Clint, 1970).

Conclusion

The general theory developed in this section can be adapted for the dynamic analysis of any rotating structure. Some special treatment of the equations (38) can be outlined to particular systems, i.e., axisymmetric or repetitive structures, but the present generality is not affected.

DYNAMIC ANALYSIS METHODS FOR STRUCTURAL ASSEMBLIES

Introduction

Although there are a number of situations in which it is useful to study the behaviour of a single blade at a time, in most practical applications the blades interact with each other and must be treated as a complete assembly. Perhaps the most common of the bladed assembly configurations is the complete bladed disk, Figure 1b, where the flexibility and inertia of the disk serve to couple the vibration of the individual blades. A variant on this arrangement is where the blades are additionally interconnected through a shroud, which may be situated at the blade tips or at a midspan station, Figure 1c. In some cases, the disk may be so stiff as to provide virtually no coupling and it is then the shroud which takes on that role. In some special cases, we may be concerned with a group of blades spanning an arc of less than the complete 360° . This refers to a 'packet' of blades in which the interconnection is applied between just a few blades at a time (Figure 1e).

All these assemblies of blades exhibit vibration characteristics which are very much more complicated than are those of the individual blade upon which the assembly is based. We shall be describing

their different types of vibration mode and response in Chapter 15, but it is appropriate here to review some of the methods which are used for analyzing such a system as a bladed assembly. The need for special methods of analysis arises from the inefficiency of the direct solution of constructing a single model for the whole structure without taking advantage of its high degree of symmetry. Also, it is sometimes found that different types of model are appropriate for the different parts of the assembly (blades, disk, shroud) and if these components can be treated independently, at least in a first stage, a more optimal analysis may be possible.

Thus, we shall outline some methods of analysis which respond to these requirements: one which requires the different components to be analyzed separately as a first stage - substructuring - and another which seeks to exploit the repetitive symmetry of a complete bladed disk - cyclic symmetry.

Substructure Methods

The basic concept of substructuring is that a more efficient analysis of a complex structural assembly can be obtained if it is first considered in its constituent component parts, or substructures. By analyzing each of these as a separate system and determining its individual vibration properties, we can (a) use the most appropriate type of model for each subsystem and (b) reduce the size of each model (if required) by retaining only the primary or major vibration modes of the component. In this way, we can ensure that the results from different types of analysis are presented in a standard format and are thus suitable for combining in an analytical equivalent of the physical connections by which the actual assembly is formed.

There are essentially two different approaches to this procedure. The first is that in which the modes of each component are first obtained by separate subsystem analyses and are then combined to predict the modes of the complete assembly. The second approach uses the frequency response properties and by deriving these characteristics for each component individually, and then combining them, it is possible to determine directly the corresponding frequency responses for the complete assembly. Of course, since we have seen from earlier sections that the frequency responses may be derived from the modal properties, these two approaches are effectively different ways of organizing the same data and do not involve any fundamentally different assumptions. Where they do differ is in the facility with which one or other type of result is obtained: if the modes of the assembly are the essential end result, then a modal coupling approach is more appropriate but if it is the responses which are ultimately of interest, then the response coupling approach is perhaps more effective. The two approaches differ in their sensitivity to errors or approximations introduced into the component

models, a point to be borne in mind when condensing or reducing a large component model in pursuit of computational economy.

Modal Coupling Methods

The first method of subsystem coupling makes use of the modal properties of each component and arranges the analysis in such a way that the coordinates used to set up the equations for the coupled structure are modal coordinates and not spatial coordinates, as is the case in other methods. Further, this method allows for the introduction of springs and/or dashpots in between the subsystems at points where they are attached to each other.

The general arrangement is shown in Figure 5. The equations of motion for subsystem A are:

$$[M_A] \{x_A\} + [K_A] \{x_A\} = \{f_A\}$$

which can be transformed into modal coordinates:

$$[I] \{\tilde{p}_A\} + [\omega_A^2] \{p_A\} = [\Phi_A]^T \{f_A\} \quad (39a)$$

Similarly for B.

$$[I] \{\tilde{p}_B\} + [\omega_B^2] \{p_B\} = [\Phi_B]^T \{f_B\} \quad (39b)$$

Combining these equations, we have

$$\begin{aligned} & \left[\begin{array}{c:c} I & 0 \\ 0 & I \end{array} \right] \left\{ \begin{array}{c} \tilde{p}_A \\ \tilde{p}_B \end{array} \right\} + \left[\begin{array}{c:c} \omega_A^2 & 0 \\ 0 & \omega_B^2 \end{array} \right] \left\{ \begin{array}{c} p_A \\ p_B \end{array} \right\} \\ &= \left[\begin{array}{c:c} \Phi_A^T & 0 \\ 0 & \Phi_B^T \end{array} \right] [K_C] \left[\begin{array}{c:c} \Phi_A & 0 \\ 0 & \Phi_B \end{array} \right] \left\{ \begin{array}{c} f_A \\ f_B \end{array} \right\} \end{aligned} \quad (40)$$

but through the connections, we can relate the forces to the responses, thus:

$$\begin{aligned} \{f_A\} &= [K_C] \{x_A\} \\ \{f_B\} &= [K_C] \{x_B\} \end{aligned} \quad (41)$$

where $[K_C]$ is the stiffness matrix for the connection and $\{x_A\}$ and $\{x_B\}$ are the geometric coordinates of the attachment. These, in turn, are related to the modal coordinates by

$$\{x_A\} = [\Phi_A] \{p_A\} \text{ etc. (see Equation 7)}$$

So, if there are no external forces applied to the coupled structure, then we have an equation of motion for the assembly

$$\left[\begin{array}{c:c} I & 0 \\ 0 & I \end{array} \right] \left\{ \begin{array}{c} \tilde{p}_A \\ \tilde{p}_B \end{array} \right\} + \left(\begin{array}{c:c} \omega_A^2 & 0 \\ 0 & \omega_B^2 \end{array} \right) \left\{ \begin{array}{c} p_A \\ p_B \end{array} \right\} = \{0\} \quad (42)$$

which can then be solved for the modal properties of the complete structure.

The second modal method to be considered is that used for most analytical substructure analyses, and is based on 'constrained' and 'constraint' modes of the subsystems. The analysis is outlined below, using the same notation as above. For subsystem A, with coordinates j at junction points and coordinates a elsewhere, we can write:

$$\left(\begin{array}{c:c} K_A^{aa} & K_A^{aj} \\ K_A^{ja} & K_A^{jj} \end{array} \right) - \omega^2 \left(\begin{array}{c:c} M_A^{aa} & M_A^{aj} \\ M_A^{ja} & M_A^{jj} \end{array} \right) \left\{ \begin{array}{c} x_A^a \\ x_A^j \end{array} \right\} = \left\{ \begin{array}{c} f_A^a \\ f_A^j \end{array} \right\} \quad (43)$$

Now define a new coordinate vector by

$$\left\{ \begin{array}{c} x_A^a \\ x_A^j \end{array} \right\} = [A] \left\{ \begin{array}{c} q_A \\ x_A^j \end{array} \right\} \quad (44)$$

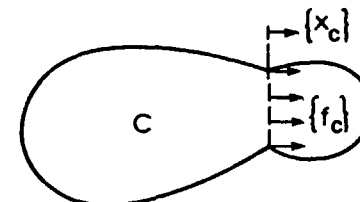
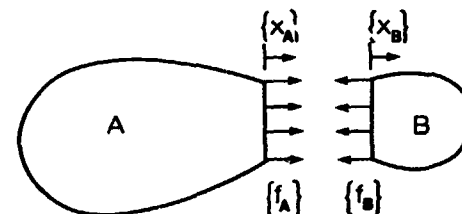


Figure 5. Coupled Structure Analysis Concepts.

where

$$[A] = \begin{bmatrix} \Phi_A^C & \Phi_A^S \\ 0 & I \end{bmatrix}$$

$\{\Phi_A^C\}$ = 'constrained' modes of system grounded at junction points.

$\{\Phi_A^S\}$ = 'constraint' modes (deflections of nonjunction coordinates for a unit displacement in one junction coordinate)

Using these transformations, the equation of motion for component A can be rewritten

$$\left(\begin{bmatrix} \omega_A^2 & 0 \\ 0 & K_A^{jj} \end{bmatrix} - \omega^2 \begin{bmatrix} I & M_A^{aj} \\ M_A^{ja} & M_A^{jj} \end{bmatrix} \right) \begin{Bmatrix} x_A^a \\ x_A^j \end{Bmatrix} = \{0\}$$

$$K_A^{jj} = [K_A^j]^j + [K_A^j][\Phi_A^S] \quad (45)$$

$$M_A^{aj} = [\Phi_A^C]^T [M_A^{aa}] [\Phi_A^S] = [M_A^{ja}]^T$$

$$M_A^{jj} = [M_A^j]^j + [\Phi_A^S][M_A^{aa}][\Phi_A^S]$$

A similar expression can be written for a second component B and the two sets of equations combined, again using the commonality (compatibility) of the junction coordinates, i.e. $(x_A^j \equiv x_B^j)$. Thus, we obtain:

$$\left(\begin{bmatrix} \omega_A^2 & 0 & 0 \\ 0 & \omega_B^2 & 0 \\ 0 & 0 & K_A^{jj} + K_B^{jj} \end{bmatrix} - \omega^2 \begin{bmatrix} I & M_A^{aj} & 0 \\ M_A^{ja} & I & M_B^{bj} \\ 0 & M_B^{jb} & M_A^{jj} + M_B^{jj} \end{bmatrix} \right) \begin{Bmatrix} q_A \\ q_B \\ q_{Xj} \end{Bmatrix} = \{0\} \quad (46)$$

$$- \omega^2 \begin{bmatrix} I & M_A^{aj} & 0 \\ M_A^{ja} & I & M_B^{bj} \\ 0 & M_B^{jb} & M_A^{jj} + M_B^{jj} \end{bmatrix} \begin{Bmatrix} q_A \\ q_B \\ q_{Xj} \end{Bmatrix} = \{0\}$$

Frequency Response Coupling Methods

The basis of this method may be quite simply stated again using the example in Figure 5: its implementation to practical structures requires appropriate organization of the data from the various component models. Turning to the example in Figure 5, we can see that the (harmonic) response at the various coordinates of interest on subsystem A can be related to the (harmonic) forces which are assumed to act at the same points by:

$$(x_A)e^{i\omega t} = [H_A(\omega)] \{f_A\} e^{i\omega t} \quad (47a)$$

and similarly for subsystem B.

$$(x_B)e^{i\omega t} = [H_B(\omega)] \{f_B\} e^{i\omega t} \quad (47b)$$

Inverting each of these equations leads to:

$$\{f_A\} = [H_A(\omega)]^{-1} \{x_A\} = [z_A(\omega)] \{x_A\} \quad (48)$$

and then the application of compatibility $\{x_C\} = \{x_B\} = \{x_C\}$ and equilibrium $\{f_A\} + \{f_B\} = \{f_C\}$ conditions as the common coordinates generate a new equation:

$$\begin{aligned} \{f_C\} &= [H_A(\omega)]^{-1} \{x_A\} + [H_B(\omega)]^{-1} \{x_B\} \\ &\equiv [H_C(\omega)]^{-1} \{x_C\} \end{aligned} \quad (49)$$

or

$$[H_C(\omega)]^{-1} = [H_A(\omega)]^{-1} + [H_B(\omega)]^{-1}$$

which thereby permits direct derivation of the frequency response function properties of the assembled structure, described by $[H_C]$. While the more representative systems consist of more numerous and complex configurations than this, the principle of the method is exactly that illustrated here.

Cyclic Symmetry Methods - Axisymmetric Modelling

As stated earlier, it is often beneficial to seek a means of exploiting the repetitive symmetry of a complex bladed assembly. If the disk and blades for a given assembly have similar stiffness, their motions are strongly coupled and simple calculation of the individual blade's properties would lead to false results. Bladed disk assemblies can effectively be classified into two groups according to their structural dynamic properties. In the first group are those assemblies having an axisymmetric behaviour characterized by mode shapes formed by simple diametral and circular nodal lines (lines of zero displacement). The structures in this group are usually characterized by a large number of blades mounted on a flexible disk, i.e., turbine wheels of jet engines and eventually some thick disks which have the blades connected in a radial plane.

The second group includes the rotationally periodic structures such as bladed disks or centrifugal impellers having few blades with or without casing or shroud. This type of structure does not exhibit purely axisymmetric mode shapes, but includes some pseudo-axisymmetric and some repetitive modes showing "scalloped" patterns (Henry, 1980). In this case, classical axisymmetric theory can no longer be applied and one has to introduce the cyclic symmetry methods using explicitly or implicitly the wave propagation concept (Henry and Ferraris, 1984). This group of structures is excluded from discussion here.

In typical gas turbine assemblies, it is found experimentally that turbine stages tend to have axisymmetric mode shapes; that is to say, the disk and blade displacement follow a simple cosine fluctuation both in time and in angular position around the circumference. In

other words, the structure vibrates with a dominant n nodal diameter mode shape having negligible contributions from other diametral orders. Thus, for example, the displacement of the j th blade can be written as:

$$\{x\}_j = \{x_n\}_j \cos \frac{2\pi n(j-1)}{N} \quad (50)$$

where n and N are the numbers of nodal diameters and blades respectively. As N is generally large, the blades can be considered to be a continuously distributed component attached to the rim of the disk. Thus, the blade array strain and kinetic energies U_B , T_B , may be obtained from the strain and kinetic energies of a single blade (U_0 , T_0), as follows:

$$U_B = \frac{N}{2} U_0 ; \quad T_B = \frac{N}{2} T_0 \quad (51)$$

For the symmetric case, i.e., when the number of nodal diameters equals 0, the coefficient $N/2$ is replaced by N . Thus, noting that U_0 and T_0 are independent of n , the stiffness and mass matrices of the vibrating blading are those of a single blade weighted by the factor N or $N/2$ according to the value of n . The axisymmetric part of the bladed assembly is modelled by axisymmetric finite elements (thin and thick), $U_A(n)$ and $T_A(n)$ are derived and the complete structure finite element energies U and T are obtained by simple summation. Applying Lagrange's equation as described previously leads to an individual governing equation for the system (Equation 38a) for each value of n . Then, the static and dynamic solutions are performed as detailed in Equations 38b and c. A practical application on a jet engine turbine stage is reported in Chapter 15.

STRUCTURAL DYNAMIC CHARACTERISTICS OF INDIVIDUAL BLADES

by

D. J. EWINS
 Imperial College of Science & Technology
 London, United Kingdom

R. HENRY
 Institut National des Sciences Appliquées
 Lyon, France

INTRODUCTION

Objective. The objective of this chapter is to provide the necessary introduction and grounding for a study of the vibration characteristics of individual turbomachine blades. We are concerned here with the structural dynamic properties only and we shall concentrate on the two most important of these - the natural frequencies and the corresponding mode shapes. Although some consideration will also be given in later chapters to the damping properties, these cannot be treated in the same analytical way as is possible for predicting the natural frequencies and mode shapes. Knowledge of these two properties is a primary requirement for a valid analysis of the aeroelastic behaviour of blades and most of the structural dynamicist's efforts are directed towards their reliable identification and prediction.

Having first outlined the basic characteristics of blade vibration properties, we shall then identify those design features which have an influence on their values. This is important since an appreciation of these effects aids our understanding of how the various vibration problems and phenomena can arise in service (often against our initial expectations) and, more importantly, how they may be treated.

For these earlier sections of the chapter we shall use relatively simple models of blades but will then progress to outline the methods which are available for the calculation of the structural dynamic properties of real blades, as required for design purposes. Throughout this chapter, we shall be dealing with individual blades only and it must be noted at the outset that in most applications the blades are grouped together in stages or assemblies and that this feature will also have an influence on their vibration properties.

Indeed, in many cases, the natural frequencies and mode shapes of a blade in its operational environment (e.g., as one of a set on a disk) may differ considerably from those calculated for the same blade as an isolated component. This topic is dealt with in detail in the next chapter (Structural Dynamic Characteristics of Bladed Assemblies) but it can be noted here that it is usually convenient in that more complex situation to relate the complete assembly's vibration properties to those of the single blade. Hence, there is considerable advantage in undertaking an individual blade analysis first, and that is the scope of the present chapter.

Outline. Before proceeding to a discussion of methods for predicting the structural dynamic properties of an individual turbomachine blade, it is appropriate to present a summary of the basic nature of these characteristics and this can conveniently be done using simple models of blades. Although the detailed geometry of a given blade will have a major influence in determining the exact values for its natural frequencies and mode shapes, these properties will be found to fall into one of a small number of categories, or families, which can be related to those of rather simpler structures than the blades themselves. Indeed, we can learn much about the vibration properties of blades by studying first those of simple beams and plates. These will be presented in the next section.

Following this basic groundwork, the influence of a number of relevant design features is examined with a view to establishing which parameters can have a marked effect on the actual values of natural frequency or mode shape. These factors include:

- complex cross section properties
- flexibility of root and/or shroud fixtures
- speed of rotation (of the blade in the machine)
- static loads
- temperature variations.

Later sections deal with prediction methods used for design calculations. These are not intended to provide a comprehensive review of the very many different methods or programs which are available for this purpose but rather to illustrate ways of dealing with a number of the difficulties often encountered in the process of predicting blade vibration properties by referring to a number of differing case studies. Perhaps the most important point to be made is the need for an appreciation of what to expect (from a calculation process) and of how to set about confirming or validating its results. It is with this aspect in mind that the early sections of the chapter are presented.

The study and analysis of the blade vibration characteristics has led to the publication of a great many technical papers, only a handful of which will be referenced here. However, there are a number of review articles which provide useful surveys of different aspects of the subject together with comprehensive lists of references, such as those by Rao (1973 and 1980) and Leissa (1981).

VIBRATION PROPERTIES OF UNIFORM BEAMS AND PLATES

Basic Structural Models for Blades. Although usually very complex in their geometric form, most turbomachine blades can generally be regarded as beam-like or plate-like in respect of their dynamic behaviour. If we review the wide range of different blade configurations used in practice, we find that the vibration modes of many of these can be well represented by a one-dimensional or beam-like model (cross section remains undeformed during vibration and deflection(s) are a function of longitudinal position only - or radial, in terms of the machine coordinates), while others with different aspect ratios require the extra dimension provided by a two-dimensional or plate-like model (for which the cross section deforms and the deflection is a function of both radial and chordwise positions); see Figure 1. In both these cases, the vibration is effectively normal to the blade longitudinal axis. There exist also a number of special cases in which there is a significant vibration displacement in the longitudinal (or radial) direction as well as the other two normal directions and the dynamics of such blades are generally not well represented by beam or plate models. These are usually very thick and/or very short blades and must be described by a full three-dimensional or solid model. However, such cases represent only a small fraction of practical blades and the predominance of the two former categories provides the basis for classifying most blades as 'beam-like' or 'plate-like.'

Beam-like blades are those which are essentially long and slender and so have a high length-to-chord aspect ratio ($L/c > 1$) and a low thickness-to-chord ratio ($d/c \ll 1$) - see Figure 1. During vibration, the time-varying deflection(s) of any point on the blade ($x, y, z, \theta_x, \theta_y, \theta_z$) depend only upon its longitudinal location (i.e., they are functions only of coordinate u). This is a consequence of an essential feature of beam-like vibration, namely that the cross section remains undeformed during vibration.

Plate-like characteristics are found in those blades which have a lower aspect ratio (typically, $L/c \leq 5$) but are still 'thin' ($d/c \ll 1$). The main difference between these blades and the beam-like ones is that the cross section itself distorts during vibration with the result that the deflection(s) of any point on the blade are now dependent on both its longitudinal and also its chordwise positions, coordinates u and v .

The vibration characteristics of blades of both types can be studied using simple-profile beams and plates for which there is considerable data already in existence (see, for example, Blevins 1979) and for which additional calculations are easy to perform.

Structural Dynamics of Simple Beams. The methods of dynamic analysis for structural elements such as uniform beams have already been summarized in the previous chapter and so we need only present some appropriate numerical results here.

Two sets of results are presented. The first set -presented in Tables 1 and 2 -give general non-dimensional natural frequency and mode shape parameters for the bending and torsion modes of vibration of a uniform beam and are obtained from direct closed-form solution to the equations of motion presented in the previous chapter. Values for the vibration properties of any specific beam can be deduced from these tabulated data by using the appropriate scaling constant, as specified in the table. The second set of results -Tables 3 and 4, and Figure 2 -relate to a specific beam model and have been computed using a simple finite element analysis, also summarized in the previous chapter. Results for this particular case may also, of course, be obtained from the non-dimensional data in the first table and the small differences which can be observed in results derived from the two sources reflect the errors associated with finite element modelling assumptions. However, this particular example is introduced here in order to provide a reference case against which to compare the properties of variations on the basic model later in the chapter.

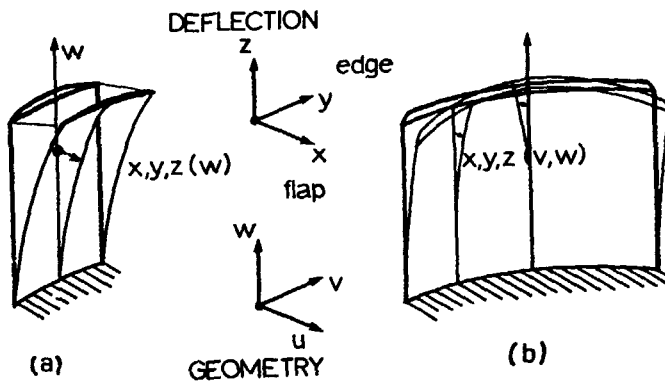


Figure 1. Essential Features of Blade Vibration Analysis

END CONDITIONS (ROOT-TIP)

MODE	C-F	P-F	F-F	C-P	C-C
1st Bend	3.516	15.42	22.37	15.42	22.37
2nd Bend	22.03	49.96	61.67	49.96	61.67
3rd Bend	61.70	104.25	120.90	104.25	120.90
1st Tors	1.57	1.57	3.14	3.14	3.14
2nd Tors	4.71	4.71	6.28	6.28	6.28

VALUES OF λ^2

To obtain natural frequencies (Hz) of a specific rectangular-section beam with dimensions: Length L, width w, thickness (in direction of bending) t, and material properties: elastic modulus E, shear modulus G, density ρ , polar moment of area I_p , use the following formulae:

$$f_{\text{bend}} = \frac{(1/2\pi)}{\lambda_{\text{bend}}} \sqrt{\frac{E t^2}{12\rho}} \text{ Hz}$$

$$f_{\text{tors}} = \frac{(1/2\pi)}{\lambda_{\text{tors}}} \sqrt{\frac{G C}{\rho I_p}} \text{ Hz}$$

Table 1. Dimensionless Natural Frequency Parameters for Uniform Section Beams

In the tables and figures below, natural frequencies and corresponding mode shapes are given for uniform rectangular section beams with five different sets of end conditions (the first of these at the root - the second at the tip - see Figure 2):

- (a) Clamped-Free (C-F)
- (b) Pinned-Free (P-F)
- (c) Free-Free (F-F)
- (d) Clamped-Pinned (C-P)
- (e) Clamped-Clamped (C-C)

These represent different conditions under which the blade might be analyzed or tested: (a) considered to be rigidly clamped or grounded at the root; (b) attached at the root but only restrained laterally - not in rotation; (c) suspended as a free object; (d) and (e) with additional constraint at the tip, such as might be provided by interconnecting tip shrouds.

The next set of results refers to a specific example consisting of a beam of length 250 mm, width (chord) 30 mm and thickness 10 mm made from a material with elastic modulus of 207 GN/m² and density 7850 kg/m³. This beam has second moments of area $I_1 = 6.77 \times 10^{-8}$ and $I_2 = 0.225 \times 10^{-7}$ m⁴ and a polar moment of area $J = 0.7902 \times 10^{-8}$ m⁴.

The natural frequencies for the first few modes computed using a finite element model of this beam are presented in Table 3(a) and the corresponding mode shapes plotted in Figure 2. For each case, we find the modes of vibration to be grouped into three families: flapwise bending (F), edgewise bending (E), and torsion about the longitudinal axis (T) with the mode shape corresponding to each natural frequency consisting of deflections in only one of these three directions. Also shown for reference is the first

longitudinal mode (A) natural frequency, although this is usually so much higher than those of the bending or torsion modes that it is of relatively little interest in practice.

In fact, for each case considered, two results can be quoted for the natural frequencies of the bending modes, as shown in Table 3(b). These are found using (i) Bernoulli-Euler theory (B-E) and (ii) Timoshenko theory (T) which respectively exclude and include the second-order effects of shear deflection (as well as bending deflections) and rotatory inertia (as well as translational inertia). From these results it is seen how the second-order terms become increasingly important as the thickness of the beam relative to its length becomes greater and the deformation shape becomes more complex. In all cases, the result of including the second-order terms is a lowering of the natural frequencies.

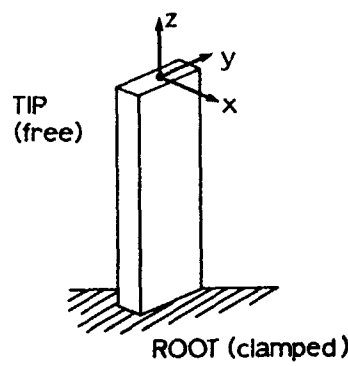
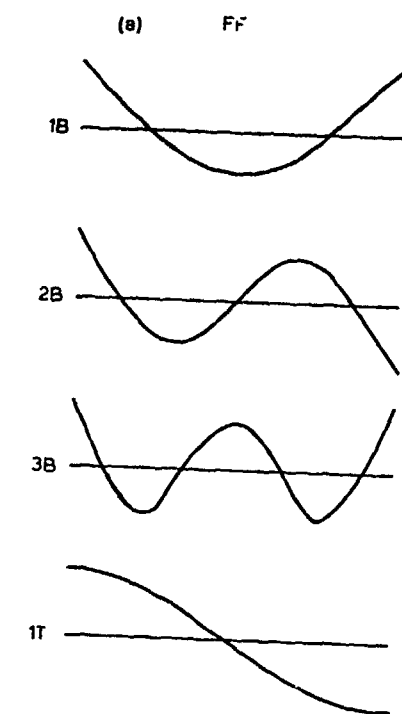


Figure 2. Mode Shapes of Uniform Beams

14-4



(b) CF

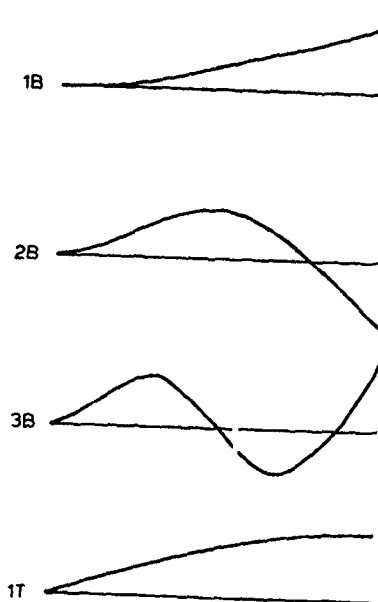
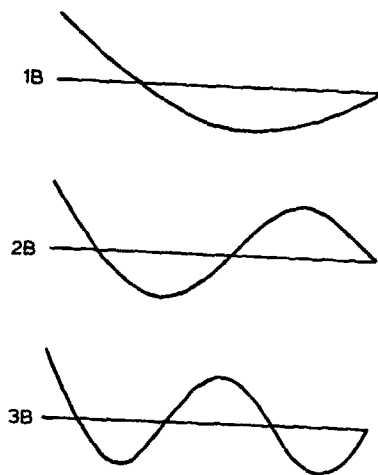


Figure 2. Mode Shapes of Uniform Beams
(a) free-free

Figure 2. Mode Shapes of Uniform Beams
(b) clamped-free

(c) PF



(d) CP

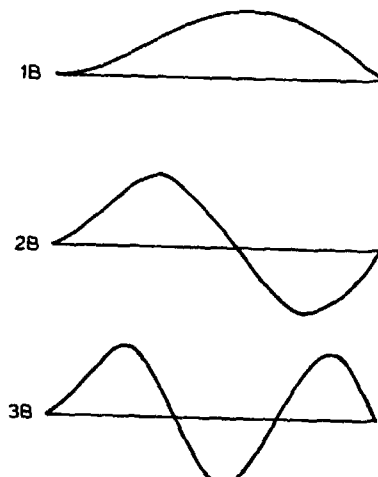


Figure 2. Mode Shapes of Uniform Beams
(c) pinned-free

Figure 2. Mode Shapes of Uniform Beams
(d) clamped-pinned

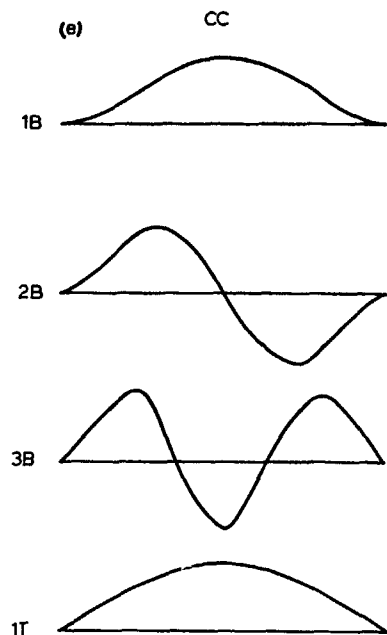


Figure 2. Mode Shapes of Uniform Beams
(e) clamped-clamped

Structural Dynamics Properties of Uniform Plates. As the aspect ratio of the blade changes so that the chord width (*c*) approaches the length (*L*), the assumption of beam-like behaviour becomes less applicable and it becomes necessary to extend the model to that of a plate in order to include the section deformation which will be present in such cases. Many studies have been reported on this approach to blade vibration analysis, ranging from early work by Dokainish and Rawtani (1973) and MacBain (1975) to more recent work by Ramamurti and Kielb (1984). A survey of the use of plate models for blade vibration analysis is presented by Leissa (1980).

In order to illustrate the particular characteristics which apply to plates, a series of case studies are presented based on a blade similar to that used previously. This blade is 250 mm in length, has a uniform rectangular cross section of 10 mm thickness and width varying from 30 to 250 mm (aspect ratio *L/c* varying from 8 to 1) - see Figure 3. The material properties are as used previously (modulus = 207×10^9 N/m², density = 7850 kg/m³) with a Poisson's ratio of 0.3, and the blade is clamped at its root. Once again, the vibration characteristics for this case are presented in tabular and graphical form with the fundamental natural frequencies given in Table 4 and the mode shapes displayed in Figure 4.

From these results it is seen that the modes become rather more complex in shape than for the beam model and are more difficult to classify. Accordingly, it is generally found that the most convenient way of describing mode shapes of blades such as these is by specifying the nodal lines - loci of points which have zero deflection during vibration. In any event, it is generally possible to follow the evolution of each mode of the reference case (30 mm wide) as the blade or plate width is increased, thereby permitting the tabulation shown below.

FACTORS WHICH INFLUENCE THE VIBRATION PROPERTIES OF BLADES

Introduction. Real blades are generally rather more complex than the simple beam and plate models which have been used so far to introduce the basic types of vibration characteristic. In this next section, we shall seek to build on the preceding groundwork by examining the influence of a number of typical blade design features which can have an influence on the structural dynamic properties of interest here - primarily, the natural frequencies and the corresponding mode shapes. Although the vibration characteristics of actual blades are similar to those already discussed, the precise natural frequency and mode shape data are of vital importance to the analyst seeking to predict a blade's vibration behaviour under operating conditions. Hence, all such influencing factors must be taken into consideration at the design prediction stage. While the finite-element based prediction methods widely used today do permit the inclusion of these various effects, as will be illustrated in the next section, it is appropriate first to extend the beam and plate models in order to explore some of the phenomena of particular interest, as has been done by many workers including: Jacobsen (1938), Carnegie (1966), Montoya (1966), Rao (1980), Irretier and Marenholz (1981) and Afolabi (1986).

In this section we shall review a number of the particular features of real blades, including:

- complex geometry (including the non-symmetric and non-uniform cross sections which are found on tapered and twisted blades and those designs for which 'simple' beam- or plate-like models are not adequate);
- attachment flexibility (the complications which arise at junctions between the blade and the disk and shroudband, or connecting blades);
- special effects of operating conditions (including the quasi-static load induced by gas pressure, centrifugal and Coriolis effects caused by rotation and by thermal effects at extreme temperatures).

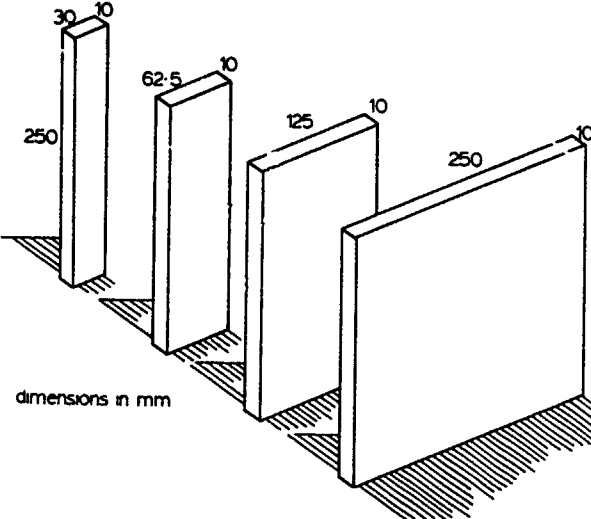


Figure 3. Uniform Plate Models

1st BENDING MODE

ROOT-TIP	F-F		C-F		P-P		C-P		C-C	
	Freq	4.730041	1 875104	3.926602	3 926602	4.730041				
C/L	DISP	STRESS	DISP	STRESS	DISP	STRESS	DISP	STRESS	DISP	STRESS
0.0	100	0	0	100	100	0	0	100	0	100
0.1	54	12	2	86	61	9	9	61	12	54
0.2	10	39	6	73	23	30	30	23	39	10
0.3	-27	69	14	59	-12	56	56	-12	69	-27
0.4	-52	92	23	46	-40	80	80	-40	92	-52
0.5	-61	100	34	34	-58	96	96	-58	100	-61
0.6	-52	92	46	23	-66	100	100	-66	92	-52
0.7	-27	69	59	14	-62	91	91	-62	69	-27
0.8	10	39	73	6	-48	69	69	-48	39	10
0.9	54	12	86	2	-26	37	37	-26	12	54
1.0	100	0	100	0	0	0	0	0	0	100

2nd BENDING MODE

ROOT-TIP	F-F		C-F		P-P		C-P		C-C	
	Freq	7.853205	4.694091	7.068583	7.068583	7.853205				
X/L	DISP	STRESS	DISP	STRESS	DISP	STRESS	DISP	STRESS	DISP	STRESS
0.0	100	0	0	100	100	0	0	100	0	100
0.1	23	30	9	52	30	26	26	30	30	23
0.2	-40	80	30	7	-29	72	72	-29	80	-40
0.3	-66	100	53	-32	-63	100	100	-63	100	-66
0.4	-48	69	68	-59	-50	88	88	-60	69	-48
0.5	0	0	71	-71	-26	38	38	-26	0	0
0.6	48	-69	59	-68	23	-28	-28	23	-69	48
0.7	66	-100	32	-53	61	-80	-80	61	-100	66
0.8	40	-80	-7	-30	70	-93	-93	70	-80	40
0.9	-23	-30	-52	-9	46	-61	-61	46	-30	-23
1.0	-100	0	-100	0	0	0	0	0	0	-100

Table 2. Mode Shapes for Uniform Beams

3rd BENDING MODE

ROOT-TIP	F-F		C-F		F-F		C-P		C-C	
	Freq	10.995608		7.854757		10.210176		10.210176		10.995608
X/L	DISP	STRESS	DISP	STRESS	DISP	STRESS	DISP	STRESS	DISP	STRESS
0.0	100	0	0	100	100	0	0	100	0	100
0.1	-5	51	23	23	2	47	47	2	51	-5
0.2	-64	100	60	-39	-61	100	100	-61	100	-64
0.3	-40	58	76	-66	-51	76	76	-51	58	-40
0.4	33	-42	53	-47	12	-14	-14	12	-42	33
0.5	71	-93	2	2	66	-88	-88	66	-93	71
0.6	33	-42	-47	53	57	-77	-77	57	-42	33
0.7	-40	58	-66	76	-6	8	8	-6	58	-40
0.8	-64	100	-39	60	-63	85	85	-63	100	-64
0.9	-5	51	23	23	-60	82	82	-60	51	-5
1.0	100	0	100	0	0	0	0	0	0	100

1st TORSION MODE

ROOT-TIP	F-F		C-F		C-C		
	Freq	3.141592654		1.570796327		3.141592654	
X/L	DISP	STRESS	DISP	STRESS	DISP	STRESS	DISP
0.0	100	-100	0	0	0	0	0
0.1	95	-95	16	-16	31	-31	
0.2	81	-81	31	-31	59	-59	
0.3	59	-59	45	-45	81	-81	
0.4	31	-31	59	-59	95	-95	
0.5	0	0	71	-71	100	-100	
0.6	-31	31	81	-81	95	-95	
0.7	-59	59	89	-89	81	-81	
0.8	-81	81	95	-95	59	-59	
0.9	-95	95	99	-99	31	-31	
1.0	-100	100	100	-100	0	0	

Data for each case

Heading : Dimensionless natural frequency parameters
 Column 1 : Position as fraction of beam length
 Cols 2, 4, etc: Relative displacement amplitudes
 Cols 3, 5, etc: Relative stress amplitudes

TABLE 2 MODE SHAPES FOR UNIFORM SECTION BEAMS

END CONDITIONS (ROOT-TIP)

MODE*	C-F	P-F	F-F	C-P	C-C
1F	132.7	582.2	845.0	582.2	845.0
2F	832.2	1891	2335	1891	2337
3F	2337	3972	4608	3977	4627
1E	398.2	398.2	2535	2535	2535
2E	2497	2497	7006	7012	7012
3E	7012	7012	13824		
1T	1807	1807	3658	3658	3658
2T	5600	5600	7675	7675	7675
1A	5156	5156	10440	10440	10440

* See Mode Shape Figures for details.

TABLE 3(a) NATURAL FREQUENCIES FOR UNIFORM SECTION BEAMS (Hz)

END CONDITIONS (ROOT-TIP)

MOD	C-F	P-F	F-F	C-P	C-C
1F (B-E) (T) (%diff)	132.7 132.6 0.08%	582.2 581.1 0.2%	845.0 843.4 0.2%	582.2 579.6 0.4%	845.0 838.3 0.8%
2F	832.2 827.8 0.5%	1891. 1878. 0.6%	2336. 2320. 0.7%	1891. 1870. 1.1%	2337. 2298. 1.7%
3F	2337. 2310. 1.2%	3972. 3919. 1.3%	4608. 4541. 1.5%	3977. 3900. 2.0%	4627. 4501. 2.8%
1E	398.2 395.4 0.7%	398.2 395.4 0.7%	2535. 2492. 1.7%	2535. 2368. 7.1%	2535. 2368. 7.1%
2E	2497. 2386. 4.7%	2497. 2386. 4.7%	7006. 6606. 6.1%	7012. 6122. 14.6%	7012. 6122. 14.6%
3E	7012. 6359. 10.3%	7012. 6359. 10.3%	13824. 12559. 10.1%		

TABLE 3(b) NATURAL FREQUENCIES OF BEAM BENDING MODES (Hz)
WITH SECOND-ORDER EFFECTS INCLUDED

PLATE WIDTH (ASPECT RATIO)

Mode	Beam	30(8.3:1)	62.5(4:1)	125(2:1)	250(1:1)
1F	132.7	134.1	134.8	135.9	137.0
2F	832.2	843.3	846.0	848.1	843.3
3F	2337.	2382.	2388.	2381.	2398.
1E	398.2	396.1	797.0	1430.	2208.
2E	2497.	2370.	4118.		
1T	1807.	2196.	1095.	590.6	340.4
2T	5600.	6634.	3386.	1929.	1240.
3T			5963.	3714.	2830.
1A	5156.	5153.	5176.	5185.	5198.
TL1	-	-	-	3689.	1078.
TL2	-	-	-	5033.	2167.

F = Flap; E=Edge; T=Torsion; A=Axial; TL=Tramline

TABLE 4 NATURAL FREQUENCIES (Hz) OF CLAMPED-FREE PLATES

CLAMPED-FREE BEAM

Mode No	UNIFORM	TAPERED	TWISTED
1	132.7 F	192.6 F	151.5 F E
2	398.2 E	576.7 E	443.3 E F
3	832.2 F	734.0 F	804.9 F E
4	1807. T	1769. F	1807. T
5	2337. F	2202. E	2279. F E
6	2497. E	3144. T	2390. E F
7	4617. F	3316. F	4600. F E
8	5156. A	5308. E	5156. A
9	5600. T	5493. F	5599. T
10	7012. E	6169. T	6731. E F

TABLE 5 NATURAL FREQUENCIES (Hz) OF TAPERED AND TWISTED CLAMPED-FREE BEAMS

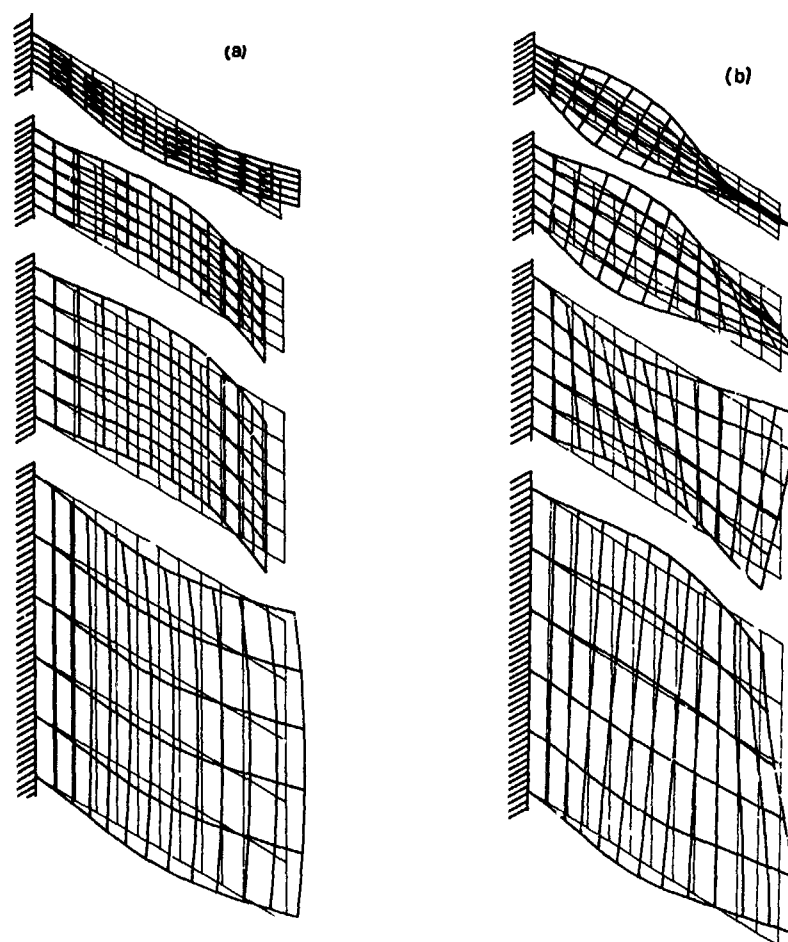


Figure 4. Mode Shapes of Uniform Blades
(a) bending mode; (b) twisting mode

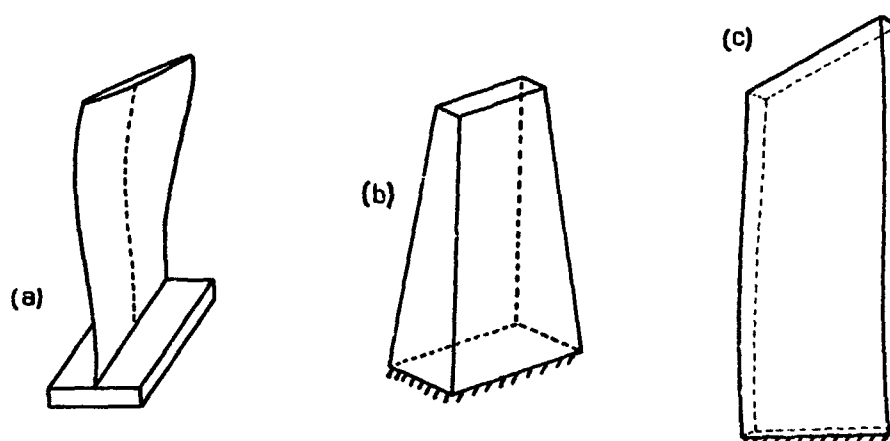


Figure 5. Non-Uniform Blade and Beam Models
(a) tapered, twisted blade;
(b) tapered beam; (c) twisted beam

Complex Geometry. The first complication to be considered is that arising from the complex geometry demanded by the aerodynamic performance requirements for the blade. In general, this results in a blade whose section varies along its longitudinal axis in one or several respects (as illustrated in Figure 5(a)):

- the section area varies (if the blade is tapered);
- the centroid of each section may not lie on the same longitudinal axis as the others;
- the stagger, or principal axes, of each section may vary in orientation (if the blade is twisted).

In addition to these features, the cross section itself is unlikely to be symmetric, as was the case in the uniform beam and plate models discussed previously. Work by Carnegie (1966), Montoya (1966), Rao (1980), Irretier et al (1981), and others has demonstrated how the beam model can be extended and refined to include these various effects and the reader is referred to their publications for full details. Also, some recent studies of plate models by Leissa et al (1986) have highlighted some of the difficulties encountered when trying to include correctly the effects of twist on the vibration properties of otherwise simple cantilevered plates.

In this section, it is proposed simply to illustrate some of the effects which can arise from the complexity of blade geometry but without making any attempt to provide a comprehensive coverage of the wide range of possibilities which are dealt with in the literature. We shall consider the changes that would be found in the previously-quoted vibration properties (for a uniform beam) if certain types of nonuniformity are introduced into the model. Two specific variations on the clamped-free beam configuration are considered: (i) taper and (ii) twist.

In the first of these cases, the rectangular cross section is reduced linearly from the root (where it is 30x10 mm) to the tip (where, in the extreme case, it is reduced to 15x5 mm), all other properties remaining unchanged: see Figure 5(b).

In the second case, the cross section is kept constant (at 30x10 mm) but is progressively rotated (about the longitudinal or radial axis) so that the tip section is aligned with a stagger angle of up to 60° relative to that at the root of the blade, as shown in Figure 5(c).

Results for these two cases -which may be taken to demonstrate the trends caused by the common geometric features of taper and twist -are summarized in Table 5 and graphically in Figures 6 and 7. In the table, an indication is given of the direction in which vibration is taking place. The essential results observed are (i) that the natural frequencies (but not the mode shapes) are significantly affected by the reduced section present in

the tapered case and (ii) that the frequencies in the twisted case are less noticeably affected, but, in this case, the mode shapes become more complex, many being combinations of motion in both the flapwise and edgewise directions simultaneously. It can be seen that if the beam's symmetry were disturbed further by misaligning the centroids of successive sections (up to now they have been thus aligned), then additional coupling would result with all modes exhibiting some contribution from each of the flap, edgewise, and torsion directions, although in many modes it is likely that just one of these directions would predominate.

Similar considerations apply plate-like blades as well and reference can be made to the recent studies by Kielb et al. (1985) who have examined the change in natural frequencies and mode shapes for a rectangular uniform cross-section cantilever plate as it is progressively twisted more and more. The purpose of that study was primarily to investigate the difficulties encountered by different methods of analysis, and to catalogue the various results which different prediction methods produce. However, it provides a convenient series of examples for the present discussion and a selection of results are included in Figure 8.

Root Flexibility. In pursuit of an accurate prediction of the natural frequencies of a blade, careful consideration must be given to the end or boundary conditions which actually obtain in practice. It is common to assume that the root presents a grounded or cantilever base to the blade but this is often not at all realistic for actual designs. Clearly, the material of the root itself (whether of fir-tree, pin or dovetail type) will possess some flexibility, as will the disk or ring onto which the blade is mounted but there will also be a 'junction flexibility' which is determined by the exact conditions of contact that exist in the joint. These various features all serve to reduce the rigidity of the boundary condition(s) for the blade and thus to lower its natural frequencies from those of the ideal clamped case.

Whether or not the root flexibility effects will be significant depends on several parameters but it is often found that the errors incurred by ignoring them are greater than others in the prediction process and than those associated with measurements. Thus, as the methods for coping with the complex geometry and other effects become more reliable, the effects of root flexibility (or at the tip, where similar comments apply to shroud attachments) emerge as important factors and have been the subject of increasing attention in recent years: Beglinger et al (1976), Irretier (1981), Afolabi (1986), for example.

A clear illustration of the effect of root flexibility can be provided using the simple beam model of a blade. Here, we suppose that the rigidity of the root end fixing is less than complete and represent

CLAMPED-FREE BEAM WITH TAPER OR TWIST

TAPER *					TWIST **				
50.%	33.%	25.%	17.%	0.%	15. ^o	30. ^o	45. ^o	60. ^o	
192.4	166.6	156.4	147.6	133.8	133.8	137.2	143.0	151.5	
596.7	499.7	469.3	442.7	398.2	400.9	409.0	423.0	443.3	
734.0	771.7	788.2	803.7	832.2	830.4	825.2	816.6	804.9	
1769.	1982.	2077.	2144.	1807.	1807.	1807.	1807.	1807.	
2202.	2364.	2579.	2167.	2337.	2335.	2327.	2311.	2279.	
3144.	2347.	2315.	2411.	2497.	2488.	2465.	2429.	2390.	

* % REDUCTION IN BOTH WIDTH
AND THICKNESS AT TIP
SECTION:
LINEAR VARIATION
ALONG LENGTH

** TWIST OF TIP SECTION RELATIVE
TO ROOT:
LINEAR VARIATION ALONG
LENGTH

Figure 6. Natural Frequencies of Tapered and Twisted Beams

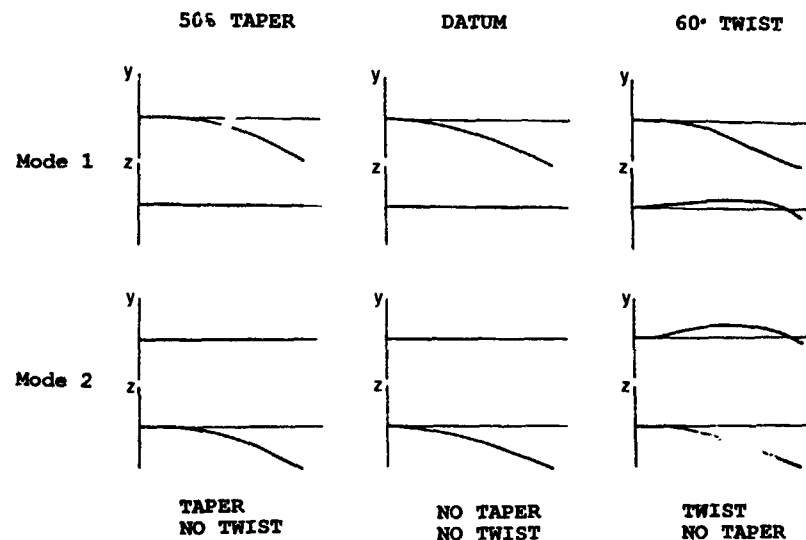


Figure 7. Typical Mode Shapes of Tapered and Twisted Beams

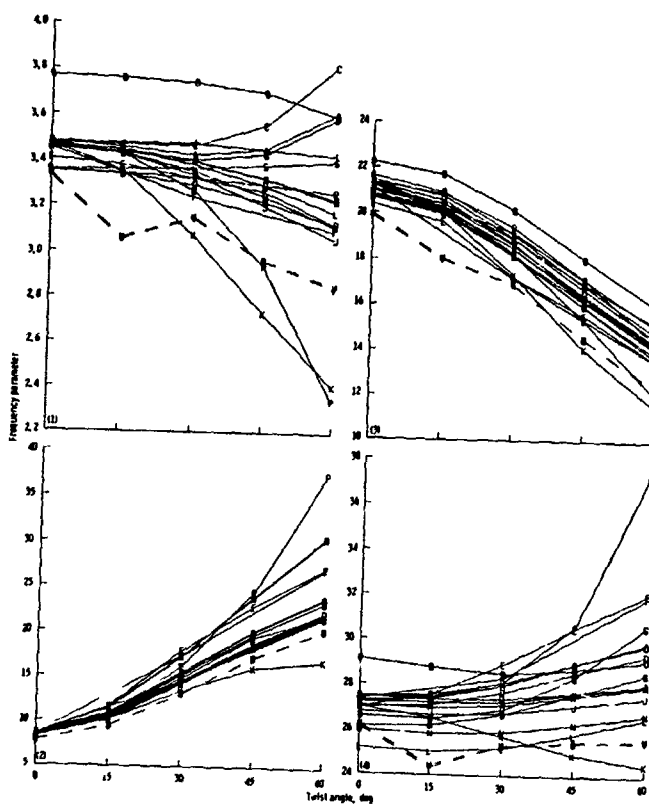


Figure 8. Natural Frequencies of Twisted Plates
Typical results from survey of different analyses for first 4 modes of twisted plate
(1) 1st bend; (2) 1st torsion; (3) 2nd bend;
(4) 1st transverse (after Kielb et al (1985))

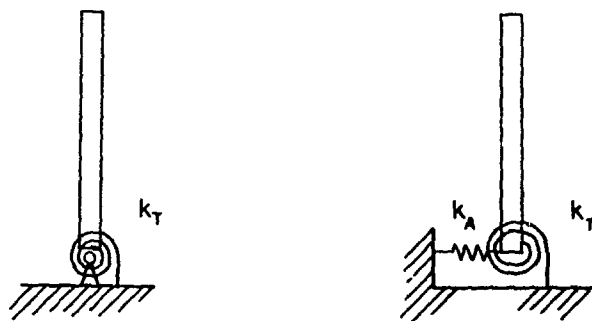


Figure 9. Effect of Root Flexibility on Beam Natural Frequency
(a) 1-coordinate flexibility; (b) 2-coordinate flexibility

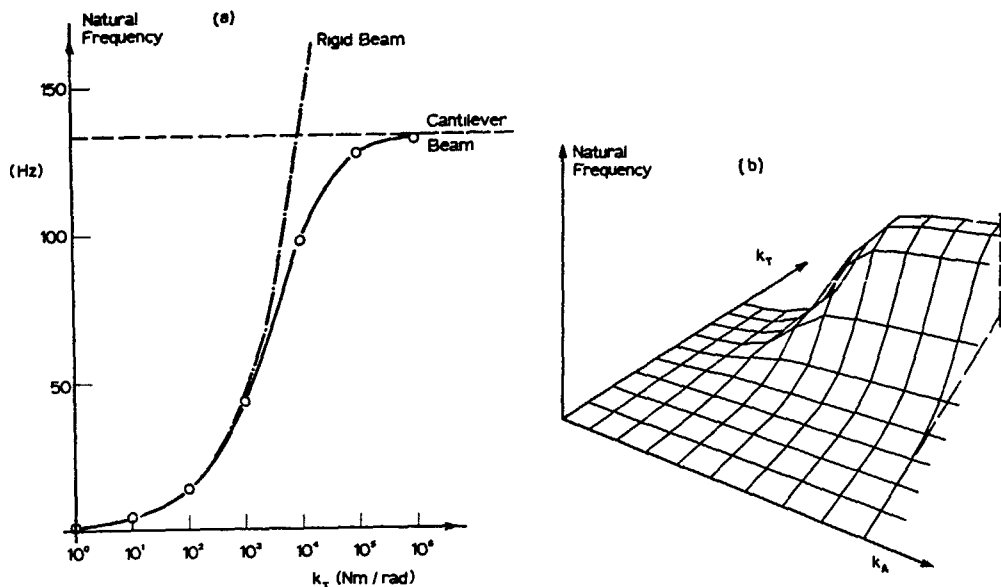


Figure 9. Root Flexibility Effects on Beam Natural Frequency
(a) 1-coordinate flexibility; (b) 2-coordinate flexibility

this effect by a boundary which prevents translational motion (i.e., which is rigid laterally) but which offers a finite stiffness k_t to any rotation of the end of the beam: see Figure 9(a). If the natural frequency of the fundamental mode of vibration is calculated for a range of values of 'root flexibility' (with k_t varying between 0 and ∞), then it is clear from Figure 9(b) that two regimes of vibration mode exist. First, for very low stiffness values, there is effectively a rigid body mode with the inertia of the beam combining with the root flexibility but involving very little bending of the beam itself. Then, for much higher values of k_t (much less flexibility in the root), the beam is found to approach the clamped-free case which might normally be assumed. However, unless the stiffness is very high, there may still be a noticeable reduction in the beam's fundamental natural frequency from that of the fully grounded case and if this discrepancy is more than 2 or 3%, then it is necessary to include the root flexibility in the analysis of the blade vibration properties.

In practice, of course, root flexibility effects are more complex than the simple model presented here but the essential results are generally similar to those shown. If we extend the previous model to include flexibility in both the rotation and translation directions (Figure 9(c)), and then consider ranges of values for both stiffness elements, we

obtain a result such as that shown in Figure 9(d), which clearly demonstrates the same basic trend as before.

Analysis of real blade designs tends to indicate that it is the rotational stiffness elements (or flexibilities) which are most likely to be the determining factors in root flexibility effects. Furthermore, it is short or otherwise very stiff blades which will be most affected by the non-rigidity of actual blade fixtures and in analyzing these, consideration of root flexibility is a primary requirement if the natural frequencies and the mode shapes are to be correctly predicted.

It should be noted that as consideration of the root flexibility effects becomes more detailed, a point is reached where it is desirable to include the flexibility of the disk also, and from there, to incorporate the interblade coupling which is provided through the disk. At this stage, it is necessary to review the whole analysis process and to employ a much more complete model - of the entire bladed assembly, or row. Such considerations are the subject of the next chapter and will not be considered further here. However, in order to define a suitable 'boundary' for the individual blade analysis, it is appropriate to include all those sections of the blade itself, plus any additional flexibilities which are introduced at the junction with the disk (e.g., fir-tree 'branch') but not of the disk or annulus itself.

Effects of Rotation. There are a number of additional factors which apply when the blade is in its operational environment and which influence the structural dynamics properties that are of interest to us here. Probably the most important are those due to the centrifugal forces which are generated by the rotation of those blades on moving rows. Very considerable forces are thus generated - for example, a 0.1 kg blade rotating at a mean radius of 0.3 m with a speed of 8,000 rev/min will experience a radial force of more than 2 tons - and, as a result, these can have a marked influence on the vibration properties of some blades.

The first consequence of the centrifugal force (and, incidentally, the other quasi-static bending forces which are generated by the gas pressure on the surfaces of the blade) is to influence the geometric form of the blade. Those blades which are heavily twisted or which have non-symmetric cross sections are liable to suffer a change in their geometric form under running conditions and this must be duly taken into account in making the design calculations of the vibration properties (see the example in the next section).

However, probably the most important consequence of the centrifugal load is the stiffening effect it has on the blade - 'CF stiffening' - which, in turn, causes an increase in the natural frequencies with some corresponding changes in mode shapes. Once again, it is possible to demonstrate the essentials of this phenomenon using simple beam-like models. Upon inspection of the mechanics of the process, it can be seen that there is a subtlety to the effect in that the CF loads have a slightly different influence on a blade mode according to the direction of its vibration: relative to the plane of the rotation. Figure 10 illustrates the basis of this feature: for vibration normal to the plane of rotation, (a) the (radial) centrifugal force, which provides an additional restoring force and hence stiffens the structure, acts purely along the blade longitudinal axis, whereas for vibration in the plane of rotation, (b) this same restoring force has a (small) un stiffening component because its line of action (again radial) is not exactly in line with the blade axis. Hence, the stagger attitude of the blade on its disk will have a small influence on exactly how much the CF stiffening affects the blade vibration modes.

A set of results is presented for the simple beam model used earlier which is now assumed to be clamped to the rim of a rigid disk of 0.56 m outer radius and rotating at speeds of up to 8000 rev/min. The 'blade' is attached such that the flap direction is in the plane of the disk - or tangential, in terms of the disk coordinates. The results of these calculations are shown in Figure 11(a) in a plot of natural frequency vs speed of rotation.

The type of plot just introduced - a Campbell Diagram - is a standard format for the presentation of blade (and bladed assembly) frequencies under operating conditions and is used even when there is no significant change in the blade's natural frequencies with running speed. It is convenient to superimpose on the basic graph lines of different 'engine orders' where the n^{th} engine order line shows what frequencies are generated by a disturbance which occurs n times per revolution of the stage. These, in turn, can help to identify potential regions of resonance - speeds at which a known excitation source will excite modes of the blade - an ability which takes on an even greater significance when dealing with bladed assemblies (next chapter) rather than individual blades.

Temperature Effect. Another effect which is present under operating conditions, and which may have an influence on the vibration modes, is a variation in the temperature of all or part of the blade. If there are any significant temperature variations, as there will often be in high pressure turbine stages, then these may result in a change in the elastic modulus of the blade material with consequent effect on its natural frequencies. If the operating temperature profile is known, along with the modulus-temperature characteristics of the blade material, then it is possible to account for this effect in calculations of the blade's vibration modes with little difficulty.

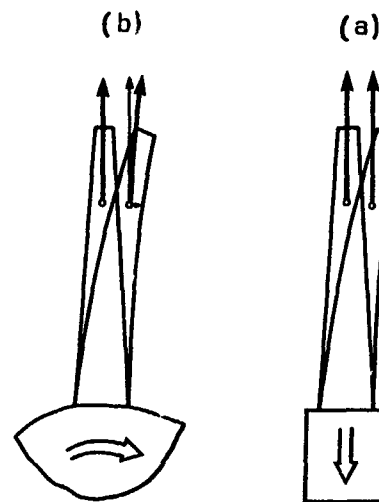


Figure 10. Centrifugal Stiffening (CF) Effects
 (1) axial vibration;
 (2) tangential vibration

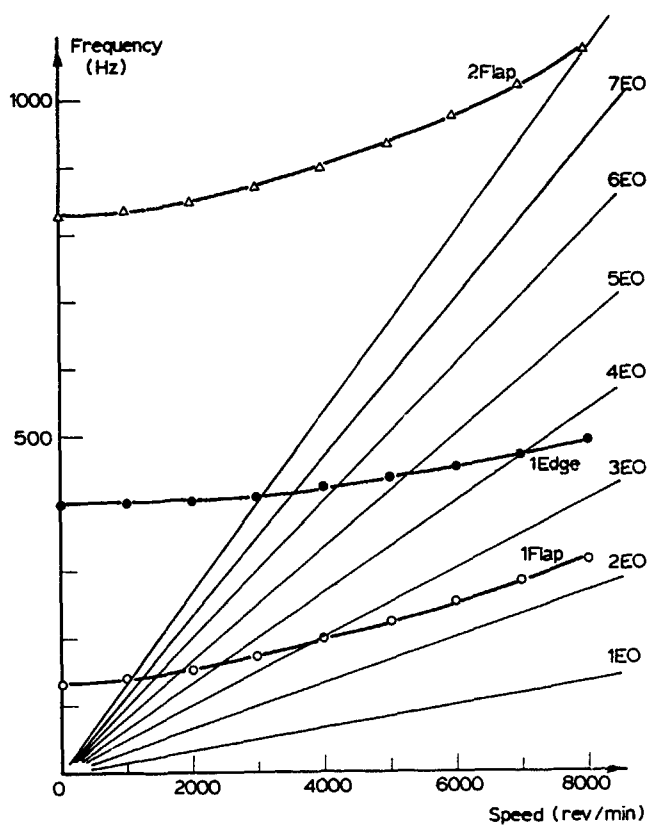


Figure 11. Campbell Diagram Showing Effects of CF Stiffening on Blade Natural Frequencies

ANALYSIS METHODS FOR PRACTICAL BLADES

Introduction. In this section, we turn our attention to the analysis methods which can be used in order to calculate the specific values for the dynamic characteristics of individual blades (as described above) for the case of practical designs. It is first appropriate to recall that the relative stiffness of the disk to that of the blades is of importance in the mechanical modelling of rotating blading. If the disk and blade stiffnesses are comparable, then their motions will be strongly coupled and dynamic analysis of the components independently is not sufficient to provide accurate estimates of the natural frequencies and mode shapes which will apply under operating conditions. However, if the disk is very stiff, its influence can be disregarded and just a single blade modelled and analyzed for use in design predictions. In any event, the properties of an individual blade are evaluated as a first step in most cases, even if the disk effects have to be added subsequently, as described in the next chapter.

Different Blade Types. As indicated earlier, blades can generally be classified into three types according to their geometric characteristics such as length, chord and thickness. If the length-to-chord aspect ratio (L/c) is high -i.e., greater than about 5 -and the thickness is small compared with the length, then the blade may be considered as a unidimensional structure and thus modelled as a beam. If the aspect ratio is low, but the thickness is still small when compared with the other dimensions, then the blade is essentially two-dimensional and should be modelled as a thin plate or shell. If the blade has a low aspect ratio and is thick, it is a three-dimensional structure and must be modelled as a thick shell.

Whatever blade type is considered, the natural frequencies and mode shapes, together with stress distributions, are generally determined using the finite element method outlined in the previous chapter. A parametric study of finite

element method modelling of all three types of blade is reported by Hitchings et al, (1980). Other methods of analysis, such as direct integration of the governing differential equations, the transfer matrix method, and others, are no longer widely used; not because of a lack of precision but because their implementation via standard computer programs is not straightforward.

Blades Modelled by Beam Elements. Generally, a beam type of model is well suited to the analysis of low pressure turbine blades. This kind of blade may be pretwisted, have an asymmetrical varying airfoil cross section and be mounted with a stagger angle. Depending on its detailed geometric characteristics, the blade can execute either uncoupled bending or coupled bending-torsion vibrations, the latter occurring when the shear centre (or centre of twist) does not coincide with the centroid of the blade cross sections, Saada (1974), Sokolnikoff (1956). Also, bending-bending coupling exists due to the pretwist and, under rotation conditions, coupling occurs between longitudinal and torsion motions (untwist due to centrifugal effects) and between longitudinal stress and bending (centrifugal stiffening). A procedure for deriving the corresponding beam element with two nodes and six degrees of freedom per node is detailed by Ferraris et al (1983) and represents a finite element version of the classical Montoya analysis, Montoya (1966).

Blades Modelled by Plate or Shell Elements. This type includes fan blades and some compressor blades. Doubly curved thin shell elements and flat plate elements can be used to model blades in this category. The only requirement is that the longitudinal (membrane) stress and bending motions coupled by the centrifugal effects are taken into account (geometric and supplementary stiffness), but as the blades in rotating axial machines are almost radial, the Coriolis effects can often be disregarded. Some studies and checks show that the flat plate triangular element with three nodes and six degrees-of-freedom per node still remains competitive for the analysis of general thin shells for practical engineering applications in spite of extensive work done with refined shell elements, Clough (1980), Olsen and Bearden (1979).

Blades Modelled by Thick Three-Dimensional Elements. All blades not included in the two previous types must generally be modelled as three-dimensional structures, e.g., short and thick turbine blades and some high pressure compressor blades. A thick shell isoparametric element with 24 nodes is widely used for this type of component, Trompette and Lalanne (1974).

Accommodation of Special Effects. As already noted in the previous section some special features of turbomachine blades have to be accounted for.

Complex Cross Section Properties. The first of these requirements concerns the derivation of the geometric characteristics of the cross sections for the beam

finite element. These characteristics are the area, the position of the centroid and that of the center of twist, the second moments of area and their principal values, the principal section axes (gives the pretwist), the torsion constant due to warping and some higher order moments of area. Some of these quantities result from performing integrals of the form:

$$I_{mn} = \iint_S x^m y^n dS \quad m, n = 0, 1, \dots, 4$$

The other parameters (torsion constant, centre of twist) are quantities related to the torsion problem of airfoil cross sections, Ferraris (1982).

As the blade profiles are usually defined by a set of points resulting from aerodynamic design calculations, it is convenient to solve the torsion problem and all the area integrals by using the boundary integral technique. A pre-processor to the blade analysis program will furnish all the required cross section properties, Ferraris et al (1983). Since the chord and pretwist tend to have rather smooth variations along the blade length, linear variations of the geometric characteristics are assumed for the blade stiffness calculations.

Root Flexibility and Platform Effect. Two approaches are possible to take account of the blade platform and root effects: the first consists of modelling the root with a large number of finite elements, while the second consists of using an equivalent but simple model.

The first method is a priori more precise but is much more costly because it increases considerably the number of degrees of freedom in the model. The second method is simpler and is most efficient for three-dimensional turbine blades. It consists of neglecting the mass of the root (because of its relatively small motion), and deriving equivalent stiffnesses calculated using simple formulas (tension, bending, and shear) for the strength of materials properties of an equivalent parallelepiped element. These stiffnesses are then distributed to the convenient nodes. The platform is relatively thin and as such acts like a mass that can also be neglected (see the section "Three-Dimensional Blade: High Pressure Turbine Blade.")

Shroud Attachment. Where appropriate, an integral shroud attachment can be modelled by equivalent stiffnesses, masses, and inertias distributed on the convenient nodes. The restrictions on the displacements are imposed by the limit conditions.

Static Loads. When using the finite element method, any inertial or external surface loads must be expressed in terms of equivalent nodal forces. The centrifugal forces are derived from the expression for the kinetic energy (see the previous chapter), and the method of introducing the aerodynamic static forces as the pressure loads is detailed in later chapters dedicated to aeroelasticity.

Coriolis Effect - Centrifugal Stiffening. It is important to take into consideration the effects of rotation on the structure, namely: the Coriolis effect and centrifugal stiffening. Their influence is reported along with the application to a fan blade in the following section. It must be pointed out that provided the blade is radial, the Coriolis effects are generally negligible. On the other hand, the centrifugal effects on the stiffness are of great importance and must be introduced, particularly for one-and two-dimensional blades, as they can produce a significant stiffening effect on the frequencies and on the untwist in rotation.

Temperature Effect. As will be seen in the following section, with an example on a turbine blade, the effects of high temperatures -generally to reduce the material stiffness -can be estimated practically by using Rayleigh's quotients through the variation of stiffness due to changes in the value of Young's modulus. In some circumstances, the temperature effect can even overcome the centrifugal stiffening and result in a net reduction of the frequencies at operating speeds. The temperature static effects require the use of a thermoelastic program that gives an initial thermal stress distribution.

REVIEW OF TYPICAL BLADE CHARACTERISTICS.

Based on the above modelling and analysis methods, the calculation of three different types of blade is now reported along with some experimental verifications of the computed results. An example of a uni-dimensional blade (from a low-pressure turbine) is used to illustrate the importance of the bending-bending-torsion coupling both at rest and when rotating. The two-dimensional example (a fan blade) includes a complete set of results: static stress distribution and untwist due to rotation, influence of the geometric stiffness on the static displacements and on the frequencies related to the speed of rotation, Henry (1973), Henry and Lalanne (1974). The influence of the Coriolis effect at operating speeds is also investigated. The last example (a high pressure turbine blade) shows some of the practical difficulties of including the rotation, temperature, root and platform effects, Trompette and Lalanne (1974). All the applications presented use the finite element modelling methods summarized in Chapter 13.

Uni-Dimensional Blade. Beam Model of an LP Turbine Blade.

Blade Finite Element Modelling. The blade used for this example has an aspect ratio of just over 6 and a maximum angle of pretwist of about 25° and this is suitable for a uni-dimensional model (Figure 12). The finite element used is a straight twisted beam element with two nodes and six degrees of freedom per node, assigned to the cross section centroid, (Figure 13). The typical element is calculated in a local coordinate system $R(G\xi\eta)$. $G\xi$ and $G\eta$ are the principal inertia axes of the cross section S . The cross section geometric characteristics are determined

by the boundary integral technique, since they are defined by points (resulting from aerodynamic design calculations). The geometric characteristics are: cross section area S , section centroid, G , principal moments of area $J_{G\xi}$ and $J_{G\eta}$ and their principal directions, leading to the pretwist angle, λ . The center of twist position $T(\xi_t, \eta_t)$ and the St. Venant torsion coefficient J_T are determined by solving the torsion problem. Finally, the remaining geometric characteristics for a complete bending-bending-torsion vibration of the blade at rest and in rotation are determined. They are of the form:

$$\begin{aligned} J_\xi &= \int_S n(\xi^2 + \eta^2) dS; \\ J_\eta &= \int_S \xi(\xi^2 + \eta^2) dS; \\ J &= \int_S (\xi^2 + \eta^2)^2 dS \end{aligned}$$

and are called higher order moments of area in the following paragraphs.

When all the cross section characteristics are known, a refined finite element is derived considering a linear variation of these characteristics along the mean line of the element. The assembly is performed using a global coordinate system XYZ fixed in the rotor, where X is directed radially outward along the mean line of the blade, Z is colinear with the rotor axis of rotation and Y is chosen to provide a right handed orthogonal coordinate system.

Dynamic Analysis Coupling Influence. The low pressure turbine blade is modelled with 12 beam elements. The tip shroud is modelled by additional masses and inertias and the blade is assumed clamped at the platform. The problem results in a model with 72 degrees of freedom for which the first six natural frequencies are calculated at rest ($\Omega = 0$ rev/min) and at the operating speed ($\Omega = 5000$ rev/min).

In order to illustrate the various coupling influences, three calculations are performed on the twisted blade. The first is made with the "refined coupling" model (noncoincident centroid and centre of twist, and higher order moments of area noted: $T \neq G$, $J_\xi \neq J_\eta$, $J \neq 0$). The second is made without the higher order inertia terms, but with noncoinciding T and G. This case is referred to as "weak coupling," ($T \neq G$ and $J_\xi \neq J_\eta$, $J = 0$). Finally, the blade is analyzed as a simple twisted beam: T and G are coincident ($T = G$) and $J_\xi = J_\eta = 0$. This last case is referred to as "no coupling." It must be remembered that in all three cases, the pretwist and the varying cross sections are included in the model.

Table 6(a) presents the results obtained for the blade at rest. The percentages indicate the influence of the coupling terms relative to those for the refined model calculations. Flapwise bending modes are labelled F, edgewise bending modes by E and torsion modes by T.

14-18



Figure 12. Low-Pressure Turbine Blade

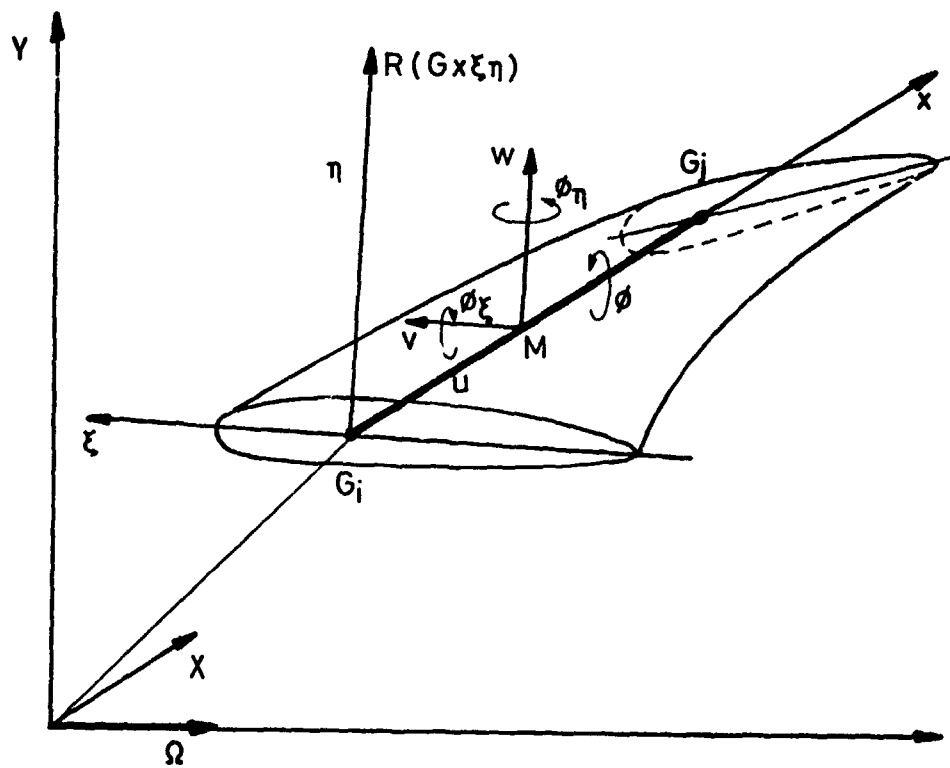


Figure 13. Twisted Beam Finite Element

Table 6(b) presents the corresponding results obtained for the operating speed while Figure 14 shows the mode shapes obtained at rest with the refined model (---), with the so-called "weak coupling" (-x-) and with the refined model at operating speed (----+---).

When examining the mode shapes presented in Figure 14 where the displacement of the mean line of the blade are projected onto the YZ plane, (X, mean line directed out of the plane), it can be seen that the first four modes are respectively 1F, 1E, 1T, and 2FE modes. The highly-coupled bending-bending-torsion modes are numbers 5 and 6, and the coupling influence is shown in Table 6(a) and (b) at rest and at the operating speed respectively. The mode shapes are only slightly modified by rotation but are very sensitive to the coupling terms, and particularly so for the torsion modes. For example, examining modes 5 and 6 for the same scaling factor, ($\alpha_x = 1$, maximum torsion angle), reveals a difference in the bending motions when the weak coupling case is considered. When no coupling is considered, it becomes impossible to make any comparison, since the 5th mode - coupled 3FE/2T - becomes 3FE uncoupled and the 6th mode - coupled 2T/3FE - becomes a purely uncoupled 2T mode, with a change in the order of natural frequencies.

Concluding Remarks.

- (i) Disregarding the various coupling terms gives overestimates for the bending frequencies and underestimates for the torsion frequencies.
- (ii) The influence of the coupling terms is quite weak for those modes which are quasi-pure in bending or in torsion, but is significant on the highly coupled modes.
- (iii) Introducing an incomplete set of coupling terms may be more disadvantageous than calculating with an uncoupled model.
- (iv) The lowest bending natural frequencies are sensitive to rotation speed, but the mode shapes are only slightly affected.
- (v) Noting that the aerodynamic forces in aeroelasticity are closely related to the frequencies and the mode shapes of the structures, it becomes clear that it is very important to use a refined finite beam element for the uni-dimensional blade model, particularly when the first bending and torsion modes are highly coupled.

Mode	Refined Coupling	Weak Coupling	% diff	No Coupling	% diff	Experimental (Clamped)
1 1F	113.4	115.2	+1.6	115.3	+1.7	113
2 1E	455	460	+1.1	464	+2.0	455
3 1T	601	574	-4.5	581	-3.3	597
4 2FE	802	814	+1.5	811	+1.1	717
5 3FE-2T	1650	1707	+3.5	1839	+11.5	1647
6 2T-3FE	1983	1872	-5.6	1790	-9.8	1967

TABLE 6(a) INFLUENCE OF COUPLING EFFECTS (AT-REST)

Mode	Refined Coupling	Weak Coupling	% diff	No Coupling	% diff
1	165.7	167.1	+0.8	167.2	+0.9
2	482	486	+0.8	491	+1.9
3	611	585	-4.3	589	-3.6
4	851	863	+1.4	861	+1.2
5	1697	1738	+2.4	1909	+12.5
6	2034	1939	-4.7	1814	-10.8

TABLE 6(b) INFLUENCE OF COUPLING EFFECTS (AT OPERATING SPEED)

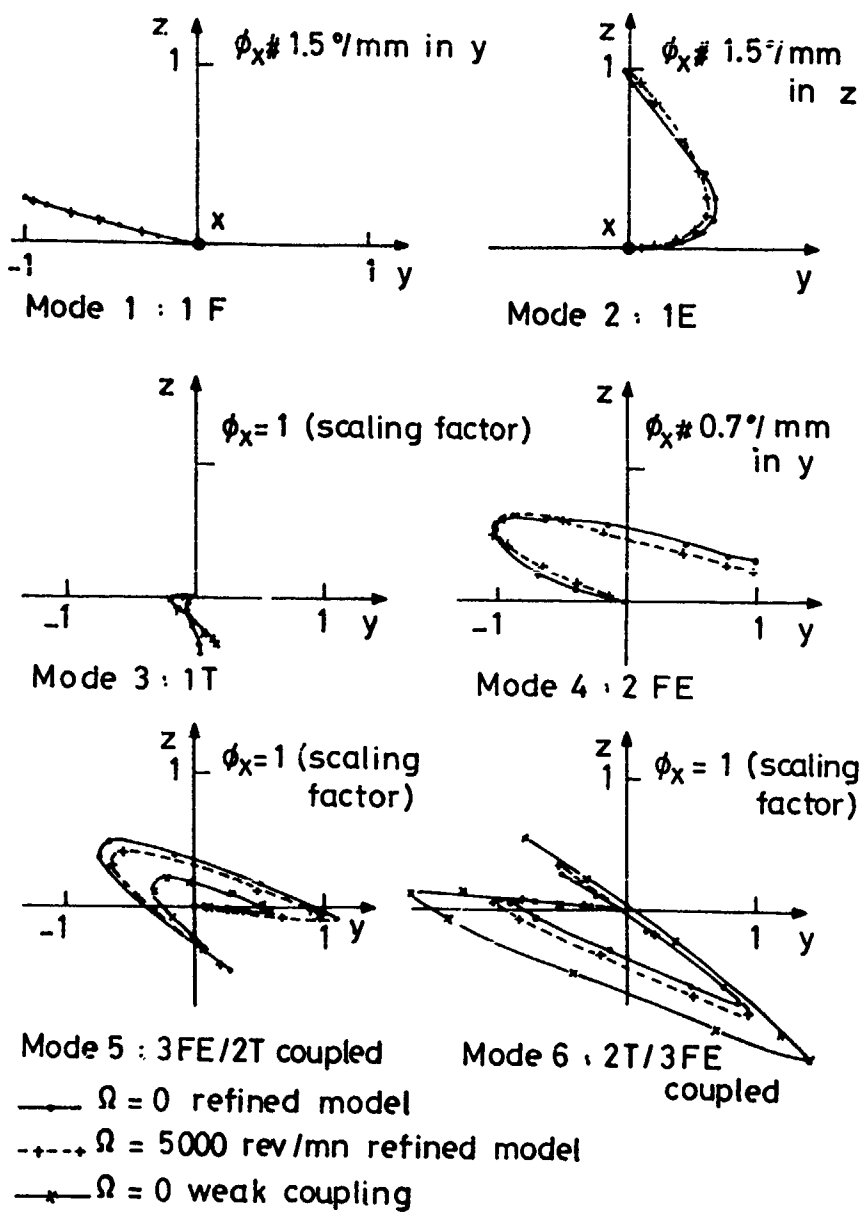


Figure 14. Mode Shapes of LP Turbine Blade

Two-Dimensional Blade Plate Model of a Fan Blade.

Blade Finite Element Modelling. This blade is modelled with 80 three-node triangular plate elements, with six degrees of freedom per node. The blade is assumed to be clamped at the platform, leading to some 300 effective degrees of freedom

(Figure 15). The plate element used is partly conforming: the displacements are continuous across the element and at the boundaries; the interpolation functions are complete and the slopes are continuous at the nodes, but not on the interelement contours. Kirshhoff assumptions are used: i.e., constant stress in membrane, linearly varying stress in bending.

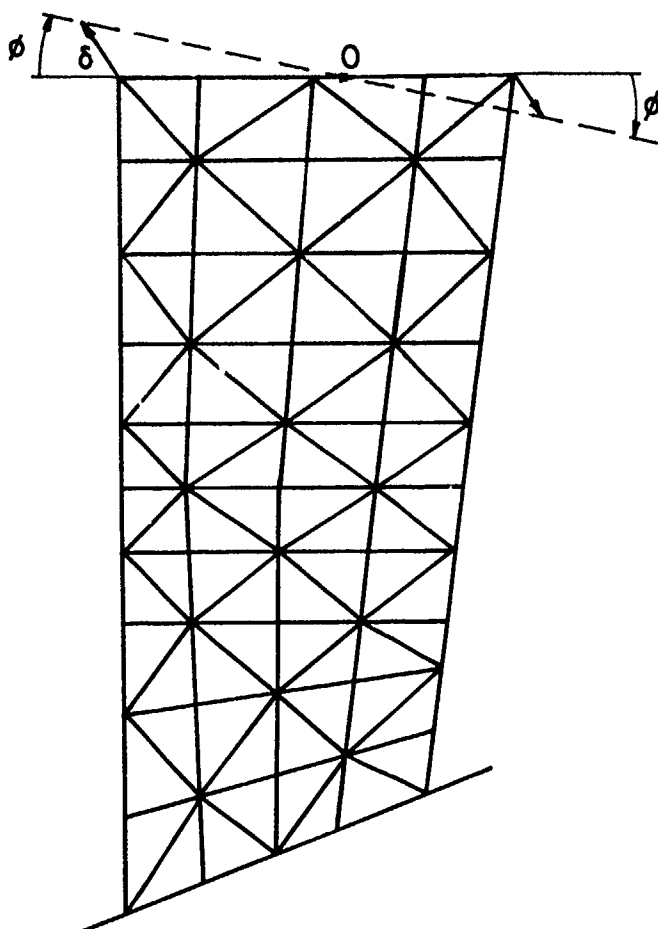


Figure 15. Finite Element Model for Fan Blade

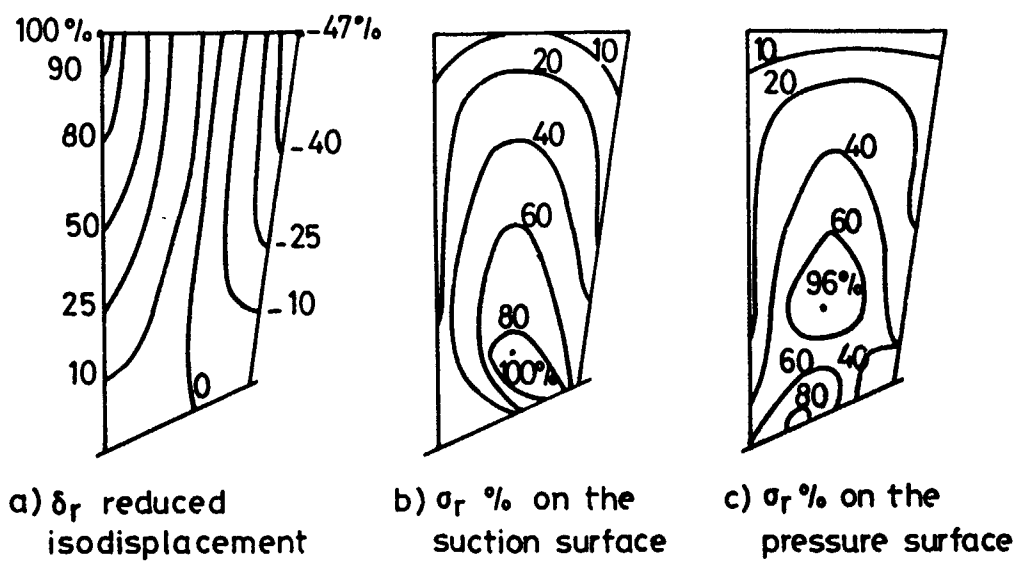


Figure 16. Static Isodisplacement and Stress for Fan Blade (at operating speed)

Stress Analysis: Displacements and Stress Distribution

At a typical operating speed, Ω_r , the steady displacements δ and the Von Mises stress σ_{VM} are determined following the procedure described in the previous chapter.

The reduced isodisplacement lines δ_r as a percentage of the maximum are presented in Figure 16(a) and one can see clearly the untwist ϕ due to rotation since the zero displacement line is located along the blade axis. The stress distribution on the suction and pressure surfaces of the blade are also presented in terms of reduced stress σ_r in Figures 16(b) and (c). When examining these two figures, it can be seen that the maximum stress is not located at the same point on the suction and pressure surfaces. This is due to the fact that the stresses at a typical point are the superposition of a membrane stress (constant across the thickness) and a bending stress (of opposite sign on the two surfaces).

These results are obtained when taking into account the centrifugal stiffening effect but, noting that these calculations require an iterative procedure, it is of some practical importance to examine the extent of this effect. In other words, in view of the higher cost of such a non-linear calculation process, is it justifiable (by an improvement in the precision of the results) to include the rotation effect (K_G , K_S) in the stiffness analysis?

Let us consider the mean untwist ϕ and the maximum displacement δ of the blade tip section in terms of Ω_r . Firstly, these quantities are calculated with the non-linear rotation effects included ($K_G \neq 0$). Secondly, the same quantities are calculated with K_G neglected ($K_G = 0$). In Figure 17, the δ and ϕ variations are presented in reduced form ($\delta_r = \delta/\delta_{max}$; $\phi_r = \phi/\phi_{max}$), where δ_{max} and ϕ_{max} are the maximum values of δ and ϕ for the maximum speed of rotation -non-linear effects included - and Ω_r is the non-dimensional speed of rotation related to the first natural frequency of the blade at rest ($\Omega_r = \Omega/\Omega_0$). It is clear that the non-linear geometric stiffness K_G cannot be disregarded, since neglecting the centrifugal stiffening will lead to significantly overestimated displacements. Remembering that the stresses are directly linked to the displacements in finite element modelling, errors in the design analysis could follow, not only in the static cases, but also in the dynamic ones.

Dynamic Analysis Ten natural frequencies and mode shapes are calculated for a range of values of the rotation speed and a Campbell diagram is plotted and presented in Figure 18(a). It can be seen that the influence of rotation is noticeable on the bending frequencies but is relatively weak on the torsion modes. Some mode shapes - those of the second and third bending and first and second torsion modes - are presented in Figure 18(b). The calculated

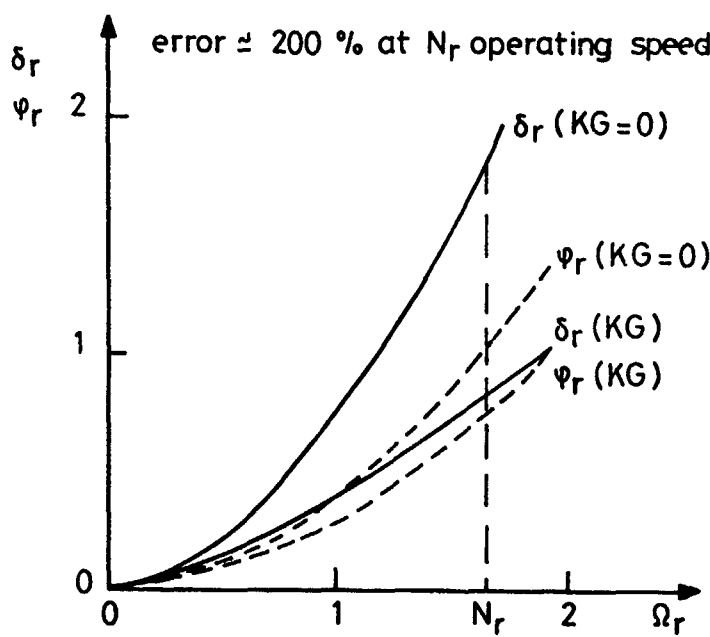


Figure 17. Influence of the CF Stiffening (K_G) on Static Deflection of Fan Blade

nodal lines for the at-rest ($\Omega_r = 0$) and rotating ($\Omega_r = 1.5$) conditions are compared together with some experimental results at rest. First, it is seen that good agreement exists at rest, and second, the calculated nodal lines in rotation show little modification when compared with those at rest.

All the preceding results have been obtained with the Coriolis effect neglected. In order to demonstrate the validity of this assumption, the first ten natural frequencies are re-calculated including the Coriolis effect for a speed corresponding to $\Omega_r = 2$, which is somewhat higher than the operating speed. The ratios of the frequencies calculated with Coriolis to the corresponding frequencies without Coriolis are in the range 0.99² to 1.0018; that is, $\pm 0.2\%$. As the computation time is about four times higher for the with-Coriolis calculation, it can be concluded that the Coriolis effect can, and indeed should, be disregarded in the analysis of practical radial and quasi-radial blades.

Comments

- (i) In principle, a "two-dimensional" blade dynamic analysis could be performed using the previously-presented beam elements but the designer must bear in mind that only the lowest modes - those which are close to beam modes - will be correctly predicted (e.g. the first four or five modes of the fan blade presented in this section). Other more complex types of mode will not be reliably predicted by a beam model.
- (ii) As was seen for the uni-dimensional blades, centrifugal effects must be included in the FEM model of two-dimensional blades.
- (iii) For classical blades which are directed radially outwards, the Coriolis effect can be neglected. However, in contrast to conventional blades, some new designs for thin and highly swept profiles give rise to large static bending and twisting deformations and also to complex vibratory characteristics. For

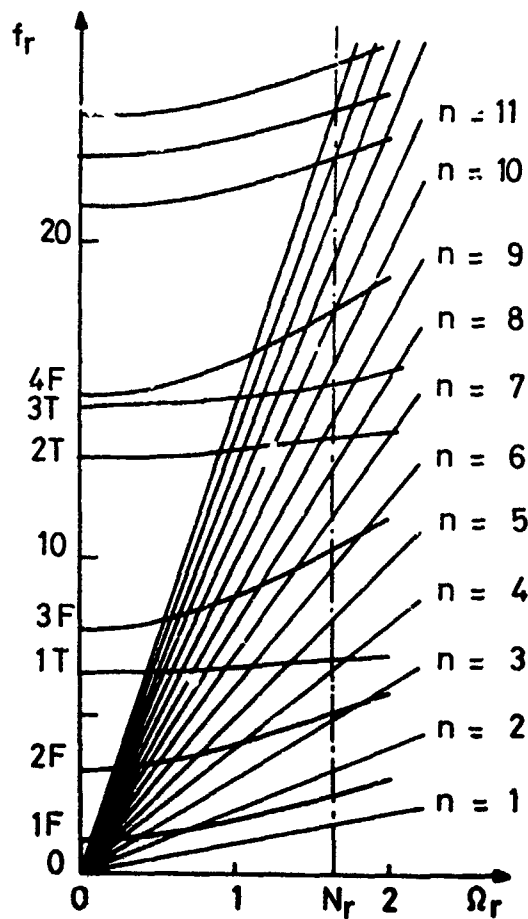


Figure 18a. Campbell Diagram for Fan Blade Natural Frequencies

these, estimating the static conditions produced by the centrifugal loading using the geometrically non-linear procedure ($K_G - \omega^2 M_G$) might not be adequate, since large displacements occur. A full non-linear analysis, using an updated Lagrangian formulation, or equivalent, might be required. For the same reasons, variations in the blades natural frequencies with speed of rotation might now result from the Coriolis effect and further investigation of this feature is strongly recommended for this type of blade.

Three-dimensional Blade: High Pressure Turbine Blade

Blade Finite Element Modelling The high-pressure turbine blade shown in Figure 19(a) is modelled with nine 24-node isoparametric thick shell elements, with three degrees of freedom per node.

The blade root and the platform can also be modelled by isoparametric elements but this is quite cumbersome and increases significantly (and unnecessarily) the total number of degrees of freedom in the model. It is generally more practical and

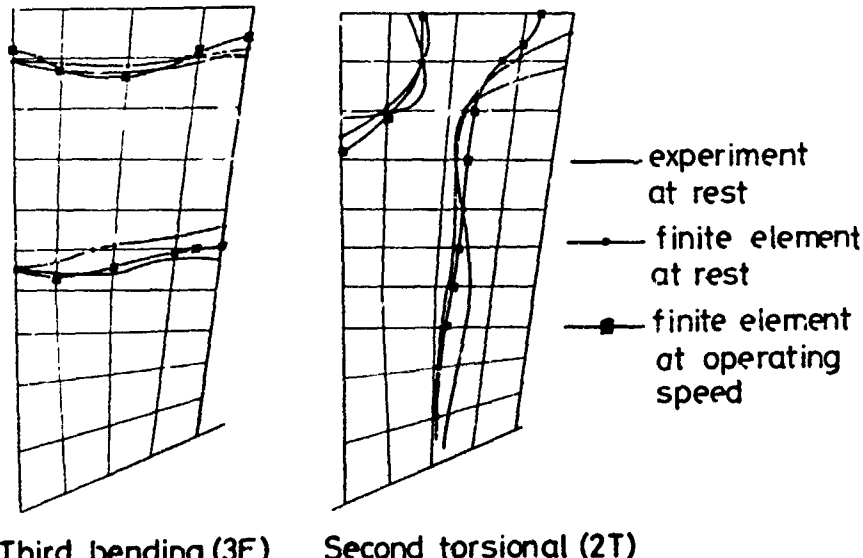
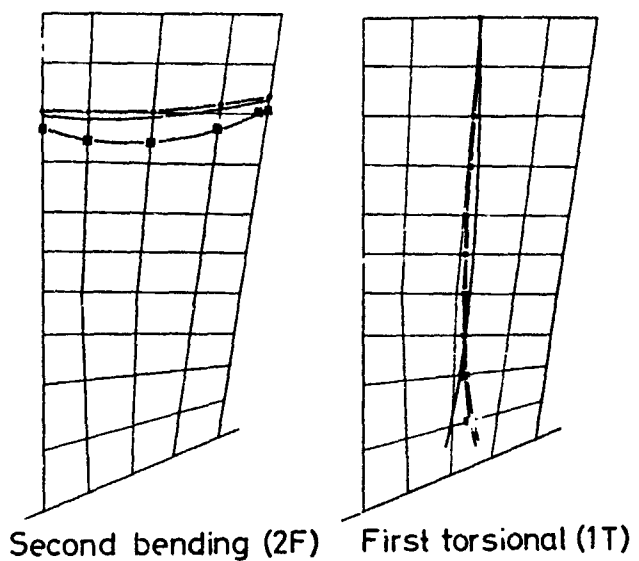


Figure 18b. Node Shapes (nodal lines) for Fan Blade Modes

convenient to choose a simpler way of taking into account the root effect using an equivalent model obtained from mechanical considerations. First, noting that the root motion is generally low, it is reasonable to suppose that its inertia influence on the kinetic energy may be neglected. The platform is thin and as such acts only as a mass (contributing negligible stiffness) and so may also be neglected. Secondly, the root is modelled by an equivalent rectangular parallelepiped whose geometrical and mechanical characteristics are defined as follows. (Figure 19(b)):

- the dimensions are the mean dimensions of the fir tree (or other) root, clamped at the first branch; and
- the stiffness characteristics in the three directions are obtained from simple strength of materials formulae for bending, shear and longitudinal effects. These stiffnesses are equally distributed to the convenient nodes of the blade base.

It is not appropriate to present again the static analysis (for centrifugal stresses) that has been detailed in the preceding section. Hence, in the following sections, only the dynamic analysis is presented and some practical considerations concerning the rotation and temperature effects are discussed.

Dynamic Analysis The finite element model results in 384 degrees of freedom. The first three natural frequencies and associated mode shapes are calculated at rest ($\Omega = 0$) and at room temperature, firstly with the blade clamped at the platform (root effects neglected altogether) and secondly including an equivalent root model. The natural frequencies are compared with experimental ones measured in situ in the engine (see Table 7). Good agreement is obtained, provided that the root is modelled, albeit with a relatively simple model.

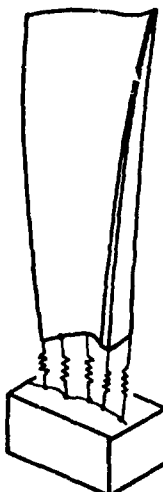
Freq. (Hz) Mode	Exp. f_0^* $\Omega = 0$	FE. %		FE %		FE + root %	
		base clamped	Equiv. root	base clamped	Equiv. root	base clamped	Equiv. root
1	1368	1588	16.1	1370	0.2	1456	6.0
2	3133	3852	23.0	3354	7.0	3401	1.4
3	4661	5248	12.6	4755	2.0	4809	1.1

* mean values for several blades

TABLE 7 TURBINE BLADE FREQUENCIES AT ROOM TEMPERATURE



19a. High Pressure Turbine Blade



springs equivalent
to the root stiffness

Figure 19b. Modelling of Root

The first mode is mainly a flap-wise bending mode; the second one edgewise bending and the third one is predominantly torsion. Still at room temperature, the blade properties are next calculated for a rotation speed of 16,000 rev/min. Examination of these results shows clearly that for this case of a three-dimensional blade, the rotation effect on the natural frequencies is weak and almost negligible on the mode shapes and this is likely to apply to most other blades in this category.

In practice, it is often recommended that the number of finite elements be increased in order to improve the accuracy of the analysis, but this will result in a higher cost, especially if several different speeds of rotation are required. However, noting that the rotation may have little or no influence on the results, a good estimate of the natural frequencies at various non-zero rotation speeds ($\Omega > 0$) can be obtained at low cost by using the at-rest results together with the so-called Rayleigh's Quotients.

Use of the Rayleigh's Quotients. It is well known that for a slight modification $[\Delta K]$ or $[\Delta M]$ to the stiffness and mass matrices $[K]$ and $[M]$ of a structure, the equation for free harmonic vibration:

$$\omega^2[M](x) = [K](x)$$

gives a first approximation to the natural frequency variation (Δf):

$$\begin{aligned} \Delta f &= \Delta\omega/2\pi \\ &= ((x)^T[\Delta K](x) - \omega^2(x)^T[\Delta M](x)) / 4\pi\omega((x)^T[M](x)) \end{aligned} \quad (1)$$

This expression is quite general and applies to whatever is the cause of the structure modification, (rotation, mass of the platform, temperature effect, etc.).

Estimation of the Rotation Effect on the Frequencies. Provided that the at-rest natural frequencies are determined using the appropriate finite element mesh, the mass matrix $[M]$ and the mode shapes (ϕ) are known. At rest, the stiffness matrix $[K]$ is the linear stiffness $[K_0]$. In rotation, the stiffness becomes $[K] = [K_0] + [K_G] - \Omega^2[M_G]$, (see Chapter 13), and consequently it can be stated that:

$$[\Delta K] = [K_G] - \Omega^2[M_G] \quad (2)$$

where $[K_G]$, the geometric stiffness matrix, and $[M_G]$, the centrifugal mass matrix, are known at the end of the static analysis.

Using Equation (1) for a typical mode, results in:

$$\begin{aligned} \Delta f_i(\Omega) &= \\ &((\phi_i)^T[K_G - \Omega^2 M_G](\phi_i)) / 4\pi\omega_i((\phi_i)^T[M](\phi_i)) \end{aligned} \quad (3)$$

or $f_i(\Omega) = f_i(0) + \Delta f_i(\Omega)$

The results presented in Table 9 for a speed of 16,000 rev/min show very good agreement when compared with those obtained by a complete finite element calculation, since the error incurred by the Rayleigh's Quotient calculation is less than or equal to 0.5%.

This procedure can be implemented directly in the finite element program and will obviate the need for a complete re-calculation at several speeds of rotation, thereby resulting in a considerable economy.

Estimation of the Platform Mass Effect. The platform mass has been modelled approximately and distributed equally to the appropriate nodes of the blade base. The resulting $[\Delta M]$ included in Equation (1) gives a less than 1Hz variation on the first three natural frequencies, demonstrating that the platform may be neglected - at least in this case.

Freq. (Hz) at room temp	FE $f_0(0)$ $\Omega = 0$	FE. $\Omega = 16000$ rev/min	Rayleigh $\Omega = 16000$ rev/min
1	1370	1456	1460
2	3354	3401	3400
3	4755	4809	4785

TABLE 8 RAYLEIGH'S QUOTIENTS FOR ROTATION EFFECT DETERMINATION

Freq (Hz) t° $\Omega = 16000$ rev/min	f_0 20°	200°C	400°C	600°C	700°C	%
1	1456	1440	1401	1360	1334	-8.4
2	3401	3359	3259	3151	3084	-9.3
3	4809	4749	4605	4451	4355	-9.4

TABLE 9 TEMPERATURE INFLUENCE AT OPERATING SPEED

Temperature Effect Large temperature variations modify the value of Young's modulus, E. Remembering that the stiffness [K] is proportional to E, then to a first approximation:

$$[\Delta K] = (\Delta E/E)[K] \quad (4)$$

and, finally,

$$\Delta f_i = ([\phi_i]^T [\Delta K] [\phi_i]) / 4\pi\omega_i ([\phi_i]^T [M] [\phi_i]) \quad (5)$$

or

$$f_t(\Omega) = f_0(\Omega) + \Delta f_t$$

In Table 9 the influence of temperature variations on the natural frequencies at the operating speed Ω is presented. When the temperature increases to a typical turbine operating level, the natural frequencies decrease and at 700°C it is clear that this effect is more important than rotation, since the frequencies at operating speed and temperature are lower than those at rest and at room temperature (20°C).

Conclusion - Practical Recommendations to the Designer. All these examples show that the finite element modelling is an efficient tool for practical rotating blade vibration analysis. However, the designer has to remember that:

- the choice of element depends primarily upon the blade geometry. If a beam model is chosen, the bending-bending-torsion coupling must be included in the finite element theory;

- the influence of rotation has to be considered through both the geometric stiffness and the centrifugal mass effects. The Coriolis effect can be neglected if the blade is directed radially outward. For prop fan blades, and other non-classical forms, further investigation is recommended before ignoring this Coriolis effect. Also, full non-linear analysis might be necessary for static behaviour in rotation;

- some account may be taken of the stiffening effects and temperature effects by using Rayleigh's Quotients, resulting in savings of time and cost, provided mode shapes are little modified by rotation;

- considerable attention has to be paid to the root modelling and the limit condition situation. Practically, at the operating speed, a rotating blade can be considered clamped if the root has a fir tree type fixation on the disk; and

- a single blade calculation is appropriate only if the disk stiffness is high compared with that of the blade. If the blade and the disk stiffnesses are comparable, then the whole assembly has to be modelled. Appropriate methods for this case are detailed in the next chapter.

ACKNOWLEDGEMENT

The authors gratefully acknowledge the contributions to this chapter made by Dr. M. Imregun, who provided many of the computed data.

STRUCTURAL DYNAMIC CHARACTERISTICS OF BLADED ASSEMBLIES

by

D. J. EWINS
 Imperial College of Science and Technology
 Department of Mechanical Engineering
 Exhibition Road, London SW7 2BX

INTRODUCTIONBackground

It is clear from the preceding chapter that considerable efforts have been expended in order to make accurate predictions for the essential structural dynamic properties of typical turbomachine blades. These components generally have quite complex profiles and the calculations involved are often lengthy since both the natural frequencies and the mode shapes are required with some accuracy: the frequencies because of their close relationship with the rotation speed(s) of the machine and the mode shapes because of their direct influence on the aerodynamics of the working fluid. One other structural characteristic which is of importance but which is far less accessible than the mode shapes and frequencies is the modal damping which derives from the various mechanical sources such as material hysteresis and slip at the mating surfaces in joints. This property, and especially the latter effect, is very difficult to predict and few attempts to do so are reported. Our comments thus concentrate on the two primary properties of natural frequency and mode shape.

In our pursuit of accuracy in these predictions, we have so far neglected one feature which may - in certain cases - have a major influence on the actual values of the vibration properties sought. That factor is the coupling between one blade and its neighbours via the structural connections which inevitably exist, either through the disk or annulus which carries the blades, or through a shroud ring which may be incorporated to stiffen the whole assembly. Although we may have included root flexibility in our single blade model (see Chapter 14), or ensured the addition of the mass of a shroud segment, these do not take into account the possibility that one blade will interact with its neighbours and thereby influence the vibration modes of the whole set. In fact, as we shall see, the structural coupling between the blades comprising one stage will usually exert a significant influence on both the natural frequencies and the mode shapes and so it is important that we extend our analysis to include it. In most cases, determining the properties of a single blade is a necessary stage in the structural dynamic analysis but is not sufficient to describe the blades' vibration properties in their operational environment: for that we must analyze the complete assembly.

Assembly Configurations

Before developing our analysis further, it is appropriate first to identify the various bladed assembly

configurations with which we shall be dealing. There are several, although they may be all classified into one of two distinct groups: (a) those which are circumferentially or cyclically symmetric and (b) those which are not. The first group comprises those assemblies in which all the blades have the same interconnections, and include:

1. unshrouded identical blades on a flexible disk (or drum);
2. continuously tip-shrouded blades on a flexible disk;
3. mid-height-shrouded blades on a flexible disk;
4. shrouded blades on a rigid disk.

The second group contains those assemblies which do not possess complete circumferential uniformity and, for our purposes here, include:

5. groups (or packets) of shrouded blades on a rigid disk;
6. shrouded blades on a flexible disk, where the shroud connections are discontinuous, resulting in a packeted bladed disk; and
7. assemblies where the blades are not identical to each other.

Although most current designs tend to fall in the first group, the second is also of interest, partly because of the possible advantages which these configurations may enjoy and partly because imperfect or non-uniform assembly conditions may (inadvertently) create them.

We have also included the implications of slight variations in the properties of the blades in one row (7), since this characteristic is likely to arise to some degree in every practical assembly and, also, because it sometimes has a very pronounced effect on the properties of interest.

Objectives and Outline of Chapter

Following the pattern set in the previous chapter, our main concern here will be to establish the essential features of the structural dynamic properties of bladed assemblies. We shall seek to illustrate the patterns of both natural frequencies and mode shapes for various assemblies and to identify the major controlling factors in each case. Thus, it is hoped that those engineers concerned with the complete aeroelastic analysis of such blading will be provided with both insight into the types of vibration mode possessed by bladed assemblies and to the design parameters which are particularly important for their exact determination.

Much of this chapter will make use of simplified mathematical models of a bladed assembly since these readily permit the detailed parametric studies necessary to determine the patterns of behaviour. The design analysis for an actual assembly will necessarily incorporate all the details of geometry and operating conditions (as was the case for the single blade), but these calculations are very expensive. As our primary interest here is to understand the interaction between the various blades, it is appropriate at each stage to consider only those features which are essential and so a number of simplified models have been devised and will be used throughout this chapter. Accordingly, the first discussion will be concerned with the development of the models themselves. The basic model, which is very simple, admits a single degree of freedom (or mode of vibration) for each blade and includes a similarly simplified representation of the disk and/or shroud coupling. The resulting discrete lumped-parameter (mass-spring) model permits rapid and cheap calculation of its vibration properties and is ideal for a parameter study but is of limited application as a design tool since the model parameters can only be specified after a complete analysis has been made of the blade and disk separately. A second group of models is used which is based on simple beam and plate components. Although, once again, not directly usable for design predictions, these models are more representative of the actual assemblies than are the first type and yet are still relatively inexpensive to analyze. Both models are suitable for studies of mistuned, as well as tuned, assemblies. The third and final type of model is that which contains few or no simplifications and is usually based on finite element techniques. These are the models used for direct design predictions but are sufficiently expensive in computation time to be inappropriate for exploratory studies and are almost always limited to tuned and/or cyclically symmetric assemblies. All three types of models will be used in this chapter.

The studies reported here will concentrate on natural frequencies and mode shapes but some consideration will be given to forced vibration response characteristics. It must be noted, however, that these latter studies will be confined to undamped or mechanically-damped systems and will be based on assumed, nominal, excitation forces. No attempt will be made at this stage to analyze the actual damping and excitation effects of the working fluid.

Throughout the chapter, our main aim is to demonstrate and to illustrate the essential structural vibration properties of various bladed assemblies. The calculation of their specific values in a practical case is largely an exercise in numerical analysis and it is probably as, if not more, important to know what to calculate and what to expect from the computed results as it is to know which coding to use and how to use it.

STRUCTURAL DYNAMICS MODELS FOR BLADED ASSEMBLIES

Lumped Parameter Models

In view of the inherent size and complexity of a typical bladed assembly, it is necessary to reduce the system model to the most basic form which is appropriate for the study in hand. Originally, this meant simplifying the usually complex geometry so that the blades could be represented by equivalent beams in order that the complete assembly could be modelled Armstrong (1955). Even then, it was necessary to assume full axisymmetry (so that the basic component consisting of a single blade/disk sector could be modelled) and to use the repetitive nature of the actual assembly, together with some knowledge of the anticipated results, in order to extract a solution.

Early attempts to study the effects of blade mistuning required a less restrictive model and one which was proposed for this purpose Dye and Henry (1969) (and derived from an earlier concept, Bishop and Johnson (1960)) now provides us with the basis of a simplified, but nonetheless very useful, model for studying bladed assemblies of all types, (Ewins 1980), Ewins and Han (1983), Griffin and Hoosac (1983). The model is a standard lumped-parameter mass-spring system of the type introduced in Chapter 13 together with the basis for its analysis. Each blade is modelled by just one or two degrees of freedom although later applications have taken the concept rather further, Jones and Muszynska (1983), and the disc or shroud by equally simple spring and mass elements. Figure 1 shows the basic model plus a number of variants which have evolved from it. It should be noted that the model can be readily extended to include damping elements as well, and some applications have made use of this facility albeit only in a rather qualitative way.

The model of this type is characterized by a mass and stiffness matrix pair such as the example which follows for model (c) in Figure 1.

$$[M] = \begin{bmatrix} \cdot & \cdot & & \\ \cdot & m_i & 0 & \cdot \\ \cdot & 0 & m_i & \cdot \\ \cdot & & \cdot & \cdot \end{bmatrix}$$

$$(K_i + K_{i-1} + k_i)$$

$$[K] = \begin{bmatrix} \cdot & -k_{i-1} & 0 & \cdot & -k_i & -K_i & 0 & \cdot & \cdot \\ \cdot & 0 & 0 & 0 & -k_i & 0 & 0 & \cdot & \cdot \\ \cdot & \cdot \end{bmatrix}$$

The main limitations of this model are (1) its restriction to a range of frequencies around the blade mode(s) represented, and (2) the difficulty of establishing suitable mass and stiffness values for a given design. The latter process is possible if the actual properties of an individual blade and the disk are known, Afolabi (1982), so that the model can be used for parameter studies, if not as a prediction tool.

Once derived, analysis of the model is straightforward, involving only the classical methods outlined in Chapter 13. In numerical solution for large assemblies, advantage can be taken of the banded nature of the stiffness matrix and, indeed, some studies have shown how a rearrangement of the sequence of the coordinates from that shown above can compact the stiffness matrix even further to gain additional computational efficiency. The model can be used just as easily for mistuned assemblies as for the perfectly tuned version and is capable of providing natural frequencies, mode shapes and forced response characteristics. The addition of damping terms to the model generally expands the computation effort by a large amount and in view of the uncertainty of their magnitude and distribution, such an extension is seldom made. It should be noted, however, that it is in the modelling - the definition of the appropriate parameter values - and not in the analysis of that model that the difficulty lies.

Beam and Plate Models

A number of models based on beam and plate components were developed prior to the widespread availability of finite element methods. Although essentially restricted to uniform - or simple geometry - components, these models are more representative than those of the lumped parameter type but are still relatively inexpensive to use. One of the earliest models of this type was devised for an axisymmetric unshrouded bladed disk using the receptance (or frequency response) coupling method, Armstrong (1955), and subsequent developments have extended this type of model to shrouded assemblies, Ewins and Cottney (1975), and to mistuned and packeted configurations, Ewins (1973), Ewins and Imregun (1983). There are now two derivatives - one for cyclically symmetric configurations and the other for the more general cases where blade-to-blade variations exist. Figure 2 shows the essential features of each type of model from which it can be seen that a degree of non-uniformity (in component geometry) can be accommodated although not to a great extent. Much the same comments concerning derivation of the model parameters in a particular case apply to this type of model as well as to the previous one although its ability to represent the behaviour of actual turbomachine stages has been demonstrated, Ewins and Cottney (1975).

The method of analysis is similar in the two types of model. Considering first the fully symmetric or tuned case (all blades identical), we can exploit the circular nature of the structure and the known properties of the connecting disk (or shroud) and assume that the variation in displacement around the assembly is essentially sinusoidal. (The validity of this assumption will be borne out by later results but its use may be likened to that of assuming simple harmonic motion (in time)). We shall thus assume that the motion at any point on the disk rim may be expressed as

$$\{x(t)\} = \{x_n\}_d \cos n\theta \cos \omega t \quad (1)$$

where the six elements in the displacement vector represent motion in the three translational and three rotational directions. θ represents the position around the disk and n the sinusoidal order of the assumed vibration pattern (and, also, the number of "nodal diameters"). If we define a vector $\{F_n\}_d$ for the corresponding harmonic forces at the disk rim, and vectors $\{x_n\}_{br}$, $\{F_n\}_{br}$, $\{x_n\}_{bt}$, $\{F_n\}_{bt}$, $\{x_n\}_s$, $\{F_n\}_s$ for the blade root, blade tip and shroud respectively, then we can relate all these parameters by applying equilibrium and compatibility at the disk/blade and blade/shroud junctions. Thus:

$$\{x_n\}_d = \{x_n\}_{br} ; \quad \{x_n\}_{bt} = \{x_n\}_s \quad (2)$$

and

$$\{F_n\}_d + \{F_n\}_{br} = \{0\} ; \quad (3)$$

$$\{F_n\}_{bt} + \{F_n\}_s = \{0\}$$

In addition, because of the assumed harmonic vibration, the displacements and forces for each component are related by its frequency response functions, thus:

$$\{x_n\}_d = [\alpha_n(\omega)] \{F_n\}_d \quad (4)$$

where $[\alpha_n(\omega)]$ is the (receptance) frequency response function matrix for the disk when vibrating in a $\cos n\theta$ (or n nodal diameters) pattern. Similar expressions apply for the shroud:

$$\{x_n\}_s = [\gamma_n(\omega)] \{F_n\}_s \quad (5)$$

and the blade:

$$\begin{Bmatrix} \{x_n\}_{br} \\ \{x_n\}_{bt} \end{Bmatrix} = \begin{Bmatrix} [\beta]_{rr} \; [\beta]_{rt} \\ [\beta]_{tr} \; [\beta]_{tt} \end{Bmatrix} \begin{Bmatrix} \{F_n\}_{br} \\ \{F_n\}_{bt} \end{Bmatrix} \quad (6)$$

Combining (2) to (6) leads to:

$$\begin{Bmatrix} ([\beta]_{rr} + [\alpha_n]) & [\beta]_{rt} \\ [\beta]_{tr} & ([\beta]_{tt} + [\gamma_n]) \end{Bmatrix} \begin{Bmatrix} \{F_n\}_{br} \\ \{F_n\}_{bt} \end{Bmatrix} = \{0\} \quad (7)$$

from which the determinantal equation

$$\det \begin{Bmatrix} ([\beta]_{rr} + [\alpha_n]) & [\beta]_{rt} \\ [\beta]_{tr} & ([\beta]_{tt} + [\gamma_n]) \end{Bmatrix} = 0 \quad (8)$$

provides a method for finding the natural frequencies and - by back substitution into the earlier equation - the mode shapes of the bladed assembly. (All the elements in the matrices $[\alpha_n]$, $[\beta]$, and $[\gamma_n]$ are frequency-dependent, and the derivation of their individual elements are detailed in Ewins and Cottney (1975) and Ewins and Imregun (1983)).

Analysis of the other, more general model follows similar lines except that it does not presuppose the $\cos n\theta$ displace-

15-4

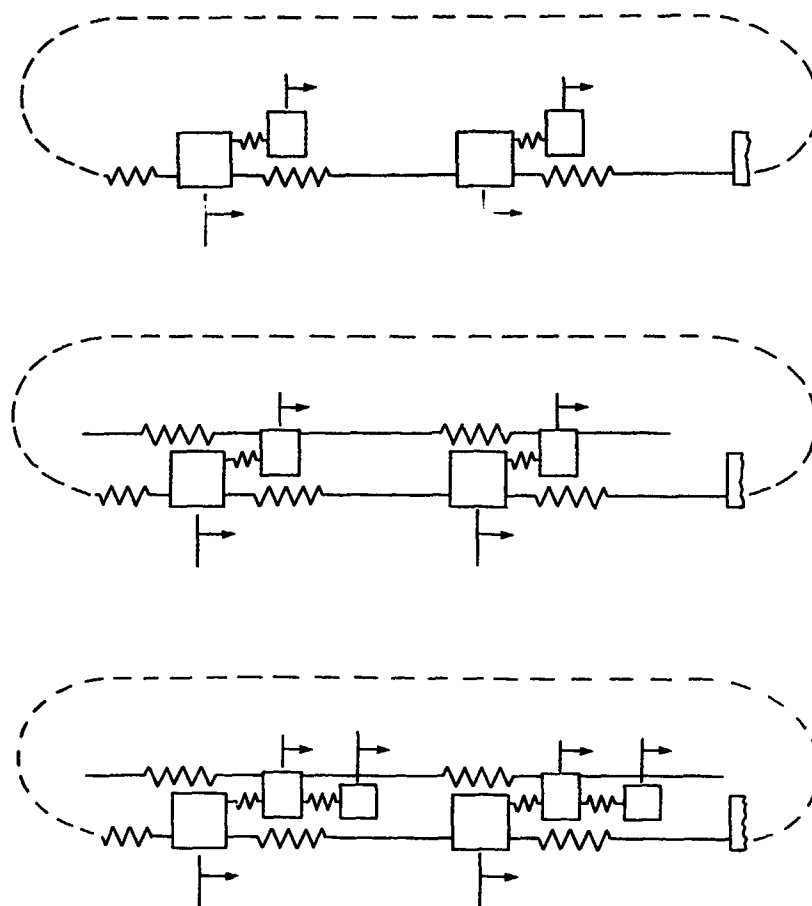


Figure 1. Simple Lumped Parameter Models of Bladed Assemblies
(a) unshrouded; (b) tip-shroud; (c) mid-height shroud

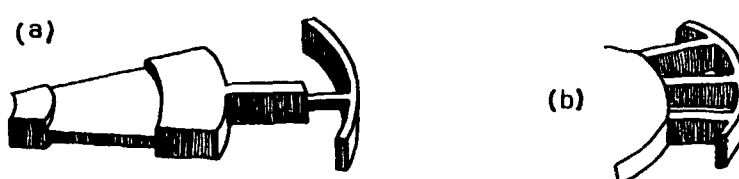


Figure 2. Beam and Plate Models for Bladed Disks
(a) cyclic symmetry; (b) general

ment variation around the disk. If we let $\{x_i\}_d$ and $\{F_i\}_d$ be the harmonic displacement and force vectors at position i around the disk, then we can write

$$\begin{Bmatrix} \{x_1\}_d \\ \{x_2\}_d \\ \vdots \\ \{x_N\}_d \end{Bmatrix} = [\alpha(\omega)] \{F\}_d \quad (9)$$

where N is the number of blades.

(Note that the disk receptance matrix used here $[\alpha(\omega)]$ is different to, and more general than, that above for a specific modal diameter pattern, $[\alpha_n(\omega)]$. A typical submatrix of $[\alpha(\omega)]$, such as $[\alpha_{ij}]$, relates the displacements at position i to a set of forces applied at position j .) Using the simple case of an unshrouded bladed disk, we derive a single set of equations:

$$\begin{bmatrix} [\alpha_{11} + \beta_1] [\alpha_{12}] \dots [\alpha_{1N}] \\ [\alpha_{21}] [\alpha_{22} + \beta_2] \dots [\alpha_{2N}] \\ \vdots \\ [\alpha_{N1}] [\alpha_{N2}] \dots [\alpha_{NN} + \beta_N] \end{bmatrix} \begin{Bmatrix} \{F_1\} \\ \{F_2\} \\ \vdots \\ \{F_N\} \end{Bmatrix} = \{0\} \quad (10)$$

which can be used to derive a determinant frequency equation, as before. The essential difference between this equation and the previous one, (7), is that in the later version, no prior assumption is made about the mode shapes and, also, every blade is individually represented so that the resulting matrix is N times larger than for the earlier case. Details for derivation of the individual beam and plate receptances may be found in Ewins, (1973) although a more general formulation using the modal properties of the individual components (if known) is outlined in Ewins and Imrequin (1983).

It should be noted that throughout the preceding analysis it has been assumed there is complete coupling at the disk/blade and blade/shroud junctions. This may not be appropriate in all cases; for example, where inter-shroud slipping is possible or where pinned blade roots are used. In such cases, the coordinates which are not coupled are simply omitted from the coupling analysis.

As noted, the analysis of this type of model is based on frequency response methods (see Chapter 13) and, consequently, the direct 'output' is itself a response function. While this can be further analyzed to yield the natural frequencies and mode shapes, because of its format it is sometimes difficult to ensure the identification of all the assembly's modes. This feature is seldom a problem when analyzing the fully symmetric assembly but can present difficulties in the other, more general, type.

Finite Element Models

One of the first published finite element models for a bladed assembly appeared in 1971 Kirkhope and Wilson (1976), and this has been followed by several others extending the capability to more and more complex designs. Undoubtedly, there are many other studies and methods developed which remain unpublished. However, as the basic blade and disk are modelled with increasing accuracy, the scale of model required to represent all the blades of an assembly individually remains prohibitive and so, here in particular, cyclic symmetry and substructure methods must be exploited to the full. Thus, the simplest type of model is one which assumes an axisymmetric structure, and this is achieved by assigning negligible circumferential stiffness to the blading but otherwise taking uniform inertial and elastic properties throughout the assembly. This type of model is more appropriate for assemblies with many blades (say, above 30) but becomes less valid as the blade number is reduced.

The next level of modelling is to construct a model of a single blade and its corresponding disk (and shroud) section. This is then considered as the basic element in a cyclically repetitive structure which may be analyzed as was the cyclically symmetric beam and plate model, above.

Lastly, a more extensive sector model can be developed, embracing several blades, and again this can be treated as a basic substructure, several of which are connected to form the whole assembly.

BASIC STRUCTURAL DYNAMIC PROPERTIES - NATURAL FREQUENCIES, MODE SHAPES

All bladed assemblies with circumferential symmetry exhibit certain well-defined types of vibration mode and these can be illustrated using any of the previously-discussed models. The most important feature is the existence of two types of mode - 'single' and 'double' - of which the latter type represents the majority. Most of a bladed assembly's vibration modes occur in pairs - double modes: these being two modes with the same natural frequency and similar mode shapes. As with other structures where there are repeated natural frequencies, no unique mode shapes can be specified for these modes. Rather, it is sufficient to specify two suitably orthogonal shapes and to note that when vibrating freely at that natural frequency the structure can assume any form given by a linear combination of the two specified shapes.

In the present case, we find that for all the 'double' modes, suitable shapes are provided by $\cos(n\theta)$ and $\sin(n\theta)$ circumferential distributions of displacement around the assembly. This means that at the corresponding natural frequency (say, ω_n), the assembly can vibrate in any combination of these two patterns - i.e., in a shape of the form $\cos(n\theta + \phi)$. What this means is that the natural frequency (or pair of identical natural frequencies) can be associated with a mode whose shape is

characterized by n "nodal diameters" since the displacement is constrained to be zero along n equally-spaced diametral lines, whatever the displacement 'shape' is in a radial section, although the orientation of these diameters will depend on some additional external influence.

Calculation of a typical assembly using the simple lumped parameter model demonstrates this pattern clearly, as shown in Figure 3 where the double modes are identified. It is also clear from this example that the assembly possesses a smaller number of 'single' modes - each with a single natural frequency and a unique mode shape - and that these fit into the pattern set by the larger number of double modes. The single modes correspond to motion with all the blades in the same amplitude of motion, either in phase with each other (0 nodal diameters) or out of phase with their neighbours ($N/2$ nodal diameters - only possible if N is even).

In addition to the sketches of mode shapes which show the relative displacements of the various blades, Figure 3(b), a second diagram is given in which each entry is obtained from a (discrete) Fourier analysis of the corresponding column from the first set of results. In this format, the diametral order of each of the modes is clearly seen and readily facilitates the graphical presentation of the results shown in Figure 3(b). This form of presentation, and where appropriate, its tabular counterpart, will be used throughout the rest of this chapter.

From the example in Figure 3 and also from a second one in Figure 4 for a more complex model, another important characteristic may be observed. As the number of nodal diameters (n) increases, the natural frequencies in each 'family' approach asymptotically one of the 'blade cantilever frequencies' - the natural frequencies of an isolated blade with the disk attachment point (or root) grounded. This behaviour is caused by the progressive stiffening of the disk as it adopts a more complex shape, and it demonstrates the relevance of performing an individual blade analysis, as in Chapter 14, even when that blade is known to be part of a coupled assembly. When the coupling is small, such as will apply with a very stiff disk, the same family characteristics are observed although, in this case, almost all the natural frequencies are very close to the blade-alone values - as would be expected - Figure 5.

Having established the main characteristics using the very simple lumped parameter model, we can confirm this behaviour using one of the beam and plate models. Taking first the more general model, a series of calculations are shown in Figure 6 for a simple unshrouded 30-bladed disk. From these results, we see the same general pattern - families of modes approaching the individual blade cantilever frequencies - but now we observe many more modes and, indeed, the full mode shape for each one of these is more complex as it describes the displacement of

all parts of the disk and the blades, including not only the circumferential variation (as before) but also a radial displacement shape. When plotted as a displacement variation with radius, it is found that each family of modes is itself associated with a number of nodal points along the radial line - much as is found for the vibration modes of a single beam - and these represent nodal 'circles' on the bladed assembly, in addition to the nodal diameters already established by the circumferential variation. The nodal diameter pattern used to identify each natural frequency on the plot is obtained by analyzing the relative displacement of each blade tip (or other selected reference location along the blade).

It should also be noted from these results that each family of modes extends only up to a maximum diametral order of $N/2$ (or of $(N-1)/2$, if N is odd). This is to be expected with the discrete lumped parameter model since higher diametral orders simply could not exist but with the continuous disk (or shroud) model, vibration of these components with higher nodal diameter patterns is possible. However, if we choose to describe the circumferential variation in amplitude by noting the relative displacement of some reference point of each blade, then we are unable to resolve higher diametral orders than $N/2$ (or $(N-1)/2$ if N is odd). A displacement shape in the disk of $\cos(n\theta)$ (where $n > N/2$) which is described in terms of the rim or blade displacement at N equal points around the disk will appear just as a mode shape in the form of $\cos((N-n)\theta)$. In other words, n nodal diameters and $(N-n)$ nodal diameters are indistinguishable to a set of N blades - see Figure 7. This phenomenon has implications for a number of bladed assemblies, including all shrouded ones (where n nodal diameters in the disk and $(N-n)$ diameters in the shroud will be directly compatible since the two components are connected only through the N discrete blades) - and those with small numbers of blades (where n and $(N-n)$ are both relatively low diametral orders).

At the lower end of each family, the 0-and 1-nodal diameter modes should also be noted for their special characteristics. These three modes (one single and one double) differ from all the others with two or more nodal diameters because they involve a net motion of the center of the disk. Movement with a 0-nodal diameter pattern involves axial or torsional disk movement while 1-nodal diameter displacements indicate rocking of the disk about a diameter or translation along a diameter. All other diametral orders are 'balanced' and involve no motion of the disk center. The main practical implication of this characteristic is that the 0-and 1-diameter modes will be influenced by the shaft and bearings which support the disk upon which the blades are mounted, while none of the other modes will be influenced at all by these other parts of the system. This, in turn, means that the model should be extended to include these components if accurate estimates of the 0-and 1-diameter modes are to be determined. However, this extra complication is not often included.

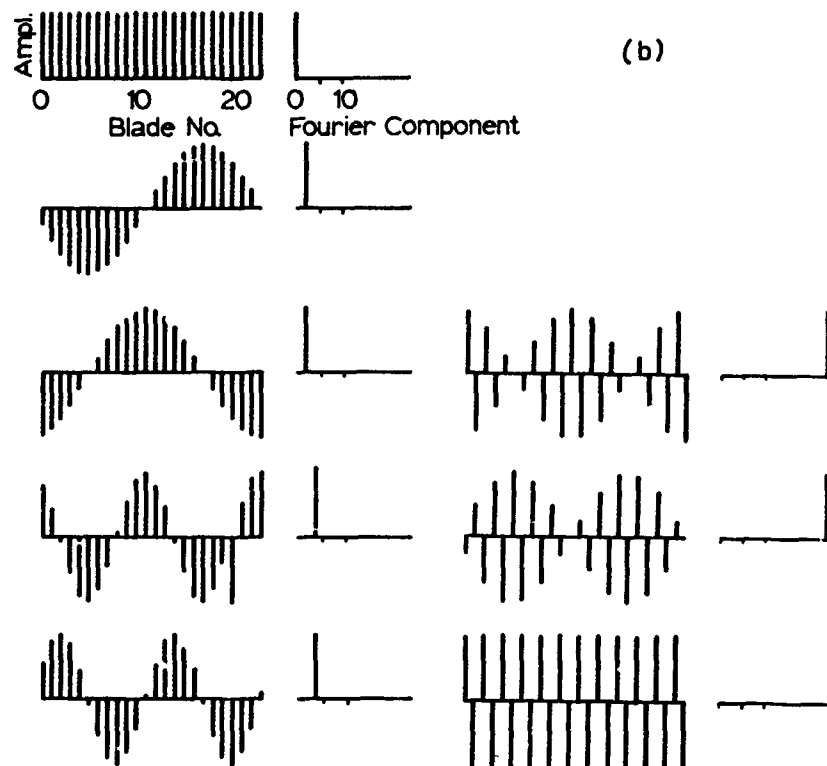
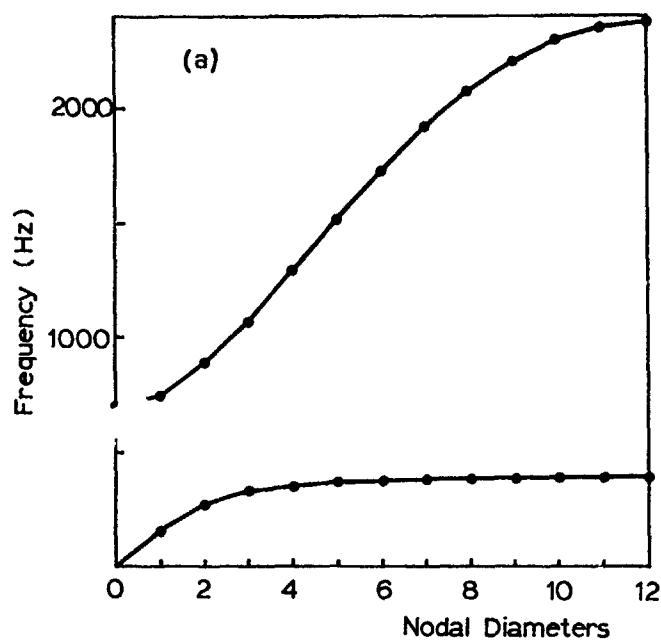


Figure 3. Natural Frequencies and Mode Shapes for Bladed Disk
(Lumped Parameter Model of 24-Bladed Disk)
(a) natural frequencies; (b) typical mode shapes

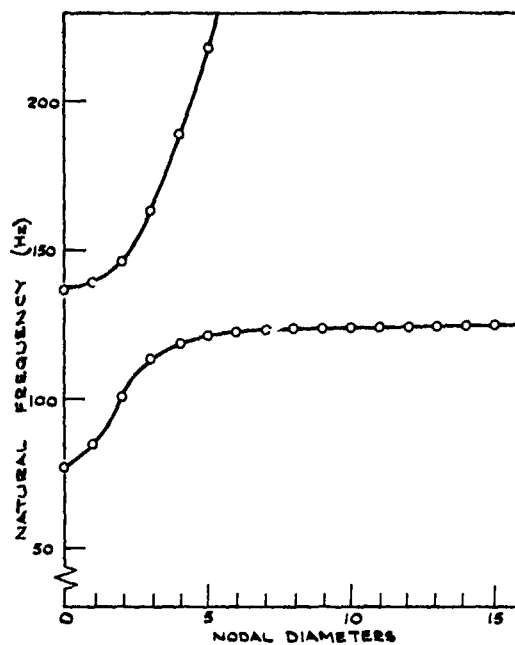


Figure 4. Natural Frequencies and Mode Shapes for Bladed Disk
(Lumped Parameter Model of 33-Bladed Disk)

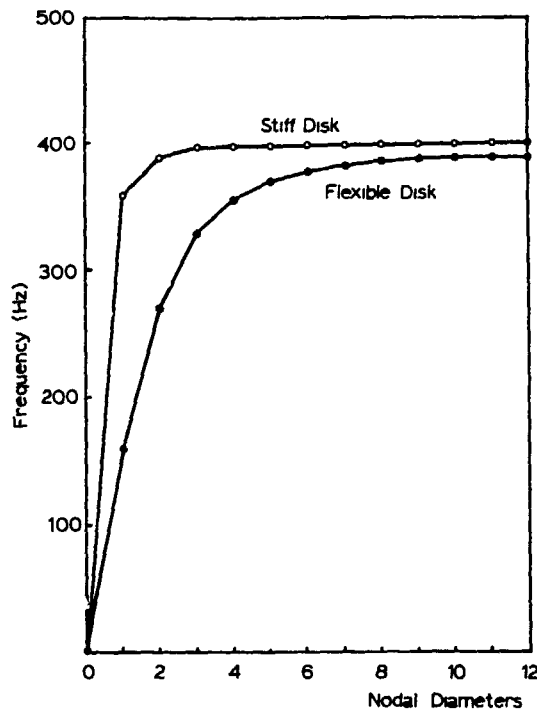


Figure 5. Vibration Properties of 24-Bladed Disk: Stiff Disk

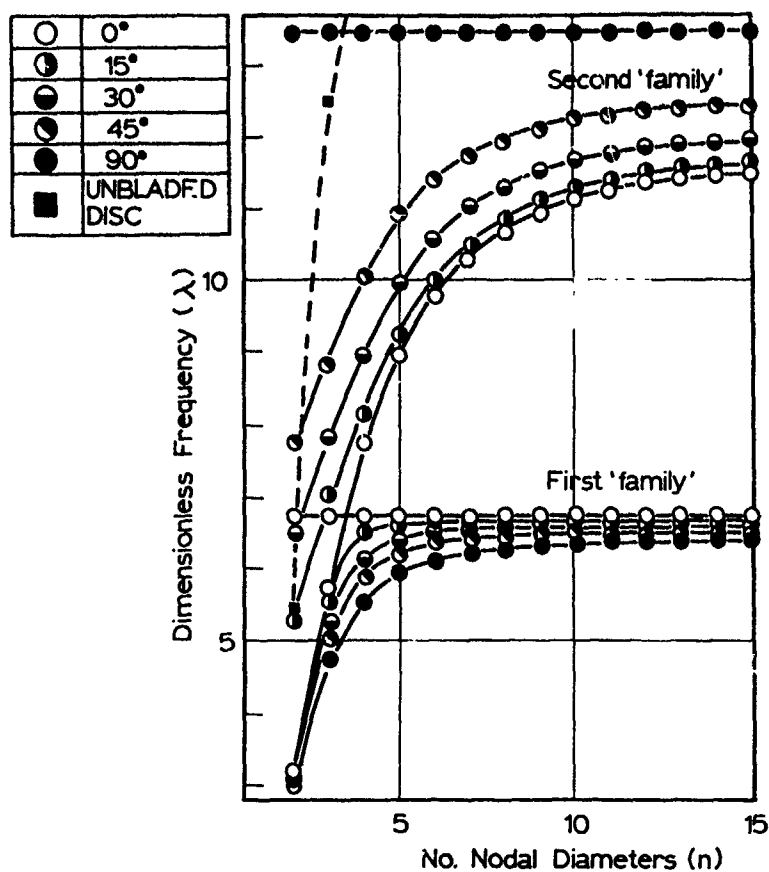


Figure 6. Vibration Properties of 30-Bladed Disk
(Beam/Plate Model - Various Stagger Angles)

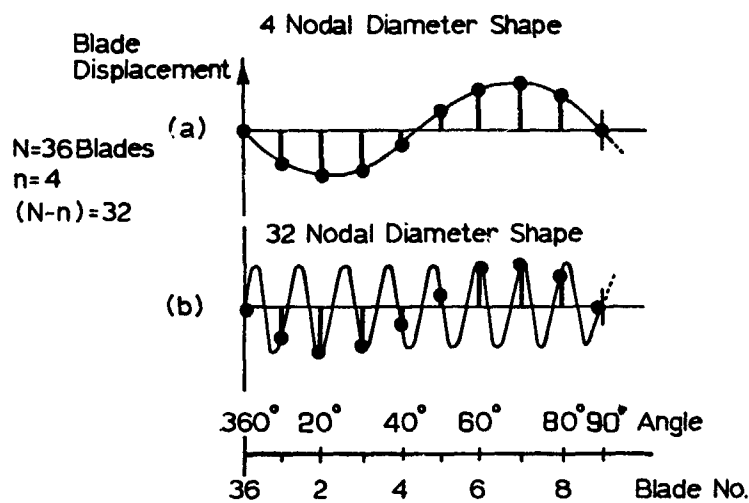


Figure 7. Discrete Descriptions of Diametral Patterns

With the bladed assembly vibration modes clearly identified, the rationale for the cyclic symmetry method of analysis is not substantiated and we can use the much simpler version of the beam and plate model (and those based on finite element models using the same approach) with some confidence. This is illustrated in Figure 8 for the 30-bladed example used above, first in the unshrouded configuration (8(a)) and the second after the addition of a tip shroud, 8(b). The latter example serves to illustrate the way in which shrouding alters the (otherwise) predictable pattern of modes and natural frequencies and will be developed further in the parameter studies and practical examples included in the next two sections.

Lastly, mention should be made of the various bladed assemblies not yet introduced here - including the cases with non-identical blades ('mistuned' assemblies) and those with deliberately non-symmetric configurations, such as blade packets. These will be discussed later, after a thorough review of symmetric, or tuned, assemblies has been completed.

MODAL PROPERTIES FOR VARIOUS BLADED ASSEMBLIES

Introduction

In this section, we shall present a series of parameter studies to illustrate the major modal properties of a range of bladed disk assemblies. No attempt is made to encompass the very wide range of configurations encountered in practical machines but a selection of parameters is made in an attempt to highlight some of the more significant influences on the natural frequencies of a bladed assembly.

The characteristics presented are based on a single reference or datum case - a simplified 36-bladed turbine. However, it is not the properties of this which are the primary interest here; rather, we shall seek to illustrate how they are influenced by changes in the system dimensions or configurations.

The system is studied in two basic configurations

- (a) unshrouded, and
- (b) shrouded

and within these groups, the influence of various design features is explored, including

- disk stiffness
- blade root flexibility
- blade stagger
- blade twist
- shroud stiffness
- shroud connection
- shroud position.

Details of the datum case are given in Figure 9.

Unshrouded Bladed Disk

(a) Datum Case

The datum system properties are shown in Figure 10 in the form of a natural frequency vs nodal diameters plot, and it is against these results that the subsequent cases will be compared.

The properties illustrate clearly the influence of both the individual (cantilever) blade properties and those of the disk alone and, indeed, indicate how these separate component data might be used to estimate the full assembly properties.

(b) Disk Stiffness

The first influence studied is that of the disk stiffness: keeping all other dimensions unchanged, the disk thickness is halved and doubled, resulting in the plots shown in Figure 11. These results are understandable and show how the assembly modes tend towards those of the components as the disk stiffness increases (so that the interblade coupling diminishes), but how the full assembly analysis becomes more important as the disk becomes more flexible.

(c) Root Flexibility

A related parameter - although quite a separate effect - is root flexibility. This is introduced to take account of the loss of rigidity which occurs at the blade/disk junction because of the root fixing used. Unlike disk flexibility, the root effect does not influence the coupling but, in effect, changes the blade stiffness with a consequent influence on the assembly properties. It is noted from Figure 12 that once the flexibility exceeds a certain level, its influence is marked but below that threshold, its magnitude is less important.

(d) Blade Stagger

In the datum case, the blades are staggered at 30° and this has the result that both flapwise and edgewise blade motions are coupled through the flexural vibration of the disc. Figure 13 shows a series of cases where the blade stagger is increased from 0° to 90° and illustrates the progressively greater influence exerted by the disk on the flapwise blade motion.

(e) Blade Twist

A further series of calculations is shown in Figure 14 for which the outer 30% of the blade is twisted (staggered) relative to the inner section. Here, it is clear how the higher families of modes are significantly influenced while the lower modes are relatively unaffected.

Shrouded Bladed Disks

(a) Datum Case

Here, the datum case is provided by adding a "standard" shroud ring around the blade tips of the 36-bladed disk used for the previous studies. The results for the

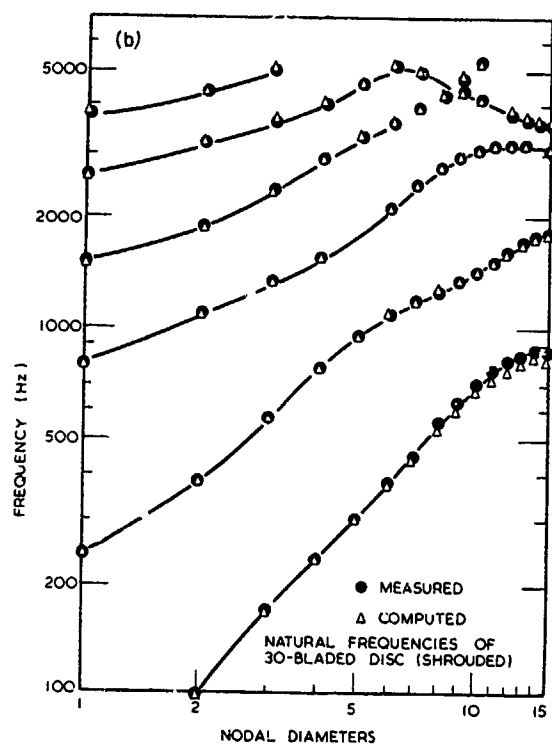
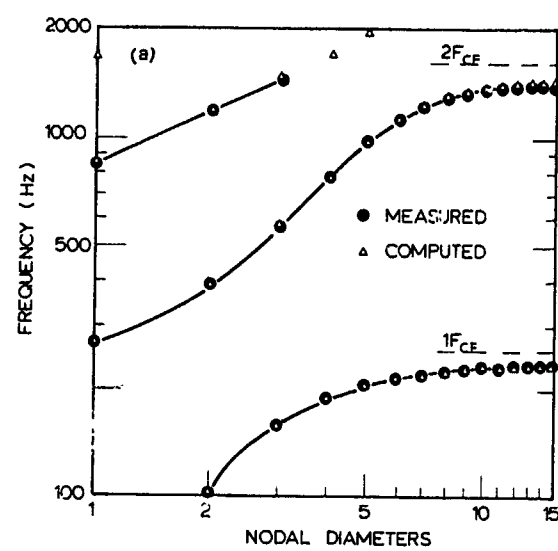
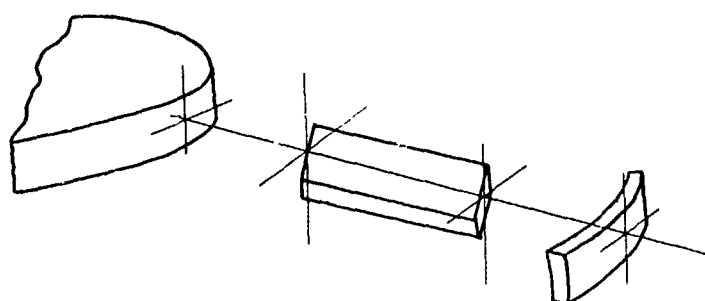


Figure 8. Vibration Properties of 30-Bladed Disk
(Cyclic Symmetry Model)
(a) unshrouded; (b) shrouded



DISK	radius = 0.050 m (inner) = 0.560 m (outer) thickness = 0.060 m	MATERIAL PROPERTIES (All components)
BLADE	length = 0.250 m width = 0.030 m thickness = 0.010 m stagger = 30° (from axis) number = 36	Modulus = 207 GN/m ² Density = 7850 kg/m ³ Poissons Ratio = 0.30
SHROUD	thickness = 0.010 m (radial) depth = 0.006 m (axial)	

Figure 9. Details of Datum Case Bladed Disk Model

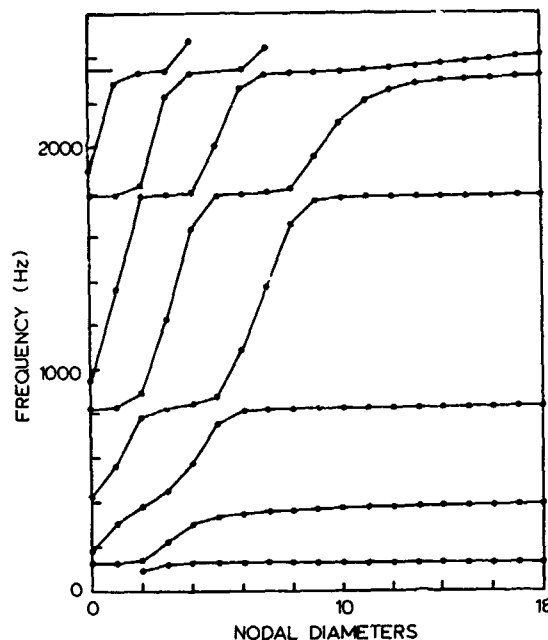


Figure 10. Natural Frequencies of Datum Case Unshrouded Bladed Disk

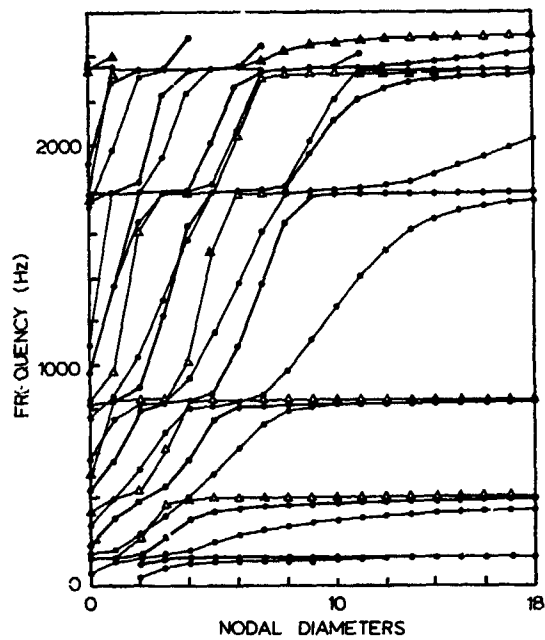


Figure 11. Effect of Disk Stiffness on Natural Frequencies
disk thickness: (o) = 0.03m; (●) = 0.06m; (Δ) = 0.09m

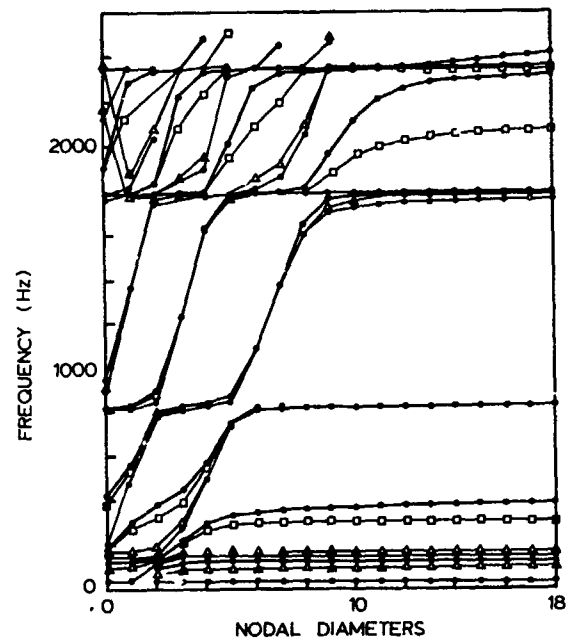


Figure 12. Effect of Root Flexibility on Natural Frequencies
(a) = 10^{-5} ; (Δ) = 10^{-4} ; (o) = 10^{-3} ; (●) = 0 Nm/rad

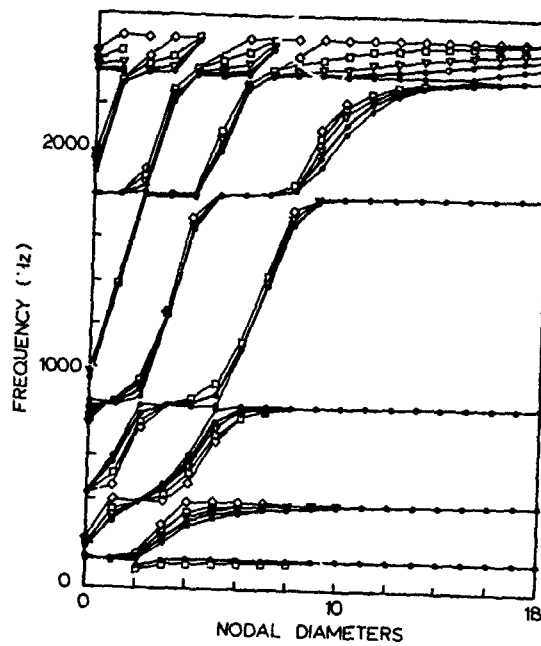


Figure 13. Effect of Blade Stagger on Natural Frequencies
 $(\circ) = 0^\circ; (\bullet) = 30^\circ; (\nabla) = 45^\circ; (\square) = 60^\circ; (\diamond) = 90^\circ$

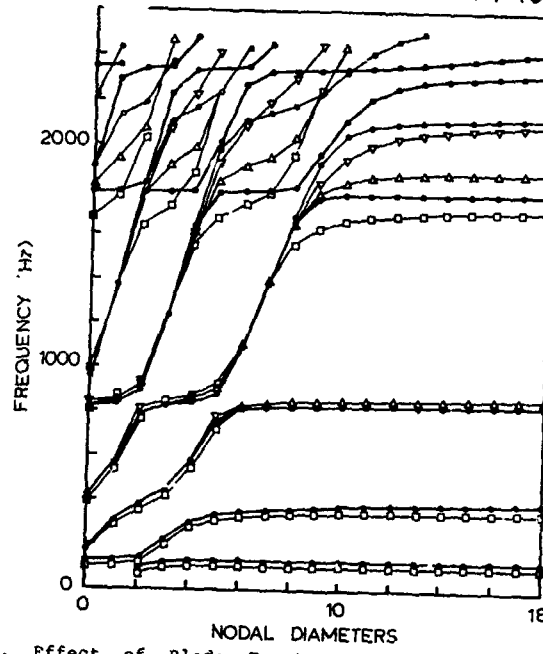


Figure 14. Effect of Blade Twist on Natural Frequencies
tip twist: $(\nabla) = -15^\circ; (\bullet) = 0^\circ; (\circ) = 15^\circ; (\Delta) = 30^\circ; (\diamond) = 45^\circ$

same frequency range as used before are shown in Figure 15(a) and immediately show rather more complex patterns of behaviour than in any of the previous cases. The main difference is that the natural frequencies in any one 'family' no longer necessarily increase steadily with the number of nodal diameters: sometimes they do, following previous experience, but sometimes not. The reason is that each mode labelled as "n nodal diameters" may indeed have n diameters, but could also (or instead) have (N-n) diameters, or (N+n) etc. (N being the number of blades). In all modes involving radial motion of the shroud, the lowest order pattern - n nodal diameters - is suppressed by the very high radial stiffness of the blades and, as a result, it is the second order, (N-n), which dominates. When the shroud is effectively dictating the coupling, as in the case when the disk is relatively stiff, then an increasing "n" involves a decreasing controlling shape, (N-n), hence the falling natural frequencies seen in this plot. This conclusion is reinforced in Figure 15(b) where the same assembly is analyzed admitting only the lowest order shroud modes to the model. This result follows the same pattern as the earlier calculations - as expected - but is clearly an inadequate representation of the actual system.

(b) Disk Stiffness

A series of calculations is included in Figure 16 where the disk is first made much more flexible than the datum case, by halving its thickness, and then much stiffer (double thickness). These results, though complex, are comprehensible. Indeed, the latter case presents an indication of the typical characteristics for an assembly of blades where virtually all the inter-blade coupling is through the shroud band.

(c) Shroud Stiffness

In the same vein, a series of calculations is shown in Figure 17 for two variants where the shroud is first less stiff and then more stiff than the reference case, this effect being achieved by halving and doubling the radial thickness of the shroud band.

(d) Shroud Attachments

In many assemblies, the connection between blades and shroud is not fully integral. Sometimes, there is a local flexibility, similar to the root flexibility, which relaxes the coupling provided by this attachment and sometimes the connections are deliberately made only in certain coordinates, or directions. In Figure 18, we see the result of making the blade/shroud attachment rigid in only 1, or 2, or 3 of the 6 coordinates previously included in the datum case. It is clear how certain modes are greatly affected by these conditions while others are barely influenced at all.

(e) Shroud Position

Lastly, we show some typical effects resulting from changing the radial location of the shroud (previously, it was at 100% blade length). In Figure 19,

results for other positions are shown alongside those of the datum case.

DYNAMIC ANALYSIS FOR PRACTICAL ASSEMBLIES (contributed by R. Henry)

Dynamic Analysis of Low Pressure Turbine Stage

Having explored the characteristics of bladed assemblies in general, we shall now present an example of a specific practical assembly analyzed by a finite element model, using the axisymmetric method outlined in Chapter 13 applied to a rotating low pressure turbine stage of a modern jet engine, Ferraris et al. (1973).

Finite Element Modelling

Figure 20 shows the finite element mesh used to calculate the natural frequencies and mode shapes of the above-mentioned turbine stage. The disk is modelled mainly with thin shell axisymmetric elements (nine elements for the flanges and ten elements for the web), connected to the disk rim using junction elements (I to VI). The rim itself is modelled with eight thick isoparametric elements. The blade is modelled with 16 twisted beam elements (see Chapter 14) and continuity of displacements and slopes at the blade root is ensured using two junction elements (VII, VIII) placed on the disk rim. The shroud element at the blade tip is modelled by additional masses and inertias in the three directions. The disk is clamped as shown in Figure 20. The blade tip is free in the X and Z directions, supported in Y and restrained in torsion. The whole model results in 288 effective degrees of freedom.

Dynamic Analysis

The first six natural frequencies and mode shapes are computed for the structure vibrating with $n = 0$ to 5 nodal diameters and at various speeds of rotation Ω . The results are presented using a dimensionless frequency parameter $f_r = f/f_{01}$, f_{01} being the fundamental natural frequency for 0 nodal diameters) and a dimensionless speed $\Omega_r = \Omega/f_{01}$. The natural frequencies related to n and Ω are presented in Figure 21(a) and (b) and the associated mode shapes are arranged in families $f_{n1}, f_{n2}, \dots, f_{n6}$ and presented in Figure 21(c) to (g).

Family I, Figure 21(c), is mainly a disk-rim vibration mode while the blades move in the XZ plane following the rim motion. It is seen that the natural frequencies of family I approach the first bending frequency of the clamped blade for increasing values of nodal diameters but that the rotation effect results in a 30 to 40% increase of the natural frequencies (Figures 21(a) and (b)).

Family II, Figure 21(d), shows a disk bending mode. Motion of the rim is limited and the blade bends in the XZ plane. It can be seen in Figure 21(d) that the rotation effect is significant on the various n diameter modes as the associated natural frequencies increase by more than 20% in the range of rotation speeds studied (from rest to operating speed).

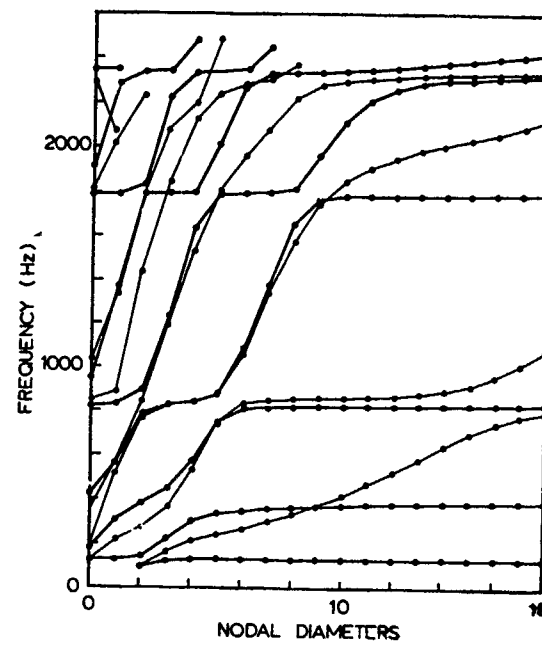


Figure 15. Natural Frequencies for Datum Case Shrouded Bladed Disk
 (a) (●) full analysis
 (b) (○) analysis omitting higher order terms

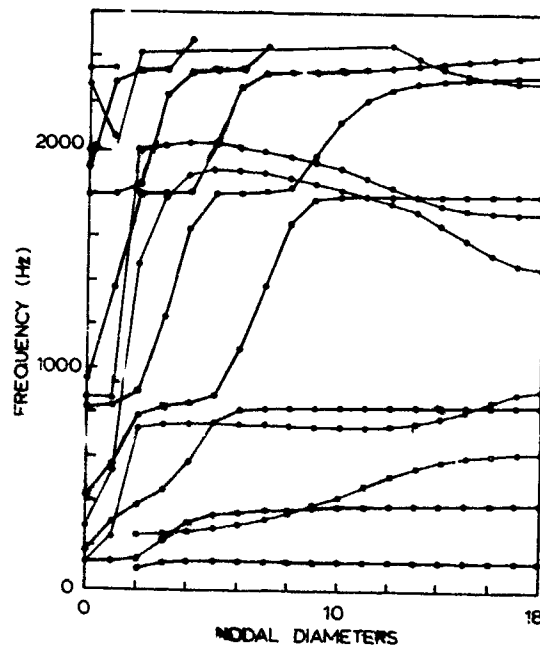


Figure 16. Effect of Disk Stiffness on Natural Frequencies
 disk thickness: (●) = 0.06m; (○) = 1.00m

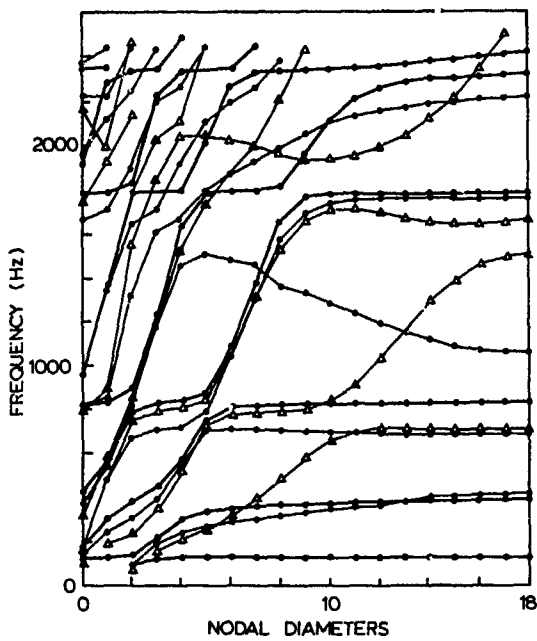


Figure 17. Effect of Shroud Stiffness on Natural Frequencies
shroud thickness: (o) = 0.006m; (*) = 0.012m; (Δ) = 0.024m

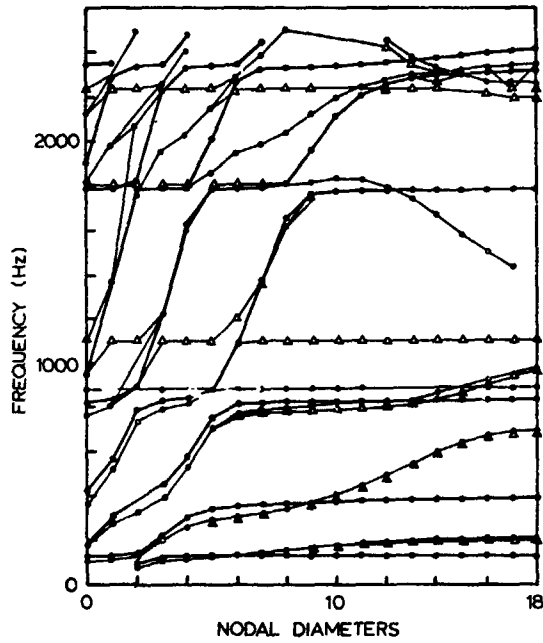


Figure 18. Influence of Blade/Shroud Connection on Natural Frequencies
tip coupling: (*) = 6 coords; (o) = 2 coords; (Δ) = 1 coord.

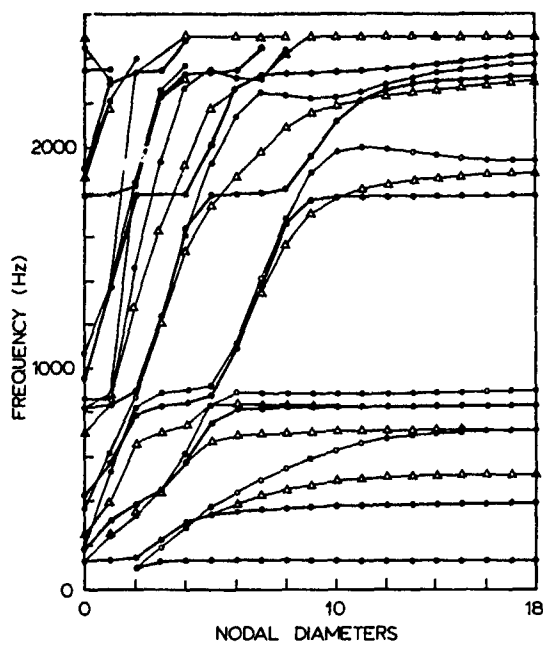


Figure 19. Effect of Shroud Position on Natural Frequencies
shroud height: (*) = 100%; (o) = 90%; (Δ) = 60% blade length

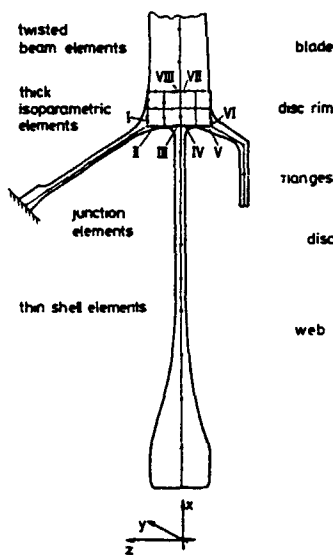


Figure 20. Finite Element Model for Low Pressure Turbine Stage

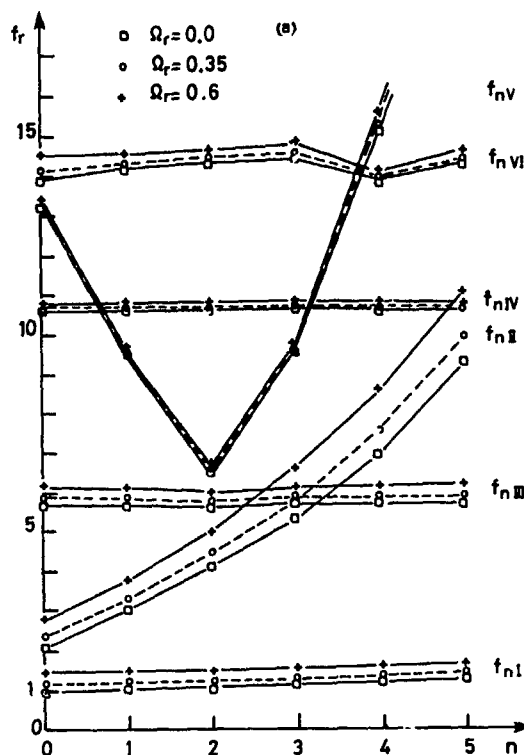


Figure 21a. Vibration Properties of a Low Pressure Turbine Stage

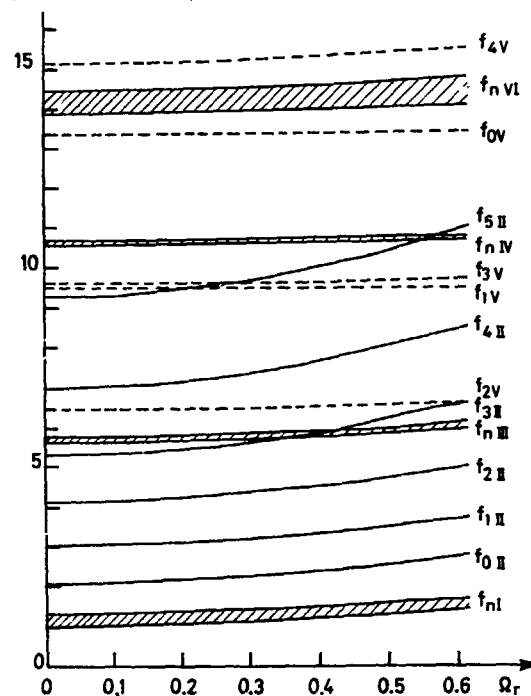


Figure 21b. Vibration Properties of a Low Pressure Turbine Stage

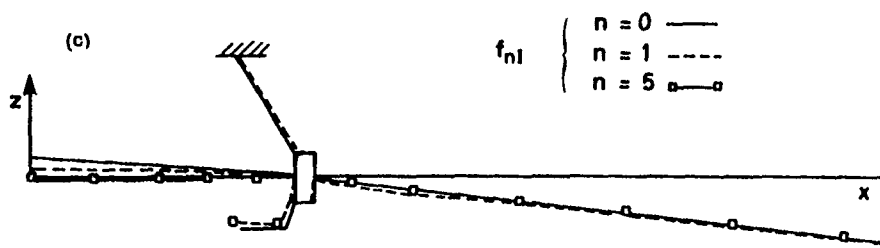


Figure 2lc. Vibration Properties of a Low Pressure Stage

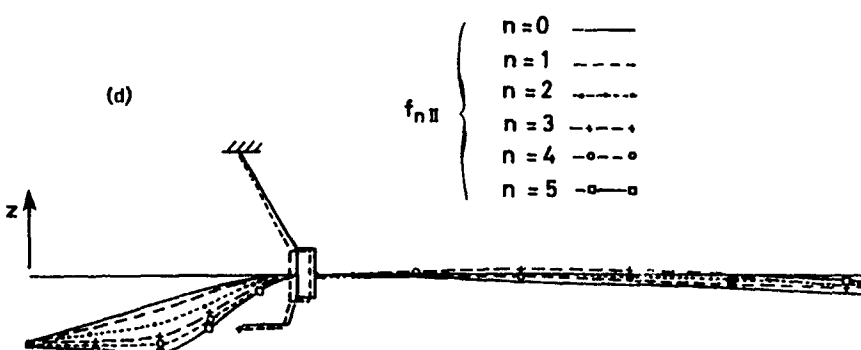


Figure 21d. Vibration Properties of a Low Pressure Stage

Family III, Figure 21(e), is mainly a blade vibration mode. Here again, the natural frequencies tend to the first flap bending frequencies of the cantilevered blade as the number of nodal diameters increases. The axisymmetric part of the stage (disk plus rim) undergoes small amplitudes of vibration, except for $n = 2$ and $n = 3$ which show large motion for the disk-rim and the disk respectively. The rotation effect results in a frequency increase of up to 8%.

Family IV mode shapes show mostly a torsional motion of the blade with very little motion of the disk. As n increases, the natural frequencies tend towards that of the first torsion mode of the cantilevered blade. For this group of modes, it can be seen in Figure 21(d) that the rotation speed has a negligible effect, never exceeding 1.5% for any value of n .

Family V, presented in Figure 21(f), shows a disk-rim vibration with strongly coupled second bending-torsion motion of the blade and, as n increases, a natural frequency tending to the second torsion mode of the cantilevered blade. Except for $n = 2$, for which the frequency increases by about 3.5%, the rotation effects are relatively small.

Family VI, Figure 21(g), is a highly coupled vibration mode with significant motion of the disk and rim, especially for $n = 1$ and 4. The blade vibrates in a coupled bending-torsion mode and the frequency tends to the second bending mode of the cantilevered blade. For this family, the rotation effects result in a rather small increase in the frequencies (2.5% for $n = 1$ to 5 and 8% for $n = 0$).

Lastly, examination of Figures 21(a) and 21(b) shows clearly that the disk influence is low for the families I, III, IV and V. It can also be noted that the families I, II and, up to a point, III are affected by the centrifugal effects.

Comments

The axisymmetric method is well suited to predicting the vibration behaviour of any rotating bladed assembly where the number of blades is high, i.e., the actual structure must have an essentially axisymmetric behaviour. The results obtained for this low pressure turbine stage example show that an adequate model of such structures must consider all the coupling effects due to the blade and disk geometry along with those due to rotation. If the number of blades is low and the blades cannot be modelled by beams (as is the case for many fan assemblies), the mode shapes are no longer axisymmetric (simple diameters and/or circles for nodal lines), and the previous hypothesis is no longer valid. In these cases, one has to introduce methods using cyclic symmetry for rotationally periodic structures.

VIBRATION PROPERTIES OF MISTUNED AND PACKETED BLADED ASSEMBLIES

Mistuned Assemblies

(a) General

All the examples presented so far have related to 'tuned' or symmetric assemblies where all the blades on one stage are identical to each other. In practice, such uniformity is seldom attained, either by chance or by design, and so it is appropriate to consider next the implications of a loss of complete cyclic symmetry for the vibration characteristics. We shall first examine 'mistuned' assemblies, where small blade-to-blade variations are admitted to the model, representing either random manufacturing variations or deliberate selection of 'light' or 'heavy' blades as is sometimes practiced during assembly. Later, we shall consider other, more extreme, departures from symmetry.

Using any of the assembly models which permit the individual representation of each blade (i.e., those models which do not presuppose cyclic symmetry), we find that a small amount of mistuning (i.e., blade variations of typically a few percent) has a relatively minor effect on the assembly natural frequencies but can introduce potentially significant changes to the mode shapes. This result is itself important because of the central role played by the mode shapes in determining the blade response characteristics.

(b) Frequency Splitting

Many of the essential characteristics of mistuned assemblies can be illustrated by the single example given in Figure 22 which relates to an unshrouded 24-bladed disk used for a series of carefully-controlled experiments. We see that as a result of random mistuning of the set of blades, each double mode degenerates from the pair of identical natural frequencies with pure n -nodal diameter mode shapes and 'splits' into two distinct modes with close natural frequencies and mode shapes which now contain several diametral components. For those double modes whose natural frequencies are well separated from each other in the tuned state - here, the low order modes with 2, 3, and 4 nodal diameters - the mistuned assembly mode shapes retain a strong resemblance to the original pure nodal diameter patterns. For many of these modes, the extra diametral components introduced by mistuning are relatively small compared with the 'parent' order. However, as we progress through the family of modes associated with one of the blade cantilever modes, we see that the contamination of the assembly mode shapes increases to the point where some of them can no longer be associated with a particular nodal diameter pattern at all. This situation arises when the tuned system natural frequencies are separated by the same order of magnitude as the frequency split induced by the mistuning. This, in turn, is related to the degree of blade mistune which can conveniently (though not uniquely) be specified in terms of the individual cantilever frequencies of the

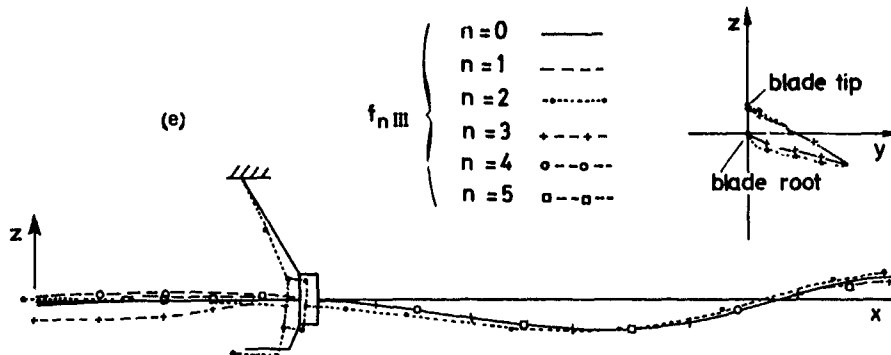


Figure 21e. Vibration Properties of a Low Pressure Stage

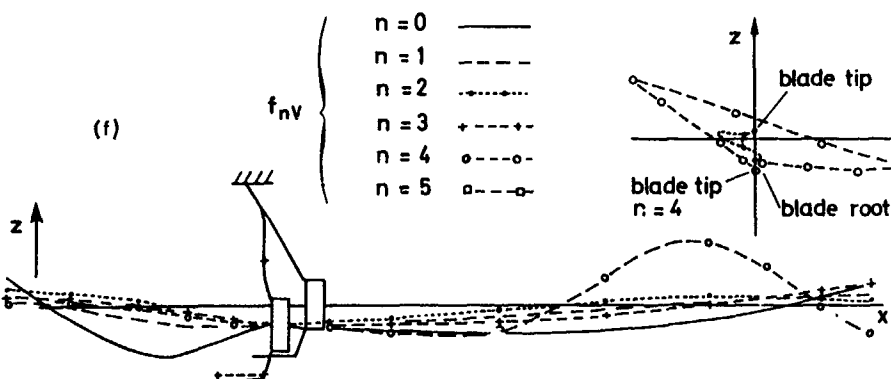


Figure 21f. Vibration Properties of a Low Pressure Stage

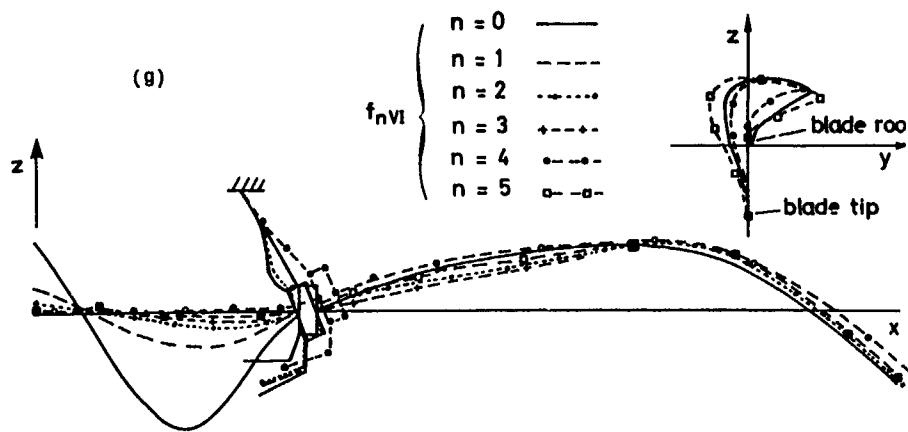
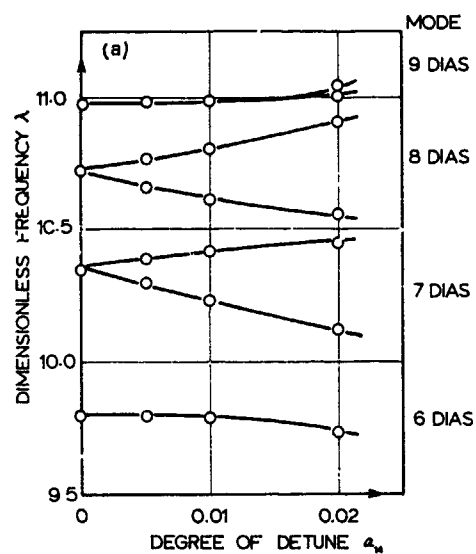


Figure 21g. Vibration Properties of a Low Pressure Stage

Figure 22a. Frequency Splitting Effect Caused by Regular Mistuning
(a) separated modes; (b) close modes

frequencies of the actual blades used. As a rough guide, a scatter of $\pm x\%$ in individual blade cantilever frequencies will generate frequency splits of up to $x\%$ in the various double modes although the exact amount will depend on the specific distribution of the blades as well.

Single modes are only slightly affected by mistuning, the variations in natural frequency and mode shape always being of the same order as the blade mistune itself.

(c) Patterns of Behaviour

Although the vibration modes can always be computed for a given assembly mistune configuration, such calculations are expensive and so it is useful to establish any patterns which may relate specific mistuning arrangements with consequent changes from the tuned system datum properties. One such pattern is found to apply to those modes which exhibit a clear frequency splitting behaviour: i.e., those modes - usually with few nodal diameters - which have well-separated natural frequencies. It is found that in order for such an n-nodal diameter mode to split due to mistuning, the variation in individual blade frequencies (the mistune arrangement) must contain a component of order $2n$. In other words, if the individual blade frequencies are given by

$$f_i = f_0 (1+x_{2n} \cos (2n\theta_i))$$

where

f_0 is the mean blade frequency,
 f_i is its individual cantilever
frequency, and
 θ_i is the position of blade i ,

then all modes with n nodal diameters will split and the extent of the frequency split will be closely related to the magnitude of x_{2n} . Modes with other nodal diameter patterns will generally not be split. This pattern ceases to apply when, as mentioned previously, the natural frequencies of the $(n-1)$ -, (n) -, and $(n+1)$ -diameter modes of the tuned system are already close together. Some examples of this effect as applied to a 30-bladed disk are shown in Figure 23 where both regimes are illustrated.

Another pattern which is observed with regular mistuning concerns the mode shapes. In all cases of mistuning, these shapes are distorted from their regular $\cos(n\theta)$ form but in the case of cosine (or other periodic) mistuning, the distortion itself is also regular, and follows a standard pattern. If the cosine mistuning is of order k , then the modes originally identified by n nodal diameters will be found to contain some component of $(n+k)$, $(n+2k)$. . . $(n-k)$, $(n-2k)$. . . etc. diameters.

The significance of the various diametral components present in each mode shape will be fully appreciated in the later discussion on forced vibration - each mode is susceptible to resonance whose severity is determined by these components.

(d) Effects of Damping

All the preceding discussion applies strictly to undamped structures, although very little change would result if proportional damping were introduced (see Chapter 13). However, it is possible that in this particular case the actual mechanical (and/or aerodynamic) damping may have a significant influence if, or because, it is distributed in a non-proportional way. In practice, non-proportional damping will result if the actual source of damping is localized and is not distributed in the same way as the mass and/or stiffness of the structure; a situation likely to apply to many bladed assemblies.

The significance of the distribution of damping lies in the fact that the modes of non-proportionally damped systems may be complex and, further, that systems with close natural frequencies are known to be more prone to significant degrees of complexity in their mode shapes. All the mode shapes illustrated so far have been real, with each blade vibrating exactly in or out-of-phase with the others and thus reaching its maximum value at the same time as all the others. In a complex mode, adjacent blades can have any relative phase difference (and not just 0° or 180°) and this can have a very marked effect on the aerodynamics.

Blade Packets

The next assembly to be considered is that of a packet of blades, often a group of up to 7 or 8 cantilevered blades connected by a shroud band. Although analysis of this configuration usually ignores the disk coupling (some examples do admit disk or root flexibility, but not inter-blade coupling), it is justified in the same way as was our earlier study of an individual blade; the vibration properties for a complete (packetized) bladed disk are related to those of the single cantilevered packet by these latter providing asymptotic values and classification of the various families of modes of the full bladed system.

The basic characteristics can be illustrated using a simple lumped parameter model, such as that shown in Figure 24(a). The natural frequencies and mode shapes for a six-bladed packet of this type are shown in Figure 24(b) from which a general trend is seen: one fundamental mode with all blades moving together which is unaffected by the 'shroud' stiffness followed by a group of five modes whose natural frequencies are grouped together and which are largely controlled by the shroud stiffness. Figure 24(c) shows a series of results based on the same very simple model incorporating two, three, and up to six blades in a single packet. The trend of one fundamental in-phase mode plus a group of $(N-1)$ modes is clearly seen throughout and it is also noted that the basic two-blade packet yields the essentials of the vibration properties of the other configurations with more blades.

The next level of model is one which represents the blades and the shroud

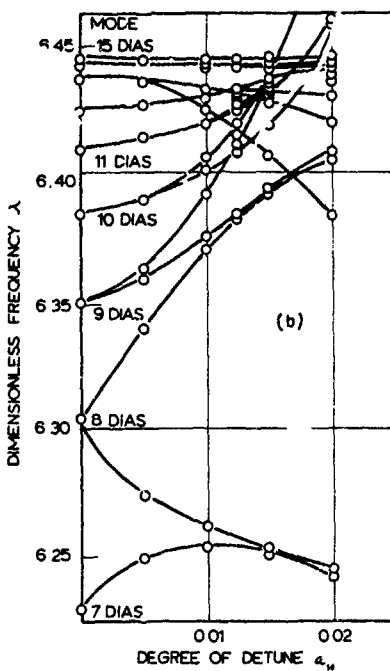


Figure 22b. Frequency Splitting Effect Caused by Regular Mistuning
(a) separated modes; (b) close modes

MISTUNED

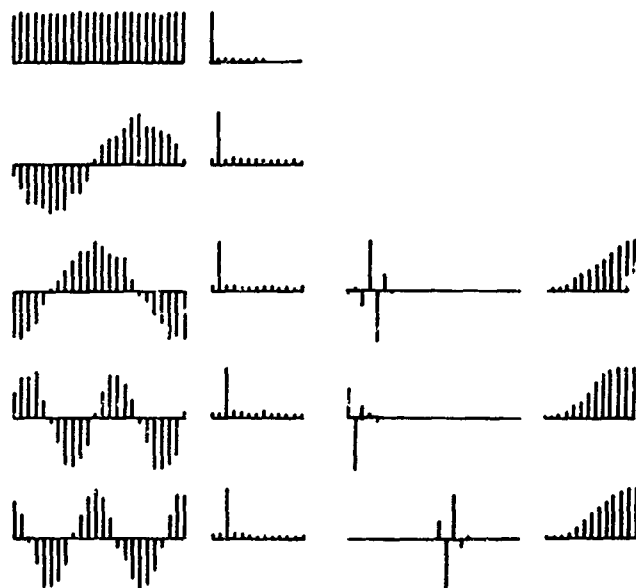
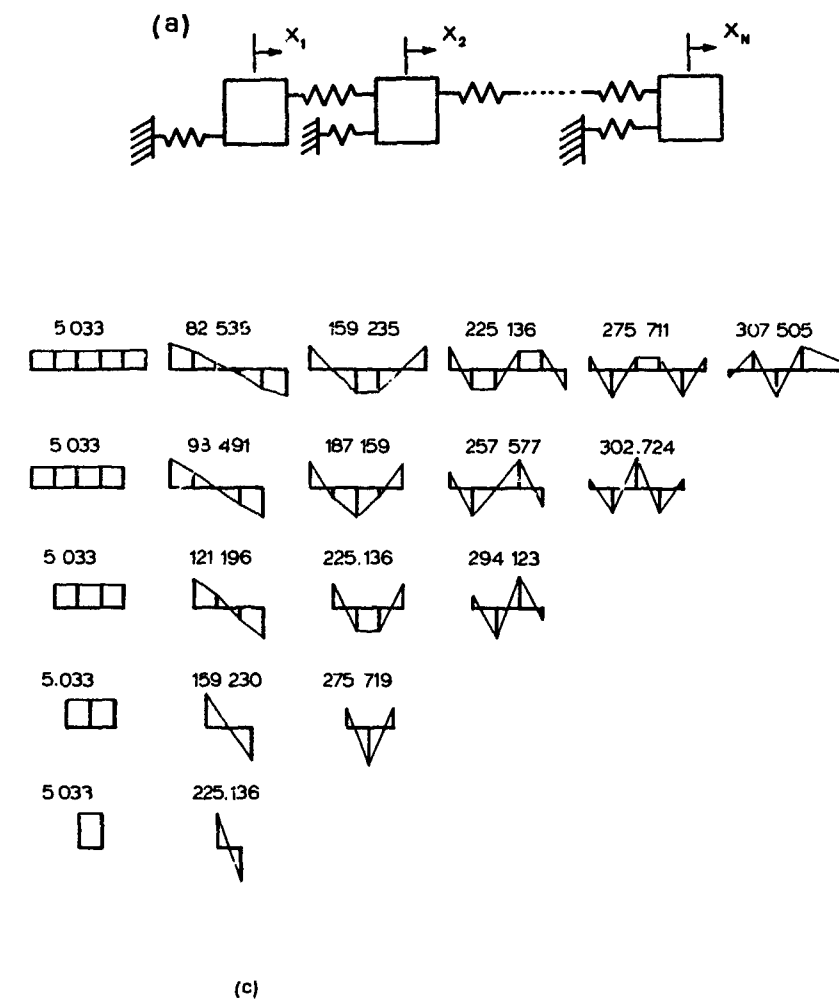
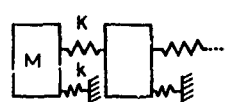


Figure 23. Vibration Properties of a Mistuned 24-Bladed Disk



(c)



$$\begin{aligned} M &= 10 \text{ Kg} \\ K &= 10^8 \text{ N/m} \\ k &= 10^3 \text{ N/m} \end{aligned}$$

Figure 24. Vibration Properties of a Simple 6-Blade Group
 (a) model
 (b) natural frequencies and their mode shapes
 (c) various group sizes

elements as beams, as shown in Figure 25(a). Results from the analysis of a specific example of this type are shown in Figure 25(b) where it is noticed that, in fact, there are two separate sets of vibration modes - the in-plane and out-of-plane modes. In this example, these two sets are totally independent of each other but this is a direct result of the zero stagger of the blades. Examining each of the separate results shows that the same trend noticed in the simple mass/spring model characteristics applies here also, with a single in-phase fundamental mode followed by a group of shroud-controlled modes in a relatively narrow frequency band. In this (more representative) mod-1, the out-of-phase modes exhibit clear and simple shapes by which the various modes are identified - the second mode being a "rocking", the third a "U", the fourth "S", and so on, depending upon the number of blades included.

A study was made using a finite element beam model to examine the significance of blade number on the packet's vibration properties, Thomas and Belek (1977). As heralded by the very simple example quoted above, it was found that the detailed analysis for a two-bladed packet could form the basis for accurate prediction of the corresponding modes of other packets containing any number of similar blades. Some results to illustrate this are shown in Figure 25(c), still based on a set of blades with 0° stagger to the plane of the 'disk'.

Finally, we consider the properties of a packet in which in-phase and out-of-phase motions are coupled by the blades being staggered. In this case, all the modes are coupled and contain some displacement in both in-plane and out-of-plane directions although, in many cases, each individual mode may be predominantly in one or the other directions. An example derived from the earlier six-bladed packet is shown in Figure 26.

Packeted Bladed Assemblies

Packeted Assembly Configurations

Probably the most complicated bladed assembly of all is the packeted bladed disk in which all the previously-discussed elements are present - disk flexibility, interblade coupling, and the lack of cyclic symmetry. The basic feature is a discontinuous shroud, there being gaps at a number of points depending on the specific packeting arrangement used. There are various possible configurations of this format, ranging from a simple case where blades are coupled together in pairs ("N/2 packets of two blades") to the most complex where blades are grouped in packets of different numbers spaced irregularly around the disk. Perhaps the most likely arrangement to be encountered is one where there exist a number of identical packets ("P packets of p blades each") - referred to as 'regular packeting'.

One way of viewing a packeted assembly is as a special type of mistuned system, the main differences from the previously discussed cases being in the regularity of the 'mistune' and also in its magnitude - likely to be considerably greater than that due to blade manufacturing tolerances. Such an approach provides some insight into what particular characteristics might be expected to apply to this type of bladed assembly since the 'mistune' applicable in this case has some similarities with regular blade mistune mentioned earlier.

Another way of viewing regularly packeted assemblies is to consider the subassembly formed by a single packet of blades as a 'superblade' so that the complete system consists of a disk with a (small) number of (identical) superblades. Since the number of 'blades' in this case would generally be small, the modes of the system would not necessarily have simple nodal diameter shapes (as is the case for a large number of blades) but would each include several prominent diametral components, although the diametral orders present in each mode would be known a priori.

Case Studies

The calculations for the vibration properties of a packeted bladed assembly are just as expensive and extensive as those already encountered for mistuned systems. As a result, it is once again of some importance to establish what patterns or trends exist in these characteristics and to seek ways of deducing or estimating them without necessarily undertaking a 'full' analysis. In this section, we shall present some results from a study made using both of the simple models of a bladed disk - the mass-spring representation and the uniform beam and plate model - in which the blades are interconnected in a variety of different packeting configurations. The latter studies are based on a simple 30-bladed disk shown in Figure 27

The first series of results shown in Figure 28 derive from the very simple mass-spring type of model and include details of the natural frequencies and mode shapes for a 36-bladed system with a number of different packeting arrangements. The results are summarized in the graph of Figure 28 where the principal diametral component has been used to classify each mode (since there is generally more than one order present in the mode shape). Also shown, on the graph axis, are the natural frequencies of the corresponding single packet of 'blades' with their roots grounded, so that the full packeted bladed disk frequencies can be seen in relation to those of the cantilevered blade packet. A pattern is clearly seen from these few examples leading us to the possibility that the full packeted assembly natural frequencies can be effectively deduced from (a) those of a single blade packet together with (b) those of the continuously shrouded assembly. Both of these two sets of calculations are very much easier to perform than those of the fully packeted assembly.

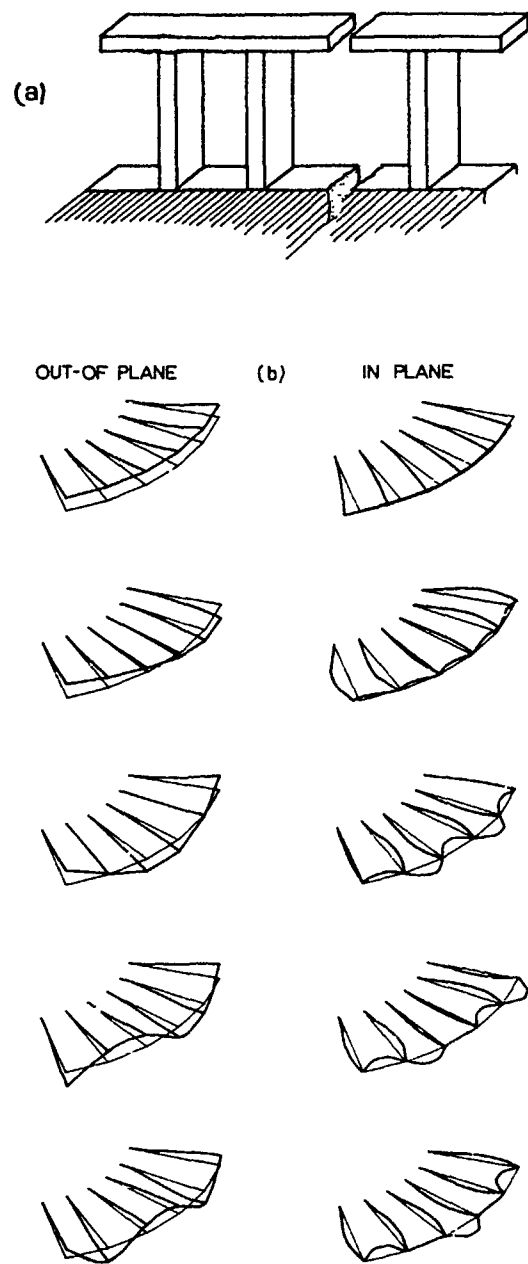


Figure 25. Vibration Properties of a Blade Packet
(Unstaggered Blades)
(a) model
(b) mode shapes

Family	p=1	p=2	p=3	p=4	p=5	p=6
1A	261.18	241.19 504.21	235.34 365.44 707.92	232.76 308.95 518.62 808.04	231.21 280.83 417.80 639.04 857.89	230.48 290.58 375.04 526.43 723.72 876.32
1T	355.20	331.25 1494.11	324.43 1490.03 1490.70	321.22 1470.67 1487.33 1496.97	319.35 1438.52 1485.34 1493.98 1497.81	325.87 1403.76 1480.34 1482.56 1491.86 1492.52
2A	1618.95	1504.78 1628.08	1468.23 1549.48 1683.70	1454.78 1502.28 1586.36 1728.97	1454.19 1477.43 1534.60 1619.48 1766.04	1451.55 1489.32 1535.88 1571.21 1649.94 1818.31
2T	2181.24	1798.31 2050.23	1758.64 1809.96 2017.31	1780.03 1798.37 1814.51 2002.58	1777.26 1790.66 1805.69 1816.69 1994.26	1761.65 1766.02 1798.30 1808.26 1814.32 2038.49
3A	3506.94	3397.82 4380.69	3335.34 3920.34 4373.06	3305.90 3760.86 4204.97 4363.18	3288.75 3629.16 3953.30 4045.29 4356.75	3287.05 3575.05 3869.36 4008.06 4053.66 4344.77

Variation of cantilevered packet natural frequencies (Hz) with number of blades in the packet (p)

A: Axial or out-of-plane

T: Tangential or in-plane

(C)

Figure 25. Vibration Properties of a Blade Packet
(Unstaggered Blades)
(c) natural frequencies for various packet sizes

15-30

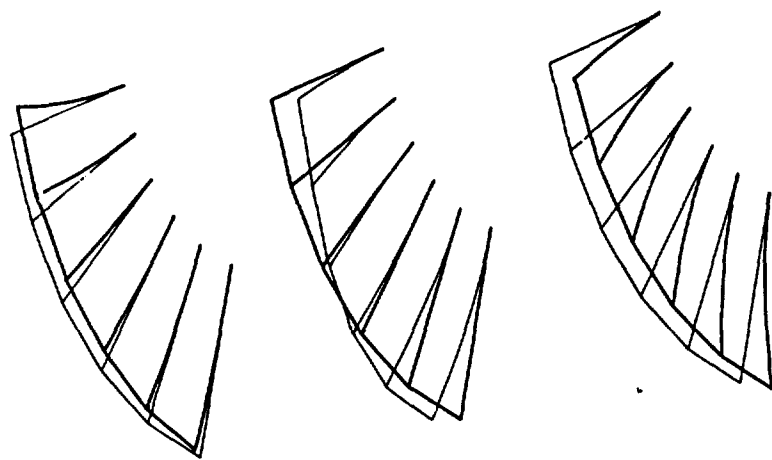


Figure 26. Mode Shapes for a Blade Packet of Staggered Blades

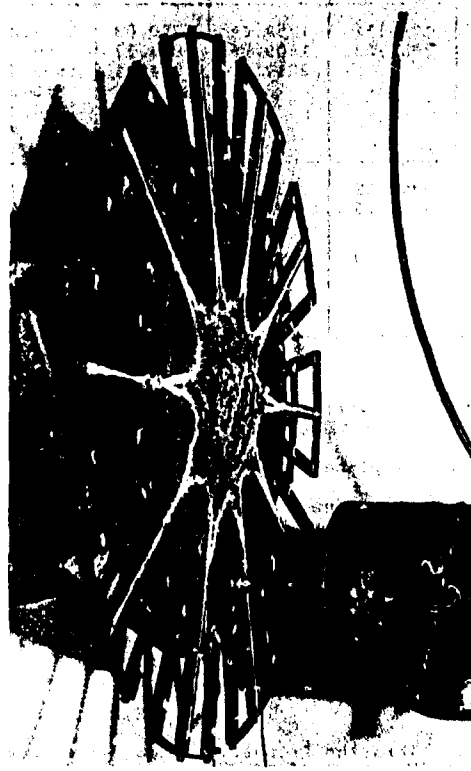


Figure 27. Packeted Bladed Disk Testpiece

A second example is shown using the more representative beam and plate type of model, again referred to a 30-bladed disk. Using the general model of this type (i.e., one which does not presuppose cyclic symmetry), we can analyze any desired packing configuration and two specific cases are illustrated in the results shown in Figure 29. Using the same form of presentation as before, we show three sets of natural frequencies on the same plot: (a) those for a single packet of blades with roots cantilevered; (b) those for the bladed disk when continuously shrouded, and (c) those for the packed bladed disk. As before, with the simpler model, there is strong relationship between the first two of these sets of results and the third, although in this case they represent more of a trend than an exact pattern. Two different packing arrangements produce the same essential result.

It was mentioned earlier that the principal diametral component of each mode shape was used to identify that mode on these plots, whereas in fact each such shape has several significant components. Once again, a pattern is observed which connects the number of blades on the disk and the number of blades in a packet with the combinations of diametral orders which appear together in the various modes. For example, taking the case cited in Figure 29, we find that each of the modes has a shape which contains one of the following sets of diametral components:

- (a) 0,5,10 or (b) 1,4,6,9,11,14 or
- (c) 2,3,7,8,12,13

A different set of diametral orders applies for other bladed assembly configurations but the connection with the essential parameters of the packing is self-evident.

FORCED VIBRATION RESPONSE

Scope of Response Analysis

Although the main objective of this chapter has been to establish the modal properties of the bladed systems of interest, we shall include some brief consideration of the forced response behaviour as well. As mentioned in Chapter 13, such a response analysis requires the introduction of additional information in the form of the definition of a specific forcing function to be considered plus the inclusion of some damping terms. In this application, both of these features involve assumptions or information which extend beyond the structural dynamics aspects that are strictly the concern of this chapter.

We shall focus our attention in this section on two specific excitation cases and one specific assumption regarding the damping effects. The first excitation case is that of a single point harmonic excitation, such as is used for most vibration test/measurement procedures. The second, and major, case will be that of 'engine-order' excitation: that which exists when a bladed disk rotates past (or through) a steady flow pattern which is nonuniform around the annulus. In such a

situation, each point on the rotating system experiences the variations in steady axial pressure or force as time-varying, and thus responds by vibrating at a frequency or frequencies directly related to the speed of rotation. Such an excitation not only has a characteristic frequency (an integer multiple of the rotation speed) but also has a characteristic shape since it is applied simultaneously to all points around the bladed assembly.

In each case, it is necessary to include some form of damping and that which is generally assumed is proportional, thereby permitting most of the computational effort to be made on the basic undamped system, introducing the damping only at the very last stage. However, it should be noted at the outset that this is a very crude approximation to the real physical conditions.

Review of Forced Response Analysis

The basis for a general forced response analysis was presented in Chapter 13; explicitly, for the single point harmonic excitation condition but also, implicitly for the more complex situation of engine-order excitation. A very important feature of all types of forced vibration is the double requirement to obtain a resonance condition: namely, an excitation at the appropriate frequency and with the appropriate shape. The former is self-evident but the latter condition is more subtle and, indeed, plays a major role in the forced vibrations of interest here. In its simplest form, it is clear that a particular mode of vibration will not be excited into resonance, even at its natural frequency, by an excitation force which is applied at a nodal point of that mode. This is a very simple example of the excitation shape being incompatible with the mode shape and we shall find other more complex ones apply in this study.

We shall consider the implications of this aspect of forced vibration for the bladed assembly whose mode shapes, as we have already seen, are conveniently described in terms of the diametral components present in the circumferential distribution of the disk and blades' displacement. Thus, we shall be looking at or for the existence of similar diametral patterns in the excitation functions as a measure of their potential ability to excite resonant vibrations in the bladed assembly. The frequency of the exciting force(s) is obviously of direct significance as well, but the shape or distribution must not be overlooked.

Consider first the single point harmonic excitation which will be assumed (for the purpose of this discussion) to be applied on a specific blade. The effective forcing function, as described in the governing equations of motion in Chapter 13, will be a vector which only has one non-zero element so that

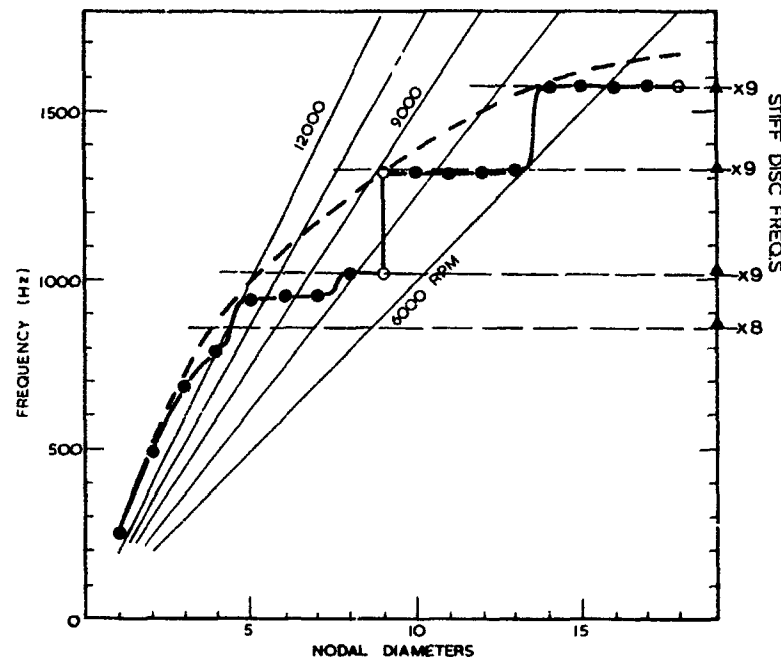


Figure 28. Vibration Properties of Packeted Bladed Disk (Simple Model)

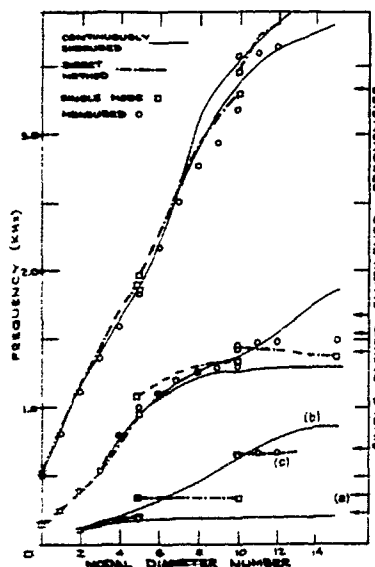


Figure 29. Vibration Properties of Packeted Bladed Disk
(Beam/Plate Model)
(a) single packet
(b) continuously shrouded
(c) packed

$$\{f(t)\} = \begin{Bmatrix} 0 \\ 0 \\ \vdots \\ f_j \\ 0 \\ \vdots \\ 0 \end{Bmatrix} e^{int} \quad (11)$$

Provided that the point of application of this force is not a node of any of the bladed assembly's modes of vibration, then it will be capable of exciting all modes. The 'effectiveness' of the excitation and the strength of the resonant response at each natural frequency will depend partly upon the proximity of the exciting frequency to the natural frequencies of the various modes and partly on the relative amplitude of each mode shape at the drive point. If any of these have a node at the drive point then the amplitude of the response will be zero but if the point is near an antinode, then a large response will be generated at resonance. It is certainly possible that any given excitation point may well find itself on or near to a node for some modes and so such a single point excitation cannot be guaranteed to excite all modes. This is important if such an excitation is being applied to measure the modes of a bladed system: several such measurements may be necessary before all the modes have been sighted.

The engine-order type of excitation is more complex but more important since it constitutes a major source of steady forced vibration in most running turbomachines. As mentioned previously, we shall consider here the excitation generated by the rotation of a bladed system past a static pressure or force field, the strength of which varies with angular position around the machine - see Figure 30. Such variations in the steady flow are inevitable consequences of upstream obstructions - vanes, bearing supports - and other maldistributions in the fluid flow. The rotation of the bladed assembly causes such variations in pressure to be experienced by the blades as time-varying forces with a frequency or periodicity based on the rotation speed. The effective excitation can be prescribed by an analysis of the following form, here based on a particular case.

Suppose the steady force has a variation (or component in its variation) of the form:

$$f(\theta) = F_n \cos n\theta \quad (12)$$

then the force exerted on blade number j , located at θ_j , where

$$\theta_j = \frac{2\pi j}{N} + nt$$

will be

$$F_j = F_n \cos(n\theta_j + \frac{2\pi j}{N}) \quad (13)$$

The total excitation experienced by the entire assembly (since the forces are exerted simultaneously on all blades) will consist of a full forcing vector (see Chapter 13, Equation 1):

$$\{f\} = F_n \begin{Bmatrix} \cos(n\theta+0) \\ \cos(n\theta+2\Delta) \\ \vdots \\ \cos(n\theta+(2j-2)\Delta) \\ \cos(n\theta+(2j-1)\Delta) \end{Bmatrix}; \Delta = \frac{2\pi n}{N} \quad (14)$$

It can be seen that this complex excitation pattern - referred to as 'engine order (EO) excitation' - can be more simply described by the sum of two harmonic components, both of the same n -diameter shape and frequency (of n times rotation speed) but with a temporal phase difference of 90° .

$$\{f\} = F_n \begin{Bmatrix} \cdot \\ \cdot \\ \cdot \\ \cdot \\ \cdot \end{Bmatrix} \cos(n\theta) + F_n \begin{Bmatrix} \cdot \\ \cdot \\ \cdot \\ \cdot \\ \cdot \end{Bmatrix} \sin(n\theta) \quad (15)$$

Engine Order Response Characteristics

From the above description of engine order forcing, it is clear that such an n th EO excitation can only excite those modes which have an n -diameter component in their mode shape. For a tuned assembly, with all blades and interconnections identical, this means that each EO excitation will only generate response in selected modes - those with n nodal diameters. Even when the excitation is exactly at the frequency of an m -diameter mode ($n \neq m$), the only response which will be generated will be the off-resonant component from the n -diameter modes: there will be zero response from the m -diameter ones. In practice, of course, there are few assemblies with such pure nodal diameter modes and most systems, having some degree of mistuning (or deliberate asymmetry), will possess several modes which have n -diameter components in their shapes. These will all be susceptible to some degree to excitation by the n EO forcing. However, the relative strengths of the resonances thus caused will reflect closely the magnitude of the n -diameter component in each mode. As was seen earlier, most modes tend to have a primary diametral component together with a number of lesser components. Thus, we can predict the general nature of engine order forced vibration response characteristics: a harmonic forcing generated at n times rotation speed causing resonances in several modes, the strength of each being dependent on the n -diameter component in that mode shape.

Lastly, we can see the possibility of the same type of aliasing phenomenon already discussed in connection with the

mode shapes themselves. Because the excitation is applied to the assembly by a discrete number of forces (one per blade), an $(N-n)$ EO excitation will be equally effective at exciting n -diameter modes as will an n EO type, although the frequency of the resulting vibration will be at $(N-n)$ times the rotation speed. It will be appreciated that with the above governing rules, the characteristics of engine-order forced vibration can be quite complicated!

A convenient way to illustrate the essential characteristics of EO forced vibration is to use a version of the Campbell or interference diagram, as shown in Figure 31. This is a plot of frequency versus rotation speed with, on the third axis, an indication of response level. Shown on the diagram are lines depicting the individual natural frequencies largely independent of speed, and also the 'order lines' indicating the frequencies of prominent excitation conditions. Where the n th EO line crosses the natural frequency 'line' of a mode of containing n nodal diameters, a resonance condition will exist. Other intersections will produce no significant response. The existence of impure mode shapes, such as those of mistuned assemblies, results in several modes exhibiting a secondary level of resonant response and this can also be indicated on the diagram. Lastly, the aliasing phenomenon - where an n th EO excitation excites modes with $(N-n)$ modal diameters - is also demonstrated on this type of plot.

In order to illustrate the engine-order forced response characteristics of bladed assemblies, a number of computed case studies will be presented, all based on the beam and plate type of model discussed earlier in this chapter. The first example, in Figure 32, shows different engine order excitations applied to a tuned bladed disk, covering the same frequency range (although, of course, this means different speed ranges). The selectivity of the excitation in generating response only in a mode whose shape is compatible with that of the engine-order forcing is quite clear in this example. Next, in Figure 33, just the 6EO forcing is applied to a slightly mistuned version of the same assembly as before and now it is clear that several modes are excited, as anticipated, although not all to a great extent. Some verification of these response characteristics has been provided by some carefully-controlled experiments, Ewins (1976), an example from which is shown in Figure 34.

In all the preceding examples, very light damping has been introduced so that the various modes with relatively close natural frequencies are still clearly distinguishable. If a higher level of damping is assumed, then several of the smaller close resonances merge together and lose their separate identity, as can be seen in Figure 35, taken from Ewins and Rao (1976). In these circumstances, it becomes almost impossible to 'anticipate' reliably the form of the response curves, although it is always possible to calculate the exact form as has been done here.

One characteristic of considerable interest is the relative response levels which will be encountered by a given bladed assembly when it is (a) perfectly tuned, (b) arbitrarily mistuned, and (c) mistuned in the most disadvantageous way. Many studies have addressed this question, focusing on the maximum possible increase in response level, and a variety of results have emerged. If only the two modes of a double mode pair are involved (i.e., only these two are coupled by virtue of the damping and separation of their natural frequencies), then only a modest increase in maximum response of up to 30% is forecast for the worst mistune case, Ewins (1969). Once the various modes' natural frequencies become 'close', then the interaction between them becomes very difficult to analyze - except by numerical calculation - and the results for this case are founded mainly on empirical observation, often based on many hundreds of case studies. One of the more comprehensive of these, Griffin & Hoosac (1983), shows response increases of up to 100% under certain special, though plausible, conditions.

At this stage, it becomes necessary to recall the assumptions which have been made concerning the damping, since departures from these can result in significant differences in response characteristics from those reported here. The uncertainty of this important parameter means that although the trends indicated by such results as those reported above are valuable, it would be inappropriate to draw too detailed a conclusion from them unless the damping model were first validated.

ACKNOWLEDGEMENT

The author wishes to acknowledge, with thanks, the assistance of Dr. M. Imregun in obtaining many of the computed data presented in this chapter.

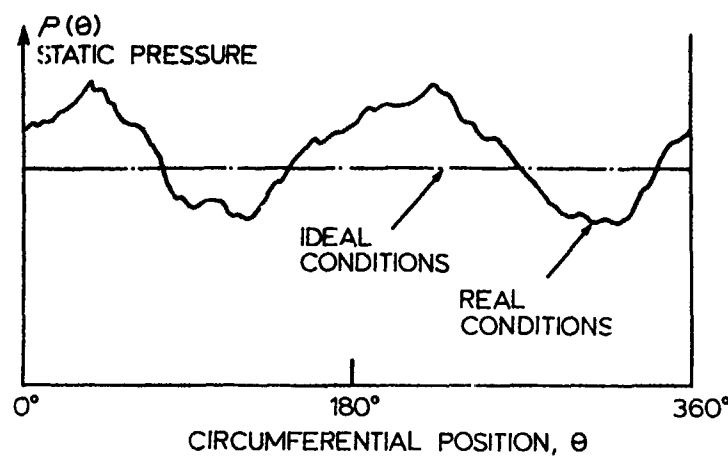


Figure 30. Variation of Working Fluid Pressure

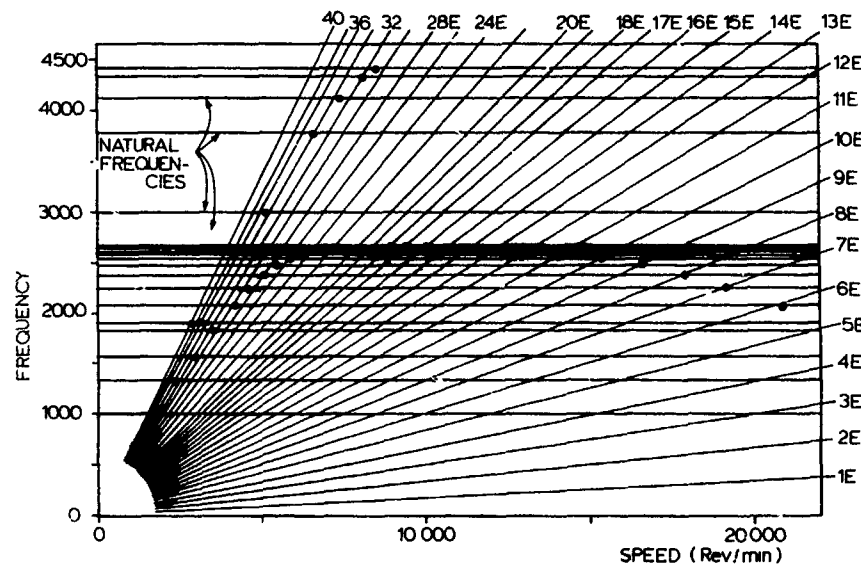


Figure 31. Interference Diagram Showing EO Forced Vibration Characteristics

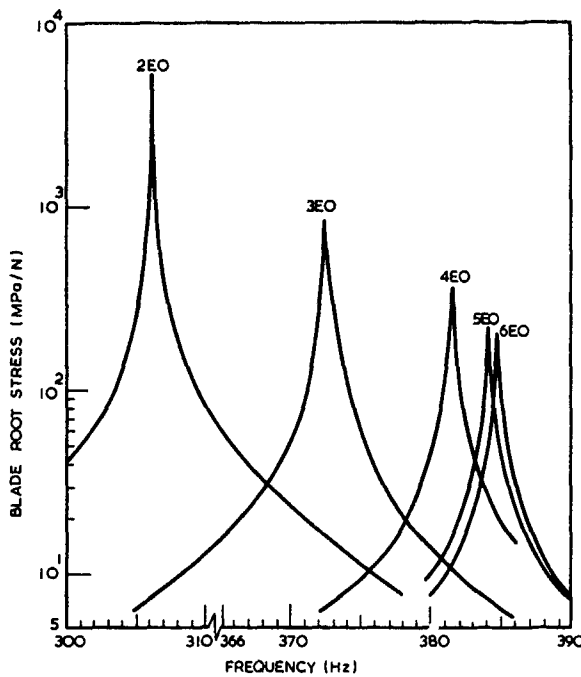


Figure 32. Various EO Excitations: Tuned Bladed Disk

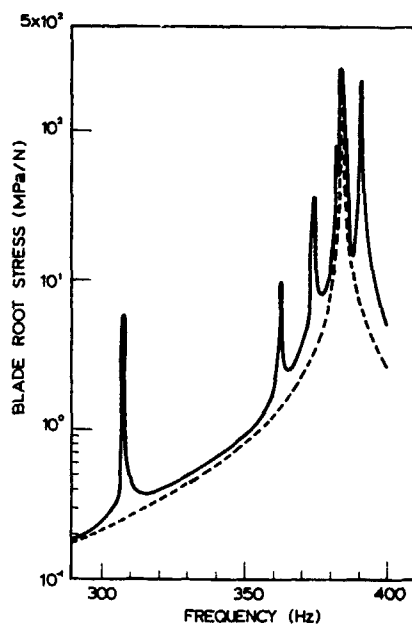


Figure 33. 6 EO Excitation: Mistuned-Blade Disk

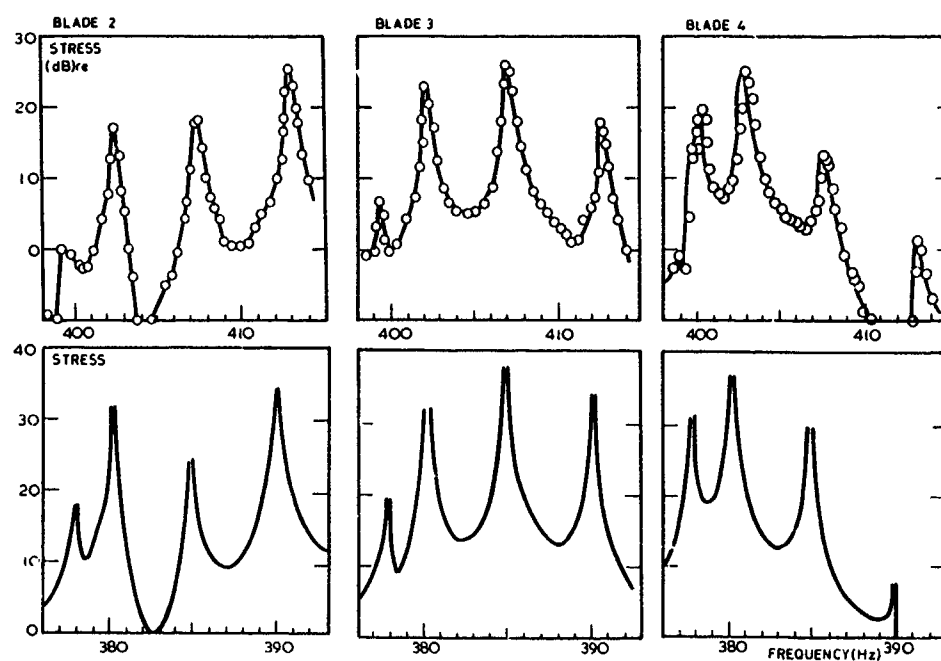


Figure 34. Measurements and Calculations of EO Excitation Response

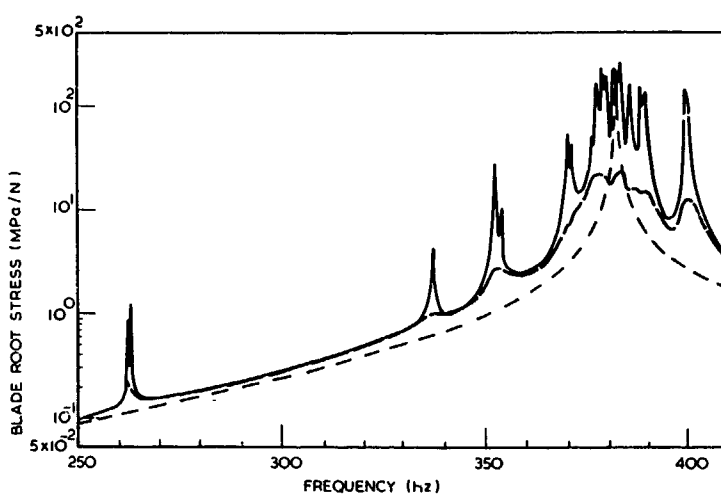


Figure 35. Calculated EO Excitation of Damped Assembly

FATIGUE AND ASSESSMENT METHODS OF BLADE VIBRATION

by

E. K. ARMSTRONG
ROLLS-ROYCE plc.
Bristol

INTRODUCTION

Ever since the initial running of gas turbines in the 1930's, their development progress has been handicapped by failures of the blading. In a large percentage of these failures the major cause was due to metal fatigue. These fatigue failures became of prime importance during the early development of the axial flow compressor, in place of the centrifugal units which were used in the early aero engines. In a fatigue failure a component suffers the development of a crack, which propagates very quickly across the section of the component. In the majority of cases this alternating stress is the direct result of the vibration of the blades, compressor or turbine, at a significant amplitude. As the fatigue crack progresses across the blade section, the level of the steady stress on the remaining part of the section increases, and final fracture takes place as this stress rises above the tensile strength of the material.

Obviously, the failure of a blade in this way - especially in an axial compressor of many stages - can create much secondary damage, as the released portion of the blade ricochets amongst the stators and high speed rotor blades. It is not uncommon for all the blading of a compressor to be fractured or severely damaged after the failure of an early stage rotor blade. The extent of this secondary damage is both governed (in a very complex way) by the design and spacing of the blading, and (to a large extent) by the impact and mechanical properties of the blading.

Published photographs of the compressors subsequent to this type of failure are not common, due, no doubt to the understandable reluctance of manufacturers to release this type of information.

However, Figure 1 is a photograph of a compressor after a major failure which illustrates the gravity of the problem.

Indeed, it can be said that if the problem of metal fatigue failure did not exist, then the study of blade vibration and the associated aeroelasticity phenomena would barely be justified. It is therefore necessary to appreciate the major factors controlling the fatigue of blading which are encountered in the actual operation of gas turbines and the practical steps which can be taken to assess the levels of vibration which are present, to ensure as far as possible that blade failures due to this cause are minimized. This is the purpose of this present chapter.

CHARACTER OF FATIGUE

The problem of metal fatigue has been of importance in mechanical engineering since the first days of the railways. In fact some of the material testing methods used today are developed from the early work of A. Wöhler (c.1860) who was involved in the investigations of the failures of axles of railway wagons, Moore (1927). Since that time much has been achieved to aid our understanding of the reasons and factors controlling the problem. However, our knowledge of the capability of a material, and so the component, has still to rely upon empirical data obtained from special "metallurgical type" fatigue testing, or actual fatigue tests on components. The aim of this section is to introduce the factors which affect the fatigue strength of a component. These have to be accommodated in any assessment concerning the importance of a level of vibration of a blade.



Figure 1. Major Compressor Failure Due To Secondary Damage After Blade Fatigue Fracture.

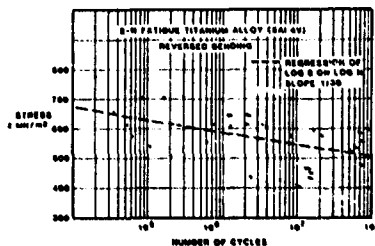


Figure 2. High Cycle Fatigue Properties.

Alternating Stress

Wöhler developed a testing machine, in which a cylindrical type specimen was rotated about its axis while subjected to a static bending moment.

These tests showed that failures could be obtained when the alternating stress levels (\pm value) were between $1/3$ and $1/2$ of the ultimate tensile strength of the material for lives of 10^6 to 10^7 cycles. With higher alternating stress levels, the test specimen broke at a reduced number of reversals. It is still the standard practice today to present a material's ability to withstand applied alternating stress on a diagram where the alternating stress is plotted against the number of reversals to failure at this stress. Because of the high number of reversals involved, it is normal to plot the number of reversals on a logarithmic scale. These diagrams are known as the S-N curves. A set of test data, for a standard titanium alloy (Ti -6Al -4V), which is used for compressor blading, is plotted in Figure 2. The tensile strength of this alloy is 990 MN/m^2 . Thus, the ratio of alternating stress to tensile strength for an endurance of 10^8 cycles is 0.51.

Further data which shows the influence of, manufacture method, microstructure, and section size, for different materials can be obtained from text books and reference manuals, Heywood (1962), E.S.D.U. (1983).

For some materials, e.g., steel alloys, it is found that failure does not occur for lives above 10^7 cycles, if the applied alternating stress is below a certain value. This threshold stress value is known as the fatigue limit of the material. For a life of a specified number of reversals 10^N , the corresponding stress is called the endurance stress for 10^N cycles. For some alloys the fatigue characteristics are found to have two slopes. At high alternating stress levels the gradient is steeper with a sudden kink or 'knee' in the S-N curve at the transition point as the curve becomes a flatter line for low alternating stress levels. The actual shape is very dependent upon the material type, its condition, and temperature.

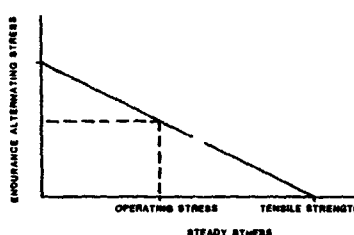


Figure 3. Modified Goodman Diagram.

Influence of Steady Stress

In an operating environment it is rare for a component to be subject to an alternating stress alone, and so experimental studies have established the influence of an applied steady stress in conjunction with the applied alternating stress.

A number of these empirical studies were correlated by Goodman, Moore (1927). He showed that for a given life there was an approximately linear relationship of the peak tensile stress on the specimen as the steady stress was reduced from the tensile stress to the tensile component of the purely applied alternating stress.

It is now common practice to use a slightly modified version of Goodman's original correlation. This is shown in Fig. 3. The Modified Goodman line connects the value of the endurance stress for a high number of reversals (10^5) to the tensile strength, or creep strength in the case of high temperature applications. As Passey (1976) points out, the Modified Goodman diagram is pessimistic for some materials, but is on the optimistic side when specimens are notched.

Because of the ease with which the diagram is constructed, coupled with the expense and difficulty in obtaining data from material tests under combined loading, the Modified Goodman diagram tends to be used in design and assessment work, in the absence of actual test data.

Notch Sensitivity

The standard S-N properties of a material are obtained from tests on specimens which are designed to give a constant stress over the test length. To overcome scatter in the test results, it is necessary to use highly polished surfaces for the test section, and so remove the effects of surface finish irregularities. It was also found that the fatigue results were also dependent on the specimen size, the larger specimens giving lower results (although work by Kelly (1971) has shown that some of these effects may be due to residual stress concentrations). In addition, it was established that all materials did not have their properties changed in the same way with a common stress concentration.

This gave rise to the concept of "Notch Sensitivity" of the material.

The definition normally used in the fatigue of materials for notch sensitivity is

$$q = \frac{K_f - 1}{K_t - 1}$$

Where q = notch sensitivity index

K_f = the fatigue strength reduction factor actually determined, i.e., ratio of fatigue strength of unnotched specimen to that of notched specimen

K_t = the theoretical stress concentration factor

The reason for subtracting 1 is to provide a scale for q which goes from zero (no notch effect, i.e., $K_f=1$) to unity (full theoretical effect $K_f=K_t$).

The value of q is dependent on the alloy strength, grain size, specimen size and degree of stress concentration -e.g., notch root radius -but it does enable materials to be compared for their ability to withstand notches. Typical values for blade materials are given below, but the values relevant for a particular component will depend upon the above factors and so its method of manufacture and component heat treatment.

Typical q values are:

- for aluminum and titanium alloys
 $q \approx 0.5$
- for steel and nickel-base alloy
 $q \approx 0.35$

Low Cycle Fatigue (L.C.F.)

In an operating engine, a large number of components are subjected to a progressively increasing stress, as the engine accelerates from idle to full power. Throughout the life of the engine these components will therefore experience many cycles of this repeated stress. With components like disks, shafts, and casings which are highly stressed, a fatigue crack can be initiated at a relatively low number of reversals - say 3×10^4 - if the applied stress is high enough.

Because of the seriousness of a failure of this class of component, much work has been done since the early 1960's, to apply the analysis of Fracture Mechanics to the propagation of a fatigue crack or the development of cracking from a defect. It is currently not feasible to apply fracture mechanics analysis to the problem of blade failure caused by high cycle fatigue. But a brief introduction to the topic is given for completeness. It is possible from its application to material tests, to obtain a better understanding of the influence of geometry, size, and stress concentration in the results of fatigue test specimen, Burdekin (1981).

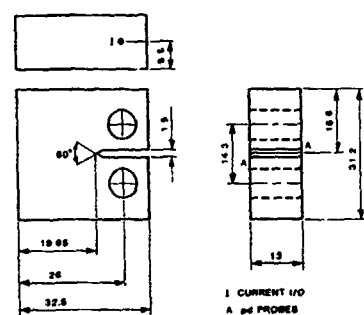


Figure 4. Compact Tension Test Piece Dimensions (mm).

Fracture Mechanics and Fatigue

In the early development of linear elastic fracture mechanics, G. R. Irwin studied the stress field in front of a growing crack in an elastic material. He showed that the stresses died away proportional to the inverse square root of the distance along a radius vector from the tip of the crack. He found that the proportionality was a function of the applied stress and the square root of the crack length, and termed this 'the stress intensity factor', K. Irwin (1957). For a crack of length $2a$ and an applied remote tensile stress σ , for a through crack in an infinite plate the stress intensity factor is given by:

$$K_I = \sigma \sqrt{\pi a}$$

The subscript I relates to the mode of opening of the crack, i.e., tensile in this case.

In the application of fracture mechanics to fatigue, the rate of crack growth under cyclic loading is related to the value of the cyclic change in the stress intensity factor at the crack tip. The resistance of a material to crack growth is established experimentally. For these tests, a thick specimen known as a compact tension specimen as shown in Fig. 1 is usually used to provide uniform conditions at the crack front and the specimen is subjected to an oscillating tension between two positive values (σ_{min} , σ_{max}). Thus the stress intensity at the tip of the crack will vary between K_{min} and K_{max} . Since both are dependent on the crack length, so will their difference. Thus, $\Delta K = \sigma_{max}(1 - \frac{\sigma_{min}}{\sigma_{max}})^{1/2}$. Normally σ_{min} is kept small. During the test, the length of the crack is measured either optically or by an electrical method and is plotted against the number of cycles. From the slope of this plot it is possible to obtain the rate of crack growth, da/dN .

For fatigue cracking it was proposed by Paris et al. (1963), that the rate of crack growth per cycle could be a function of the power of the stress intensity factor range, under the cyclic loading.

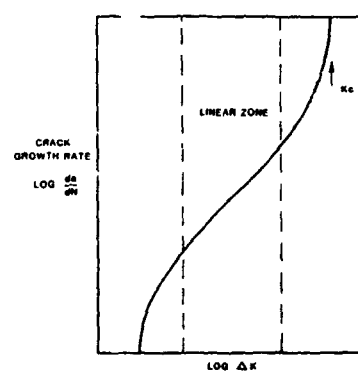


Figure 5. Range Stress Intensity Factor.

$$\text{Thus } \frac{da}{dN} = C(\Delta K)^m$$

resulting in plots as shown in Fig. 5.

At very low values of ΔK there is a threshold below which the crack appears not to develop, while in the central zone most materials exhibit a fairly linear relationship. At high values of ΔK , the crack propagation rate becomes high as ΔK approaches the critical values K_{IC} , which is termed the fracture toughness of the material. With this value the propagation of the crack is extremely rapid to eventual failure.

Application of Fracture Mechanics

Apart from an improved understanding of 'metallurgical type' fatigue test data, and the characterization and comparison of the fatigue properties of materials, the main application of fracture mechanics has been to the analysis of low cycle fatigue (L.C.F.) life of disk and other similarly stressed components. If the fracture face of a component which has undergone L.C.F. testing is examined under high levels of magnification, for example with an electron beam microscope, it is possible to identify striations on the surface. Laboratory test piece specimen analysis has shown that each striation is associated with a cycle of fatigue loading. It is therefore possible to obtain values of da/dN by measurement from the fracture face of the disk. This information, together with the crack propagation rate of the alloy, enables the operating stress level to be determined, together with an estimate of the number of cycles since crack initiation. Such data are valuable evidence when seeking the conditions which have given rise to a failure. The application of fracture mechanics to this type of component also enables crack propagation rates to be established with confidence under the stresses caused by L.C.F. conditions, which then permits component lifing techniques to be adopted. However, the necessary conditions for fracture mechanics to be applied do not exist in the case of compressor and turbine blading. This is because of the following

two major factors. In general the unknown fluctuating nature of blade vibration amplitude is often so great that the evaluation of da/dN is unreliable, also the operating stress field is not sufficiently constant in the crack zone to be consistent with the underlying analysis of fracture mechanics. In addition, the bulk of the blade life is associated with crack initiation which cannot normally be dealt with by a fracture mechanics approach. Once a crack is established then the remaining life is short because the high frequency of stressing propagates the crack very quickly.

Residual Stress and Surface Treatments

It has already been explained that the fatigue strength is influenced by the presence of a steady stress. However, this steady stress need not be due to an external force system, but may arise from an internal system of stresses. One significant cause is residual stresses resultant from the method of manufacture, either forging or machining. In some instances these stresses result from cold setting of blading to correct stagger errors, or forging manufacture distortions. Obviously, the value of these stresses is not known, but their variability must contribute to the scatter in fatigue strength of blades.

The surface finish of a component has a significant influence on the fatigue strength, because the vibratory stresses will be highest at the surface. The susceptibility to fine polishing scratches will depend upon the notch sensitivity of the material, and the thickness of the local blade section, for example at the trailing edge. In most cases, these surface effects can be mitigated by superimposing a residual compressive stress in the surface and this can be achieved by a cold work of the surface by controlled shot peening, or vapor blasting, for example. Fig. 6 shows the improvements in fatigue properties obtained by this technique, Metal Improvement Co (1980), Manson (1971).

Other surface processes like plating, anodic treatments, or antierosion or oxidation coatings may reduce the properties, by the creation of a residual tensile stress, or by the fact that the coating itself lacks ductility and will cause micro cracking which then propagates into the parent material. The influence of these effects is best established by carrying out fatigue tests on actual components with the treatment applied.

Material Structure

In most materials which are used for blading, the fatigue properties are dependent upon the grain structure of the metal, which is determined by the way the component is made. A forging, in which the aerofoil is forged to size from an extruded bar stock, provides possibly the best grain flow and with the optimum heat treatment, the finest grain size, to obtain the highest fatigue properties for

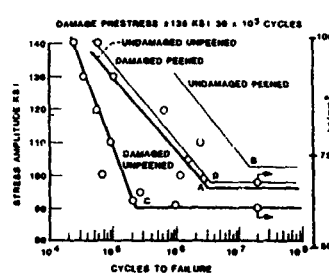


Figure 6. Shot Peening as a Means of Overcoming Prior Fatigue Damage with 4340 Steel Tested in Rotating Bending.

aterial. A titanium blade made by this method will have superior fatigue properties by some 20% above a similar blade machined from conventional bar stock. Also, within the same aerofoil, the fatigue properties will vary, dependent upon the degree of forging work done at various stations. Thus, the properties of the material around the junction of an aerofoil and a snubber will be different than those in the aerofoil midway between the platform and the snubber.

The importance of process control, of both temperatures and degree of working, at the various stages in manufacturing is given in the section on process control of titanium alloys p. 82, Meetham (1981), Figure 7 showing the difference in grain size between standard and premium quality of Ti 6AL 4V is taken from Meetham (1981).

Scatter in Fatigue

In previous sections, a number of reasons for scatter in fatigue properties have been given. However, to these must be added the geometric variations between blades which are made to comply with the same drawing. These differences will arise due to the manufacturing tolerances on thickness, chordal length, blade length, aerofoil shape and local variations in stress concentration areas like fillet radii, and trailing edge thickness. Thus, if a large number of blades are vibrated in the same mode and at the same level of vibration, then there will be a scatter in time to failure. As might be anticipated, where the stress at the crack initiation point is affected by a large number of factors, the failure lives fall into a log normal distribution, i.e., a normal distribution of the logarithm of blade life. Figure 8 is taken from Hunt (1972) which shows that the scatter in life from the shortest to longest life of a group of 44 blades tested under the same conditions is 200:1 and that their distribution approximates very closely to a log normal distribution. It is a feature of fatigue properties of components, that



Figure 7. Typical Macrostructure of Standard and Premium Quality Ti 6-4 Forging Stock (350 mm Diameter).

with a higher number of reversals to failure than there is a larger scatter in life. For low cycle fatigue at say 10^4 cycles the scatter in life is more of the order of 2:1.

Fretting Fatigue

One major problem which occurs in engineering structures is the phenomenon known as fretting. It occurs when two components are loaded together, and when the interface is subjected to an oscillating shear type of force or movement. Under these conditions the surfaces of the interface become marked or damaged, and this is known as fretting damage. These situations exist in the blading of gas turbines, where the blades are connected onto the rest of the engine structure, e.g., rotor blade fixing onto the disk; stator vane outer fixing into casings and the inner ends of variable stator vanes. Laboratory tests, Waterhouse (1981), shows that the fatigue strength of some materials can be reduced to 1/3 of the standard strength. Attention to detail design and antifretting coatings, Waterhouse (1981), can help to reduce these serious effects.

Variation of Stress Level

In the majority of engineering applications, levels of alternating stress are not constant with time, and so consideration has been given to ways in which this might be accommodated in any analysis to establish how a variation in amplitude will affect the fatigue strength. For the analysis of gust loads, on aircraft structures, Miner (1945), suggested a relatively simple method of damage accumulation. His concept was, that the accumulated damage can be expressed in terms of the number of cycles applied, divided by the number to produce failure at the given stress level. Further, this cumulative damage theory assumes that failure from fatigue will occur when the summation of the various contributions of damage equals unity.

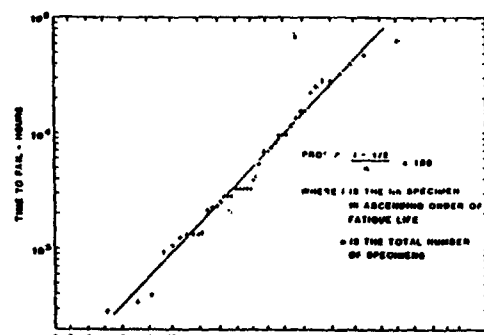


Figure 8. Log Normal Probability Plot (44 Blades in Fatigue).

Thus $\frac{n}{N} = 1$

when n = number of cycles applied at stress S

N = number of cycles for a specimen to fail at stress S alone

In Chapter 12 of Sires (1959), Miner considered some of the other more complex proposals to integrate the fatigue damage. However, the more extended specimen testing needed for the alternative method was not considered justified.

Indeed even today Miner's simple proposal, given above, is widely used for the usual blade materials -aluminium, titanium, and steel. This is because the reasonable accuracy given by the method does not justify employing a much more complex analysis.

Corrosion, Erosion, and Damage

The blade surfaces of a gas turbine are often operating in a severe environment. Because of the high, air or gas, speeds over their surface any dirt or grit in the air will scour the surface and may damage any protective coating or treatment. The corrosion which will follow will cause a loss of properties by two mechanisms. There is the stress raising effect due to the geometry of the corrosion pit, and also there may be a detrimental change in the chemistry of the material on the exposed surface, with possible preferential attack along the grain boundaries. Losses in properties due to these effects must be considered when determining the service life of blading.

In the case of local damage to blade aerofoils as a consequence of small objects (metal or stones) being ingested into compressors, the blading may suffer significant nicking on the leading edges. The loss in fatigue strength which results from these nicks, depends upon the notch sensitivity of the material having been subjected to the manufacturing and heat treatment processes. In some cases these

nicks may also have incipient tear cracks at the root of the notch. The actual shape and type of crack will be dependent upon the detail of the foreign body as well as its size, velocity, and the tangential speed of the rotor blade. Only by fatigue testing correctly damaged blades can the loss of properties be correctly determined.

OBSERVATIONS ON BLADE FATIGUE

During the running of research compressors, or in the early development of aero engines, fatigue cracking or failure of blading may occur.

This experience over the years has allowed certain aspects of the blade fatigue problem to be appreciated and techniques developed, in addition to those covered in the previous section which can be of value in the task of overcoming these fatigue failures. Those associated with fatigue rather than amplitude assessments will be covered in this section.

Fracture Characteristics

The fracture face of a fatigue failure has a very distinct and unique appearance. The fatigue zone has a relatively smooth appearance compared with the near crystalline texture of the final tensile fracture zone. This is because the fatigue crack propagates in a transgranular manner in a series of very small increments; each increment notionally being associated with a stress cycle. In the case of low cycle fatigue with the higher stress levels, this is indeed the case, and the analysis of electron microscope examinations permits fracture mechanics techniques to be applied. However, with the more complex amplitude histories involved with blade vibration, similar deductions are not possible, but the short periods of high vibration do produce the concoidal marking which are centered about the fatigue nucleus. A photograph of a fracture face of titanium blading is reproduced in Fig. 9. This type of fatigue cracking exhibits practically no ductility until the final tensile failure. Thus, it is very difficult to detect the presence of the crack development in an operating compressor. The high steady stress in the blade form also causes the crack to propagate quickly, and as a consequence it is unusual to find cracks in compressor rotor blade aerofoils before one blade fails. When the cracking nucleates in the blade root fixing, where the mean steady stress is lower, then the cracks are slow to propagate and so cracks in the roots may be found prior to failures.



Figure 9. Typical Fracture Faces Due to Fatigue of Titanium Compressor Blades.

Influence of Alternating Stress Level

In engineering components it is the stress concentrations present which locate the positions of the fatigue nuclei. When the stress level is very high, then experience shows that fatigue cracking will start at a number of sites apparently simultaneously. A good example is repro-

duced in Fig. 10 taken from Armstrong (1966a) where a shaft was subjected to high alternating stress ± 40 tons/sqin which caused failure in 5×10^4 cycles and multiple cracks were found. A bladed disk may be considered to be an assembly, with many similar stress concentrations in the blading. If it is found that a lot of fatigue crack systems are present, then it is most likely that they have been caused by a high amplitude -for example a strong flutter condition.

However, if only one blade is cracked or broken then it is likely to have resulted from a moderate amplitude, maybe a resonance. Of course, it may be that because of the spread in natural frequencies, only one blade was vibrating. Such a situation is not usually the case.

Determination of Properties

It is often necessary to establish the fatigue strength of a blade. Two typical reasons are (1) to provide data for the assessment of the amplitudes of vibration measured in an engine, or (2) to establish the change in properties which may result from the adoption of a different method of manufacture. The previous section covers many of the reasons why the fatigue properties of the blade may be expected to differ from the figures which are obtained from a series of basic "metallurgical type" fatigue tests. One method of carrying out fatigue tests on components is covered in detail in Armstrong (1966b).

However, the problem remains concerning how the test program is to be controlled. As explained above it is standard practice for metallurgical laboratory tests to be carried out and presented in the form of an S-N diagram. Where great attention is paid to the surface finish condition, i.e., mirror finish and stress relief in a vacuum, Kelly (1970), then scatter is small, and one or two specimens only need be tested at each stress level required to determine the shape of the S-N curve at stresses above the fatigue limit. However, where the surface finish is not to this high standard, and where possible residual stress is present to some degree, as will be the case with engine components, then the scatter will be very significant, and it is necessary to test at least 3 to 4 blades at each stress level. Because of the large variation in life - say 10:1 - and also the fact that the mean life is initially unknown for a given level of vibration amplitude, it is often a very time consuming and costly rig test program to establish the S-N curve for blade components.

These practical problems can be illustrated in the following questions:

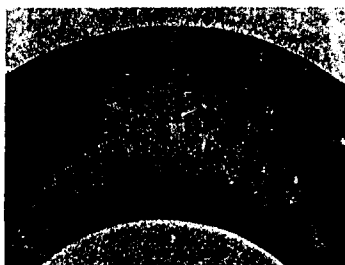
(a) What should be the amplitude of the first test where knowledge of the properties are not known to better than 20-30%? This lack of knowledge may be due to a new blade shape, new manufacturing process, new material.

(b) What further test program should you follow when the first blade has run for 10⁴ reversals and is unfailed? The necessary test time with 100 Hz blade is nearly 30 hours.

(c) How do you run the second test if the first test failed early; was it a weak blade at the bottom end of the scatter, or was the amplitude too high? Remember, the mean life will vary by at least 10:1 for a 20% change in stress level, Koff (1978), Armstrong (1966b).

(d) How do you plan a series of fatigue tests to solve a development or manufacturing problem and be able to fix a completion date?

(e) Can you do anything worthwhile with only a small number of blades; for example, three or four?



(a) FORWARD BAND



(b) CENTRE BAND



(c) REARWARD BAND

Figure 10. Cracks Beneath Stiffening Bands on Completion of Endurance Test.

Some of these problems can be avoided by the adoption of an incremental method, Hunt (1972), Armstrong (1966b), Armstrong (1967). The purpose of the test is not to provide data which replaces the basic metallurgical type of S-N curve, but to provide an effective engineering answer to the questions; how do these two standards of blade compare in fatigue properties? What is the scatter and mean fatigue strength of this blade for use in assessing the level of vibration in an engine? Remember, the blades in an engine do not vibrate at constant amplitude, and are only subjected to relatively short periods of vibration during the engine life, and so the results of an S-N curve cannot be applied directly. This is dealt with more fully in the section "Amplified Ratio Method."

In an incremental fatigue test such as that illustrated in Figure 11, the amplitude of vibration is increased regularly every half hour. The starting level of vibration is standardized for a particular material so that results will be more comparable. A value of about one third the failure amplitude is normal, and ensures that time is not wasted at very low ineffective amplitudes, but also provides ample accommodation for specimens with very low fatigue strength. The time axis was selected in hours rather than number of cycles, as engine life is in hours rather than reversals, and so the standardized test method will be equally relevant to blades of all frequencies. During the test each blade is stepped through the increments of increased amplitude each lasting for 30 minutes.

The incremental steps are fixed at a constant value. If the amplitudes are measured in 'af' (see the section "Mechanical Aspects of af"), then this is either 0.5 ft/sec or 0.2 mHz. At some amplitude level, the blade will fail, and the time in the increment is recorded together with the level and site of fatigue crack on the component.

The major advantage of the above method is that all specimens are taken through the same test cycle until failure occurs. By plotting the results in a simple form, Figure 12, a ready appraisal of the relative strengths of two groups of blades can be obtained. By using an anal-

ysis based on Miner fatigue damage simulation, and with the statistical tests, Student's 't' and 'F' test, see "Blade Fatigue Capability," a more formal assessment of the results may be obtained. Because a valid result is obtained from each specimen, an informative result can be obtained with as few as three specimens. The limited duration for each test also allows the test sequence to be planned, which is often a useful advantage when faced with an engine development problem.

A comparison between constant-amplitude and incremental tests is hard to form, as it depends entirely upon the purpose of the test.

If the purpose of the tests is to establish a "full" knowledge of the fatigue properties of the blade, then perhaps the constant amplitude tests are the best. This will involve testing over the full S-N curves, or say from 10^4 to 10^8 reversals, although to cover 100 hours for a frequency of 3 kHz the number of reversals would need to be 1×10^9 . A number of specimens will be needed to establish the degree of scatter. This type of testing is hardly, if ever, required other than for research purposes. Also, in doing this type of testing, certain data like the slope of the S-N curve for the material are reassessed. One criticism of the incremental test is that the number of reversals during an amplitude increment is low. For 300 Hz these are 5.4×10^5 reversals in half an hour which of course could be extended at the expense of a longer testing time. However, the testing procedure integrated in an assessment method, Armstrong (1966a and 1966b), seems to provide a very satisfactory method.

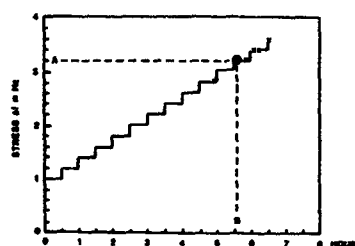


Figure 11. Incremental Test Programme X - Fatigue Failures (Example ③).

BLADE TEST NO	STANDARD BLADES									
	1	2	3	4	5	6	7	8	9	10
1										
2										
3										
4										
5										
6										
TESTING										
INCREMENT OF STRESS	0.0	0.0	0.0	0.0	0.0	0.0	0.0	0.0	0.0	0.0
TIME IN HOURS	0.0	0.0	0.0	0.0	0.0	0.0	0.0	0.0	0.0	0.0

Figure 12. Comparison of Two Test Groups Tested by Incremental Method.

Strength and Life

Problems in fatigue generally fall into one of two groups. They are either those dominated by problems of low cycle fatigue and repeated high stress levels, or those of vibration and high cycle fatigue. Two of the features of fatigue which contribute to this identification of two problem classes, are the shape of the S-N curve of materials, and the distribution scatter.

In the case of the repeated high steady stress, the level of applied stress is relatively well-known, and so with knowledge of the S-N curve and the reduced scatter with high stress, the life of the order 10^4 is also known. A change in material processing which changes this life by a factor of 3 is very relevant. However, in the case of high cycle fatigue, the levels of vibration are not known or measured to anything like the same accuracy as the L.C.F. stress levels and typically a factor of 2 is relevant. Thus, it is more meaningful to quote the results of a comparison of fatigue properties between two groups in terms of stress level, rather than in terms of mean life. Remember that 20% in stress is equivalent to a factor of at least 10:1 in life.

FACTORS AFFECTING BLADE AMPLITUDES OF VIBRATION

A method of assessing the severity of blade vibration must make allowance in some way for the factors which control the vibration. These factors can be summarized as the mode of vibration, and the form of excitation. The mode shape influences the fatigue strength and its scatter, while the excitation controls the level of vibration and the variation during the flight life of the engine. Excitation can be divided into two major groups. Self excitation or flutter, which is due to the interplay between the blade's vibratory motion, and the resultant change in aerodynamics forces on the blade, which is the subject of the earlier chapters of this handbook. Flutter is a serious problem, because the amplitudes of vibration are limited by nonlinear effects. The other class of vibration is the larger group, and a number of sources of excitation can be grouped together, because the response is due to the forced resonant characteristics of a single or multi-degree-of-freedom system.

Identification of Modes and Excitation

The identification of the modes of vibration of a blade, or bladed assembly, must be derived from the observed frequency of vibration, and a knowledge of the calculated values or experimental frequencies obtained on a static test for frequency determination of the individual blade. Modern signal frequency analyzers enable the results from engine or compressor strain gauge tests to be presented in a compact and readily appreciated form. Figures 13-16 are taken from Armstrong (1977).

The format is similar to the conventional Campbell interference diagram, with axes of frequency and rotational speed. However, in the figures, the brightness indicates the amplitude of vibration, and is usually proportioned to the logarithm of the amplitude. To obtain this form of presentation, of the response from a blade strain gauge, the amplitude signal from a frequency analyzer is used to modulate the intensity of an oscilloscope. The y axis deflection of the oscilloscope is driven from the signal from the analyzer proportional to the analysis frequency while the x axis deflection of the oscilloscope is controlled by a signal proportional to the rotational speed of the engine as derived from the tacho signal. During a slow acceleration, the display is photographed, and at 10⁴ increments in speed, the frequency calibration marks are applied, thus producing the array of spots which are used for reference purposes.

Fig. 13 shows the result of a single strain gauge attached to an early stage compressor rotor blade. There is sufficient turbulence in the air stream to cause the blade to respond at its natural frequencies, and to give a strain gauge signal above the background noise level. The responses of the first flexural (1F), second flexural (2F), and first torsional mode (1T) are clearly seen. Multiple lines in the 2F zone are associated with the effects of blade-disk coupling. For the flexural modes, the rise in natural frequency with centrifugal stiffening is clearly seen; this is absent on the 1T mode, thus confirming the modal identification.

The sloping lines of various intensities are the strain responses of the rotating blade, due to the air flow not being uniform round the compressor annulus. In fact, in this engine there are 3 intake vanes and this is the reason why the third sloping line labelled 3 E.O. for the third engine order is stronger than the others. The brightness of the

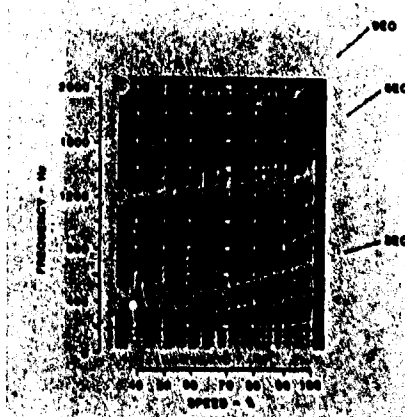


Figure 13. Frequency V Speed Plots Engine with Venturi Intake Component: 'O' Compressor Rotor Blade.

second engine order line is stronger towards 100% than lower in the speed range. While the excitation strength is expected to rise with engine power, an additional reason is the proximity of the excitation to the 1F natural frequency line. It will be seen that there is no resonance of the 1F mode between 70% of full speed-flight-idle, and 100%. In fact, as a result of this form of testing, a minimum frequency limit was imposed on the 1F mode to ensure that a second engine order resonance did not occur on a blade with a particularly low 1F natural frequency. In the region below 60% engine speed, and at frequencies between 200 Hz and 800 Hz, excitation lines additional to the engine orders can be seen. These are due to the presence of rotating stall cells.

Fig. 14 is a reproduction of a frequency analysis from a strain gauge on a fan rotor blade. The fan blade has a snubber or part-span shroud. In this particular engine test, the blades were assembled with a clearance between the snubber contacting faces of 0.060 inches. Under the influence of the centrifugal field, the blades untwist, until the inter-snubber gap closes, and then the snubber ring acts as a ring coupling the blades together, and producing assembly, rather than blade modes.

The characteristics of the above effects can be readily seen from Figure 14. At speeds below 60% full speed the cantilever natural frequencies 1F, 2F, 1T, 3F can be seen. Between 60% to 70% full speed, a signal which has intermittent components over the whole frequency range is evident. Experience has shown that this type of signal is usually present when two surfaces are in intermittent contact. Above the 70% speed condition a new set of natural frequencies are present. These are the natural frequencies of the bladed assembly, all the blades being coupled with the ring formed by the stubbers. The modes are characterized by the presence of nodal diameters.

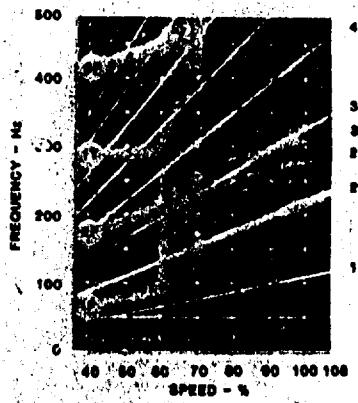


Figure 14. Frequency V Speed Plots Engine with Aircraft Intake Components; 1st Fan Rotor Blade 0.060" Snubber Gap.

The one marked 3D is so identified since it is resonant with the 3 engine order (EO) excitation. Notice also that the 2 EO signal is stronger than the 1, 3, and 4 EO components; this is because the engine was run behind an aircraft intake with a bifurcated inlet.

Because of the difficulty of accurately predicting whether flutter will be present on a compressor rotor blade, strain gauge testing is usually carried out to establish if flutter is in the operating range. Fig. 15 shows an analyzed strain gauge signal from a rotor blade having part-span shrouds. For this test the engine speed was progressively increased, and the frequency data are presented against time rather than engine speed, as is normal for a Campbell diagram.

In the early part of the record, the natural frequencies of the blades can be easily distinguished from the engine order excitations. At the flutter condition it will be seen that the strain gauge signal, at the natural frequency, is greatly increased. This is, of course, characteristic of self excitation, and unmistakably different from the response due to a forced resonant type of vibration. Since the flutter involves a periodic change in the aerodynamics of the blading, the resultant variations in pressure can be detected on the casing. In Fig. 16 also reproduced is a record of a pressure pick-up installed in the casing at the time of the flutter incident. It can be seen that the two signals are coincident in time.

However, the difference in the frequency of the signals is because the strain signal is taken from the rotating blade, and the pressure pick-up is on the casing. By using these two frequencies, it is possible to establish the number of lobes in the rotating pattern and the speed of rotation.

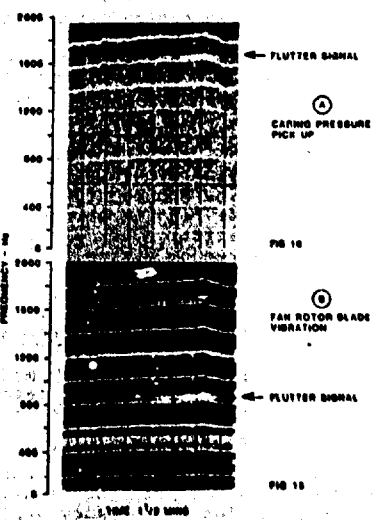


Figure 15. & 16. Frequency V Time Plots Engine Research Compressor Test Component Fan Rotor Blade and Casing Pressure 2U.

Amplitude - Time Variations

Amplitudes of blade vibration at a steady engine condition are seldom constant with time, and are only so when at the peak of a forced resonant condition of high amplitude or a serious flutter condition. Examples of stress against time can be found in early references, Carter (1957), or more recently in Cardinale (1980), from which Figure 17 and 18 have been taken. These show responses in conditions of turbulent flow and rotating stall, while Figure 19 shows conditions of stress at the strain gauge in a flutter condition.

Variations of amplitude with engine speed will occur, due to the change in aerodynamic conditions, e.g., rotating stall and resonance. Typical results can be seen in Fig. 19 and is reproduced from Armstrong (1960) and Fig. 20 is reproduced from Cardinale (1980). It will be seen that, in both cases, large amplitudes of vibration exist over a relatively small increment of speed range, as a result of resonances between the natural frequencies and specific engine orders of excitation. The shape of these amplitude speed curves is controlled by the total aerodynamic and mechanical damping in the system. Typical values from published papers, e.g., Hunt (1972), Armstrong (1967), give values of Q of about 30 which correspond to log dec of 0.1. However, values for high modes are given in Cardinale (1980) for integrally bladed assemblies.

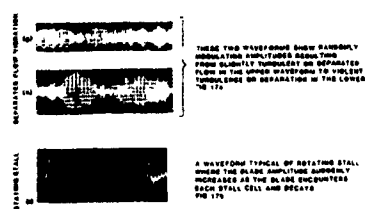


Figure 17. Induced Flow Vibrations.

Note

$$Q = \frac{1}{\text{Loss Factor } (\eta)} \cdot \text{Log Decrement } (\delta)$$

Mode	Log Decrement (δ)
1F	.04 - .08
1T	.02 - .03
2F	.005 - .015
2T	.01 - .03
1-2S	.005 - .01

It is also stated that data of axial dovetail designs appear to fall in the above range. When it is remembered that a reduction of 20% in stress amplitude results in at least an increase of more than 10:1 in life, then the potential life at stresses less than half the peak amplitude will be between 10^3 to 10^6 times longer than that associated with the peak stress level. Therefore, because of the high Q of blading, it is only necessary to consider the response at their natural frequencies, and not the responses at off-resonant conditions.

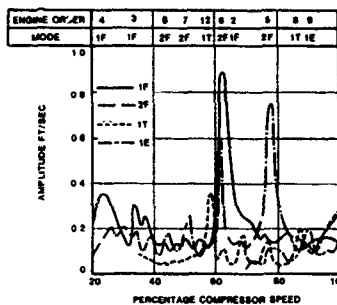


Figure 19. Engine Order Vibration.

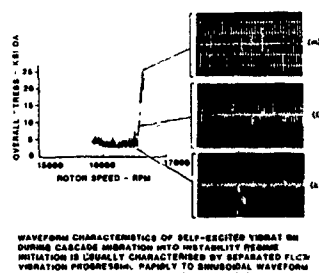
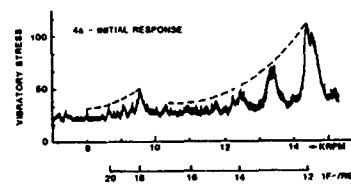


Figure 18. Self-Excited Vibration.



Characteristics of Types of Vibration

The assessment of the degree of vibration of a blade or vane, in terms of it causing a fatigue failure, must be made on the evidence from one or more blades of a stage, and possibly from a limited amount of engine running. As previous sections have shown, the vibration can be due to one of many sources of excitation. However, the consequences in terms of consistency of the stress level is very dependent on the particular type of excitation under consideration. The Table, Figure 21, has been drawn together from Danforth (1975, 1974) Armstrong (1967, 1960), Cardinale (1980). The data in this table provide a good indication of the dependence of the amplitude of vibration on the operating conditions of the engine, but it must not be taken as exclusive of additional factors, nor new types of problems which will become evident as the rating and performance of compressors and turbine designs are extended. The section "Design Assessment" addresses the problem of how an engine test series should be conducted.

METHODS OF ASSESSMENT

Strain gauges were first used on compressor blading in the late 1940's, see discussion Carter (1957), to establish the reason for the fatigue failure of blading. This early work set the obvious style for investigations of this sort and the strain gauges were positioned at the sites of fatigue nucleation. Under these conditions of high alternating stress, and with the very early strain gauges, the instrumentation life was very short. However, as the quality of the strain gauges and their installations improved, their use became more commonplace. With this

greater use and ability to help diagnose the cause of failure, it was realized that by their early application, it should be possible to detect potential failures and their source of excitation. This would then enable early modifications to be made prior to any failures, and thus to avoid their attendant disruptions to engine development programs. However, this aspect of the work places new requirements on the assessment method which is adopted.

Assessment Requirements

The prime requirement of any assessment method must be to establish whether a particular stage of blading will give a satisfactory service life. As the introduction to Cardinale (1980) states, "the evaluation of aeromechanical behaviour must consider practical operational effects and sensitivities, including aircraft maneuver and flight transition distortion, and the integrated effects of a number of other variables, including variable geometry, bleed, power extraction, operating line, and other engine and inlet transient conditions, such as those associated with environmental and weapon delivery gas ingestion. The long range effects of deteriorations, foreign object damage, airfoil erosion and potential control malfunctions also need to be addressed. Predictions of vibratory responses, fundamental mode instability margins, and surge-induced stresses are not yet adequate to eliminate the need for experimental validation of these effects. Overall experience, guided by the aeromechanical fundamentals, serves to establish systematic design verification procedures with considerations given to the total engine system."

ENGINE/AIRCRAFT CONDITION	TYPE OF VIBRATION			
	FLUTTER AND SURGE	ROTATING STALL AND SEPARATED FLOW	LOW ENGINE ORDER	STRUCTURAL VANE WAKES
OPERATING LINE Throttle Derivative(s)	High Operating Line	High Operating Line Generally Aggravates		
Afterburner Transients	Reduces Margins	Affected Stage Depends on Setting & Aero Design May Reduce Amplitudes Depending on Schedule		
Stator Schedule	Malfunction May Cause Flutter			
Idle Speed Variation		May Cause Longer Running Time in Amplitude Bands		May Result in Longer Time on Resonance
DISTORTION Aircraft Intake				
Circumferential Radial	May Increase Margin Likely to Reduce Margin	Can Cause Large Amplitudes on Segment of Stator Vanes	Introduction of Additional Resonances Creates 3rd Engine Order	May Result in Large Stator Wakes
Cross Wind • Magnitudes Depend on Flight Conditions, e.g., Incidence, Tsv.				
FLIGHT OPS				
Intake Temperature	Reduction of Margin	Speed Range Controlled by Corrected Speed,		Introduction of some Resonances at High RPM Due to Drop in Natural Frequencies with Temperature.
Inlet Pressure	Reduction of Margin	Increases in Amplitude with Pressure		Possible Increases in Amplitude.
CHARACTER OF VIBRATION				
Modes of Vibration	1P or 1P with Canti-Lever Blading Low Diameters with Bladed Assemblies	Low Modes		High Modes Including Plate Mode
Amplitude Variation	Impulsive for Surge Very Sudden Increase in Amplitude with Engine Condition for Pitch	Similar Peak Amplitude v All Blades for a Condition Ripples in Character	Classical Resonance Fluctuates on Peak	Peaks Separated Due to Frequency Scatter Often High 'N' Values
Differences Between	Very Variable for Flutter Similar for All Blades in Surge	Consistent Between Blades	Consistent	Very Variable

Figure 21. Character and Changes of Compressor Blade Vibration.

In addition to the primary task of assessing a particular design, it is also important to be able to relate the results of a particular investigation with similar data from other engines or rig test results. This comparison across a field of experience then allows a feedback to take place into the design processes for new engines. Ideally, this type of information should be in a form which will be of use at the earliest project stage, and often before the details of the mechanical design are finalized. Thus, there are the two important aspects of the aeromechanical behaviour to be considered in the assessment method; the excitation and the response in terms of ability to withstand the vibration.

Aerodynamic and Mechanical

There is no doubt that the factors which are relevant in blade vibration fatigue problems can be divided into two major groups. This is illustrated in Figure 22 which is taken from Armstrong 1980. The degree of vibration in the operating environment is controlled by a number of factors of which perhaps the following are the most important, for a particular condition of resonance.

- A. Basic blade aerodynamics and nominal flow conditions.
- B. Individual blade geometry, stagger angle, aerofoil shape, and thickness.
- C. The mode shape of the blade which is in resonance.
- D. Aerodynamic factors controlling the balance between excitation and damping.
- E. The mechanical damping.
- F. The flight condition and the mode of operation of engine and aircraft.
- G. The consistency between engines and aircraft.

While these, and others control the level of the vibration, another group establish the ability of the blade to withstand the vibration, for example:

- A. The material of the blade which will control the fatigue strength.

- B. The surface finish and the finishing process, e.g., shot peened.
- C. The actual local profile, e.g., any local undercutting or thinning.
- D. Variations in the manufacture process heat treatment.
- E. Method of manufacture whether it be forged, machined, or degree of cold setting.
- F. Level of steady stress in blading.

Each group will contain variations in the values of the factors, and so they will create some form of distribution as indicated in the Figure 22. It is evident that when the two distributions are well separated, i.e., the upper end of the amplitude distribution is well below the low end of the fatigue capability, then failure will not occur. It will be equally obvious that failure is certain to occur when the fatigue capability is below the engine amplitude distribution. The most difficult problems are when the two distributions just overlap as indicated in Figure 22.

The desire to separate the problems associated with blade fatigue capability from the level of vibration in the engine, has resulted in a method of assessment being developed which is an alternative to the more direct technique of stress measurement.

Stress Method and Amplitude Ratio Techniques

The two methods which have been developed have much in common, and both are effective in satisfying the basic requirement of evaluating the seriousness of a particular vibration incident. Unfortunately, the degree of expertise invested in each method, and the extensive experience gained and success with its operation, rather precludes the possibility of a serious assessment of the benefits and disadvantages of the alternative method. In the following sections each method will be introduced and a brief comparison will be attempted.

AMPLITUDE RATIO METHOD

The amplitude ratio method of assessment has been developed by the Bristol Division of Rolls-Royce, and is reported in Armstrong (1966b, 1967), and is a development of the early work on assessment of blade vibration work which was reported in Blackwell (1958). In this work the level of vibration is determined in terms of the product of tip amplitude of vibration of the blade (a), and the frequency of vibration (f). As will be shown, this product ' af ' is a very useful measure of the fatigue strength of the blade. It had been shown earlier in Pearson (1953) and Tarry (1954) that the product ' af ' was also a measure of the aerodynamic excitation, assuming that quasi-static conditions exist (i.e., zero frequency parameter) and also that mechanical damping maybe neglected in comparison with the aerodynamic forces. This analysis is repeated below.

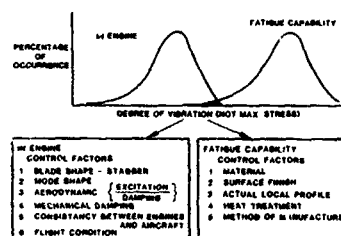


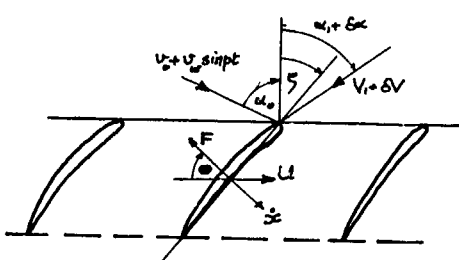
Figure 22. Factor Influencing Failures.

Thus, while these aerodynamic assumptions are not valid in absolute detail, the approach does provide the ability to relate the degree of excitation to other similar experience without introducing the detailed geometry of the blading. A decision can then be made concerning the strength of the excitation, and whether it will have to be reduced, or whether the blade can withstand it. It is also of assistance in relating the measured level of vibration to the fatigue strength of the blading, and so predicting the likelihood of blade failure in service.

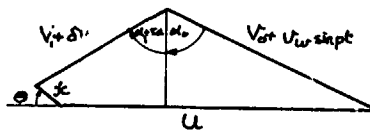
Aerodynamic Excitation and 'af'

This analysis under quasi-static conditions, i.e., zero frequency parameter, is based on that given in Pearson (1953) and Parry (1954) for wake excitation of compressor blading.

Cascade Notation



Vector Diagram



where

V_o absolute gas inlet velocity (steady)

V_1 gas relative inlet velocity (steady)

$V_o + v_w \sin pt$ absolute gas inlet velocity with wake component

U blade speed

F lift force on blade in direction of vibration

$\dot{x} = a \omega \sin(\omega t + \epsilon)$

= vibrational velocity of blade

α_0 absolute gas inlet angle

α_1 relative gas inlet angle

ζ stagger angle

θ inclination of vibration to U direction

$\delta v, \delta \alpha_1$ increments due to vibration

From the vector diagram

$$(V_1 + \delta v) \cos(\alpha_1 + \delta \alpha_1) =$$

$$(V_o + v_w \sin pt) \cos \alpha_0 - \dot{x} \sin \theta \quad \dots \dots \dots 1$$

$$(V_1 + \delta v) \sin(\alpha_1 + \delta \alpha_1) =$$

$$U - (V_o + v_w \sin pt) \sin \alpha_0 - \dot{x} \cos \theta \quad \dots \dots \dots 2$$

Expanding the L.H.S. and using the approximation for small quantities

$$\cos \delta \alpha_1 = 1 \quad \sin \delta \alpha_1 = \delta \alpha_1 \quad \delta v_x \delta \alpha_1 = 0$$

we get

$$(V_1 + \delta v) \cos(\alpha_1 + \delta \alpha_1) =$$

$$V_1 \cos \alpha_1 - V_1 \delta \alpha_1 \sin \alpha_1 + \delta v \cos \alpha_1 \quad \dots \dots \dots 3$$

$$(V_1 + \delta v) \sin(\alpha_1 + \delta \alpha_1) =$$

$$V_1 \sin \alpha_1 + V_1 \delta \alpha_1 \cos \alpha_1 + \delta v \sin \alpha_1 \quad \dots \dots \dots 4$$

Now from 1 & 2, for steady state

conditions, i.e., $v_w = \dot{x} = \delta v = \delta \alpha_1 = 0$

$$V_1 \cos \alpha_1 = V_o \cos \alpha_0 \quad \dots \dots \dots 5$$

$$V_1 \sin \alpha_1 = V_o \sin \alpha_0 + U \quad \dots \dots \dots 6$$

Therefore, using equations 1 to 6, we obtain

$$-V_1 \delta \alpha_1 \sin \alpha_1 + \delta v \cos \alpha_1 =$$

$$v_w \sin pt \cos \alpha_0 - \dot{x} \sin \theta \quad \dots \dots \dots 7$$

$$V_1 \delta \alpha_1 \cos \alpha_1 + \delta v \sin \alpha_1 =$$

$$-v_w \sin pt \sin \alpha_0 - \dot{x} \cos \theta \quad \dots \dots \dots 8$$

Multiplying 7 by $\cos \alpha_1$ and 8 by $\sin \alpha_1$ and adding we get

$$\delta v = v_w \sin pt \cos(\alpha_0 + \alpha_1) - \dot{x} \sin(\theta - \alpha_1)$$

Multiplying 8 by $\cos \alpha_1$ and 7 by $\sin \alpha_1$ and subtracting we get

$$V_1 \delta \alpha_1 = -v_w \sin pt \sin(\alpha_0 + \alpha_1) + \dot{x} \cos(\theta - \alpha_1)$$

Now with F the force on the blade

$$\delta F = \frac{\partial F}{\partial \alpha_1} \delta \alpha_1 + \frac{\partial F}{\partial v_1} \delta v_1 \quad \text{and } F = F_o + \delta F$$

Therefore,

$$F = F_o + \dot{x} \left[\frac{1}{v_1} \frac{\partial F}{\partial \alpha_1} \cos(\theta - \alpha_1) - \frac{\partial F}{\partial v_1} \sin(\theta - \alpha_1) \right]$$

$$-v_w \sin pt \left[\frac{1}{v_1} \frac{\partial F}{\partial \alpha_1} \sin(\alpha_0 + \alpha_1) - \frac{\partial F}{\partial v_1} \cos(\alpha_0 + \alpha_1) \right]$$

$$= F_o + A \dot{x} - B v_w \sin pt$$

The vibrational energy gained per second by the blade is W with frequency

$$f = \frac{\omega}{2\pi}$$

D = mechanical damping work done per second. We have:

$$W = f \int_0^T (-F\dot{x}) dt - D$$

$$= -A \frac{\omega}{2\pi} \int_0^{2\pi} \dot{x}^2 dt + B \frac{\omega}{2\pi} \int_0^{2\pi} \dot{x} \sin pt - D$$

With

$$\dot{x} = a \omega \sin(\omega t + \epsilon)$$

$$W = -A \frac{\omega}{2\pi} \int_0^{2\pi} a^2 \omega^2 \sin^2(\omega t + \epsilon) dt$$

$$+ B \frac{\omega}{2\pi} v_w \int_0^{2\pi} a \omega \sin(\omega t + \epsilon) \sin pt dt - D$$

The value of the first term, which is a damping term, is independent of the value of ϵ whereas the second excitation term will be a maximum when $\omega = p$ (i.e., on resonance) and when $\epsilon = 0$. Therefore,

$$W = -\frac{1}{2} A a^2 \omega^2 + \frac{1}{2} B v_w a - D$$

Assuming that the mechanical damping D is small and can be neglected, we have for a steady state vibration (i.e., when $W = 0$) and for no increase in energy in the vibration.

$$a\omega = \frac{B}{A} v_w \quad \text{or} \quad af = \frac{B}{A} \frac{v_w}{2\pi}$$

Thus, the product of (amplitude of vibration) times (frequency) is proportional to the velocity strength of the wake.

Clearly the expression:

$$af = \frac{B}{A} \frac{v_w}{2\pi} = \\ = \frac{\left[\frac{1}{v_1} \frac{\partial F}{\partial \alpha_1} \sin(\alpha_0 + \alpha_1) - \frac{2F}{3v_1} \cos(\alpha_0 + \alpha_1) \right]}{\left[\frac{1}{v_1} \frac{\partial F}{\partial \alpha_1} \cos(\theta - \alpha_1) - \frac{2F}{3v_1} \sin(\theta - \alpha_1) \right]} \times \frac{v_w}{2\pi}$$

is not a precise prediction of the response of the vibrating blade, but as was pointed out in Pearson (1953) and Parry (1954) and in the Blackwell contribution the discussion of Carter (1957) and Blackwell (1958) the product of af is a very convenient method of assessing the relative strength of the aerodynamic excitation from the results of a strain gauge test on a compressor or turbine.

The above analysis also holds in the case of flutter, but with $v_w = 0$. Thus, for energy to be fed into the vibration to overcome the mechanical damping, the term $\frac{1}{2} A a^2 \omega^2$ must be positive. Hence A must be negative but again the term is proportional to $(af)^2$.

In the next section it will be shown that the product (af) is also a very useful and general method for specifying the intensity of a vibration from a mechanical aspect.

Mechanical Aspects of af

Perhaps the first reference to velocity being an important criterion for the assessment of vibration stress, was given in Appendix 1 of the paper by H. G. Yates (1948). He proposed the following general proposition based on reasoning from a dimensional type of analysis.

"Mechanical vibrating systems, having geometrical similarity and constructed of the same materials, when vibrating freely in the same mode with equal linear velocities, will suffer the same vibrational stresses."

He then extends his reasoned argument to the case of transverse vibration of a cantilever beam. However, this can be confirmed by mathematical analysis which is given in full in Appendix I.

The analysis follows the standard type, e.g., Timoshenko (1937) for a beam of constant section. The assumption is made that the beam is vibrating harmonically with time and that the applied load intensity on the beam is due to the reversed mass inertias as a result of the beam's motion. The constants in this general solution are determined by the end conditions for the beam - fixed and free - for a cantilever. This, therefore, yields the frequency relationship equation, the roots of which define the natural frequencies. Using this frequency equation in conjunction with the expressions for the bending moment at the root section, and the amplitude 'a' at the free end of the cantilever, it is possible to derive the following expression, which is valid for all flexural frequencies since the frequency relationship equation was used in the analysis.

$$af = \frac{1}{2\pi} \cdot \frac{k}{y} \cdot \frac{\sigma}{\sqrt{Em}}$$

Where a = the tip amplitude of vibration

f = the natural frequency of the flexural mode

k = radius of gyration

y = distance of the highest stress fiber from the neutral axis

σ = stress on the fiber

E = Young's modulus

m = mass per unit volume

This is the important relationship for cantilevers, relating the product of the (tip amplitude) times (frequency) with the material properties of Young's modulus E , mass density m and the alternating stress σ at the root section. It has been shown by Blackwell (1958) and Yates (1948) that k/y is reasonably constant for similar section shapes. Thus, if the stress σ is taken as the value for an endurance life of say 10^7 reversals for a particular material, then all cantilevers in that material will fail at the corresponding fixed value of af irrespective of the length, breadth, and thickness of the beam.

Typical values of $\frac{\sigma}{\sqrt{Em}}$ for blade type materials are given in the table.

Alloy	Young's Modulus E GPa	Density m Mg/m ³	Endurance Stress σ MPa	$\frac{\sigma}{\sqrt{Em}}$
Aluminium	72.4	2.71	145	10.35
Steel	214	7.83	591	14.44
Titanium	113	4.43	550	24.58
Nickel Based	214	7.86	340	8.29

The relative values of $\frac{\sigma}{\sqrt{Em}}$ in this table illustrate the ability of blading in the various materials to withstand vibration as a cantilever. It will be noted that whilst the endurance stress of steel is some four times that of aluminium, the actual performance as blading will be only some 40% better. This is because of the high Young's modulus and the higher density of the steel material.

The lower values of E and m for titanium enable the titanium blading to demonstrate its far greater superiority in a vibration environment.

Similar relative values obtained from fatigue tests on blades are taken from Armstrong (1960). The values being for 10^7 reversals.

Aluminium 5.5 ft/sec
Steel 6.5 ft/sec
Titanium 11.0 ft/sec
Glass fiber laminates 12.0 to 13.0 ft/sec.

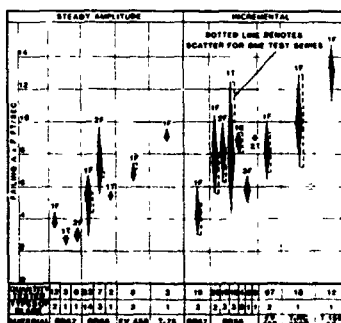


Figure 23. Compressor Blade Fatigue Strength for Different Materials and Blade Designs.

The analysis given above applies to the flexural modes only, since a similar exact analysis does not exist for non-circular sections vibrating in torsional modes. However, Yates (1948) refers to simple calculations for non-circular sections, and states that the ratio of maximum shear stress to maximum linear velocity is nearly equal to $\frac{Gm}{E}$ where G is shear modulus. This is borne out by correlations of fatigue tests on blades in the torsional modes, where the amplitude is measured at the leading edge. The early work reported by Backwell (1958) shows that the failing values of af in torsion are very similar to those in flexure - see Figure 23 which is reproduced from this reference.

Whilst the relationships developed above for flexural vibration of uniform cantilever beams are exact, the benefits which are gained by using af as a measure of the severity of vibration from a mechanical aspect, derive from the ability to compare the performance and fatigue properties of blading covering a wide range of designs, sizes, and methods of manufacture. It is not intended, as Passey (1976) comments, to be an alternative to stress as a criterion of fatigue of material, but rather as an indicator of the ability of the whole blade to withstand vibration. This must, and does, involve all the mechanical aspects of the blade.

The Measurement of af

A strain gauge positioned on a vibrating blade in an engine, will indicate the strains due to all the modes which may be excited. Each mode will of course be identifiable by the frequency content of the signal. As reported in Armstrong (1960) it is possible to find a position on a blade which provides almost equal response in a number of modes. The unit of response for this comparison is strain gauge output per unit tip af , and so to a first approximation the modal output from the strain gauge is a correct indication of the seriousness of the vibration. Initially, the position of the strain gauge was determined experimentally on a static rig, where the blade was vibrated in each mode in turn, for the modes of interest, and the corresponding gauge output and tip amplitude measured. Changes to the strain gauge position normally resulted in one being satisfactory for 3 or 4 modes. If more modes are required, then an additional position can also be used. In these calibrations, it is important to measure the tip amplitude in an identical way to that which is used during the fatigue testing on the blade. Normally, this is the leading edge, but when a nodal line is close to this edge then it is more reliable to measure the amplitudes at the trailing edge for that particular mode.

Whilst the above methods relied upon experimentally determined positions of the strain gauge to cover a number of modes, it is now possible to predict the likely sites and orientations of the strain gauges by working with data from the blade design detail using Finite Element (F.E.)

analysis methods. It is expected that an empirical calibration will be performed to calibrate the strain gauges prior to engine build but the finite element analysis route will minimize the experimental work required.

The use of tip af, as a measure of the importance of the intensity of vibration, has also led to the development of methods other than the use of strain gauges to measure blade vibration. One of these, which is particularly useful where slip rings cannot be fitted to the shaft, is the F.M. (frequency modulated) grid.

In this method - which is fully described in Eccles (1962) and Raby (1970) - a small magnet is inserted in the tip of a rotor blade. In the casing, above the track of this magnet, is fixed an accurately pitched zig-zag conductor, and the near axial portions of this conductor are spaced at 2 degree intervals. As the blade rotates at a uniform speed, a series of electrical impulses is generated in the conductor. Because of the uniform speed and the accurate pitch of the bars of the conductor, the frequency of the impulses will be constant. If, however, the blade is also vibrating while it is rotating, then the frequency of the impulses will vary. By the use of pulse shaping techniques and filtering the signal it is possible to frequency demodulate the signal and to produce a signal which is proportional to the alternating velocity of the magnet in the blade tip. As the signal is proportional to the component of the blade's vibrating velocity at right angles to the bars of the conductor, it is necessary to calibrate the direction and amplitude of the magnet for the blade's modes of vibration relative to the blade's leading edge amplitude.

As the signal generated is a frequency-modulated one, the signal strength -which is dependent upon the magnet to grid clearance -is unimportant, and so the technique is not dependent on blade tip clearance. Normally, 2 or 3 grids per stage can be incorporated. The temperature limit is that of the materials used to bond the conductor into the casing.

The tip af method of assessment also allows ready use to be made of the data obtained from measurements of the blade tip displacements as reported in Raby (1970) and Koff (1978) from probes mounted on the casing.

Blade Fatigue Capability

As explained before, the fatigue properties of a blade depend upon many factors, and in general these are not known very accurately. So the Amplitude Ratio method relies upon a comparison between the measured af in the engine and the fatigue capability of the blade as determined by test. To predict the strength of the blade in the engine, it is necessary to apply a number of correction factors to the fatigue tests, and these will be covered in this section. The majority of this section is taken from Armstrong (1966b).

A. Incremental and Constant Amplitude

It was explained before that significant benefits can be gained by using the incremental fatigue test techniques when carrying out test work, to establish the fatigue capability of a blade standard. However, it is necessary to convert the results into a form which can be compared with the amplitudes measured in the engine. The method which has been adopted is to convert the experimental fatigue results to constant amplitude data. This then allows the effect of scatter to be allowed for easily because, as explained before, the scatter properties of a blade population form a normal distribution of the log life at a constant amplitude or alternating stress.

The conversion from the incremental tests to the life at a specific amplitude is done by the use of Miner's fatigue damage summation. Thus for r steps in the incremental test:

$$\sum_{x=1}^{x=r} \left(\frac{n_x}{N_x} \right) = 1$$

represents a criterion for failure.

Where N_x is the life (number of cycles) at the amplitude S_x and n_x is the time increment (number of cycles) during the fatigue test at the amplitude S_x . It has been found that metallurgical constant-amplitude fatigue test data for blade materials when presented as a plot of log (stress) against log (number of reversals) approximates well to a straight line. Thus, the relationship:

$$SN^d = \text{constant}$$

holds and obtain

$$SN^d = \left[\sum_{x=1}^{x=r} (n_x S_x)^{\frac{1}{d}} \right]^d$$

Thus, by carrying out a small number of constant amplitude fatigue tests, it is possible to obtain a value for the index d for the material. From the above equation it is possible to obtain values of N and log N for a specific constant amplitude of vibration.

B. Scatter in Properties

One of the difficulties in the assessment of blade fatigue problems is allowing for the scatter in properties. However, this can be achieved in the following way. From the results of a small number of blades tested in the relevant mode, it is possible to establish the mean of the log life of the group at a specified amplitude.

Because we are only a small number in the sample, their mean value is likely to be different from that of the population from which they have been taken. By using a statistical technique, it is possible to estimate within a 95% confidence level, a lower limit on the mean of the whole group. This lower limit is given by

$$\frac{t\hat{\sigma}}{\sqrt{n}}$$

where t is the Students t value for a chosen confidence level.

$\hat{\sigma}$ is the best estimate of the standard deviation of the population (see below) and

n is the number in the sample.

For 95% confidence level the values of t for different sample sizes are:

n	3	4	5	6
t	4.3	3.2	2.8	2.6

With a knowledge of the mean of total population, and an estimate of the standard deviation, it is possible to predict the lowest log life in a large number of blades. Armstrong (1966b) considered the lowest one in 10,000 which is $3.72\hat{\sigma}$ below the population mean. These relationships are shown graphically in Figure 24.

In the previous paragraph, a value of the standard deviation has to be used. An accurate value will not be obtained solely from a small sample size, but it is not unreasonable to consider that the standard deviation σ is common for a similar design of blade in a certain material. Thus, it is possible to obtain a good estimate of σ from an overall consideration of all the blades tested. Hunt (1975) has done this and Figure 25 is reproduced showing how the values of σ tend to definite values for each of the three examples of typical blade materials. The bounds for each of the trends are the chi-square distribution for $n-1$ degrees of freedom, and are given by:

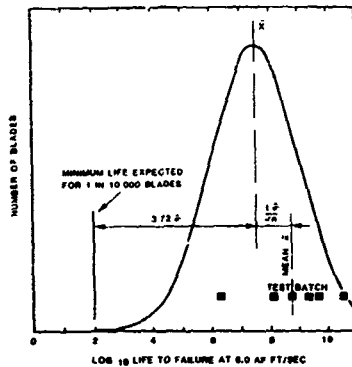


Figure 24. Statistical Determination of 1 in 10,000 Level.

$$\frac{(n-1)\hat{\sigma}^2}{x_2^2} < \sigma^2 < \frac{(n-1)\hat{\sigma}^2}{x_1^2}$$

The values of x are obtained from statistical tables, found in most statistics books, which are based on the Biometrika Tables for Statisticians, Vol. 1, Table 8.

C. Effect of Temperature

To allow for the effect of temperature on the failing amplitudes of blades, Armstrong (1966b) proposed that test data from metallurgical specimens from rotating bend tests conducted over the temperature range may be used. This information would allow a correction to be applied to the mean property, and also the index 'd' defining the slope of the $\log S$ vs $\log N$ curve. In applying this it is assumed that these changes apply directly to the material in blade form.

In the absence of more detailed information on the actual variation of the blade's operating temperature with engine speed, it is assumed that the metal temperature will vary on a speed squared law. Therefore we have

$$T = 20 + \frac{N^2}{R} (T_T - 20)$$

Where $N_R = \frac{\text{actual rev/min}}{\text{maximum rev/min}}$

T = metal temperature

T_T = metal temperature at maximum rev/min

D. Amplitude for Given Life

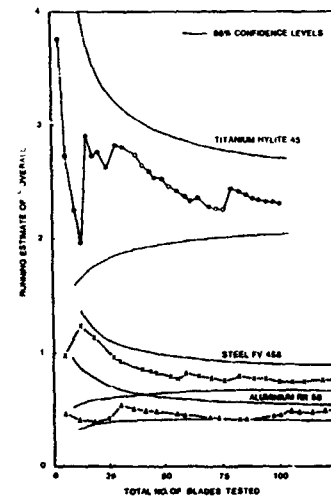


Figure 25. Best Estimate of Standard Deviation.

With the application of the foregoing sections, it is possible to predict the failing amplitude of the weakest blade in a large population in the absence of steady stresses. The effect of steady stress can be allowed for by the use of a Goodman type diagram, if the equivalent to the alternating stress axis can be established. To do this it is necessary to 'use' a realistic life and Armstrong (1967) explained that a value of 100 hours was chosen for this purpose as this is a mean on a logarithmic scale between 10 hours and 1,000 hours. It must be noted that the material properties are such, that a 20% change in stress level is worth a factor of at least 10 to 1 on life, and the time to be considered is the time at maximum vibration amplitude and not the total blade life.

E. Steady Stress Correction

In allowing for steady stress effects, Armstrong (1966b) used a Goodman type of correction and so:

$$\frac{S_s}{S_0} = 1 - \frac{S}{S_u}$$

where S_0 is the allowable alternating stress or a_f at zero mean stress:

S_s is the allowable alternating stress or a_f at steady stress and S_u is the effective ultimate stress at the operating temperature.

It is assumed in their analysis that the steady stress varies with rotor speed as follows

$$S = S_t \times N_R^2 + \frac{S_b N_R^2 \sqrt{1+x}}{\sqrt{(1+xN_R^2)}}$$

Where S_t is the direct centrifugal stress;

S_b is the total bending stress (allowing for the restoring centrifugal moment),

$$\text{and } x = \left[\left(\frac{M_{xy}}{M_{xx}} \right)^2 - 1 \right]$$

Where M_{xy} and M_{xx} are the uncorrected and corrected gas bending moments respectively for a radial blade.

The positions on the blade for which these steady stresses are evaluated, are those at the positions of the fatigue crack in the mode in question. If the position of cracking varies from blade to blade, in the batch of the fatigue tested blades, then the most severe steady stress is taken.

As discussed in the next section with the possibility of the results of finite element analysis being available today, to establish the value of steady stresses, these results may be more applicable than the relationships given above.

F. 100 Hour Amplitude Curves

It is now possible, with the steady stresses applicable for a particular engine speed, to obtain from the Goodman type diagram the amplitude of vibration, a_f , for the 100 hour life. If this is completed for all speeds, a series of curves can be drawn, one for each mode of vibration under consideration. A typical curve is presented by Armstrong (1966b) in Figure 26 for four modes of vibration.

These curves can be used directly in comparing the measured a_f , from an engine test, in order to assess the seriousness of the vibration.

Amplitude Ratio and Rules

It has been explained before that an informative way to assess the importance of a vibration amplitude, which may cause a high cycle fatigue problem, is to form a comparison between the measured amplitude and that which will cause failure. This therefore gave rise to the concept of an amplitude ratio which is defined as:

Amplitude ratio % =

$$= \frac{\text{Maximum measured amplitude} \times 100}{\text{Amplitude for 100 hour life}}$$

A survey of the observed amplitude ratios, as determined above, was compared with the service experience of the blading, and is reported by Armstrong (1966b and 1968). From the results of this correlation it was possible to propose the following design/development rules.

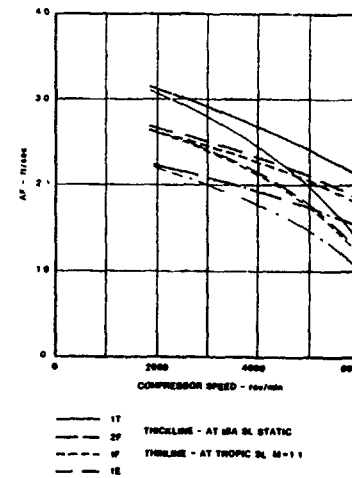


Figure 26. Typical 100 Hour Life Curves.

- A. If the amplitude ratio in any mode is found to be greater than 100%, then adequate engine restrictions must be imposed until satisfactory engine modifications have been incorporated. Service evidence has shown that short life failures had taken place with amplitude ratios greater than 100%.
- B. When the amplitude ratio lies between 50% and 100% then failures during long service use may be expected. In these cases, long term rectifications and improvements should be prepared.
- C. For amplitude ratios less than 50%, the vibration may be considered to be acceptable for the full service use.

These rules have proved to be satisfactory for the last 20 years, Armstrong 1980, but it is emphasized that to obtain a thorough assessment it is necessary to carry out the strain gauge survey at all flight conditions. See also the section "Flight Testing" further below.

Foreign Object Damage (F.O.D.) and Ex Engine Blades

During engine service use, the blading suffers foreign object damage (F.O.D.) or in some cases the surface of the blades deteriorate due to corrosion and erosion. This results in the problem of establishing what should be the limits of acceptance for this form of damage, and in the case of blades showing corrosion and erosion on engine overhaul, to determine if they are acceptable for engine rebuild.

The amplitude ratio method provides a technique for readily answering these queries. Fatigue tests are carried out on the defective blades, in the modes which exhibit cracking where the damage is most severe. Or alternatively in those modes with the highest amplitude ratios. From these results it is possible to establish a new 100 hours life for this standard of blading. With the originally measured bench or flight amplitude data it is possible to create a new assessment which can be called an Effective Amplitude Ratio. Obviously, the same rules for acceptance can be used as for the new blades.

STRESS LEVEL METHOD

The stress level method of assessing the severity of a blade vibration is basically very straightforward, and follows directly from the strain gauge investigation work of the early days of jet engine development. In essence, the alternating stress at the most critical part of the blade is measured by the use of strain gauges, and then this level is compared with the material properties. The problems which arise are a consequence of the complex stress distributions of current high performance blading and the lack of sufficient knowledge of the material properties. However, these problems have been overcome, and a number of companies employ these techniques very successfully in their assessment methods. However, its successful operation does rely upon a good background of practical knowledge and ex-

perience, and so only the basic aspects of the methods, which are published in the technical press may be reviewed here.

Steady Stress Distributions

A knowledge of the steady stress distribution is equally vital to both the Amplitude Ratio Method as it is to the Stress Level Method, because the level of steady stress, through the Goodman or equivalent type of diagram, establishes the level of vibration which may be permitted. It is discussed here because some aspects are also applicable to the study of the alternating stress distributions.

Modern finite element analysis methods permit the stress distributions over the whole of the blade surface to be predicted. However, to obtain a sufficient accuracy does demand a fairly small grid size, and for the modelling of the blade platform and root fixing zones, solid or brick elements will be required. As is reported by Koff (1978), it is possible to confirm these calculated values either by strain gauge measurements or by photoelastic tests and analysis. The obvious advantage of the finite element analysis is that it is possible to perform the calculations for various combinations of the steady state force systems which might be present.

In order to appreciate the results of the detailed finite element analysis, it is beneficial to understand the physical representations of the force systems which are present, and also the reasons for the stress/strain distributions which will be observed in practical blading. The steady state forces may be considered, for cantilever blading, to be caused by four force systems.

- A. Centrifugal forces acting on the blade sections. In the absence of high degrees of twist if the centers of mass of each section lie on a radial line, then these forces will be a radial force giving rise to an average P/A type stress; at sections remote from the fixing.
- B. Because of the variation in stagger angle of the blade from root to tip, the centrifugal body forces acting on the leading and trailing edge zones of the blade will not be normal to the blade sections. Thus, there will be a component of force, in addition to the radial force, which will act in the tangential plane and cause a twisting moment which will alter the blading stagger angle.
- C. The aerodynamic forces on the blade sections. There will be both forces which cause bending of the blade about its two principal axes, and also an aerodynamic twisting moment.
- D. If, as is the usual practice for large and medium size blades, design causes the centers of mass of the blade sections to lie off a radial line through the root section of the blade, then the centrifugal forces will also result in bending moments

about the blades' principal axes. It is customary to design the blade shape so that the combined gas bending moment, and the centrifugal bending moments, provide the optimum stress condition. Note the gas bending moment will be a function of the flight condition, and so the optimum arrangement will depend upon the aircraft duty.

The stress distribution within the blade aerofoil which would be obtained by the application of the elementary Euler beam theory, under the action of the above forces, will be modified by a number of effects. These modifying factors are discussed by Danforth (1975) and Shorr (1961).

Warping Stress due to End Restraint

If a thin rectangular beam is rigidly fixed at its end, then under the action of a torque, the Saint Venant shear stress distribution (which would be obtained in a free beam) is modified. The edges of the section undergo a bending type of distribution as in Figure 27 from Danforth (1975). For a thin rectangular section the bending stress can be 2.9 times the shear stress.

Effect of Partial Chord Root Fixing

It is unusual in the design of the root fixing for the root to be the same chordal width as the aerofoil at the station above the platform. Thus, the leading and trailing edge zones of the blade will not be fully supported, and the stress distribution as determined by a completely rigid fixing will be modified. Figure 28 from Danforth (1975) shows this effect of axial width reduction. This effect would be much more severe in the case of blades which are carried in a circumferential slot, where the axial width of the portion below the platform may be only 1/3 or less of the aerofoil chord.

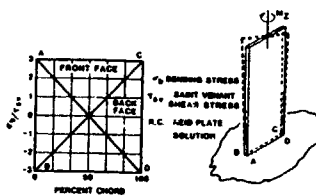


FIG. 27 - ILLUSTRATIVE ELEMENTARY END EFFECT STRESS BENDING AT ROOT OF CANTILEVER BAR IN TORSION

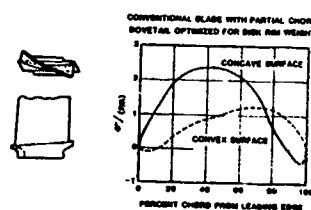


Figure 28. Illustrative End Effects Stress Blade Root in Spanwise Pull Compared to Nominal Pull/Area Stress.

Blades with High Rate of Stagger Change

When a blade has a high rate of change of stagger along the blade span, and when it is subjected to a torque load, the twist distortion is accompanied by tensile stresses in the leading and trailing edge zones of the blade. In order to provide the equilibrium of forces normal to the aerofoil section, a stress of opposite sign and reduced magnitude is set up over the central zones of the blade.

Blades with Root Camber and High Degree of Stagger Change

Shorr (1961) explained that when a high rate of change of stagger was present with highly cambered sections, then the three force systems, - radial load, torsional twist, and bending moment about the least moment of inertia - are all coupled with their corresponding displacement strains.

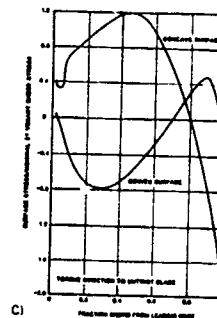
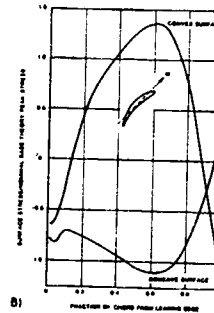
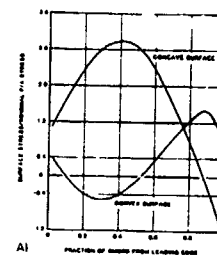


Figure 29. End Effect Stresses for Illustrative Fan Blade Root Section (A) Spanwise Pull, (B) Moment, and (C) Torque Load.

Danforth (1975) provides the stress distribution around the root section periphery, for a fan blade design, as shown in Figure 29. Where the loading is, in turn, that of a pure pull load—the radial component of the centrifugal field—a pure bending moment about the section axis with the least second moment of area, and a pure torque. The stress magnitudes are normalized with respect to their respective beam theory counterparts.

Results for Typical Fan Blade

The actual stress distribution for a particular blade will depend upon its detail geometry and blade/disk root design, but the values may be obtained by the application of finite element analysis, photoelastic test, or an approximate numerical solution following the work of Zbirohowski-Koscia (1967). Koff (1978) provides a comparison of the strain distribution at an aerofoil root of a fan blade, determined both by strain gauge test and by finite element analysis. These results are reproduced in Figure 30. It will be seen that the character of the distributions is of the same form of those given in Figure 29.

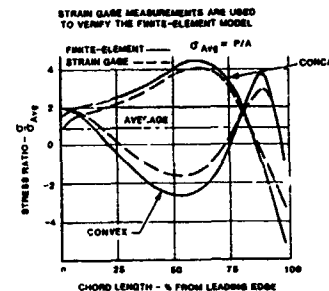


Figure 30. Fan Blade Stress Analysis - Comparison of Finite-Element and Strain Gage Measurements at Airfoil Root.

Alternating Stress Distributions

The stress distributions of a rectangular section cantilever beam when vibrating in the flexural modes are relatively straightforward, and in Figure 31 are presented the variations of stress for three different taper ratios. However, as in the case of the steady stress distribution the distributions become more complex, when actual blade geometries are considered. In the case of vibration, as opposed to steady loading, the situation is more involved. As for each mode of vibration, the modal shape, and so the frequency, are dependent upon the elastic distortion of the blades under the action of major inertia force systems. Thus, on

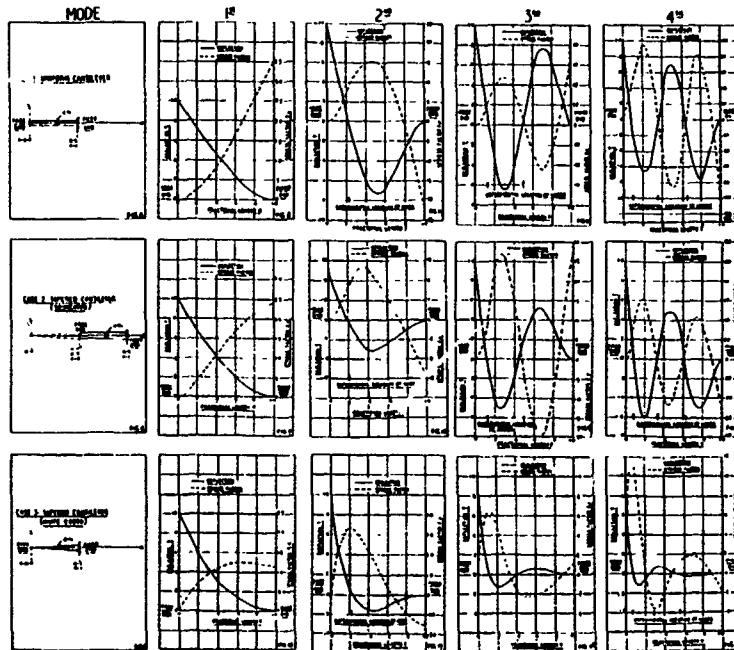


Figure 31. Deflection and Stress Distributions for Tapered Cantilevered Beams.

a fan blade, which has at its root, both high camber, and a rapid rate of change of stagger at sections above the platform, then in the 1F mode, which is predominantly bending about the axis of minimum second moment of area, the stress distribution will be similar to that of Fig. 29. These coupling effects, primarily due to end effects, will therefore result in motion in the torsional and edgewise coordinates being present in the mode. These additional distortions together with the associated inertia forces result in a change in the natural frequency, from the 'Euler beam' frequency value which would neglect these effects.

Experimental Determination of Strain Distributions

As reported in Passsey (1976), a visual impression of the strain distributions of a blade may be obtained by carrying out an incremental vibration test, with the aerofoil surface coated by a strain sensitive brittle lacquer. This then gives a series of strain contours and so the strain distribution.

In Figure 32 are presented the results for the 1F, 2P, 3P, and 1T modes of the first stage rotor blade of an LP compressor. It will be seen that, for the 1F mode, the maximum strain on the concave form is in the central zone of the aerofoil, as would be anticipated from Fig. 29 for the bending moment about the minimum axis. This is also true of the root stations for the higher modes, but the peak strains in these modes are found in areas nearer the blade tips. Also in Fig. 32 are the strain distributions for the 1T mode, which shows the peak strain to be present in the leading and trailing edges, and not in the areas of maximum aerofoil thickness as one would expect from torsional strains of a beam with long thin sections. The reason was discussed in the section "Blades with High Rate of Stagger Change."

These alternating strain distributions will of course be altered to some degree under the action of the centrifugal field. The extent of the change will depend upon the mode, the stagger angle, the hub to tip ratio of the stage, and the blade aspect ratio, but the general pattern will remain.

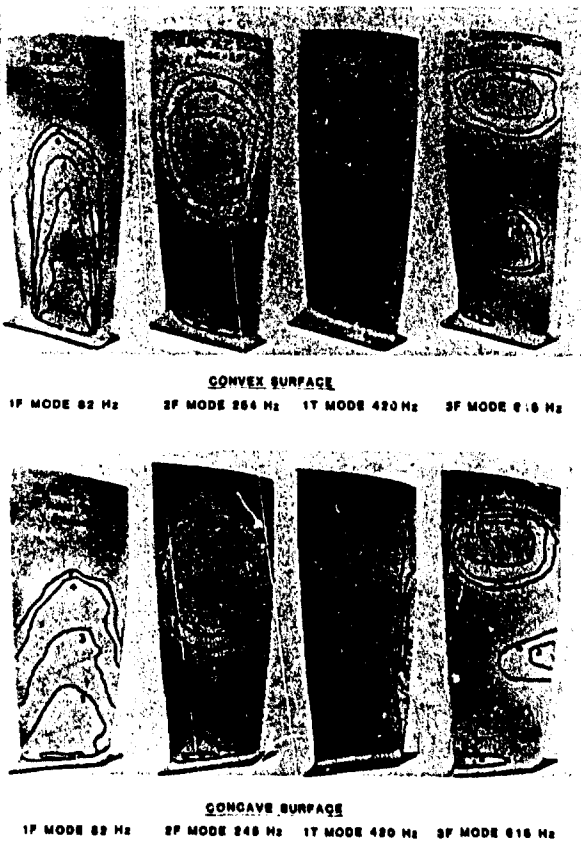


Figure 32. Surface Strain Distributions.

It is of course possible to obtain an indication of the strain distribution by the use of a matrix of strain gauges, but the accuracy and degree of appreciation will depend upon the number of gauges employed.

Calculation of Strain Distribution

It is also possible to calculate these strain distributions, from a finite element analysis of the blade, provided that the element size is sufficiently small, and that the blade fixing is modelled accurately enough. Such an investigation of a turbine blade has been reported in Peterson (1978) for the assessment of the levels of blade vibration measured by strain gauge testing. Figure 33 is taken from that paper, and shows the finite element model which employed three-dimensional isoparametric elements, which are formulated either as solid or thin shell versions, to allow the representation of thin airfoils and attachments with the same element configuration. The result in Figure 34 shows the steady state effective stress distribution. In Figure 35 is presented the strain of the 7th mode which was in resonance with the nozzle guide vane order.

Material Properties

One of the major considerations, in the stress level method of assessment, is the knowledge of the material properties,

which are necessary to derive the allowable values for comparison with the stress, as determined from the strain gauge measurement. In the work of Danforth (1975), Peterson (1978), Passey (1976) use is made of a Modified Goodman type of diagram or stress range diagram. Fig. 36 and its description is taken from Danforth (1975) and represent the typical form. "Curve 'C₁' represents the upper bound of alternating stress for unlimited life, vs mean stress as given for statistically "minimum" properties. Curve 'C₁' reflects undamaged material manufactured according to prescribed blade surface preparation, and without concentration. Curve 'C₂' represents the blade fatigue strength in terms of the nominal stress in the presence of a notch, (whether of design geometry, foreign-object damage induced, or a notch-equivalent degradation induced by instrumentation surface preparation for test vehicles). The level and shape of curve 'C₂' relative to 'C₁', depends upon the notch concentration - the higher the concentration, the lower and more concave is curve 'C₂'. Curve 'C₃' is in a sense the limiting case of the curve 'C₂' family. It represents the upper bound of alternating stress, consistent with crack propagation avoidance, a level of significance for blade durability in the presence of extreme F.O.D.".

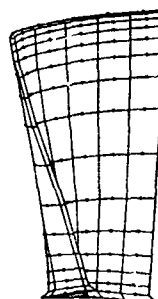


Figure 33. Turbine Blade Finite - Element Model

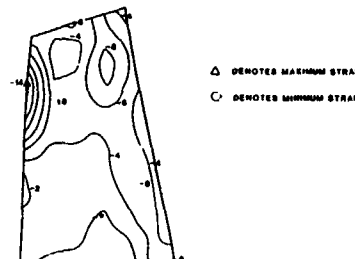


Figure 35. Vibratory Strain (Plus Three Standard Deviations) on Turbine Blade Pressure Surface (Micro-Strain $\times 10^{-2}$).

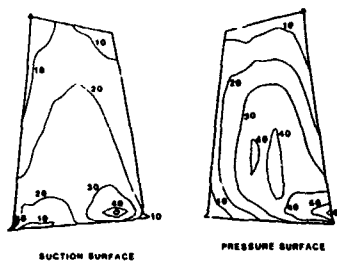


Figure 34. Turbine Blade Steady-State Effective Stress KN/cm^2 .

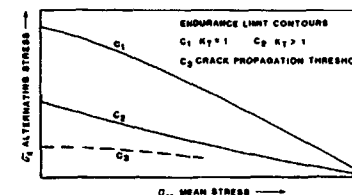


Figure 36. Schematic of Typical Stress Range Diagram.

For development work, the severity of a measured stress may be expressed as a "percentage endurance", by comparing the measured alternating stress with the alternating endurance stress from curve 'C₂' having applied the correct mean steady stress.

Typical values of alternating stress which may be used are seldom reported, although Passey (1976) does provide the following table of safe levels of alternating stress.

SAFE ALTERNATING STRESS RANGE

<u>Material</u>	<u>(Peak-Peak) lb/sq in</u>
Aluminium Alloy	10,000
Titanium Alloy	25,000
Steel	25,000
Nickel-Iron Alloys	35,000

Passey attributes the low level of these stresses to the influence of damage and surface imperfections.

Koff (1978) expresses the opinion "that the actual fatigue strength of engine components is best evaluated by bench testing, where the parts are subjected to vibratory load to induce failure." Tests are carried out on instrumented blades to evaluate the design, material, and manufacturing process under partially simulated conditions, i.e., heating coils are used to raise the temperature to provide hot fatigue testing. From the testing, it is possible to compare the results with anticipated properties for the parent material, and also to complete a fatigue limit diagram for use in blade assessment, i.e., curve 'C2' of Figure 36.



Figure 37. Ceramic Versus Thin Film Strain Gages.

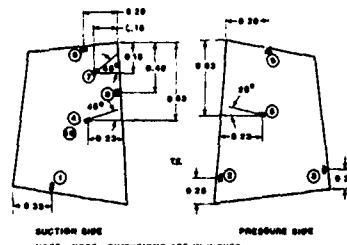


Figure 38. Typical Turbine Blade Strain Gauge Installation.

Strain Gauge Position and Operation

The number of gauges which are used on a blade may be restricted by the size of the blade and the lead out wire arrangements. Normally 3 or 4 strain gauge locations are used per stage, and 4 blades in a stage will be instrumented to allow for blade to blade variation and gauge failure. However, the problem of gauge failure is much reduced by the adoption-
 Koff (1978)- of thin film gauges Figure 37. It is stated that thin film gauges offer higher quality, lower cost, improved test survivability, and a 60% improvement in the strain level that can be measured. The usual ceramic strain gauges fail at approximately half the amplitude necessary to produce an aerofoil failure, whereas tests with thin film gauges have permitted measurements of strain levels up to the failure amplitude.

The ability of the strain gauge to withstand high levels of alternating strain, will also control the positioning of the gauges. The requirements are, that it should be able to measure a significant response in more than one mode, but if its fatigue strength is limited, then it must not be used in anticipated areas of the highest alternating strain. With 3 or 4 gauges, up to 8 modes can easily be covered. Figure 38 from Peterson (1978) shows the positions selected for a small turbine blade. The detailed investigation, see later, centered on the 7th mode. Because of the small blade size, in this instance, only one gauge per blade could be accommodated.

By rig test calibrations for each mode in turn the relative sensitivity of the gauge positions may be established, and related to the level of the highest alternating stress on the blade.

This data, coupled with a knowledge of the stress distribution over the surface of the blade makes it possible to obtain a ratio between the critical point vibratory stress, to the apparent stress sensed by the strain gauge ($\frac{\sigma_{CP}}{E_{\theta}}$). This stress distribution will have been established by one of the methods discussed above. Danforth (1975) uses this form of ratio to establish the "scope limits" for use during live strain gauge testing, to assess the severity of a vibration.

$$\sigma_{sc} = \frac{2\sigma_{acp}}{K_v \cdot K_e} \cdot \frac{\sigma_{cp}}{E_{e\theta}}$$

Where σ_{app} is the stress range diagram endurance stress for the critical point under the given operating conditions.

$\frac{\sigma_{cp}}{E_{\epsilon\theta}}$ is the stress ratio as above and will be mode and speed dependent.

K_v is an experience - derived factor greater than one, implying the presence of a blade in the stage more active than the one directly observed.

K_e is a mode frequency dependent function to allow for frequency response of equipment.

The factor 2 is dependent upon whether the oscilloscope is calibrated, using 'peak-to-peak' signals or not.

Correlations and Criteria For Failure

One of the major problems in the assessment of blade vibration test data is the variability of the information between blades and strain gauges. The test data presented in Peterson (1978) illustrate this point. During this turbine test, 6 strain measurements were made for the 9 strain gauge positions, Figure 38. If all the blades had been vibrating at a common amplitude, then the scale factors to apply for the calculated stress pattern, which is necessary to provide a common level at the point of maximum stress, would have been the same. The mean and standard deviation of these 54 scale factors were calculated, and then applied to the strain at the measurement position. These are compared with the measured data in Figure 39.

The reasons which are given as contributing to the variation in the scaling factors for the nine gauges and six time points are:

- Blade to blade variations in dimensions, material, properties, temperatures, loading, damping, etc.
- Variations in engine conditions and excitation levels in the operating range, including acceleration rates, pressures, temperatures.
- Gauge position and wiring routing influences.

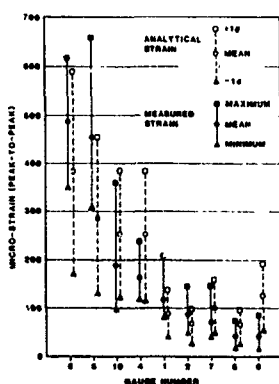


Figure 39. Ranges of Measured and Analytical Strain Data.

The predicted maximum strain was obtained by using a scale factor of 3 standard deviations above the mean. This resulted in the principal strain distribution on the pressure surface shown in Figure 35. It shows a peak level at a position removed from a measurement point, and some 4 times the highest peak measured.

The test data was presented also on a modified Goodman diagram, and is reproduced in Fig. 40 where it will be seen that the points all lie below the nominal endurance line. However, the fact that the critical points may not be represented in the measured data was highlighted by the inclusion of Fig. 41. This plots all the calculated points from the finite element analysis nodes, with the alternating levels scaled to correspond to the empirical data. It will be seen that two points with high steady strains are above the endurance line.

COMPARISON OF METHODS

It is important in discussing the pros and cons of the two methods of assessment which have been reviewed, to identify the purpose of the investigation. The prime purpose in this handbook is to be able to assess those situations where failure is principally due to high cycle

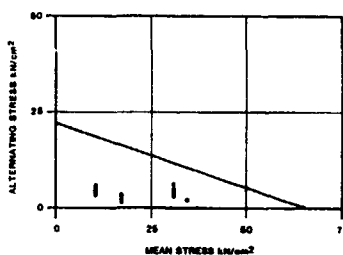


Figure 40. Modified Goodman Diagram for Peak Strains Measured in Engine Test.

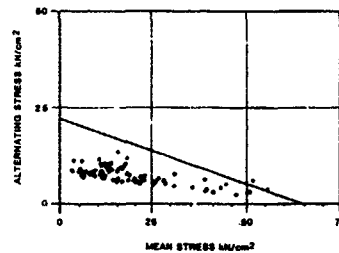


Figure 41. Modified Goodman Diagram Including Analytical Data.

fatigue, i.e., if there were no vibration the component would not fail. If this purpose is accepted, then it automatically rules out that portion of the modified Goodman diagram where the magnitude of the applied steady stress is comparable with the ultimate tensile strength. The repeated application of these steady flight flightstresses would cause a failure which is basically an L.C.F. type of failure. Under these conditions of high steady stress the failure will be aggravated by the presence of high cycle vibration and so the problem will not be corrected by reduced aerodynamic vibration - it is essentially a steady stress problem, which is identified by stress analysis and not strain gauge and vibration testing.

Company Organization and Size

There can be no doubt that both methods have been developed to provide accurate and practical tools for assessment purposes. However, each method does require significant expertise and experience and background data. Much of this data, especially the material test data for the stress level method, is not available in the open literature, and can only be obtained by extensive testing, which is usually only practicable in large companies. Equally, the amplitude ratio method may require a high content of experimental rig testing on components. The facilities for these tests will require moderate investment, as long as the number of components to be reviewed is not large.

Which of the two methods is adopted will depend to a large extent upon the way in which the technical departments in the company interact, and also the engineering style which has been adopted by the company. The 'af' aspects of the amplitude ratio method enable some aspects of the aerodynamic excitation to be assessed independently of the mechanical stress analysis/fatigue considerations of the problem. This will be of prime interest to the aerodynamic design departments, while the development groups will be more familiar with stress levels and material properties.

Defect Investigation

When it is necessary to investigate the cause of a fatigue crack, defect or failure, then it must be the correct procedure to ensure that a strain gauge is positioned at the crack location. Care must be taken to be sure that the gauge is applied to the relevant surface, if the crack is in a thin section like a trailing edge. In these investigations, it will be prudent to use other strain gauge positions in addition and to cross-calibrate the gauges for all possible modes so that should the gauges at the crack location fail, then the testing may continue by monitoring the alternative gauges. In this aspect the methods are very similar, especially if the amplitude of the leading edge is used as a reference.

Fatigue and Amplitude Scatter

There can be no doubt that the biggest problem which has to be overcome by the adopted assessment method, is the scatter in fatigue capability of blades, and the variation of amplitudes between blades in the fleet of engines to be assessed. Many factors contribute to the scatter in the fatigue strength of blading, and it would appear to be very difficult to allow for all these factors effectively by correcting the results of laboratory type fatigue tests which might be obtained from special specimens, both notched and un-notched. As inferred by Koff (1978), even for the stress level method, fatigue testing of representative blades is the optimum way to establish the fatigue capability of the blade. From these tests, it has been shown that a satisfactory allowance for the fatigue scatter can be made.

Equally difficult to accommodate is the scatter in amplitude between blades within a stage, and within a group of engines. The stress level method uses a special factor k_y to account for the anticipated variations. However, its value is obtained from experience, and so is difficult to obtain initially. By using the maximum modal amplitude from a small number of instrumented blades, together with a survey of service experience, it has been possible with the amplitude ratio method to set up assessment rules which have not needed to be altered during some 20 years of use Armstrong (1966) to Armstrong (1980). One advantage of this method is that it does not involve any experience factors other than the interpretation of likelihood of long term failures, when the amplitude ratios are between 50% and 100%.

For Cantilever Assemblies

One failing of the amplitude ratio method is when the blades form part of an assembly, e.g., a part span bladed disk design. In these circumstances it is not practicable to carry out fatigue tests in the correct modes. For these conditions, the method adopted compares closely with the stress level method, although the fatigue strength of the section can be derived from instrumented blade fatigue tests in a mode which approximates to that of the assembly mode of interest. Under conditions when the anticipated amplitude ratio is becoming high, it is possible to carry out a calibrating fatigue test on a whole bladed assembly, in a facility similar to the rotating fatigue test in the whirligig facility, Koff (1978).

Of course, the assessment of complete assemblies by the stress level method should provide few problems above those encountered for cantilever blading.

Ex Engine and Damaged Blades

The consequences of surface damage on blading after service engine running can be readily assessed from the amplitude ratio method using the effective amplitude ratio. For the stress ratio method, if the fatigue properties of ex engine blades are compared to new blades by fatigue tests, then they can easily be incorporated into the method. Otherwise, it is difficult to see how they can be assessed by the stress level method, because of the difficulty of reproducing the damage on laboratory type fatigue test specimens.

These same comments also apply to the necessary approval process which has to be cleared before a repair technique can be used for damaged blades.

Optimum Method

No doubt the optimum technique is a blend between the two methods. Calibration of the strain gauges to a movement of the blade's tip section, allows the severity of the aerodynamic excitation to be quantified. The application of this calibration may also reduce one of the sources of scatter when deriving the degree of vibration of the blades. The fatigue strength of blading could be measured by fatigue tests on instrumented blades, and after corrections for the environment, scatter and steady stresses, the results could be compared with strain gauge measurements from engine test. In this way bladed assemblies could be handled, and the benefits of both general methods obtained.

STEPS OF ASSESSMENT AND TEST CONDITIONS

The assessment of blade vibration must be a continuous process throughout the life of an engine, from the project stage right through to the evaluation of engine blading during service use. At the project stage, the general vibration characteristics of the blading should be considered when the scantlings of the major engine components, compressors and turbines, are being sized. Detail adjustment can then be made during the design phase. The design predictions must then be verified as early as possible during compressor and turbine rig testing. Full engine development then follows, including, tests in altitude facilities and flight testing where appropriate, as well as bench testing.

The above sequence of testing provides the ability to obtain the earliest indication possible of any likely major problems. This is advantageous in two ways. Not only does it give the best protection against possible component failure, but the early knowledge that a new component or change in operation is required minimizes the quantity of components which will be scrapped or need modification. By minimizing the cost of the alterations in this way, it enables the correct change to be adopted without risk of compromise.

Design Assessment

It is now possible with modern finite element analysis to predict the natural frequencies of cantilever blades, bladed assemblies, and bladed disks including the necessary allowance for temperature and centrifugal effect. Thus, it is possible at the design stage to construct a Campbell diagram of frequency against engine speed. This diagram will be completed by adding the major sources of excitations due to non-uniform variations of flow around the blading annulus, e.g., structural struts, intake distortions, numbers of blades in adjacent rows.

Types of Vibration

Blade vibration phenomena fall into two major categories. That due to self excitation, and that due to forced resonance type of excitation. The methods of accommodating each by the assessment method is quite different.

Self Excitation

For the cases of self excitation or instability, i.e., subsonic stall, supersonic stall, supersonic shock, conditions of choke, disk shroud system subsonic stall, etc., it is generally accepted, Cardirale (1980), Danforth (1975), Armstrong (1960), Danforth (1967), that sufficient operational margin must always be provided.

Methods of calculating the conditions for this type of self excitation are provided in other chapters of this handbook but, because of the difficulty of performing these calculations, it will always be necessary to verify that sufficient operational margin is provided. At the design stage, in addition to the prediction for the nominal conditions, it will also be necessary to allow for other additional effects. For instance intake distortion and intake air density under flight conditions, Figure 42 and Figure 43, are taken from Halliwell (1978) as examples.

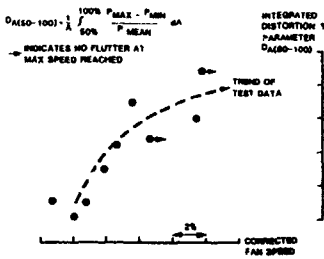


Figure 42. Correlation of Integrated Distortion Parameter with Average Flutter Onset Speed For Different Intake Types.

Forced Response and Resonance Conditions

The location of possible resonant conditions can be obtained from the predicted Campbell diagrams. However diagrams will indicate many resonances, especially if the harmonics, as well as the basic frequencies generated from obstructions in the air stream are included. The problem exists as to which of these resonances may be accepted in the design, and to identify those which should be removed, either by modification to the blade to change the frequency or by adopting a different number of obstructions, e.g., struts across the air stream.

Currently, the ability of theoretical methods to predict the amplitudes of these resonances is not very good, and so recourse has to be made to experience based design rules. Armstrong (1960), Danforth (1967) recommended that resonances with the lowest 4 modes, and a recognized circumferential disturbance should not exist in the high portion of the speed range. Armstrong (1960) suggests that the lower limit of this speed band should extend down to the idle zone, and also that this rule should apply to two stages adjacent to the source of excitation. It is also stressed in Danforth (1967) that a "two per rev" resonance in the idle to maximum speed range should not be accepted, as some degree of this excitation pattern will always be present.

The presence of low engine orders is especially relevant when considering the early stages of a compressor, and the possible excitation due to intake distortion patterns. Armstrong (1965) reports on some early work which was carried out to predict the levels of fan blade vibration from aircraft intake distortion patterns. With today's improved analysis procedures, it is expected that this type of prediction could be much improved.

Danforth (1974) outlines the type of analysis which will be required to predict fully the levels of vibration from distortion patterns. However, there is little published data showing the accuracy attained by these more complex and thorough analyses.

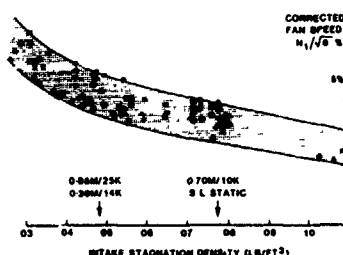


Figure 43. Effect of Intake Air Density on Supersonic Flutter Onset - Accumulated Test Data For -30 MPa Stress.

For obstructions downstream of a rotor blade, Armstrong (1967) suggests that if the obstruction in the air stream can be approximated to an aerofoil, then it is possible to estimate the velocity variations of the flow by employing a potential flow calculation for the equivalent standard shape. It was found that the best correlation was obtained by a comparison of the measured 'af' of the resonant blade and the relevant harmonic of the excitation. This correlation is reproduced in Figure 44 from which an anticipated 'af' can be obtained from the magnitude of the flow disturbance.

Rotor to Stator Resonance

With close pitching of rotor to stator blade rows in a compressor, there is a possibility of the flow disturbance arising from the blades in the adjacent blade row. Because of the relatively high numbers of blades in a row, the modes of vibration which will be excited are normally the higher modes. Cardinale (1980) discusses this problem and considers designing the appropriate adjacent blade rows with the required aspect ratio to avoid the rotor's or stator's first two stripe (1-2s) panel mode resonance with its adjacent row's passing frequency. This is illustrated in Figure 45 from the reference. Based on their current solidity trends, they found the criterion to be satisfied when the ratio of blade to stator aspect ratio was approximately 0.6.

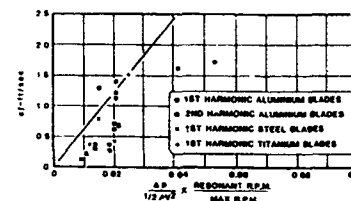


Figure 44. Comparison of Downstream Excitation.

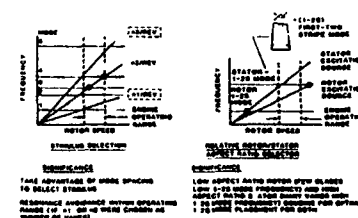


Figure 45. Schemes for Frequency Tuning.

Rotating Stall and Separated Flow

Until the mid 1960's, there was a significant problem of compressor blade failure due to unsteady rotating stall or separated flow type of excitation. Armstrong (1960) in the Design Rules for Blade Vibration the following is proposed, "so that the general level of vibration and the lower levels of random type of vibration can be accommodated, the compressor blades should be stressed to withstand a minimum vibration of ± 2.0 ft/sec".

With the aluminium (and to a lesser extent with the steel) alloys which were used for blades, this anticipated level of vibration, together with the steady stresses would be very significant, and in some cases would not provide an acceptable blade design. Two things have eased the problem. The first is the wider use of the titanium alloys with their inherent ability to withstand higher levels of vibration, thereby making it easier to comply with the above design rule. The second major factor is the wider use of variable geometry within the compressor. This results in a reduced speed range zone with rotating stall, or separated flow, and often the excitation is of reduced intensity.

It is, however, a prudent design rule to adopt wherever possible, to enable unanticipated minor excitations to be withstood.

Design Verification

In the design process, many assumptions have to be made in order to idealize the problem until it becomes one which is tractable. It is therefore necessary throughout the engine development process, to carry out testing to ensure that the behaviour of the parts is in acceptable agreement with the predicted characteristics of the idealized systems.

Mechanical Aspects

Testing therefore has to establish the following characteristics of the basic components.

- A. The natural frequencies are as predicted with a representative type of fixing.
- B. The fatigue strength of the blade is as anticipated.
- C. The natural frequencies in the operating machine are not unexpectedly influenced by touching platforms, shrouds, spacer constraints, etc.
- D. The combined bladed disks assembly frequencies are as predicted.

The levels of vibration for a given set of component characteristics will be dependent upon the aerodynamic test conditions, and the mode of operation of the unit which will be briefly discussed below. However, these amplitudes may also be influenced by factors which cannot be readily allowed for by calculation, and so it is necessary to obtain test data from

at least a small number of blades. Usually, 4 blades are instrumented an identical way. This will then allow for differences in manufacturing tolerances, which may affect the mechanical damping, etc., to be covered in a general way. One factor which should be specifically accounted for is the influence of blade frequency variations on the amplitudes of vibration. Research work has shown that the largest and smallest amplitudes of a blade row are often predicted to occur on either of the blades, with the highest or lowest frequencies. It is therefore advisable to select these blades and to include them in the smaller number to be instrumented.

Rig Compressor Testing

Aerodynamic rig tests provide an ideal opportunity to establish the vibration characteristics of the blading over the whole performance map of the unit. In this way it will be possible to establish the zones of self excitation in relationship to the anticipated work line. In this connection, it is worth reminding the reader that it is often the practice with large compressor tests to throttle the intake to reduce the power requirements. As we have seen, this will have the effect of increasing the onset speed for flutter.

With units incorporating variable stator vanes, it is normal to carry out testing with the full range of variable angle settings, to establish the extent of rotating stall zones, and any possible flutter conditions on the following rows. This information is essential to set satisfactory operating control laws for the vanes, so that a satisfactory margin from these flutter conditions is determined.

A number of the techniques employed in this type of testing with variable stator geometry are covered in Cardinale (1980).

Engine Development Tests

If design verification is to be applied satisfactorily, it is essential that engine components are instrumented in engine use as early as possible. Priority should be given to the first and last two rows of compressors, as well as to stages adjacent to variable geometry stators. This testing will confirm, on the correct engine component parts, the indications obtained during compressor testing. This testing, however, will be representative of engine use, as it will be operated over the correct work lines. It is normal practice to carry out recordings over slow accelerations and decelerations at the rate of approximately 2,000 rpm/min Armstrong (1960), Armstrong (1967), and in addition, slam accelerations and deceleration should also be recorded. This type of testing is included in the table Figure 21 of conditions to be surveyed and includes data from Danforth (1975).

As part of the engine development program, tests should always be carried out with the engine fitted behind an aircraft intake. This will confirm whether any additional forcing excitations are

present in the intake flow. The bench test program should also include the consequences of likely malfunction of the engine control system; examples being; sudden opening of reheat nozzle, mal operation of variable vanes or blow off valve, operation of deicing air.

Strain gauge testing should also be employed during any testing in engine altitude test facilities, as this will provide an early anticipation of the influence of the worst flight conditions. As Fig. 43 would imply, high intake densities, i.e., high aircraft speeds at low levels, may cause a worsening of any flutter condition.

Flight Testing

A series of flight tests will be essential to ensure that service failures can be avoided. Normally it will be the early stage blading which will be instrumented because they will be affected most by the special flight conditions. These conditions will result from the aircraft operations which cannot be simulated in the altitude test plant. Typically, they will be:

- A. Intake conditions during the take-off phase for supersonic aircraft.
- B. Operation of single and dual engines in installations where the intake of one will affect the second.
- C. Aircraft incidence.
- D. Aircraft yaw.
- E. High speed 'q' turns and spirals.
- F. Approach and landing conditions; reverse thrust.
- G. Firing of any armament.
- H. Operation of reheat.
- I. Aircraft intake operation for supersonic flight.

The testing should include any special aircraft maneuvers as listed above but recordings of deceleration and accelerations should also be made during high and low speed flight at a range of altitudes throughout the flight envelope. Finally, it is prudent to carry out recording throughout normal flights or sortie patterns.

Normally, in this work the early stage blading will be instrumented. However, because of the knowledge from previous testing, if specific engine orders are generated, which may cause problems on later stages, then on subsequent flights these too should be included for verification.

CONCLUSIONS

Fatigue is the failure mode of a metal which has been subjected to a large number of applications of stress. Under conditions of high-frequency vibration, which is typical for the blading of gas

turbines, the level of vibration may be sufficiently high to cause fatigue failure. It is normal for these high-cycle fatigue cracks to propagate very quickly and as there is no prior elongation of the material the final fracture takes place without warning. The fatigue strength of a component is dependent upon many factors, e.g., material characteristics, manufacturing methods which determine the material structure and residual stress, applied steady stress, stress concentration and surface condition. The materials which are used conventionally for gas turbine blading exhibit a high degree of scatter in their fatigue strength and this characteristic, combined with the variability of manufacture of components, creates one of the major problems in the assessment of blade vibration levels.

The blading of a gas turbine is continuously subjected to forces which will cause it to vibrate. The most difficult vibration situation to assess is that which may cause a long-term service failure to occur. Under these conditions, experience shows that it will be necessary to carry out fatigue tests on the component to obtain a sufficiently accurate measure of the blade's fatigue strength. A high fatigue strength requires attention to detail design and also to ensure that a good distribution is obtained for the applied steady stress as well as the alternating stress caused by the vibration. The use of the af - tip amplitude times frequency - techniques helps to verify that a high fatigue strength has been obtained.

It is expected that it will always be necessary to confirm by engine testing that a design is satisfactory from a vibration point of view. Blades can be subjected to two major classes of excitation - self excitation, e.g., flutter, or forced resonant vibration. In the case of self excitation the published data recommend that a margin of operation from the onset of flutter be available throughout the total operation of the engine. Self excitation can be distinguished from forced resonance response by detailed analysis of the strain gauge signal from the vibrating component. For flutter, the response will be at the natural frequency of the component or assembly and is not dependent upon a forcing function being present. With a forced resonant condition the essential forcing frequencies are likely to be seen away from resonance and the response of the vibrating component will increase as the forcing frequency coincides with the natural frequency.

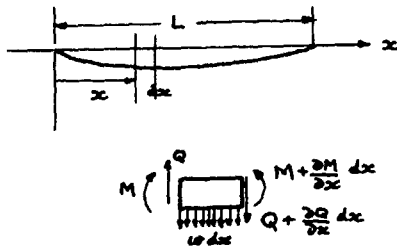
As it is generally not possible to operate engines without forced resonances being present in the running range, it is necessary to ensure that the levels of vibration will not give rise to an unacceptable incidence of fatigue failure during the engine working life. This can be achieved by the measurement of the maximum alternating stress present on the blade and then forming a comparison with the fatigue properties of the material. In this process it is necessary to allow for the material scatter, the influence of steady stresses and temperature, stress concentrations and the degradation of

properties due to erosion, corrosion, and fretting. A good data bank in conjunction with experience of application is required to ensure all factors are accommodated correctly. An alternative method of assessment measures the level of vibration achieved in engine operation for each of the normal modes of vibration of the component and then compares this level with an acceptable one which is derived from fatigue tests on the component. Experience has shown that, when measured amplitudes are double those which are satisfactory for service then failures with short lives are likely to take place. The advantage of the method lies in the ability to allow for the variation of the fatigue strength of components and can easily be extended to include surface deterioration effects, e.g., erosion and corrosion. Because the vibration is measured in the amplitudes of the normal modes rather than the maximum stress, one strain gauge, or some other convenient method of vibration measurement, can be used to cover a number of modes and this is an advantage in the testing for design verification. A disadvantage is that the method is not directly applicable to vibration involving an assembly mode because of difficulty of carrying out the necessary fatigue tests and calibrations.

The 2:1 range of amplitudes between those which are acceptable for long life and those which may result in a dangerously short life ensures that it will always be necessary to measure the operating amplitudes in an engine in order to assess them accurately. It is difficult to see how predictive methods can become a practical alternative due to the largely unknown factors which must be considered to achieve the amplitude accuracy. The factors which have to be considered include mechanical damping, all sources of excitation including variations in aircraft intake distortions over the full flight envelope, the influence of blade to blade coupling due to variation in natural frequencies. However, the role of the predictive methods must be to ensure that designs are not considered which would generate extremely short life failures. The aeroelastic work will also indicate the best way in which a design can be modified, to reduce the level of excitation, should an unacceptable level be measured during the engine design verification testing.

APPENDIX ITHE DERIVATION OF THE 'af' RELATIONSHIP FOR CANTILEVERS

The vibration velocity can be used as a criterion for the assessment of vibration stress. The proposition, which is outlined in a general way by H.G. Yates (1948), can be developed analytically for a cantilever beam of constant cross section when it is vibrating in its flexural mode. The analysis follows a standard type of text, e.g., Timoshenko (1937).



Positive directions as shown

With the usual assumptions that the cross sectional dimensions are small compared with the length of the beam, and that it is vibrating in one of its principal planes of flexure, then the following will define the deflection curve.

$$EI \frac{d^2y}{dx^2} = -M$$

where EI is the flexural rigidity

M is the bending moment at any cross section

Differentiating twice:

$$\frac{d}{dx} (EI \frac{d^2y}{dx^2}) = -\frac{dM}{dx} = -Q$$

$$\frac{d^2}{dx^2} (EI \frac{d^2y}{dx^2}) = -\frac{dQ}{dx} = w$$

The last equation is for a bar subject to a distributed load of intensity w . This load can be due to the inertia load of the vibrating beam itself; the intensity being equal to the reversed mass inertia of the cross section. Therefore, with m = mass per unit volume, A the cross sectional area:

$$\frac{\partial^2}{\partial x^2} (EI \frac{d^2y}{dx^2}) = -mA \frac{\partial^2y}{\partial t^2}$$

For a beam of uniform cross section, EI is constant and we have

$$\frac{\partial^2y}{\partial t^2} + b^2 \frac{\partial^4y}{\partial x^4} = 0$$

where

$$b^2 = \frac{EI}{mA}$$

If we assume that the beam is vibrating at a natural frequency ω and so, with $y = X \sin \omega t$ where X is the mode shape and is a function of x

$$\frac{d^4X}{dx^4} = \frac{\omega^2}{b^2} X \quad \dots \quad A.1$$

By using the notation

$$\frac{\omega^2}{b^2} = \frac{\omega^2 mA}{EI} = p^4 \quad \dots \quad A.2$$

it can easily be verified that $\sin px$, $\cosh px$, $\sinh px$, and $\cosh px$ are solutions of A.1 and thus that the general solution can be of the form

$$X = c_1(\cosh px + \sinh px) + c_2(\cosh px - \sinh px) \\ + c_3(\sin px + \sinh px) \\ + c_4(\sin px - \sinh px) \quad \dots \quad A.3$$

with the values of c_1 , c_2 , c_3 , and c_4 being determined by the particular end conditions for the beam. In the case of a cantilever beam for the fixed end

$$x=0, X=0 \quad \text{and} \quad \frac{dX}{dx} = 0 \quad (\text{i.e., deflection}$$

and slope zero);

for the free end

$$x=L, \frac{d^2X}{dx^2}=0 \quad \text{and} \quad \frac{d^3X}{dx^3}=0 \quad (\text{i.e., bending moment and shearforce are zero}).$$

$$\text{Thus at } x=0 \quad X=0=c_1$$

$$\frac{dX}{dx} = -c_2 p (\sin px + \sinh px) + c_3 p (\cosh px + \sinh px) \\ + c_4 p (\cosh px - \sinh px) \quad \dots \quad A.4$$

$$\text{with } x=0 \quad \frac{dX}{dx} = 0 = c_3$$

$$\text{Therefore } \frac{d^2X}{dx^2} = -c_2 p^2 (\cosh px + \sinh px)$$

$$-c_4 p^2 (\sin px + \sinh px) \quad \dots \quad A.5$$

$$\frac{d^3X}{dx^3} = c_2 p^3 (\sin px - \sinh px)$$

$$-c_4 p^3 (\cosh px + \sinh px) \quad \dots \quad A.6$$

16-34

$$\text{At } x=L \quad \frac{d^2x}{dx^2} = 0 \quad \frac{d^3x}{dx^3} = 0$$

$$0 = -c_2 p^2 (\cosh pL + \cos pL) - c_4 p^2 (\sinh pL + \sin pL)$$

$$c_2 = -c_4 \frac{(\sinh pL + \sin pL)}{(\cosh pL + \cos pL)}$$

From A.6

$$0 = -c_4 (\sinh pL + \sin pL) \cdot \frac{(\sinh pL + \sin pL)}{(\cosh pL + \cos pL)}$$

$$-c_4 (\cosh pL + \cos pL)$$

$$0 = \sin^2 pL - \sinh^2 pL + \cos^2 pL + \cosh^2 pL$$

$$+ 2 \cosh pL \cos pL$$

Remembering $\sin^2 \theta + \cos^2 \theta = 1$

$$\text{and } \cosh^2 \theta - \sinh^2 \theta = 1 \quad \dots \dots \dots \text{A.7}$$

we have $\cosh pL \cos pL = -1 \quad \dots \dots \dots \text{A.8}$

This is the frequency relationship which determines the natural frequencies of a cantilever beam in flexure, the first six roots of which are:

$p_1 L$	$p_2 L$	$p_3 L$	$p_4 L$	$p_5 L$	$p_6 L$
0	4.730	7.853	10.996	14.137	17.279

The frequencies can be obtained using the definition of p from equ. A.2

$$f_2 = \frac{\omega}{2\pi} = \frac{(p_2 L)^2}{2\pi L^2} \sqrt{\frac{EI}{m}}$$

etc. for higher roots.

We now proceed to obtain the relationship between the bending moment and stress at the fixed end $x=0$ for the amplitude of vibration at the free end $x=L$

$$M_x = c_0^2 = -EI \left[\frac{d^2x}{dx^2} \right]_{x=0} = 2EI c_2 p^2 \text{ from A.5}$$

For half total tip amplitude a at $x=L$ from A.3 as $c_1 = c_3 = 0$

$$a = c_2 (\cosh pL + \cos pL) + c_4 (\sinh pL + \sin pL)$$

$$= c_2 (\cosh pL + \cos pL) + c_2 (\sinh pL + \sin pL) \cdot$$

$$\cdot \frac{(\sinh pL + \sin pL)}{(\cosh pL + \cos pL)} \quad \text{from A.6}$$

$$= c_2 \frac{[-2 \sinh pL \sin pL]}{\cosh pL + \cos pL} \quad \text{with the}$$

relationship A.7

Squaring both sides we have

$$a^2 = \frac{4c_2^2 \sinh^2 pL \sin^2 pL}{\cosh^2 pL + \cos^2 pL + 2 \cosh pL \cos pL}$$

$$= \frac{4c_2^2 \sinh^2 pL \sin^2 pL}{\cosh^2 pL + \cos^2 pL - 2} \quad \dots \dots \dots \text{A.10}$$

by using the frequency relationship A.8. Thus, the following relationships between stress and tip amplitude will be valid for any of the flexural natural frequencies.

From A.8 and A.7 $\cos^2 pL \cosh^2 pL = 1$

therefore,

$$\cosh^2 pL = \frac{1}{\cos^2 pL} = 1 + \sinh^2 pL \quad \dots \dots \dots \text{A.11}$$

therefore,

$$\sinh^2 pL = \frac{1 - \cos^2 pL}{\cos^2 pL} = \frac{-\sin^2 pL}{\cos^2 pL} \quad \dots \dots \dots \text{A.12}$$

From A.10 and A.7

$$a^2 = \frac{4c_2^2 \sinh^2 pL \sin^2 pL}{-\sin^2 pL - \sinh^2 pL} = \frac{4c_2^2 \sin^2 pL}{\cosh^2 pL - \sin^2 pL - \left(\frac{1 - \cos^2 pL}{\cos^2 pL} \right)}$$

$$= \frac{4c_2^2 (\sin^2 pL - \sin^2 pL \cos^2 pL)}{-\sin^2 pL \cos^2 pL + \sin^2 pL} = 4c_2^2 \quad \dots \dots \dots \text{A.13}$$

$$a = 2c_2 \quad \dots \dots \dots \text{A.14}$$

Hence using A.9

$$M_{x=0} = EI p^2 a$$

From normal bending theory the stress σ on a section of 2nd moment of area $I = Ak^2$ where k = radius of gyration and y is the distance of stressed fiber from the neutral axis then with A.14

$$\sigma = \frac{y}{I} M = y E p^2 a = y E a \omega \sqrt{\frac{m}{EI}}$$

$$\text{Therefore } af = \frac{1}{2\pi} \frac{k}{y} \frac{\sigma}{\sqrt{Em}}$$

LIFE TIME PREDICTION: SYNTHESIS OF ONERA'S RESEARCH
IN VISCOPLASTICITY AND CONTINUOUS DAMAGE MECHANICS,
APPLIED TO ENGINE MATERIALS AND STRUCTURES

BY

R. LABOURDETTE
Office National d'Etudes et de Recherches Aeroespaciales
BP 72 - 92322 CHATILLON CEDEX, France

INTRODUCTION

Improvements in the metallurgy of superalloy materials make it possible to use them at higher temperatures. This is of great importance in aeronautics, where gas turbines are widely used for propulsion. In addition, new cooling techniques for turbine blades lead to increased turbine inlet temperatures and therefore better turbine efficiency.

However, it follows from this increase in temperature that more severe thermo-mechanical problems are encountered when dealing with the design and life prediction of turbine blades (and disks).

Roughly speaking, two phenomena are to be described for such a prediction: creep and fatigue, with particular emphasis on low cycle fatigue.

This part of the chapter deals with the method of life prediction developed at ONERA whose main steps are:

- Behavior of the macroscopic volume element.
- Damage accumulation under creep-fatigue conditions.
- Numerical methods of stress and damage calculation in complex structures undergoing thermomechanical loading, i.e., submitted to generalized viscoplastic behavior.

Although it was developed for gas turbines, the method presented here can be applied to any kind of structure undergoing thermomechanical loading. We

describe now the above mentioned steps of the life prediction method. Most of them are described in more detail in the cited references.

It must be mentioned that all the results obtained here were obtained in the course of a very close and fruitful cooperation between ONERA and SNECMA.

BEHAVIOR OF MACROSCOPIC VOLUME ELEMENT

General Remarks

Two main thermodynamical concepts are generally considered when describing the mechanical behavior of materials, Odquist and Hult (1962).

- A. - the present state of the material depends on the present values and past history of observable variables only (such as: total strain, temperature...)
- B. - or it depends only on the present values of both observable and internal variables.

All the developments made at O.N.E.R.A. are derived from the second one, and assume the existence of a thermodynamic potential (the free energy for example) from which the relations between the state variables and thermodynamic forces are defined; it is also considered that dissipative potentials, associated with the generalized normality rule, allow the a priori verification of the second principle, Mandel (1962).

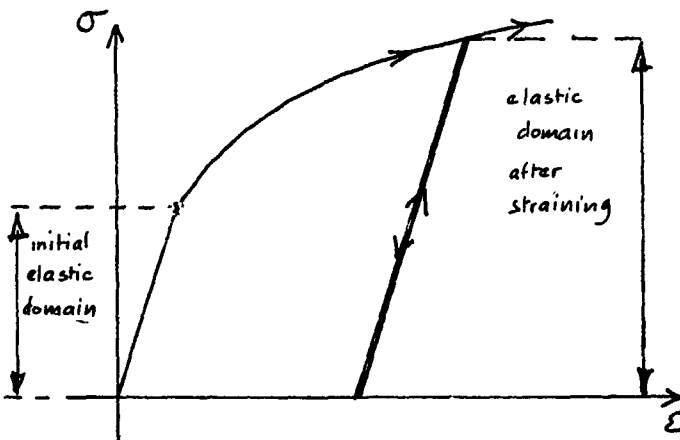


Figure 1. "Hardening" Effect due to Straining.

In the context of plasticity and viscoplasticity, such general concepts have been applied by many workers, giving rise to a coherent tool, especially for the classical flow rules, Halphen and Nguyen (1975), Sidoroff (1975).

In the next sections we shall derive and present a model able to describe complex behavioral effects such as: cyclic hardening or softening, time recovery, aging and strain memory.

Description of the Model of Viscoplastic Behavior

Strain hardening

The inelastic straining of a material almost always results in hardening. This is perceptible macroscopically, e.g. after a plastic flow under tensile stressing: the apparent yield strength increases and the material exhibits a greater resistance to a subsequent plastic flow (Fig. 1). The decrease in the strain rate during the primary phase of creep tests also results from work-hardening. We thus associate an increase in the inelastic strain with an increase in the density of the dislocations, which lose their mobility by piling up on obstacles or by forming cells.

The cumulated plastic strain p is thus a natural hardening parameter. It is defined by:

$$\dot{p} = \left(\frac{2}{3} \dot{\epsilon}_{p,ij} \cdot \dot{\epsilon}_{p,ij} \right) \quad (1)$$

The hypothesis of strain hardening (SH) is more accurate than the time hardening one (TH) as can be seen from a two-level creep test. Figure 2 shows, schematically, what should be the results of a two level creep test according, respectively, to the SH and TH hypothesis. In that sort of test, the higher level (σ_2) follows the lower one (σ_1). Experimental data confirms, generally, the SH hypothesis, Rabotnov (1969), Larson and Storakers (1978).

In order to describe this kind of behaviour, it is worthwhile to use a state equation written as:

$$F(\sigma, \epsilon_p, \dot{\epsilon}_p) = 0 \quad (2)$$

In order to describe this kind of behaviour, it is worthwhile to use a state equation written as:

$$F(\sigma, \epsilon_p, \dot{\epsilon}_p) = 0 \quad (2)$$

(for the one-dimensional case).

A product of power functions gives good results over a wide range for the primary creep as well as for the tensile test or relaxation test, Lemaitre (1971).

$$\sigma = K \epsilon_p^{1/m} \cdot \dot{\epsilon}_p^{1/n} \quad (3)$$

This three-coefficient relation is easily generalized to the three-dimensional form if we assume an isotropic hardening hypothesis. With the Von-Mises criterion, we can say that:

$$J(\sigma) = \left(\frac{3}{2} \sigma : \sigma' \right)^{1/2} = K p^{1/m} \cdot \dot{p}^{1/n} \quad (4)$$

where p is given by (1) and σ' is the deviatoric stress tensor.

The viscoplastic strain occurs at constant volume and we have:

$$\dot{\epsilon}_p = \frac{3}{2} \dot{p} \frac{\sigma'}{J(\sigma)} \quad (5)$$

This elementary theory of viscoplasticity with isotropic hardening is valid in the case of nearly proportional monotonic loadings.

For other kinds of loadings, internal stress must be introduced in the equations.

The various internal stresses

The idea of internal stress is not new. It was introduced in the thirties by Orowan to provide a better way of expressing the observed macroscopic behavior, in particular, in polycrystal and multiphase materials. In these materials, the exponent in the secondary creep phase law (Newton's law), for example, is very high:

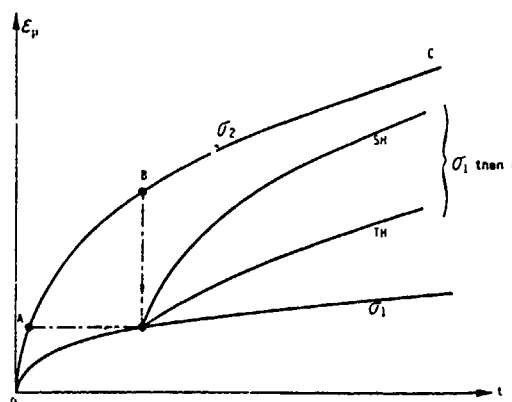


Figure 2. Time and Strain Hardening Visualized Schematically by Two-Level Creep Tests.

$$\dot{\epsilon}_p = \left(\frac{\sigma - \sigma_i}{K}\right)^n \quad (6)$$

Among other things, introducing an internal stress σ_i makes it possible to reduce this exponent greatly, to values of 2, 3, or 4, as justified by physical theory. The internal stress can be measured in the secondary phase of creep by successive unloadings, modifying the law as follows, Culie et al. (1982).

$$\dot{\epsilon}_p = \left(\frac{\sigma - \sigma_i}{K}\right)^n \quad (7)$$

The internal stress may be a scalar or a tensor depending on the type of interaction considered. On the macroscopic level, four types of internal stresses can be introduced, corresponding to an additive decomposition of the applied stress. In 3-D form we can write:

$$J(\sigma - X) - k - R - R^* - K_p^{1/n} = 0 \quad (8)$$

which, under pure tensile stress, reduces to:

$$\sigma = X + k + R + R^* - K_p^{1/n} = 0 \quad (9)$$

where

$$\sigma = \sigma_i + K_p^{1/n}$$

- X is a second-order tensor, called the back stress or rest stress corresponding to long-distance interactions: intergranular stress induced by the nonhomogeneous plastic strains from one grain to the other, interactions between dislocations and precipitates, as exact calculations have shown on the precipitate scale, Carry and Strudel (1978).

- k is Orowan's isotropic (or scalar) stress. It corresponds to the initial yield strength of the material and, among other things, depends on the volume fraction of precipitates and the initial density of the dislocations. This flow

threshold k also depends on the size of the precipitates, because of the various bypasses of shear forces making the dislocations move across the precipitates. Let us note immediately that a macroscopic model has been developed to express the variations in this internal stress, induced by temperature changes (partial dissolution of the medium-size precipitates, followed by reprecipitation of a finer phase), Chabache and Cailletaud (1979).

This model has been shown to describe, very accurately, the additional hardening induced by overheating periods for the IN 100 alloy in the range of 900-1000°C.

- R is the variation in Orowan's stress induced by a plastic strain. It is directly related to the increase in the dislocation density, but may also depend on the dislocation configuration, e.g. creation of dislocation cells, size, and fineness of the cell, etc.

- R^* , sometimes called R_{SOL} or the drag stress, is included to describe the hardening as seen by the atoms or particles in solution. This hardening slows down the movement of the dislocation by a drag phenomenon.

- The last term, $\sigma_v = K_p^{1/n}$ is the viscous stress itself (viscous friction) which can be approximated initially by a power function. Of course, equation (8) can be rewritten in the ordinary form (1):

$$\dot{\epsilon}_p = \frac{J(\sigma - X) - k - R - R^*}{K} \quad (10)$$

Many models have been developed to describe the variations in the internal stresses X , R , R^* .

Constitutive equations for viscoplasticity

The law of viscoplasticity (10) derives from a viscoplastic potential of the form, Chaboche (1977):

$$\dot{\phi} = \frac{K}{n+1} \left(\frac{J(\sigma - X) - k - R - R^*}{K} \right)^{\frac{n+1}{n}} \quad (11)$$

Using expression (10) for the modulus p of the plastic strain rate, we again find:

$$\dot{\epsilon}_p = \frac{\delta \dot{\phi}^*}{\delta \sigma} = \frac{3}{2} \dot{p} \frac{\sigma' - X'}{J(\sigma - X)} \quad (12)$$

$J(\sigma - X)$ designates, for example, the second invariant of the deviator $\sigma' - X'$ of $\sigma - X$, for a von Mises type material.

This model brings in a flow threshold, given by $k_e = k + R + R^*$. Figure 3 indicates schematically the actual domain of elasticity centered at X , of radius k_e , in the deviator plane of the stress state. The surface of equal dissipation (or of equal rate p) is found by similarity.

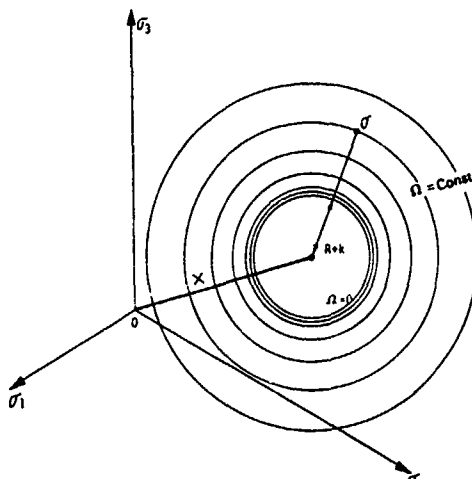


Figure 3. Elastic Domain and Viscoplasticity Equipotentials.

It can be noted that, in the limit case of a very slightly viscous material, (n being very large) the present theory must be replaced by a time-independent theory of plasticity which will not be described here.

Non-linear kinematic hardening

Let us first take $R = R^* = 0$. The only hardening effect is kinematic: a translation of the surfaces in the stress space. This type of hardening is predominant in many situations, and, consequently, must be accurately described if one wishes to predict the cyclic behaviour of a material.

The simplest kinematic model is linear, and was originally developed by Prager (1949). It reads:

$$X = \frac{2}{3} c \cdot \epsilon_p$$

or

$$dX = \frac{2}{3} c \cdot d\epsilon_p$$

This linear kinematic model has two disadvantages: 1) The stress-strain curve is poorly expressed in the limit case of time-independent plasticity. 2) It cannot describe the controlled-stress ratchet effect or the effect of the mean stress relaxation, under controlled cyclic strain. Figure 4a shows how the model stabilizes at the first cycle.

Introducing a recall term to express an evanescent plastic strain memory effect brings a significant improvement, Armstrong and Frederick (1966).

$$dX = \frac{2}{3} c \cdot a \cdot d\epsilon_p - cX dp; \quad X(0) = 0 \quad (14)$$

Let us clearly note the essential difference between the two plastic strain increase terms $d\epsilon_p$ and dp . Under tensile-compressive loading, for example, we have:

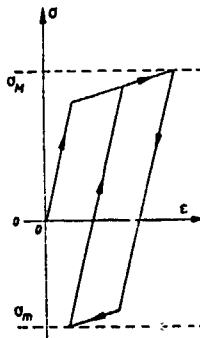


Figure 4a. Immediate Stabilization of the Linear Kinematic Model
(Time-Independent Scheme).

$$dX = c a d\epsilon_p - cX |d\epsilon_p| \quad (15)$$

The nonlinearity introduced by the recall term is thus not the same during a flow under tensile or under compressive loading: the relation is nonunique between X and ϵ_p , and the concavity of the stress-strain curve is correctly reproduced, even in the limiting case of plasticity (Fig. 4b). At each half cycle, beginning with ϵ_{po} , X_0 , the kinematic model (15) is integrated explicitly:

$$X(\epsilon_p) = v_a + [x_0 - v_a] \exp(-c(\epsilon_p - \epsilon_{po})) \quad (16)$$

and the stress is then expressed by:

$$\sigma = X(\epsilon_p) + v_k + v K_p^{1/n} \quad (17)$$

where $v = \pm 1$ gives the direction of the flow. Figure 3b shows this stress decomposition schematically.

The kinematic model gives the shape of the hysteresis loop, but also the relation between the amplitudes at the stabilized cycle (here stabilization is very fast for a periodic symmetrical loading).

$$\frac{\Delta \sigma}{2} = a \cdot \tanh \left(c \frac{\Delta \epsilon_p}{2} \right) + k + K_p^{1/n} \quad (18)$$

For the viscoplastic material, they depend on the rate.

This model of viscoplasticity, using only the five temperature-dependent coefficients n , K , k , a , and C , already gives a very good approximation of the cyclic behaviour, as illustrated for IN 100 alloy in the Figures 5 and 6. In a rather limited strain domain (<0.5%) the model correctly reproduces the cyclic curves, the hysteresis loop and the effect of the loading rate or hold time in cyclic creep tests.

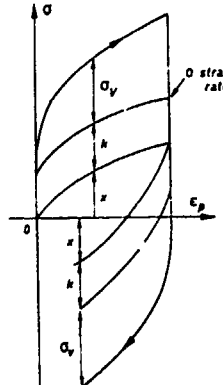


Figure 4b. Nonlinear Kinematic Model: Stress Decomposition.

Note that the cycles stabilize in the nonlinear kinematic model only if the loading is symmetrical (zero mean stress). Qualitatively, the model thus describes the ratchet effects (nonzero σ_{mean}) under tensile-compressive loading as well as, for example, the cyclic torsion superimposed on a constant tensile stress, and also describes the effects of the mean stress relation under controlled strain loading (nonzero σ_{mean}).

The valid strain range is widened and the quantitative description of the ratchet effects is improved when we superimpose several models of the same types as follows, Krempl (1977):

$$X = \sum_{k=1}^m X_k \quad (19)$$

$$dX_k = \frac{2}{3} c_k \alpha_k d\epsilon_p - c_k X_k d_p$$

One of the models can be linear, for example:

$$dX_j = \frac{2}{3} c d\epsilon_p \quad (20)$$

For proportional loading, the work-hardening model is still integrated explicitly. Figure 7 illustrates the modeling possibilities.

Isotropic hardening

In order to obtain a better fit of the monotonic hardening curve, and of the cyclic softening or hardening ones, it is necessary to describe an isotropic hardening, that is to introduce an equation for R evolution. A simple form of such an equation, similar to the kinematic case, is:

$$dR = b \cdot (R_s - R) \cdot dp \quad (21)$$

$$R(0) = 0$$

This internal stress varies as a function of the cumulated plastic strain p . After a certain number of cycles (less as the strain amplitude increases) it stabilizes at the value R_s . This is necessary, or else the only possible stabilized cycle would be elastic. We integrate to get:

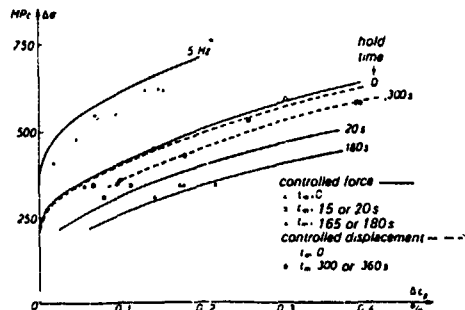


Figure 6. Modelization of the Cyclic Curves for the IN 200/Alloy at 1000°C.

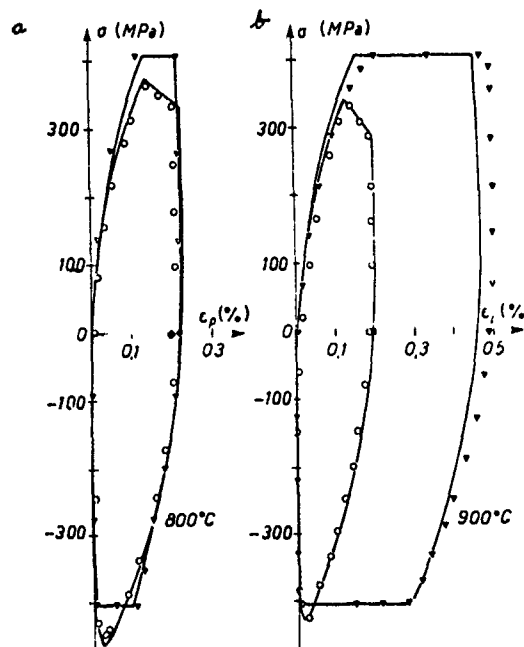


Figure 5. The Model of Viscoplasticity Applied to the IN 100 Alloy: Stabilized Hysteresis Loop.

$$R(p) = R_s(1 - \exp(-bp)) \quad (22)$$

Coefficients b and R_s depend on the temperature. Tensile-compressive stress is now expressed in the form:

$$\sigma = X(\epsilon_p) + v_k + vR(p) + vK \cdot p^{1/n} \quad (23)$$

For a controlled strain amplitude (alternating, for simplicity), we have at each cycle:

$$\sigma_M = X_M(\Delta\epsilon_p) + k + R(p) + K \epsilon_p^{1/m} \quad (24)$$

where ϵ_{pM} is the plastic strain rate for the maximum stress. In this loading configuration ϵ_{pM} is not very different from the total controlled strain rate; in any case, it can be considered to be approximately the same at each cycle. Furthermore, X_L is little different from a $\text{Th } C \Delta\epsilon_p / 2$. Applying relation (24) to each cycle, to the stabilized cycle and to the first cycle, considering the approximations we have mentioned, we get:

$$\frac{\sigma_M - \sigma_{MO}}{\sigma_{MS} - \sigma_{MO}} + \frac{R}{R_s} = 1 - \exp(-bp) \quad (25)$$

where σ_{MS} and σ_{MO} are the stress peaks in the stabilized cycle and in the first cycle.

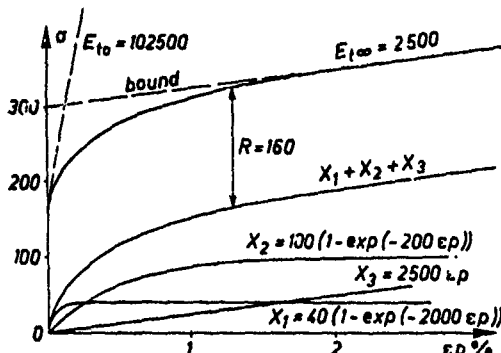


Figure 7. Stress-Plastic Strain Curve Obtained by Superimposing Three Kinematic Variables.

Thermodynamical aspects

The present approach has been developed in a general thermodynamic framework of irreversible processes with internal variables, Germain (1973), Sidoroff (1975), Halphen and Nguyen (1975).

Let us summarize this theory briefly as it applies to small quasistatic transformations, using T for the temperature, ϵ_e for the internal variable that describe the current state of the volume element.

Two potentials are used: a thermodynamic potential, e.g. the free energy:

$$\Psi = \Psi(\epsilon_e, T, \alpha_j) \quad (26)$$

The total strain is divided into thermoelastic strain ϵ_e and plastic strain $\epsilon = \epsilon_e + \epsilon_p$. The second potential controls the dissipation:

$$\phi = \phi(\epsilon_e, \alpha_j, \epsilon_e, T, \alpha_j) \quad (27)$$

The variables ϵ_e , T , α appearing in this potential are considered as parameters. The Clausius-Duhem inequality, expressing the second principle, leads to:

$$\sigma = \rho \frac{\partial \Psi}{\partial \epsilon_e}, \quad \zeta = -\frac{\partial \Psi}{\partial T}, \quad A_j = \rho \frac{\partial \Psi}{\partial \alpha_j} \quad (28)$$

where σ is the stress tensor, ζ is the entropy, ρ is the density and A_j are the thermodynamic forces associated with the internal variables α_j .

$$D = \sigma : \dot{\epsilon}_p - A_j \cdot \dot{\alpha}_j - \frac{1}{T} q \text{ grad } T \geq 0 \quad (29)$$

This must be positive because of the second principle. This is automatically the case if we adopt the hypothesis of generalized normality, using the potential ϕ^* obtained from ϕ by a Legendre-Fenchel transformation on the variables

$$\dot{\epsilon}_e, \dot{\alpha}_j.$$

$$\phi^* = \phi^*(\sigma, A_j, \epsilon_e, T, \alpha_j) \quad (30)$$

For a theory with time (or rate) effects the generalized normality is expressed by:

$$\dot{\epsilon}_p = \frac{\partial \phi^*}{\partial \sigma}, \quad \dot{\alpha}_j = -\frac{\partial \phi^*}{\partial A_j} \quad (31)$$

We see that the intrinsic dissipation is necessarily positive if ϕ^* is convex, positive and equal to zero at the origin ($\sigma = A_j = 0$):

$$D_i = \sigma : \dot{\epsilon}_p - A_j \cdot \dot{\alpha}_j = \sigma : \frac{\partial \phi^*}{\partial \sigma} + A_j \frac{\partial \phi^*}{\partial A_j} \geq 0 \quad (32)$$

To fit the viscoplasticity law with nonlinear kinematic hardening and isotropic hardening into this thermodynamic framework, we simply use the following expressions for the two potentials:

$$\rho \Psi = \frac{1}{2} \Lambda : \epsilon_e : \epsilon_e + \frac{4}{3} c a \alpha : \alpha + W(p) \quad (33)$$

$$(34)$$

$$\phi^* = \frac{K}{n+1} \left(\frac{G - (3/4a)X : X + (1/3)c^2 a \alpha : \alpha}{K} \right)^{n+1}$$

where G expresses the elastic range:

$$G = J(\sigma - X) - R - k \leq 0 \quad (35)$$

assuming here that $R^* = 0$. We get the associated variables from the first potential:

$$\sigma = \rho \frac{\partial \Psi}{\partial \epsilon_e} = \Lambda : \epsilon_e; \quad X = \rho \frac{\partial \Psi}{\partial \alpha} = \frac{2}{3} c a \alpha \quad (36)$$

$$R = \rho \frac{\partial \Psi}{\partial \alpha} = W'(p)$$

The hypothesis of normal dissipativity leads successively to:

$$\dot{\epsilon}_p = \frac{\partial \phi^*}{\partial \sigma} = \frac{3}{2} \rho \frac{\sigma' - X'}{J(\sigma - X)} \quad (37)$$

$$\dot{\alpha} = -\frac{\partial \phi^*}{\partial X} = \frac{\partial \phi^*}{\partial G} = \left(\frac{2}{3} \dot{\epsilon}_p : \dot{\epsilon}_p \right)^{1/2}$$

$$\dot{\alpha} = -\frac{\partial \phi^*}{\partial X} = \dot{\epsilon}_p - \frac{3}{2a} X \cdot \dot{p}$$

From the last relation we get:

$$\dot{X} = \frac{2}{3} c a \dot{\alpha} = \frac{2}{3} c a \dot{\epsilon}_p - c X \dot{p} \quad (38)$$

which is identical to (14) in the non-linear kinematic model. We note that p is actually the cumulated plastic strain. Using (34) and (35), we get the plastic strain rate modulus by:

$$\dot{p} = \frac{\partial \phi^*}{\partial G} = \left(\frac{G + (3/4a)X : X - (1/3)c^2 a \alpha : \alpha}{K} \right)^n \quad (39)$$

and, using $X = \frac{2}{3} C a \alpha$, we find the relation (10) again exactly, with $R^* = 0$.

DAMAGE DESCRIPTIONGeneral Remarks

In the previous paragraph, we have seen that a model with internal variables is able to describe the macroscopic mechanical behaviour of a metallic material undergoing viscoplastic straining. Yet, during this straining, and particularly under cyclic conditions, microscopical phenomena take place, such as dislocation motion, which lead to macroscopical defects of significant size classically known as cracks.

Since the presence of cracks can markedly reduce the strength of a structure, it is obvious that the prediction of crack initiation is of paramount importance in engineering design. For instance, the assessment of the structural integrity of a turbine disk must be achieved before any usage of the engine, since the burst of such a disk can lead to very serious damage to the passengers and the airframe, and even to complete loss of the aircraft.

The classical way to predict crack initiation was to use the so-called "parametric failure relations." Since the original idea and work of Kachanov (1958) and Rabotnov (1969) on the concept of "macroscopic damage," we, at ONEKA, have contributed to develop an alternate way of prediction known as "Continuous Damage Mechanics."

The objectives of this paragraph are to briefly introduce the theory, review its specific advantages compared to the classical approach, illustrate it by the results obtained for some materials and finally open the discussion on its applicability and possible future developments.

The Continuous Damage Approach:
One-Dimensional AspectsMechanistic concept of a macroscopic internal variable.

Before any damage theory can be developed, it is necessary to define what we mean by the ultimate stage of the damage processes. Current Continuous Damage Mechanics assumes that this final stage corresponds to the macroscopic crack initiation, that is the presence of a material discontinuity, sufficiently large as regards the microscopic heterogeneities (grains, subgrains...). In such a case, the main macroscopic crack is assumed to be developed through several grains, in order to show a sufficient macroscopic homogeneity, in size, geometry and direction, leading to a possible treatment through the Fracture Mechanics concepts (see the schematic illustration in Figure 8). Let us remark that, contrary to the usual definitions, the present one can be approximately associated with the breaking up of a uniaxial specimen subjected to tension-compression.

The theory is supported by the physical idea that crack initiation is preceded by a progressive internal deterioration of the material, which induces a loss of strength in terms of strain as well as in terms of remaining life. Kachanov (1958) first proposed to relate these two aspects through a macroscopic damage variable, introduced with the effective stress concept. The phenomenological idea of a damage parameter D taking into account, on a macroscopic scale, the microscopic deteriorations (voids, decohesions, micro-cracks...) is generally accepted, Krempl (1977), with the following limiting values: $D = 0$ for the initially unstressed material, $D = D_c$ at failure, that

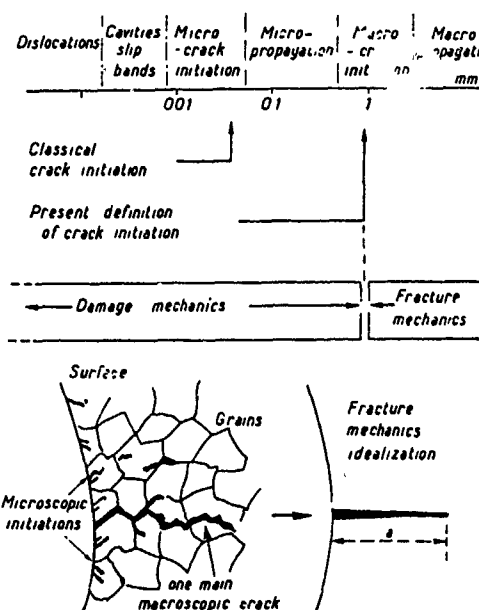


Figure 8. Schematic Illustration of a Macroscopic Crack Initiation Concept.

is at the macroscopic crack initiation time (in several works the critical value D_c is taken as 1). The effective stress concept is used to describe the effect of damage on the strain behaviour: a damaged volume of material under the applied stress σ shows the same strain response as the undamaged one submitted to the effective stress (Fig. 9).

$$\tilde{\sigma} = \sigma / (1 - D)$$

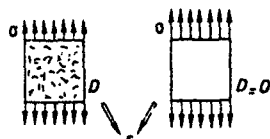


Figure 9. The Effective Stress Concept.

Under this definition D represents a loss of effective area taking into account decohesions and local stress concentrations through homogenization concepts, Duvaut (1976).

Depending on the concerned areas, different microscopic measures of damage have been used in the past: in addition to density changes or electric resistivity measurements, Cailletaud et al (1980), one can distinguish between:

- measures of the remaining life as used in creep, Woodford (1973), or in fatigue, Klemers (1945).
- measures of the reduction in fatigue limits, Bui Quoc et al (1971), which need many tests to define the damage evolution curves,
- measures of the stress-strain behaviour, which are now retained because of their easier applicability in each test (independently of the others). They can be obtained in terms of elastic strain (Young's modulus), Lemaitre and Dufailly (1977), plastic strain range, Chaboche (1974), or stress range.

In the particular case of stress controlled tests, measurements of plastic strain range evolution, lead to damage measurements through the classical Manson-Coffin equation for the undamaged stabilized stress-strain behaviour and the effective stress concept for the last part of the test. According to this hypothesis:

$$\Delta\epsilon_p = \left[\frac{\Delta\sigma}{K(1-D)} \right]^m \quad (40)$$

Stabilized conditions correspond to:

$$\Delta\epsilon_{ps} = (\Delta\sigma/K)^m \text{ where } m \text{ is}$$

determined from a number of cyclic tests. The damage follows from, Chaboche (1974),

$$D = 1 - (\Delta\epsilon_{ps} / \Delta\epsilon_p)^{1/m} \quad (41)$$

Figure 10 shows the example of IN 100 refractory alloy tested at 1000°C, at 5 Hz, under completely reversed stress control. Let us underline the high non-linearity of damage evolution and the stress dependency.

Using similar procedures, directly deduced from the initial propositions of Kachanov one can obtain the creep damage evolution during creep tests (Lemaitre and Chaboche (1975), (Fig. 11)). Eq. (1) corresponds to the initial theory of Kachanov. Actually, the microscopic damage process can give little loss of effective area before crack initiation, especially under fatigue loading; this gives rise to very small values of the D parameter until a large fraction of life is consumed, which induces highly non-linear damage evolution curves. However, it must be emphasized that small values of D can lead to large reductions in life: using the present approach, the damage is no longer proportional to N/N_f .

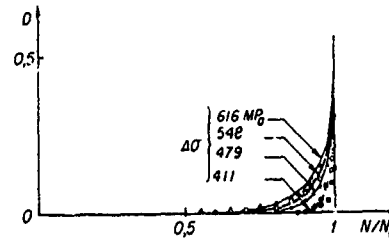


Figure 10. Fatigue Damage Evolution Curves as Measured Through Plastic Strain Range and Effective Stress Concept: IN 100 Alloy, 1000°C, 5 Hz Frequency, Load.

The lost area interpretation can be considered under many situations but constitutes a first approximation only. It applies mostly to the ultimate crack micropagation stage of the tests. Future improvements could be obtained by introduction of two damage parameters corresponding to the micro-initiation and macropagation stages, as in the simplified approach of the Double Linear Cumulative Damage Rule, Manson et al (1965).

Development of damage constitutive equations

Let us begin with an important remark: these equations have to be developed in differential form: an expression of D as a function of time, for example, constitutes only a response of the material to a particular forcing parameter. All equations using the consumed potential as a damage parameter are thus eliminated.

Second general remark: if nonlinear cumulative effects are needed, these equations must have unseparable variables in terms of damage and the chosen forcing parameter, Krempel (1977), Duvaut (1976), Cailletaud et al (1980), Woodford (1980), Kommers (1945), Bui Quoc et al (1971), Lemaitre and Dufailly (1977), Chaboche (1974). In other words, the damage response functions have to be different under different loading conditions, Bui Quoc et al (1971).

Three types of damage evolutions can be considered: as a function of stress in the static plastic failure (or in fatigue), as a function of time for the creep processes (σ , for corrosion or irradiation processes), and as a function of cycles for the fatigue processes. Each of them has to be identified by some specific tests, independently of the others, leading to the determination of the corresponding differential damage equations. Their one-dimensional isothermal form is, Lemaitre and Chaboche (1975).

$$\begin{aligned} dD_1 &= F_1(\phi, \alpha, D_1, \dots) d\sigma \\ dD_2 &= F_2(\phi, \alpha, D_2, \dots) dt \\ dD_3 &= F_3(\phi, \alpha, D_3, \dots) dN \end{aligned} \quad (42)$$

Here ϕ denotes the chosen forcing variables: stress or strain or plastic strain, and α represents the internal variables, describing for example the hardening state of the material.

When several processes act simultaneously, the interaction effect has to be determined through special tests: for example, the combination of creep and fatigue effects could be treated by introducing coupling terms in eq. (42)

$$\begin{aligned} dD_2 &= F_2(\phi, \alpha, D_2, D_3, \dots) dt \\ dD_3 &= F_3(\phi, \alpha, D_2, D_3, \dots) dN \end{aligned} \quad (43)$$

Although some microphysical studies use such coupling parameters, most of the present day cumulative damage theories are based on the simplifying hypothesis that damage variables (here D_2 and D_3) are of similar nature and interact in an additive manner, which corresponds to the special forms:

$$\begin{aligned} dD_2 &= F_2(\phi, \alpha, D_2 + D_3, \dots) dt \\ dD_3 &= F_3(\phi, \alpha, D_2 + D_3, \dots) dN \end{aligned} \quad (44)$$

As shown in several applications, the nonlinearities of the interaction processes can effectively be described, because of the different nonlinearities in functions F_2 and F_3 . Under this hypothesis only one damage variable has to be considered for the general case. Combination of eqs. (42) leads to:

$$\begin{aligned} dD &= F_1(\phi, \alpha, D) d\sigma + F_2(\phi, \alpha, D) dt \\ &\quad + F_3(\phi, \alpha, D) dN \end{aligned} \quad (45)$$

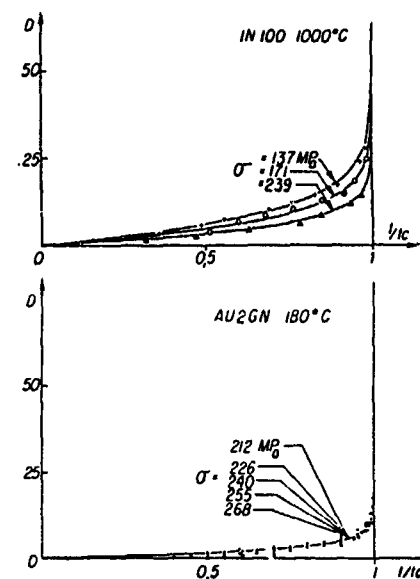


Figure 11. Creep Damage Evolution Curves as Measured Through Strain Rate and Effective Stress Concept: IN 100, 1000°C., AU2GN, 180°C.

Application to the Refractory Alloy IN 100

Creep-fatigue interaction

The creep and fatigue damage were independently characterized from pure creep and pure fatigue (high frequency) tests, through failure measurements and damage measurements.

Equations of damage, Lemaitre and Chaboche (1975), Manson et al (1965), Chaboche et al (1978), can be explicitly integrated (see Figs. 10, 11). This leads to the possibility of description of sequence effects as in the case of two level fatigue tests (see Fig. 12). As already mentioned by several workers, Bui Quoc et al. (1971), Lemaitre and Dufailly (1977), Chaboche (1977), Lemaitre and Chaboche (1975), Manson et al (1965), these sequence effects are consistent with the stress dependency. Figure 13 illustrates how the linear Palmgren-Miner rule does not hold in such cases.

Two types of non-fatigue situations can be considered. First, the two level tests where a portion of life is spent in fatigue (resp. creep), the remaining life is being measured under creep (resp. fatigue). For IN 100, such testing leads to nonlinear effects with life summations greater than 1 (resp. smaller than 1), because the measured fatigue damage rate (Fig. 10) is much smaller than the creep damage rate (Fig. 11) when they are normalized by the total life. This has been experimentally checked and compared quite satisfactorily with damage equations (Fig. 14).

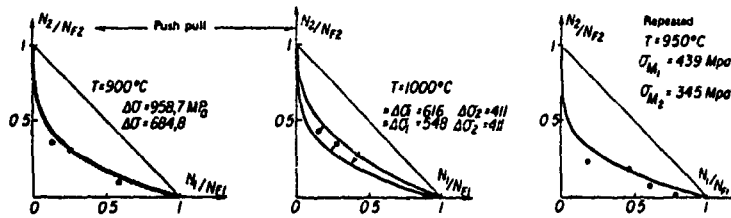


Figure 12. Prediction of Two-Stress-Level-Fatigue Tests - IN 100 Allow.

The second case, more important for the applications, appears when creep and fatigue act simultaneously during each cycle: low frequency stress controlled or strain controlled cyclic tests, cyclic creep, cyclic tests with hold times under strain control. In such cases the developed damage equations, Chaboche et al (1978), are numerically integrated, the nonlinear interaction effect being reproduced through the different damage rates under creep and under fatigue for a given damage state. This is supported by the physical idea that creep cavities nucleate early in the life and accelerate the nucleation and the propagation of fatigue microcracks.

Figure 15 shows that such a theory predicts nonlinear creep-fatigue interaction with a stress range dependency: the lower the stress, the greater the interaction that is the greater the life reduction by comparison with pure fatigue. Such predictions are consistent with experimental results reported in the literature, Krempel and Walker (1968), and agree fairly well with results of cyclic creep tests performed with IN 100. For this material the Low-Cycle High Temperature fatigue, with or without hold times, is predictable from damage equations determined under pure creep and pure fatigue conditions, as shown in Figure 16. Let us emphasize that the predictions shown in Figures 15 and 16 have been made with equations whose constants have been determined only from pure creep and pure fatigue tests.

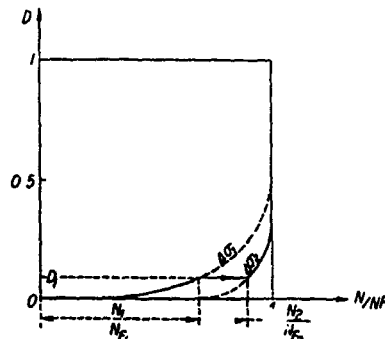


Figure 13. Schematic Explanation of Non-Linear Cumulative Effects From the Damage Evolution Curves.

Stress-strain behaviour of the damage material

In the case of high temperature viscoplastic behaviour of some refractory alloys, particular strain rate equations have been developed, using isotropic and nonlinear kinematic hardening rules, Chaboche et al (1978), consistent with a general thermodynamical framework. For IN 100 alloy, the one-dimensional isothermal equations are:

$$\dot{\epsilon}_p = \left(\frac{|\sigma - x| - R}{K} \right)^n \cdot \text{sign}(\sigma - x) \quad (46)$$

$$\dot{x} = c F(p) (a \dot{\epsilon}_p - x | \dot{\epsilon}_p | - b | x |^m \text{sign}(x)) \quad (47)$$

$$F(p) = t + (1-t) \exp(-\beta p) \quad (48)$$

$$p = \int_0^t |\dot{\epsilon}_p(t)| dt$$

where p and x are isotropic and kinematic internal variables and n , K , c , a , b , m , β , t are coefficients.

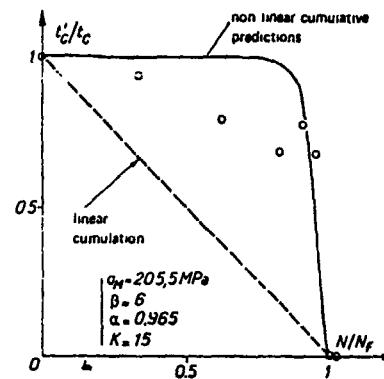


Figure 14. Creep Rupture after Pure Fatigue Cycling; IN 100, 1000°C. (○ tests, — predictions).

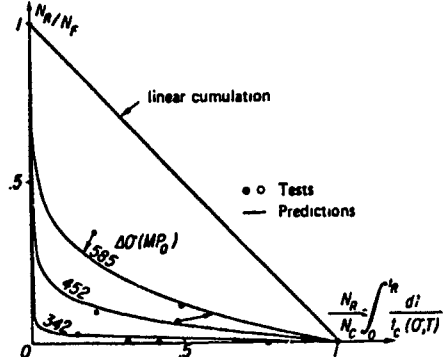


Figure 15. Creep-Fatigue Interaction for Cyclic Creep Tests (IN 100, 1000°C.).

This formulation brings together concepts and equations proposed by several workers and contains many descriptive possibilities of nonlinear hardening, creep and relaxation, Bauschinger effects, with the strain rate equation (46) and the non-linear kinematic hardening (47), stabilized cyclic behaviour, cyclic hardening or softening through isotropic hardening dependence (48), time softening (high temperature recovery effects) induced by the last term in eq. (47).

Moreover, some microstructural hardening effects induced by temperature changes can be described through the introduction of additional internal variables, Chaboche and Cailletaud (1979).

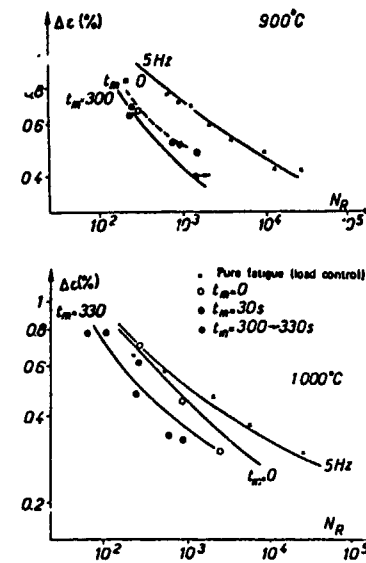


Figure 16. Prediction of Strain Controlled Cyclic Tests on IN 100, from the Measured Stabilized Loops and the Non-Linear Creep-Fatigue Damage Equations.

Introduction of the coupling with damage effect is easily done by the effective stress, replacing σ by $\sigma/l-D$. Consistency in the hardening rule needs also the modification of X by $X/l-D$.

This makes possible to describe tertiary creep effects as shown for IN 100 in Fig. 17.

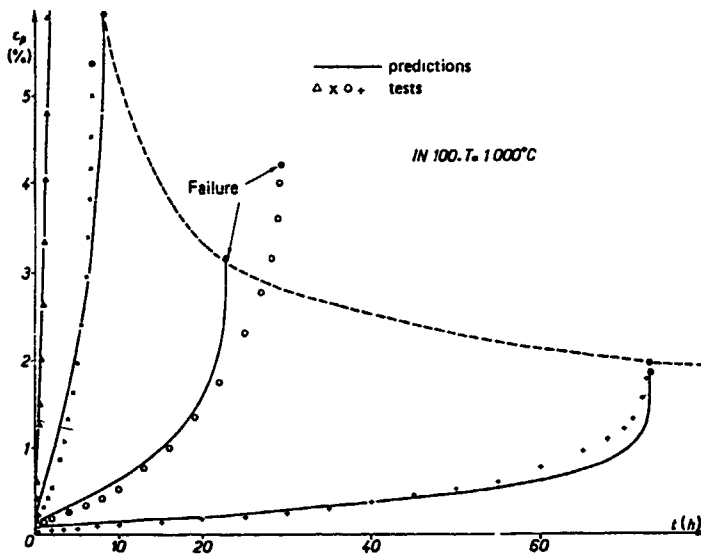


Figure 17. Prediction of Creep Curves and Creep-Fatigue through Coupled Viscoplastic and Damage Equations IN 100, 1000°C.).

STRUCTURAL LIFE PREDICITON AT HIGH TEMPERATURE, UNDER COMPLEX LOADINGS, CHABOCHE AND CAILLETAUD (1984)

Structure Analysis in viscoplasticity

The object of this paragraph is to present the "structural" aspect of life time prediction, i.e., the numerical methods and tools which have been developed at O.N.E.R.A. to integrate the results described in the two previous sections.

This has resulted in a finite element code named 'EVPCYCL', suitable for treating two-dimensional structures under plane stress, plane strain, or axisymmetrical cases.

This code exhibits a great versatility concerning the choice of constitutive equations; for instance, one can choose to describe isotropic hardening or kinematical hardening or both, etc.... Time dependent temperature fields are also accepted. We describe now some features of this code.

EVPCYCL Finite Element Code

Finite element aspects

This part of the code is quite classical: the unknowns are the nodal displacements (q), which are linked to the displacements (u) and strains (ϵ) within the elements through the matrices N and B , giving:

$$\begin{aligned} u &= N \cdot q \\ \epsilon &= B \cdot q \end{aligned} \quad (49)$$

The total strain is the sum of three terms:

ϵ_e : elastic strain

ϵ_p : viscoplastic strain

ϵ_{th} : thermal strain ($= \alpha \theta$)

so that Hooke's law leads to:

$$\sigma = D\epsilon - D\epsilon_p - Da\theta \mathbb{I} \quad (50)$$

where α is the thermal expansion coefficient,

θ the temperature,

\mathbb{I} unit tensor in R_3 space.

The last two terms can be considered as an initial stress, so that one can write:

$$K \cdot q = F + F_0 \quad (51)$$

where K is the classical stiffness matrix (depending on the elastic constants of the material and not on the viscoplastic behaviour).

F and F_0 are the nodal forces equivalent to external loads and initial stress.

In some isothermal problems, K is then triangularized and assembled only once; for the time dependent temperature cases, we use a linear interpolation of the inverse of K between two exact values, in order to minimize the computation cost.

Viscoplastic algorithm

As already seen, we can write the constitutive equations as:

$$\begin{aligned} \dot{\epsilon}_p &= F(\sigma, a_j, T) \\ \dot{a}_j &= g(\sigma, a_j, T) \end{aligned} \quad (52)$$

where the a_j are scalar or tensorial variables describing the hardening state of the material, and T is the temperature. It follows that a step by step integration process is required; several options are offered in EVPCYCL:

- completely explicit
(Euler, second order)
- semi-implicit
(Euler-Cauchy), Chaboche (1978)

The most often used is the second order one, developed at ONERA, Savalle and Culie (1978). In this method we perform an automatic computation of the time integration step before the time increment, by using the first and second derivatives of ϵ_p and a_j which are explicit at time t , since, if \dot{y} designates the stage variable vector (ϵ_p and a_j) one can write:

$$\begin{aligned} \dot{y}(t) &= Y(y(t), t) \\ \ddot{y}(t) &= \left(\frac{\partial Y}{\partial t} \right) \dot{y}(t) + \frac{\partial Y}{\partial t} \end{aligned} \quad (53)$$

One feature of the chosen algorithm is to increment only the state variables ϵ_p and a_j which leads to:

$$\begin{aligned} (\epsilon_p)_{t+\Delta t} &= (\epsilon_p)_t + (\dot{\epsilon}_p)_t \cdot \Delta t + (\ddot{\epsilon}_p)_t \cdot \frac{\Delta t^2}{2} \\ (a_j)_{t+\Delta t} &= (a_j)_t + (\dot{a}_j)_t \cdot \Delta t + (\ddot{a}_j)_t \cdot \frac{\Delta t^2}{2} \end{aligned} \quad (54)$$

The first order terms are obtained after expressing equilibrium at time t , (51) giving the knowledge of ϵ_p ; the second order terms are obtained by solving

$$\dot{K}q = \dot{F} + \dot{F}_C \quad (55)$$

where \dot{F}_C depends on $\dot{\epsilon}_p$, \dot{a}_j .

We can then obtain the third order term in ϵ_p and a_j , which allows the optimal determination of the time increment, by assessing that the third order term in the Taylor expansion must be negligible compared to the sum of the first and second order terms.

The time increment is obtained from equation (56):

$$|\dot{y}(t)| \frac{\Delta t^2}{6} = n |\dot{y}(t) + \ddot{y}(t) \cdot \frac{\Delta t}{2}| \quad (56)$$

n being a precision factor of roughly $5 \cdot 10^{-2}$. Although this method is not rigorously established, it leads to a remarkably safe algorithm. In addition, it has the advantage of needing only the approximate incrementation of ϵ_p and a , which avoids the cumulation of errors and gives good stability to the algorithm (although, by nature, an explicit algorithm is less stable than an implicit one).

Example of an Application: Biaxial Fatigue Disk

The geometry and mesh are indicated in Figure 18, the elements used are triangles, the problem is axisymmetrical.

Loading conditions

The temperature is assumed as uniform and constant. Two cases were studied:

- 550°C , low rotation speed :
1500 r.p.m
high rotation speed:
27700 r.p.m/10 s
- 650°C , low rotation speed :
1500 r.p.m
- high rotation speed:
24000 r.p.m/90 s

Results

For the stresses, results are shown in Figures 19, 20, and 21 for the two temperatures. At the lower temperature, the material is only slightly viscous and stress redistribution is essentially plastic; in contrast, at 650°C the viscosity is present, so that we observe viscoplastic flow during the hold time.

For the 550°C case, two computations were made, one using a complete model describing the behaviour continuously from the first cycle until obtaining the stabilized one, and a second one where only the model describing the stabilized cycle is used. Figures 19 and 20 show the great qualitative difference between these two cases, in particular, the zone under high stress being much more extended in the first case. This would lead to large differences in predicting life time.

Finally, a comparison was made with a corresponding test where the increase in the diameter of the bore was measured as .04 mm. The computed values were .04 and .07 mm respectively at the external surface and in the plane of symmetry which shows good agreement.

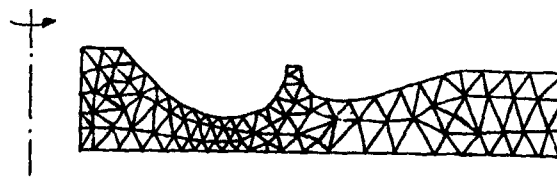


Figure 18. Mesh for F.E.M. Analysis.

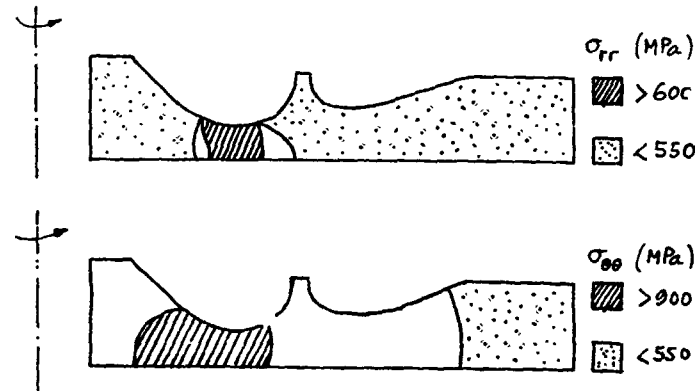


Figure 19. $T = 550^{\circ}\text{C}$. - Stress Distribution with Complete Behaviour Described.

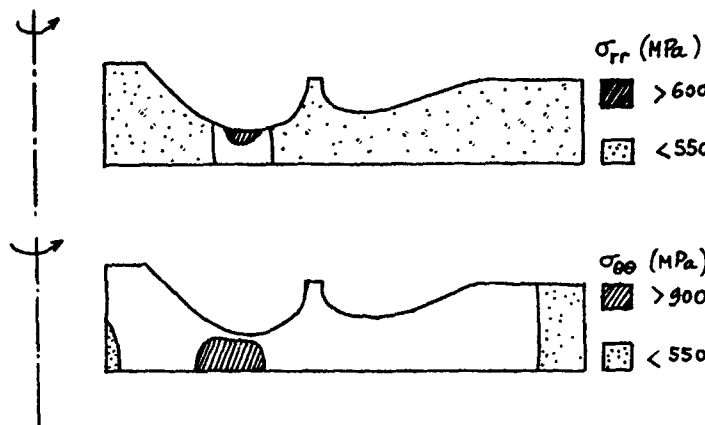


Figure 20. $T = 550^{\circ}\text{C}$. - Stress Distribution with Behaviour of Stabilized Cycle.

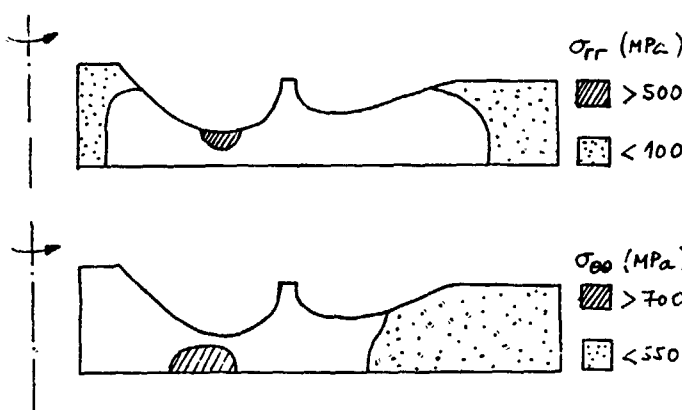


Figure 21. $T = 650^{\circ}\text{C}$. - Stress Distribution (Complete Behaviour).

Life time prediction of turbine blades

The general method previously described, i.e.:

- structure analysis under viscoplastic behaviour
- damage cumulation for creep-fatigue interaction has been applied to the case of two turbine blades with different cooling ducts, but made of the same material, the IN 100 refractory allot.

In this case, the structure analysis was performed using Bernoulli's kinematical hypothesis for beams, Chaboche and Culie (1980); the damage behaviour was described using the Manson-Coffin equa-

tions, Manson (1954), Coffin (1954), for fatigue, and the Kachanov-Rabotnov equation for creep, Rabotnov (1969).

The computed crack initiation numbers of cycles were compared (Fig. 22) to the experimental ones obtained through tests on actual blades with thermal and centrifugal loadings (see Fig. 23 for the description of the experimental set-up).

All this work is fully described by Policella and Culie (1981). It can be shown, from Figure 22, that the predictions fall reasonably in the experimental scatter zone, the number of cycles to initiation being determined by extrapolating the curves of crack length versus number of cycles toward zero length.

CONCLUSIONS

The Continuous Damage Mechanics has been proved to be an accurate tool for prediction of crack initiation.

It must be noted that it is a complex tool, either in its numerical implementation on computers, or concerning the experimental determination of behaviour and damage models, particularly for multi-dimensional situations. Yet, this complexity allows one to treat very difficult problems, where, for instance, the materials undergo microstructural changes during the period of loading, as already pointed out.

For the time being, extensions of this approach are in progress concerning the following items:

- description of viscoplastic behaviour and damage of materials exhibiting a high initial anisotropy, like single crystal alloys;
- numerical treatment of fully three-dimensional structures and behaviour. It must be noted that this requires very powerful computers.

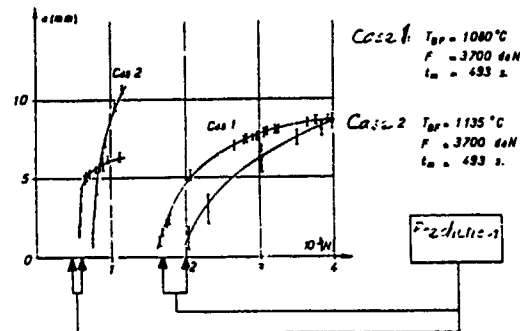


Figure 22. Comparisons of Predicted Number of Cycles to the Test Results.

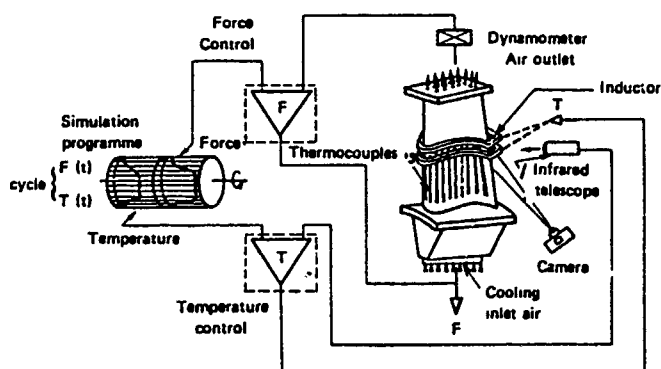


Figure 23. Description of the Experimental Set-Up.

AEROELASTIC COUPLING - AN ELEMENTARY APPROACH

by Franklin O. Carta
 United Technologies Research Center
 East Hartford, CT 06108
 USA

INTRODUCTION

In the Introduction and Overview of Volume 1, the wide diversity of flutter and vibration instabilities of turbomachinery blade rows faced by the designer have been described. Common to all of these instabilities are two necessary requirements for them to occur: 1) an available energy supply (i.e., the moving air stream) and 2) a zero or negatively damped system. In the most elementary sense, the word "system" refers to the combination of the blading and the airstream. Taken alone, the blades have positive damping. The inclusion of the airstream will either increase or decrease the damping of the system, and in the case of a negatively damped system, will lead to self-excitation or flutter.

It should be noted that the emphasis on self-excited phenomena in this chapter does not imply that this is the only important vibratory problem faced by the engine designer. Indeed, there are several chapters in this Manual (Chapters 9, 16, 17, 19, 20, 22) that are concerned with forced vibration, resonant response, and fatigue of engine structures. Nevertheless, most or all of these phenomena involve the close coupling and interaction of aerodynamics and structures, and for this reason, the present topic was chosen to introduce the reader to the subject of coupled aeroelasticity in axial flow turbomachines, in preparation for the chapters that follow.

It is historically appropriate to initiate this chapter with a brief review of the evolution in engine design that led to the occurrence of coupled flutter, and to its subsequent analysis and prediction by the energy method. Prior to the early 1960s the observed flutter of turbomachinery blading was usually a single-degree-of-freedom instability associated with high blade loading, and was invariably called "stall flutter" (cf. Chapter 7). Although several multiblade unsteady aerodynamic theories existed (Lane and Wang 1954, Sisto 1952, and Whitehead 1960), they were all based on linear potential flow of an incompressible fluid past infinitely thin flat plate airfoils. Clearly, none were applicable by virtue of the nonlinear nature of the governing aerodynamics. Hence, empiricism was the only tool available to the designer.

The empiricism took the form of a plot of reduced velocity (U/U_{∞}) vs. incidence angle (Fig. 1) in which the lower left portion of the plot was flutter free and represented "goodness", while the upper right portion, above the curved boundary, was a region of progressively increasing torsional stress, leading ultimately to blade failure (cf. Fig. 2 of the Introduction of Vol. 1, and Fig. 2 of Chapter 7). If a blade design yielded an operating condition at "1", within the flutter regime, the designer could apply a series of corrections that would lead to a reduction in angle of attack (which would yield a lower pressure rise and was therefore unfavorable), or a reduction in velocity (having the same unfavorable effect on performance), or an increase in torsional frequency, ω_t , which would also decrease the value of the ordinate of the operating point to "2" in Fig. 1.

Within limits, the increase in torsional frequency was a viable fix to this problem. It was generally accomplished by increasing the thickness of the blade, which had the effect of increasing engine weight. Early designs were based on steam turbine technology, in which thick blades were the norm, and the percentage increase in bulk was not prohibitive to the overall system operation. However, as higher performance was required of the engine, thin blades of higher aspect ratio were found to provide this extra performance margin, and unfortunately, both of these blade characteristics were found to place the operating point securely within the flutter region of Fig. 1. Further discussions of these early problems can be found in Shannon (1945), Armstrong and Stevenson (1960), and Sisto and Ni (1970).

The introduction of part-span shrouds (called snubbers or clappers in Great Britain) provided an additional constraint that dramatically raised both the torsional and bending frequencies of the blades without materially affecting the overall weight, and in some instances permitted the use of thinner (and hence lighter) hardware. The need for this configuration was driven by the introduction of the fan engine, which required one or more stages of extra long blades at the compressor inlet to provide an annulus of air to bypass the central core of the engine. This solved the stall flutter problem, but introduced a more insidious problem, initially termed "non-integral order flutter", which was impossible to predict with the available empirical tools. The term "non-integral order" was chosen because the flutter, which involved the coupling of bending and torsion modes, did not occur exclusively at the intersections of the engine order lines and the natural frequency curves of the Campbell diagram (cf. Fig. 3 of the Introduction to Vol. 1). The problem was further exacerbated by the relative supersonic speeds at which the blade tips operated.

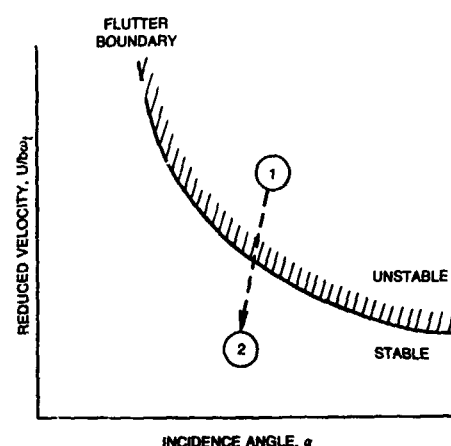


Figure 1 Schematic stall flutter map.

At this time (in the early 1960s) there were no applicable aerodynamic theories capable of modeling the complex flow field in the tip region of the new fan jet geometry, shown schematically in Fig. 2. Here the axial velocity was subsonic, but its vector sum with the wheel speed yielded a supersonic relative speed that placed the leading edge Mach waves ahead of the leading edge locus of the blade row. Thus the relatively simple theory of Lane (1957) for supersonic through-flow was inapplicable. Furthermore, the incompressible theories cited above were inappropriate for compressible flow, and were far too complicated for routine computations on existing computer hardware, and hence could not be used even for trend studies.

The present chapter will review the first published work to provide a means for identifying the phenomenon and for predicting its behavior (Carta 1967). Although the initial paper relied on unsteady aerodynamic theories for isolated airfoils in an incompressible flow, the fundamental principle was sound, and its later use with the supersonic cascade theory of Verdon (1973) and subsequent aerodynamic theories was shown to be accurate as a predictive design tool by engine manufacturers (Nikolaiczak et al 1975, Hallivell 1975, 1980).

The object of this chapter is to introduce the reader to the concept of the coupled, multiblade flutter instability. The fundamental aeroelastic equations linking aerodynamic forces and moments with elastic blade deformations will be manipulated to yield a prediction of the work per cycle of coupled motion, leading to a stability prediction. Although superseded by more modern approaches and techniques this will serve to highlight the need to understand both the aerodynamic and the structural contributions to the phenomenon. The remainder of this two volume work has been devoted to satisfying this need.

NOMENCLATURE

a	dimensionless distance of pivot axis of the midchord, in semichords	K	stiffness, lb/ft
A	lift function	K_E	kinetic energy, ft-lb
A_n	amplitude of n th wave	L	lift, lb (positive upward), or lift function
b	semichord, ft	m	mass, $\text{lb}\cdot\text{sec}^2/\text{ft}$
B	moment function	M	moment, ft-lb (positive nose up), or moment function, or Mach number
c	damping, $\text{lb}\cdot\text{sec}/\text{ft}$	n	number of blades
c_{cr}	critical damping, $\text{lb}\cdot\text{sec}/\text{ft}$	N	number of waves, or number of nodal diameters
$C(k)$	Theodorsen function	r	radius, ft
f	frequency, cps	s'	peripheral distance along rim, ft
F_d	damping force, lb	$s = s'/S$	dimensionless peripheral distance along rim
$F(k)$	real part of Theodorsen function	S	peripheral wave length, ft
$G(k)$	imaginary part of Theodorsen function	t	time, sec
h'	bending deflection, ft (positive downward)	T	period of damped motion
$h = h'/b$	dimensionless bending deflection, in semichords	U	velocity relative to moving blade, ft/sec
i	$\sqrt{-1}$	w	work, ft-lb
$k = b\omega U$	reduced frequency parameter	x	displacement, ft
$k_c = 2kM/(M^2-1)$	compressible reduced frequency	α	twist angle, rad, or incidence angle, deg (positive nose up)
		α_{ch}	chordal stagger angle, deg
		γ	damping ratio

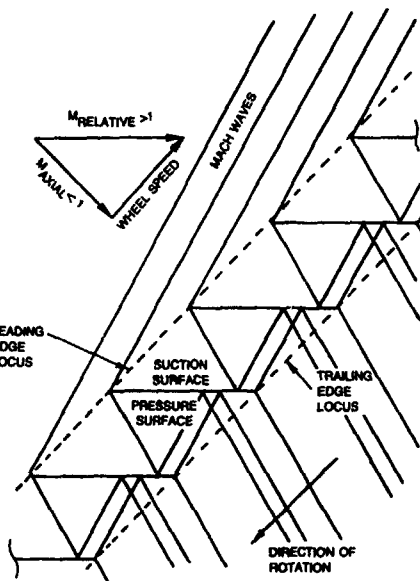


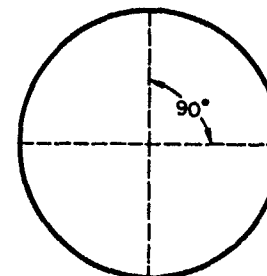
Figure 2 Supersonic cascade with subsonic leading edge locus.

δ	logarithmic decrement, or blade deflection, ft
η	dimensionless spanwise station
θ	phase angle between bending and torsional motions, rad
λ	normalized work term
μ	real part of eigenvalue
ν	imaginary part of eigenvalue
ρ	air density, $\text{lb-sec}^2/\text{ft}^4$
r	gap, ft
σ	interblade phase angle
ω	frequency, rad/sec
Subscripts	
ax	axial
B	bending term
C	coupling term
d	damped value
h	due to bending
I	imaginary part
0	root radius or natural frequency
P	pitching term
R	real part
t	torsional
tan	tangential
T	tip value
TOT	total
α	due to pitch
Superscripts	
$(\bar{\ })$	amplitude or average over one cycle
$(\prime), (\prime \prime)$	first and second derivatives with respect to time

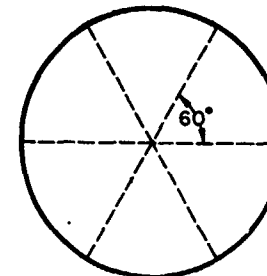
SYSTEM MODE SHAPES

The vibratory mode shapes which can exist on a rotor consisting of a flexible blade-disk-shroud system are well known to structural dynamicists in the turbomachinery field and are discussed in detail in chapter 15 of this volume. Although both concentric and diametric modes can occur, the latter are the only system modes which are of interest in the present chapter. These diametric modes are characterized by node lines lying along the diameters of the wheel and having a constant angular spacing. Thus, for example, a two-nodal diameter mode would have two node lines intersecting normally at the center of the disk, and a three-nodal diameter mode would have three node lines intersecting at the disk center with an angular spacing of 60 deg between adjacent node lines (see Fig. 3). These diametric modes are the

physical embodiment of the eigensolutions of the system, and it can be shown, using standard structural dynamical techniques, that the system frequency for each mode is primarily a function of the physical distribution of the system mass and stiffness and is only slightly affected by the rotation of the system. Thus the system frequencies do not necessarily coincide with integral multiples of the rotor speed, and in fact, such coincidences of frequency are avoided for the lower frequencies if possible.



a) TWO NODAL DIAMETER PATTERN



b) THREE NODAL DIAMETER PATTERN

Figure 3 Typical diametric node configurations.

A graphic depiction of these coupled disk modes can be found in the "rubber wheel" experiment performed by Stargardter (1966) in which a flexible multiblade rotor, with integral part-span ring, was spun over a range of rotational speeds and subjected to integral order excitations with air jets. The deformation mode shapes were exaggerated relative to a "real" rotor, but left no doubt about the physics of the problem and the key role played by the part span shroud in coupling the bending and torsion modes. Figure 4, taken from the work that led to the paper, shows the flexible wheel in plan view, and two other edgewise views of two- and three-nodal diameter vibrations. Of necessity, these are integral order modes because of the use of an excitation source that was fixed in space. However, they differ from the nonintegral order flutter modes only in that they are stationary in space while the nonintegral modes are traveling waves.

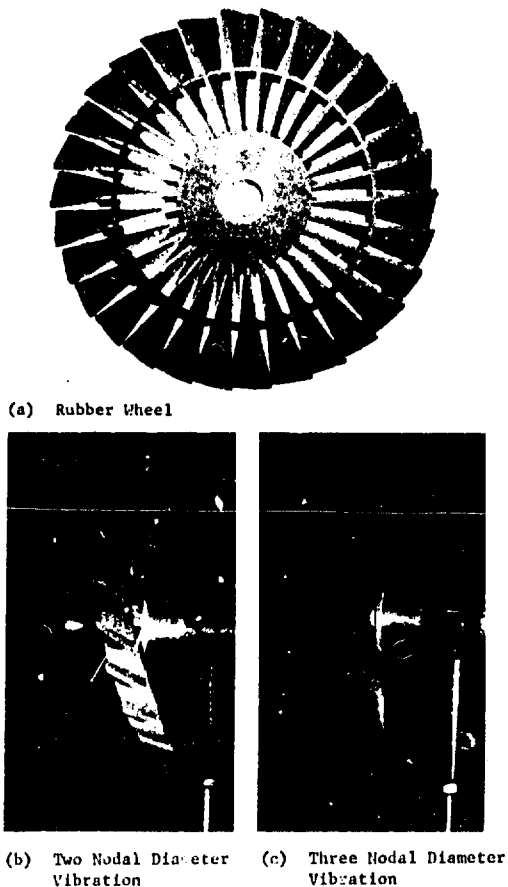


Figure 4 Rubber wheel deformation.

In the early 1960s, a number of instances of nonintegral order vibrations at high stress occurred in both engine and test rig compressor rotors. The stress levels reached in a number of cases were sufficiently high to severely limit the safe operating range of the compressor. Attempts to relate these vibrations to the stall flutter phenomenon or to rotating stall failed, largely because the vibrations often occurred on or near the engine operating line. Subsequent analysis of these cases revealed that the observed frequencies of these instabilities correlated well with the predicted frequencies of the coupled blade-disk-shroud motion described previously.

The initial object of the 1967 analysis was to explore the underlying mechanism of this instability and to show that under certain conditions of airflow and rotor geometry this coupled oscillation was capable of extracting energy from the airstream in sufficient quantities to produce an unstable vibratory motion. A further objective was to make the analysis sufficiently general to permit its use with advanced aerodynamic and/or structural dynamic theories, and ultimately, to provide the designer with a tool for flutter free operation.

ANALYSIS

Two-Dimensional Section Coefficients

The unsteady aerodynamic theory of a two-dimensional thin airfoil executing simple harmonic motion in vertical translation and/or twist has been extensively investigated by a number of authors (Theodorsen 1935, Scanlan and Rosenthal 1951, Bisplinghoff, Ashley, and Halfman 1955) and will not be discussed in any great detail in this chapter. However, for clarity in the ensuing derivation, it is expedient to describe briefly the physical system being considered and to define the nomenclature to be used in the analysis.

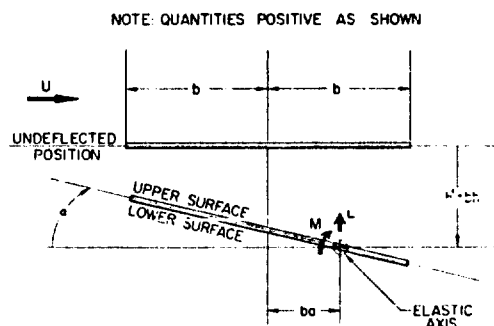


Figure 5 Airfoil section notation showing both undeflected and deflected blade.

Figure 5 is a schematic representation of a two-dimensional airfoil section displaced in both vertical translation (normal to the chord) and twist. The effects of translation of the airfoil parallel to the chord are of second order (Whitehead 1960) and have been neglected herein. The complex, time-dependent unsteady lift and moment per unit span are given by

$$L = L_h + iL_I = -mb^3\omega^2 \left[A_h \frac{h^2}{b} + A_{h\alpha}\alpha \right] \quad (1)$$

$$M = M_h + iM_I = mb^4\omega^2 \left[B_h \frac{h^3}{b} + B_{h\alpha}\alpha \right] \quad (2)$$

where A_h , $A_{h\alpha}$, B_h , and $B_{h\alpha}$ represent the standard unsteady aerodynamic coefficients -- lift due to bending, lift due to twist, moment due to bending, and moment due to twist, respectively. For example, if Theodorsen's theory (1935) for an isolated airfoil at zero incidence oscillating in an incompressible, two-dimensional flow is used, these quantities may be rewritten in the form of Smilg and Wasserman (1942) as

$$\left. \begin{aligned} A_h &= L_h \\ A_{h\alpha} &= L_{h\alpha} - (\frac{1}{2} + \alpha)L_h \\ B_h &= M_h - (\frac{1}{2} + \alpha)L_h \\ B_{h\alpha} &= M_{h\alpha} - (\frac{1}{2} + \alpha)(L_{h\alpha} + M_h) + (\frac{1}{2} + \alpha)^2L_h \end{aligned} \right\} \quad (3)$$

where, in turn, L_h , L_a , M_h , and M_a are tabulated in both Scanlan and Smilg. (Note that in these sources the positive lift and vertical translation are both directed downward which accounts for the negative right-hand side of equation (1).) Appropriate coefficients for other aerodynamic conditions may be inserted for A_h , A_a , B_h , and B_a , and it is shown in Mikolajczak (1975) and Hallivell (1975) that this leads to an accurate prediction of the instability boundary. At present, though, the development will be based on the coefficients A_h , A_a , B_h , B_a , and consequently will be quite general.

It is well known from unsteady aerodynamic theory that the forces and moments acting on an oscillating airfoil are not in phase with the motions producing these forces and moments. A convenient representation of this phenomenon is obtained on writing the steady coefficients in complex form as $A_h = A_{hR} + iA_{hI}$, etc., and the time dependent displacements as

$$\left. \begin{aligned} h &= h_R + ih_I = \bar{h}e^{i\omega t} = \bar{h} \cos \omega t + i\bar{h} \sin \omega t \\ a &= a_R + ia_I = \bar{a}e^{i(\omega t + \theta)} \\ &= \bar{a} \cos(\omega t + \theta) + i\bar{a} \sin(\omega t + \theta) \end{aligned} \right\} \quad (4)$$

where, in general, it has been assumed that the torsional motion leads the bending motion by a phase angle, θ . In this equation, $h = h'/b$ is the dimensionless bending displacement, and \bar{h} and \bar{a} are the dimensionless amplitudes of the motion in bending and torsion, respectively.

Two-Dimensional Work Per Cycle

The differential work done by the aerodynamic forces and moments in the course of this motion is obtained by computing the product of the in-phase components of force and differential vertical displacement and of moment and differential twist. Accordingly, the work done per cycle of motion in each mode is obtained by integrating the differential work in each mode over one cycle. The total work done per cycle of coupled motion is given by the sum

$$W_{TOT} = -b \oint L_R dh_R + \oint M_R da_R \quad (5)$$

where the minus sign is required because h and a are defined to be positive in opposite directions. It is important to note that in equation (5), positive work implies instability since these equations represent work done by the air forces on the system.

To compute these integrals, L_R and M_R are obtained from equations (1) and (2), the real parts of equations (4) are differentiated, and these quantities are substituted into equation (5) to yield

$$\begin{aligned} W_{TOT} = -\pi b^4 \omega^2 [& \bar{h} \oint [A_{hR} \bar{h} \cos \omega t - A_{hI} \bar{h} \sin \omega t \\ & + A_{aR} \bar{a} \cos(\omega t + \theta) - A_{aI} \bar{a} \sin(\omega t + \theta)] \sin \omega t d(\omega t) \\ & + \bar{a} \oint [B_{hR} \bar{h} \cos \omega t - B_{hI} \bar{h} \sin \omega t + B_{aR} \bar{a} \cos(\omega t + \theta) \\ & - B_{aI} \bar{a} \sin(\omega t + \theta)] \sin(\omega t + \theta) d(\omega t)] \end{aligned} \quad (6)$$

The line integrals over one cycle of motion are equivalent to an integration over the range $0 \leq \omega \leq 2\pi$; after the indicated integrations in equation (6) are performed and the equation is simplified, the total work done on the system is given by

$$W_{TOT} = \pi^2 b^4 \omega^2 [A_{hR} \bar{h}^2 + [(A_{aR} - B_{hR}) \sin \theta \\ + (A_{aI} + B_{hI}) \cos \theta] \bar{h} + B_{aI} \bar{a}^2] \quad (7)$$

In this equation, the quantities A_{hI} and B_{aI} represent the damping in bending and the damping in pitch, respectively. For an isolated airfoil oscillating at zero incidence in an incompressible flow, both of these damping terms will be negative and hence will contribute to the stability of the system.

The sign of the cross-coupling term in equation (7) (the term enclosed by the square brackets and multiplied by the product $\bar{a}\bar{h}$) is strongly dependent on the phase angle between the motions, θ . In the usual classical flutter analysis, the phase angle remains an unknown until the end of the calculation, at which time it may be evaluated as an output quantity. For the configuration presently under consideration, however, the physical constraint of the structure on the mode shape fixes θ to be a specific input quantity, as will be shown in the next section. This quantity within the square brackets is dominant in specifying regions of unstable operation.

Relations Between Blade Motions and Disk Deformation

It is assumed that a given rotor system consists of a set of flexible blades uniformly distributed on the periphery of a flexible, rotating disk. To determine the phase relations between the components of blade vibration, consideration is given to the portion of the blade which is in the immediate neighborhood of the disk rim. The nomenclature for a compressor blade row is illustrated in Fig. 6, in which the blades have been schematically represented as a series of flat plates oriented at a chordal stagger angle α_{CH} relative to the line connecting the leading edges of all blades.

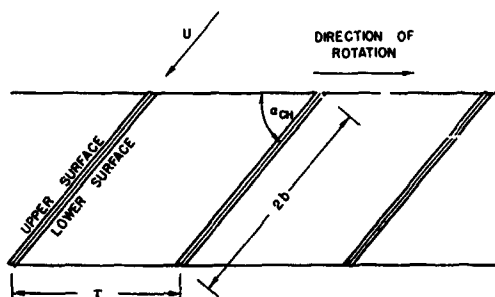


Figure 6 Cascade geometry.

The disk deformation, which is primarily in the axial direction, is denoted by $\delta_{ax}(s')$ at the disk rim, where s' is the peripheral distance along the rim, measured from a diametric node point. It can be assumed that for small amplitudes of vibration the rim mode will be sinusoidal and given by the formula

$$\delta_{ax} = \bar{\delta}_{ax} \sin(2\pi s'/s) = \bar{\delta}_{ax} \sin 2\pi s \quad (8)$$

where s is the dimensionless peripheral distance measured in units of the wavelength, S , and where $\bar{\delta}_{ax}$ is the amplitude of the peripheral wave at the disk rim.

The blade embedded in the rim of the compressor disk may now be represented by the intersection of a line segment (i.e., the blade) and a portion of the disk deformation curve, with the angle of intersection between the line segment and the tangent to the curve equal to α_{CH} . This is shown in Fig. 7, in which both a deflected and an undeflected rim are depicted.

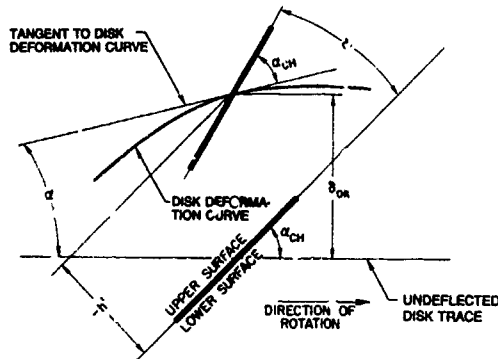


Figure 7 Blade deformation notation for disk deformation at blade root showing both undeflected and deflected blade.

Figure 7 shows that the blade twist, α , is given by the slope of the disk deformation curve, and upon differentiating equation (8), the result is

$$\begin{aligned} \alpha &= \tan^{-1}(d\delta_{ax}/ds') = \tan^{-1}\left[\frac{2\bar{\delta}_{ax}}{s} \cos 2\pi s\right] \\ &\approx \frac{2\bar{\delta}_{ax}}{s} \cos 2\pi s \end{aligned} \quad (9)$$

for a sufficiently small angle, α . The figure also shows that the dimensionless normal deflection is given by

$$\begin{aligned} h &= h'/b = -\frac{\bar{\delta}_{ax}}{b} \cos \alpha_{CH} \\ &= -\frac{\bar{\delta}_{ax}}{b} \cos \alpha_{CH} \sin 2\pi s \end{aligned} \quad (10)$$

where use has been made of equation (8). Equations (10) and (9) will now be set equal to the real parts of h and α , respectively, from equations (4) with the result

$$h \cos \omega t = -\frac{\bar{\delta}_{ax}}{b} \cos \alpha_{CH} \sin 2\pi s \quad (11)$$

$$\bar{\alpha} \cos(\omega t + \theta) = \frac{2\bar{\delta}_{ax}}{s} \cos 2\pi s \quad (12)$$

The amplitudes of the periodic functions must be equal, and therefore

$$h = \frac{\bar{\delta}_{ax}}{b} \cos \alpha_{CH} \quad (13)$$

$$\bar{\alpha} = \frac{2\bar{\delta}_{ax}}{s} \quad (14)$$

Hence equations (11) and (12) become

$$\left. \begin{aligned} \cos \omega t &= -\sin 2\pi s \\ \cos(\omega t + \theta) &= \cos 2\pi s \end{aligned} \right\} \quad (15)$$

In order to satisfy this set simultaneously, one possible solution for the phase angle is $\theta = -\pi/2$ (i.e., the bending motion leads the torsional motion by 90 deg). This result can also be obtained intuitively (at least for the magnitude of the phase angle) from the fact that at the nodal points in the disk rim the blade will experience maximum twist with no normal displacement, whereas at the antinodes in the disk rim the blade will have no twist, but will experience maximum normal displacement, as shown in Fig. 8.

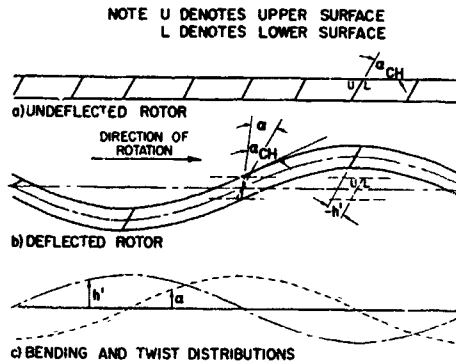


Figure 8 Torsion and bending motions caused by coupled blade-disk-shroud interaction.

Thus far the development has been carried out at the disk rim. (Actually, the disk participation in the coupled motion is usually quite small, and it will be seen later that the major contribution to the coupling between bending and torsion often derives from the presence of a part-span shroud.) In considering any arbitrary outboard station on the blade span, it can be assumed that the same phase angle, $\theta = -\pi/2$ will exist between the bending and torsion motions. However, the amplitude h will be different from that given by equation (13) by an amount obtained from the vector sum of the blade deformation relative to the disk rim in the axial and tangential directions, and the amplitude $\bar{\alpha}$ will be different from that given in equation (14) by an amount equal to the blade twist relative to the root position. Use was made of an existing structural dynamics computer program to determine the characteristic vibration modes and frequencies of a typical rotor system consisting of disk, blades and part-span shroud. (As stated earlier, these procedures are discussed in detail in Chapter 15.) The computed

quantities relevant to the present study are δ_{ax} and δ_{tan} , the axial and tangential deformations of the blade at the given radial station, measured relative to the original blade position in the plane of the undeformed disk, and $\bar{\alpha}$, the total twist distribution. Thus, at any arbitrary radial station outboard of the rim, the bending amplitude will be computed from the formula (see Fig. 9).

$$\delta = \frac{1}{b} \sqrt{\delta_{ax}^2 + \delta_{tan}^2} \cos \left[\alpha_{CH} + \tan^{-1} \frac{\delta_{tan}}{\delta_{ax}} \right] \quad (16)$$

$$= \frac{\delta_{ax}}{b} \cos \alpha_{CH} - \frac{\delta_{tan}}{b} \sin \alpha_{CH}$$

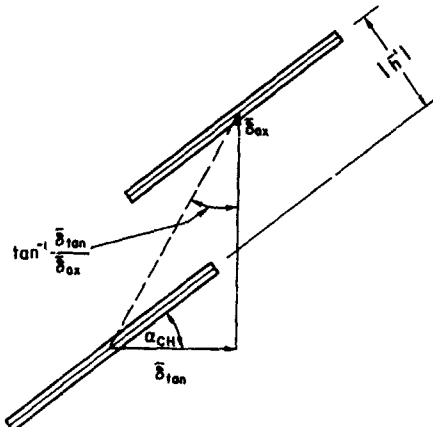


Figure 9 Blade deformation notation outboard of blade root showing both undeflected and deflected blade.

Stability of Blade-Disk-Shroud System

The value of the phase angle, $\theta = -\pi/2$, may now be substituted into equation (7) and the resulting two-dimensional aerodynamic work per cycle at each spanwise station reduces to

$$W_{TOT} = \pi^2 \rho b^2 U^2 [k^2 A_{HI} \bar{h}^2 - (k^2 A_{OR} - k^2 B_{HR}) \bar{\alpha} \bar{h} + k^2 B_{OI} \bar{\alpha}^2] \quad (17)$$

where $k = \omega U / h$ is the reduced frequency parameter. (The use of the combinations $k^2 A_{HI}$, $k^2 A_{OR}$, $k^2 B_{HR}$, and $k^2 B_{OI}$ in the original 1967 paper was dictated by convenience and by this availability of the aerodynamic coefficients in this form.)

Equation (17) is an expression for the two-dimensional aerodynamic work per cycle at any arbitrary span station, say at radius r , as measured from the engine centerline. The work done on the entire blade is obtained by integrating equation (17) over the blade span, from the root, at $r = r_0$, to the tip, at $r = r_T$, after normalizing the deformations, \bar{h} and $\bar{\alpha}$, with respect to the tip bending deflection, \bar{h}_T , this gives

$$\frac{W}{h_T^2} = \pi^2 \int_{r_0}^{r_T} \rho b^2 U^2 \left[k^2 A_{HI} \frac{\bar{h}^2}{h_T^2} - (k^2 A_{OR} - k^2 B_{HR}) \frac{\bar{\alpha}}{h_T} \cdot \frac{\bar{h}}{h_T} + k^2 B_{OI} \left(\frac{\bar{\alpha}}{h_T} \right)^2 \right] dr \quad (18)$$

It was stated earlier that the stability of the system was related to the algebraic sign of the work expression; i.e., positive aerodynamic work implies instability and negative aerodynamic work implies stability. As shown in equation (18), the aerodynamic work done on the system is a direct function of the squares and products of the oscillatory amplitudes which are ordinarily obtained from a numerical solution of the characteristic equation for the vibratory system. It is well known from elementary vibration theory that the results of such a calculation are given in the form of relative amplitudes rather than absolute amplitudes. Therefore, the aerodynamic work can only be calculated on a relative basis and in its present form it cannot be used to predict either the absolute stability level of a particular configuration or the relative stability levels between two configurations. Since one of the objects of the original study was to devise a prediction technique that would permit the evaluation of alternative rotor designs from the standpoint of system stability, the theoretical development was necessarily extended to overcome this deficiency.

In addition to the relative amplitudes of motion, the structural dynamics solution provides average kinetic energy of vibration of the entire blade-disk system, based on the relative amplitudes of motion. It is shown in Appendix 1 that for a simple, linear, spring-mass-dashpot system, the ratio of damping work per cycle to average kinetic energy is proportional to the logarithmic decrement of the system, which is independent of the absolute amplitudes of the system. A comparable ratio of the aerodynamic work done per cycle on the entire blade-disk-shroud system to the average kinetic energy of vibration of the system may be made and this will be equal to the logarithmic decrement of the system. First, however, the normalized aerodynamic work per cycle obtained for one blade in equation (18) must be multiplied by the number of blades on the entire disk, n , and then by the proportionality factor, $1/4$, from equation (26) in Appendix 1. The result is

$$\delta = - \frac{nW/h_T^2}{4Kg/h_T^2} \quad (19)$$

where Kg/h_T^2 is the average kinetic energy of the system, also normalized with respect to h_T^2 , and where a positive value of δ represents stable operation. Equation (19) yields an absolute measure of system stability which is independent of relative amplitudes. Hence the results obtained may be used to evaluate both the absolute stability of a particular configuration and the relative stability between two or more configurations.

RESULTS

Calculation Procedure

To illustrate the use of this theory, the stability characteristics of a typical rotor were investigated and the results are presented below. The input quantities for use in equation (18) were obtained both from experiments and analytical studies conducted on an actual rotor at a given rpm. These data consisted of: (a) the geometric parameters for the configuration, α_{CH} , b , r_0 , r_T , and n ; (b) the steady-state aerodynamic parameters, ρ and U ; and (c) for each prescribed disk nodal diameter pattern and blade mode, the relative amplitudes of the blade deformation components, δ_{ax} , δ_{tan} , and $\bar{\alpha}$, the average system kinetic energy, K_g , and the system natural frequency, ω_0 . For each nodal diameter, equation (16) was used to calculate \bar{h} from $\bar{\delta}_{ax}$ and $\bar{\delta}_{tan}$ and both \bar{h} and $\bar{\alpha}$ were then normalized with respect to the tip bending deflection, \bar{h}_T , and plotted in Figs. 10 and 11 as functions of the dimensionless spanwise variable $\eta = (r - r_0)/(r_T - r_0)$. In both of these figures the shroud location at $\eta = 0.653$ is indicated by short tick-marks on each curve.

The stability analysis of the rotor system for any given nodal pattern was performed by calculating the spanwise variation of the reduced frequency parameter, k , and using this to obtain the spanwise variations in the unsteady aerodynamic coefficients, $k^2 A_{HI}$, $k^2 A_{QR}$, $k^2 B_{HR}$, $k^2 B_{QR}$, which are functions of k . These quantities were then inserted into equation (18) together with the normalized mode shapes and other spanwise variables and integrated numerically. Finally, the logarithmic decrement, δ , was computed from equation (19). The relevant details of this analysis are described in the subsequent sections of this chapter.

Structural Dynamics of Typical Rotor System

The dynamic system chosen for analysis in this chapter consists of a blade-disk-shroud configuration in which the blade oscillates in its first bending and first torsion modes, and

the overall system vibration modes encompass 2 through 8 nodal diameters. Figures 10 and 11 contain the spanwise variations of bending deflection and blade twist, both normalized with respect to the bending deflection at the blade tip for the specific nodal diameter under consideration. Figure 10 shows that as the number of nodal diameters increases the bending mode shape undergoes a consistent change in which the deformation of the tip region, outboard of the shroud, increases relative to the inboard region.

In Fig. 11, however, it is seen that the torsional content of the vibration (relative to the tip bending) first increases and then decreases with increasing number of nodal diameters. This suggests a variable amount of coupling between bending and torsion as the system mode changes from one nodal diameter to another. Furthermore, the major change in twist distribution for each curve occurs over the portion of the blade inboard of the deformed shroud, which imposes a twisting moment on the blade as a result of this deformation. Hence, the presence of a deformed shroud produces the coupling between blade twist and bending, and the degree of this coupling is modified by the diametric modal pattern.

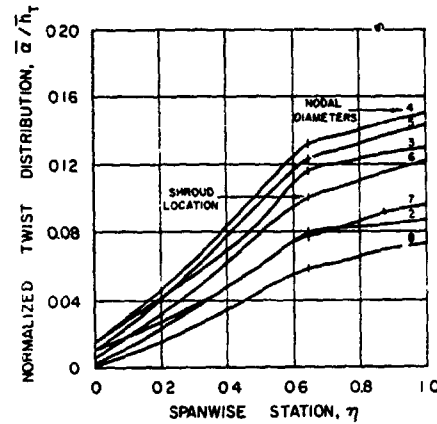


Figure 11 Spanwise variation of twist distribution normalized with respect to tip bending deflection for each nodal diameter.

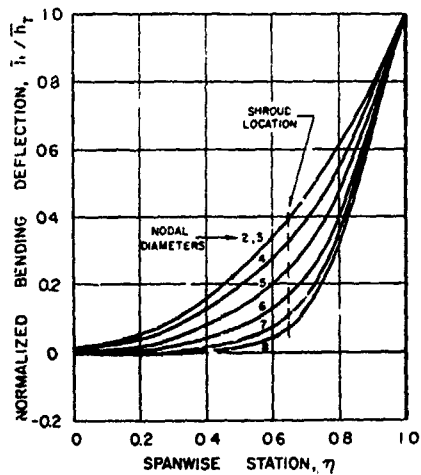


Figure 10 Spanwise variation of bending deflection normalized with respect to tip bending deflection for each nodal diameter.

A very revealing and informative plot is shown in Fig. 12, in which only the tip value of the normalized deformation ratio $(\bar{\alpha}/h_T)_T$ has been plotted as a function of frequency. This figure indicates a very strong variation of $(\bar{\alpha}/h_T)_T$ with the number of nodal diameters (i.e., with natural frequency); it is relatively small at both small and large nodal diameters and reaches a maximum value at approximately 4 or 5 nodal diameters. Thus, it appears that torsion-bending coupling is a maximum for intermediate nodal diameters, with a predominantly bending motion occurring at either extreme. This increase in coupling for intermediate nodal diameters may be regarded as either a relative increase in blade twist or a relative decrease in blade bending. The absolute deformations are unimportant since the stability equations (18) or (19) are expressed solely in terms of the normalized deformations \bar{h}/h_T and $\bar{\alpha}/h_T$.

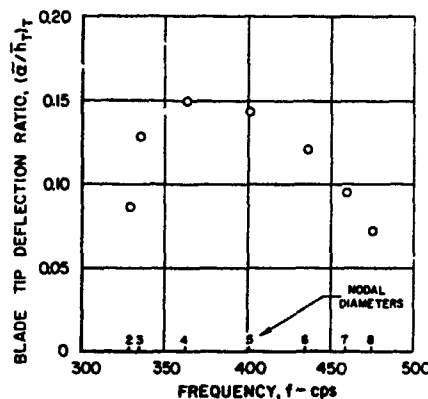


Figure 12 Variation of blade tip deflection ratio with frequency.

Stability Analysis Using Isolated Airfoil Theory

The stability of the system was originally determined using equations (18) and (19) and employing unsteady isolated airfoil theory as described in Appendix 2. The logarithmic decrement, δ , was calculated for each nodal diameter (2 through 8) at the resonant frequencies appropriate for each case. Results of these stability calculations are found in Fig. 13. The natural frequency in each case is denoted by the circled point. System stability is indicated by positive values of δ and instability is indicated by negative values of δ . It is seen from this figure that the system is stable for the 2, 6, 7, and 8-nodal-diameter modes and is unstable for the 3, 4, and 5-nodal-diameter modes, with minimum stability (i.e., maximum instability) occurring at four nodal diameters. A comparison of Fig. 13 with Fig. 12 reveals a rather strong correlation between maximum system instability and maximum torsion-bending coupling, represented in Fig. 12 by the maximum values of $(\bar{\alpha}/\bar{h}_T)_T$ at four nodal diameters. Similar results were obtained for a number of rotor configurations which were analyzed using these procedures. Thus it was tentatively concluded that the greater the degree of coupling between torsion and bending in a shrouded rotor, the greater the likelihood of a flutter instability.

Comparison Between Theory and Experiment

The theoretical procedure for an isolated airfoil at zero incidence described in a previous section was modified slightly (by the engine development group) for use in evaluating various rotor configurations. An iterative procedure was developed which produced the rotor parameter values for the neutrally stable condition, $\delta = 0$, in which the incompressible isolated airfoil theory of Theodorsen (1935) was used at low speeds, and the supersonic isolated airfoil theory of Garrick and Rubinov (1946) was used at high speeds. A number of rotors were considered in this study, and in each case, values of blade tip deflection ratio, $(\bar{\alpha}/\bar{h}_T)_T$, and reduced velocity at the blade tip, $(U/b\omega_T)_T$, were obtained for the condition of zero logarithmic decrement, $\delta = 0$. The locus of points so obtained yielded a narrow band of scattered points through which a faired curve was drawn. This formed a single zero damping stability boundary valid for all configurations, as shown in Fig. 14. It is interesting to note that the theoretical curve

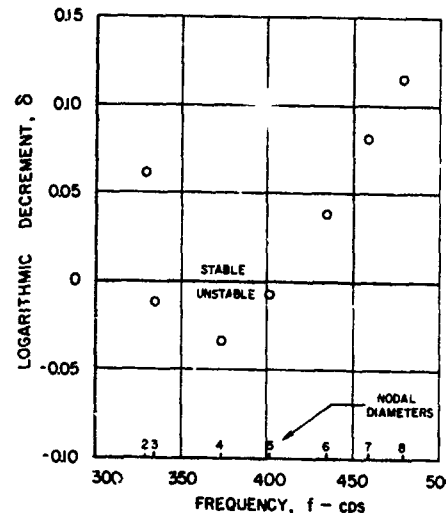


Figure 13 Variation of logarithmic decrement with frequency using isolated airfoil theory.

— LOCUS OF POINTS FOR WHICH $\delta=0$ (THEORY)
 ● CONFIGURATIONS WHICH FLUTTER
 △ CONFIGURATIONS WHICH DID NOT FLUTTER
 ○ → DENOTES REDESIGN OF UNSTABLE
 CONFIGURATION TO OBTAIN STABILITY

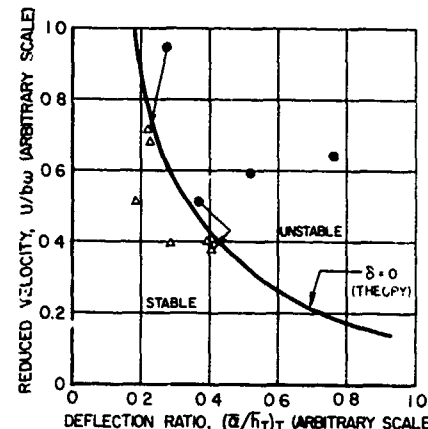


Figure 14 Stability boundary — comparison between theory and experiment.

of Fig. 14 may also be confirmed by interpolating Figs. 12 and 13 to $\delta = 0$, through fictitious curves passed through the circled eigensolutions. This was done for several configurations in the report (Carta 1966) that formed the basis for the 1967 paper.

In Fig. 14 the region beneath and to the left of the curve represents stable operation, and the region above and to the right of the curve represents unstable operation. Superimposed on this curve are the results of a number of engine and rotor tests. The solid circular symbols represent configurations which fluttered and the open triangular symbols represent stable configurations. It is seen that the engine experience and the theoretical

prediction were in good agreement for these early cases. Furthermore, two of the unstable configurations were redesigned to yield stable rotors, as indicated by the arrows connecting two pairs of points. Hence, it was felt that the theory had some merit in predicting as well as explaining the occurrence of coupled blade-disk-shroud flutter. However, it was also felt that the agreement achieved through the use of incompressible, isolated airfoil theory on a high speed, multiblade system was tenuous at best, and a major effort was continued by a number of researchers to extend the aerodynamic model to include more realistic effects. Before these modern developments are discussed, a brief review of the energy distribution among the modes will be made, and a portion of a parametric study of coupling effects will be examined.

Spanwise Variations in the Damping and Coupling Terms

In the previous section on Stability Analysis, the major emphasis was placed on the variation in stability parameter with changes in frequency (i.e., number of nodal diameters). In this section, some brief considerations will be given to the individual terms in the work equation and their spanwise variations as they are affected by changes in frequency.

For convenience the expression for the work per cycle at each spanwise station, equation (17), will be rewritten as

$$W_{TOT} = W_B + W_C + W_P \quad (20)$$

where

$$W_B = \pi^2 \rho b^2 U^2 k^2 A_{hi} \bar{h}^2 \quad (21)$$

is the local two-dimensional work due to bending,

$$W_C = -\pi^2 \rho b^2 U^2 (k^2 A_{or} - k^2 B_{hr}) \bar{a} \bar{h} \quad (22)$$

is the local two-dimensional work due to coupling and

$$W_P = \pi^2 \rho b^2 U^2 k^2 B_{oi} \bar{a}^2 \quad (23)$$

is the local two-dimensional work due to pitch. Before these quantities can be usefully investigated, they must be normalized in such a way that meaningful comparisons between various cases may be made. In the course of this study, it was found that the tip value of the local work due to bending,

$$W_{BT} = \pi^2 (\rho b^2 U^2 k^2 A_{hi} \bar{h}^2)_{TIP} \quad (24)$$

was negative and non-zero for all values of frequency in all cases considered. (It will be recalled that negative work implies stability since this represents work done by the air on the blade.) Therefore, in view of the negative definite behavior of W_{BT} , it was decided to normalize all three local work terms, W_B , W_C , and W_P , with respect to this tip value of W_B for the specific number of nodal diameters being considered. The normalized quantities are defined below.

$$\lambda_B = \frac{W_B}{W_{BT}} = \frac{\rho b^2 U^2 k^2 A_{hi} \bar{h}^2}{(\rho b^2 U^2 k^2 A_{hi} \bar{h}^2)_{TIP}} \quad (25)$$

$$\lambda_C = \frac{W_C}{W_{BT}} = \frac{\rho b^2 U^2 (k^2 A_{or} - k^2 B_{hr}) \bar{a} \bar{h}}{(\rho b^2 U^2 k^2 A_{hi} \bar{h}^2)_{TIP}} \quad (26)$$

$$\lambda_P = \frac{W_P}{W_{BT}} = \frac{\rho b^2 U^2 k^2 B_{oi} \bar{a}^2}{(\rho b^2 U^2 k^2 A_{hi} \bar{h}^2)_{TIP}} \quad (27)$$

It was stated earlier that the quantity W_{BT} was always a negative, non-zero number, and hence implied a stable condition for this parameter at the blade tip. By definition the value of λ_B at the tip will be +1.0 since at this point W_B is divided by itself. Hence a positive value of any of the normalized work terms will indicate a stable tendency (in contrast to a negative value of the absolute work parameter) and a negative value of any of the normalized work terms will indicate an unstable tendency.

From Fig. 13 the most unstable condition was a 4 nodal diameter vibration, while the most stable was an 8 nodal diameter vibration. The quantities λ_B , λ_C , and λ_P are plotted versus dimensionless span station for these two conditions in Fig. 15. An examination of this plot provides a great deal of insight into the mechanism involved in this flutter phenomenon. In both panels, the distributed work is negligible inboard of the midspan, and is significant only over the outer 1/3 of the span. The normalized work in bending, λ_B , is always positive (stabilizing), and reaches its normal value of 1.0 at the tip. In both instances the normalized coupling work, λ_C , is negative (destabilizing), and the normalized work in pitch λ_P , is of second order and can be ignored. For the 4 nodal diameter case, the bending and coupling work both reach approximately the same value at the tip, but the distribution over the span is such that the destabilizing integrated work in coupling is greater in magnitude than the stabilizing integrated work in bending. This leads to a net instability of the system in this mode. (A similar situation, with less obvious differences between bending and coupling distributions, is found for the less unstable 3 nodal diameter mode in Fig. 31 of Carta (1966).) In contrast, the spanwise distributions for the 8 nodal diameter mode show that the stabilizing work in bending is significantly greater in magnitude than the coupling work over the entire span, and accordingly, the system is stable at this condition.

Use of Advanced Aerodynamic Theories and Typical Rotor Shapes

These results in Fig. 15 were for a so-called first family spanwise mode. More typical higher order family modes, having additional circumferential nodes lines, were examined independently by Mikolajczak, et al (1975) and by Hallivell (1975), for state-of-the-art compressors of the mid 1970s. Hallivell used the aerodynamic theory of Nagashima and Whitehead (1974) and obtained the spanwise distribution of work per cycle shown in Fig. 16 for the second family modes. This confirms the

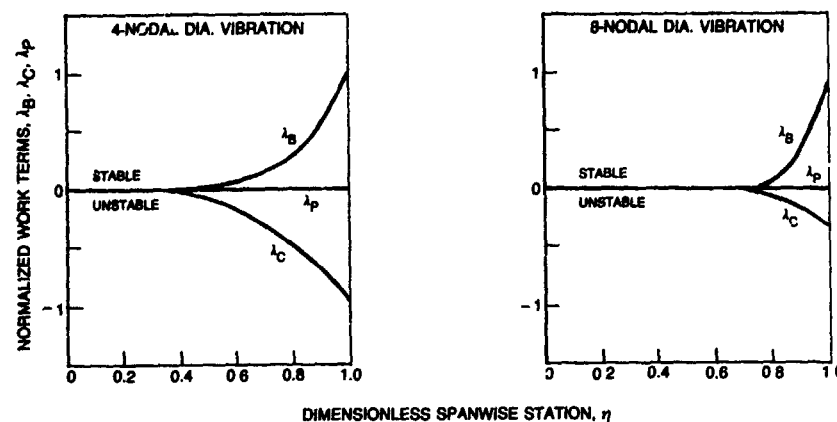


Figure 15 Variation of normalized work terms with span.

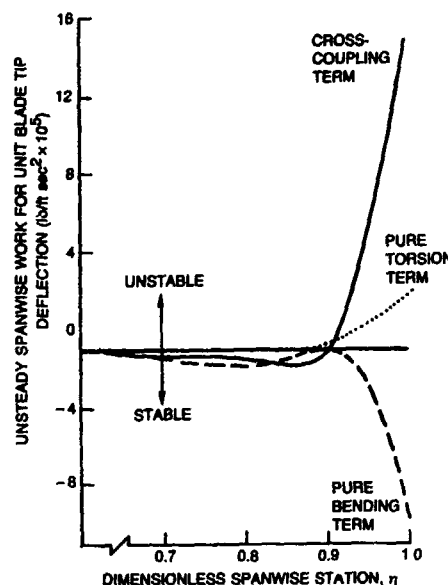


Figure 16 Fan unsteady work components at 100 per cent speed four-diameter second family mode (from Halliwell 1975).

distributions of work shown in Fig. 15. Note that Halliwell's results are dimensional, and are inverted relative to Fig. 15. He further computed the integrated work per cycle for each component of the stability equation, and the results are shown in Fig. 17 as a function of nodal diameter number, again for the second family mode. Here again the coupling term is destabilizing, and opposite to the bending term. An overall system instability for the 4, 5, and 6 nodal diameter forward traveling waves was predicted, and was confirmed as 4 nodal diameters for the test compressor.

The work by Mikolajczak et al (1975) concentrated on the overall aerodynamic damping of several compressor designs. This was preceded by the cascade study of Snyder and Commerford (1974) which also examined the

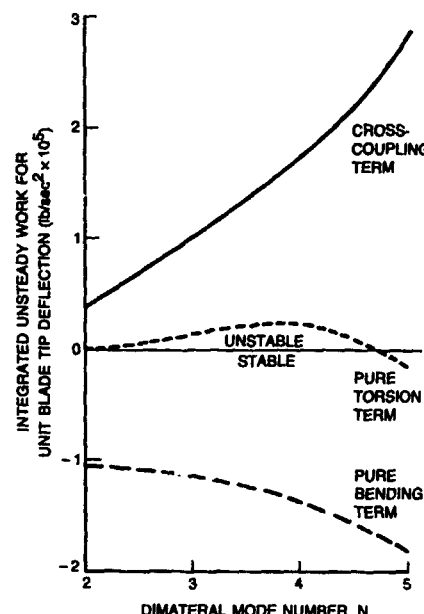


Figure 17 Fan unsteady work components at 100 per cent speed variation with second family mode number (from Halliwell 1975).

typical compressor designs. The work by Mikolajczak and his co-authors employed several aerodynamic theories, depending on the local aerodynamic conditions. For the supersonic relative flow (with subsonic axial Mach number) use was made of Verdon (1973), and for subsonic flows Smith's theory (1971) was used. In addition, cambered thin airfoils were treated using an extension of Whitehead's early work (1960) or the analysis of Sistio and Ni (1974).

Three radial modes were examined in this work, which concentrated on two compressor rotors. Rotor A was designed specifically to be susceptible to an unstalled supersonic flutter in its second radial mode. It experienced flutter at 13,700 rpm in its second mode with a 4 nodal diameter vibrational pattern. The

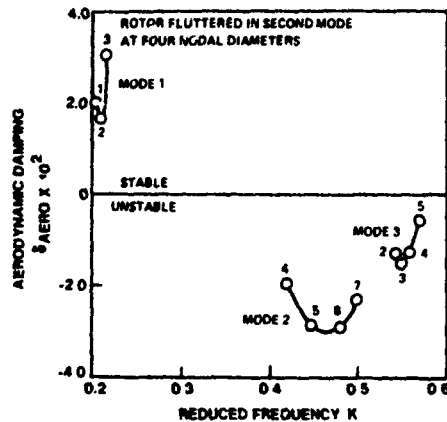


Figure 18 Damping predictions for P&WA research rotor at flutter speed.

predicted aerodynamic damping for the three modes, plotted as a function of reduced frequency, is found in Fig. 18. This clearly shows the second mode to be the least stable mode, although the 5 and 6 nodal diameter patterns appear to be theoretically more unstable than the 4 nodal diameter pattern. The sensitivity of predicted stability to rpm for Rotor A is shown in the prediction of Fig. 19 for the second radial mode. Rotor B (a NASA 1800 fps design) was specifically designed to be flutter free over its performance range. It was tested successfully with no flutter up to 12,464 rpm. The predicted aerodynamic damping for the first three radial modes was positive for all nodal diameters, as shown in Fig. 20. In a summary of these and several other rotor designs, the Mikolajczak paper shows that the use of the analytical prediction techniques described here were consistently conservative (at least up to the date of publication) and generally capable of predicting the correct flutter mode, when it occurred. This is shown in Fig. 21, where the predicted minimum aerodynamic damping for each of several rotors is plotted horizontally for the first three radial modes. The tabulation at the right of this figure briefly describes each rotor and indicates the observed flutter mode when it occurred. It should be noted that the estimated mechanical damping of a typical rotor system (the sum of material and frictional damping) was approximately 0.03. Thus, it can be seen from Fig. 21 that whenever flutter was observed, the analysis predicted a level of negative aerodynamic damping which was comparable to this expected level of mechanical damping of the rotor.

PARAMETRIC VARIATIONS

Effect of Shroud Location

In the original 1966 report a parametric study was made of the effect of part span shroud location on system stability. The results already discussed were for the standard configuration having a part span shroud at the 65.3% span station. Additional locations of 50%, 60.5%, 69.1%, and 80% span were also examined. As before, this study was constrained by the use of isolated flat plate aerodynamic theory, but it is believed that the physical principles involved are sound and that the relative changes in predicted stability are correct.

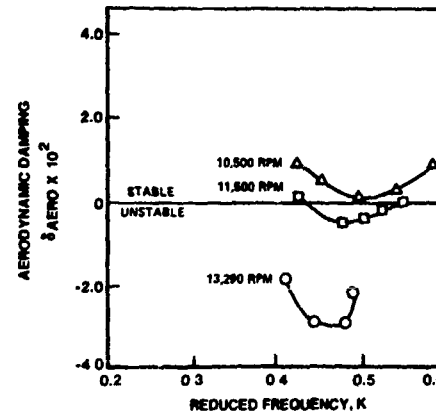


Figure 19 Second mode damping as a function of rotor speed.

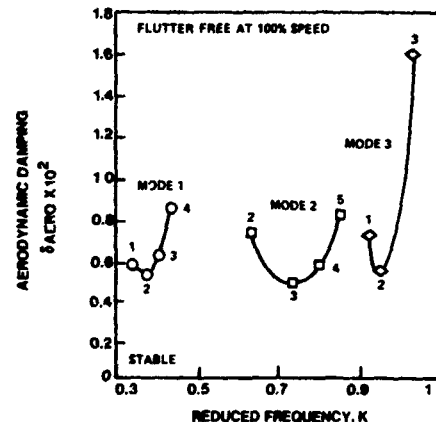


Figure 20 Damping prediction for NASA 1800 fps rotor at 100% speed.

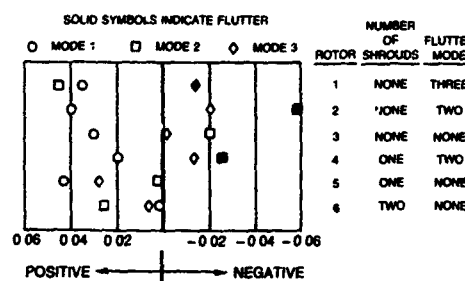


Figure 21 Damping analysis as an unstalled supersonic flutter prediction tool.

The most important finding of this study was that the stability of the system decreases rapidly as the shroud is moved outboard. This is shown in Fig. 22 in which a number of normally stable conditions for the basic configuration became quite unstable as the shroud was moved outboard. This unstable tendency is caused by the associated increase in coupling between the torsion and bending modes, shown in Fig. 23, in which a number of curves of the normalized twist distribution have been plotted as a function of spanwise station for three values of nodal diameter number (4, 6, and 8) and five shroud locations. For each nodal diameter, curves have been plotted for the shroud location at the 50%, 60.5%, 65.3%, 69.1%, and 80% span station. The position of the shroud has been indicated by a short tic mark on each curve.

The primary effect to be noted in Fig. 23 is the increase in coupling (i.e., the increase in normalized twist value) within each nodal diameter plot as shroud location is moved outboard. This increase in coupling is caused by two factors. First, as the shroud is moved outboard, a larger portion of the blade (the inboard portion) is subjected to the oscillating twisting moment of the shroud at resonance in the system mode vibration, and a smaller portion of the blade (the remainder of the blade outboard of the shroud) is driven at an off-resonance condition. (Actually, for the 6 and 8 nodal diameter vibrations with an 80% shroud position it appears that the outboard portion may also be at or near a resonance condition, but it is felt that this is an isolated phenomenon and is not important in general.) Second, as the shroud is moved outboard, the portion of the blade outboard of the shroud becomes stiffer in bending; consequently, the tip bending deflection, which is the normalizing factor in the denominator of α/h_q , becomes relatively smaller, and therefore the entire level of the curve is raised. In effect, the torsional motion has increased at the expense of the bending motion.

Finally, it is obvious that as the shroud is moved inboard the system stability increases — at least for the type of coupled flutter instability being considered herein. However, another effect of moving the shroud inboard is to increase the cantilever length of the blade portion outboard of the shroud, which reduces both the cantilever bending and cantilever torsion frequencies of this part of the blade.

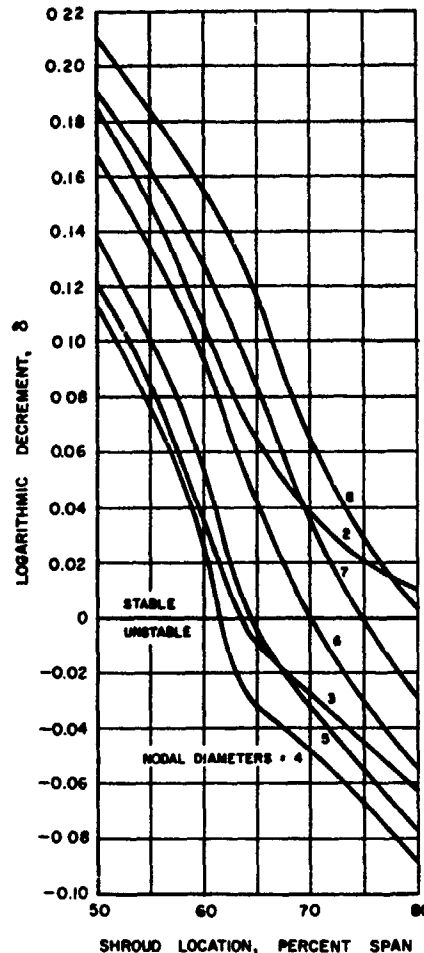


Figure 22 Effect of shroud location on stability parameter.

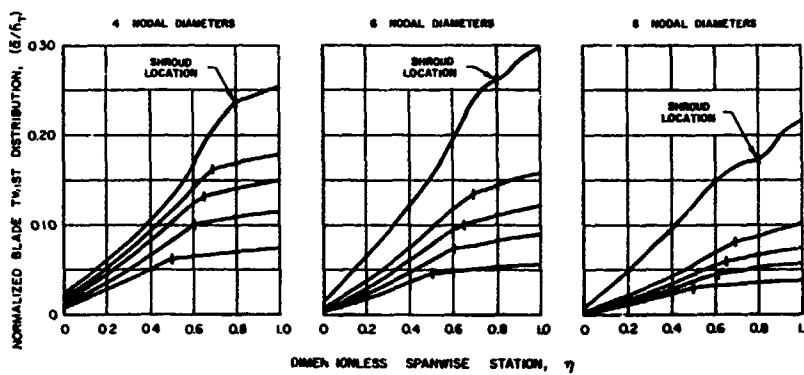


Figure 23 Effect of shroud location on normalized twist distribution.

This reduction in frequency at a fixed value of resultant velocity into the stage produces an increase in reduced velocity, U/bw , and the blade system outboard of the shroud may become susceptible to either a torsional stall flutter, a bending buffet, or both. Clearly in any design procedure a compromise must be made between a flutter-free configuration relative to the coupled flutter phenomenon, and a flutter-free configuration relative to either torsional stall flutter or bending buffet.

Interblade Phase Angle

In most of the early work described above the interblade phase angle was necessarily a quantity fixed to the configuration under examination, and not usually subjected to parametric scrutiny in a sensitivity analysis. By virtue of its definition it was inextricably tied to the fixed number of blades in the rotor, n , and to the number of disturbances over the rotor circumference, N , by the formula

$$\sigma = -2\pi/(n/N) = -2\pi N/n \quad (28)$$

where the minus sign is associated with a backward traveling wave relative to the rotor, and where N is also the number of nodal diameters that forms the basis of this chapter. Note that in general the forward traveling wave is associated with system instability (Hallivell 1975).

Physically, the interblade phase angle is a measure of the phase lag or lead of adjacent blades, and has been the subject of several experimental studies at low supersonic speeds of its important effect on aerodynamic damping (Carta and St. Hilaire 1980, Carta 1983), primarily in cascade. An analysis of the effect of varying σ for a single degree of freedom pitching motion of a supersonic cascade of thin blades operating in a subsonic axial flow was presented by Verdon and McCune (1975). It is well known (e.g. Carta 1983) that the stability of an airfoil executing a pure pitching motion depends only on the sign of the imaginary part of the pitching moment. (Note that in this case, with $h = 0$, equation (17) reduces to the form

$$W_{TOT} = \frac{1}{2} \rho b^2 U^2 k^2 B_{01} \bar{\sigma}^2 = \bar{M}_I \bar{\sigma} \quad (29)$$

where the last term is a consequence of using equation (2). If \bar{M}_I is positive, then the work per cycle is also positive, which represents an unstable condition. Figure 24 is a phase plane plot of the complex moment coefficient, taken from Verdon and McCune (1975) for this condition. The open points connected by curves represent increments of $\Delta\sigma = 30$ deg relative to the specified values of $\sigma = 0, \pi/2, \pi, 3\pi/2$. Each curve is for a different compressible reduced frequency, $k_c = 2KM/(M^2 - 1)$, from 0.5 to 2.0. Corresponding values of the complex moment coefficient for an isolated flat plate airfoil in a supersonic flow, computed from the theory of Garrick and Rubinov (1946), are represented by the solid symbols. Two concepts are revealed by this figure. The first, which is obvious, is that isolated airfoil theory is inadequate to predict the extent of the unstable region for this single degree of freedom oscillation. The second, which is also obvious, but which has subtle implications, is that the interblade phase angle has a significant effect on system stability. For the analysis described here, which was an

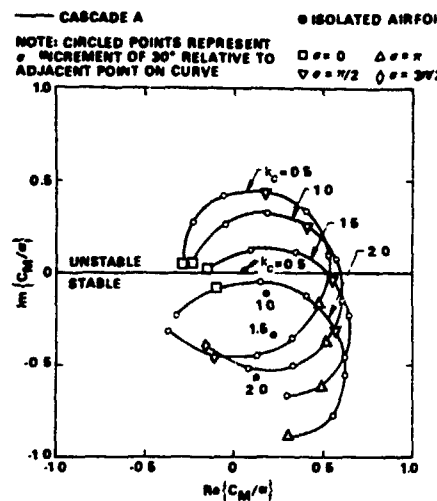


Figure 24 Moment coefficients due to pitching motions of cascade A and isolated airfoil.

infinite cascade of theoretical airfoils, the points and their connecting curves represent a continuum of valid and realizable solutions. Thus, any interblade phase angle can be represented by this plot. It will be shown presently, however, that for a rotor with a finite number of blades, a similar closed diagram is generated by the stability analysis of a coupled motion, in which the only valid solutions are for the specific values of interblade phase angle that satisfy equation (28). Under these circumstances, a variation in σ implies a corresponding change in number of blades, and the effect on stability will be profound.

An illustration of the assertion that the number of blades has a strong effect on system stability through the interblade phase angle is discussed in the papers by Kaza, et al (1987a, 1987b) which deal with single rotation propfans. Both papers deal with thin, flexible, low aspect ratio blades susceptible to large, nonlinear deflections in a strongly three-dimensional flow. To further complicate matters, the blades have large sweep and twist which couples blade bending and torsional motions within each blade, and their flexibility and proximity to one another engenders an aerodynamic coupling similar to that caused by part span supports. In addition, a flexible hub also contributes to the system coupling.

An analysis of the stability of the basic propfan, denoted by SR3C-XZ, was performed for an eight blade, a four blade, and a single blade configuration. The results are presented in Fig. 25 (taken from the 1987a paper), which is a root locus plot of the complex eigenvalues, consisting of the real part, μ (proportional to damping), and the imaginary part, ν (proportional to frequency). Thus, in this phase plane plot the stable/unstable boundary is at $\mu = 0$, with flutter occurring for a positive real part. The single blade system has a single eigenvalue, located well within the stable region of the phase plane. The four blade system has four eigensolutions, represented by interblade phase angles 90 deg apart. This configuration is also fully stable. However, the eight blade system, with eight eigensolutions spaced $360^\circ/8 = 45$ deg

apart, surrounds the two other system solutions, and borders on the unstable region for $\sigma=180$ deg and 225 deg. In this instance it would appear that an increase in the number of blades has intensified the interblade coupling, possibly through the cascading effect, and has caused a deterioration of the system stability. (The prediction is shown to be in good agreement with theory in Fig. 15 of this paper.)

An extension to a mistuned case was the subject of the Kaza 1987b paper. Once again the SR3C-X2 rotor was analyzed, together with a rotor designated the SR3C-3. Both of these were tuned rotors, as in the 1987a paper. In addition, a deliberately mistuned rotor, the SR3C-X2/SR3C-3, was analyzed. It was modeled as an idealized alternately mistuned rotor having four identical blade pairs with two different blades in each pair, one from the SR3C-X2 rotor, and one from the SR3C-3 rotor. The analysis yielded the plots shown in Fig. 26, taken from the 198/b paper. In this case all three rotors have eight eigensolutions. The SR3C-X2 (circled points) was already discussed in the previous paragraph. It was an unstable rotor, with a measured flutter condition that coincided with the real part of the eigenvalues equal to zero. Conversely, the SR3C-3 (triangular points) was a stable rotor during the experiments, and yielded eigensolutions comfortably away from the stable/unstable boundary. The aerodynamic coupling of the mistuned rotor (square points) appears to be gone, and the eigensolutions are divided into two nested groups, with the high frequency group near the center of the SR3C-X2 eigensolutions, and the low frequency group in the vicinity of the SR3C-3 solutions.

The previous paragraphs serve to point out the complications associated with multiblade system coupling, and the need for accurate modeling of the interblade phase angle effects. They also introduce the reader to the concept of mistuning as it affects system stability, although the discussion is restricted to ideal paired mistuning. A detailed study of arbitrary or random mistuning is beyond the scope of the present chapter, and the reader is referred to the several papers by Kaza and Kielb (1982, 1984, 1985), Kielb and Kaza (1983, 1984), Bendiksen (1984), and to the chapter that follows.

CONCLUSION

It was shown in the original 1967 paper that the energy method, using unsteady isolated airfoil theory, and applied to actual multiblade rotors, yielded results that were remarkably accurate. This fortuitous agreement was sufficiently encouraging to foster a continuing development of the technique and its constituent aerodynamic and structural dynamic components. As shown in these two volumes and in the several citations to advanced analyses, current practice has gone well beyond the relatively simplistic view of this early paper. The aerodynamic input now encompasses multiblade systems subjected to compressible flows, and structures are modeled to include nonlinearities and mistuning. Nevertheless, the paper has served its purpose well. In its original form it set the stage for the continual improvement of engine flutter prediction methods, and in this Manual it provides the reader with a vehicle for coordinating the separate disciplines which, together, represent the modern approach to flutter prediction of turbomachine, blade rows.

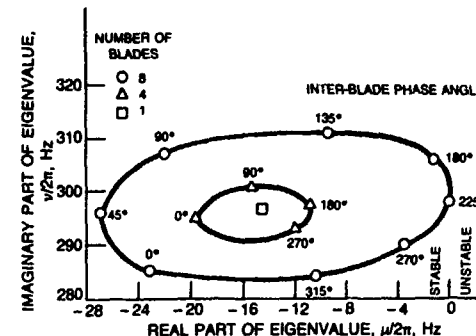


Figure 25 Root locus plot of the mode with least damping: $M = 0.59$, $\Omega = 6080$ rpm, SR3C-X2 rotor.

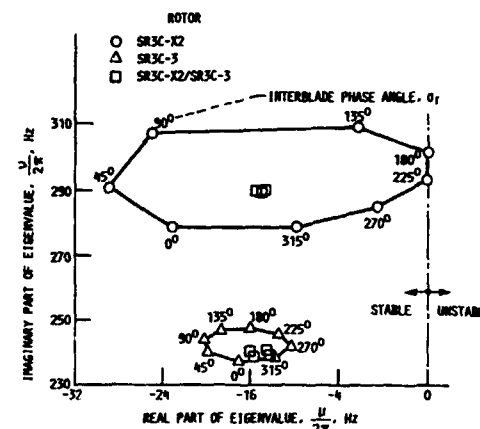


Figure 26 Calculated root locus plot of the lowest damped mode for the SR3C-X2, SR3C-3, and SR3C-X2/SR3C-3 rotors at 6320 rpm and 0.528 freestream mach number.

APPENDIX 1

Logarithmic Decrement for Simple Linear System

The simple spring-mass-dashpot system is governed by the linear differential equation

$$\ddot{x} + 2\omega y \dot{x} + \omega^2 x = 0 \quad (30)$$

where (see Scanlan and Rosenbaum 1951)

$$\begin{aligned} \omega &= \sqrt{k/m} = \text{undamped natural frequency} \\ \gamma &= c/c_{cr} = \text{damping ratio} \\ c_{cr} &= 2m\omega = \text{critical damping} \end{aligned} \quad \left. \right\} \quad (31)$$

The damping force always opposes the velocity and is given by

$$F_d = -c\dot{x} = -\gamma c_{cr}\dot{x} = -2\gamma m\omega \dot{x}$$

Hence the differential work done by the damper is

$$dW = F_d dx = -2\gamma m \omega_d \dot{x} dx = -2\gamma m \omega_d^2 dt$$

Therefore, the work done per cycle of motion is

$$W = -2\gamma m \omega_d \oint \dot{x}^2 dt \quad (32)$$

At any instant of time the kinetic energy due to the motion is

$$K_E = \frac{1}{2} m \dot{x}^2$$

and hence the average kinetic energy over one cycle of the motion is

$$\bar{K}_E = \frac{1}{T} \oint K_E dt = \frac{m}{2T} \oint \dot{x}^2 dt = \frac{m\omega_d}{4\pi} \oint \dot{x}^2 dt \quad (33)$$

where $T = 2\pi/\omega_d$ is the period of the damped motion. It can be shown (cf. Scanlan) that the damped frequency is given by $\omega_d = \omega\sqrt{1-\gamma^2}$.

If the ratio of the work per cycle to average kinetic energy for the same cycle is taken, then from equations (32) and (33),

$$\frac{W}{\bar{K}_E} = -\frac{8\pi\gamma}{\sqrt{1-\gamma^2}} \quad (34)$$

On page 58 of Church (1957), the logarithmic decrement of a damped motion is given by

$$\delta = \log(A_n/A_{n+1}) = \frac{\pi c}{m\omega_d} = \frac{2\pi\gamma}{\sqrt{1-\gamma^2}} \quad (35)$$

and A_n and A_{n+1} are the amplitudes of two consecutive waves. A comparison of equations (34) and (35) yields

$$\delta = -\frac{W}{4\bar{K}_E} \quad (36)$$

which is the required result.

APPENDIX 2

Unsteady, Incompressible, Potential Flow Theory for Isolated Airfoil

The appropriate unsteady aerodynamic coefficients for incompressible, inviscid, potential flow past a two-dimensional isolated flat plate airfoil have been previously mentioned in equation (3). On page 399 of Scanlan and Rosenbaum (1951), the coefficients L_h , L_a , M_h , and M_a are related to the Theodorsen (1935) circulation function $C(k) = F(k) + iG(k)$, by the equation

$$\left. \begin{aligned} L_h &= 1 - \frac{2i}{k} C(k) \\ L_a &= \frac{1}{2} - \frac{i}{k} [1 + 2C(k)] - \frac{2}{k^2} C(k) \\ M_h &= \frac{-i}{2} \\ M_a &= \frac{3}{8} - \frac{i}{k} \end{aligned} \right\} \quad (37)$$

In these equations the reduced frequency, k , is based on the freestream velocity component, U , parallel to the flat plate airfoil.

After $C(k)$ and equation (37) are substituted into equations (3), multiplied through by k^2 and separated into real and imaginary parts, the required coefficients in equation (18) are given by

$$\left. \begin{aligned} k^2 A_{hI} &= -2kF \\ k^2 A_{aR} - k^2 B_{hR} &= -2F + 2kG \\ k^2 B_{aI} &= -(\frac{1}{2} - a)k + 2(\frac{1}{2} + a)G + 2(\frac{1}{4} - a^2)kF \end{aligned} \right\} \quad (38)$$

AEROELASTIC FORMULATION FOR
TUNED AND MISTUNED ROTORS

by

EDWARD F. CRAWLEY
Gas Turbine Laboratory
Massachusetts Institute of Technology
Cambridge, Massachusetts

INTRODUCTION

In previous chapters, the analytic tools necessary to approach the problem of aeroelastic analysis have been presented. In the terminology of Bisplinghoff and Ashley (1962), three operators, Inertial, Structural, and Aerodynamic, are needed in the appropriate form. The current state of the art techniques for determining the aerodynamic operators, which are contributed by the unsteady aerodynamicist, have been presented in Chapters 2 through 7. The inertial and structural operators, which together form the structural dynamic model have been reviewed in chapters 12 through 14.

The task of the aeroelastic analysis is to combine the formulations of the structural dynamic and unsteady aerodynamic model in a consistent manner, to solve the resulting aeroelastic model for the desired results (e.g., stability, forced vibration), and to interpret those results for both qualitative trends, and quantitative detail. This task of formulation of the aeroelastic problem and interpretation of the results will be the subject of this chapter.

Specifically, the topics to be addressed are: the formulation of the aeroelastic problem, including a summary of the relations necessary to transform various diverse structural and aerodynamic models to a consistent notation; a brief review of the solution techniques applicable; the trends in aeroelastic stability for tuned rotors; and the effects of mistuning on stability.

In order to understand the motivation for a lengthy discussion of aeroelastic formulations, one must appreciate the challenges and dilemmas faced by the working aeroelastician. First, the starting point of the analysis can vary. Typical starting points can include experimentally or analytically determined mode shapes of the entire blade-disk assembly, mode shapes of individual blades, or the properties of a simple typical section. Secondly, the objective or end point of the analysis may vary. Most often in current practice, a simple assessment of the stability of the turbomachinery stage is desired. Increasingly, however, the full forced vibration response to aerodynamic disturbances is of interest. In principle, the ultimate objective is to develop a completely coupled, time accurate dynamic and aerodynamic model which can be used in such diverse analysis as stall and surge loading, and analysis of

mechanical disturbances such as FOD impact, blade loss, rubs, etc. The third challenge facing the working aeroelastician is that all the required analytic tools to progress in an orderly and rigorous manner from the starting point to the end point are not available within the state of the art. For example, a three-dimensional, heavily loaded, large shock motion unsteady aerodynamic operator for the analysis of transonic fan aeroelasticity simply does not exist as of this writing. Therefore existing tools, experimental data and empirical rules must be combined to yield an appropriate engineering solution to the aeroelastic problem.

To illustrate these three problems, varying start points, various goals, and unavailability of analysis tools, consider the very general flow chart for aeroelastic analysis shown in Figure 1. The figure is largely self-explanatory, especially in view of the discussion in earlier chapters, but presents a consistent strategy for combining and extending those topics. What is important to note are the start points, end points, and limitations that prevent full implementation of the charted procedure.

Essentially, three starting points are available, either a structural model of the blade alone, of the nonrotating blade-disk assembly or the rotating blade-disk assembly. In each case, assumed modes, calculated eigenmodes, or measured eigenmodes are possible forms of the starting data. After inclusion of thermal and shaft/rotor support effects, the first possible end point is reached, the rotating natural frequencies, which can be used in traditional Campbell diagram analysis of forced vibration. It is reasonable to say that all of the analytic tools necessary to reach this point on the flowchart are reasonably well developed, and the temporal dependence of the motion can be expressed either in the time or frequency domain. As soon as the next step in the chart is taken, the inclusion of the homogeneous unsteady aerodynamic forces, two limitations appear. First, as has been discussed in Chapters 2 through 7, aerodynamic operators do not exist for all flow regimes, and secondly, intrinsic to the development of these operators is the assumption of sinusoidal motion of the blade row. If the ultimate end point is only the flutter behavior, the assumption of sinusoidal behavior is not limiting, as well known techniques exist for assessing stability even under the assumption of the sinusoidal motion.

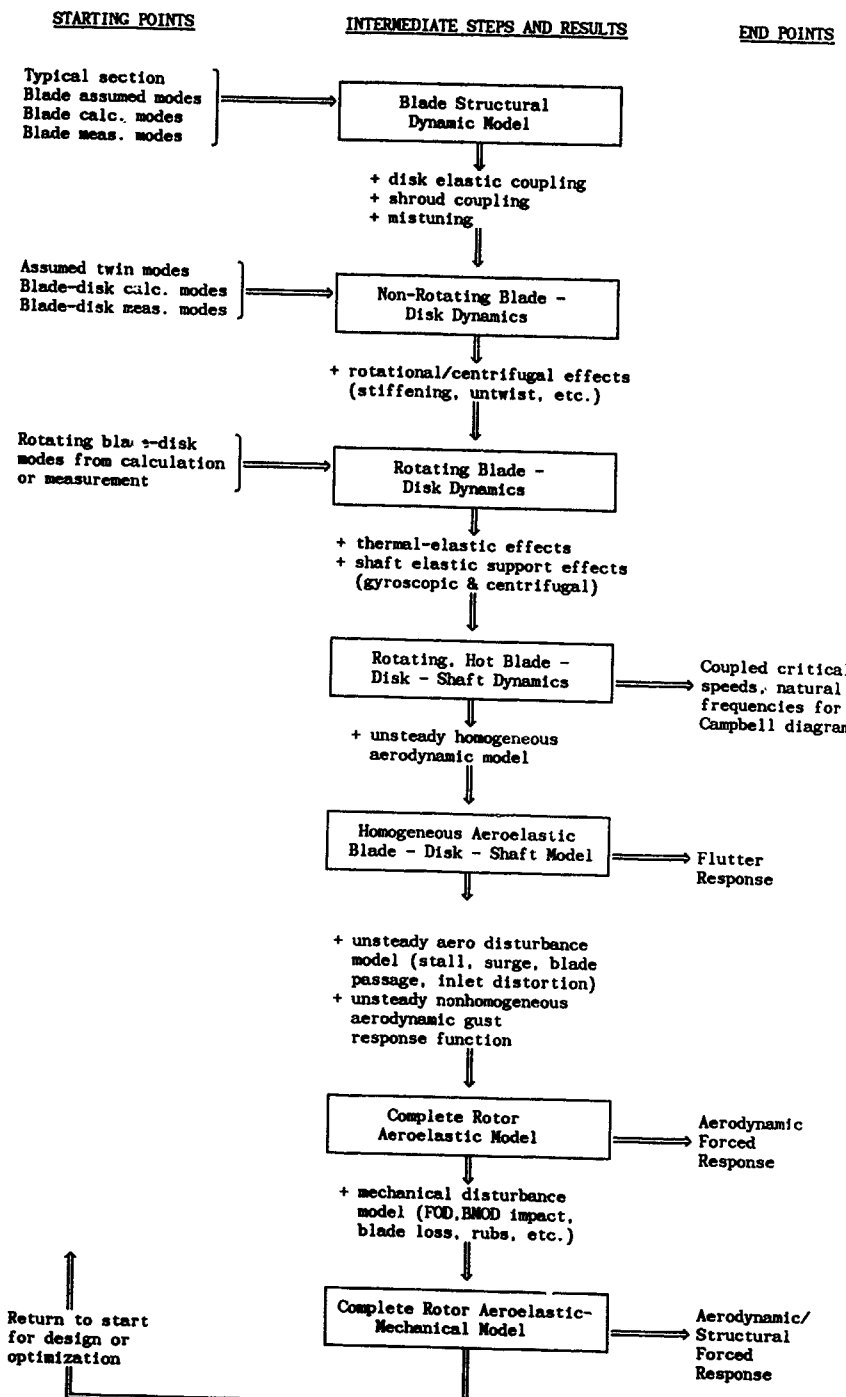


Figure 1. Flowchart for Aeroelastic Analysis

At the next step, however, the addition of the unsteady aerodynamic disturbances and unsteady aerodynamic "gust" response function, even fewer analytic tools are available, and the assumption of sinusoidal motion becomes limiting. Techniques will be presented below to transform the aerodynamic influences derived in the frequency domain, back to the time domain.

Of course, the complete model would include the capability to couple the structural dynamic, aeroelastic and mechanical disturbance models to produce a complete, time accurate model of the turbomachine aeromechanical response. However, due to lack of the proper analytic tools, this is probably not possible at the current time. Ultimately, iteration takes place over this entire procedure, either in the form of heuristic design or formal optimization.

Over the past decade, as the state of the art of aeroelastic analysis has progressed, a number of different formulations of the aeroelastic problems have evolved. These have included travelling wave formulation, individual blade formulations, and standing mode formulations, Kielb and Kaza (1983), Crawley and Hall (1985), Dugundji and Bundas (1984). These formulations have been applied to single and two degree of freedom typical section models, and to blade modal models, Srinivasan (1980), Bendiksen and Friedmann (1981), Srinivasan and Fabunmi (1984). In some models the effect of disk and shroud elastic coupling has also been included, Kielb and Kaza (1984). There has been some doubt as to whether these various formulations are equivalent, and as to which is most appropriate. One of the objectives of this chapter is to review and summarize these formulations in a consistent notation for single blade degree of freedom analysis, and to show that they are mathematically equivalent. This does not imply that in a given situation one may not be preferred over another due to its ease of application or insight contributed, but merely that simple similarity transforms are available to transform easily from one formulation to another. The direct extension of the one degree of freedom formulation to multiple section or blade modal degrees of freedom is also demonstrated.

In the next section the mathematical formulations and transformations which allow coupling of the various existing analytic tools along the lines of the flowchart of Fig. 1 will be presented.

FORMULATION AND SOLUTION OF THE AEROELASTIC PROBLEM

Basic Relationships

At the foundation of the aeroelastic analysis of turbomachines and propellers are three fundamental relationships: a structural dynamic model of the bladed disk; a kinematic relationship between various expressions for blade motion; and an unsteady aerodynamic model of aerodynamic forces. The most general possible model of the single degree of freedom aeroelastic response of a typical blade

section of the i th blade is given as

$$m_i \ddot{q}_i + m_i \omega_i^2 q_i = f_i^M + f_i^D \quad (1)$$

where m_i is the generalized mass, ω_i its natural frequency, q_i its displacement, f_i^M the motion dependent aerodynamic forces, and f_i^D the aerodynamic disturbance forces acting on the i th blade. When modelling a typical section, the generalized mass and force traditionally have units of mass per span and force per span. The assembly of N structurally uncoupled blades would then be governed by

$$\left[m_1 \right] \ddot{\left[q_1 \right]} + \left[m_1 \omega_1^2 \right] \left[q_1 \right] = \left\{ f_1^M \right\} + \left\{ f_1^D \right\} \quad (2)$$

where equation (2) represents N "independent" equations, which will be recoupled by the motion dependent aerodynamic forces f_i^M . In its most general form, the motion dependent force can be written as

$$\begin{aligned} f_i^M = & f_0(q_i, \dot{q}_i, \ddot{q}_i, y_i) + \\ & + f_{+1}(q_{i+1}, \dot{q}_{i+1}, \ddot{q}_{i+1}, y_{i+1}) + \\ & + f_{-1}(q_{i-1}, \dot{q}_{i-1}, \ddot{q}_{i-1}, y_{i-1}) + \\ & + \text{etc.} \end{aligned} \quad (3)$$

$$\begin{aligned} \text{with } y_i &= \int_0^t \dot{q}_i(\tau) h_0(t-\tau) d\tau \\ y_{i+1} &= \int_0^t \dot{q}_{i+1}(\tau) h_{+1}(t-\tau) d\tau \\ y_{i-1} &= \text{etc...} \end{aligned}$$

where, of course, f_0 , f_{+1} , f_{-1} depend on the Mach No., reduced frequency, and geometry of the blade and cascade. Equation (3) expresses in a very general way the dependence of the force acting on the i th blade due to its motion and the motion of its neighbors, and on the time history of those motions through lags due to shed vorticity and finite speed of sound. These lag effects are explicitly represented by the augmented state variables y_i .

Unfortunately, within the state of the art, the aerodynamic operators are not available in the very general form of eq. (3). In fact, they are derived for a very specific temporal and spatial motion pattern: sinusoidal in time and fixed interblade phase along the cascade in space. The kinematic relationship between these travelling wave coordinates and the displacement of the i th blade is

$$q_i = \sum_n \bar{q}_n e^{j(\omega t + i\beta_n)} \quad (4)$$

where \bar{q}_{β_n} is the amplitude of the travelling wave of interblade phase β_n . The sum in n can be taken as

$$n = 0, 1, 2, \dots, N-1$$

or, equivalently for N an odd number of blades,

$$n = -\frac{(N-1)}{2}, \dots, -1, 0, 1, \dots, \frac{(N-1)}{2} \quad (4a)$$

or, for N an even number of blades,

$$n = -\frac{N}{2} - 1, \dots, -1, 0, 1, \dots, \frac{N}{2}$$

since for a rotor of N blades there are N possible interblade phase angles, and small negative angles are equivalent to large positive ones

$$\beta_{-n} = \beta_{N-n} = \frac{2\pi(-n)}{N} \approx 2\pi - \frac{2\pi n}{N} \quad (4b)$$

It will be convenient to rewrite equation (4) as

$$\{q_i\} = [E]\{\bar{q}_{\beta_n}\} e^{j\omega t} \quad (5)$$

$$\text{where } [E] = \begin{bmatrix} E_{0,0} & \cdots & E_{0,N-1} \\ \vdots & \ddots & \vdots \\ E_{N-1,0} & \cdots & E_{N-1,N-1} \end{bmatrix} \quad E_{k,\ell} = e^{\frac{j2\pi k\ell}{N}} \quad (6)$$

The aerodynamic forces per span are usually derived assuming that the blades are undergoing the travelling wave motion of eq. (4), Whitehead (1966), Smith (1972), Adamczyk and Goldstein (1978). Under this assumption the forces per span acting on the zeroth blade undergoing the nth travelling wave, constant interblade phase angle motion of eq. (4) can be expressed as

$$f_o^n = \pi \rho b^2 \omega^2 \epsilon_{\beta_n} \bar{q}_{\beta_n} e^{j\omega t} \quad (7)$$

where \bar{q}_{β_n} is the amplitude of the nth travelling wave pattern, and the complex force coefficient due to β_n is ϵ_{β_n} .

The force on the ith blade due to the superposition of all the interblade phase angle waves is

$$f_i^n = \pi \rho b^2 \omega^2 \sum_{n=0}^{N-1} \epsilon_{\beta_n} \bar{q}_{\beta_n} e^{j(\omega t + i\beta_n)} \quad (8)$$

$$\text{or } \{f_i^n\} = \pi \rho b^2 \omega^2 [E] \left[\epsilon_{\beta_n} \right] \left\{ \bar{q}_{\beta_n} \right\} e^{j\omega t}$$

At this point the three fundamental equations of the aeroelastic problem are at hand and will be repeated for clarity. The first is the dynamic governing equation of motion, as would be derived by the structural dynamicist (eq. 2).

$$[\mathbf{m}_1] \left[\ddot{q}_i \right] + [\mathbf{m}_1 \omega_i^2 (1+jg_i)] \left[q_i \right] = \{f_i\} \quad (9)$$

where the structural damping factor g has been added. The second is the kinematic relationship between individual and traveling wave blade motion (eq. 5)

$$\{q_i\} = [E] \left[\bar{q}_{\beta_n} \right] e^{j\omega t} = \left\{ \bar{q}_i \right\} e^{j\omega t} \quad (10)$$

where the last relation simply assumes sinusoidal motion of the individual blades.

The third is the relationship between travelling wave motion and unsteady aerodynamic forces, supplied by the aerodynamicist (eq. 8)

$$\{f_i^n\} = \pi \rho b^2 \omega^2 [E] \left[\epsilon_{\beta_n} \right] \left\{ \bar{q}_{\beta_n} \right\} e^{j\omega t} \quad (11)$$

These three fundamental relationships can be combined to yield the governing aeroelastic equations in several ways. First, the equations can be expressed in terms of interblade phase angle "modes". This requires transformation of the structural dynamic equation (9) to interblade phase coordinates. Second, the equations can be expressed in terms of individual blade displacements. This requires transformation of the aerodynamic forces, eq. (11) to individual blade coordinates. And third, the equations can be expressed in terms of standing modes of the bladed disk, such as sine and cosine modes, or structural eigenmodes. This requires transformation of both the dynamic equations and aerodynamic forces. Each of those approaches has some value, as will be discussed.

Travelling Wave Formulation

The aeroelastic eigenvalue problem was first formulated in travelling wave coordinates, that is in those coordinates for which the aerodynamic forces are derived, Whitehead (1966). In order to derive the equations in traveling wave coordinates, equations (10) and (11) are substituted into equation (9), giving:

$$\begin{aligned} -\omega^2 [\mathbf{m}_1] [E] \left[\bar{q}_{\beta_n} \right] e^{j\omega t} + \\ + [\mathbf{m}_1 \omega_i^2 (1+jg_i)] [E] \left[\bar{q}_{\beta_n} \right] e^{j\omega t} \\ = \pi \rho b^2 \omega^2 [E] \left[\epsilon_{\beta_n} \right] \left\{ \bar{q}_{\beta_n} \right\} e^{j\omega t} \end{aligned} \quad (12)$$

premultipling by E^{-1} , and cancelling the time variation $\exp(j\omega t)$ gives

$$\begin{aligned} -\omega^2 [E]^{-1} [\mathbf{m}_1] [E] \left[\bar{q}_{\beta_n} \right] + \\ + [E]^{-1} [\mathbf{m}_1 \omega_i^2 (1+jg_i)] [E] \left[\bar{q}_{\beta_n} \right] \\ = \pi \rho b^2 \omega^2 \left[\epsilon_{\beta_n} \right] \left\{ \bar{q}_{\beta_n} \right\} \end{aligned} \quad (13)$$

Equation (13) now represents the formulation of the aeroelastic problem in terms of travelling wave coordinates. It has the advantage of using the aerodynamic force coefficients in exactly the form in which they are derived. Furthermore, if the blades have a single degree of freedom and if the blades are uniform in mass and stiffness such that

$$\begin{aligned} \left[m_1 \right] &= m[I] \\ \text{and } \left[m_1 \omega_1^2 (1+jg_1) \right] &= m\omega_0^2 (1+jg)[I] \end{aligned} \quad (14)$$

then equation (13) becomes

$$\begin{aligned} -m\omega^2 [I] \left\{ \bar{q}_{\beta_n} \right\} + m\omega_0^2 (1+jg) \left\{ \bar{q}_{\beta_n} \right\} &= \\ = \bar{\epsilon}_{\beta_n}^2 \left[\bar{\epsilon}_{\beta_n} \right] \left\{ \bar{q}_{\beta_n} \right\} & \end{aligned} \quad (15)$$

which is the governing homogeneous equation for single degree of freedom flutter for a perfectly tuned rotor. Note that the separate equations in equation (15) are completely uncoupled. This implies that for a tuned rotor, the travelling wave coordinates are the normal aeroelastic eigenmodes, and the eigenvalues associated with each mode are directly related to the unsteady aerodynamic coefficients for that interblade phase angle.

$$\begin{aligned} -m\omega^2 + m\omega_0^2 (1+jg) &= \bar{\epsilon}_{\beta_n}^2 \omega^2 \\ \text{or } \omega^2 &= \frac{\omega_0^2 (1+jg)}{(1+\bar{\epsilon}_{\beta_n}^2 \omega^2)} \end{aligned} \quad (16)$$

It is an advantageous coincidence that the kinematic assumption of constant interblade phase travelling wave coordinates made by the unsteady aerodynamicist eventually turn out to be the eigenmodes of the aeroelastic problem for a tuned rotor. The disadvantage of this formulation is that it requires transforming the structural model to travelling wave coordinates, in effect forcing the structural representation into a form chosen for its convenience in the unsteady aerodynamic problem. Although not inconvenient for tuned rotors, transformation of the governing equations to this form makes it very difficult to interpret the aeroelastic response of mistuned rotors with non-uniform blades, and difficult to explicitly include the effects of shroud and disk elastic coupling, Crawley and Hall (1985), Kielb and Kaza (1984). Although the representation of the aerodynamic forces in this form obscures the real physical dependence of forces on specific blade motions, Szechenyi et al (1984), much more insight into these aspects is gained by examining the equations formulated in terms of individual blade coordinates.

Individual Blade Formulation

In order to formulate the problem in terms of individual blade coordinates, the

aerodynamic forces must be transformed by substituting equation (10) into equation (11), yielding

$$(f_i^m) = \bar{\epsilon}_{\beta_n}^2 \omega^2 [L] \left\{ \bar{q}_i \right\} e^{j\omega t} \quad (17)$$

where $[L] = [E] \left[\bar{\epsilon}_{\beta_n} \right] [E]^{-1}$

The flutter equation is found by substituting into equation (9)

$$\begin{aligned} -\omega^2 \left[m_1 \right] \left\{ \bar{q}_i \right\} + \left[m_1 \omega_1^2 (1+jg_1) \right] \left\{ \bar{q}_i \right\} &= \\ = \bar{\epsilon}_{\beta_n}^2 \omega^2 [L] \left\{ \bar{q}_i \right\} & \end{aligned} \quad (18)$$

which is the aeroelastic equation in terms of individual blade coordinates. The principal advantage of this formulation is that it is expressed in a coordinate system which is a natural one for the structure. Thus, if any complicating features are added to the structure, such as disk elastic coupling, shroud elastic coupling, blade nonuniformity or mistuning, or multiple blade degrees of freedom. This is a simpler starting point for the resulting model than the travelling wave form.

Another advantage of this formulation is that although the aerodynamic coefficients must be transformed into the $[L]$ matrix form, the aerodynamic coefficients as they appear in the $[L]$ matrix give tremendous insight into the unsteady aerodynamic interactions in a cascade. Each term in the aerodynamic influence matrix $[L]$ has a unique physical significance (Fig. 2). The term in the first row and the second column, for example, designates the force acting on the first blade due to the motion of the second blade. By the symmetry of the rotor, assuming that the blades are geometrically identical, this must be the same as the force felt by the second blade due to the motion of the third. Likewise, each term on the diagonal represents the force felt by a blade due to its own motion. The $[L]$ matrix has the form in which there are only N independent complex terms, and the entries of each column are the same, with each column permuted one row relative to the adjacent columns.

$$[L] = \begin{bmatrix} L_0 & L_{N-1} & L_{N-2} & \cdots & L_1 \\ L_1 & L_0 & L_{N-1} & \cdots & L_2 \\ \vdots & \vdots & \vdots & & \vdots \\ L_{N-1} & L_{N-2} & L_{N-3} & \cdots & L_0 \end{bmatrix} \quad (19)$$

The most significant term in $[L]$ is the diagonal term L_0 , which expresses the force acting on any given blade due to its own motion, in effect the blade self-stiffness and self-damping. It has been shown that this is the only term in the influence coefficient matrix which can provide a net stabilizing influence on the rotor, Crawley and Hall (1985), Szechenyi et al (1984).

Mathematically, the individual blade aerodynamic forces L_k are related to the travelling wave forces through a complex Fourier transform relationship

$$L_k = \frac{1}{N} \sum_{n=0}^{N-1} e_{\beta_n} \exp\left(j \frac{2\pi k n}{N}\right) \quad (20)$$

and

$$e_{\beta_n} = \sum_{k=0}^{N-1} L_k \exp\left(-j \frac{2\pi k n}{N}\right) \quad (21)$$

Equation (20) shows that L_k is just the k th coefficient of the discrete Fourier series representation of β_n given in equation (21). So, for example, if a plot of the aerodynamic coefficients versus β is dominantly the first harmonic of β and an average offset, this implies that $[L]$ is almost tridiagonal, and the physical interpretation is that only the two adjacent blades to a given blade and the blade itself have any direct effect on the blade (Figure 2). If the plot of β_n vs. β has higher harmonics in β , then the influence of more distant blades is relatively more important.

Standing Mode Formulation

When the starting point of the aero-elastic formulation is a set of calculated or experimentally measured standing structural eigenmodes of the bladed disk assembly, it is desirable to formulate the aeroelastic problem in terms of these modal coordinates, Brooker and Halliwell (1984), Crawley (1983).

If the rotor is tuned, then there will be pairs of repeated structural eigenvalues. In this case, there is not a unique representation of the eigenvectors. Two natural ways to represent the mode shapes are by forward and backward traveling waves, or by sine and cosine standing waves, Dugundji and Bundas (1984). Expressing the motion of the rotor in terms of sine and cosine modes, also known as twin orthogonal modes or multiblade coordinates, gives the representation

$$\begin{aligned} q_i &= b_{co} + \frac{1}{N} b_n \cos(n\theta_i) + \frac{1}{N} a_n \sin(n\theta_i) \\ n &= 1, 2, \dots, \frac{N-1}{2} \text{ for } N \text{ odd}, \\ n &= 1, 2, \dots, \frac{N}{2} \text{ for } N \text{ even}, \\ \theta_i &\equiv \frac{2\pi i}{N} \end{aligned} \quad (22)$$

which still allows arbitrary time dependence of the motion. If the motion is assumed to be oscillatory, the displacement is

$$\bar{q}_i = \bar{q}_{co} + \frac{1}{N} \bar{q}_{cn} \cos(n\theta_i) + \frac{1}{N} \bar{q}_{sn} \sin(n\theta_i) \quad (23)$$

which can be written

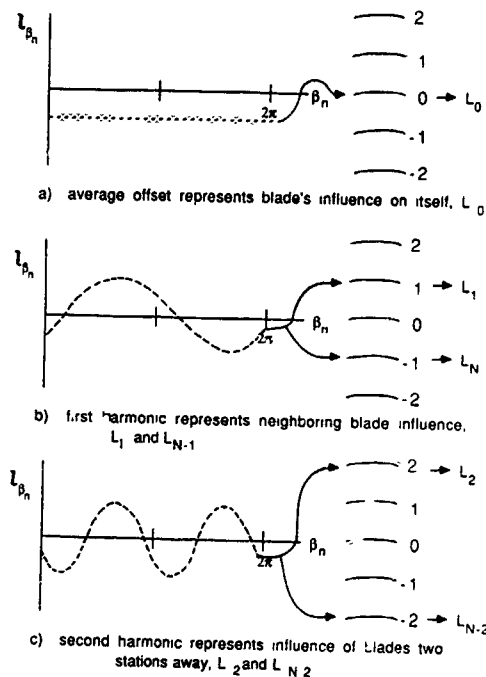


Figure 2. Graphical Relationship Between Aerodynamic Forces in Inter-blade Phase and Complex Influence Coefficient Form

$$\{\bar{q}_i\} = [P] \begin{bmatrix} \bar{q}_{co} \\ \bar{q}_{cn} \\ \bar{q}_{sn} \end{bmatrix} = [P] \begin{bmatrix} \bar{q}_{co} \\ \bar{q}_{c1} \\ \bar{q}_{s1} \\ \bar{q}_{c2} \\ \bar{q}_{s2} \\ \vdots \end{bmatrix} \quad (24)$$

$$[P] = \begin{bmatrix} C_{0,0} & C_{0,1} & S_{0,1} & C_{0,2} & S_{0,2} & \cdots \\ C_{1,0} & C_{1,1} & S_{1,1} & C_{1,2} & S_{1,2} & \cdots \\ C_{2,0} & \vdots & \vdots & \vdots & \vdots & \vdots \\ C_{3,0} & & & & & \vdots \\ \vdots & & & & & \\ C_{N-1,0} & \cdots & & \cdots & S_{N-1, \frac{N-1}{2}} & \end{bmatrix} \quad (25)$$

for N odd

$$C_{k,\ell} \equiv \cos \frac{2\pi k \ell}{N} \quad \text{and} \quad S_{k,\ell} \equiv \sin \frac{2\pi k \ell}{N}$$

Since equation (23) expresses the relationship between the individual and sine/cosine modal coordinates, the aero-elastic formulation can be transferred to these coordinates by simply substituting equation (24) into equation (18) and pre-multiplying by P^{-1} giving

$$\begin{aligned}
 & -\omega^2 [P]^{-1} \left[\begin{bmatrix} \ddot{q}_{cn} \\ q_{sn} \end{bmatrix} \right] \\
 & + [P]^{-1} \left[\begin{bmatrix} \omega_1^2(1+jg_1) \\ 0 \end{bmatrix} \right] [P] \left[\begin{bmatrix} \ddot{q}_{cn} \\ q_{sn} \end{bmatrix} \right] \\
 & = \bar{\rho} b^2 \omega^2 [P]^{-1} [L] [P] \left[\begin{bmatrix} \ddot{q}_{cn} \\ q_{sn} \end{bmatrix} \right]
 \end{aligned} \quad (26)$$

The process of deriving equation (15) from equation (8) is a similarity transform, in which eigenvalues are preserved.

The unique aspect of the pure sine and cosine standing modes is that a pair of like nodal diameter modes can be directly superimposed to form a traveling wave mode. By comparison of equation (10) and equation (24), it can be seen that

$$\left[\begin{bmatrix} \ddot{q}_{\beta_n} \\ q_{sn} \end{bmatrix} \right] = [E]^{-1} [P] \left[\begin{bmatrix} \ddot{q}_{cn} \\ q_{sn} \end{bmatrix} \right] \quad (27)$$

If the rotor is mistuned, or contains coupled bending torsion motion of the blades, it is no longer simple to relate the standing and travelling waves, but it is still straightforward to relate the standing blade-disk modes to the individual blade deflections. The i th blade deflection is given as

$$q_i = \sum_{n=0}^{N-1} \phi_i^{(n)} q_n \quad (28a)$$

which can be written

$$\{q_i\} = [\Phi]\{q_n\} \quad (28b)$$

where Φ is the matrix whose columns are the traditional structural modes, and q_n are the coordinates of those modes. Comparison of equation (24) and equation (29) show that for perfect sine and cosine twin orthogonal modes that P matrix is just a special case of the normal modal vector matrix Φ under the assumption of sinusoidal motion.

$$\left[\begin{bmatrix} \ddot{q}_i \\ q_n \end{bmatrix} \right] = [\Phi] \left[\begin{bmatrix} \ddot{q}_n \\ q_n \end{bmatrix} \right] \quad (29)$$

and substitution into equation (18) and premultiplication by Φ^T gives the aerelastic formulation in terms of arbitrary blade-disk modal coordinates

$$\begin{aligned}
 & -\omega^2 [\Phi]^T \left[\begin{bmatrix} \ddot{q}_i \\ q_n \end{bmatrix} \right] [\Phi] \left[\begin{bmatrix} \ddot{q}_n \\ q_n \end{bmatrix} \right] + [\Phi]^T \left[\begin{bmatrix} \omega_1^2(1+jg_1) \\ 0 \end{bmatrix} \right] [\Phi] \left[\begin{bmatrix} \ddot{q}_n \\ q_n \end{bmatrix} \right] \\
 & = \bar{\rho} b^2 \omega^2 [\Phi]^T [L] [\Phi] \left[\begin{bmatrix} \ddot{q}_n \\ q_n \end{bmatrix} \right]
 \end{aligned} \quad (30)$$

Note that the left hand side of equation (30) will now be uncoupled, since Φ are the structural normal modes, but these modes will be aerodynamically coupled by the terms on the right hand side.

The advantage of this formulation is that the starting point is the set of blade disk normal modes, which can incorporate all forms of blade, disk, and shroud elastic coupling. The disadvantage is that the aerodynamic forces in the form in which they appear in equation (30), and the resulting flutter eigenvectors may be difficult to interpret physically.

FORMULATION FOR MULTIPLE SECTION DEGREES OF FREEDOM

So far the various formulations for single blade degree of freedom flutter have been outlined. However, it is often desirable to include multiple degrees of freedom for each blade in the aeroelastic model, Bendiksen and Friedmann (1980), Kielb and Kaza (1984).

For such a model, such as a bending-torsion coupled typical section analysis, the equations presented above are still valid, but must be generalized appropriately. This generalization process essentially consists of letting each scalar quantity in the equations (9), (10), and (11) take on a sub-matrix nature. The three fundamental relations for one degree of freedom system are summarized here again. The dynamic equation of equilibrium is

$$\left[\begin{bmatrix} \ddot{q}_i \\ q_n \end{bmatrix} \right] + \left[\begin{bmatrix} \omega_1^2(1+jg_1) \\ 0 \end{bmatrix} \right] \left[\begin{bmatrix} \ddot{q}_i \\ q_n \end{bmatrix} \right] = \{f_i\} \quad (9)$$

the kinematic relationship between standing and travelling waves is

$$\left[\begin{bmatrix} \ddot{q}_i \\ q_n \end{bmatrix} \right] e^{j\omega t} = [E] \left[\begin{bmatrix} \ddot{q}_{\beta_n} \\ q_n \end{bmatrix} \right] e^{j\omega t} \quad (10)$$

The dependence of the aerodynamic force on motion is

$$\{f_i\} = \bar{\rho} b^2 \omega^2 [E] \left[\begin{bmatrix} \ddot{q}_{\beta_n} \\ q_n \end{bmatrix} \right] e^{j\omega t} \quad (11)$$

If each section is allowed a translational and pitching degree of freedom, then the generalized coordinate sub-matrix may be

$$q_i \rightarrow \tilde{q}_i \equiv \begin{bmatrix} h/b \\ \alpha \end{bmatrix}_i \quad (31)$$

where h is the translation of the section, and α is the pitch. The other terms in the equation (9), therefore, map as follows

$$\mathbf{z}_1 \rightarrow \mathbf{z}_1 = \begin{bmatrix} 1 & s/b \\ s/b & L/b^2 \end{bmatrix}_1 \quad (32)$$

$$\omega_1^2(1+jg_1) \rightarrow [\omega_1^2(1+jg)]_1 = \begin{bmatrix} \omega_B^2(1+jg_B) & 0 \\ 0 & \frac{I_{\alpha T}^2}{b^2}(1+jg_T) \end{bmatrix}_1 \quad (33)$$

$$\mathbf{f}_1 \rightarrow \mathbf{f}_1 = \begin{bmatrix} -L/b \\ M/b^2 \end{bmatrix}_1 \quad (34)$$

In this typical section analysis all of the generalized mass and force terms are defined on a per unit span basis.

The pitch motion is defined about the elastic axis, such that the stiffness, sub-matrix in equation (33) is diagonal, but the inertia matrix is populated. Note that the usual (unfortunate) aeroelastic convention for positive signs has been used (Figure 3). In modifying the kinematic relationship (equation (10)) the traveling wave coordinates also take on two coordinates for each interblade phase angle

$$q_{\beta_n} \rightarrow q_{\beta_n} = \begin{bmatrix} h_{\beta_n} \\ a_{\beta_n} \end{bmatrix} \quad (35)$$

The E matrix is now fully populated by sub-matrix blocks

$$E_{k,\ell} \rightarrow E_{k,\ell} = \begin{bmatrix} E_{k,\ell} & 0 \\ 0 & E_{k,\ell} \end{bmatrix} \quad (36)$$

so that the E matrix has the form

$$[E] = \begin{bmatrix} E_{0,0} & 0 & E_{0,1} & 0 & E_{0,2} & 0 & \dots \\ 0 & E_{0,0} & 0 & E_{0,1} & 0 & E_{0,2} & \dots \\ E_{1,0} & 0 & \dots & & & & \\ 0 & E_{1,0} & \dots & & & & \\ \vdots & \vdots & & & & & \end{bmatrix} \quad (37)$$

Finally, the aerodynamic forces and moments now depend on translation and pitch, so that

$$\begin{aligned} f_1 &\equiv \begin{bmatrix} -L/b \\ M/b^2 \end{bmatrix}_1 \\ &= \begin{bmatrix} \sum_{n=0}^{N-1} [e_n^{hh} h_{\beta_n} + e_n^{ha} a_{\beta_n} + e_n^{hw} w_{\beta_n}] U \\ \sum_{n=0}^{N-1} [e_n^{ah} h_{\beta_n} + e_n^{aw} a_{\beta_n} + e_n^{ww} w_{\beta_n}] U \end{bmatrix} e^{j(\omega t + i\beta_n)} \end{aligned} \quad (38)$$

where equation (38) includes the effects of impinging wakes of velocity w_{β_n} and of periodicity β_n being convected into the cascade. Equation (38) can be written

$$\begin{bmatrix} -L/b \\ M/b^2 \end{bmatrix}_0 = E p b^2 \omega^2 [E] \begin{bmatrix} e_{\beta_n} \\ e_{w_n} \end{bmatrix} \begin{bmatrix} q_{\beta_n} \\ q_w \end{bmatrix} e^{j\omega t} \quad (39)$$

$$\begin{bmatrix} -L/b \\ M/b^2 \end{bmatrix}_{N-1} + E p b^2 \omega^2 [E] \begin{bmatrix} e_{\beta_n} \\ e_{w_n} \end{bmatrix} \begin{bmatrix} q_{\beta_n} \\ q_w \end{bmatrix} e^{j\omega t}$$

provided E has the definition of equation (37), q_{β_n} has the definition of equation (35), and i is defined as

$$e_{\beta_n} \equiv \begin{bmatrix} e_n^{hh} & e_n^{ha} \\ e_n^{ah} & e_n^{aw} \end{bmatrix} \quad \text{and} \quad e_{w_n} \equiv \begin{bmatrix} e_n^{hw} \\ e_n^{ww} \end{bmatrix} \quad (40)$$

With these relationships, the bending torsion aeroelastic problem has the same notation as the single degree of freedom problem and all the the transformations developed above can be employed. The aeroelastic problem can be formulated in terms of travelling modes, individual blade deflections and standing modes of bending-torsion deflection.

FORMULATION FOR MULTIPLE SPANWISE BLADE MODES

In order to gain a more accurate model of the aeroelastic behavior of a turbo-machine component, it is necessary to integrate the unsteady aerodynamic forces over the entire span. Whether two-dimensional strip theory operators (Chapter 3) or a full three-dimensional model is used (Chapters 4 and 5) will depend on the availability and refinement of such operators. The inclusion of spanwise integration of aerodynamic forces in the aeroelastic formulation is a straightforward extension of the results of the last section. The governing dynamic equation for the $i = 1, 2, \dots, N-1$ blades is now

$$\begin{aligned} [M]_i \{ \ddot{q}_m \}_i + [K(1+jg)]_i \{ q_m \}_i \\ = \{ F_m \}_i \end{aligned} \quad (41)$$

with $m=1, 2, \dots, N$ for every $i=0, 1, \dots, N-1$

where the generalized displacements and generalized forces of the i^{th} blade are now represented at $N/2$ spanwise stations

$$\begin{aligned} \{\ddot{q}_m\}_i &= \begin{bmatrix} h_1/b \\ a_1 \\ h_2/b \\ a_2 \\ \vdots \\ a_{N/2} \end{bmatrix}_i & \{F_m\}_i &= \begin{bmatrix} -L_1 Ar_1/b \\ M_1 Ar_1/b^2 \\ -L_2 Ar_2/b \\ M_2 Ar_2/b^2 \\ \vdots \\ M_{N/2} Ar_{N/2}/b^2 \end{bmatrix}_i \end{aligned} \quad (42)$$

Note that the mass matrix of equation (41) now has units of mass, rather than mass per span, and the other matrices have been redimensioned accordingly. The formulation of equation (41) still assumes that shroudless blades are rigidly fixed to a stiff disk, such that no structural coupling exists between blades.

Rather than solve the coupled structural-aerodynamic problem, the usual procedure is to solve equation (41) for the structural normal modes of the i^{th} blade, (i.e., with f_i set to zero), by solving

$$\begin{bmatrix} M \end{bmatrix}_i \{\ddot{q}_m\}_i + [K(1+jg)]_i \{q_m\}_i = 0 \quad (43)$$

The result of the structural eigenvalue problem for the i^{th} blade is a set of M natural frequencies and mode shapes.

$$\omega_p^{(p)} \varphi_i^{(p)} = \begin{bmatrix} h_1/b \\ a_1 \\ h_2/b \\ a_2 \\ \vdots \\ a_{N/2} \end{bmatrix}_i \quad p = 1, 2, \dots, M \quad (44)$$

and an associated set of blade modal coordinates η_p .

In the aeroelastic problem, only a few of the blade modes are generally of interest. Let the number of modes of interest be P , so that the displacement of the i^{th} blade is expressed in terms of P modes

$$\{q_m\}_i = \begin{bmatrix} \varphi^{(1)} & \varphi^{(2)} & \dots & \varphi^{(P)} \end{bmatrix}_i \begin{bmatrix} \eta_1 \\ \eta_2 \\ \vdots \\ \eta_P \end{bmatrix}_i \quad (45)$$

and upon substitution into equation (41)

$$\begin{bmatrix} [M_p]_i \end{bmatrix} \{\ddot{\eta}_p\}_i + \begin{bmatrix} M_p^2(1+jg_p) \end{bmatrix}_i \{\eta_p\}_i = \{F_p\}_i \quad (46)$$

with $p=1, 2, \dots, P$ for every $i=0, 1, \dots, N-1$

where the modal mass, modal stiffness, and modal force associated with these P modes are

$$[M_p]_i \equiv [\varphi^p]_i^T [M]_i [\varphi^p]_i \quad (47)$$

$$[M_p^2(1+jg_p)]_i \equiv [\varphi^p]_i^T [K(1+jg)]_i [\varphi^p]_i \quad (48)$$

$$\{F_p\}_i \equiv [\varphi^p]_i^T \{F_m\}_i \quad (49)$$

With these definitions the left hand side of equation (46) is completely uncoupled and the mapping of the multiple spanwise blade mode problem to the simple single degree of freedom problem of equation (9), (10), and (11) is possible.

For the displacements, the generalized displacements map to the blade modal coordinates

$$q_i \rightarrow \{\eta_p\}_i = \begin{bmatrix} \eta_1 \\ \eta_2 \\ \vdots \\ \eta_P \end{bmatrix}_i \quad (50)$$

for the inertia term the inertia maps to the modal inertia

$$m_i \rightarrow [M_p]_i = \begin{bmatrix} M_1 \\ M_2 \\ \vdots \\ M_P \end{bmatrix}_i \quad (51)$$

and the stiffness terms map to the modal stiffness

$$\begin{aligned} M_1 \omega_1^2 (1+jg_1) &\rightarrow [M_p^2(1+jg_p)]_i = \\ &= \begin{bmatrix} M_1 \omega_1^2 (1+jg_1) \\ \vdots \\ M_P \omega_P^2 (1+jg_P) \end{bmatrix}_i \end{aligned} \quad (52)$$

and, finally, the blade force f_i maps to the blade modal forces

$$f_i \rightarrow \{F_p\}_i = \begin{bmatrix} F_1 \\ F_2 \\ \vdots \\ F_p \end{bmatrix} \quad (53)$$

The proper transformation of the blade aerodynamic forces acting on the blade modes is somewhat complex. Careful attention must be paid to keeping track of effects at the same spanwise location around the rotor versus effects along the blade.

When written in the notation of equation (53), the forces acting on the blade modes of the N blades in terms of the motion of the modes of the individual blades is given by equation (54). Note that the form assumes that aerodynamic strip theory has been used. The transformation matrix T is used to change the order of notation for blade degrees of freedom from that used for the structural problem (inner loop on the blade DoF) to that used in the aerodynamic problem (inner loop on the cascade-wise coordinate).

$$\begin{aligned} \begin{bmatrix} (F_p)_{i=0} \\ (F_p)_{i=1} \\ \vdots \\ (F_p)_{i=N-1} \end{bmatrix} &= \frac{\rho b^2 \omega^2}{2} \begin{bmatrix} [\psi^p]_{i=0} \\ [\psi^p]_{i=1} \\ \vdots \\ [\psi^p]_{i=N-1} \end{bmatrix} \begin{bmatrix} T^T & \Delta r_{m=1}[I] & [E] & [E] & \cdots & [E] \\ & \Delta r_{m=2}[I] & & & & \\ & & \ddots & & & \\ & & & \Delta r_{m=M}[I] & & \end{bmatrix} \begin{bmatrix} [\psi^p]_{i=0} \\ [\psi^p]_{i=1} \\ \vdots \\ [\psi^p]_{i=N-1} \end{bmatrix} \\ &\left[\begin{bmatrix} e_{\beta_n} \\ e_{\beta_n} \\ \vdots \\ e_{\beta_n} \end{bmatrix}_{m=1} \begin{bmatrix} e_{\beta_n} \\ e_{\beta_n} \\ \vdots \\ e_{\beta_n} \end{bmatrix}_{m=2} \cdots \begin{bmatrix} e_{\beta_n} \\ e_{\beta_n} \\ \vdots \\ e_{\beta_n} \end{bmatrix}_{m=M} \right] \begin{bmatrix} [E]^{-1} & & & & & \\ & [E]^{-1} & & & & \\ & & \ddots & & & \\ & & & [E]^{-1} & & \end{bmatrix} \begin{bmatrix} [\psi^p]_{i=1} \\ [\psi^p]_{i=2} \\ \vdots \\ [\psi^p]_{i=N} \end{bmatrix} \begin{bmatrix} (\eta_p)_{i=0} \\ (\eta_p)_{i=1} \\ \vdots \\ (\eta_p)_{i=N-1} \end{bmatrix} e^{j\omega t} \quad (54) \end{aligned}$$

where the transformation
[T] is defined by :

$$\begin{bmatrix} (q_1)_{m=1} \\ (q_1)_{m=2} \\ \vdots \\ (q_1)_{m=M} \end{bmatrix} = [T] \begin{bmatrix} (q_m)_{i=0} \\ (q_m)_{i=1} \\ \vdots \\ (q_m)_{i=N} \end{bmatrix}$$

inner loop over i blades inner loop over
a blade stations of the ith blade

If the aerodynamic forces were derived from a three-dimensional aerodynamic model which assumed a travelling wave pattern of an assumed blade mode shape, then the aerodynamic forces are

$$\{F_p\}_i = \frac{\rho b^2 \omega^2 \Delta r}{2} \begin{bmatrix} [E] \end{bmatrix} \begin{bmatrix} s_{3-D} \end{bmatrix} \begin{bmatrix} [E] \end{bmatrix}^{-1} \{F_p\}_i e^{j\omega t} \quad (55)$$

where the s_{3-D} matrix is the representation of travelling wave three-dimensional unsteady aerodynamic forces due to travelling wave motion (Chapters 4 and 5).

It may be desirable to express the aeroelastic equations of motion of a complete rotor in terms of both spanwise blade modes and coupled blade-disk circumferential modes. In this case the formulation for blade modes of this section can be coupled with the formulation for standing blade-disk modes given above to yield the governing equations of motion.

To this point all the necessary transformations and formulations have been rigorously developed to express the spatial (i.e., spanwise and circumferential) dependencies of the aeroelastic formulation. However, the entire formulation to this point, except for the basic equations (3), (4), and (9) have assumed temporally sinusoidal motion. This is due to the assumptions inherent in the derivation of the aerodynamic operators. In the next section, solution techniques for the sinusoidal formulation will be presented, and in the following section, an approximate transformation to an explicit time accurate formulation will be discussed.

SOLUTIONS FOR SINUSOIDAL TEMPORAL REPRESENTATIONS

Under the assumption that the aerodynamic operators are only available for sinusoidal motion, the steps remaining after formulation of the aeroelastic problems are its proper nondimensionalization and solution for stability and forced response. For reference, the dynamic equation of equilibrium, assuming sinusoidal motion is

$$-\omega^2 \left[\bar{q}_1 \right] (\bar{q}_1) e^{j\omega t} + \left[\bar{q}_1 \omega_1^2 (1+jg_1) \right] (\bar{q}_1) e^{j\omega t} = \{ f_1 \} \quad (56)$$

Generalized forces on the i th blade due to the n th travelling displacement wave pattern and the wake forced vibration terms are

$$f_1 = \frac{\pi \rho b^2 \omega^2 [E]}{M/b^2} \left[\left[\bar{q}_{\beta_n} \right] \left(\bar{q}_{\beta_n} \right) + \left[\bar{q}_{w_n} \right] \left(\frac{\bar{v}_{\beta_n}}{U} \right) \right] e^{j(\omega t + \beta_n i)} \quad (57)$$

This will be referred to as the ℓ formulation of aerodynamic forces. Note that the forces are nondimensionalized in time by the square of the frequency of oscillation, and therefore have the form of virtual inertias. A second common form of the aerodynamic operators is (Chapter III)

$$\left[\begin{array}{c} \bar{F} \\ \bar{M}/c \end{array} \right] = \frac{\pi \rho U c}{b} \left[\begin{array}{cc} C_{F_q} & UC_{F_\alpha} \\ C_{M_q} & UC_{M_\alpha} \end{array} \right] \left[\begin{array}{c} \bar{q}_{\beta_n} \\ \bar{q}_{\beta_n} \end{array} \right] - \left[\begin{array}{cc} C_{F_W} & UC_{F_\alpha} \\ C_{M_W} & UC_{M_\alpha} \end{array} \right] \left[\begin{array}{c} \bar{v}_{\beta_n} \\ \bar{v}_{\beta_n} \end{array} \right] e^{j(\omega t + \beta_n i)} \quad (58)$$

in which q (unfortunately) stands for the translational velocity, and α for the pitch angle (Fig. 3). If the assumption of sinusoidal motion is made, and the coordinates are assumed to be the translational and pitch displacements, and wake velocity amplitude, then equation (58) can be manipulated to have the form of equation (57).

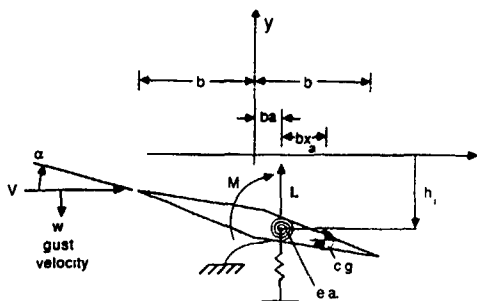


Figure 3a. Notation Convention for 2-dof Model in the ℓ Force Notation

$$f_1 = \frac{[-L/b]}{[M/b^2]} \quad (59)$$

$$= \frac{\pi \rho U^2}{b} \left[\left[\begin{array}{cc} 2jkC_{F_q} & 2C_{F_\alpha} \\ 4jkC_{M_q} & 4C_{M_\alpha} \end{array} \right] \left[\begin{array}{c} \bar{h}_{\beta_n} \\ \bar{a}_{\beta_n} \end{array} \right] - \left[\begin{array}{cc} 2C_{F_W} & \bar{v}_{\beta_n} \\ 4C_{M_W} & \bar{v}_{\beta_n} \end{array} \right] \left[\begin{array}{c} \bar{v}_{\beta_n} \\ \bar{v}_{\beta_n} \end{array} \right] \right] e^{j(\omega t + \beta_n i)}$$

This will be referred to as the c_ℓ formulation for the aerodynamic forces.

If the homogeneous aerodynamic force due to translation and moment due to pitch are examined in the C_ℓ form, they are

$$f_1 = \frac{-L}{b} = \frac{\pi \rho U^2}{b} \left[2jkC_{F_q} \right] \left(\bar{h}_{\beta_n} / b \right) \quad (60)$$

$$f_1 = \frac{M}{b^2} = \frac{\pi \rho U^2}{b} (4C_{M_\alpha}) \bar{a}_{\beta_n} \quad (61)$$

In contrast to the ℓ formulation, the aerodynamic forces in the c_ℓ formulation are nondimensionalized in time by the square of free stream velocity in the case of the moment (eq. 61), and by the velocity and frequency, in the case of the force, (eq. 60). Therefore these terms appear in the equations of motion as virtual stiffness and damping like terms, respectively. Note that in the ℓ form there is an explicit frequency dependence but no explicit dynamic pressure dependence, whereas in the c_ℓ form, there is explicit dynamic pressure dependence, and the explicit frequency dependence is different from that in the former. Thus in comparing reduced frequency dependence of the nondimensional aerodynamic forces, one must keep in mind that the form of the nondimensionalization impacts the apparent trend as the reduced frequency is varied. Of course, as always, one must pay close attention to the sign convention for positive moment and displacement, and for the chord location which is used for the coordinate system reference. A summary of these conventions for the ℓ and c_ℓ forms is given in Appendix B. The nondimensionalization and solution techniques will be developed for the simple single degree of freedom equations (9), (10), and (11), since it was shown above that the problems with multiple blade degrees of freedom were simply extensions of the one DOF per blade formulations.

Continuing with only the ℓ form, combinations of eq. (9), (10), and (11) give the aeroelastic problem formulated in individual blade coordinates as

$$\begin{aligned} -\omega^2 \left[\bar{q}_1 \right] \left(\bar{q}_1 \right) + \left[\bar{q}_1 \omega_1^2 (1+jg_1) \right] \left(\bar{q}_1 \right) &= \\ = \pi \rho b^2 [E] \left[e_{\beta_n} \right] [E]^{-1} \left(\bar{q}_1 \right) &= \\ = \pi \rho b^2 [L] \left(\bar{q}_1 \right) \end{aligned} \quad (62)$$

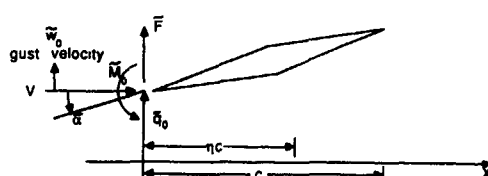


Figure 3b: Notation Convention for the 2-dof Model in the C_ℓ Force Notation [Chapter 3]

Division by the blade mass of a section of the nominal blade gives us the nondimensional form of the problem

$$\eta^2 \left[\left[1 + \epsilon_i \right] + \frac{1}{\mu} [L] \right] \{ \bar{q}_i \} = \left[(1 + jg_i)(1 + \delta_i) \right] \{ \bar{q}_i \} \quad (63)$$

where ϵ_i and δ_i are the fractional mass and stiffness mistuning of the i th blade, η is the nondimensional eigenfrequency, $\eta = \omega/\omega_R$, and μ is the section mass density ratio

$$\mu = \frac{\rho}{\rho_{pb}} \quad (64)$$

which premultiplies all of the aerodynamic terms in the governing equations. Note that in the form of equation (64) the mistuning or nonuniformity effects appear explicitly in the formulation.

Equation (63) is of the form of a traditional aeroelastic eigenvalue problem used to determine the stability of the system. The task is to solve for the complex eigenvalues of equation (63). The eigenvalues in general will have a negative real part or a positive real part, indicating mode stability or instability, respectively. The contradiction present in the formulation is, of course, that the system eigenvalues are either exponentially damped or unstable, but in general not purely sinusoidal, while the aerodynamic forces were derived assuming pure sinusoidal motion. Furthermore, these aerodynamic terms depend implicitly on the reduced frequency, but the actual frequency of oscillation is not known until after the eigenvalues are determined.

The traditional solution to this problem is the so-called V-g method, in which the structural damping is assumed uniform, and treated as a free parameter, Bisplinghoff and Ashley (1966). Rewriting equation (63) under these assumptions

$$\left[\left[1 + \epsilon_i \right] + \frac{1}{\mu} [L] \right] \{ \bar{q}_i \} = z \left[\left[1 + \delta_i \right] \{ \bar{q}_i \} \right] \quad (65)$$

where $z = \frac{1+jg}{\eta^2}$

For a fixed reduced frequency η_R , the eigenvalue problem is then solved for the complex eigenvalues, and for each the frequency of oscillation and damping factor are calculated

$$\Omega = (\Omega z)^{-1/2} \quad (66)$$

$$g = \Im(z)/\Re(z)$$

where g is interpreted as the degree of structural damping necessary to provide neutral (oscillatory) dynamic behavior. The corresponding velocity is then

$$U = \Omega U_R \quad (67)$$

For a N degree of freedom system this will produce N points on the V-g diagram, as shown in Figure 4. By choosing various values of k , families of curves of required damping can be plotted. The stability boundary is then defined as the velocity at which the required damping exceeds the structural damping actually present in the rotor.

Unlike in aeroelastic analysis of aircraft, a key simplification of this process can usually be made for gas turbines. Since the mass ratio is usually large ($\mu > 10$), the aerodynamic forces are very small compared to the inertial and elastic forces acting on the blade, that is $\Omega/\mu \ll 1$. Therefore the oscillatory component of the aeroelastic eigenvalue is usually very close to the reference frequency, implying that the reduced frequency for all of the eigenvalues is very close to the reduced frequency associated with the natural frequency.

This relative weakness of the aerodynamic terms leads to treating equation (63) as a standard eigenvalue problem. That is, a reference value of the reduced frequency is calculated based on the structural frequencies at speed but in vacuum. The aeroelastic eigenvalues are all then calculated and used as is, since little difference between aeroelastic and in vacuum frequency is present.

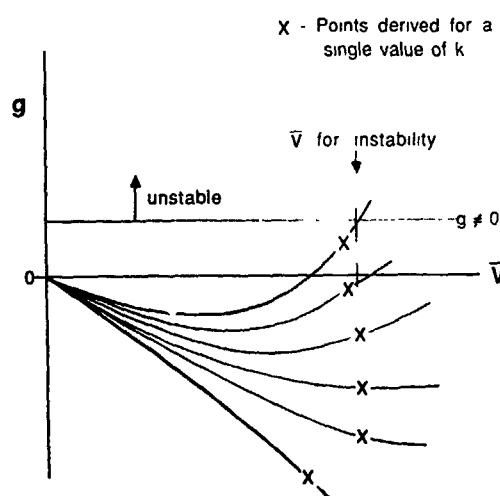


Figure 4: V-g Representation of System Stability

If more accuracy is desired, then two approaches are available. In an iterative approach, after the first calculation, the reduced frequency is modified based upon the calculated oscillatory component of the most critical aeroelastic eigenvalue. This iteration is then continued until the reduced frequency assumed in determining the aerodynamic coefficients, and the calculated reduced frequency of the most critical eigenvalues converge. This procedure resembles the traditional p-k method of aeroelastic analysis.

A second procedure which eliminates the need for this iteration is based on expanding the explicit functional dependence of L on k. If the aeroelastic coefficients are locally fit by a least squares procedure to an expression of the form

$$L(\Omega) = L_0 + L_1 \frac{1}{\Omega} + L_2 \frac{1}{\Omega^2} \quad (68)$$

$$\Omega = \omega/\omega_R = k/k_R$$

Substitution into equation (63) gives a new eigenvalue problem

$$\left[\Omega^2 \left[1 + \epsilon_1 \right] + \frac{1}{\mu} [L]_0 \right] + \frac{\Omega}{\mu} [L]_1 + \frac{1}{\mu} [L]_2 \{ \bar{q}_1 \} = \\ = \left[(1+jg_1)(1+\delta_1) \right] \{ \bar{q}_1 \} \quad (69)$$

which can be rewritten as a standard eigenvalue problem and solved directly for the aeroelastic eigenvalues.

The results of these formulations are aeroelastic eigenvalues which can be plotted in the complex plane. If the traditional complex s-plane interpretation is desired, then the plot must be of

$$s = j\Omega \quad (70)$$

as shown in Figure 5a for a single value of reduced frequency k. If a range of k is plotted, the root locus of the individual eigenvalues plot out as curves originating at $(0 + j\Omega)$ in the case of no structural damping. Instability is then defined to occur as the first root crosses into the right half planes (Fig. 5b).

There remains in all this analysis the contradiction that the system behavior is non-oscillatory, while the aero forces were derived for oscillatory behavior. Where accuracy is most needed, at the point of neutral stability, the behavior is truly oscillatory, so the aerodynamic forces are exact. Common sense would dictate that for lightly damped and marginally unstable systems, the stability margin would approximate the true damping ratio of the system. This, in fact, has been shown to be the case, but a proof requires the expression of the aerodynamic forces in time explicit form, Dugundji and Bundas (1984). An approximate scheme for this time accurate representation will be shown in the next section.

EXPLICIT TIME DEPENDENT FORMULATION OF AERODYNAMIC FORCES

While sinusoidal representation of motion is adequate for stability analysis, it is sometimes desirable to express the aeroelastic equations of motion with explicit time dependence of the unsteady aerodynamic terms. Examples of when this might be needed are when the excitation or response is expected to differ from a sinusoidal behavior. Such non-sinusoidal behavior occurs in certain forced vibration phenomena, such as impacting or mechanical rubs, and time unsteady aero disturbances, such as rotating stall and surge. Furthermore, whenever time marching calculations are to be done, it will be necessary to have the aerodynamic forces in a time domain representation.

Unfortunately, the unsteady aerodynamic operators have been derived assuming sinusoidal behavior in time and travelling wave constant interblade phase angle in space. In the special transformations above, a complex inverse discrete Fourier transform (eq. 17) was used to remove the restriction of assumed travelling waves, and to express the aerodynamic forces in terms of the individual blade motions. The resulting form was

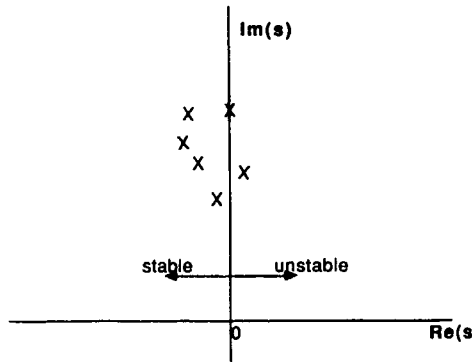


Figure 5a Complex s-Plane Interpretation of Aeroelastic Eigenvalues for a Single k

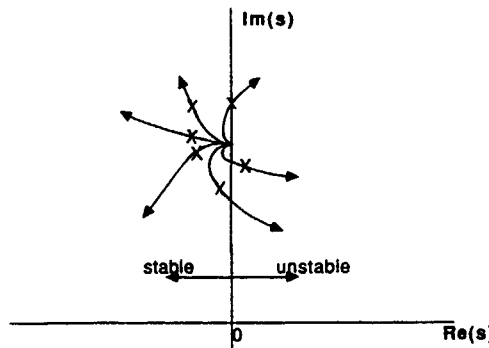


Figure 5b: Complex s-Plane Interpretation of Eigenvalue Root Loci for Increasing k

$$\{f_i\} = \frac{\pi \rho b^2}{U^2} \omega^2 [L] \left\{ \bar{q}_i \right\} e^{j\omega t} \quad (71)$$

where each column of L was identical, and shifted down one row relative to its neighbor. Thus all the diagonal terms are L_{00} , the blade's aerodynamic force on itself, the first diagonal below the principal is L_{10} , the effect of the adjacent blade downstream, etc. (eq. 19). The elements of the matrix L are of course complex and functions of the reduced frequency k . The restriction of sinusoidal temporal behavior was therefore still present.

In principle, a complex inverse Fourier integral in the reduced frequency parameter k , allowing k to range from zero to infinity, could be taken of the elements of L in order to explicitly transform them to the time domain. In practice, the frequency dependence of the L terms is either expressed as a very complicated expression of k , or, if L is found through computational techniques, never written as an analytic function of k . Thus approximate transform techniques from the frequency to time domain must be used.

The most popular approximate transform technique for unsteady aerodynamic forces involves the so-called Pade approximation of exponential lags in the aerodynamic forces, Edwards et al. (1979). In order to prepare the aerodynamic coefficients for this approximation procedure, it is necessary to convert the coefficients to a form in which the frequency does not appear explicitly in the nondimensionalization

$$\{f_i\} = \frac{\pi \rho U^2}{U^2} \left[\frac{b^2}{U^2} [L] \right] \left\{ \bar{q}_i \right\} e^{j\omega t} = \frac{\pi \rho U^2}{U^2} [C]_L \left\{ \bar{q}_i \right\} e^{j\omega t} \quad (72)$$

$$\text{where } [C]_L = k^2 [L]$$

The C_L form of the coefficients is similar, but not identical to the c_L form. Now a general approximation to the time dependent form of the aerodynamic forces is introduced

$$\begin{aligned} \{f_i\} &= \frac{\pi \rho U^2}{U^2} \left[\frac{b^2}{U^2} [C]_2 (\ddot{q}_i) + \frac{b}{U} [C]_1 (\dot{q}_i) + [C]_0 (q_i) \right. \\ &\quad \left. + \sum_{j=0}^N \left\{ y_i^{(j)} \right\} + \sum_{j=1}^N \left\{ y_i^{(1)} \right\} + \sum_{j=2}^N \left\{ y_i^{(2)} \right\} + \dots \right] \end{aligned} \quad (73)$$

where C_2 , C_1 and C_0 are real circulant matrices of the same form as L (i.e., only N unknowns, all columns identical but shifted). The matrices C_2 , C_1 , and C_0 represent the inertial, damping, and stiffness effects of the aerodynamics. The matrices G_0 , G_1 , G_2 , etc. are sparse real circulant matrices with only one entry per column. They contain the impact of the relative lags in the aerodynamics on the blade forces. G_j , for example, contains the coefficient which expresses the lagged forces of the $i+j$ blade on the i blade.

The vectors of y_i are augmented states, related to q_i by

$$\frac{b}{U} \dot{y}_i^{(t)} + g_t y_i^{(t)} = \frac{b}{U} \dot{q}_i \quad \text{for } i=0,1,\dots,N-1 \quad (74)$$

In other words, the y_i variable is a first order lag of time constant g_t , on the rate of change of the displacement q_i . The time constants are the same for all the nominally identical blades. Such approximations are motivated by their success in approximately unsteady aerodynamic forces in external flows and cascades.

In order to evaluate the unknown constants in C_2 , C_1 , C_0 , G_0 , G_1 etc., equations (73) and (74) are expanded to examine the forces acting on the zeroth blade. Equation (73) gives

$$\begin{aligned} f_0 &= \frac{\pi \rho b^2}{U^2} \left[\frac{b^2}{U^2} (C_{0,2} \ddot{q}_0 + C_{1,2} \ddot{q}_1 + \dots + C_{N-1,2} \ddot{q}_{N-1}) \right. \\ &\quad + \frac{b}{U} (C_{0,1} \dot{q}_0 + C_{1,1} \dot{q}_1 + \dots + C_{N-1,1} \dot{q}_{N-1}) \\ &\quad + (C_{0,0} q_0 + C_{1,0} q_1 + \dots + C_{N-1,0} q_{N-1}) \\ &\quad \left. + (G_{0,0} y_0^{(0)} + G_{1,0} y_1^{(1)} + \dots + G_{N-1,0} y_{N-1}^{(N-1)}) \right] \end{aligned} \quad (75)$$

$$\frac{b}{U} \dot{y}_i^{(t)} + g_t y_i^{(t)} = \frac{b}{U} \dot{q}_i \quad \text{for } i=0,1,\dots,N-1 \quad (76)$$

Assuming pure sinusoidal motion

$$\{q_i\} = \left\{ \bar{q}_i \right\} e^{j\omega t} \quad (77)$$

then substitution into equations (75) and (76), and combining the two, the force on the zeroth blade can be written

$$\begin{aligned} f_0 &= \frac{\pi \rho U^2}{U^2} \left[\left[-k^2 C_{0,2} + jk C_{0,1} + C_{0,0} + G_{0,0} \frac{k^2 + jkg_0}{g_0 + k^2} \right] \bar{q}_0 e^{j\omega t} \right. \\ &\quad + \left[-k^2 C_{1,2} + jk C_{1,1} + C_{1,0} + G_{1,0} \frac{k^2 + jkg_1}{g_1 + k^2} \right] \bar{q}_1 e^{j\omega t} \\ &\quad \left. + \dots \right] \end{aligned} \quad (78)$$

If equation (72) is expanded in a manner similar to equation (78), then the force on the zeroth blade is

$$\begin{aligned} f_0 &= \frac{\pi \rho U^2}{U^2} \left[\left[\Re(C_{L_0}) + j\Im(C_{L_0}) \right] \bar{q}_0 e^{j\omega t} \right. \\ &\quad + \left[\Re(C_{L_1}) + j\Im(C_{L_1}) \right] \bar{q}_1 e^{j\omega t} \\ &\quad \left. + \dots \right] \end{aligned} \quad (79)$$

By comparing equations (78) and (79) term by term, the following relations are apparent

$$-k^2 C_{r,2} + C_{r,0} + G_{r,r} \frac{k^2}{g_r^2 k^2} = \text{Re}(C_{Lr}) \quad (80)$$

$$kC_{r,1} + G_{r,r} \frac{k^2}{g_r^2 k^2} = \text{Im}(C_{Lr}) \quad r=0,1,\dots,N-1$$

where the C 's, G 's, and g 's are real constants to be determined, and C_{Lr} is a complex function of k .

All that remains is for the real unknowns to be determined by a fitting procedure, such as a least squares fit to C_{Lr} versus the reduced frequency k for each value of the index r . Such experience in fitting sometimes produces an adequate fit using the single lag pole shown. This is true for the case of an incompressible cascade, Dugundji and Bundas (1984). More accuracy is attained by introducing a second set of poles g' and associated constants G' . The classic Jones approximation to the Theodorsen function is an example of this kind of two pole fit, Bisplinghoff and Ashley (1962).

Once the aerodynamic constants have been determined, the governing equation of equilibrium, equation (9), and the time domain expression for the aerodynamic forces can be combined into a single expression.

$$\begin{aligned} & \left[-\epsilon_1 \right] (\ddot{q}_1) + \left[\epsilon_1 \omega_1^2 (1+jg_1) \right] (q_1) = \\ & \eta \mu U^2 \left[\frac{b^2}{U^2} [C]_2 (\ddot{q}_1) + \frac{b}{U} [C]_1 (\dot{q}_1) + [C]_0 (q_1) \right. \\ & \left. [G]_0 \{y_1^{(0)}\} + [G]_1 \{y_1^{(1)}\} + [G]_2 \{y_1^{(2)}\} + \dots \right] \quad (81) \end{aligned}$$

$$\text{where } \frac{b}{U} \{y_1^{(\ell)}\} + \left[g_\ell \right] \{y_1^{(\ell)}\} = \frac{b}{U} \{\dot{q}_1\} \quad \ell = 0,1,\dots,N-1$$

If a similar procedure is used to represent the unsteady wake or gust response function, then a complete time accurate time domain representation of the aeroelastic behavior can be achieved.

TRENDS IN AEROELASTIC STABILITY

As with many engineering analyses, there are certain dominant trends in the analysis of the aeroelastic stability of turbomachine rotors. Some, such as the role of the mass ratio or the importance of blade mistuning can be determined simply from careful examination of the governing equations. Others require solutions for ranges of parameters to determine overall trends. In this section four trends will be addressed: the stabilizing and destabilizing influences in a cascade, and the critical role of the blade self-damping; the effects of bending-torsion coupling; the real rotor effects of loading, three-dimensionality and stall; and the differences in analysis of actual rotors and "rubber" designs.

Stabilizing and Destabilizing Influences in Cascades.

Simply from examination of the stability eigenvalue problem, certain stabilizing and destabilizing effects can be identified for a single degree of freedom flutter model. The nondimensional form of the stability problem, equation (63), is

$$\frac{1}{\eta^2} \left[(1+jg_1)(1+\delta_1) \right] \left\{ \bar{q}_1 \right\} = \left[\left[1+\epsilon_1 \right] + \frac{1}{\mu} [L] \right] \left\{ \bar{q}_1 \right\} \quad (82)$$

in which g is the structural damping δ , and ϵ the stiffness and mass nonuniformity, and L , the complex aerodynamic influence coefficients of the form

$$[L] = \begin{bmatrix} L_0 & L_{N-1} & L_{N-2} & \cdots & L_1 \\ L_1 & L_0 & L_{N-1} & \cdots & L_2 \\ L_2 & L_1 & L_0 & \cdots & L_3 \\ \vdots & \vdots & \vdots & \ddots & \vdots \\ L_{N-1} & L_{N-2} & L_{N-3} & \cdots & L_0 \end{bmatrix} \quad (83)$$

In order to identify the stabilizing and destabilizing influences, we simplify the problem by allowing the blades to be uniform in stiffness and structural damping. The governing equations for one degree of freedom per blade flutter are then

$$\frac{1}{\eta^2} \left\{ \bar{q}_1 \right\} = \frac{1-jg}{1+g} \left[\left[1+\epsilon_1 \right] + \frac{1}{\mu} [L] \right] \left\{ \bar{q}_1 \right\} \quad (84)$$

The remaining parameters in the problem are the structural damping g , the mass mistuning ϵ_1 , the mass ratio μ , and aerodynamic coefficients L_0 through L_N . Each of these terms somehow influences the eigenvalues Ω .

The complex eigenvalues of equation (84) form a pattern in the s -plane, with $s = j\Omega$, as shown in Figure 6. This pattern can be considered to have a centroid, and the eigenvalues are distributed about this centroid.

The location of the centroid is critical to the stability. If the centroid is in the right half plane, then by definition some eigenvalues will be in the right half plane, and the system will be unstable. Thus, to assure system stability the centroid must be in the left half plane. Returning to equation (84), it has been shown, Crawley and Hall (1985), that the only terms which can exert a net stabilizing influence on the rotor are the structural damping g , and the term L_0 , which expresses the aerodynamic force felt on the blade due to its own motion. To show the importance of this term, consider the problem of equation (84). Making use of the matrix property that the sum of the eigenvalues of a matrix equals the trace of the matrix, we have the following relationship for the sum of the eigenvalues:

$$\sum_{k=0}^{N-1} \frac{1}{\Omega_k^2} = \left[1 + \frac{L_0}{\mu} + \sum_{i=0}^{N-1} \epsilon_i \right] \left[\frac{1-g}{1+g^2} \right] \quad (85)$$

In the absence of unsteady aerodynamic forces, the reference blade vibrates at the nondimensional eigenfrequency $\Omega = \Omega_R = 1$. In the presence of aerodynamic forces, which are small compared to the elastic and inertial moments, Ω will still be nearly equal to Ω_R . The eigenfrequency can be expressed as a sum of its reference value and a perturbation from the reference value Ω_R .

$$\Omega = \Omega_R + \tilde{\Omega} = 1 + \tilde{\Omega} \quad (86)$$

The last step in eq. (86) is due to Ω_R being unity (see Eq. 68). Hence the eigenvalues of eq. (85) can be expanded as

$$\frac{1}{\Omega^2} = \frac{1}{1 + 2\tilde{\Omega} + \tilde{\Omega}^2} = 1 - 2\tilde{\Omega} + O(\tilde{\Omega}^2) \quad (87)$$

For convenience, let $s = \Omega j$. Substitution of eq. (87) into eq. (85) yields that the centroid of the eigenvalues (Fig. 6) is given approximately by

$$\begin{aligned} \text{Re}(s) &= \frac{1}{2} \text{Re} \left[\frac{L_0}{\mu} \right] - \frac{1}{2} g \\ \text{Im}(s) &= 1 - \frac{1}{2} \text{Re} \left[\frac{L_0}{\mu} \right] - \frac{\langle \epsilon \rangle}{2} \end{aligned} \quad (88)$$

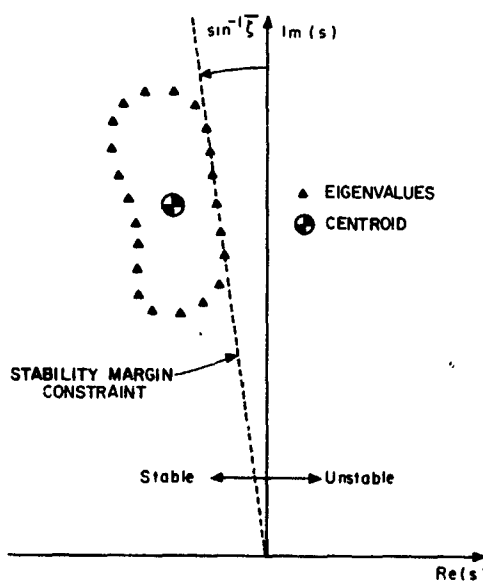


Figure 6. s -Plane Interpretation of Eigenvalues Showing Centroid and Stability Margin Constraint

That is, in the absence of structural damping, the real part of the centroid, $\langle s \rangle$, depends on the imaginary part of L_0 , and the structural damping g . The imaginary part of the centroid depends on the real part of L_0 and the mean value of the mistuning.

The location of the eigenvalues in the s -plane can be considered to be distributed around the centroid. Recalling that the system will be unstable if any eigenvalue is in the right half plane, the objective is to assure that the least stable eigenvalue is as far to the left as possible. If the rotor is unstable, increases in stability can be achieved either by moving the centroid to the left, or by reducing the size of the distribution about the centroid, which pulls the rightmost eigenvalue to the left.

Interpreted in this light, eq. (88) is an important result. It shows that in the absence of structural damping the centroid of the eigenvalues lies in the left plane if and only if $\text{Im}(L_0)$ is less than zero. Since a necessary condition for aeroelastic stability of the rotor is that the centroid of the eigenvalues lies in the left half plane, it can be deduced that a necessary but not sufficient condition for stability is that $\text{Im}(L_0)$ be less than zero. This is equivalent to the condition that the blades be self damped.

The location of the centroid is set by the average value of the mass (and stiffness), of the blades, the structural damping, and the blade self damping term. The distribution of the eigenvalues about the centroid is controlled by the nonuniformity in the mass and stiffness and by the off-diagonal terms in the aerodynamic influence coefficient matrix equation (83) (i.e., the unsteady cascade influences in the aerodynamics).

Note that any amount of off-diagonal aerodynamic influence, that is any unsteady aerodynamics effects due to neighboring blades, will distribute the eigenvalues about the centroid, and therefore move some of the eigenvalues to the right, destabilizing the cascade. Thus, unsteady aerodynamic interactions amongst the blades in a cascade are destabilizing.

The distribution pattern of eigenvalues about the centroid is influenced by the pattern of stiffness and mass mistuning of the blades, but the location of the centroid is not influenced by the pattern of mistuning so long as the average value is zero. Thus, the effect of mistuning is to reduce the influence of the blade to blade aerodynamic coupling and move the less stable eigenvalues toward the centroid. Note that no amount of mistuning will cause the centroid to move in a stabilizing direction and no amount of mistuning can increase the stability margin of the rotor beyond that given by the blade self damping.

Finally, the importance of the mass ratio and structural damping can be seen for a one degree of freedom flutter by examining equations (84) and (88). It is clear that all of the aerodynamic influences are scaled by the mass density ratio. In particular, if a necessary stability criterion is that the centroid of the eigenvalues is in the left-half plane then for stability

$$\operatorname{Re}(s) \leq 0 \quad (89)$$

$$g_m \left[\frac{L_0}{\mu} \right] - g \leq 0$$

A similar relationship is derived from the previous tuned rotor analysis in which a sufficient condition for stability of a tuned rotor was that

$$g_m \left[\frac{e_{Bn}}{\mu} \right] - g \leq 0 \quad (90)$$

for the largest positive value of the aerodynamic coefficient e_{Bn} . In each of these cases, the relative contribution of the aerodynamic component and structural damping is scaled by the mass density ratio μ .

In the limiting case of no structural damping, the stability boundary is independent of the mass ratio, since even a small amount of destabilizing aerodynamic influence will cause the rotor to go unstable. However, in the presence of a fixed nonzero structural damping ratio, the mass ratio sets the magnitude of destabilizing aerodynamic effect which can be tolerated before the system becomes unstable. If the rotor speed is increased past the reduced velocity corresponding to neutral aerodynamic stability for a fixed structural frequency and damping, a rotor blade with a larger mass ratio will be more stable than a rotor with a smaller mass ratio, as shown in Figure 7. The mass ratio of course can be changed by either changing the gas density, or by a change in the blade material.

The stabilizing and destabilizing effects for a single degree of freedom flutter model can be summarized as follows:

1. In the absence of structural damping, the blade must be self damped, so that the centroid of the eigenvalues lies in the left half plane.
2. In the presence of structural damping, blades of larger mass ratio are relatively more stable than those of smaller mass ratio for the same damping g .
3. The cascade unsteady aerodynamic influences are destabilizing.
4. Structural mistuning does not change the location of the centroid, but can rearrange the eigenvalues to increase the stability of the least stable root. The

limit to the potential effectiveness of mistuning is the centroid of the eigenvalues of the tuned rotor.

While these four trends are rigorously true for single degree of freedom per blade flutter, they are generally applicable to any turbomachine in which the flutter dominantly involves a single degree of freedom per blade. This is generally true of solid metallic blades. In the case of hollow or composite blades with significant bending torsion coupling, more judgment should be used in interpreting these stabilizing and destabilizing cascade influences.

Bending-Torsion Coupling

Several authors have investigated the impact of modeling cascade flutter as a classical bending-torsion coupled problem. In order to not confuse issues, two distinct mechanisms of bending-torsion coupling must be distinguished:

- A. Single mode coupling -this occurs when a single torsional mode has some translational component, or a single bending mode has some torsional component. Although its origin may be dynamic, this is essentially a kinematic coupling. It may be due to the root not being supported along a line normal to the elastic axis (i.e., structural sweep), the presence of an offset between the elastic axis and center of mass, the presence of anisotropic materials or fibers, or the presence of shrouds at tip or mid-span;
- B. Dynamic coupling between two modes -which is the case when two independent modes dynamically interact to cause a classic bending-torsion like coalescence flutter.

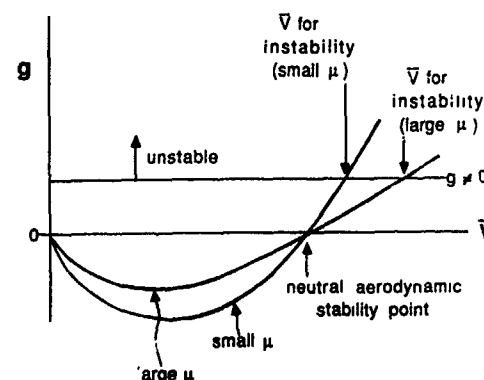


Figure 7: Sensitivity of Rotor Stability to Mass Ratio for Single Degree of Freedom Flutter

In gas turbine blading, the first or single mode kinematic coupling can be very important. The presence of shrouds or the distribution of mass will often cause a vibrational mode not to be pure torsion or pure bending, and this mixture must be taken into account. Often the presence of some bending in a dominantly torsional mode will exert a stabilizing influence.

However, in gas turbine blading, the dynamic bending-torsion coalescence coupling is more important when the structural modes are very close in frequency, or when blades are hollow or composite. The lesser importance of this dynamic interaction between modes can again be traced to the large mass ratios usually found in turbine components. The aerodynamic forces are simply not strong enough to significantly shift the structural frequencies, unless they are already in close proximity. Thus the aeroelastic instability found in most gas turbine components is not the classic bending-torsion coalescence flutter, but instead a cascade induced blade-to-blade interaction flutter.

The Effects of Loading and Three-Dimensionality

Actual turbomachine components work in a complex heavily loaded, three-dimensional flow environment which is not easily modeled in unsteady aerodynamic models. The aerodynamic loading and associated turning of the flow impact the aeroelastic problem in at least two ways. First, the presence of the loading can push the blading to a near stall condition. In this heavily loaded condition, the additional load per unit of incidence is known from quasi-steady analysis and cascade experiments to diminish. Translated into an unsteady aerodynamic effect, this implies that the forces on the blade for a unit of motion diminish. These forces per motion of the blade on itself are expressed in the L_0 unsteady aerodynamic coefficient, which was shown to be pivotal to system stability in the discussion above. Thus, any slight reduction in the $Im(L_0)$ the blade self damping term, might lead to flutter. This could be the origin of heavily loaded flutter occurring near the stall line.

A second effect of the turning is to introduce swirl into the flow. This swirl vastly complicates the downstream flow, and couples the acoustic, vorticity and pressure fields. Even current three-dimensional aerodynamic analyses do not take this into account. The implications on the unsteady aerodynamic forces of this swirling downstream flow have yet to be considered.

Trends with Reduced Velocity

In considering aeroelastic trends with reduced velocity, or reduced frequency, it must be remembered that those parameters are in fact used in two ways: first, as a general measure of the unsteadiness of the flow, and, secondly, as a way to non-dimensionalize the relative strength of the structural and dynamic pressure forces

$$\bar{V}^2 = \frac{U_b^2 b^2}{\omega^2} = U_b^2 b^2 \left[\frac{m}{k} \right] \sim \frac{\text{dynamic pressure}}{\text{structural stiffness}}$$

Generally, these two influences on aeroelastic stability are opposing, that is, the flow is more unsteady at high k , low V , but the dynamic pressure is greater at low k , high V .

Further, when aeroelastic trends such as the V-g diagram of Figure 8 are plotted versus V , attention must be paid to whether the trends are at constant Mach number, or if the Mach number changes with V . The former, which is the traditional V-g diagram, is useful in the analysis of rubber engines, i.e., in considering design trades, since V can be changed at constant Mach number and temperature only by changing b and ω . These are parameters which are only variable in design. For analysis of an actual component, a V-M-g diagram is required, i.e., one in which Mach number changes in proportion to V , as determined by the operating line of the rotor on the performance map. Such diagrams then represent the performance of a given component running on an operating line.

When plotting both V-g and V-M-g diagrams, it is useful to plot the performance of a tuned rotor, and one with a nominal degree of mistune as in Fig. 8. In limiting case a mistuned rotor asymptotically approaches the stability associated with the blade self damping.

EFFECTS OF MISTUNING ON STABILITY

All rotors are, by the nature of the manufacturing process, mistuned to some degree. Here mistuning is defined as a distribution in the frequencies of the blades in the cascade. It has been suggested that the level of mistuning be deliberately increased to further augment the stability margin of the rotor, and that this mistuning be introduced in specific patterns.

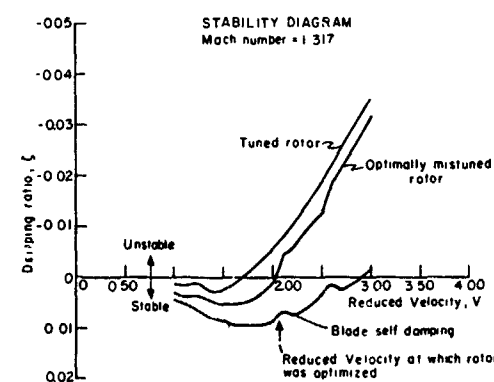


Figure 8. V-g Stability Diagram of a Tuned and Optimally Mistuned Rotor ($\tau=0.002$), with the Limiting Case of the Blade Self Damping

In considering the effect of mistuning on stability, one must understand the mechanisms of mistuning; that is, what physical effects cause change in stability. The auxiliary questions are then: how much mistuning must be present to consider a rotor mistuned, how much change in stability margin can be achieved by mistuning; what is the optimal pattern of mistuning; and what are the limitations to mistuning for stability augmentation.

When deliberately introducing mistuning for stability, one would like to pick an arrangement of mistuning which provides a large increase in stability for a given level of structural mistuning. It has been suggested, for example, that alternate mistuning may be nearly optimal in increasing the stability of shroudless fans. In this first section, an appropriate criterion for optimal mistuning will be defined and typical optimal mistuning patterns examined. In the next section, the mechanisms and limitations of mistuning will be discussed.

The selection of a definition of an optimal mistuning pattern is of course necessarily subjective. One must determine how to weigh the unlike quantities of stability, mistuning level, and forced response of the rotor. One choice is to implement the level of mistuning as a cost function to be minimized, and the desired level of stability of the least stable eigenmode as a constraint. Hence, the optimal mistuning problem can be posed as a constrained optimization problem.

The cost function which represents the level of mistuning in the rotor should of course strongly penalize large amounts of mistuning in any single blade. The cost function used by Crawley and Hall (1985) is given by

$$\varphi = \left[\frac{\sum \epsilon_i^n}{N} \right]^{1/n} \quad (90a)$$

where n is in general some positive integer. In particular, n was chosen to be 4. Since this cost strongly penalizes large amounts of mistuning in any single blade, no blade mistuning becomes excessively larger than that of any other blade. That is to say that there will be no "rogue blades" in the optimal mistuning pattern.

The designer of a fan might wish to specify that a fan have at its operating point some minimum stability level. Hence the stability requirements are simply that the damping ratio of every eigenmode of the mistuned fan be greater than some minimum damping ratio. This is expressed symbolically as

$$\theta_i = \xi_i - \bar{\xi} \geq 0 \quad i=1,2,\dots,N \quad (91)$$

where ξ_i is the damping ratio of the i th eigenvalue, and $\bar{\xi}$ is the desired stability margin. This requirement is shown graphically in Figure 6.

At this point, the optimization statement has been completely specified. The cost function to be minimized is a measure of the level of mass mistuning to be introduced into the rotor while the constraints are that the rotor meet minimum stability requirements. The independent variables are the individual mass mistuning of the blades or stiffness and the governing system equation is equation (63). This problem can be solved using appropriate numerical optimization techniques.

To illustrate the results of optimal mistuning, consider a specific high bypass ratio shroudless fan. The aeroelastic behavior is modelled using a typical section analysis by assuming a single torsional degree of freedom per blade. At the typical section, the relative Mach number, M_r , is 1.317; the reduced frequency, k , is 0.495; the solidity, s , is 1.404; the mass ratio, ρ , is 182; and the nondimensional radius of rotation, r , is 0.4731. Because the computational difficulty of the optimization problem rises quickly as the number of blades increases, the number of blades of the fan was taken to be 12, 13, or 14.

The unsteady aerodynamic model used is the supersonic linearized model of Adamczyk and Goldstein (1978). The aerodynamic influence coefficients found from this model are shown in Figure 9. Note that $\text{Im}(L_{ik})$ is less than zero indicating that the blades are self-damped. Hence, although the tuned rotor is unstable, mistuning may stabilize the rotor as previously discussed. Figure 9 also shows that the neighboring blades and the blade itself exert the dominant forces on a given blade. Therefore, the aerodynamic influence coefficient matrix is strongly banded.

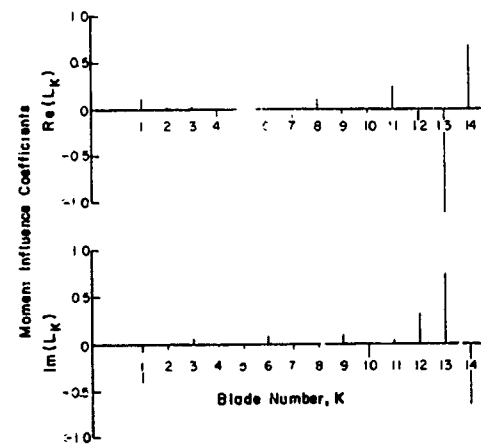


Figure 9. Unsteady Aerodynamic Moment Coefficients Showing the Influence of the i -th Blade on the 14th Blade in a 14-Bladed Rotor

Figure 10 shows the eigenvalues of the 14-bladed tuned rotor in nondimensional form. Note that four of the 14 eigenvalues lie in the right half plane and are therefore unstable. Since the blades are self-damped, the centroid of the eigenvalues lies in the left half plane.

Next the rotor is optimally mistuned by numerically finding a mistuning pattern which minimizes the cost function and satisfies all the constraints. Figure 11 shows the cost of the optimal mistuning pattern versus the desired amount of stability margin for the 12, 13, and 14-bladed cases. Also shown is the cost of alternate mistuning for the 14-bladed case. Two important points are clearly illustrated. First, although it has been previously thought that alternate mistuning may be nearly optimal (in the sense that a small amount of mistuning is necessary) this is not the case. For a desired damping ratio of 0.002, alternate mistuning requires nearly twice the level of mistuning as optimal mistuning. Second, it appears that the number of blades on the rotor is unimportant when optimally mistuning the rotor, and also that the optimal cost for 12, 13, and 14-bladed rotor are very similar.

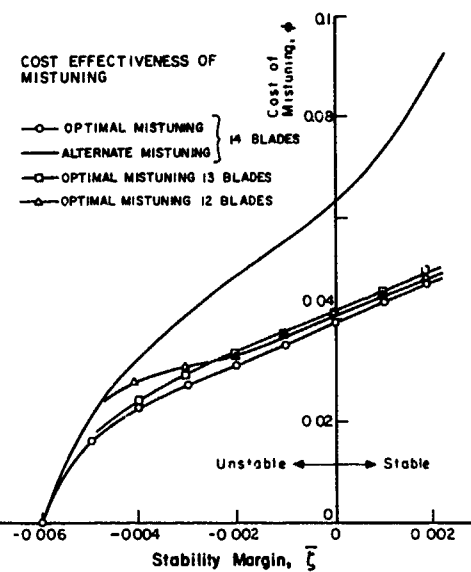


Figure 11. Cost of Mistuning for 12, 13, and 14-Bladed Rotors

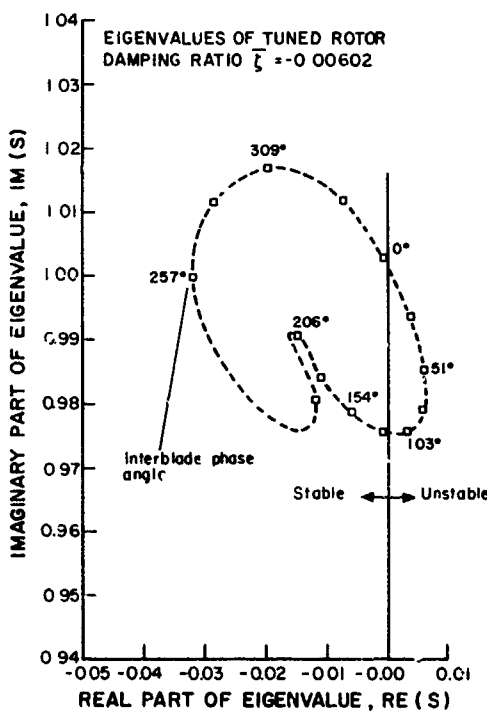


Figure 10. Eigenvalues of a Tuned Rotor

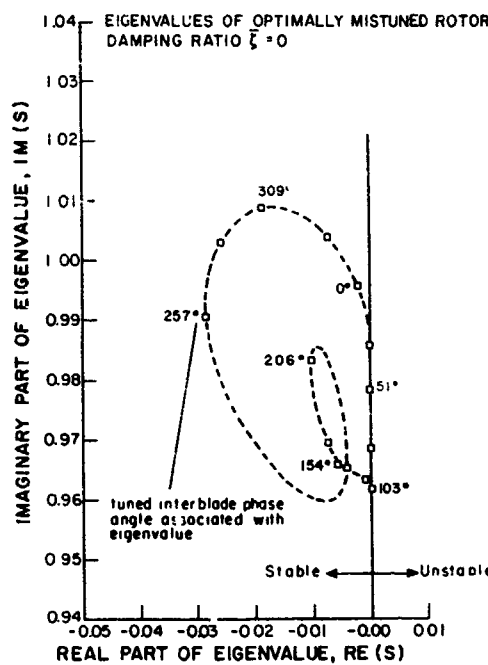


Figure 12. Eigenvalues of Optimally Tuned Rotor

Mechanisms and Limitations of Mistuning

Some insight into why mistuning is effective can be gained by examining the eigenvalues of the tuned and mistuned rotors in the complex plane. Figures 10, 12, and 13 show the eigenvalues for the tuned case and the $\zeta = 0.0$ and the $\zeta = 0.002$ optimally mistuned cases for the 14-bladed rotor. As mistuning is introduced the eigenvalues are "pushed" to the left as much as necessary to satisfy the constraints.

The optimal mistuning patterns found in the optimization procedure for the 14-bladed rotor are shown in Figure 14. Beginning with the $\zeta = -0.005$, the pattern of mistuning is "almost alternate" mistuning. The odd numbered blades have little or no change from their nominal mass. As the stability margin is increased, the nearly alternate blade mistunings become more and more apparent.

Upon examination of a number of optimal mistuning patterns such as these, certain characteristic trends become apparent. An almost alternate pattern is evident which serves to reduce the dominant influence of the neighboring blades. This almost alternate mistuning pattern, however, is usually broken at one or two points around the rotor. It is thought that these breaks disrupt the communication of longer "wavelength" forces, that is, the smaller but nonzero influence coefficients from non-neighboring blades.

Finally, there is a certain fine structure to the mistuning pattern. The details of this structure depend on the details of the minimization, and it is difficult to predict what this structure will look like without actually performing the numerical optimization.

Unfortunately, the strict optimal mistuning pattern is sensitive to errors in implementation. Although the designer may specify a certain mistuning pattern, the manufacturing process may place limits on the tolerances which can actually be achieved. Hence, it is necessary to consider the sensitivity of a given mistune pattern to errors in implementation. For instance, if one wishes to implement an optimal mistune pattern on an actual rotor, the actual mistuning pattern which is implemented will be given by

$$\xi_i = \xi_{i\text{specified}} + \epsilon_i \quad (92)$$

where ϵ_i is the error in mistuning the rotor. The stability of this actual pattern may be significantly less than the one desired, depending on the errors introduced.

To investigate this problem, errors were introduced into the optimally mistuned 14-bladed rotor with a stability margin of 0.002. The procedure was to compute the worst case arrangement of the error and then assess the degradation in stability due to that case.

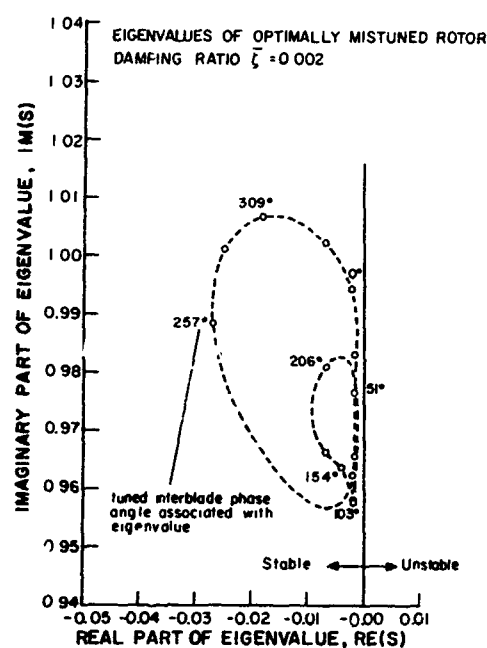


Figure 13. Eigenvalues of Optimally Tuned Rotor
 $\zeta = 0.002$

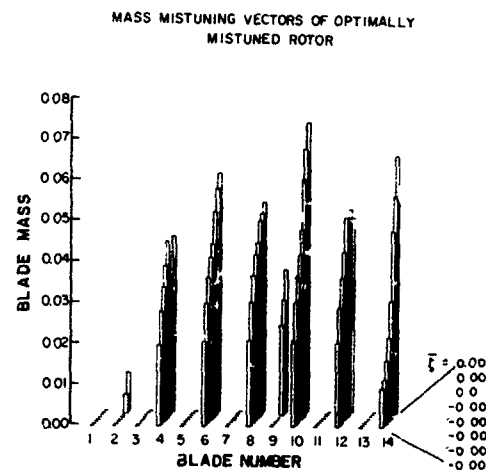


Figure 14. Optimum Mistuning Patterns of 14-Bladed Rotor

For an RMS scatter of 1 percent in mass mistuning, it was found that the stability was reduced from 0.002 to -0.00317 (Figures 15 and 16). The optimally mistuned rotor is extremely sensitive to errors in mistuning.

Hence we have seen that even though the optimal mistuning is the best possible mistuning pattern in one sense, that is, it requires the lowest level of mistuning to achieve a desired level of stability, it is clearly not practical to implement a pattern of mistuning which requires very close tolerances on the natural frequencies of the blades. As an alternative, consider the case of alternate mistuning. As was shown earlier, this mistune pattern is not nearly as effective as the optimal mistuning in terms of required levels of mistuning. However, the pattern is not as susceptible to errors in implementation as the optimal mistuning pattern. The same sensitivity analysis was applied to an alternately mistuned rotor with a perfectly mistuned stability margin of 0.00171. For a 1 percent RMS scatter in mass mistuning, the stability margin was reduced from 0.00171 to 0.00047 as shown in Figure 16. Therefore, although alternate mistuning is not as cost effective as optimal mistuning, it is clearly much more robust to errors in implementation.

Some insight into this difference in sensitivity can be gained by examining the trends shown in Figure 16. These trends can be divided into three regions. For the first few percent of mistuning introduced into the tuned rotor, very little change in stability occurs. In fact, it

can be shown that for the first increment of mass mistuning of blades with a single degree of freedom, no change in stability occurs. Thus, on average, a rotor must have several percent mistuning before it begins to exhibit the behavior of a mistuned rotor.

Beyond the first few percent in mistuning, the trend enters an approximately linear region of sensitivity, that is, linearly increasing stability with increasing mistuning. Beyond this region, one moves into a region of diminishing returns. Eventually, the asymptotic limit of stability, the centroid of the eigenvalues, is approached and the level of mistuning required per increase in stability rises sharply.

This idealized trend can be used to explain the sensitivity of the optimum mistuning patterns. Figure 9 shows that the optimum cost curve has a very shallow slope in the region of $\xi = 0.002$. This implies that a small amount of mistuning, if introduced correctly, can greatly increase the stability of the rotor. But for the same reason, small errors in mistuning can cause large decreases in stability. On the other hand, alternate mistuning is relatively insensitive to errors in mistuning but is not nearly optimal. Thus there is a clear design trade-off between the level of mistuning and the robustness of the design.

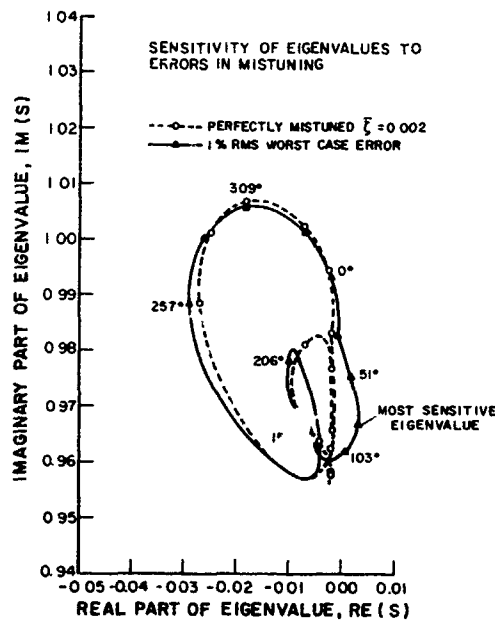


Figure 15. Sensitivity of Optimally Mistuned Eigenvalues to Errors in Mistuning

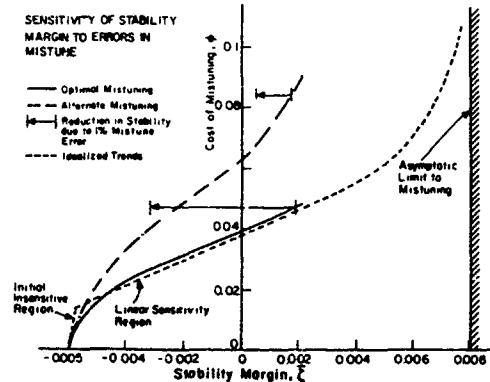


Figure 16. Sensitivity of Stability Margin to Errors in Mistuning

Summary Comments

In this chapter an attempt has been made to outline a complete and generalized formulation for the aerelastic problem and its solution. This includes information necessary conventions of the aerodynamic and structural dynamic operators. The most important lesson to be learned from this review is that in the case of linear analysis, all of these analyses are equivalent, and the practicing engineer should use the one which gives the most insight into a particular problem.

In addition, a brief review of the most common trends in stability analysis was conducted; the destabilizing influences in cascades, the influence of kinematic vs. dynamic bending torsion coupling, the effects of mistuning, and the yet largely unmodelled effects of three-dimensionality.

Much of what has been presented in this chapter, except for the treatment of explicit time dependent motion in a cascade, exists in fragments distributed throughout the literature. But, here an attempt has been made to unite all of this material in a common formulation, and reference it to the remaining chapters of this Manual.

APPENDIX A: SUMMARY OF TRANSFORMATION RELATIONSHIPS

Basic relationships (for single degree of freedom per blade):

Structural dynamics:

$$[M]\{q_1\} + [K]\{q_1\} = \{f_1\} \quad (A1)$$

Unsteady aerodynamics:

$$\begin{aligned} f_1 &= \bar{\rho} b^2 \omega^2 \sum_{n=0}^{N-1} e_{\beta_n} \bar{q}_{\beta_n} e^{j(\omega t + i\beta_n)} \\ \{f_1\} &= \bar{\rho} b^2 \omega^2 [E] \left[e_{\beta_n} \right] \{q_{\beta_n}\} e^{j\omega t} \end{aligned} \quad (A2)$$

Kinematics:

$$\{q_1\} = [E] \left\{ \bar{q}_{\beta_n} \right\} e^{j\omega t} = \{\bar{q}_1\} e^{j\omega t} \quad (A3)$$

For blade coordinates:

transform equation 2 using equation 3

$$\begin{aligned} -\omega^2 [M]\{\bar{q}_1\} + [K]\{\bar{q}_1\} &= \{f_1\} \\ &= \bar{\rho} b^2 \omega^2 [E] \left[e_{\beta_n} \right] [E]^{-1} \{\bar{q}_1\} \end{aligned} \quad (A4)$$

For travelling wave coordinates:

transform equation 1 using equation 3

$$\begin{aligned} -\omega^2 [E]^{-1} [M][E] \left\{ \bar{q}_{\beta_n} \right\} + [E]^{-1} [K][E] \left\{ \bar{q}_{\beta_n} \right\} &= \\ = \bar{\rho} b^2 \omega^2 \left[e_{\beta_n} \right] \left\{ \bar{q}_{\beta_n} \right\} & \end{aligned} \quad (A5)$$

For standing mode coordinates (sin/cos):

transform eqn. 4 for q_1 and premultiply by $[P]^{-1}$

$$\begin{aligned} -\omega^2 [P]^{-1} [M][P] \left[\begin{array}{c} \bar{q}_{cn} \\ \bar{q}_{sn} \end{array} \right] + [P]^{-1} [K][P] \left[\begin{array}{c} \bar{q}_{cn} \\ \bar{q}_{sn} \end{array} \right] &= \\ = \bar{\rho} b^2 \omega^2 [P]^{-1} [L][P] \left[\begin{array}{c} \bar{q}_{cn} \\ \bar{q}_{sn} \end{array} \right] & \end{aligned} \quad (A6)$$

For standing mode coordinates (general):

transform eqn. 4 for q_1 and premultiply by $[\phi]^T$

$$\begin{aligned} -\omega^2 [\phi]^T [M][\phi] \left\{ \bar{q}_n \right\} + [\phi]^T [K][\phi] \left\{ \bar{q}_n \right\} &= \\ = \bar{\rho} b^2 \omega^2 [\phi]^T [L][\phi] \left\{ \bar{q}_n \right\} & \end{aligned} \quad (A7)$$

Other useful transformation relationships:

$$q_1 = \bar{\rho} \left\{ \bar{q}_{co} + \sum_{n=1}^{(N-1)/2} \bar{q}_{cn} \cos n\theta_1 + \sum_{n=1}^{(N-1)/2} \bar{q}_{sn} \sin n\theta_1 \right\} e^{j\omega t}$$

$$\left\{ \bar{q}_1 \right\} = [P] \left[\begin{array}{c} \bar{q}_{cn} \\ \bar{q}_{sn} \end{array} \right]$$

$$\left[\begin{array}{c} \bar{q}_{co} \\ \bar{q}_{cl} \\ \bar{q}_{sl} \\ \bar{q}_{c2} \\ \bar{q}_{s2} \\ \vdots \end{array} \right] = \left[\begin{array}{c} \bar{q}_{cn} \\ \bar{q}_{sn} \end{array} \right]$$

$$[P] = \left[\begin{array}{cccccc} C_{0,0} & C_{0,1} & S_{0,1} & C_{0,2} & S_{0,2} & \cdots \\ C_{1,0} & C_{1,1} & S_{1,1} & C_{1,2} & S_{1,2} & \cdots \\ C_{2,0} & \vdots & \vdots & \vdots & \vdots & \cdots \\ C_{3,0} & \vdots & \vdots & \vdots & \vdots & \cdots \\ \vdots & & & & & \cdots \\ C_{N-1,0} & \cdots & & & & \cdots \end{array} \right]$$

where $C_{k,\ell} = \cos 2\pi \frac{k\ell}{N}$ and $S_{k,\ell} = \sin 2\pi \frac{k\ell}{N}$

$$[P]^T [P] = [D] = \left[\begin{array}{ccccc} N/2 & & & 0 & \\ & N/2 & & & \\ & & N/2 & & \\ 0 & & & \ddots & \end{array} \right] \cdot [P]^{-1} [D]^{-1} [P]^T$$

$$\bar{q}_i = \sum_{n=0}^{N-1} \bar{q}_{\beta_n} e^{j(\omega t + \beta_n)} \quad (1)$$

$$\{\bar{q}_i\} = [E]\{\bar{q}_{\beta_n}\}$$

$$[E] = \begin{bmatrix} E_{0,0} & \dots & E_{0,N-1} \\ \vdots & \ddots & \vdots \\ E_{N-1,0} & \dots & E_{N-1,N-1} \end{bmatrix} \quad E_{k,\ell} = e^{\frac{j2\pi k \ell}{N}}$$

$$[E]^{-1}[P] \begin{bmatrix} \bar{q}_{cn} \\ \bar{q}_{sn} \end{bmatrix} = \{\bar{q}_{\beta_n}\}$$

$$[E]^{-1}[P] = \begin{bmatrix} 1 & 0 & 0 & 0 & 0 & 0 & 0 & 0 & \dots & \dots \\ 0 & \frac{1}{2} & -\frac{1}{2} & 0 & 0 & 0 & 0 & 0 & \dots & \dots \\ 0 & 0 & 0 & \frac{1}{2} & -\frac{1}{2} & 0 & 0 & 0 & \dots & \dots \\ \vdots & \ddots & \ddots \\ 0 & 0 & 0 & \frac{1}{2} & \frac{1}{2} & 0 & 0 & 0 & \dots & \dots \\ 0 & \frac{1}{2} & \frac{1}{2} & 0 & 0 & 0 & 0 & 0 & \dots & \dots \end{bmatrix}$$

APPENDIX B: FORCE AND MOMENT NOTATION

Force notation usually used with the C notation

The forces and moments are initially defined to be acting at the leading edge (see figure 3b), and the displacements and wake velocities are:

$\tilde{q}_0 e^{j\omega t}$ leading edge velocity

$\tilde{\alpha}_0 e^{j\omega t}$ angular displacement

$\tilde{w}_0 e^{j\omega t}$ wake velocity at leading edge

The forces and moments acting at the leading edge are:

$$\tilde{F}_0 = \pi b U c (C_{FQ} \cdot \tilde{q}_0 + U \cdot C_{Fa} \cdot \tilde{\alpha}_0 - C_{Fw} \cdot \tilde{w}_0) \cdot e^{j\omega t} \quad (B1a)$$

$$\tilde{M}_0 = \pi b U c^2 (C_{Mq} \cdot \tilde{q}_0 + U \cdot C_{Mx} \cdot \tilde{\alpha}_0 - C_{Mw} \cdot \tilde{w}_0) \cdot e^{j\omega t} \quad (B1b)$$

If the axis of pitch is shifted to a point ηc behind the leading edge, the coefficients about this axis (designated by subscript η) are derived by considering the transformation in coordinates and forces:

$$\tilde{q}_\eta e^{j\omega t} = \tilde{q}_0 e^{j\omega t} + \eta c \frac{d}{dt} (\tilde{q}_0 e^{j\omega t})$$

$$\tilde{\alpha}_\eta e^{j\omega t} = \tilde{\alpha}_0 e^{j\omega t}$$

$$\tilde{w}_\eta e^{j\omega t} = \tilde{w}_0 e^{-j\lambda \eta c} e^{j\omega t}$$

$$\tilde{F}_\eta = \tilde{F}_0$$

$$\tilde{M}_\eta = \tilde{M}_0 - \eta c \cdot \tilde{F}_0$$

where $\eta = 0$ at the leading edge, 1 at the trailing edge, and $\lambda = \omega c/U$. The new coefficients are:

$$\begin{aligned} (C_{FQ})_\eta &= (C_{FQ})_0 \\ (C_{Fa})_\eta &= (C_{Fa})_0 - j\lambda \eta (C_{FQ})_0 \\ (C_{Fw})_\eta &= e^{j\lambda \eta} (C_{Fw})_0 \\ (C_{Mq})_\eta &= (C_{Mq})_0 - \eta (C_{Fa})_0 \\ (C_{Mx})_\eta &= (C_{Mx})_0 - \eta (C_{Fa})_0 - j\lambda \eta (C_{Mq})_0 + j\lambda \eta^2 (C_{FQ})_0 \\ (C_{Mw})_\eta &= e^{j\lambda \eta} (C_{Mw})_0 - \eta e^{j\lambda \eta} (C_{Fw})_0 \end{aligned} \quad (B2)$$

$$\begin{aligned} \tilde{F}_\eta &= \pi b U c [(C_{FQ})_\eta \cdot \tilde{q}_\eta + U (C_{Fa})_\eta \cdot \tilde{\alpha}_\eta \\ &\quad - (C_{Fw})_\eta \cdot \tilde{w}_\eta] \cdot e^{j\omega t} \end{aligned} \quad (B3a)$$

$$\begin{aligned} \tilde{M}_\eta &= \pi b U c^2 [(C_{Mq})_\eta \cdot \tilde{q}_\eta + U (C_{Mx})_\eta \cdot \tilde{\alpha}_\eta \\ &\quad - (C_{Mw})_\eta \cdot \tilde{w}_\eta] \cdot e^{j\omega t} \end{aligned} \quad (B3b)$$

Force Notation used with the ℓ notation

The forces and moments are assumed to be acting at the elastic axis (see figure 3a), and the displacements and wake velocities are:

$$\begin{aligned} h &= \tilde{h} \cdot e^{j\omega t} : \text{displacement of the reference axis} \\ \alpha &= \tilde{\alpha} \cdot e^{j\omega t} : \text{angular displacement} \\ w &= \tilde{w} \cdot e^{j\omega t} : \text{wake velocity of the reference axis} \end{aligned}$$

And the forces and moments are written as:

$$\frac{L}{b} = \pi b^2 \omega^2 (\ell^{hh} \cdot \frac{\tilde{h}}{b} + \ell^{ha} \cdot \tilde{\alpha} + \ell^{hw} \cdot \frac{\tilde{w}}{U}) \cdot e^{j\omega t} \quad (B4a)$$

$$\frac{M}{b} = \pi b^2 \omega^2 (\ell^{ah} \cdot \frac{\tilde{h}}{b} + \ell^{aa} \cdot \tilde{\alpha} + \ell^{aw} \cdot \frac{\tilde{w}}{U}) \cdot e^{j\omega t} \quad (B4b)$$

By comparison of the two conventions,

$$\begin{aligned} \tilde{F}_\eta &= L \\ \tilde{M}_\eta &= -M \\ \tilde{q}_\eta &= -\frac{dh}{dt} = -j\omega \cdot \tilde{h} \\ \tilde{\alpha}_\eta &= -\tilde{\alpha} \\ \tilde{w}_\eta &= -\tilde{w} \\ c &= 2b \end{aligned}$$

and with these conventions:

$$\begin{aligned} \ell^{hh} &= \frac{2j}{k} (C_{FQ})_\eta & \ell^{ah} &= \frac{4j}{k} (C_{Mq})_\eta \\ \ell^{ha} &= \frac{2}{k^2} (C_{Fa})_\eta & \ell^{aa} &= \frac{4}{k^2} (C_{Mx})_\eta \\ \ell^{hw} &= \frac{-2}{k^2} (C_{Fw})_\eta & \ell^{aw} &= \frac{-4}{k^2} (C_{Mw})_\eta \end{aligned}$$

FAN FLUTTER TEST

by

HANS STARGARDTER
 United Technologies Corporation
 Pratt & Whitney Aircraft
 East Hartford, Connecticut 06108

INTRODUCTION

The object of this chapter is to describe an aeroelastic investigation of fan flutter. Discussion includes test procedures for flutter evaluation, data acquisition and reduction, safety, and instrumentation. Some data contents are included, but are not the primary concern of this document. Initially, a complete sequence of preparation, testing and analysis of an ideal fan flutter test is presented. This is followed by identification of dangerous blade vibrations, a case history of a NASA/Pratt & Whitney Subsonic/Transonic Flutter Study, and a discussion and analysis of the program results. Lastly, a summary relating this test to the overall discussion of fan flutter testing is presented. It will be noted that many of the steps in the ideal test situation have been omitted in the actual case history. Most of these differences are in the test preparation area because the case history used a previously tested design in which much of the preliminary work and safety screening had already been accomplished.

TEST PROCEDURE FOR A FLUTTER EVALUATIONWhat is to be measured?o Flutter Boundaries

Locations on compressor map, intensity gradients, stress gradients

o Response in Flutter

Frequencies, coherence, modulation, phase, mode shapes, amplitude variations from blade to blade

o Blade Running Position

Steady untwist, camber changes, unsteady mode shapes, variations from blade to blade, variations with speed, temperature, pressure

o Aerodynamic - Steady Performanceo Aerodynamic - Unsteady Performance

Incidence, pressure and velocity fluctuation, in-passage fluctuations, airfoil surface fluctuation

o Rig Safety

Vibration, critical speed, temperatures, tip tabs, sudden changes in performance or signals

Pretest Analysiso Blade Steady Stress

Goodman Diagram

Check for steady-state stresses

Check for safe steady-state deflections

o Resonant Vibration

Campbell Diagram

Avoid known resonant stimuli

o Stability

Supersonic unstalled flutter

Transonic stall flutter

Other flutter

Test Preparationo Blade Selection and Acceptance Criteria

Dimensional verification

Frequency checks

Instrumentationo Strain Gages

Select blades for instrumentation based on measured frequencies. Place strain gages at locations where strain is high on modes of vibration anticipated in test (root leading edge is normally good location).

o Number of Instrumented Blades

Strain gage of high and low frequency blades

o Mirrors

Select locations

Decide installation technique

Recognize limitation that optical path must be clear

o Kulites

Mount on blade and/or case; concentrate on leading edge region where most of the flutter action will be.

o Hot Films

Blade-mounted hot film good only for qualitative data. Amplitude cannot be calibrated.

o Include Steady State Performance Instrumentso Safety

Determine steady state safety limits

Determine transient state safety limits

Test Plano Define number of test points required to get satisfactory data for flutter boundaries, resonances, surge, etc.

- o Establish flutter boundaries
- o Establish safe operating regime
- o Obtain most important information first; flutter tests can end abruptly

Test Procedure

- o Safety and exploring new regimes

During first acceleration, overshoot all steady points by a small margin to assure a safe condition on all blades, including those not instrumented.

- o Accuracy

Verify accuracy of test stand observations by careful playback.

- o Fatigue Damage

To assess fatigue damage keep records of time above fatigue limits, estimate amplitude and number of cycles above limits, visually inspect blades using borescopes, if necessary, inspect often for foreign object damage, i.e., nicks, gouges, erosion, tip rub burrs and temperature discoloration.

Data Acquisition

- o Frequency Response

Recovery of wave forms requires an order of magnitude margin above highest anticipated blade frequency. If sampling is used watch for loss of frequency spectrum.

- o Determine calibrations for amplitude.

- o Determine calibrations for phasing (spectral and fast Fourier Transform). Use a common clock on all recorders by paralleling a prime signal from the strain gages.

Strain Gage Signals

Each aeroelastic phenomenon has a characteristic signature or wave form that can be identified on the oscilloscope during the test or on playback. The major signals are identified below.

- o Flutter - coherent
- o Resonant vibration
 - Buffeting (also called separated flow vibration, bending flutter)
- o Rotating stall
- o Surge or stall
- o Tip rub
- o Bas signals (faulty slip ring, breaking gages, etc.)

IDENTIFICATION OF BLADE VIBRATION

Rapid identification of blade vibration signals observed on the test stand is essential. Certain potentially

dangerous conditions require instantaneous reaction, while other situations allow more time for control. A description of various types of blade vibrations associated with excessive amplitudes follows, along with the required test control actions.

- o Flutter

Flutter is identified on the monitor scope as a sinusoidal signal usually on all blades but isolated to one stage. It is probably the most dangerous aeroelastic event, often associated with rapid increases in amplitudes. The observed frequency of flutter is not an integral multiple of the engine rotational frequency. Safe test stand practice requires backing off the flutter boundary quickly by reversing the operating changes that caused penetration into the flutter boundary. Hysteresis associated with the flutter boundary is rare.

Figure 1 shows typical unfiltered strain gage responses associated with a high-speed torsional condition. This figure shows a coherent flutter response, i.e., all blades vibrating at the same frequency with the inter-blade phase angle fixed. Rarely flutter may occur in a less coherent manner with variable amplitude and variable phase, each blade vibrating at its own natural frequency.

- o Resonance

Resonance is excited when the frequency of periodic aerodynamic forces (wakes) matches the blade's natural frequency. Some sources of resonant vibration are inlet distortion, structural struts, instrumentation, burner cans or nozzles. The blade response frequency is an integral multiple of the engine rotation.

Resonant vibration can be recognized on the test monitor by constant amplitude sinusoidal wave forms that appear to stand still when the scope sweeps are triggered by the engine per-revolution signal. For example, a two per-revolution signal displays two full waves on the scope; a six per-revolution shows six full waves. See Figure 2.

While the only safe reaction to flutter is to back off, resonant vibration can be avoided by either acceleration or deceleration of the test vehicle. How far to stay away from a dangerous resonance depends on the instrumentation. Enough margin must be allowed to keep non-instrumented high and low frequency blades out of danger. Usually 5 to 10 percent change in speed in either direction is sufficient. However, in the case of a new machine it is prudent to accelerate to a slightly higher speed than the intended new data point and then back down to the intended design speed. This will assure the absence of resonant vibration of non-instrumented high frequency blades that may be excited to dangerous amplitudes.

HIGH SPEED TORSIONAL FLUTTER
TIP M_{REL} = 1.6

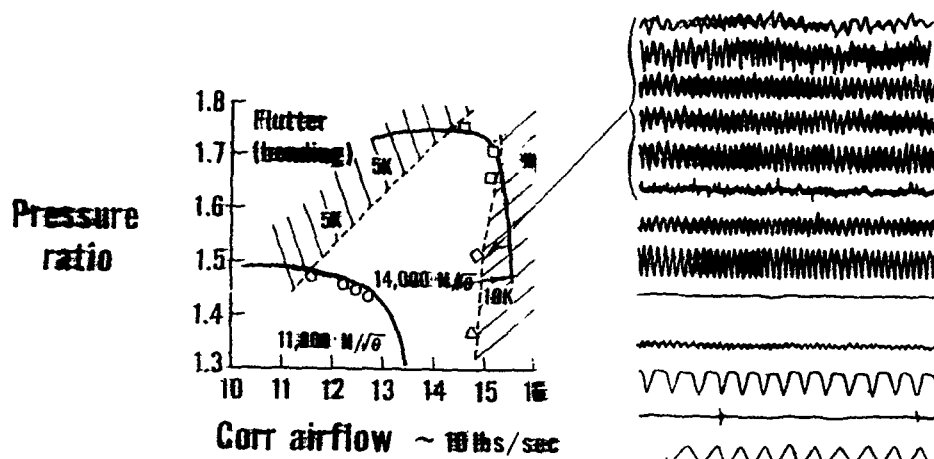


Figure 1. High Speed Torsional Flutter

BLADE RESONANT VIBRATION OSCILLOGRAPH
FROM STRAIN GAGE
 4E primary signal with weaker 2E

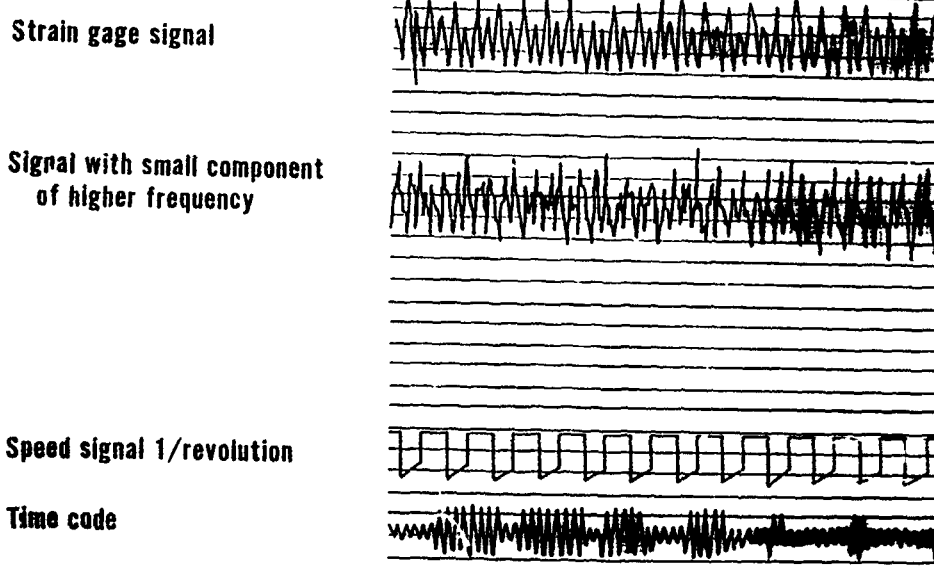


Figure 2. Blade Resonant Vibration Oscillograph

o Buffeting

Buffeting, also called separated flow vibration or bending flutter, is an irregular motion of the blades excited by turbulence in the flow field. It usually shows on the scope as a first mode response with amplitude varying randomly. Buffeting is associated with high incidence angles and often occurs toward the stall line or preceding flutter. It is also common on front stages of multistage compressors at part speed.

This vibration is not necessarily dangerous because penetration into the buffeting regime normally increases slowly. However, occasionally a threatening situation occurs when the buffeting shifts rapidly into true torsional coherent flutter. Typical responses to this condition are shown in Figure 3.

o Rotating Stall

Rotating stall, although often mentioned as a cause of blade vibration, is rarely a threat. Blade frequencies are usually too high for one-sector excitations, and multi-sector excitations provide only transient weak stimuli. Therefore, the required excitation-response conditions do not often exist for a rotating stall to cause blade vibration.

FAN FLUTTER TEST, A CASE HISTORY

Fan Rig Description

A stall flutter test was conducted on a single stage fan research rig. The fan rig combined moderate tip speed with a high pressure ratio, high flow rate per unit annulus area, and good efficiency. The 3.6 blade aspect ratio was aeroelastically aggressive even with a single partspan shroud. The stage, with its 81.8 cm (32.21 in.) rotor tip diameter, was large enough to permit good definition of the unsteady flow, blade deflections, and mode shapes during flutter.

The rig is schematically represented in Figure 4. Stage design parameters are listed in Table I, and rotor blade specifications, in Table II.

Blade Inspection

Blade leading and trailing edge angles were determined. The maximum, minimum, and average edge angles at fourteen span locations are compared with design values in Tables III and IV.

The second mode bending frequency of the isolated blades was considered to be representative of blade flutter frequencies. Therefore, the second mode frequency with clamped root and unrestrained shrouds was measured for each of the thirty-two rotor blades. The minimum measured frequency was 241 Hz; the maximum, 249 Hz. The blade positions in the rotor (Figure 5) were selected to minimize differences in frequency between adjacent blades and provide a smooth

frequency variation around the rotor.

Instrumentation and Data Acquisition System

Instrumentation provided full documentation of both steady-state and non-steady aerodynamics and for rotor structural behavior in and out of flutter. The location of instrumentation is shown in Figures 6 and 7; Table V lists the instrumentation and readout systems.

A fully computerized steady-state data acquisition system was used during testing. Data were transmitted to a computer located in the control room and then to an automatic data reduction computer which performed preliminary data reduction and returned the results to the control room for use directing the test program. Positioning and readout of all the traverse probes at the rotor inlet, rotor exit, and stator exit were controlled by the rig automatic traverse system.

Unsteady data recording systems for the Kulites, hot films, and strain gages recorded a common 1:1 speed signal, common time code, and a common strain gage signal. Before the start of testing, a common sine wave and white noise signal were recorded on all system channels in order to calibrate frequency and phase response.

Data from the blade mirror system were recorded on still photographs, movie film and video tape.

Steady-State Aerodynamic Instrumentation

Wedge probes measured total pressure, static pressure, and air angle. Combination probes measured total pressure, static pressure, air angle, and total temperature. Wall taps were used for measuring wall static pressures, and total pressure rakes were used for measuring stator exit total pressures.

The pressures sensed by the probes, fixed rakes, and static taps were measured by transducers and recorded in millivolts by the automatic data acquisition system. The accuracy of the pressure measurement was ± 0.1 percent of fullscale value. All temperatures were measured with Chromel-Alumel, type K thermocouples connected to reference junctions attached to uniform temperature reference blocks located in the test cell. Temperature elements were calibrated for Mach numbers over their full operating range. The thermocouple leads were calibrated for each temperature element. Overall rms temperature accuracy was estimated to be $\pm 0.56K$ ($1.0^{\circ}R$).

Compressor speed was measured using an impulse-type pickup, which counted time. The data were recorded through a frequency-to-DC converter. Accuracy was ± 1 rpm.

Airflow was measured with an orifice calibrated to International Standards Organization/BIS 5167 Standards. Accuracy of the airflow measurement was within one percent.

TABLE I

TS22 FAN STAGE DESIGN PARAMETERS

<u>Aerodynamic</u>	
Pressure ratio	
Rotor Stage	1.702
	1.67
Adiabatic Efficiency	
Rotor Stage	0.871
	0.838
Corrected Flow	95.56 kg/sec (210.67 lbm/sec)
Specific Flow	202.78 (kg/sec/m ²) (41.53 lbm/sec/ft ²)
<u>Geometric</u>	
Rotor Tip Diameter	0.8178m (2.7 ft)
Number of Blades	32
Hub Solidity	2.60
Tip Solidity	1.315
Hub/Tip Ratio (rotor leading edge)	0.32
Partspan Shroud Location (percent span from hub)	62

TABLE II

TS22 BLADE DESCRIPTION

Corrected Design Speed	11,042 rpm
Airfoil Series	Multiple Circular Arc
Aspect Ratio	3.6
Taper Ratio	1.5
Tip Speed	472.4 m/sec (1550 ft/sec)
Root Diameter	
Inlet	26.2 cm (10.3 in.)
Tip Diameter	
Inlet	81.7 cm (32.2 in.)
Exit	79.7 cm (31.4 in.)
Beta 1*(a)	
Root	54.999 deg
Tip	27.0399 deg
Beta 1* Suction Surface(b)	
Root	48.503 deg
Tip	25.398 deg
Chord Length	
Root	7.47 cm (2.94 in.)
Tip	10.42 cm (4.10 in.)

Notes:

(a) Beta 1* is the leading-edge metal angle, β^* , the angle between the tangent to the mean camber line and the meridional direction.

(b) Leading-edge metal angle based on suction surface.

Type of vibration	Characteristics	Wave form
Resonance	Multiple of engine order Individual blade response occasionally full stage response	Sinusoidal
Flutter	Not multiple of engine order Usually all blades at same frequency	Sinusoidal
Buffet	Not multiple of engine order Individual blade response usually first bending mode	Random amplitude

Figure 3. Identification of Blade Vibration

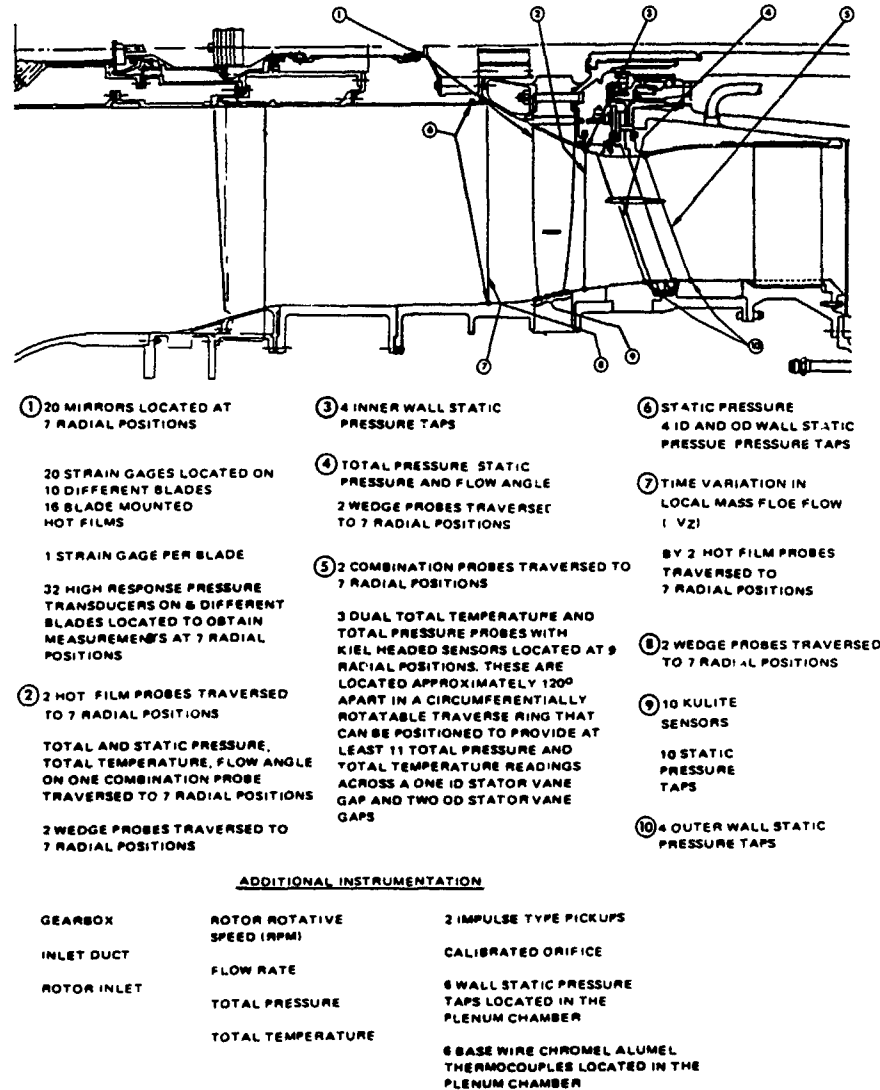


Figure 4. Schematic Diagram of TS22 Rig

TABLE III
LEADING EDGE ANGLE
BLADE INSPECTION RESULTS

<u>Percent (a) Span</u>	<u>Design</u>	<u>Minimum</u>	<u>Maximum</u>	<u>Average</u>	<u>Design Value Minus Average Value</u>
0.08	47054°	47040°	48012°	47050°	.0004°
0.12	46010°	45024°	4600°	45044°	.0026°
0.22	42054°	42016°	43012°	42042°	.0012°
0.32	40054°	39028°	39046°	39037°	.0030°
0.43	37058°	37018°	37040°	37029°	.0029°
0.52	36052°	3608°	3700°	36029°	.0023°
0.55	3704°	36050°	3700°	36055°	.009°
0.58	37010°	36010°	36028°	36018°	.0052°
0.62	35026°	350°	3508°	3502°	.0024°
0.66	34036°	33030°	34054°	34015°	.0021°
0.72	320°	31048°	31052°	3105°	.0055°
0.82	28050°	28024°	28044°	30029°	.0014°
0.92	25024°	2504°	25050°	25029°	-.0005°
0.99	23010°	22056°	2304°	22058°	.0012°

Note: (a) Percent Span From Hub

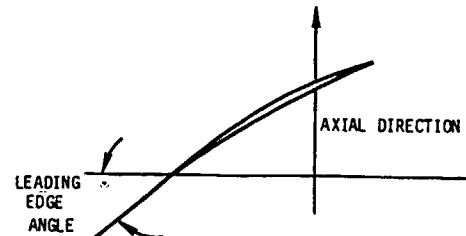
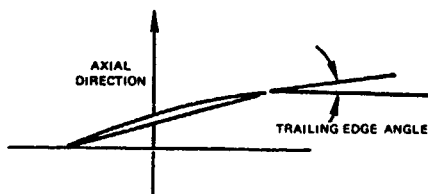


TABLE IV
TRAILING EDGE ANGLE
BLADE INSPECTION RESULTS

<u>Percent (a) Span</u>	<u>Design</u>	<u>Minimum</u>	<u>Maximum</u>	<u>Average</u>	<u>Design Value Minus Average Value</u>
0.08	96050°	95050°	9602°	95054°	.0056°
0.12	87010°	86014°	86042°	86028°	.0042°
0.22	69056°	6900°	70016°	69037°	.0029°
0.32	58028°	57058°	58034°	58014°	.0014°
0.42	4908°	48042°	4900°	48040°	.0018°
0.52	44034°	43044°	44040°	4407°	.0027°
0.55	43042°	43024°	43030°	43028°	.0014°
0.58	43014°	42022°	42046°	42037°	.0037°
0.62	4100°	4004°	40028°	40015°	.0048°
0.66	39042°	4904°	39052°	39025°	.0017°
0.72	35028°	35026°	35038°	35032°	.004°
0.82	30028°	30014°	30048°	30029°	.001°
0.92	24024°	24024°	250°	24041°	-.0017°
0.99	21058°	21038°	21056°	21044°	.0014°

Note: (a) Percent span from hub



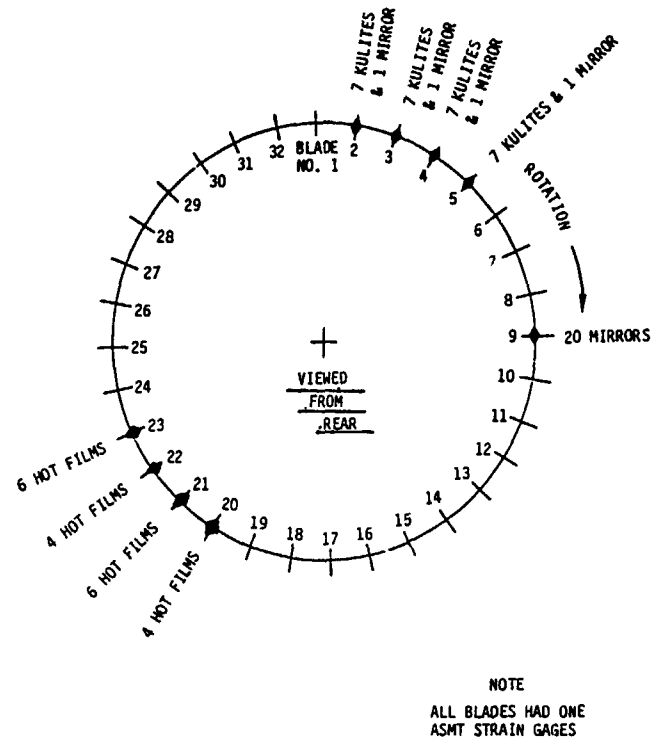


Figure 5. Circumferential Location of Blade Instrumentation

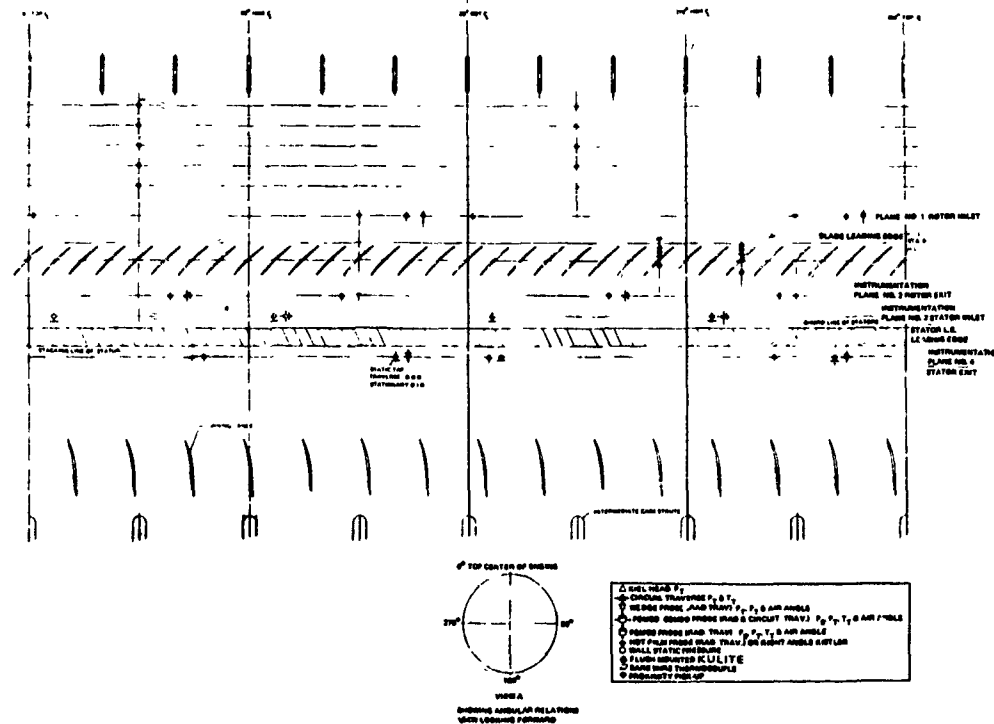


Figure 6. Circumferential Schematic View of T-22 Compressor Instrumentation

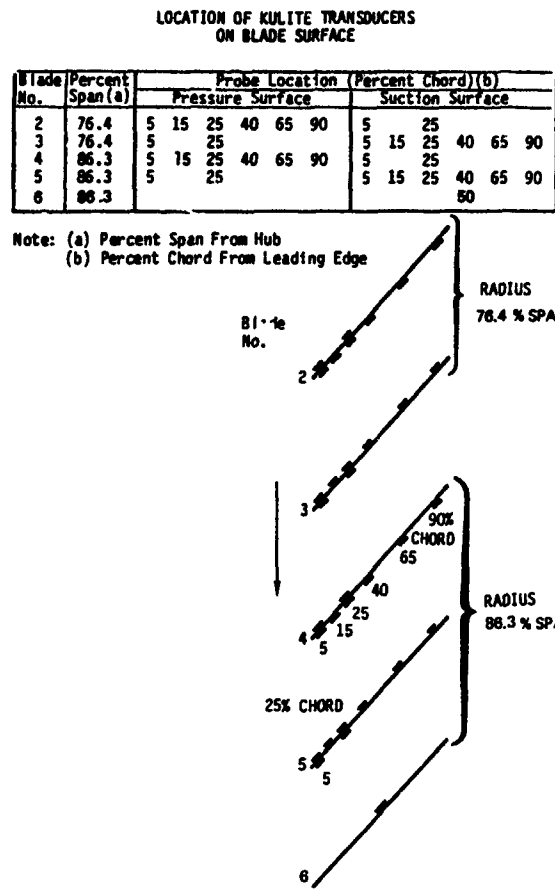


Figure 7. Installation Locations for Blade-Mounted Kulite Pressure Transducers

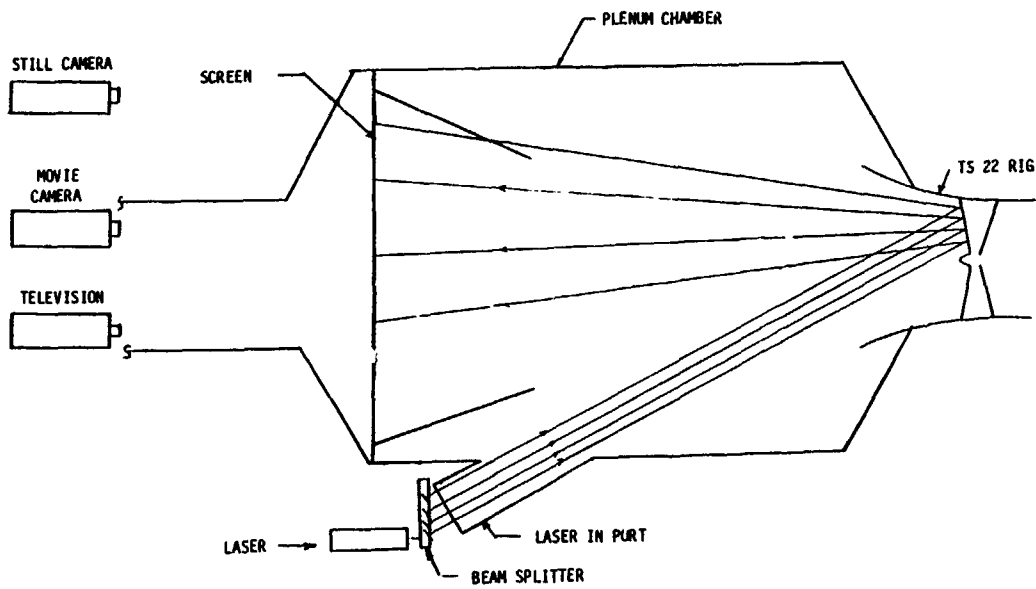


Figure 8. Schematic of TS22-X204 Laser Configuration

TABLE V
INSTRUMENTATION AND READOUT EQUIPMENT

Non-Steady Instruments Recorded

- 32 Strain gages
 - 24 Hot films - blade mounted
 - 4 Stationary hot film probes
 - 10 Wall Kulites
 - 32 Blade mounted Kulites
 - 102 Sensors
- Recorders
- 1 70 channel multiplex
 - 2 9 channels Sangamo
 - 3 11 channels Sangamo
 - 4 12 channels strain gage console
 - 5 4 channels strain gage console
 - 106 channels

Each of the five recorders had strain gage 3 in parallel as a common signal to permit time correlations between any of the 102 sensors.

TABLE VI
HIGH RESPONSE INSTRUMENTATION SPECIFICATIONS

Kulite - Model XCQL-8V-808	
Rated Pressure:	17.24 N/cm ² (25 lbf/in. ²)
Sensitivity:	3.8 x 10 ⁻⁴ mV/N/m ² (2.62 mV/lbf/in. ²)
Temperature Compensation:	278K to 422K (40°F to 300°F)
Acceleration Sensitivity:	
Traverse	0.00004% Full Scale Gage
Perpendicular:	0.0002% kHz
Natural Frequency:	230 kHz
Non-Linearity and Hysteresis:	±0.75% full scale maximum
Kulite - Model LQL5-080-255	
Rated Pressure:	17.24 N/cm ² (25 lbf/in. ²)
Sensitivity	3.8 x 10 ⁻⁴ mV/N/m ² (2.62 mV/lbf/in. ²)
Temperature Compensation:	278K to 422K (40°F to 300°F)
Acceleration Sensitivity:	
Transverse:	0.00008% Full Scale Gage per g
Perpendicular:	0.0004% Full Scale Gage per g
Natural Frequency:	125 kHz
Quartz Hot Film	
Thermo-systems model 1210-60	
0.0154 cm (0.006 in.) quartz rod with platinum sensor deposited 0.203 cm	
(0.080 in.) between posts	
Temperature coefficient of resistance = 0.0026 ohm/ohm-°K	
Frequency Response at 91.44 m/sec (300 ft/sec): 200 kHz	

TABLE VII
TS22 NASA FLUTTER TEST
TEST MATRIX

Run Number	Speed Code	Point Number	Unsteady Record	Percent Speed	Percent Design Flow	Rotor Pressure Ratio	Remarks
<u>Shakedown All Mirrors</u>							
001	70	01	20-27	70	72.8	1.228	Wide Open Discharge
--	--	--	28	70	--	--	Closing Discharge Valve, Transient into Flutter
001	70	05	43	70	66.9	1.2722	Check Point wide Open Discharge
--	--	--	64T	--	--	--	Transient
003	63	01	71	63	65.8	1.1776	Wide Open Discharge
003	63	03	76-84	63	53.4	1.2374	Stress Level Fluctuating, Shakedown Complete
<u>Performance All Mirrors</u>							
003	73	01	86-94	73	74.7	1.2687	Wide Open Discharge
003	73	02	100-108	73	60.0	1.3317	Maximum Flutter
<u>3 Watt Laser 4 Rows Mirrors (Above Shroud)</u>							
004	70	03	128-135	70	59.8	1.3004	70% Low Flutter Point
004	67	01	136-143	67	68.5	1.1890	Wide Open Discharge
004	75	01	176-183	75	75.3	1.2840	Wide Open Discharge
004	75	04	195-202	75	60.3	1.3369	Maximum Flutter
005	73	08	220	70	56.5	1.2978	
<u>All Mirrors 3 Watt Laser</u>							
007	66	01	239	66	54.5	1.26	Maximum Flutter
007	60	01	242-249	55	52.0	1.1530	Near Surge (Rotating Stall)
007	65	02	279-286	65	85.8	1.3792	Wide Open Discharge
--	--	--	287	--	--	--	Transient To Surge
007	65	05	288-295	65	75.1	1.4862	Near Surge

BLADE MIRROR LOCATION

BLADE NUMBER	PERCENT SPAN (a)	PERCENT CHORD (b)
2	86.3	50
3	86.3	50
4	66.0	50
5	66.0	25
9	95.2	5 25 50 70
	66.3	5 25 50 70
	76.4	5 25 50
	66.0	5 25
	55.0	5 25 50
	47.0	5 25
	38.0	5
	20.0	5

Note: (a) Percent Span From Hub TIP

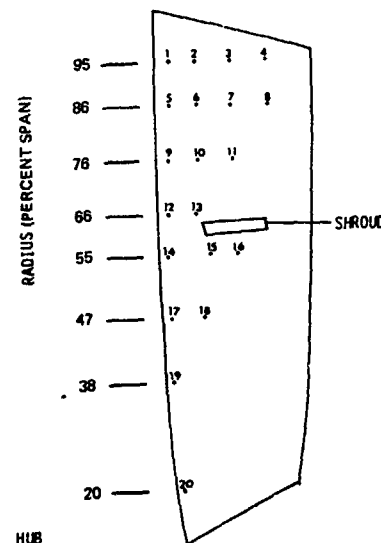


Figure 9. Mirror Installation Locations

Structural Instrumentation

Blade deflections were measured by a mirror system. Steady state and unsteady deflections were recorded using the techniques described in Stargardter (1977) and Stargardter (1979). One strain gage was placed on each blade to measure unsteady stresses and to the onset of flutter.

Optical Mirror System

Rotor blade deflections were measured both in and out of flutter. During stable operation these deflections were due to centrifugal and aerodynamic forces. When in flutter, vibrational mode shapes had to be determined. A patented system Stargardter (Patent 4080823) of optical mirrors and reflected laser light was used to measure rotor blade surface angle changes from which blade deflections were determined.

The optical mirror system consisted of an array of mirrors installed on the blades, a laser light source, and a readout and recording system, shown schematically in Figure 8. The laser light was split into several beams, each directed to the radial location of one of the mirrors. Variable beam splitters were adjusted to provide equal intensity of all the light beams. Each splitter was mounted on a five-axis adjustment system to facilitate accurate aiming of the light beams. The laser light and mirror system for measuring the instantaneous blade surface positions used a 604.5 cm (238.0 in.) optical path upstream of the test stage inlet. This path was long enough to provide light spot deflections to detect blade motion of 0.1 degree rotation in bending or torsion. As the instrumented blade rotated through the beams, the mirrors reflected the beams back to the readout system to separate points that had been selected to avoid pattern interference during flutter.

The mirrors were attached to the blades with epoxy cement. Additional details of the mirror system and mounting techniques are given in Stargardter (1977). Twenty mirrors were installed on one blade to provide full coverage of the blade in the region above the midspan shroud and along the leading edge below the shroud. Additional mirrors were mounted on other blades. The complete array of mirrors is shown in Figure 9. Circumferential locations of instrumented blades are shown in Figure 5.

Two windows were installed in the inlet section walls of the test facility: one to provide laser light entry; the other to provide a screen for receiving the reflected light beams. The interior of the inlet was frosted in selected locations to prevent secondary reflections from interfering with the laser beam signal.

The optical data were recorded with a movie camera, and video tape. The cameras were placed to receive the maximum scattered light when the beams were on the output window. A oscil-

loscope beneath the output window was photographed simultaneously with the light spots to correlate the time code and rotor speed signals with the mirror deflection.

Strain Gage on Blades

To ensure safety and to measure the response of all blades in flutter, one strain gage was installed on each rotor blade immediately above the shroud at the midchord location. This location was selected because it is sensitive to the second coupled mode expected in flutter. Signals from these gages were transmitted through a slipring and recorded on magnetic tape.

The frequency response of the strain gage data was limited by the bandwidth of the data recording system. The accuracy of any given strain gage was statistically determined to be approximately ± 5 percent, representing one standard deviation for typical data.

Unsteady Aerodynamic Instrumentation

The instrumentation for measuring unsteady aerodynamic effects included: 1) Kulites on the case over the rotor blade tips, 2) an array of Kulite high response pressure transducers on the rotor blades, 3) traversing hot-film probes at the inlet and exit locations of the rotor, and 4) an array of hot-film anemometers on the rotor blades.

The fan case Kulites and the hot-film probe outputs were recorded on two wide band FM tape recorders having a capacity to 40 kHz center frequencies and 40 kHz output filters. In addition to the data signals, 60:1 and 1:1 speed signals were recorded along with 1 kHz IRIG B Format Time Code Signal.

Data from all blade-mounted Kulites were recorded on a constant bandwidth frequency-division multiplex system, which provided a frequency response of 2 kHz with a resolution of 690 N/m^2 (14.4 lbf/ft^2) and an error no greater than $\pm 1 \text{ dB}$. Each of the 12 tracks on the system recorded six data signals plus a time code signal. One data channel on each track was used to record a reference strain-gage signal for phase determination. The hot-film anemometer data were also recorded on this multiplex system.

Case and Blade Mounted Kulites

Thirty-two Kulite, high-response pressure transducers were distributed over the pressure and suction surfaces of four blades (Figure 7) instrumented in pairs such that the instrumentation locations on the suction surface of one blade matched those on the pressure surface of the adjacent blade across the flow channel. Transducer specifications are shown in Table VI. The data from these transducers provided detailed mapping of the pressure fluctuations during flutter.

Signals from the rotating Kulite transducers were amplified before passing through the slipring to the record-

ing device by an amplifier package which rotated with the rotor assembly.

The rotating Kulite pressure transducers were calibrated both before and after mounting on the blade surfaces. The accuracy of the calibration facility was 0.1 percent full scale over a range of zero to 345 N/cm² (550 lbf/in.²).

Hot Film Anemometers

Radially traversing hot-film probes, two located at the inlet and exit of the rotor, respectively, measured fluctuations in inlet and exit flow during stable and flutter operation. The hot-film probes were calibrated at ten different flow velocities. Hot-film anemometers were located on the rotor blades to characterize the flow over the blade surfaces in and out of flutter and during transition from stable flow to flutter. The sensors were oriented with their length tangent to the case and perpendicular to the rig axis.

The frequency response of the probes and the associated data acquisition system was 40 kHz with a resolution of 1.0 percent of the mean flow velocity. The dynamic accuracy of the probes was 1 dB for axial Mach numbers below 0.4. The accuracy at higher Mach numbers was less because of a loss in sensor linearity caused by flow compressibility.

Twenty hot-film sensors were installed on four blades above the shroud at positions corresponding to those of the blade-mounted Kulite pressure transducers.

The film with its polyimide backing was mounted on a 0.041 cm (0.016 in.) Kapton film substrate to minimize heat transfer to the blades. The grid was oriented in the direction of flow with the leadwires routed off the trailing edge to avoid an additional turbulence source.

The sensors were calibrated to identify strain induced errors, but their nonlinear response and the difficulty in simulating the test situation in the laboratory made calibration to obtain quantitative data unrealistic. Therefore, their function was limited to qualitative characterization of the flutter. However, comparing the flutter response from one data point to another gave useful data on suction surface nonsteady flow characteristics. These sensors and associated data acquisition system provided a frequency response to 2 kHz.

Tests

Overall aerodynamic performance and high response aerodynamic and aeroelastic data were obtained at all operating points, and surge points were determined at several speeds between 63 and 85 percent of design.

Testing involved mapping the extent of the flutter boundary by taking data at operating conditions both in and out of flutter. Test points are listed in Table

VII. Flutter boundary was defined as the flow at which a vibratory stress of $\pm 2068 \text{ N/cm}^2$ ($\pm 3000 \text{ lbf/in.}^2$) was attained.

Data Reduction Procedures

Parameters calculated for all data points:

- o Overall stage performance
- o Blade element performance
- o Blade untwist and uncamber
- o Flutter frequency on all blades
- o Blade stress level on all blades
- o Vibratory mode
- o Pressure contours over the blade tips
- o Incidence angle at seven radial stations
- o Reduced velocity for seven radial stations

More extensive data reduction was performed for six of the data points. This reduction provided:

- o Analysis of the mirror data for amplitudes and phase relations on one blade correlated with strain gage signals and other non-steady signals to define the blade and stage mode shape and its relationship with the instantaneous aerodynamics.
- o Average steady pressure distribution at the wall for two blade passages.
- o Unsteady pressure distribution at the wall for two blade passages.
- o Amplitude and phase angles of all fluctuating signals from rotor-mounted sensors — both amplitude and phase angle were determined relative to the reference signals from the No. 3 blade.

The blade centrifugal untwist and uncamber resulting from centrifugal and gas bending loads were determined directly from the blade deflection data obtained with the optical mirror system. Images from twenty of the twenty-six blade mounted mirrors were used to determine blade movement.

The steady pressure contours indicated that flutter may alter the blade passage pressure distribution.

The contour maps of unsteady pressure amplitude revealed regions of high amplitudes near the leading edge, lower amplitudes near the trailing edge, and nodes near the midchord position.

Steady Deflections

Steady deflections were determined for speeds from 25 to 85 percent of design. Photographs taken at selected speeds in nine percent increments were used to determine steady blade movement.

The vertical position of each spot on each photograph was measured. Using the idle spot positions as a baseline, the movement of the spots for any speed was scaled. This movement on the screen was then converted to angle of twist and change in bending slope.

Unsteady Data Reduction

The reduction of the high frequency response data from the hot-film probes, wall-mounted Kulites, blade-mounted hot-film sensors, blade-mounted Kulites and blade-mounted strain gages was done by signal enhancement, signal phasing from rotating instruments, and signal phasing between rotating and stationary instruments.

Signal Enhancement

The signal enhancement, a time domain technique, extracted or enhanced particular frequency components from a broadband signal. The technique involved averaging numerous time segments of a broadband signal, the start of each segment being triggered by a reference signal. Each successive time segment was summed and averaged in a storage memory. The result was an enhancement or reinforcement of those components that were synchronous with the triggering signal and suppression of components that were not.

Phasing of Signals from Rotating Instrumentation

Phase information between the reference strain-gage signal on the No. 3 blade and all other strain-gage and rotating Kulite and hot-film signals was produced at the flutter frequency, using cross spectral density techniques. The analysis range for the task extended to 2 kHz. An 800 element spectral resolution was selected. To produce each final plot, 128 sweeps from the analyzer were averaged. The analysis was conducted from zero to 2000 Hz. The analyzer filter bandwidth yielded a spectral resolution of about 3.75 Hz. All resulting phase angles were corrected for errors introduced by the signal conditioning and recording systems.

Phasing of Signals Between Rotating and Stationary Instrumentation

Phasing between signals from the rotating blades and the stationary wall instrumentation was determined using a variation or extension of the cross-spectral density technique.

The vibration of the individual blades in a stage in flutter is fully defined by the sum of a finite series of circumferential harmonic waves where the number of component waves equals the number of blades, N , in the stage. The associated unsteady pressure, p , at a particular axial coordinate, x , varies with tangential coordinate, y , and time, t , is described by the sum of an infinite series of forward and backward rotating harmonic waves having all integer numbers of cycles around the circumference of the stage. This function is expressed in terms of sets of responses to individual

orders, m , of blade vibration where $1 \leq m \leq N$.

$$P_m(x, y, t) = \sum_{n=-\infty}^{\infty} P_{mn}(x) \exp\{i(\beta_{mn}y + \omega t)\} \quad (1)$$

where n , the number of full waves per intrablade passage, is added to the fractional number represented by m waves around the full circumference. ω is the flutter frequency common to all phenomena in the rotating system. The unsteady periodicity condition defines the wave number.

$$\beta_{mn} = \frac{\theta_m + 2\pi n}{s} \quad (2)$$

where the interblade phase angle,

$$\theta_m = \frac{2\pi x}{N} \quad (3)$$

$$\text{and blade spacing, } s = \frac{2\pi r}{N}$$

where r is radius

$$\text{hence } \beta_{mn} = \frac{m + Nn}{r}$$

In the stationary system, the coordinates x' and y' are related to their rotating counterparts by

$$\begin{aligned} x &= x' \\ y &= y' + \Omega rt \end{aligned} \quad (4)$$

where Ω is the rotor speed. Equation (1) then becomes

$$\begin{aligned} P_m(x', y', t) &= \\ \sum_{n=-\infty}^{\infty} P_{mn}(x') e^{i\beta_{mn}} (y' + (\Omega r + \omega/\beta_{mn})t) \end{aligned} \quad (5)$$

This is in the form of waves having wavelength $2\pi/\beta_{mn}$, moving at velocity $(\Omega r + \omega/\beta_{mn})$. The frequency was measured by a stationary probe is the product of the wave number mn and the wave velocity. Hence

$$\omega_s = \beta_{mn}\Omega r + \omega = \Omega n + \omega + \Omega m \quad (6)$$

where Ωm is a multiple of shaft speed, and Ωn is a positive or negative multiple of blade passing speed. Therefore, the single flutter frequency, ω , in the rotating system becomes a spectrum when detected by a stationary sensor. The observed frequencies, ω_s , are spaced at multiples of shaft speed, Ω . The index m identifies the associated harmonic wave component of blade vibration and the index n identifies the added number of waves within a passage between adjacent blades.

Because flutter was seen at many frequencies by the case-mounted Kulites, phase information could not be produced directly. Instead, an averaging technique was used. By averaging on of the

sampling rate to equal the rotational frequency, both the rotating and stationary transducer flutter signals were transformed to a new coordinate system in which a single flutter frequency existed for both sets of signals. Phasing of the signals in question could then be performed. The one-per-revolution speed pip was used as the sampling rate command.

Two different procedures were used to produce phase information. One procedure was to allow all the flutter components in the stationary signal to be aliased. The other procedure was to isolate individual spectral components of the flutter with a narrow filter before aliasing. This latter technique extracted a single nodal diameter signal plus its harmonics at multiples of the rotor speed. In all cases, the sampling command was properly conditioned to allow the rotor to be in a selected orientation before a data sample was taken. Corrections to the final phase angle were included for influences of all signal conditioning and the aliasing process.

Strain Gages

Each of the 32 blades was instrumented with one dynamic strain gage located near the maximum thickness point above shroud at 64 percent span. The stage flutter response was obtained from the strain-gage signals consisting of amplitude, frequency, and phase. The amplitude and frequency characteristics of the individual blades were obtained from power spectral density (PSD) plots from 0 to 2 kHz. Phases relative to the gage on the No. 3 blade were obtained by using the cross spectral analysis technique described above. The strains were of the form $S_v e^{i\omega t}$ where the complex number, S_v , representing the strain in the No. 3 blade, defined phase as well as amplitude. The S_v numbers, where $1 \leq v \leq N$, may be represented by the finite summation

$$S_v = \sum_{m=1}^N a_m e^{\frac{i2\pi mv}{N}} \quad (7)$$

where a_m is the amplitude of a series of patterns having numbers of lobes, m , where $1 \leq m \leq N$, rotating with respect to the disk at speed w/m . From the known amplitude and phase of each strain gage, S_v , the complex coefficients, a_m , of the series in Equation (7) may be determined by mathematical inversion to give the strength of the m th modal component or spatial harmonic and its phasing with respect to all other components.

The broadband and flutter frequency amplitudes for all strain gages and rotating Kulites were plotted versus time to help establish the stability of the data during the two-minute steady-state records. The plots were also used as a cross-check with the power spectral density curves to help identify possible errors in engineering unit conversions.

Mirrors

Blade mode shape was determined by analysis of the laser optics mirror data. Blade deflection amplitudes were determined from the mirror data. For the blades without mirrors, the deflection amplitudes and relative phases were determined through correlation of the strain gage data and the mirror data.

Typical still photographs of the mirror data in and out of flutter are shown in Figure 10. The difference in width of the same spot in the two images is proportional to the torsional amplitude and the difference in height is proportional to the axial component of the bending slope.

The 16mm film record of the reflected laser beams was digitized using a Spatial Data Systems Scanner. The measurement accuracy was better than ± 0.00254 cm (0.001 in.). The data were stored on magnetic tape for computer processing. A fast Fourier transform was used to convert the data from the time domain to the frequency domain. This procedure allowed the calculation of power spectral densities and cross-spectral densities to determine amplitude and phase angles for the different mirrors.

Case Mounted Kulites

The case-mounted Kulites were used to obtain nodal diameter patterns present in the rotor system during flutter, contour maps of the pressure distributions over the blade tips during stable operation, contour maps of the unsteady pressures during operation with flutter, and contours of the real and imaginary components of the unsteady pressure and relative phase during flutter.

The nodal diameter patterns in the rotor system during flutter operation were determined through Fourier analysis of the signals from the case-mounted Kulite pressure transducers.

The contour maps of pressure distributions over the blade tips were obtained from wall Kulite and wall static tap data. The one-per-revolution speed signal was the reference signal used in the enhancement. Data from 512 rotor revolutions were averaged to produce the final plots. The enhancements were timed to allow a selected group of blades to occupy a desired orientation relative to the wall Kulites. These enhancement techniques produced a signal-to-noise improvement factor of about 22.6

Plots of pressure versus time were digitized to obtain an array of pressures representing the variation from the mean at the specific axial location. A minimum of ten samples per blade gap was digitized. The time location of each pressure sample was translated into a rotating frame, with the leading edge of the No. 2 blades used as the zero reference. The wall mean static pressure for each axial location was added to the local variation to obtain the steady state pressures. The array of local static pressures was input into a contour plotting package, which linearly inter-

polates in space to find specified levels of pressure. The lines of constant pressure were normalized as percentages of the maximum local steady-state static pressure sampled, and contour maps of the constant percentages of pressure were machine plotted.

When the contour maps at the blade tips were plotted, the pressure field with respect to the blade leading edges was observed to be shifted about three degrees tangentially in the direction of rotation, corresponding to a time delay of about 30 microseconds. However, this shift, which was nearly independent of rotor speed, did not appear in the nonsteady pressure plots obtained from the same data. The shift is, therefore, believed to have resulted from the data reduction procedure used to obtain the steady-state plots. Although the source was not found, the location of the blades was evident from the plots. Each steady pressure plot in the report has been corrected to place the blades in the proper positions.

Blade-Mounted Kulites

Blade-mounted Kulites provided unsteady pressure amplitude and phase distribution for both the pressure and suction surfaces of the airfoil at two radial positions. Amplitudes were determined from the power spectral density for each signal over a frequency range of 0 to 2 kHz. The power spectral density data were confirmed by backup plots of amplitude against time during the two-minute test period. Cross-spectral density functions were used to determine the phasing of the pressure signals relative to the strain-gage signal from No. 3 blade.

Blade-Mounted Hot-Film Sensor

Blade-mounted hot-film sensors provided air velocity measurements on the blade suction and pressure surfaces at two radial positions. The flutter response from these sensors consisted of frequency, amplitude, and phase. Amplitude and frequency were obtained from the power spectral density for each signal over a frequency range of 0 to 2 kHz. The measured amplitude had a repeatability of ±20 percent, making it possible to relate the data from one point to another. The strain gage on the No. 3 blade was used as the reference for determining phase angle.

Blade-Work Interaction Calculation

The flutter characteristics of the test rotor and the types of data obtained allowed for an evaluation of a theory of energy transfer that takes place during flutter. The assumptions associated with this theory are:

- o Self-excited vibrations occur in a bladed rotor when the energy supplied by the air stream exceeds the energy dissipated through the structural damping associated with that mode.
- o The complex rotor vibration mode can be defined as a summation of simple circumferential harmonic responses

(i.e., Fourier decomposition).

- o The net aerodynamic energy of a mode is the algebraic sum of the aerodynamic energy associated with each harmonic response.
- o The susceptibility of a rotor vibration mode to flutter is a function of the stability of the individual harmonic responses.

An aerodynamic damping exists for each harmonic response. This damping is defined by the log decrement parameter, which is proportional to aerodynamic work divided by kinetic energy of the harmonic

$$\delta_{\text{aero}} = \frac{W_m}{E_m}$$

For positive values of the aerodynamic damping parameter, the energy flow is from the structure to the flow stream and in the reverse direction for negative values.

The aerodynamic work per cycle done by each of the individual harmonics is computed by integration.

$$W_m = \iint_0^{2\pi} \Delta P_m \frac{dh_m}{d(\omega t)} d(\omega t) db$$

where:

ΔP_m = pressure jump across the airfoil from the mth harmonic and is of the form $\Delta P_m = P_m(x, y_p, t) - P_m(x, y_s, t)$

where:

y_p and y_s are blade surface coordinates on the pressure and suction surfaces at axial location x

h_m = deflection normal to the airfoil surface of the mth harmonic

(ωt) = position angle during the vibration cycle

b = chordwise location

ω = flutter frequency

t = time

The pressure at the airfoil tip at any axial location is the summation of the distribution resulting from individual blade harmonic motions.

$$P(x, y, t) = \sum_{m=1}^N P_m(x, y, t,)$$

The pressure of each harmonic is defined by a Fourier series described above.

$$P_m(x, y, t) = \sum_{n=-\infty}^{\infty} P_{mn}(x) e^{i(\omega t + \beta_{mn} y)}$$

These pressure waves are translated into the stationary system using the relationships given above.

$$P_m(x', y', t) = \sum_{n=-\infty}^{\infty} P_{mn}(x') e^{i((\omega + (m+n)n)\Omega t + \theta_{mn})}$$

The values of P_{mn} at frequencies ($\omega_{mn} = (m+n)\Omega$) are obtained by processing the casing wall Kulite signals through a wave analyzer. The frequency band of the recorded data was 40 kHz which at the maximum rotational test speed of the rotor permitted ten harmonics (i.e., $-10 \leq n \leq +10$) to be determined.

Since no direct measurement was made of the mode shape at the blade tip, a NASTRAN analysis was used to predict the deflections.

The predicted mode shapes were scaled and phased in accordance with the measured strain components to define the tip motion, h_m , required to calculate the energy transfer in three dominant harmonic components. The NASTRAN mode shape energy levels were scaled in proportion with the strain component amplitude squared to determine the kinetic energy level of the individual harmonic responses.

The kinetic energy per cycle of the individual harmonics was computed by integration:

$$E_m = \frac{1}{2} \iint \mu \tau \omega^2 (f_m^2 + g_m^2 + h_m^2) d\theta db$$

where:

μ = airfoil material density
 τ = airfoil thickness

f_m , g_m , h_m = spatial components of deflection in the m th harmonic

t = spanwise location coordinate
 b = chordwise location coordinate
 ω = flutter frequency

PROGRAM RESULTS

The following conclusions are based on test results:

- o Deviations from uniform phase angle from blade-to-blade, previously attributed to insignificant anomalies in the data, are important, being indicative of a complex flutter characteristic.
- o Flutter alters the passage steady-pressure pattern only slightly, as shown in the steady-pressure contours.
- o Work input is concentrated near the leading edge, as shown in the unsteady-pressure contours.
- o Local supersonic flow is required in order for this flutter to occur.

Test Matrix

Tests were run over a range of corrected speeds from 54 to 85 percent of design. A transient was run at each of several speeds from wide-open-throttle to

surge, and the points of flutter initiation as well as the surge were determined. Data along the 70 percent speed line are shown in Figure 11.

The data points in Figure 11 were taken during a slow transient in which equilibrium conditions were not fully established. Furthermore, the pressure ratios were obtained from arithmetic averages of a limited number of rake readings. As noted on Figure 11, flutter was first indicated by the hot-film gages at about 67 percent of design flow, and the first indication of flutter on the strain gages appeared at about 63 percent of design flow. Surge occurred at about 56 percent of design flow.

A composite map for all test speeds is shown in Figure 12. These data were obtained at fully stabilized conditions and represent mass-weighted average performance. Flutter occurred at speeds between 63 and 75 percent of design. The flutter boundary shown in Figure 12 represents a blade vibratory stress level of $\pm 2068 \text{ N/cm}^2$ (3000 lbf/in.^2) as measured on the strain gage just above the shroud. Surge was encountered before flutter at speeds below 63 or above 75 percent of design.

Structural Deformations

Steady-state structural deformations of the blades were determined from data from the optical mirror system. Unsteady deformations during flutter were determined from the optical mirror system, the strain gages, and by analysis of the high response pressure data.

Steady-State Deformations

Local steady-state untwist at from 35 to 85 percent of the design speed are shown in Figure 13 for the 95 percent span location. Above 25 percent speed the amount of untwist varied as the square of the rotational speed, the midspan shroud was not seated, and the untwist varied in an unpredictable manner.

The distribution of untwist along the span at 73 percent speed is shown in Figure 14. Approximately equal amounts of untwist occurred above and below the shroud, which was at the 62 percent blade span and constrained untwist to near zero at this location. Untwist was essentially a function of speed only. The effects of gas loading were negligible. As shown in Figure 15, the variation of untwist with flow at 75 percent speed was less than 0.1 degree for a flow change from 70 to 59 kg/sec (155 to 130 lbm/sec), corresponding to a blade tip D-factor increase of 0.1764.

Measured untwist as a function of chordal position is shown in Figure 16 for 73 percent speed. Uncambering was significant at all stations above the shroud, exceeding 0.3 degrees near the blade tip.

Figure 17 shows both the measured untwist and predicted by NASTRAN analysis for rotor speed at 75 percent speed. The measured uncambering at the

tip was slightly higher than predicted. However, the deformations in this region, where the airfoil was very thin, were sensitive to the actual airfoil thickness, and slight variations within specified tolerance might have been sufficient to cause the observed discrepancies.

Unsteady Deformations

Previous to this program, fan flutter had been visualized as a sinusoidal, circularly traveling wave superimposed on the rotor, forming a single multinodal pattern, each rotor blade deflecting sinusoidally in sequence as the wave traveled around the rotor, Bendat and Piersall (1971).

Such a wave was characterized by concentric ring nodes and traveling nodal diameters or diametral lines of zero deflection. Figure 18 shows such a system with two ring nodes and three nodal diameters. This pattern is referred to as a vibration in the second mode with three nodal diameters. On a rotating stage, the radial lines travel either forward or backward, and adjacent blades experience a relative time delay or phase difference (interblade phase angle) as the wave passes. With such a concept, all blades are assumed to flutter at the same frequency and amplitude, with uniform phase angles between adjacent blades.

The results of the current program revealed a different picture: All blades fluttered at the same frequency, but not at the same amplitude and interblade phase angles were not equal. Typical amplitudes and phase angles observed during the program are shown in Figures 19 and 20, respectively. These data were obtained from the strain-gage measurements. Amplitudes in Figure 19 are expressed in terms of measured stress. The patterns shown represent a family of spatial harmonics described by the superposition of a number of rotating nodal diameter patterns, each characterized by a different number of nodal diameters with different but uniform amplitudes and different but uniform phase indexing, with each pattern rotating at a speed that results in the same flutter frequency.

The detailed definition of the amplitude and phase for each nodal diameter pattern was determined from wall Kulite data. A result of this analysis is presented in Table VIII. As shown in the table the fifth nodal diameter pattern had the strongest signal at 67 percent speed. The seventh nodal diameter pattern was strongest at 73 percent speed, and the eighth was slightly stronger than the others at 75 percent speed.

To further study the complex mode shapes of the rotor and blading, stability calculations were made for the fifth, seventh, and ninth nodal patterns at 70 percent design speed. These patterns represented strong signals and one weaker signal. The results of these calculations are given in Table IX in terms of the logarithmic decrement

which is 2 times the ratio of available damping to critical damping. Since this number represents the percentage rise or decay of the signal, a negative of the logarithmic decrement represents an unstable or flutter condition. Complex pressures used in the stability calculations are listed in Table IX and plotted in Figures 21, 22 and 23 for the upper and lower surfaces of the airfoil. The chordwise position of the pressures is the same as for the wall mounted Kulites from which the data was obtained.

Table IX shows that the fifth harmonic was the principal source of instability at 70 percent speed. The seventh harmonic was marginally unstable; the ninth, marginally stable. The results suggest that the effect of asymmetries, or "mistuning," on the system in flutter is to couple secondary modes into the instability. This is an important result, clearly demonstrating that any future flutter analysis that is to be correlated against test data for a mistuned bladed disk system must be capable of handling several spatial harmonics.

The present analysis is not capable of explaining the mechanism that determines what patterns will occur or what their relative indexing will be. However, the mechanism probably relates to the mistuning of the stage, which results from small dimensional differences among these airfoils. These airfoils had been deliberately grouped by frequency when the rotor was assembled, see Figure 24. And it may be significant that the group of airfoils with the highest flutter amplitudes were those that individually had natural vibratory frequencies equal to the average frequency for the blade set. It may also be significant that only forward traveling waves (traveling in the same direction as the rotor) were observed.

Pressure Distributions

Increasing rotor speed on a given operating line resulted in a strengthening of the expansion waves and normal shock and a rearward shift of the shock. Moving up a speed line to higher loading and incidence shifted the shock forwards towards the leading edge. Crossing the flutter boundary produced little change although the normal shock appeared to have spread, which is probably indicative of shock oscillation.

Steady-State Pressure Distributions

At 63 percent outside of flutter, data from the case-mounted Kulites showed that high loading occurred at the leading edge and that the flow was subsonic (Figure 25). Moving up to a high operating line into flutter is shown in Figure 26.

At 67 percent speed on the low operating line, expansion waves occurred behind the leading edge, culminating in a shock at about 15 percent chord (Figure 27). At the flutter boundary at 67% speed, the shock appeared to be a gradual compression, which may be indicative of an oscillating shock (Figure 28).

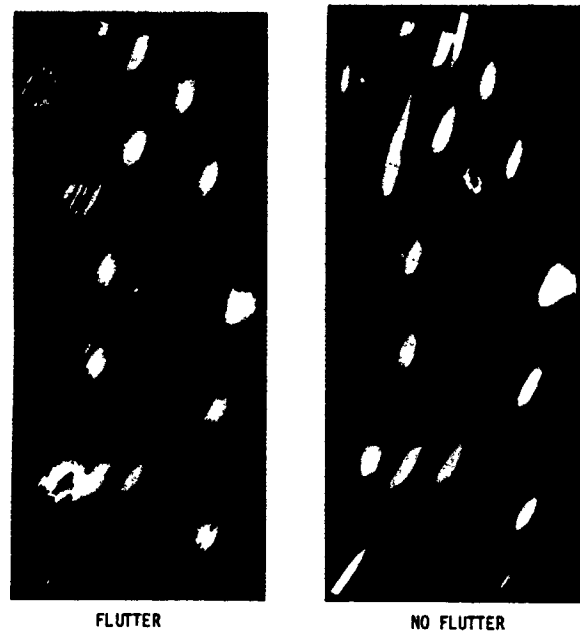


Figure 10. Typical Laser Mirror Results for Operation at 67 Percent Speed In and Out of Flutter

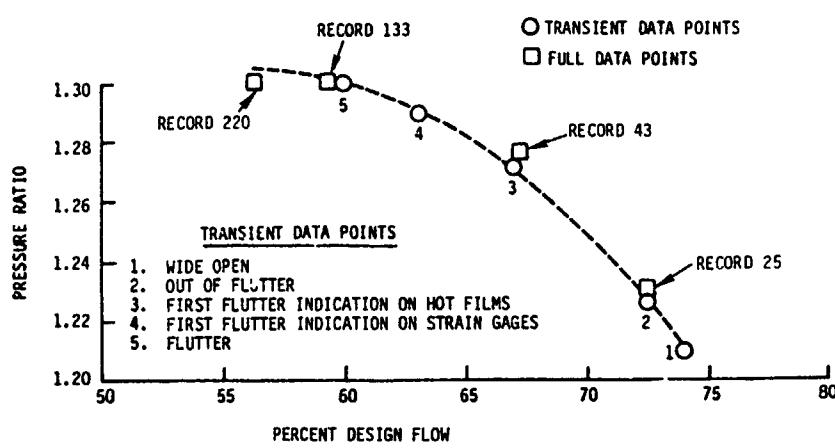


Figure 11. Identification of Data Points at 70 Percent Speed, Including Transient from Open Discharge Into Surge

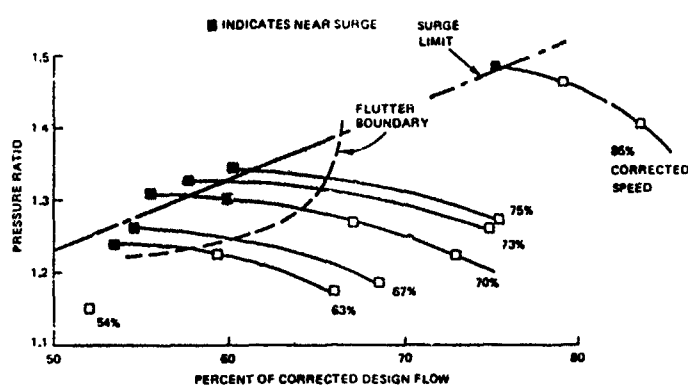


Figure 12. TS22 Performance Map Showing Test Points in Relationship to Flutter Boundary

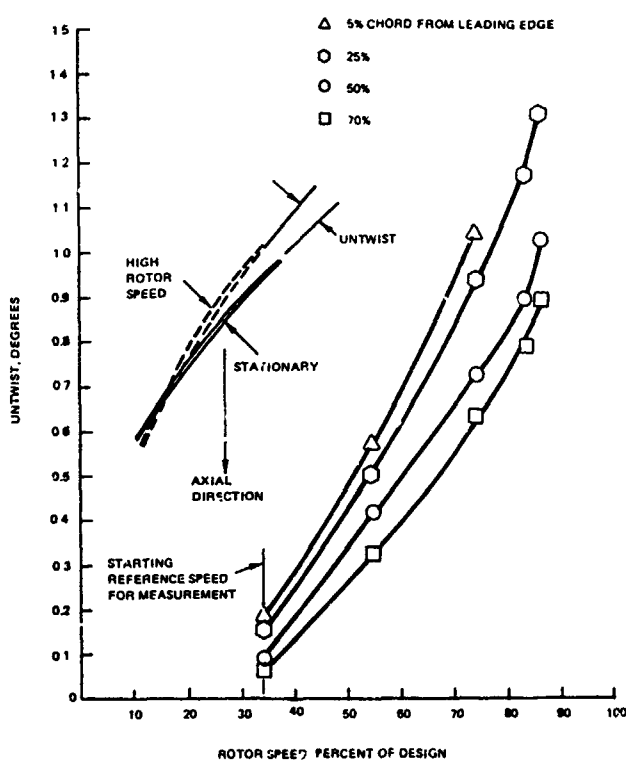


Figure 13. Measured Untwist for TS22 Fan Blade as a Function of Rotor Speed at 95 Percent Span

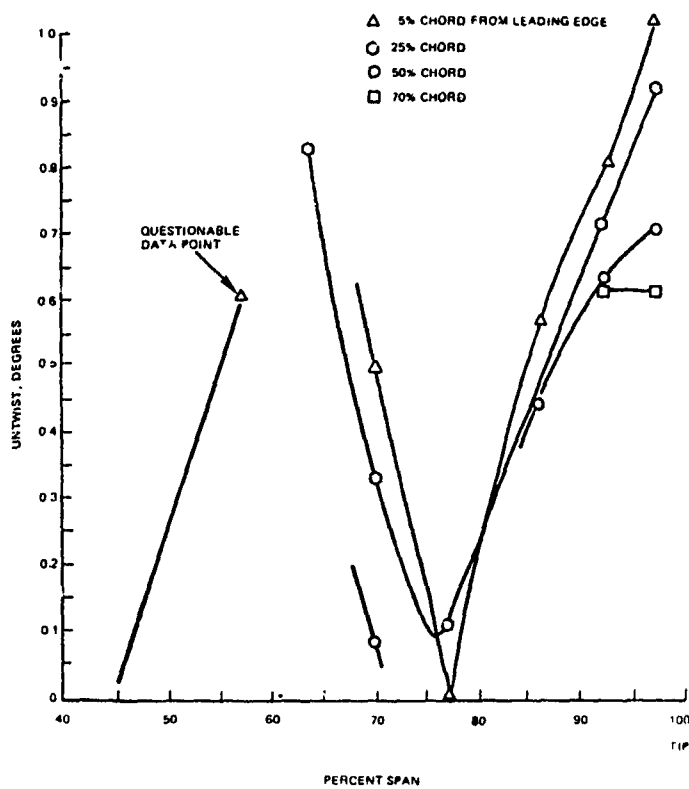


Figure 14. Measured Untwist for TS22 Fan Blade at 73 Percent Speed Relative to Untwist at 25.4 Percent Speed

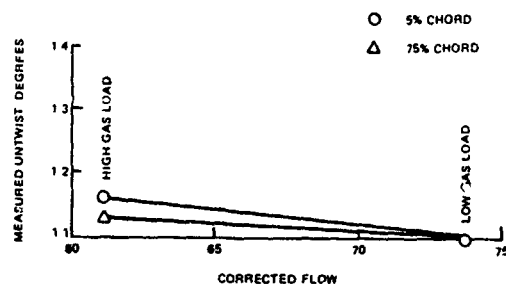


Figure 15. Measured Untwist for TS22 Fan Blade as a Function of Flow Rate at 75 Percent Speed

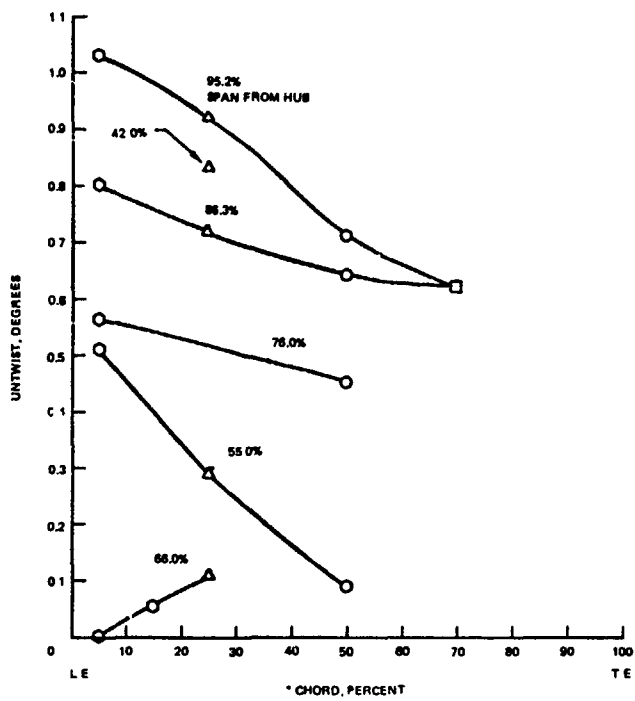


Figure 16. Measured Untwist for TS22 Fan Blade as a Function of Chord at 73 Percent Speed

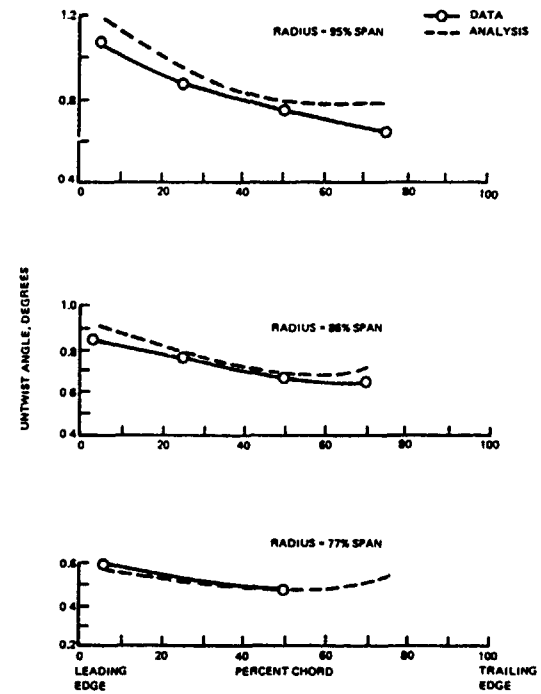


Figure 17. Measured Untwist for TS22 and Predicted by NASTRAN Analysis for Rotor Speed at 75 Percent Speed

TABLE VIII

UNSTEADY WALL PRESSURE AMPLITUDES FOR INDIVIDUAL
NODAL DIAMETER PATTERNS FUNDAMENTAL MODES ONLY
(NO HARMONICS)

Nodal Diameters	Relative Power Spectral Density									
	-55.4	-15.1	-3.8	9.4	22.2	34.6	47.5	73.4	99.3	141.4
<u>67 Percent Speed</u>										
2										
3										
4										
5										
6										
7										
8										
9										
10										
<u>73 Percent Speed</u>										
2										
3										
4										
5	9	25								
6	10	32								
7	24	84	96	68	165	240	180	340	270	280
8	35	77		130	165	150	140	160	150	120
9				110		88	75	44	35	38
10	26				125		80	34	31	24
<u>75 Percent Speed</u>										
2										
3										
4										
5					50	100	55	39	45	60
6					50	80	78	70	70	100
7						120	70	50	45	45
8						140	110	78	55	75
9						120	85	45	35	35
10										

TABLE IX

COMPUTED DAMPING IN DOMINANT HARMONICS
AT 70 PERCENT SPEED

Harmonic	Log Decrement
5	-0.012
7	-0.001
9	+0.002

Complex pressures used in damping calculation normalized to 1600 N/m²
(0.232 lbf/in.²).

Percent Chord	Upper Real	Upper Imaginary	Lower Real	Lower Imaginary	
-3.4	0.039	-0.091	0.022	-0.022	5 Nodal Diameters
9.4	0.573	-0.681	0.056	-0.134	
22.2	0.504	-1.000	-0.254	-0.060	
34.6	0.095	-0.125	-0.059	-0.060	
47.5	0.030	-0.246	-0.086	-0.142	
73.4	0.138	-0.086	-0.108	-0.086	
99.3	0.198	-0.026	-0.228	-0.039	
-3.4	-0.065	0.017	0	0.043	7 Nodal Diameters
9.4	-0.250	0.190	0.039	0.026	
22.2	-0.177	0.384	-0.091	0.241	
34.6	-0.031	0.056	-0.121	0.052	
47.5	-0.095	0.060	-0.129	0.052	
73.4	-0.129	-0.004	-0.112	0.004	
99.3	-0.112	-0.052	-0.147	-0.043	
-3.4	-0.112	-0.099	0.009	-0.009	9 Nodal Diameters
9.4	-0.030	-0.259	-0.069	-0.134	
22.2	-0.181	-0.134	-0.129	-0.091	
34.6	0.017	-0.034	-0.043	-0.043	
47.5	-0.030	-0.172	-0.052	-0.164	
73.4	-0.043	0.056	-0.017	0.060	
99.3	0.043	-0.194	0.022	-0.233	

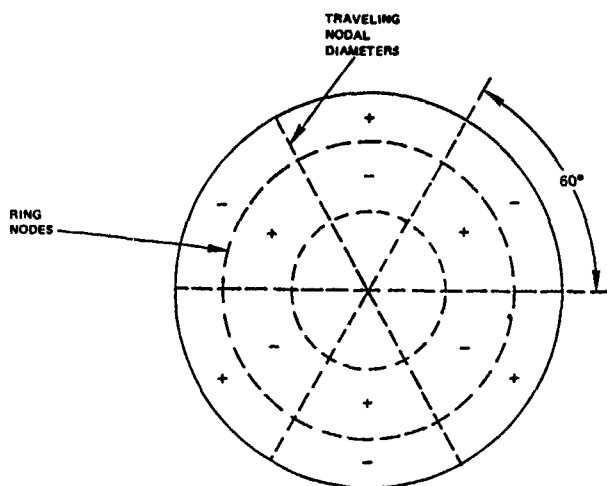


Figure 18. Three Nodal Diameter Pattern Second Mode - Previous Theory Predicted the Presence of only one Nodal Diameter Pattern at Any Time

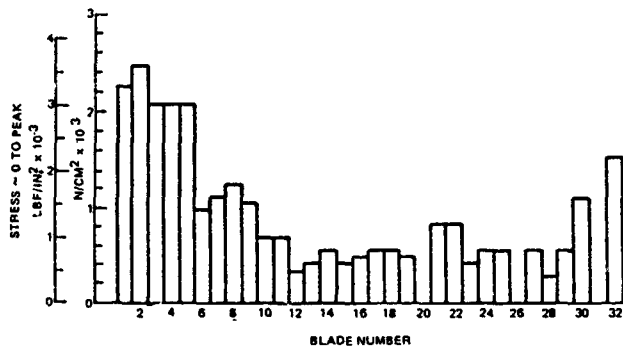


Figure 19. Blade Flutter Amplitude for TS22 Rotor at 67 Percent Speed from Strain-Gage Measurements

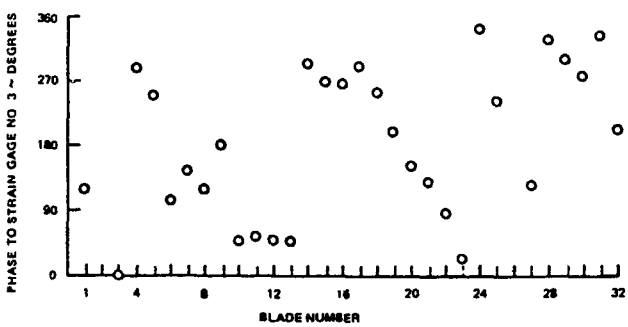


Figure 20. Blade Flutter Phase Angles for TS22 Rotor at 67 Percent Speed from Strain-Gage Measurements

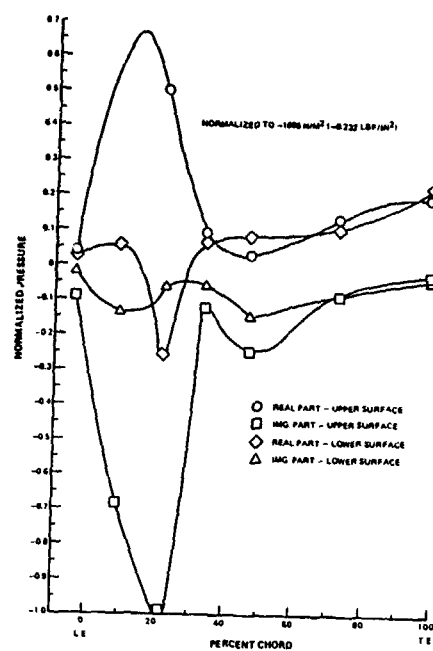


Figure 21. Complex Pressures Used in Damping Calculation,
Five Nodal Diameters

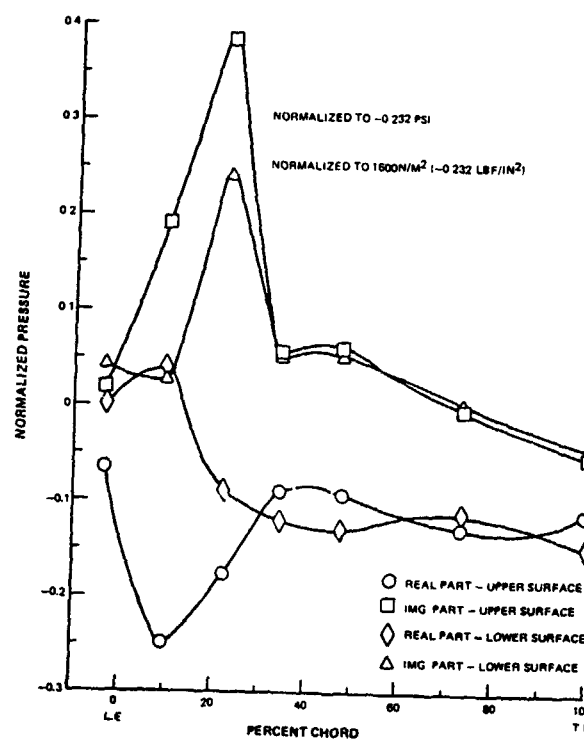


Figure 22. Complex Pressures Used in Damping Calculations,
Seven Nodal Diameters

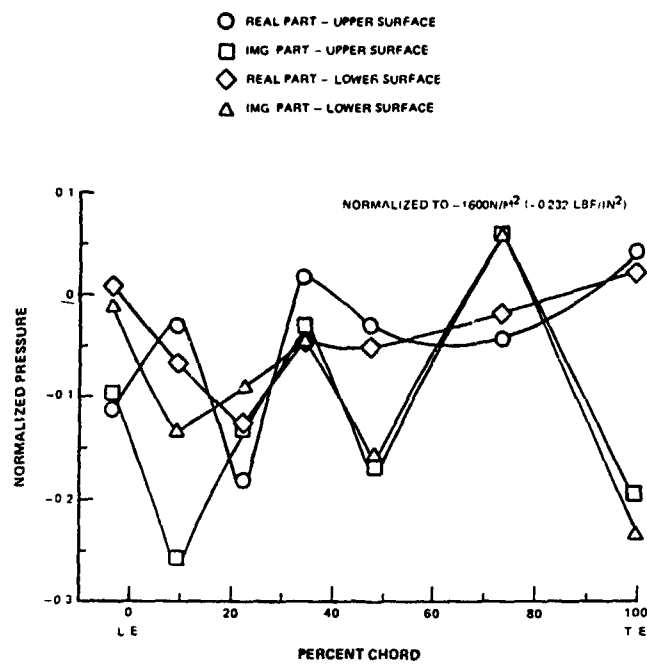


Figure 23. Complex Pressures Used in Damping Calculations,
Nine Nodal Diameters

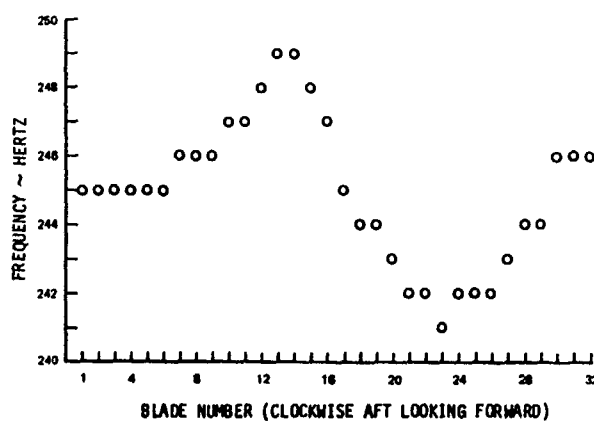


Figure 24. Distribution of Natural Second Mode Vibration Frequencies of Blades in Assembled Rotor

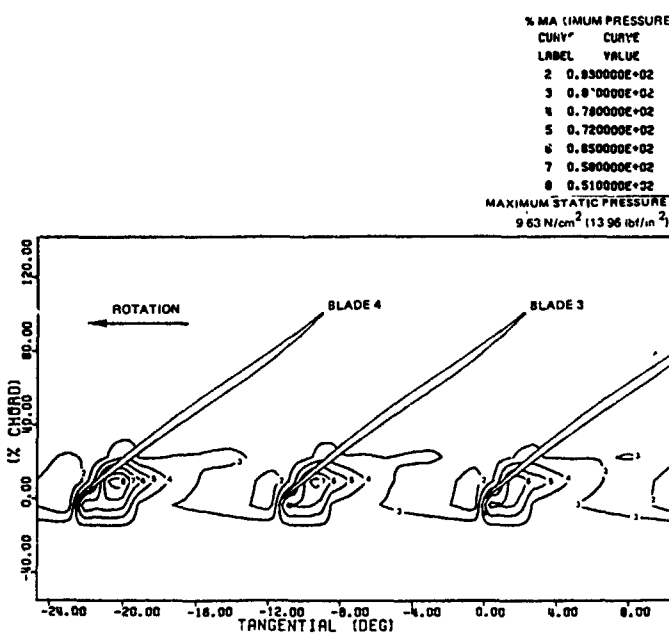


Figure 25. Steady-State Pressure Contours at Blade Tip at 63 Percent Speed Outside of Flutter on a Low Operating Line

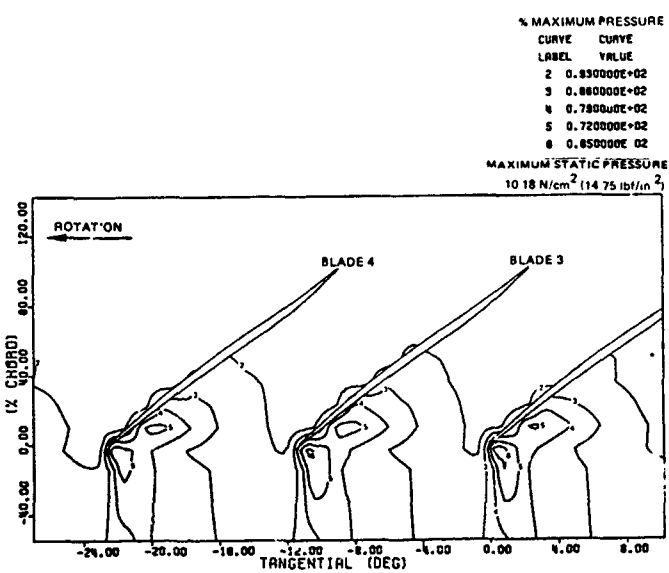


Figure 26. Steady-State Pressure Contours at Blade Tip at 63 Percent Speed Inside of Flutter on a High Operating Line

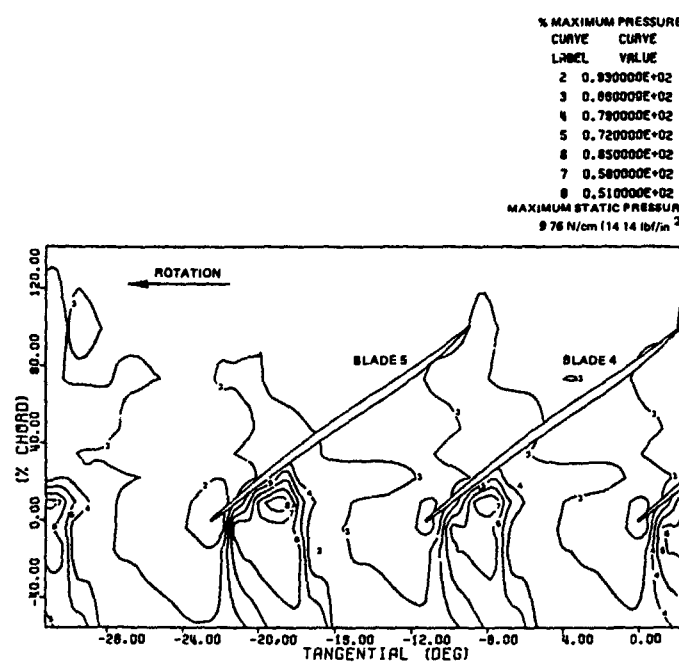


Figure 27. Steady-State Pressure Contours at Blade Tip at 67 Percent Speed Outside of Flutter on a Low Operating Line

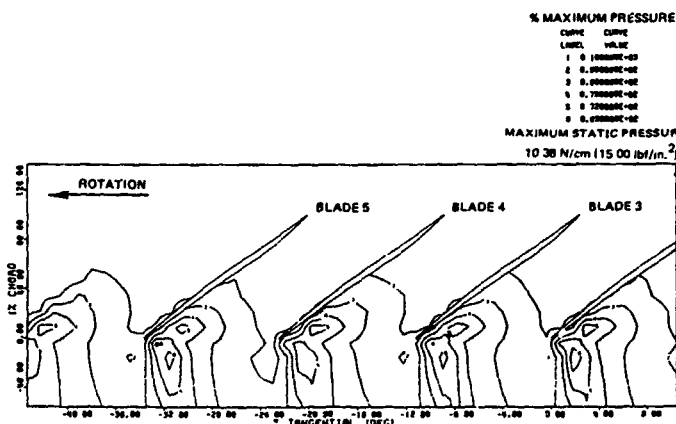


Figure 28. Steady-State Pressure Contours at Blade Tip at 67 Percent Speed Inside of Flutter on a High Operating Line

At 70 percent speed outside the flutter boundary, supersonic Mach number expansion at the leading edge was more clearly evident, and the normal shock moved rearward to the 20 percent chord position (Figure 29). At the flutter boundary, the shock moved forward, very close to the leading edge (Figure 30). Near surge the leading edge expansions appeared to be weaker, but the passage shock appeared stronger (Figure 31).

At 73 percent speed on a low operating line the shock moved further rearward to about the 30 percent chord position. Moving into flutter the principal loading remained at the leading edge with the data showing considerable smearing of the normal shock. Essentially identical trends occurred at 75 percent speed.

At 85 percent speed, surge occurred before flutter. On the low operating line significant reacceleration occurred behind the shock and the compression process was far from optimum, with negative lift occurring on the aft portion of the blade. Moving up the operating line resulted in a high Mach number with strong leading edge expansion and a strong detached bow shock. Operating near surge produced little change in this pattern.

Unsteady Pressure Distributions

Unsteady pressure data were reduced to contours of unsteady pressure amplitude and contours of the real and imaginary components of the unsteady pressure to provide relative phasing information. A typical plot is presented in Figure 32. To interpret these plots it should be noted that the real and imaginary components represent the instantaneous unsteady pressures at two time phases separated by 90 degrees. Hence, the square root of the sum of the squares of the real and imaginary amplitudes shown in Figures 33 and 34 is equal to the amplitudes shown in Figure 32, and the relative phase angle of the unsteady pressure is equal to the arctangent of the ratio of the real and imaginary components.

The data showed high unsteady pressures near the leading edge (back to approximately the 25 percent chord position), relatively low values near the trailing edge, and minimum amplitude near midchord. Similar trends were evident in the blade unsteady surface pressures measured by the blade-mounted Kulite (see Figure 35). The arrow lengths in this plot represent unsteady amplitudes and the directions represent phase angle as referenced to the strain-gage signal from the No. 3 blade. As shown, significant unsteady pressure amplitudes were confined to the leading edge portion of the airfoils.

These results clearly indicate that the major portion of the action was concentrated in the first quarter of the airfoil, implying that future flutter research should concentrate on the aerodynamics near the leading edge.

Velocity Fluctuations

Upstream and Downstream Velocity Fluctuations

Enhanced wave forms from the hot-film probes ahead of and behind the rotor are shown in Figure 36 for two test points at 73 percent speed: One at wide open discharge, the other in the flutter region. Because these signals were not calibrated for amplitude, the magnitudes of fluctuation are not known. For the open discharge condition, the inlet signal at the blade tip showed a velocity fluctuation of blade passing frequency that was caused by the passage of expansion and shock waves emanating from the blades. There was no defined pattern at the inlet near the shroud and at the blade root where the relative inlet velocity was subsonic. At the rotor exit, a well defined blade wake pattern existed for all three radial positions. The inlet probe patterns in flutter were similar to those for the nonflutter condition. Behind the rotor at the hub, the pattern was also similar to that for wide open throttle. However, at the near shroud and tip exit position, the blade wakes were not as well defined as for the nonflutter condition. The tip pattern had some random fluctuations at other than blade passing frequency, but did not show a significant fluctuation at flutter frequency.

Blade Surface Unsteady Velocities

Unsteady velocities and phase angles were determined from the hot-film gages mounted on the rotor blades. Data for a flutter condition at 67 percent speed are shown on Figure 37. The arrow length in this plot represents the amplitude of the unsteady velocity relative to the maximum fluctuation observed for that test point. The direction of the arrow indicates the phase angle referenced to the strain-gage signal from the No. 3 blade. The major fluctuations of velocity occurred on the forward part of the airfoil, but some significant fluctuations also occurred at midchord and near the trailing edge.

Reduced Velocity Versus Incidence Angle

Empirical correlations of reduced velocity versus incidence angle have been used extensively as a stall flutter criterion. The range of design types over which any specific correlation will accurately predict flutter boundaries, however, is questionable. Existing correlations were based on measured air angles, but blade metal angles were usually taken as the calculated metal angle at design speed. In this program, actual metal angles were measured. Figure 38 presents a plot of reduced velocity versus measured incidence angle. Incidence angles were based on the blade leading-edge mean-line metal angle. The reduced velocity parameter, v/bw , is the ratio of the relative inlet velocity, V_1' , to the product of the blade half-chord, b , and the rotational flutter frequency, w , in radians per second.

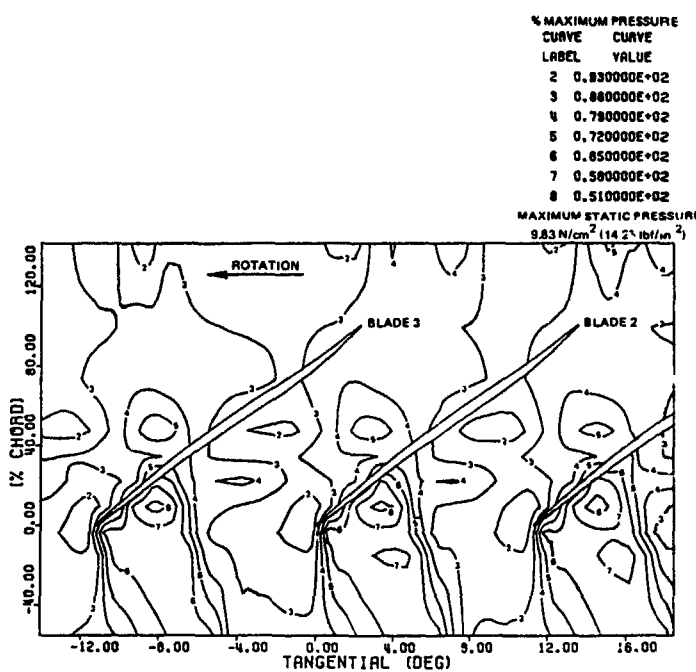


Figure 29. Steady-State Pressure Contours at Blade Tip at 70 Percent Speed Outside of Flutter on a Low Operating Line

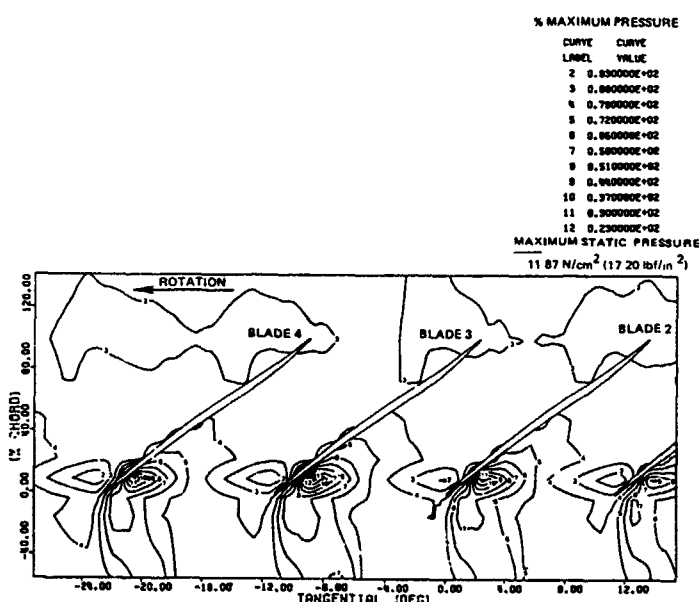


Figure 30. Steady-State Pressure Contours at Blade Tip at 70 Percent Speed Inside of Flutter on a High Operating Line

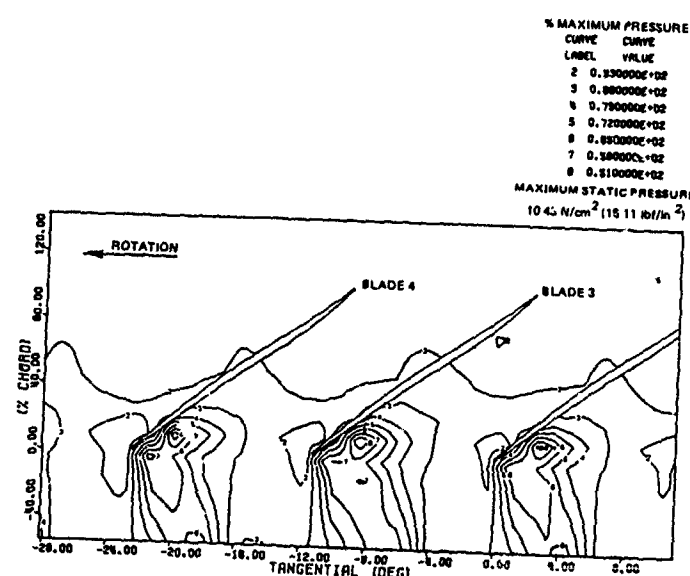


Figure 31. Steady-State Pressure Contours at Blade Tip
 at 70 Percent Speed Near Surge

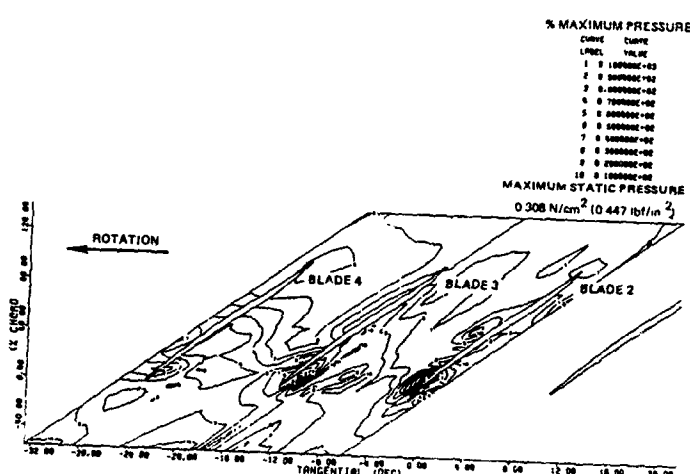


Figure 32. Unsteady Pressure Amplitude Contours for
 TS22 Rotor in Flutter at 73 Percent Speed

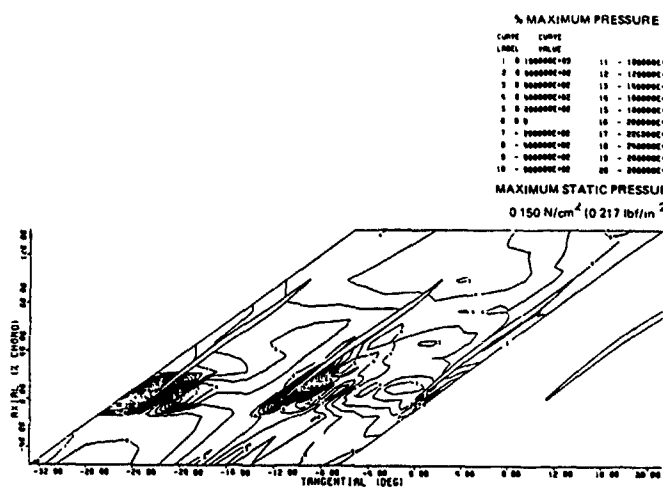


Figure 33. Real Component of Unsteady Pressure in Flutter at 73 Percent Speed

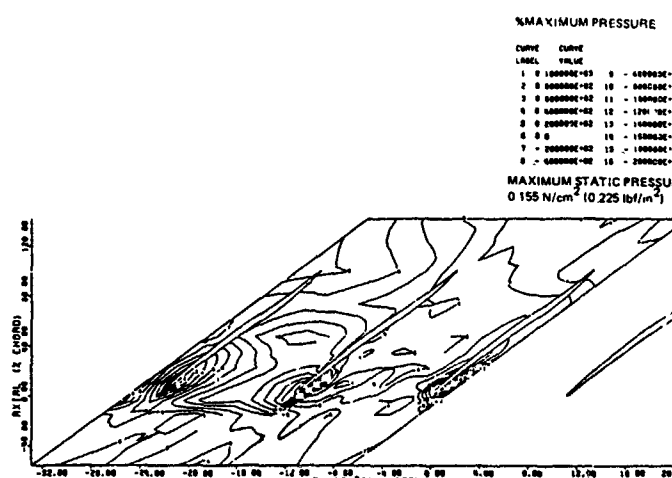


Figure 34. Imaginary Component of Unsteady Pressure in Flutter at 73 Percent Speed

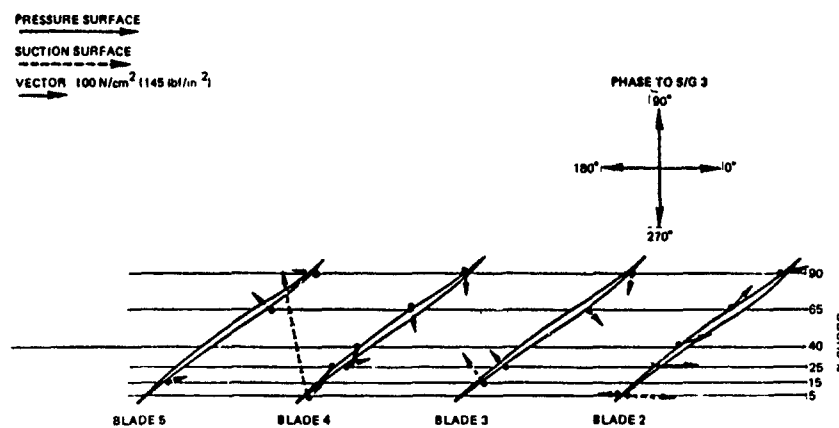


Figure 35. Blade Mounted Kulite Unsteady Pressure Amplitude and Phase Obtained in Flutter at 67 Percent Speed

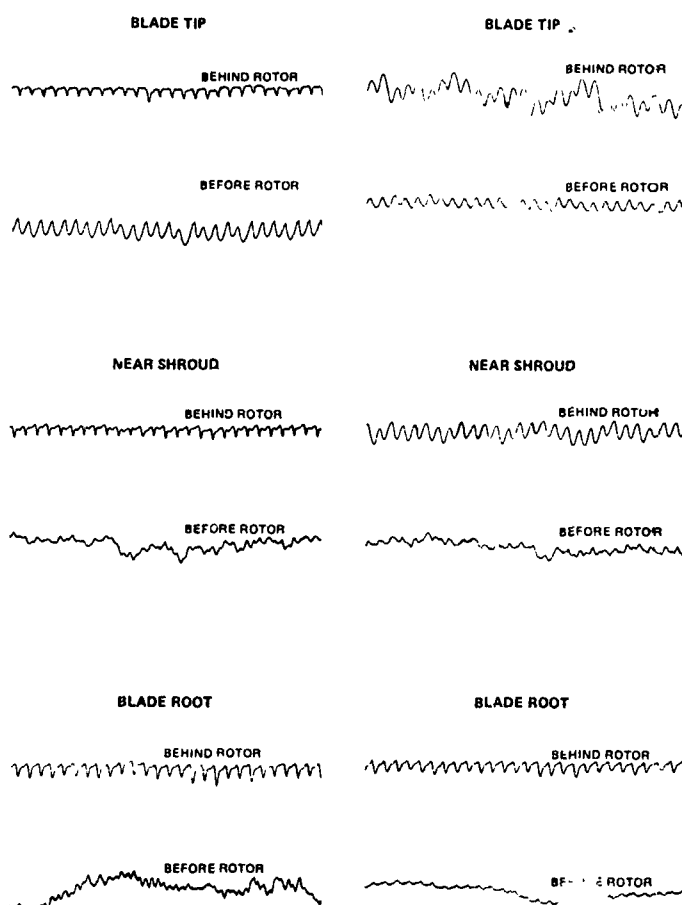


Figure 36. Signal Enhanced Wave Forms of Hot Film Probes at 73 Percent Speed (Noncalibrated Amplitudes)

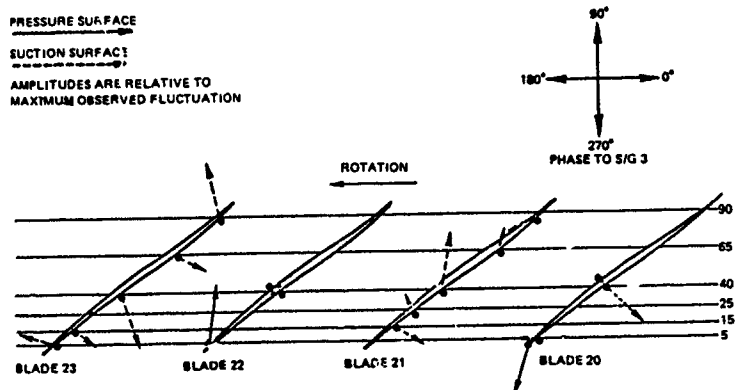


Figure 37. Blade Mounted Hot Film Unsteady Velocity Amplitude and Phase Obtained in Flutter at 67 Percent Speed

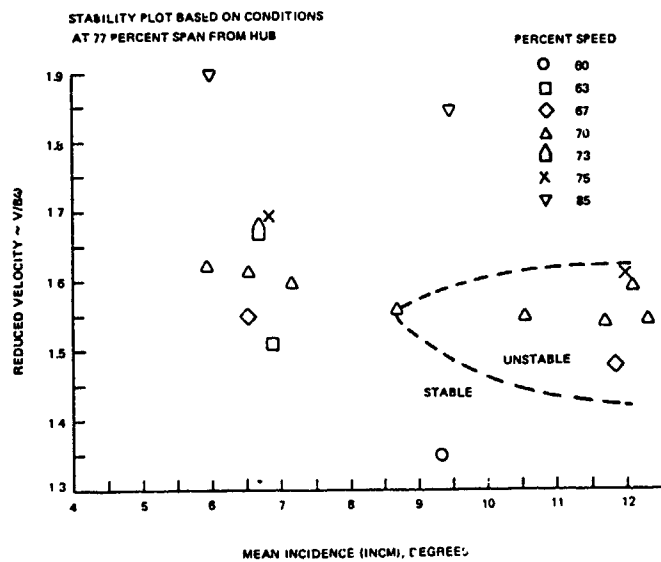


Figure 38. Observed TS22 Flutter Boundary Correlation of Reduced Velocity as a Function of Incidence

Figure 38 shows that flutter occurred at high incidence angles only over a limited range of reduced velocity values, with flutter-free operation being obtained at reduced velocities both above and below those at which flutter was achieved for a given incidence. A possible explanation is that locally supersonic flow may be required for flutter and that this was not achieved at low rotor speeds and velocity ratios, even at high incidence. At very high speeds and velocity ratios, the incidence was too low even at surge to support flutter.

SUMMARY

This chapter describes the procedure of conducting a fan flutter test. The experience of an actual test is used as an example. Test preparation includes a test plan, selection of blades, and description of measurement instrumenta-

tion. Test execution includes the testing procedure as well as data acquisition, reduction and analysis. Safety procedures are outlined. Included is a description of the on-test appearance of several aeroelastic phenomena and an assessment of corrective actions to prevent fatigue failures due to over-stress.

ACKNOWLEDGMENT

The author gratefully acknowledges the assistance of the following individuals in the performance of the program: Robert A. Arnoldi, and Ron-Ho Ni for providing technical guidance, Arthur R. Guerette for providing instrumentation and data reduction, William N. Dalton, III, for reducing the laser mirror data and performing the analysis, and Dr. John J. Adamczyk for providing technical direction.

AEROELASTIC THERMAL EFFECTS

by
 JAMES D. JEFFERS, III
 9321 Forest Hills Drive
 Tampa, Florida 33612

INTRODUCTION

The adverse effect of increasing temperature on the stability of turbomachinery airfoils has long been recognized but remains today one that is not fully understood. The quantitative effect on the reduced frequency parameter, $k^* \omega c/V$, which has been experimentally and analytically shown to be one of the most influential stability parameters, is readily calculated. The effects of increasing temperature on the parameters that comprise reduced frequency, i.e., the frequency of the unsteady airfoil motion and relative flow velocity, are well known. Unfortunately, the resulting effect on aerelastic stability, particularly for "stall" flutter, is not.

This inability to completely assess thermal effects, among others, was dramatically underscored by an occurrence of subsonic stall flutter in the first stage fan rotor of the F100 turbofan engine early in its development program. The severity of the problem prompted an intensive experimental test program and analysis to first determine a solution and, further, to assess the design techniques used to avoid the problem. As a result, a decade of extensive analytical and experimental research has been conducted at the Government Products Division of Pratt & Whitney Aircraft, the United Technologies Research Center, and the NASA Lewis Research Center. The following is a summary of some of the findings of these investigations.

HISTORICAL BACKGROUND

In late September of 1972, a prototype F100 engine was tested at simulated high-Mach-number flight conditions in preparation for military qualification tests (Jeffers & Meece, 1975). The F100 engine is a twin-spool, high thrust-to-weight ratio, turbofan engine developed for the F-15 and F-16 fighter aircraft.

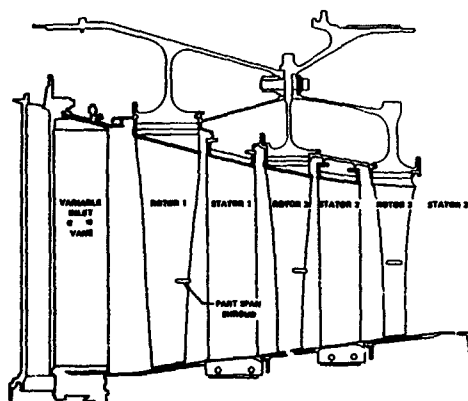


Figure 1. F100 Fan Cross-Section.

The fan has three rotating stages, each with partspan shrouds, as shown in figure 1. The original configuration of the first stage fan blade, which is located immediately behind a variable inlet guide vane, had a shroud mounted aft of the airfoil midchord at approximately 65% span.

Upon completion of the initial test, airfoil fatigue failures were discovered in several first stage blades. Materials laboratory tests indicated that the failures were high-cycle fatigue cracks caused by a high amplitude response in a predominantly torsional mode of vibration. Both the nature of the failure and the aerodynamic environment of the airfoil at the time of failure suggested that the first stage had experienced sub-sonic stall flutter.

Initial Flutter Analysis

The design system used to predict the sub-sonic stall flutter margin of the F100 first stage consisted of a stability boundary that is a function of two variables (Figure 2). One of the variables is reduced velocity, $V_r = V/c_w$, which is the inverse of the reduced frequency. The second is a normalized incidence parameter, β_{lf} , which is defined as

$$\beta_{lf} = (\beta_{min} - \beta_1) / (\beta_{min} - \beta_t) \quad (1)$$

The flow angles, β , in this expression are determined from nonrotating two-dimensional cascade loss correlations which generate "loss buckets". β_1 represents the actual inlet flow angle, β_{min} is the flow angle at minimum loss, and β_t is the flow angle at a specified loss on the stalled side. Thus, β_{lf} is a measure of the degree of stalling.

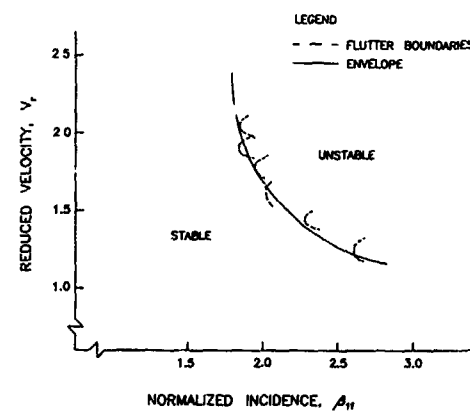


Figure 2. Torsional Stall Flutter Experience

The two-dimensional bi-variate experience limit was generated by enveloping the available stall flutter experience at a reference span to create a "conservative" stall flutter boundary.

Extensive rig component testing was conducted early in the development program to evaluate the aerodynamic design and structural durability of the F100 fan. The testing included heavily instrumented fan rigs that were operated at ambient inlet conditions in sea level facilities at both normal and off-design engine operating conditions. Instrumentation included standard steady state temperature and pressure probes at stator leading edges and strain gages placed at strategic locations as dictated by modeling and laboratory tests.

During off-design testing of an F100 fan rig, a response at a non-integral order frequency was observed in the first stage rotor at low corrected speed and high pressure ratios, well away from the normal operating line (Figure 3). The flutter frequency was very near that calculated for a 5 nodal diameter, blade-shroud-disk system mode, but phasing of the strain gage responses proved inconclusive. In the 5 nodal diameter system mode, the blade motion is calculated to be comprised primarily of bending motion with a high degree of shroud coupling. At these near surge operating conditions, the first stage experiences very high incidences, and consequently the response was designated as stall flutter.

Correlation of the rig stall flutter data on the empirical experience curve indicated that it was indeed a conservative operating limit (Figure 4). The rig data formed a "nose curve" similar to the correlations of previous Pratt & Whitney Aircraft flutter data considerably beyond the experience boundary. Because many of the variables not included in a two-dimensional flutter were reasoned to not appreciably change, the rig boundary was used to assess the stability of the F100 first stage fan at the elevated temperatures and pressures of high Mach

number flight. For flight inlet conditions, the normalized incidences of the first stage were calculated to be the same as those in the rig at part corrected speed on the normal operating line. However, the increased temperatures did increase the reduced velocities (decrease the reduced frequencies) such that the flutter region on a fan map was projected to enlarge (Figure 5). The enlargement was small, and therefore the engine was predicted to be flutter-free throughout the flight envelope. Obviously, the blade failures experienced during flight testing indicated that the prediction was in error.

Engine Test Results

A full-scale engine test program was initiated to investigate the blade failures. Strain gages were placed on the first stage fan as dictated by laboratory tests that reproduced the failure. Aerodynamic instrumentation was sparse due to the difficulty of the twin-spool engine environment. The engine was placed in an altitude test facility capable of simulating flight inlet conditions in excess of Mach 3.0 and 70,000 ft.

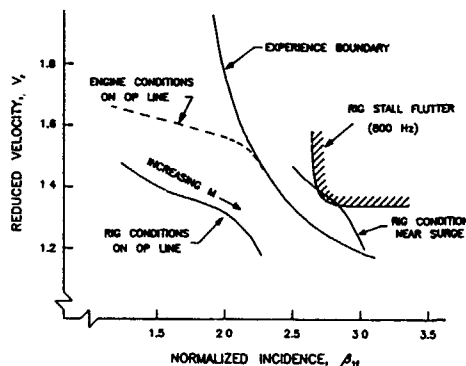


Figure 4. Prediction of First-Stage Fan Blade Stability at Engine Flight Conditions.

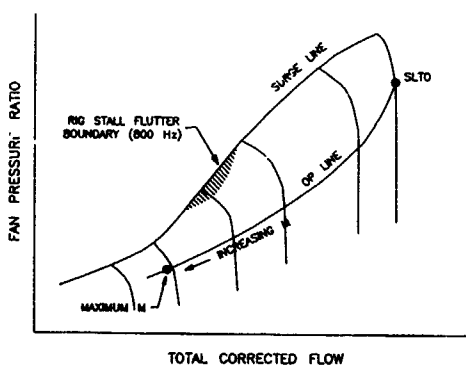


Figure 3. F100 Rig Stall Flutter Fan Map.

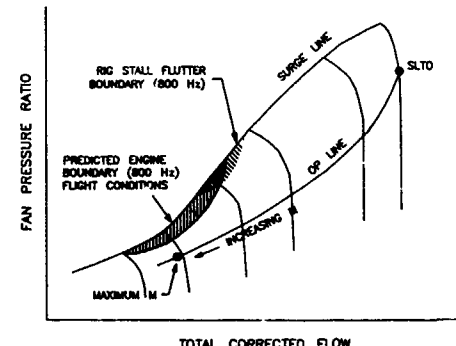


Figure 5. Predicted Stall Flutter Boundary at Engine Flight Conditions on Fan Map.

The flutter region was probed by two basic paths, as illustrated in three formats in Figure 6. Initially, inlet conditions were set at a maximum safe experience point based on endurance testing (point A). Inlet temperature was then steadily increased to simulate a high Mach number excursion into the failure region (point B). Above a certain Mach number, the engine is scheduled such that the fan corrected speed decreases with increasing temperature to avoid aircraft inlet instabilities. On a fan map, the fan approaches lower corrected flows and pressure ratios as temperature or flight Mach number is increased. During this temperature excursion, the first stage fan experiences increasingly higher normalized incidences but only slightly decreasing reduced velocities. Temperature was increased until stability was encountered.

The second basic path employed suppressed speed excursions to flutter onset (points A to C, Figure 6). Speed was decreased at constant temperature by circumventing the engine control system. The fan followed an off-schedule operating line at increasing higher pressure ratios as speed and corrected flow were reduced. As a result, flutter was generally encountered at higher normalized incidences but lower reduced velocities than on the temperature transients.

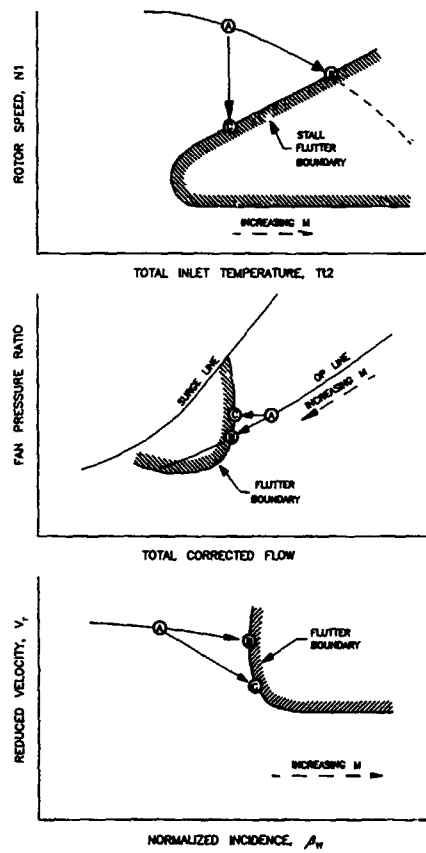


Figure 6. Engine Operation to Encounter Flutter.

The F100 engine data determined the first stage durability problem was in fact the result of an aeroelastic instability that was a function of stalled incidence. The engine flutter exhibited a marked difference from that observed in the component rig tests; i.e., the flutter response changed from an 800-Hz, coupled bending-torsion system mode to a 1000-Hz, above-shroud torsion mode (Figure 7). Because phasing of the strain gage data again proved inconclusive, the engine flutter mode could have been either a high-nodal-diameter, second coupled mode or a low-nodal-diameter, third coupled mode.

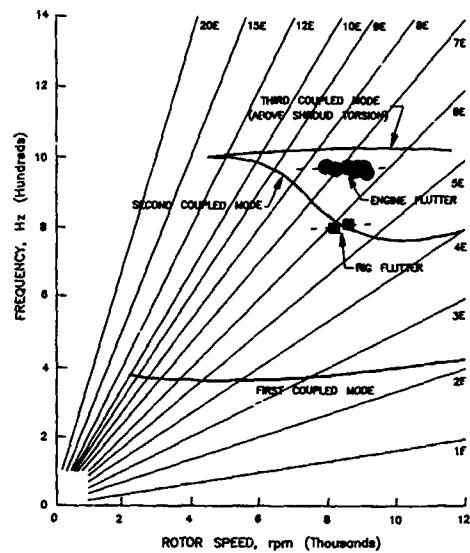


Figure 7. Rig vs. Engine Stall Flutter Frequency Response.

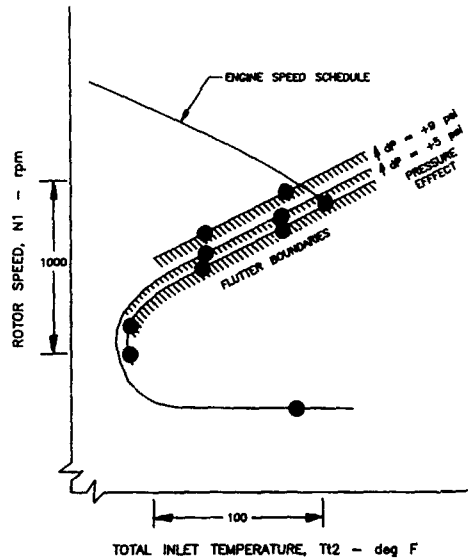


Figure 8. Stall Flutter Boundaries From Engine Tests.

The data confirmed the destabilizing effect of increased temperature, but in addition demonstrated that increasing pressure is destabilizing, a fact not previously documented. This pressure dependence was readily seen when the engine stall flutter boundaries were presented on a speed-versus-inlet-temperature plot (Figure 8). Subsequent testing of candidate redesigns substantiated the pressure effect as illustrated in a correlation of pressure-versus-temperature flutter boundaries (Figure 9). As pressure was increased, flutter occurred at lower temperatures.

When plotted on the empirical V_r -versus- β_{1f} correlation, the engine flutter was shown to occur at considerably lower reduced velocities and normalized incidence than previous stall flutter experience (Figure 10). In fact, the engine V_r -versus- β_{1f} boundary would have predicted the first stage fan to have fluttered on the normal operating line at low temperature and pressure. Nevertheless, the general stability trends represented by the empirical correlation were used to redesign a flutter-free first stage fan. The thickness-to-chord ratio in the airfoil tip region was increased to increase the torsional frequency from 1000 Hz to 1240 Hz and thereby decrease the reduced velocity. The airfoil thickness increase also improved the loss characteristics resulting in lower calculated normalized incidence at a given operating condition. A finite element analysis (NASTRAN) of the steady-state aerodynamic loading on the blade also indicated that the destabilizing effects of increased pressure were, at least in part, due to increased blade deflections and consequently the cascade geometry. The increased stiffness in the tip region created by the thickness increase minimized the cascade geometry changes and the accompanying increase in normalized incidence.

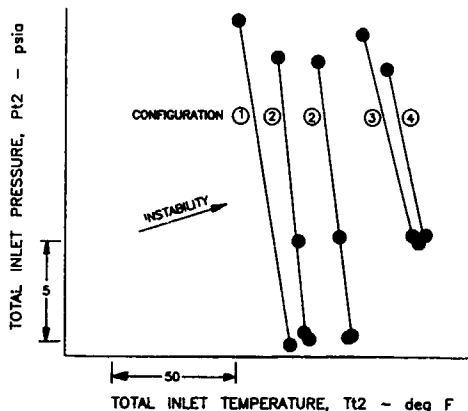
The redesigned first stage blade was demonstrated to be free of flutter throughout the aircraft flight envelope in tests of the F100 engine in altitude test facilities and in F-15 and F-16 aircraft. Concern remained, however, for the F100 stall flutter problem had revealed grave inadequacies in the state of the art of stall flutter prediction.

FOLLOW-ON RESEARCH

In recent years, the emphasis on light-weight, high performance engine designs has resulted in flutter problems similar to the one encountered in the F100 engine. Efforts have intensified in academia, industry and government to develop accurate and reliable flutter prediction systems that go beyond the limitations of the empirical method.

Carta (1967) proposed the aerodynamic damping approach to flutter prediction in which the unsteady aerodynamic work over one oscillatory cycle is normalized by four times the system kinetic energy to obtain the logarithmic decrement commonly denoted as δ_{aero} . The total system logarithmic decrement is the sum of δ_{aero} and the mechanical logarithmic decrement, δ_{mech} , which is always positive or dissipative. Thus, instability occurs only when δ_{aero} is negative and of a magnitude such that δ_{mech} is overcome. The unsteady aerodynamic work for the entire blade is obtained by summing the contributions from two-dimensional strips of constant airfoil cross section along the blade span in an attempt to account for three-dimensional effects.

The aerodynamic damping approach requires an unsteady aerodynamics model to predict the unsteady lift and moment responses to the unsteady motion, which is assumed to be that of the system natural modes. Unsteady aerodynamic modeling has investigated two areas for the subsonic stall flutter problem. Some investigators



have probed the effects of high loading due to incidence and blade shape for attached flow (Atassi & Akai, 1978, Verdon & Caspar, 1982), while others have studied the effects of flow separation (Sisto & Perumal, 1974, Chi, 1980, Chi & Srinivasan, 1984). The Chi model, which assumes that the flow separates at a fixed point along the blade chord, was very successful in predicting the relative stabilities of the two flutter modes observed during F100 first stage fan tests at the disparate temperature and pressure inlet conditions. Further research may establish a means of determining the separation point as a function of the steady-state operating conditions. However, although some of the results have been encouraging, no fully substantiated model has as yet been developed.

A semiempirical unsteady aerodynamics model for stall flutter (Jeffers, et. al., 1978) was evaluated using F100 engine data from tests at the NASA Lewis Research Center. The model was moderately successful in that the above-shroud torsion mode was calculated to be the least stable and the destabilizing effect of increasing inlet pressure was satisfactorily represented. However, other inadequacies, most notably the inability of the model to fully account for the effects of inlet temperature, led to the conclusion that a conservative design system was possible only within certain limits. More importantly, the aero elastic data used to assess the model yielded valuable information concerning the stall flutter phenomena.

NASA Flutter Data

The objectives of the F100 engine tests at NASA Lewis were to further define the parametric effects of inlet temperature and pressure, determine flutter responses as a function of operating conditions, and to generate a data bank for future research. The instrumentation included strain gages on all fan rotors and stators and total temperature and pressure probes at the leading edges of all stators. In addition, a traversing flow angle probe was placed behind the inlet guide vane to more accurately define the inlet flow angles to the first stage fan. The more atypical instrumentation included high-response pressure probes and optical sensors mounted in the engine case directly over the tip of the first stage rotor. A high-response wake probe was also placed downstream of rotor 1. These sensors recorded the unsteady airfoil motion and the aerodynamic responses to the blade motion during stall flutter.

A broad range of inlet temperatures and pressures as well as fan operating conditions were surveyed to generate stall flutter data. The stability trends associated with changing inlet temperature and pressure were in agreement with those observed in the earlier F100 tests (Mehalic, Dicus & Kurkov, 1977). Of most interest were the flutter responses measured in the stationary reference frame. As reported by Kurkov (1978, 1980, 1981) and Jeffers, et. al., (1978), the

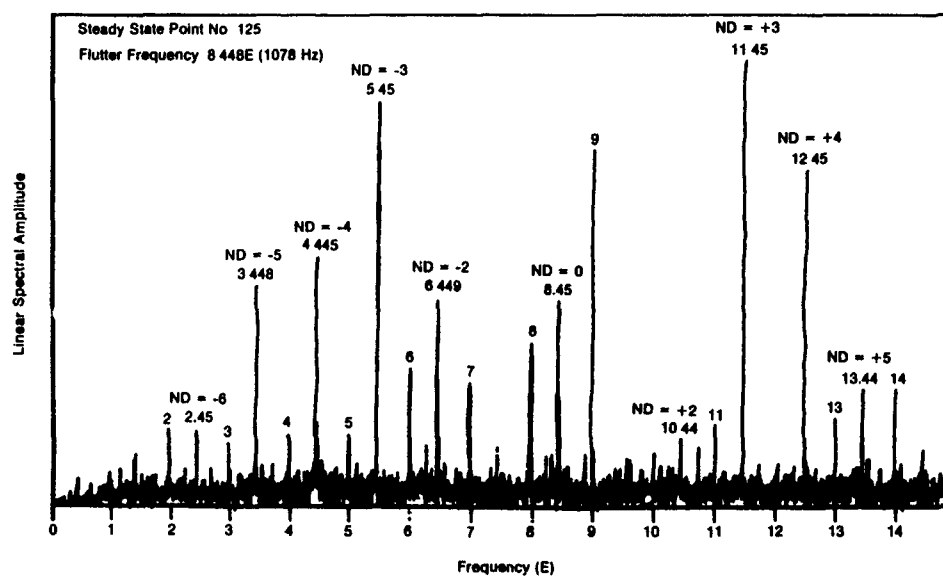


Figure 11. Static Pressure Transducer Frequencies During Flutter Indicate Presence of Several Nodal Diameter Modes and Wave Directions.

stationary sensors in combination with the rotating strain measurements showed that although stall flutter occurred at a single frequency relative to the rotating reference frame, the flutter mode shape was comprised of several nodal diameter patterns traveling in both the forward and backward directions with respect to disk rotation. In the stationary reference frame, the frequency of the contributing mode was displaced from the non-integral flutter frequency by positive or negative multiples of engine order depending upon nodal diameter and wave direction (Figure 11). The blade-to-blade maximum amplitude response varied considerably around the circumference of the disk similar to that observed for forced excitation of mistuned blade-disk assemblies (Ewins, 1974). Further, the modal contributions and the resulting blade-to-blade amplitude and phase angle responses were found to vary with inlet and engine operating conditions.

Thus, stall flutter occurs in complex modes whose contributors are determined by aerodynamic and structural asymmetries. Although mistuning has been shown to be stabilizing and a conservative design system could be based on tuned aero-mechanical systems, a comprehensive flutter prediction system capable of verifying an unsteady aerodynamics model for stall flutter would have to account for mistuning effects.

CONCLUDING REMARKS

An encouraging amount of progress has been made over the past decade in the understanding of the stall flutter phenomenon. The parametric effects of inlet flow, particularly temperature and pressure, and of engine operating conditions have been extensively demonstrated in experiment. Analytical aerodynamic and structural modeling has become more ambitious and sophisticated with, in many cases, promising results. However, no fully substantiated stall flutter prediction system has as yet been developed.

FORCED VIBRATION AND FLUTTER DESIGN METHODOLOGY

by

Lynn E. Snyder and Donald W. Burns
 Allison Gas Turbine Division
 General Motors Corporation
 Indianapolis, Indiana 46206

INTRODUCTION

Prevention of high cycle fatigue in turbomachinery components is the aim of the structural designer. High cycle fatigue considerations account for a significant percentage of development and operational costs of a gas turbine engine. In development, costly time delays and redesign efforts may be incurred due to high cycle fatigue failures of components. Decreased reliability, shortened time between overhauls, and increased need for spares may be associated with high cycle fatigue failures. These also add to the costs of operation of gas turbine engines. Based on the accumulated knowledge of the cause of high cycle fatigue, empirical and analytical design tools to aid the designer have been and continue to be developed. Proper application of these design aids leads to the ultimate goal of eliminating high cycle fatigue from gas turbine engines through judicious design of turbomachinery components.

This chapter will cover the aeroelastic principles and considerations of designing blades, disks and vanes to avoid high cycle fatigue failures. Two types of vibration that can cause high cycle fatigue, flutter and forced vibration, will first be defined and the basic governing equations discussed. Next,

under forced vibration design the areas of source definition, types of components, vibratory mode shape definitions and basic steps in design for adequate high cycle fatigue life will be presented. For clarification a forced vibration design example will be shown using a high performance turbine blade/disk component. Finally, types of flutter, dominant flutter parameters, and flutter procedures and design parameters will be discussed. The overall emphasis of this chapter is on application to initial design of blades, disks and vanes of aeroelastic criteria to prevent high cycle fatigue failures.

CHARACTERISTICS OF FLUTTER AND FORCED VIBRATION

The classification of the two types of vibration which can cause high cycle fatigue failures is delineated by the relationship between the component displacement and the forces acting on the component. Forced vibration is defined as an externally excited oscillating motion where there are forces acting on the component which are independent of the displacement. Where the nature of the forces acting on the component are functions of the displacement, velocity or acceleration of the component, and

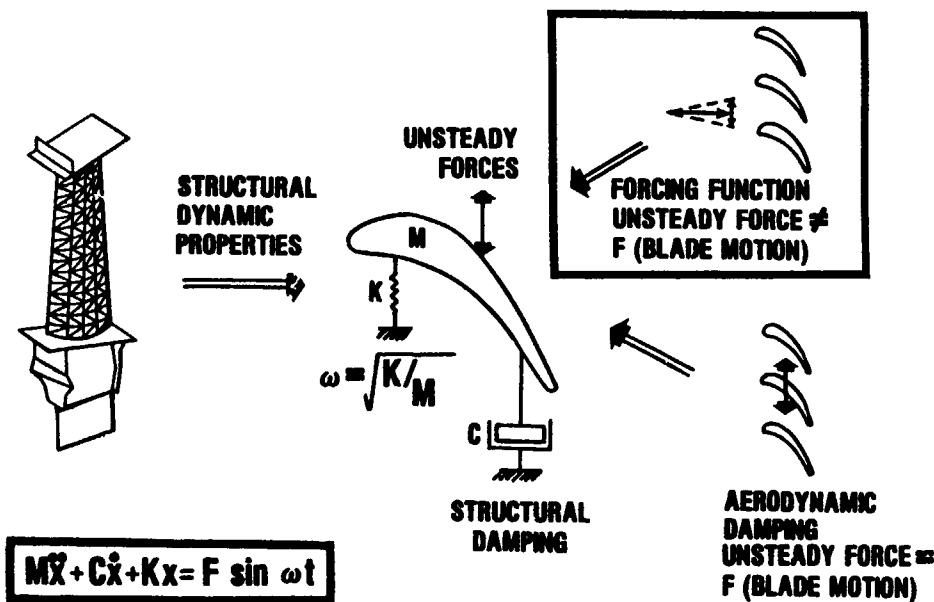


Figure 1. Primary Elements of Flutter and Forced Vibration.

these forces feed energy into the system, the self-induced oscillations are classified as flutter. Therefore to avoid forced vibration and flutter through design requires an accurate knowledge of the forces and the dynamic properties of the structural component involved.

A simplified view of the forces and the dynamic characteristics of the structural component are shown in Figure 1. The basic equation of motion shown combines the structural dynamic properties on the left side of the equation with the forcing function on the right. The dynamic properties of the component are based upon the mass (M) and stiffness (K) matrices of the system from which natural undamped frequencies (ω) and mode shapes are determined. The force required to move the component in each mode shape is dependent on the structural damping (C) of the system.

Definition of the forcing function is divided to distinguish between external and self-induced forces. External forcing functions which are independent of component displacement can be generated by such things as air flow nonuniformities or by mechanical mechanisms such as rub. The aerodynamic force which is created as a result of the component's displacement is classified as a self-induced force called aerodynamic damping. This self-induced force may either be stabilizing (positive aerodynamic damping) or destabilizing (negative aerodynamic damping).

For either forced vibration or flutter, the response (equilibrium amplitude) of the component is equal to the work done by the component. For forced vibration, the equilibrium amplitude is reached when the work done on the component by the external forcing function is equal to the work done by the structural damping force and by the aerodynamic damping force. This work balanced is expressed as:

$$\text{WORK/CYCLE)}_{\text{IN}} = \text{WORK/CYCLE)}_{\text{OUT}} \quad (1)$$

$$\text{WORK/CYCLE)}_{\text{FORCING}} \quad (2)$$

$$\text{FUNCTION}$$

$$= \text{WORK/CYCLE)}_{\text{STRUCTURAL}}$$

$$\text{DAMPING}$$

$$+ \text{WORK/CYCLE)}_{\text{AERODYNAMIC}}$$

$$\text{DAMPING}$$

For flutter, equilibrium is reached when the work on the component by the self-induced force, aerodynamic damping, is equal to and opposite in sign to the work done by the component by the structural damping force. This is expressed as:

$$\text{WORK/CYCLE)}_{\text{AERODYNAMIC}} \quad (3)$$

$$\text{DAMPING}$$

$$- \text{WORK/CYCLE)}_{\text{STRUCTURAL}}$$

$$\text{DAMPING}$$

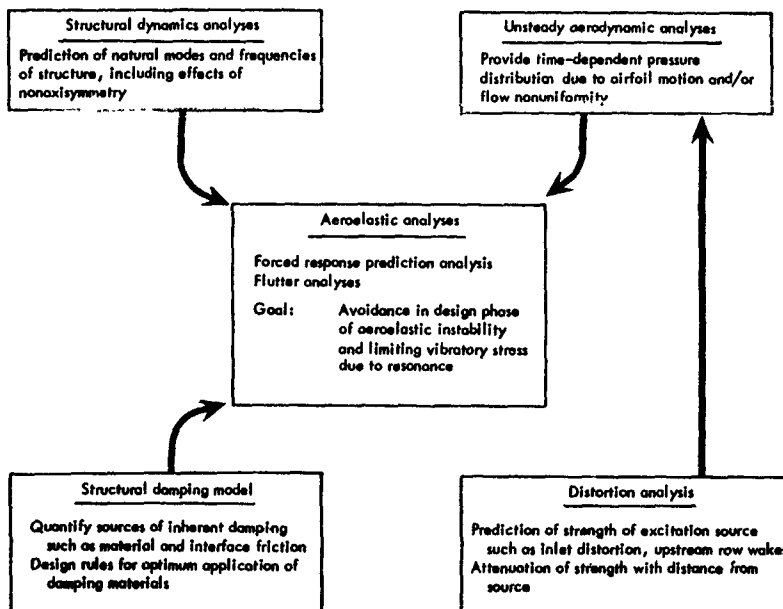


Figure 2. Elements of an Aeroelasticity Design Analysis.

The key elements of an analytical design system for aeroelastic response prediction is shown in Figure 2. This system can be used to predict steady state (equilibrium) response of turbomachinery components to forced response or flutter with the ultimate goal being elimination of HCF failure in the design phase. The basic elements of the equation of motion are shown here with the structural dynamic properties on the left side and the forcing function on the right. The structural dynamics analyses used presently are based on finite element techniques and are able to accurately predict natural modes and frequencies of blade, disk and vane structures. Structural damping is defined by qualifying the various sources of damping such as material and interface friction. Recently structural damping has been measured by Srinivasan (1981) and Jay (1983). Damping materials have been identified for optimum application to various designs to improve flutter characteristics and/or reduce forced vibration responsiveness. D.I.G. Jones (1979) gives an extensive list of efforts to increase/add structural damping to components. Prediction of the strength of the forcing function due to aerodynamic disturbances is also required. Research to acquire data and model such disturbances to provide an experimentally verified analytical prediction system has been carried out by Gallus (1982a, 1982b). Research to develop unsteady aerodynamic analyses to calculate the time-dependent pressure distribution due to airfoil motion and/or flow uniformity has been conducted by Smith (1971), Caruthers (1980). All of the elements shown are necessary to adequately design components for forced vibration or flutter considerations.

The preceding definitions and equations form the basis for the design systems used for preventing high cycle fatigue of gas turbine blades, disks and vanes. These design systems are largely centered on defining the sources and/or mechanism of forcing function generation and accurately predicting the aeroelastic properties of the component. The success of a design system is directly dependent on how well it can define these elements of forced vibration and flutter. Use of empirical relationships are still required as a substitute for exact definitions of some elements. Estimates of values of certain elements based on experience are needed. These approximations compromise the ability of the designer to completely avoid high cycle fatigue of blades, disks and vanes but are used to prevent most high cycle fatigue problems. As more exact definitions of these elements are obtained through experimental and analytical approaches, the designer will be able to more adequately attain the goal of elimination of high cycle fatigue failure in turbomachinery components.

Additional references on aeroelasticity are Scanlan (1951), Bisplinghoff (1955, 1962), and Fung (1955).

FORCED VIBRATION DESIGN

Forced vibration is the result of

external forces acting on the blade, disk or vane component. The type of component geometry can be tailored to limit or lessen the effects of these forces through displacement limitation, frequency tuning, mode selection and/or damping control. Accurate calculation of the undamped natural frequencies and mode shapes is required to effect an acceptable geometry for forced response. These areas will be discussed and an example of the basic steps in forced vibration design will be presented in this section.

Sources of Unsteady Forces

The most common aerodynamic sources of forced vibration are shown in Table 1. Aerodynamic sources due to structural blockages to the flow are mainly due to the upstream or downstream airfoil rows. Upstream vanes and struts create a periodic unsteady flow field for downstream rotating blade rows. Likewise the viscous flowfield of rotating blade rows creates a periodic unsteady flowfield for downstream stationary vanes and struts. Generally, vanes, struts and blades are equally spaced circumferentially but if they are nonuniform in a) circumferential location b) shape (i.e., thickness, camber, trailing edge thickness, chord) or c) setting angle, for example, then the unsteady downstream flowfield will contain harmonics of the pattern which may coincide in the operating speed range of the engine with a natural frequency of a downstream airfoil structure.

Downstream vanes and struts can also create a periodic unsteady flow field for upstream rotating blade rows. Likewise potential flow effects of rotating blade rows create a periodic unsteady flowfield for upstream vanes and struts.

Asymmetry in the stationary flowpath can cause unsteady forces on rotating (rotor) airfoils. Examples of flowpath asymmetry are a) rotor off center, b) non-circular case and c) rotor case tip treatment.

Circumferential inlet flow distortion can be a source of unsteady forces on rotating blade rows. A non-uniform inlet flow condition creates unsteady forces on the rotating (rotor) airfoils. The strength and harmonic content of the forcing function produced will be dependent on the magnitude of the velocity/pressure/temperature defect and the radial and circumferential extent of the distortion.

Table 1.

Sources of Unsteady Forces in Rotating Turbomachinery Structures.

- Aerodynamic sources
 - Upstream vanes/struts (blades)
 - Downstream vanes/struts (blades)
 - Asymmetry in flowpath geometry
 - Circumferential inlet flow distortion (pressure, temperature, velocity)
 - Rotating stall
 - Local bleed extraction
- Mechanical Sources
 - Gear tooth meshes
 - Rub

Circumferential inlet flow distortion taking the form of velocity, pressure or temperature variations at the inlet to the compressor or turbine can induce high sinusoidal forces through the length of the compressor or turbine. Crosswinds or ducting at the compressor inlet may produce distortion patterns of low order harmonic content. Combustor cans, because of the variations in operation, may produce temperature patterns of low order harmonic content. Even annular combustors may produce velocity/temperature patterns of low order harmonic content which are due to circumferential flow variations.

Rotating stall zones are another source of aerodynamic blockage which can produce high response in blade, disk and vane components. Stall zones are formed when some blades reach a stall condition before others in a the row. A zone(s) of retarded flow is formed which due to variations of angle of attack on either side of the zone begins to rotate opposite the rotor rotation direction. This speed of rotation has been observed to be less than the rotor speed. Thus, the zone(s) alternately stalls and unstalls the blades as it rotates. The number, magnitude and extent of the zones and the relative speed between zone rotation and blade, disk or vanes determines the magnitude and frequencies of the forcing function available for component excitation. High stresses observed with this source of excitation can lead to quick failure of turbomachinery components.

Local bleed extraction, where air flow is not removed uniformly around the case circumference, may produce unsteady forcing functions which may excite natural modes of blade and disk components. Stages upstream and downstream of the bleed locations have been observed to respond to harmonics of the number of bleed ports.

Tooth meshing of a gear that is hard mounted on the same shaft is a common mechanical source of blade forced vibration excitation. Rotor blade failure is possible when the rotor system is excited in a natural mode in which there is high vibratory stress at the blade root. The mechanism of this excitation can be illustrated by examining two examples.

Consider a rotating rigid rotor system vibrating in a fixed plane, the instantaneous direction of acceleration that is applied to each blade root differs from blade to blade for a total variation of 360° around the rotor. Each blade will resonate when its natural frequency (f_c) equals either the sum or difference of the rotor translation frequency (f_{TR}) and the rotational frequency (f_N).

$$f_c = f_{TR} \pm f_N \quad (4)$$

This equation defines phase equality between the vibrating blade and the forcing function dynamics. If the rotor was not rotating only those blades which were normal to the plane of translation would be resonant due to common phase equality.

Gear tooth (N_T = number of teeth) meshing can be a source of such translation motion of the rotor system ($f_{TR} = N_T \times f_N$). Therefore whenever the blade frequency matches the order frequency due to the number of gear teeth plus or minus one, excitation is possible ($f_c = (N_T \times f_N) \pm f_N$ or $f_c = (N_T \pm 1) f_N$).

Considering the case of torsional vibration of a rigid rotor, all blades experience the same in-phase excitation forces at any instant, independent of whether the rotor is turning. Each blade will resonate when its natural frequency (f_c) equals the rotor torsional vibrating frequency.

$$f_c = f_{TR} \quad (5)$$

Again, gear tooth meshing can be a source of such torsional motion of the rotor system ($f_{TR} = N_T \times f_N$). Therefore whenever the blade frequency matches the other frequency due to the number of gear teeth, excitation is possible.

Rub, as a source of forcing function, can produce high response in components. Contact of a rotor blade tip with the stationary casing locally, may cause an initial strain "spike" of the blade followed by strain decay in a natural mode. At its worst the rub excitation frequency will be equal to a blade natural frequency. Causes of contact may be related to rotor unbalance response, ovalizing of the case, casing vibration characterized by relative blade to case radial motion, casing droop, and non-uniform blade tip grind.

Types of Turbomachinery Blading

There are many types of turbomachine blades and vanes. Table 2 is a partial list of the types of blades and vanes. Each of these descriptors have a definite impact upon the dynamic properties of the components. They describe some aspect of the component design from how it is supported, general shape, structural geometry, material, to its aerodynamic design.

Some examples of turbine blade and disk geometries are presented in Figure 3. As shown, blades may be integrally cast with blades or may be separate and have attachments at the blade root. The differences in dynamic characteristics of each of the blades must be accurately considered during the design of testing phases.

Table 2.

Types of Turbomachinery Blades and Vanes

Blades	Vanes
Shrouded/shroudless	Cantilevered/inner banded
Axial/circumferential attachment	High/low aspect ratio
Stiff/flexible disk	Solid/hollow
High/low aspect ratio	Metal/ceramic
High/low speed	Compressor/turbine
Solid/hollow	
Fixed/variable	

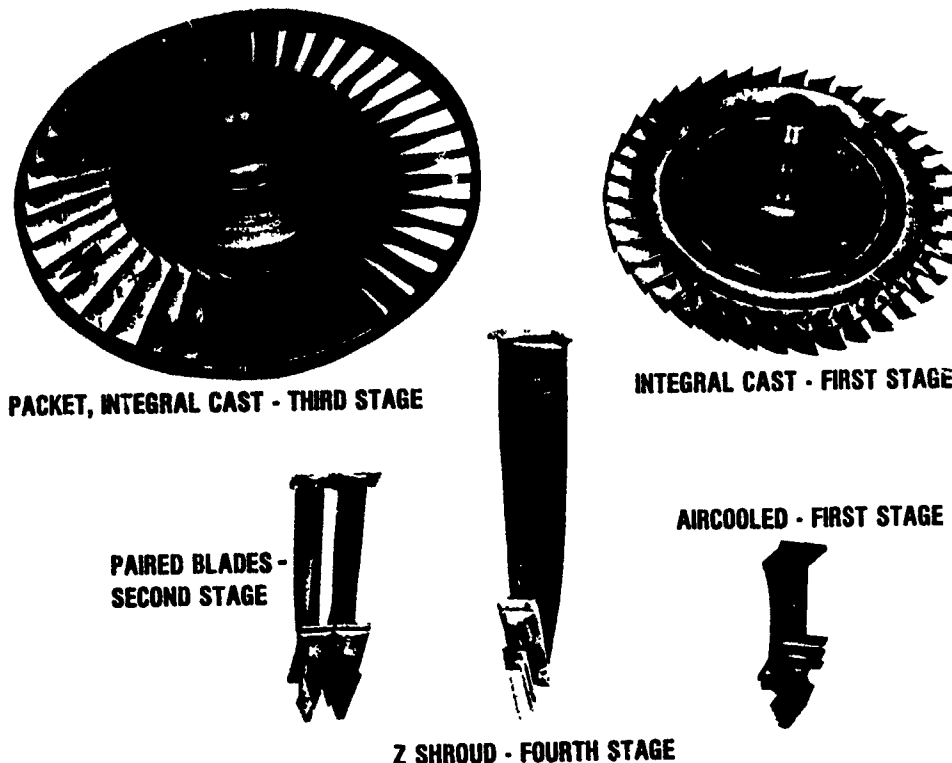


Figure 3. Turbine Blade Configurations.

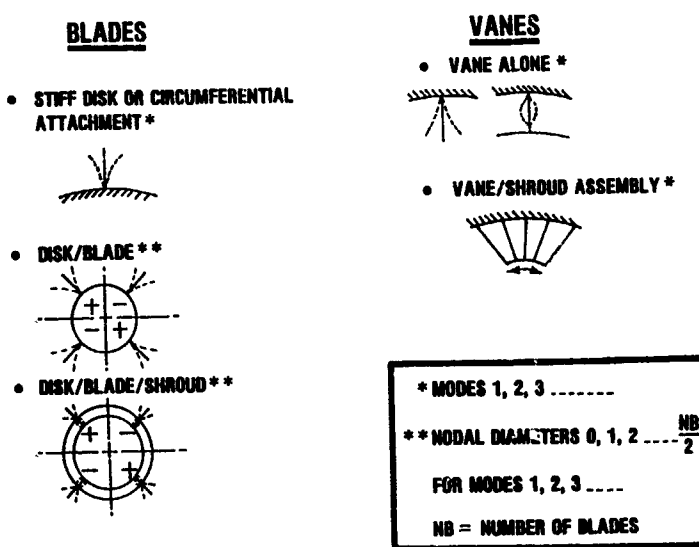


Figure 4. Types of Blade and Vane Vibratory Modes.

Metal/ceramic/composite
High/low hub-to-tip radius ratio
Compressor/turbine
High/low pressure ratio

Natural Modes

Natural modes and frequencies of the components are defined by the physical geometry of the component. These natural modes are described by the location of node lines (zero motion) and general mode deflection. Generic types of natural modes are shown in Figure 4.

The first, lowest frequency, mode of a beam-like component is that mode which has no nodes present on its unfixed surface. This is illustrated by the stiff disk and vane alone modes. For a blade or vane fixed at one end the motion is one of bending from side to side of the whole structure. The fixed blade or vane at both ends bends like a bow string in its first mode. For both types of fixity the second, third, etc. modes become more complex with node lines appearing on the blade or vane.

Actual holographic and calculated mode shapes for an unshrouded compressor blade are shown in Figure 5. The fixity of this

first stage compressor blade is at the bottom (hub) end of the airfoil. A variety of mode shapes characterized by node lines are identified as either basically bending (B), torsion (T), edgewise (EW), lyre (L) or chordwise bending, or complex (C). The finite element method used to calculate the frequency and mode shapes shows the excellent accuracy possible by analytical means. This ability to predict natural modes is necessary in order to have accurate forced response and flutter design systems.

When several blades or vanes are tied together and/or are a part of a flexible disk, the combined dynamic properties of the components couple to produce additional modes called system modes (see Figure 4). Packets of blades or vanes tied together have assembly modes in which combined bending/twisting of all blades take place at one natural frequency. Flexible disk natural mode shapes are characterized by line of zero motion across the diameter called nodal diameters (ND). These may couple with the blade natural modes to produce system modes with elements of motion from each component's natural mode but at a new natural frequency. Circumferential node lines also may describe higher frequency natural modes of blade/disk systems.

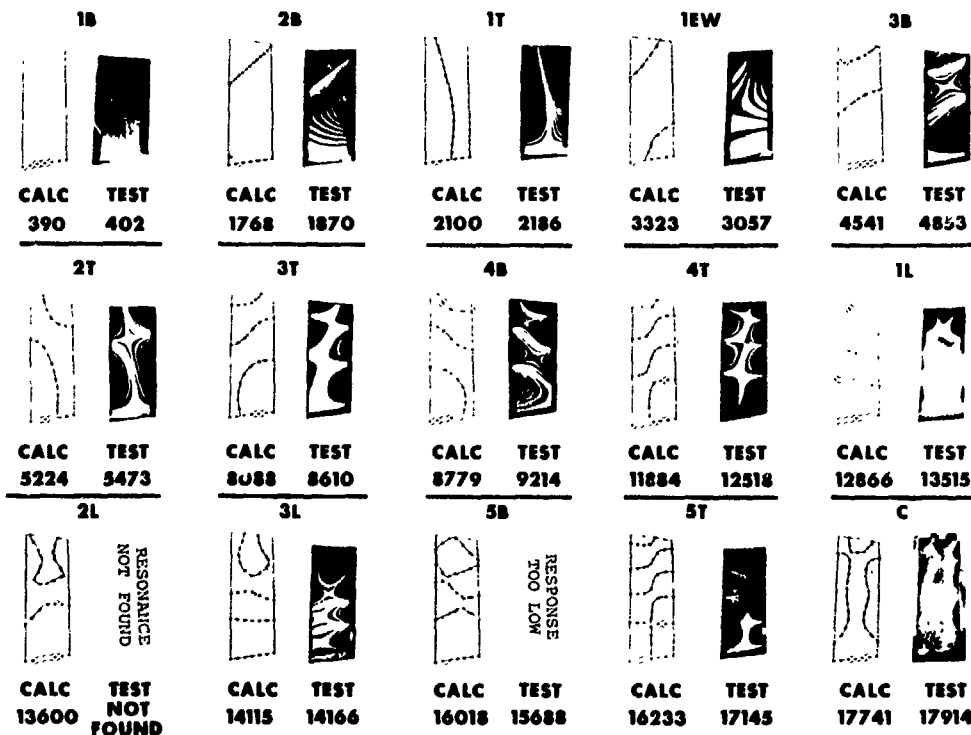


Figure 5. Frequency and Mode Shape Correlation

Holographic photographs (see Figure 6) of a blade/disk system illustrate the relationship between nodal diameter pattern and mode number. Three nodal diameter patterns are shown with the 3ND pattern family expanded for the first three modes. The second mode is characterized by one circumferential node while the third mode has two.

Ten Steps of Forced Vibration Design

The ten basic steps in designing to prevent high cycle fatigue due to forced response are listed in Figure 7. These steps involve evaluating the environment in which the component must operate (steps 1, 2, 5), predicting the aero-elastic characteristics of the component (steps 3-8), investigating possible design changes (step 9), and finally the actual measurement of the dynamic response of the component in the engine environment (step 10). These steps will be illustrated by examining the design of a second stage gasifier turbine blade/disk component. The choice of a turbine instead of a compressor component was arbitrary since the steps are the same for each.

The example blade is an aircooled design incorporating the features listed in Figure 8. It is a shrouded blade which is integrally bonded to the disk. The

hollow blade is a low aspect ratio (length to width) design, with twenty-two (22) airfoils in the stage. A nickel alloy which has good structural properties at high temperature and stress conditions is used in this design.

Step one calls for an identification of possible sources of excitation (forcing function) while step two requires the definition of the operating speed ranges the component will experience. For the example turbine the possible sources and speed ranges are shown in Figure 9. Several sources of aerodynamic excitation exist and are listed. Two upstream and two downstream sources have been identified. Each of these sources creates a periodic forcing function relative to the rotating second stage blade/disk component. The relevant content of these forcing functions will be the harmonics associated with the second stage blade passing these stationary sources. The frequency of the forcing function is dependent upon the rotating speed of the second stage blade. The speeds of possible steady state operation are between idle and design. Any resonance occurring below idle would be in a transient speed range implying lower chance of accumulating enough cycles for failure or maintaining high enough response to produce failure.

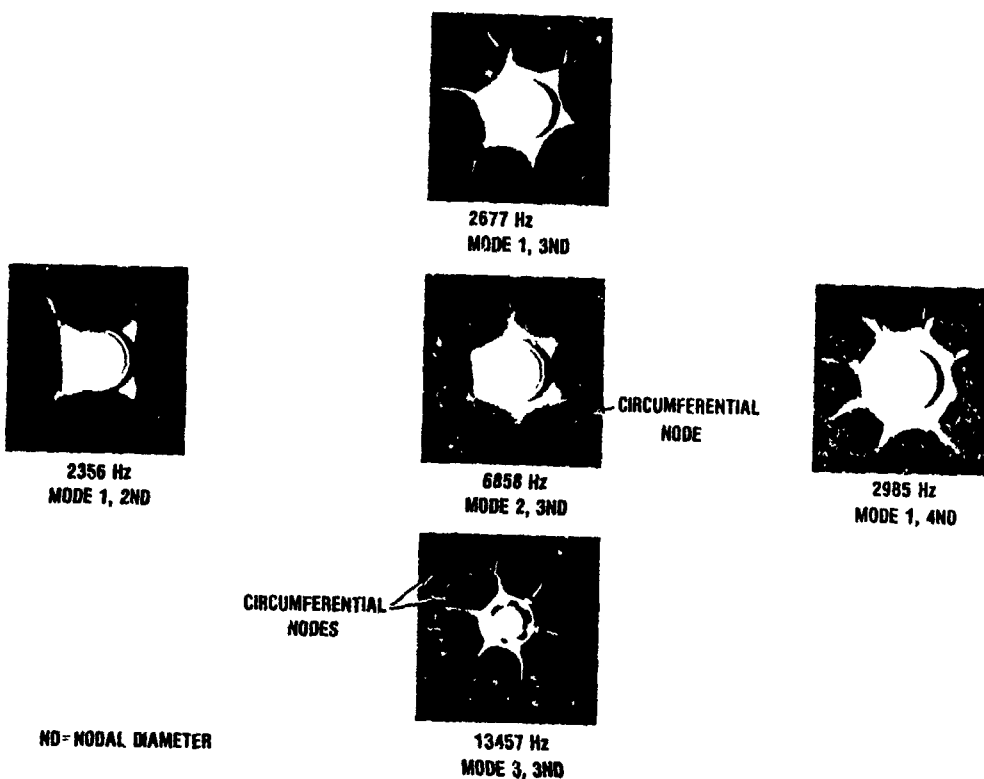


Figure 6. Mode Number and Nodal Diameter Pattern.

- STEP 1 IDENTIFY POSSIBLE SOURCES OF EXCITATION**
- STEP 2 DETERMINE OPERATING SPEED RANGES**
- STEP 3 CALCULATE NATURAL FREQUENCIES**
- STEP 4 CONSTRUCT RESONANCE DIAGRAM**
- STEP 5 DETERMINE RESPONSE AMPLITUDES**
- STEP 6 CALCULATE STRESS DISTRIBUTION**
- STEP 7 CONSTRUCT MODIFIED GOODMAN DIAGRAM**
- STEP 8 DETERMINE HIGH CYCLE FATIGUE (HCF) LIFE (FINITE OR INFINITE)**
- STEP 9 REDESIGN IF HCF LIFE IS NOT INFINITE**
- STEP 10 CONDUCT STRAIN GAGED RIG/ENGINE TEST TO VERIFY PREDICTED RESPONSE AMPLITUDES**

Figure 7. Summary of Basic Steps in Designing to Prevent High Cycle Fatigue Created by Forced Vibration.

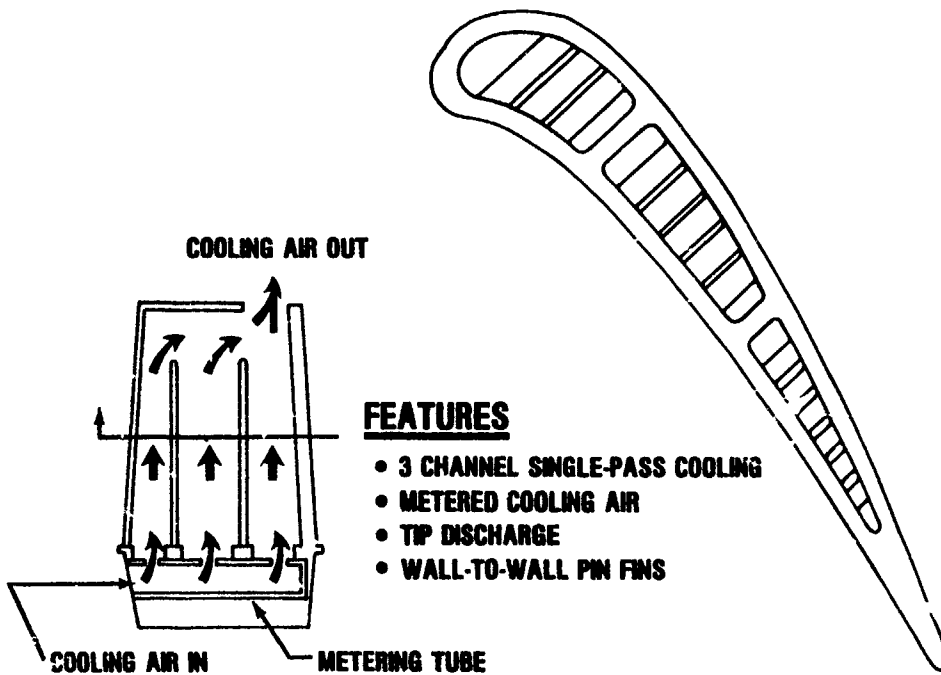


Figure 6. Gas Generator Second Stage Blade Cooling Geometry.

Figure 9 also notes that the spacer and disk have been designed to be in constant contact throughout the engine operating conditions. This contact limits the disk flexibility and eliminates the disk participation in the assembly modes. Therefore accurate prediction of natural modes, step 3, can be made for this type of design by modeling only the blade geometry and fixing the blade at the proper radial location.

The natural modes of a blade as complicated as this example, can be calculated using finite element techniques developed especially for rotating turbomachinery components. The natural frequencies of the blade have been calculated using a model constructed with triangular plate elements. The elements have been used to simulate the hollow airfoil, platform, and stalk geometry as shown in Figure 10. The stiffness and mass matrices formed by these elements are solved to compute the natural frequencies. The more elements used, the closer to the actual blade is the mathematical model.

This method of calculation is shown to be accurate by the comparison of frequencies and mode shapes of test holograms with those of the finite element model. This comparison is for zero RPM and room temperature conditions. Additional calculations are made for various temperature and rotational speeds to determine natural modes at the actual operating conditions.

To determine if the natural frequency of a blade coincides with the frequency of a source, resonant condition, a resonance diagram is constructed (step 4). A resonance diagram relates frequency to rotational speed as shown in Figure 11. Since the forcing function frequency is dependent on rotational speed, lines of concurrent frequencies can be drawn for various harmonics (i.e., 1,2,3,... 10, ...13,...19,...21... sine waves per revolution of the rotor) of engine speed for which sources exist. Placing of the calculated natural frequencies on the diagram with the lines of concurrent frequencies, engine order lines, of the known sources, identifies possible resonant conditions of a component natural frequency coinciding with a forcing function, source frequency. In this example, a dropping of natural frequency with rotor speed indicates that temperature effects are dominant over centrifugal stiffening within the operating speed range.

The possible resonant conditions are identified by intersection of natural frequencies and order lines which occur within or near to the steady state operating speed range. The strongest expected aerodynamic sources of excitation are those immediately upstream (in front of) and downstream (behind) the blade. The amount of response (step 5), depends not only on the strength of the forcing function, but also upon the aeroelastic characteristics of the component. For this example, the dynamic

DESIGN SPEED=48,500 RPM

IDLE SPEED=32,000 RPM

**DISK BOUNDARY CONDITION = SPACER AND DISK
IN CONSTANT CONTACT**

SOURCES:

- 13 1ST STG VANES**
- 19 2ND STG VANES**
- 21 LP1 VANES**
- 5 EXIT STRUTS
(NOT SHOWN)**

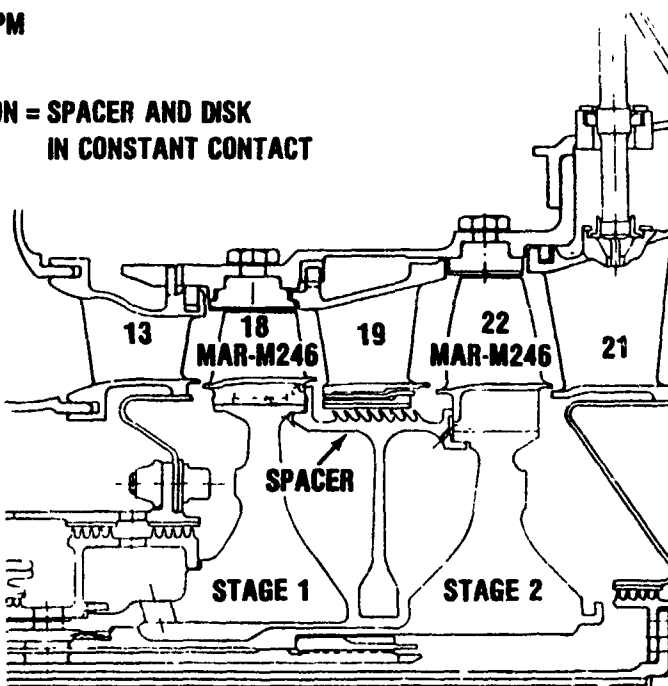


Figure 9. Gas Generator Turbine General Arrangement.

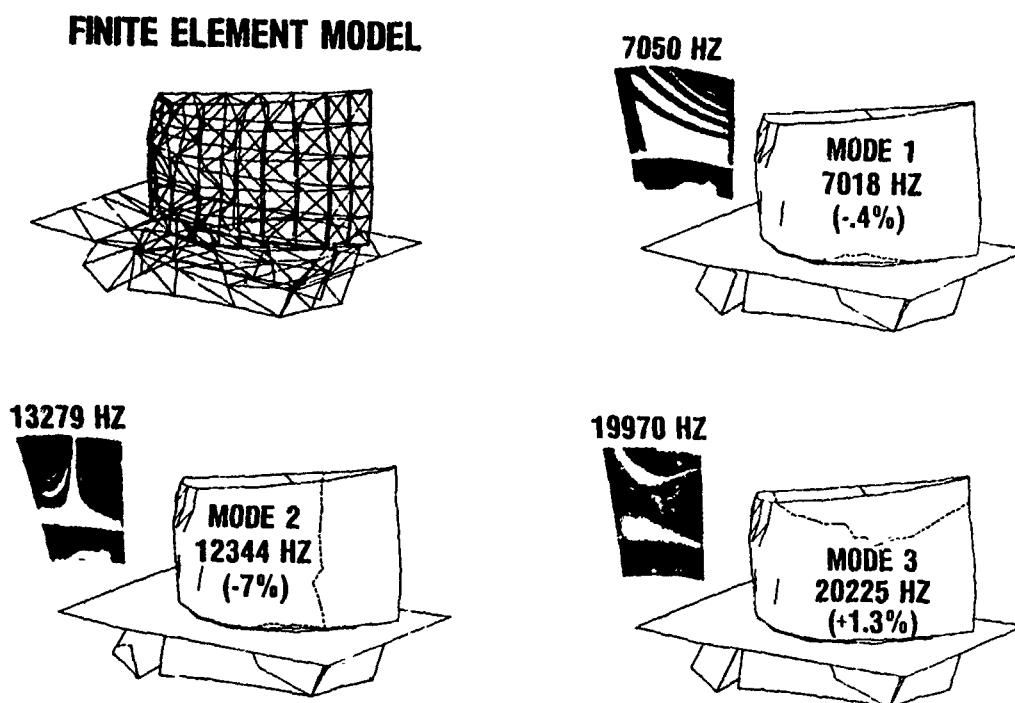


Figure 10. Calculation of Natural Frequency for Second Stage Blade.

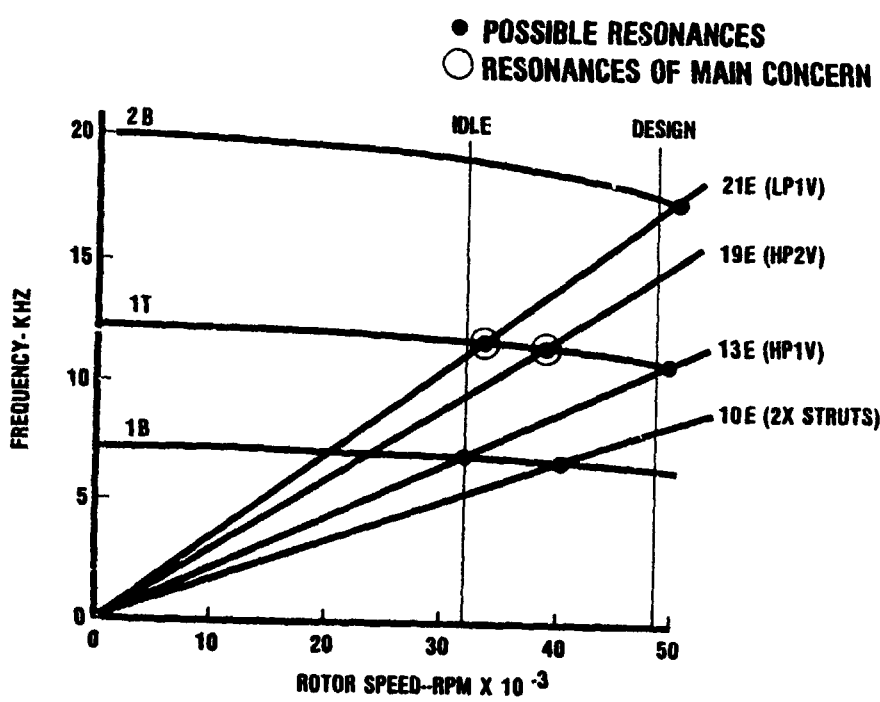


Figure 11. Resonance Diagram for Second Stage Blade.

characteristics for the first torsional mode (1T), mode shape and damping are significant in determining possible response amplitudes.

The response of modes of blades due to aerodynamic sources of excitation have been empirically defined based on experience. This empiricism groups typical blades by common mode shape, damping, type of source, and distance from the source to correlate with response experience. The use of an empirical method for estimating response is due to a current inability to adequately predict the strength of the forcing functions produced and the damping present in the gas turbine environment.

For example, the response of first torsional modes of turbine blades due to an upstream vane source might be empirically defined as in Figure 12. A plot of axial gap/vane axial chord (rate of decay of forcing function) versus the vane overall total to static expansion ratio (forcing function) may allow the designer to pick the combination of variables that will ensure a viable design. A range of blade gap/chord values is defined for the second stage based upon build up tolerances from engine to engine of the various rotor components. This range indicates that a maximum dynamic stress of six to ten thousand psi would be expected for the first torsional mode coincidence with the upstream vane order line.

The response of turbine blade modes to the turbine downstream vane source of excitation has been shown to be related to the variation of static pressure in front of the vane source, Figure 13. $\Delta P/Q$ is a calculated value based on the aerodynamically predicted static pressure field created by the presence of the vane in the airflow stream. This pressure field is dependent upon aerodynamic characteristics (velocity triangles, mass flow, etc.) and vane cross-sectional geometry. Plotting $\Delta P/Q$ versus a normalized value of axial gap allows the designer to space (gap) the blade-vane row to avoid a large forcing function. A specified limit would be based upon turbine blade experience to date and represents the maximum value of $\Delta P/Q$ that is considered acceptable. The second stage blade range (based on build tolerances) indicates an acceptable value of $\Delta P/Q$ and thus indicates that a low response due to the third vane row is expected.

Calculation of dynamic stress distribution, step 6, is necessary for determining locations of maximum vibratory stress for high cycle fatigue assessment and as an aid in the placement of strain gages to measure strain due to blade motion during engine operation. A number of these gages placed in various positions on the airfoil can be used to qualify the relative responses of the blade at each location for each natural mode. A distribution of stress for each mode is thus identified.

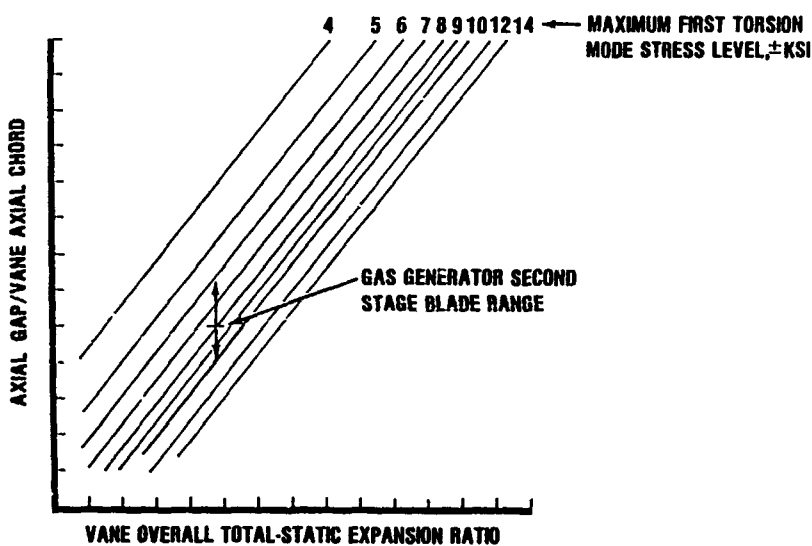


Figure 12. Prediction of Response due to Second Stage Vane.

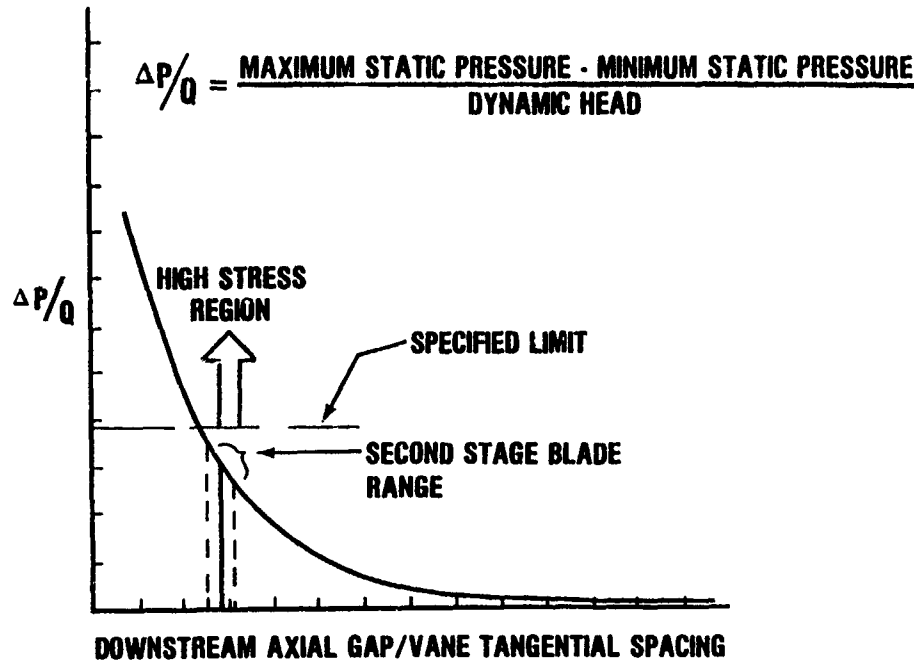


Figure 13. Prediction of Response due to Third Stage Vane.

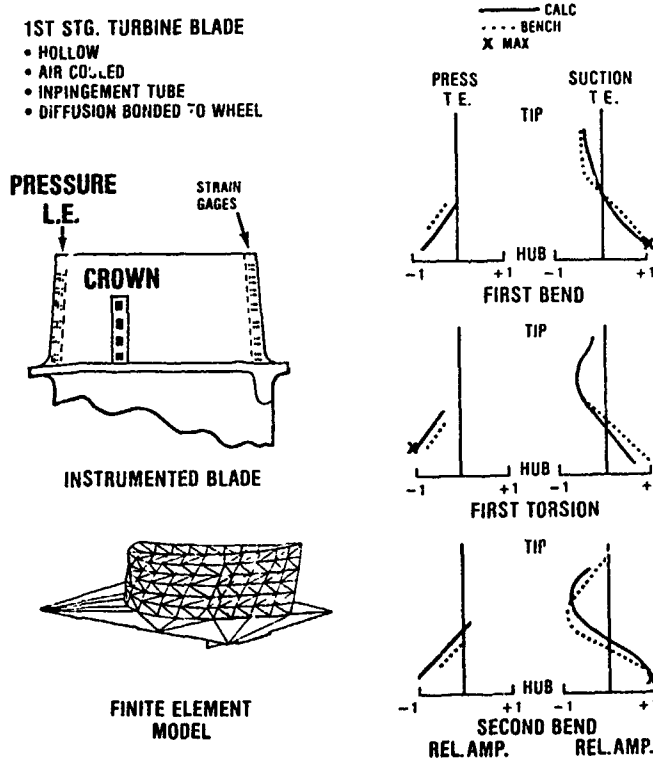


Figure 14. Calculation of Dynamic Stress Distribution for First Stage Blade--Trailing Edge.

An example of a first stage turbine blade stress distribution is shown in Figures 14 and 15. The analytical results are based upon finite element calculations and show good correlation with test data. The results of the bench test are limited to the number of and direction of the gages, while the analytical results cover all locations and directions. Use of analytical stress distributions to pick a limited number of gage locations on the blade helps to ensure the best coverage of all modes of concern. It should be noted that one gage location may not cover all modes of concern since maximum locations vary with mode shape.

To determine the allowable vibratory stress for various locations on the blade a diagram relating the vibratory and steady state stress field is used, step 7. A typical modified Goodman diagram is shown in Figure 16. Material properties are normally obtained through testing at several temperatures with smooth bar samples, no notches or fillets. From these properties mean ultimate strength at zero vibratory stress and mean fatigue strength at 10^7 cycles (or infinite life) of vibration at zero steady stress are placed on the diagram. A straight line is drawn between these two values which, for most materials, is a conservative mean fatigue strength as a function of loading (steady stress).

Parameters which can affect the distribution of mean fatigue strength and, thus allowable vibratory stress, are notch factor, data scatter, and temperature. These are illustrated in Figure 17. The fatigue notch factor is related to a stress concentration factor which is a ratio of the maximum steady stress to the average steady stress of a particular geometry (notches, fillets, holes). The relationship between fatigue notch factor (K_f), and stress concentration factor (K_t), is dependent upon the notch sensitivity of the material. The one-sigma scatter, which is obtained from test data, accounts for variations in mean fatigue strength due to compositional changes of the material and processing differences from piece to piece. A minus three sigma (-3σ) value of fatigue strength used accounts for 99.865 percent of all pieces having a fatigue strength greater than this value. The temperature affects both the ultimate and fatigue strengths. The example shows a dip in fatigue strength with temperature which is characteristic of some alloys used in turbine blades.

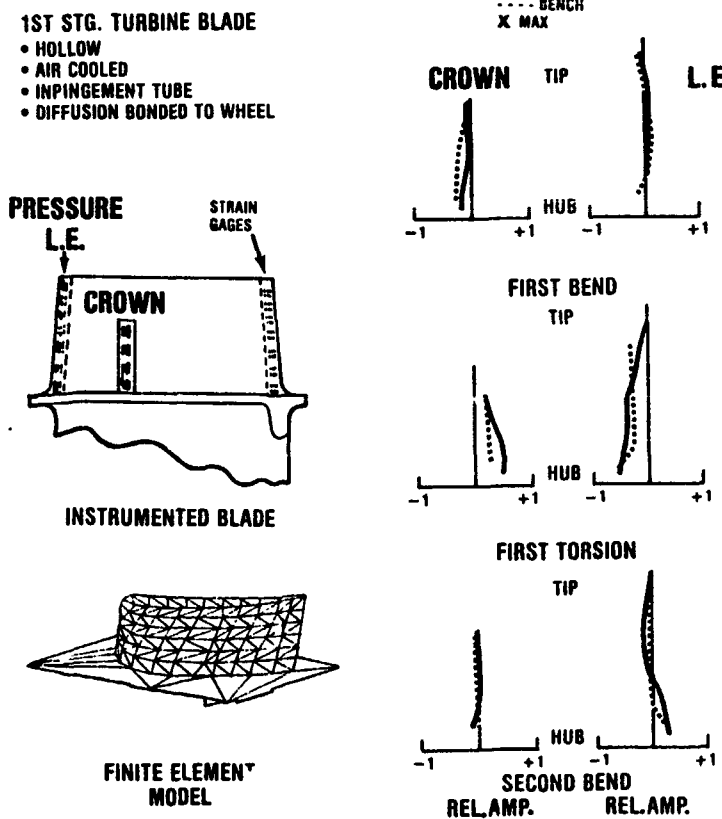


Figure 15. Calculation of Dynamic Stress Distribution for First Stage Blade--Leading Edge and Crown.

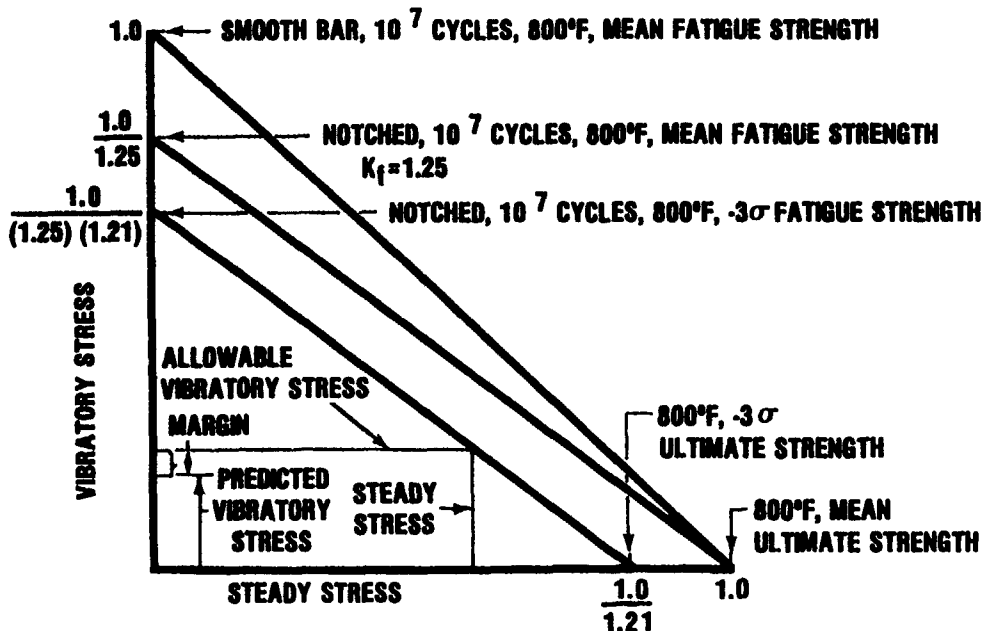
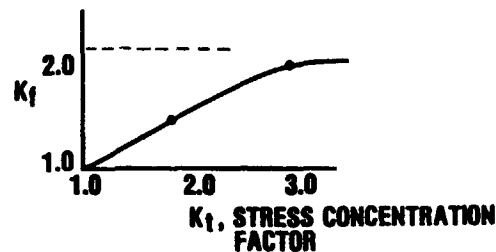


Figure 16. Typical Modified Goodman Diagram.

- **FATIGUE NOTCH FACTOR, K_f , ACCOUNTS FOR NOTCHES (FILLETS, NICKS, FOD, HOLES)**



EXAMPLE ON PREVIOUS CHART
ASSUMES $\sigma = 7\%$
 $\therefore -3\sigma = 21\% \text{ DEGRADATION}$

- **TEMPERATURE AFFECTS ULTIMATE AND FATIGUE STRENGTH**

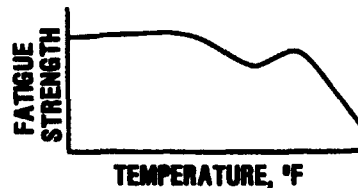


Figure 17. Parameters which Affect the Allowable Vibratory Stress.

Returning to Figure 16, degradation of the line representing the mean distribution of fatigue strength is made for notches, scatter and temperature. Where notches or fillets exist, it is necessary to degrade the mean fatigue strength by the notch fatigue factor (K_f). Lowering of both the mean fatigue and ultimate strengths for -3 σ scatter effects is made. Temperature effects which also affect both fatigue and ultimate strengths was included initially in establishing their values. The lowest line now represents the distribution of fatigue strength versus steady stress at temperature for a specified notch factor and for which 99.865 percent of blades produced will have a greater strength.

This diagram is now entered at the steady stress value based on the resonance speed and specific component location of concern. The maximum allowable vibratory stress level for infinite life, 10^7 cycles in this case, is then read. The difference between the maximum allowable vibratory stress level and the predicted vibratory stress level is called the vibratory stress margin.

The modified Goodman diagram for the example second stage blade is based on MAR-M2465 material properties at 1300°F, Figure 18. The mean ultimate and the mean fatigue strengths are 142 and 31 thousand pounds per square inch (ksi) respectively. The one-sigma scatter for each strength is 8 and 2.2 ksi, respectively. The stress concentration factor (K_t) for the hub fillet radius is 1.36. For this material and fillet radius, this gives a notch factor (K_f) of 1.18. Degrading the mean strengths by the respective factors and entering the steady

stress values for the two locations of concern, yields maximum allowable stresses of 15.3 and 14.3 ksi. These values of maximum allowable vibratory stress are above what is expected based upon evaluation of the upstream and down stream vane row sources. Thus, the high cycle fatigue life is predicted to be infinite and no redesign is required.

Redesign, step 9, was not necessary in this example, but if it had been, design changes such as those listed in Table 3 would have been reviewed. Redesign considerations fall under the categories of changes to the source, component geometry, fixity, damping, material and possible maximum amplitude. Changing the proximity of sources may lower the forcing function strength and thus blade response. The frequency of resonance may be moved to occur outside the operating range by changing the number of sources and thus forcing function frequency. Geometry changes to the sources may be made to lower the disturbance factor (i.e., $\Delta P/Q$).

Table 3

Typical forced vibration redesign considerations

- Proximity of sources (gap/chord, $\Delta P/Q$)
- Number of sources (resonance speed)
- Geometry of sources (lower disturbance)
- Geometry of resonant piece (stiffness and mass distributions)
- Boundary conditions (type of fixity)
- Increase system damping (coating, fixity)
- Amplitude limitation (shroud gap)
- Increase fatigue strength (geometry, material, temperature)

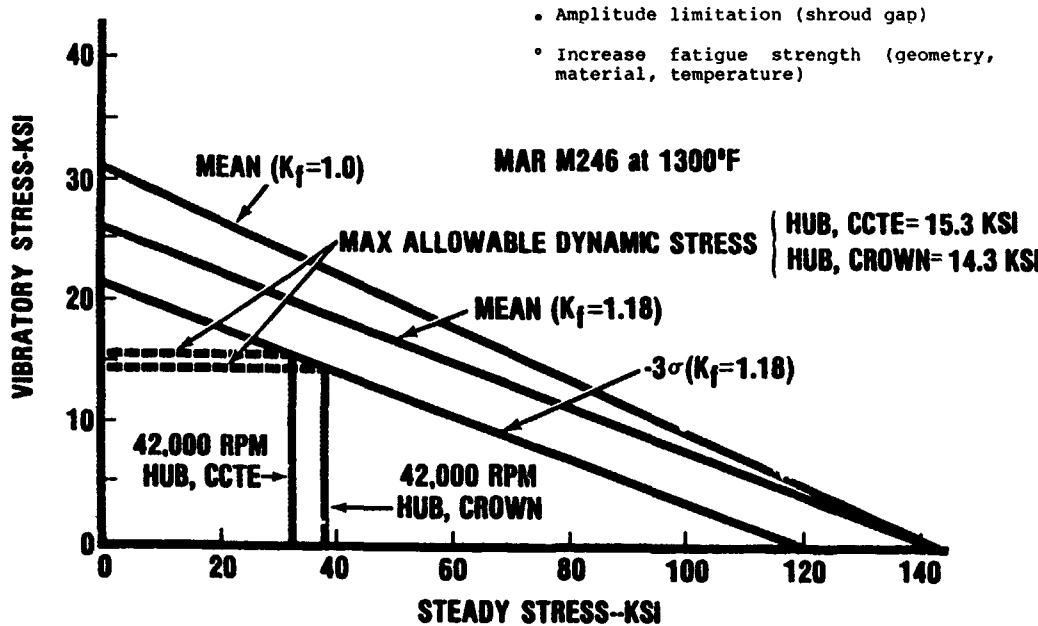


Figure 18. Modified Goodman Diagram for Second Stage Blade.

Component geometry changes such as variations in thickness or chord distribution which change stiffness and mass distributions can be used to raise or lower natural frequencies and thus move resonances above or below operating speed limits. Geometry modifications such as changing of fillet sizes or local thickening can be used to lower notch effects and thus increase allowable vibratory stress.

Changes to boundary conditions to raise or reduce fixity may be used to raise and lower natural frequencies, again to move resonances above or below operating speed limits. Some examples of fixity changes which affect blades and vanes include disk rim restraint as in our example, slot and tang restraint of vanes, blades and vanes cast rigidly to support structure, use of Z shrouds for turbine blades, pinned retentions for compressor blades and packing of blades and vanes together. These changes may also increase or decrease damping by modifying the frictional losses. Damping may also be increased by application of a selected coating to the blade or vane surface.

Amplitude limitation has been used mainly in turbines to reduce the amount of response. Reducing gaps between adjacent shrouds will limit motion in modes where the adjacent blades are not in phase when at resonance. Application of a wear resistant coating to the shroud faces is usually required to limit material loss due to wear.

To maintain or increase fatigue strength material or processing changes may be required. Choosing materials which increase corrosion resistance, decrease notch sensitivity or increase temperature capability can help the designer to attain the necessary high cycle fatigue strength. Processes such as airfoil coating, peening, brazing, grinding, heat treating all affect fatigue strength and should be considered in the design process.

For the example chosen, testing to verify the predicted response amplitudes, step 10, was accomplished using a gasifier turbine rig with the instrumentation configuration shown in Figure 19. The amount and location of the vibratory instrumentation to cover the rotating components is shown. The testing prior to rig running included determining frequencies, mode shapes, stress distributions and fatigue strengths for the second stage blade. Note that in the absence of the low pressure turbine, the third stage vane row was not present.

The vibratory responses of the second stage blade obtained during the gasifier test are shown on the predicted resonance diagram in Figure 20. The two strain gage locations of crown and concave trailing edge are denoted by the circle and triangle symbols respectively. The percent gage sensitivity for the first torsion and first bend modes are bracketed directly below the symbols. The maximum vibratory allowables for these locations are ± 14.3 and ± 15.3 ksi.

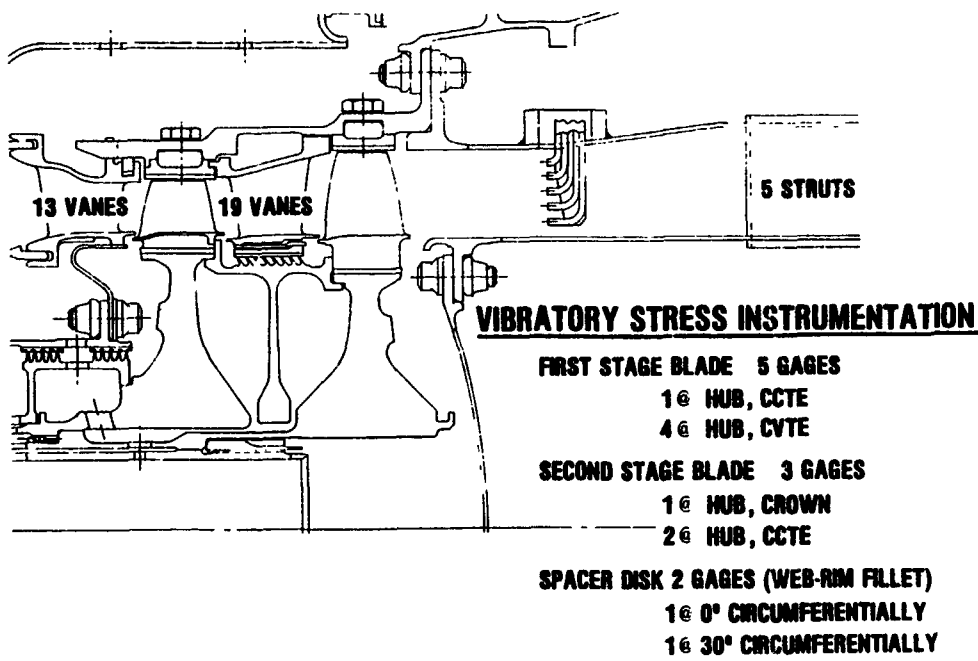


Figure 19. Gasifier Test Configuration.

Maximum measured stresses were ± 6.3 to ± 8.8 ksi for the 1T mode and upstream vane resonance. This compares to a ratioed maximum 1T response of ± 13.3 ksi. The predicted response was estimated to be $\pm 6 - 10$ ksi. The design shows a minimum vibratory margin of 7.5% or 11 ksi using the ± 13.3 ksi as a maximum response.

Based on these measured responses this design should exhibit infinite high cycle fatigue life. Additional instrumented tests during actual engine running will assure that adequate HCF margin is present by better defining the vibratory response distribution (scatter) among blades.

This completes the discussion of forced response. Basic sources of excitation, component geometries, natural mode shapes and frequencies have been presented. Fundamental steps in designing for forced response included discussion of sources, environment, resonance and Goodman diagrams, calculation of natural frequencies, mode shapes and stress distributions, determination of response amplitudes and high cycle fatigue life, redesign considerations, and strain gage testing to verify the design.

FLUTTER DESIGN

Designing to avoid flutter is an important part of the aeroelastic design process for aircraft engine fan and compressor blades. Although there is much more to be learned about turbo-machinery flutter, there are basic principles that have been developed. In this section these principles will be presented. This presentation will contain a discussion of the types of fan/compressor flutter and the dominant design parameters associated with each. A definition of the ideal flutter design system and the overall flutter design procedure will also be included. Finally, a detailed review of five types of fan/compressor flutter and empirical and analytical design systems for each will be presented.

Description of Flutter

The designer is interested in predicting the onset of flutter rather than predicting a specific vibratory response level as in forced vibration. As discussed earlier, the blade vibration present during flutter is not caused by an unsteady external force but instead by the fact that the blade is absorbing energy from the flow around the blade.

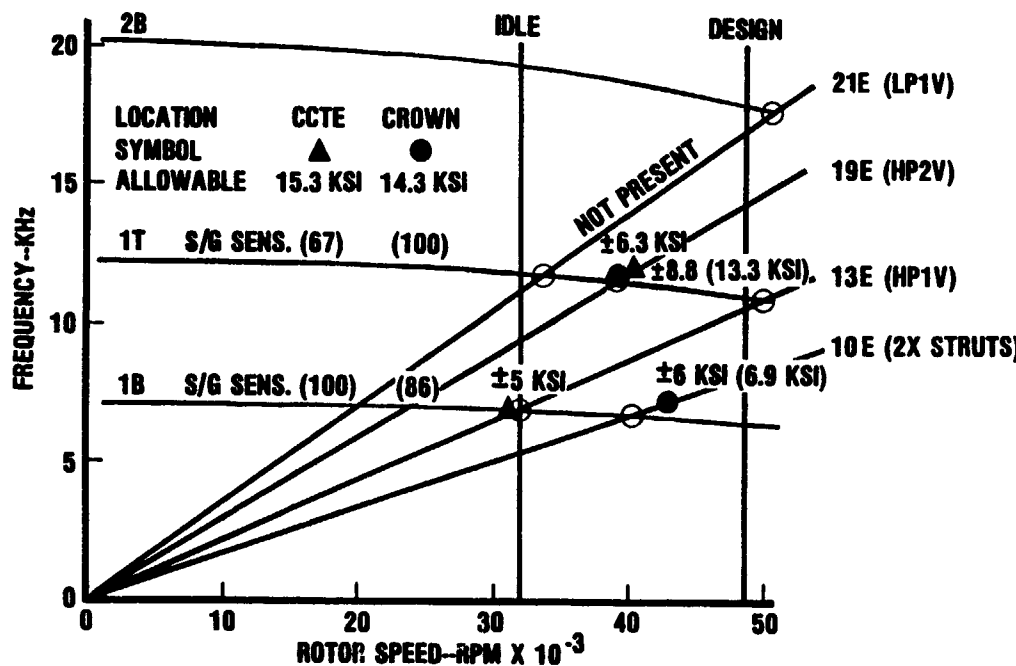


Figure 20. Resonance Diagram for Second Stage -- Gasifier Test Configuration.

Once any random excitation causes a small vibration of the blade, if the blade aerodynamic damping is negative, the blade will absorb energy from the airstream as the blade vibrates. If the energy absorbed from the airstream is greater than that dissipated by the structural damping, the blade vibratory amplitude will increase with time until an energy balance is attained. Random excitation is always present at low levels in the turbomachinery environment. Thus predicting the onset of flutter entails predicting the aeroelastic conditions that exist when the absorbed energy due to negative aerodynamic damping equals the dissipated energy due to structural damping at the equilibrium vibratory stress level.

For most blade/disk/shroud systems, structural damping (i.e., frictional damping, material damping, etc.) is not large. Therefore, the stability (design) criterion essentially becomes positive aerodynamic damping. Aerodynamic damping is proportional to the nondimensional ratio of unsteady aerodynamic work/cycle to the average kinetic energy of the blade/disk/shroud system.

δ_{AERO} = AERODYNAMIC DAMPING

$\sim \frac{\text{UNSTEADY AERODYNAMIC WORK}}{\text{BLADE/DISK/SHROUD KINETIC ENERGY}}$ (6)

$$\delta_{AERO} = \frac{(\text{NB})(\text{ROOT-TO-TIP INTEGRATED UNSTEADY WORK/CYCLE})}{(4)(\text{AVERAGE KINETIC ENERGY of B-D-S-SYSTEM})} \quad (7)$$

The criterion for stability requires that the unsteady aerodynamic work/cycle remain positive (i.e., system is not absorbing energy). The unsteady aerodynamic work/cycle is the integral over one vibratory cycle of the product of the in-phase components of unsteady force (pressure times area) and unsteady displacement.

$$= \int F_0 \exp(i(\omega t + \phi)) \cdot d(h_0 \exp(i\omega t)) \quad (8)$$

$$= \int_0^{2\pi} F_0 \exp(i(\omega t + \phi)) \cdot i h_0 \exp(i\omega t) d(\omega t) \quad (9)$$



Thus positive aerodynamic damping is related to the aerodynamic characteristics of the flow field (unsteady forces) and vibratory mode shape (displacement).

Dependence upon the flow field is noted by the names given to five types of fan/compressor flutter which have been observed and reported during the last thirty-five years. These five are presented in Figure 21 on a compressor performance map. Each of these types of flutter is characterized by a distinct aerodynamic flow field condition. Each of these types will be discussed later with respect to avoidance of flutter in design. References for this section are Carta (1966) and Snyder (1974).

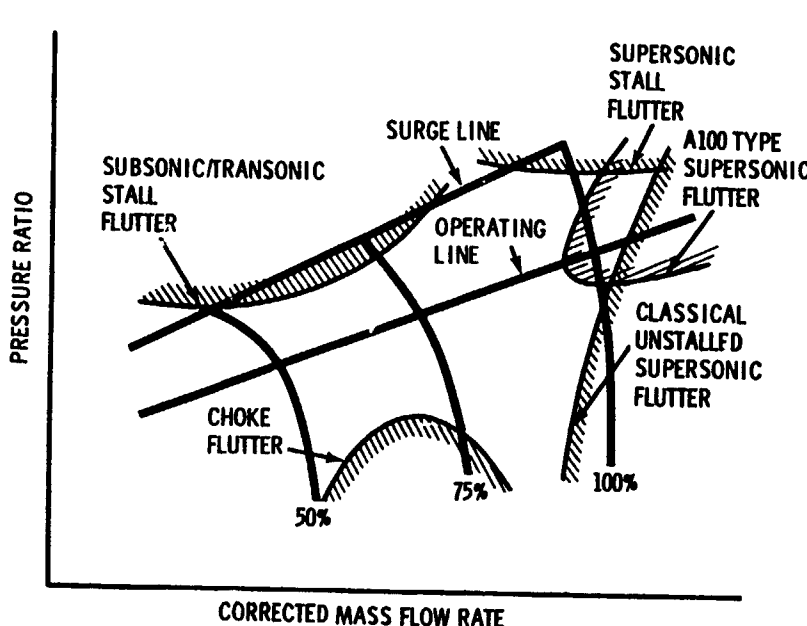


Figure 21. Types of Fan/Compressor Flutter.

Dominant Design Parameters

Since the distinct flutter regimes are identified by the type of flow present, it is not surprising that four of the five dominant flutter design parameters involve aerodynamic terms. The five are as follows:

1. Reduced velocity
2. Mach number
3. Blade loading parameter
4. Static pressure/density
5. Vibratory mode shape

The fifth parameter, vibratory mode shape, is necessary since the vibratory displacement directly affects the magnitude and sign of the unsteady aerodynamic work per cycle. All five design parameters are pertinent to each type of flutter and are important elements of the flutter design system.

The first two dominant design parameters are dimensionless and appear in the governing equations for unsteady flow over a vibrating airfoil. Mach number is a parameter which describes the nature of the unsteady flow field whether it be subsonic, transonic or supersonic. It has been seen that Mach number and reduced velocity are key parameters in correlating flutter data and developing empirical design systems. Reduced velocity is de-

fined as the ratio of relative inlet velocity to the product of blade vibratory frequency and blade semi-chord length.

$$\text{Reduced velocity} = \frac{V}{b\omega} \quad (10)$$

Decreasing this parameter is stabilizing. In general, the reduced velocity parameter is between 1 and 5 at the flutter stability boundary. Examination of the unsteady flow equations for flow through a cascade of airfoils shows that the unsteady flow terms are important for these levels of reduced velocity.

Blade loading parameters have also been used in correlations of flutter data. Incidence or non-dimensional incidence, pressure ratio, diffusion factor and margin to choke are parameters which have been used to describe the blade loading. Blade shape geometry descriptors such as leading edge radius, maximum thickness/chord ratio and the maximum thickness location also indicate the magnitude and distribution of aerodynamic loading.

Either static density or pressure can be used as a design parameter if static temperature is held constant and the flow of a perfect gas, $p = \rho RT$, is being considered. The primary effect of changing air density (or pressure) is a proportional change in unsteady aerodynamic work/cycle and therefore in aerodynamic damping.

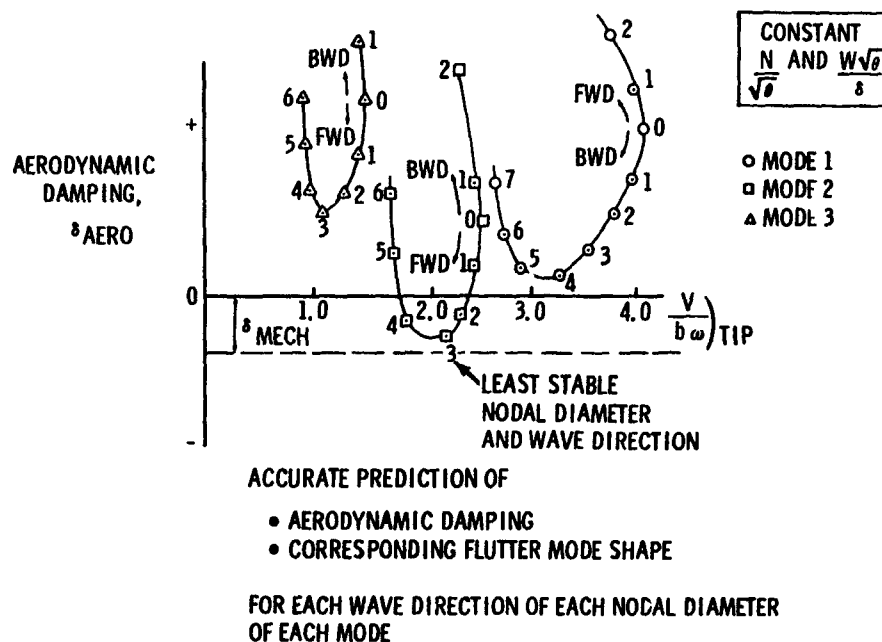


Figure 22. Definition of Ideal Flutter Design System.

Increasing the gas density is stabilizing if aerodynamic damping is positive. Likewise, increasing the gas density is destabilizing if aerodynamic damping is negative. An indirect effect of changing gas density is that of changing the flutter mode shape which is a weak function of mass ratio. Thus aerodynamic damping is also a function of density through the effect of air density on the flutter mode shape. Aerodynamic damping is also a function of density through the effect of density on the Reynolds number and the effect of Reynolds number on the unsteady flow field.

The final dominant design parameter is vibratory mode shape. The unsteady aerodynamic work per cycle of blade motion is a function of both the unsteady surface pressure created by the blade's motion in the air flow and the vibratory mode shape. Thus, since the blade unsteady surface pressure distribution is also a function of the blade mode shape (motion), the aerodynamic damping is a strong function of the vibratory mode shape. Vibratory mode shape may be described as pure bending or torsion of the airfoil or a coupling of bending and torsion. Rigid body bending or translation of the airfoil is displacement of the airfoil perpendicular to the minimum moment of inertia axis. Rigid body torsion or pitching is rotation

of the airfoil about the minimum polar moment of inertia axis. Some cases of flutter have been encountered in a chordwise bending with node lines nearly perpendicular to the airfoil chord. Since blade modes generally contain chordwise bending, bending and torsion motions, the modes can best be described in terms of a generalized mode shape where motion perpendicular to the mean line is expressed as a function of radial and chordwise position.

References for this section are Pines (1958) and Theodeorsen (1935).

Design System and Steps

This dependence of flutter or vibratory mode shape is illustrated in Figure 22 in the definition of the ideal flutter design system, an experimentally verified analytical prediction system. Classical supersonic unstalled flutter is one type of flutter for which such a design system exists. The analysis which is a part of an ideal flutter design system considers the mode shape and frequency for each nodal diameter of each mode. It also considers both forward and backward traveling wave directions, Campbell (1924). There is a least stable nodal

STEP 1 - AERODYNAMIC DESIGN AND ANALYSIS

DESIGN

- PRESSURE RATIO/STAGE
- SPECIFIC FLOW
- H_1
- T/inlet & exit
- FLOWPATH TYPE
- BLADE ASPECT RATIO
- THICKNESS/CHORD RATIO
- BLADE SERIES
- TAPER RATIO

ANALYSIS

- RELATIVE VELOCITY AND MACH NUMBER
- BLADE CAMBER AND CHORD
- INCIDENCE, D_f , MARGIN TO CHOKE
- STATIC AIR TEMPERATURE
- STATIC AIR DENSITY AND PRESSURE



STEP 2 - BLADE STRUCTURAL DESIGN AND ANALYSIS

DESIGN

- BLADE MATERIAL
- NO. OF SHROUDS

ANALYSIS

- STEADY STATE
- BLADE/(DISK/SHROUD) VIBRATORY MODE SHAPES AND FREQUENCIES



STEP 3 - FLUTTER ANALYSIS AND REDESIGN

ANALYSIS

- BLADE STABILITY MARGIN

REDESIGN

- CHANGE ASPECT RATIO
OR
- CHANGE BLADE THICKNESS
OR
- CHANGE TAPER RATIO
OR
- CHANGE SHROUD LOCATION



Figure 23. Flutter Design Procedure.

diameter and wave direction for each mode and of these there is a least stable mode (i.e., mode 2) for the structure. The design system must accurately calculate the aerodynamic damping and corresponding flutter mode shape for each of these modes in order to predict the stability of the blade. Stability is determined by maintaining positive total damping (i.e. above dashed line) for all modes and all nodal diameters and wave directions. Furthermore, the aerodynamic damping must be determined at the least stable fan/compressor steady state aerodynamic operating point. The impact of the steady state aerodynamic operating point will be discussed in more detail in later sections.

The three steps in the flutter design procedure are outlined in Figure 23. The first step is to perform the aerodynamic design of the blade and to obtain the pertinent aerodynamic parameters that have an impact on aerodynamic damping. This should be accomplished at the most critical points within the predicted operating envelope of the engine. The definition of the modal displacement and frequencies of the blade/disk/shroud system is the next step. This can be done by conducting a structural dynamic analysis using a finite element model of the blade/disk/shroud system to determine the modal frequencies and mode shapes of the natural modes of the system (i.e. ND = 0, 1, 2,...for modes 1, 2, 3...). The final step is to conduct the analysis to combine the steady state aerodynamics and dynamics results and conduct a flutter analysis (unsteady aerodynamics analysis plus stability analysis). Depending on the type of flutter this analysis may entail an actual calculation of the aerodynamic damping (e.g. classical supersonic unstalled flutter) for each mode or may involve an empirical correlation of flutter data (stalled flutter) using the dominant design parameters.

If the blade is predicted to exhibit flutter within the desired operating range, a redesign effort must be initiated. Changes are usually in the form of geometry modifications which not only affect the system modal characteristics (displacement and frequency) but also the flow characteristics (velocity and blade loading). These changes are aimed at obtaining a design which exhibits stability, positive total damping, throughout the engine operating environment.

Detailed Review, Types of Flutter and Design

The types of flutter will now be discussed with respect to the dominant design parameters and the available analytical tools. The purpose of this discussion is to demonstrate how to avoid fan/compressor flutter through judicious design. Five types of flutter and the location of their boundaries on a compressor map are shown in Figure 21. The order of discussion will be subsonic/transonic stall flutter, classical uninstalled supersonic flutter, A100 supersonic flutter, choke flutter and supersonic stall flutter.

The first documented type of turbomachinery flutter, subsonic/transonic stall, was first reported almost at the same time that the performance of the first axial compressor was reported. At first, this type of flutter was confused w/ rotating stall. Characteristics of the subsonic/transonic stall flutter vibratory stress response are non-integral order, sporadic amplitude with time, stress holds or increases with increasing stage loading and blades vibrate at different frequencies and amplitudes in same mode, whether bending, torsion or coupled modes.

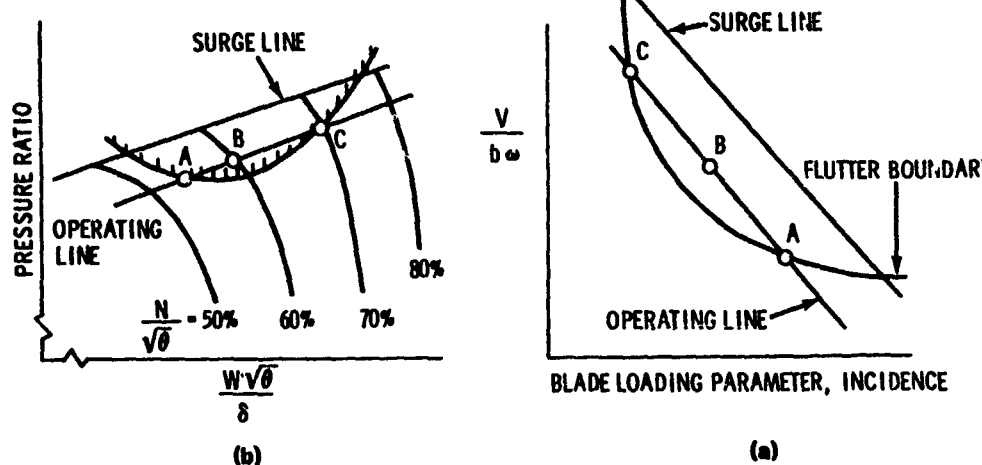


Figure 24. Subsonic/Transonic Stall Flutter Design System Using Reduced Velocity and Blade Loading Parameter.

All five dominant flutter design parameters are needed to describe subsonic/transonic stall flutter (S/TSF). By its very name, S/TSF is dependent on Mach number. The shape of the flutter boundary on the compressor map shows its dependence on a blade loading parameter such as incidence or diffusion factor. The simplest S/TSF design system is a correlation of flutter and no flutter data on a plot of reduced velocity versus a blade loading parameter such as incidence (see Figure 24). Experience has shown that with such a correlation with parameters chosen at a representative spanwise location it is possible to separate most of the flutter and no flutter data with a curved line. This curve is then called the flutter boundary. The relationship between points A and C on the flutter boundary on the compressor map and the same points on the design system flutter boundary are shown. This example shows that S/TSF flutter can prevent acceleration along the operating line of the compressor. For the case where the boundary falls between the operating line and surge line the flutter boundary can become a limiting characteristic of the compressor performance if distortion, increased density or temperature or changes in the operating line occur. The design goal is to have all points on the surge line be below the flutter boundary with an adequate margin.

Based on this empirical design system, a blade design may be stabilized by lowering the blade loading parameter. This may be accomplished by modifying the position of the operating line as shown in Figure 25a. This change may be made through rescheduling stators or re-twisting the airfoil. Likewise, by changing the blade shape, the position of the flutter boundary may be moved. Such changes to shape would include leading edge radius, camber of leading edge, blade thickness and maximum thickness location. All of the above changes demonstrate the effect of lowering the blade loading parameters (i.e. diffusion factor, incidence) to increase the stability of the blade in the operating environment (Figure 25b).

Another way of avoiding a potential flutter problem suggested by this empirical design system is to lower the reduced velocity. This is most commonly done by increasing the product of semi-chord times frequency, $b\omega$. Increasing the chord or lowering blade thickening, adding part span shrouds (also called nubbers, dampers, bumpers and clappers) or changing taper ratio have been used. Use of composite materials have been made to change the material modulus/density ratio to increase frequency. The effects of increasing $b\omega$ are shown graphically in Figure 26. The change shows up as a relocation of the operating and surge lines in the correlation plot (Figure 26a) while it is a shift in the flutter boundary on the performance map.

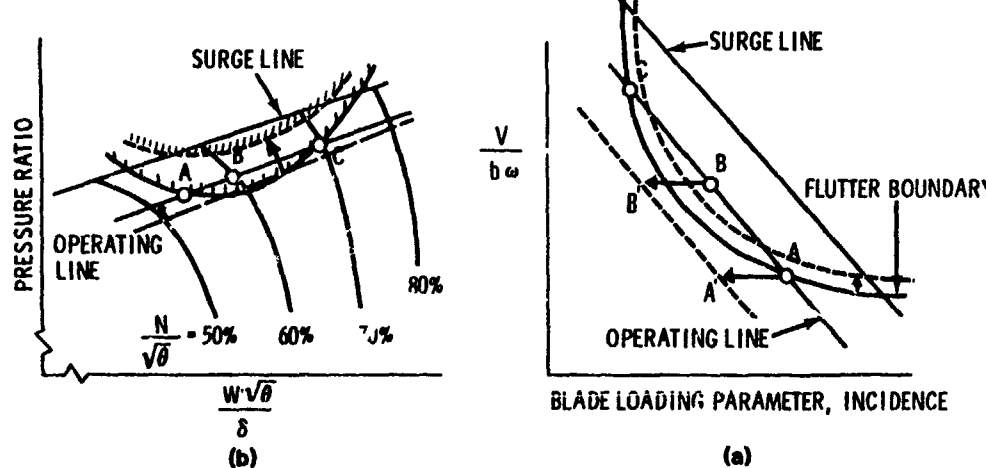


Figure 25. Stabilizing Effect of Lowering Blade Loading Parameter.

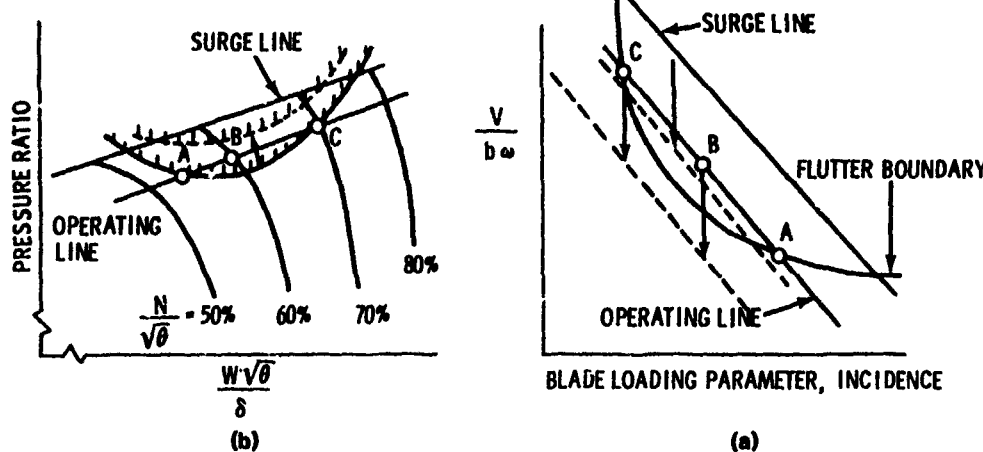


Figure 26. Stabilizing Effect of Increasing the Product $b\omega$.

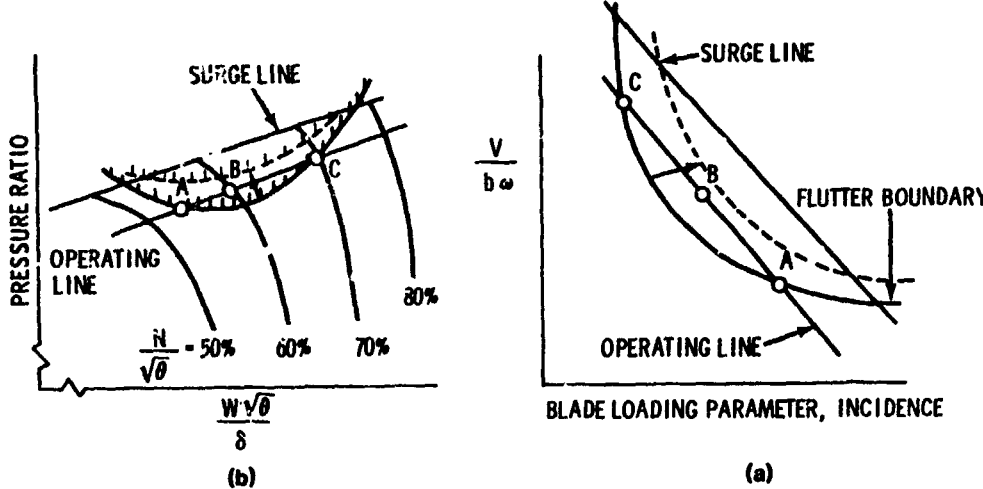


Figure 27. Stabilizing Effect of Lowering Static Pressure/Density at Constant Static Temperature

Blade inlet static density (or static pressure) changes may occur as the aircraft changes altitude and/or flight speed or as the engine changes speed. As discussed earlier aerodynamic damping is proportional to static density. If the aerodynamic damping is positive, increases in static density are further stabilizing. If the aerodynamic damping is negative, decreases in static density are stabilizing. The latter is shown in Figure 27 on both the compressor map and the S/TSF design system as shifts in flutter boundary. Changes in aircraft altitude and/or flight speed also affect blade inlet static temperature. However, to properly predict the independent effects of density and temperature changes, they should be considered independently. After they are considered independently, the two effects can be combined.

Changes in blade inlet static temperature affect the relationship between Mach number and velocity. If Mach number is held constant and static temperature is decreased, velocity is decreased and, therefore, reduced velocity is reduced. Thus, reducing static temperature and holding static density will be stabilizing. The effect of such a change is shown on both the compressor map and the S/TSF design system plot in Figure 28.

In gas turbine engine applications, temperature and density changes generally occur simultaneously. Such is the case as aircraft flight speed is changed. As aircraft flight speed is increased, the blade inlet static temperature increases, corrected speed drops if there is a mechanical speed limiter and blade inlet static density increases. These effects can cause a S/TSF boundary to move nearer to the compressor operating region, while at the same time causing the engine operating point to move closer to the S/TSF region. This is illustrated in Figure 29.

Sufficient flutter margin must be designed into a new compressor or fan such that flutter will not be encountered under any aircraft operating point.

Vibratory mode shape is a dominant S/TSF design parameter. For a given reduced velocity a bending mode is much more stable than a torsional mode (Figure 30a) with node-line located at mid-chord. This implies the need of the designer to evaluate the S/TSF flutter margins of both bending and torsion modes. If bending and torsion modes are coupled by the presence of a flexible disk or part span or tip shroud, the ratio of bending to torsional motion and the phase angle between them must be considered in the flutter analysis. This is illustrated in Figure 30b.

References for subsonic/transonic stall flutter are Shannon (1945), Graham (1965), Huppert (1954), Pearson (1953), Sisto (1953, 1967, 1972, 1974), Schnittger (1954, 1955), Carter (1955a, 1955b), Armstrong (1960), Rowe (1955), Halfman (1951) and Jeffers (1975).

Classical unstalled supersonic flutter (USF) is a design concern if a significant portion of the blade has supersonic relative inlet flow. The term unstalled is used because USF is encountered at the lowest corrected speed when the stage is operating at the lowest pressure ratio. Classical is used because of its similarity to classical aircraft wing flutter. The stress boundary is very steep with respect to speed as shown in Figure 21, thus, preventing higher speed operation. The stress level does not usually fluctuate with time and all blades vibrate at a common frequency unlike S/TSF. Experience to date has been predominately in torsional modes but has occurred in coupled bending/torsion modes or chordwise bending modes. Four dominant design parameters are used to describe USF. They are reduced velocity, Mach number, vibratory mode shape, and static pressure/density.

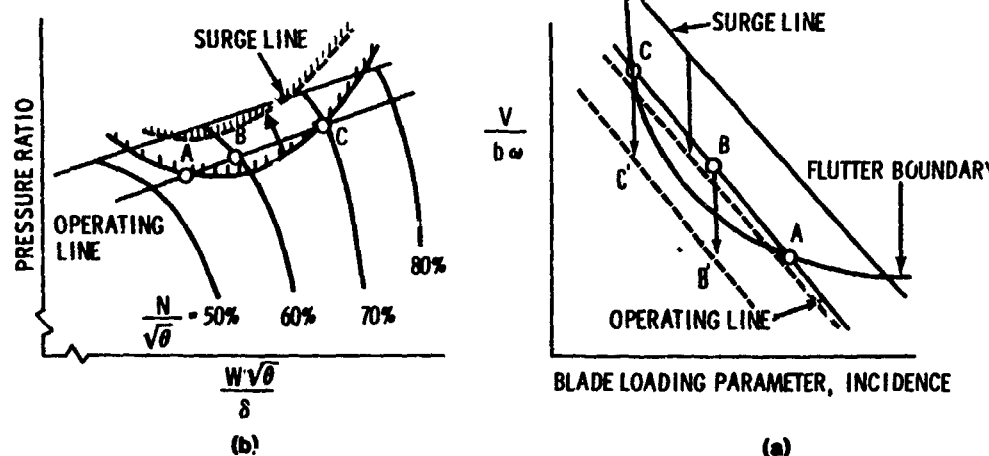


Figure 28. Stabilizing Effect of Reducing Inlet Static Temperature at Constant Static Density.

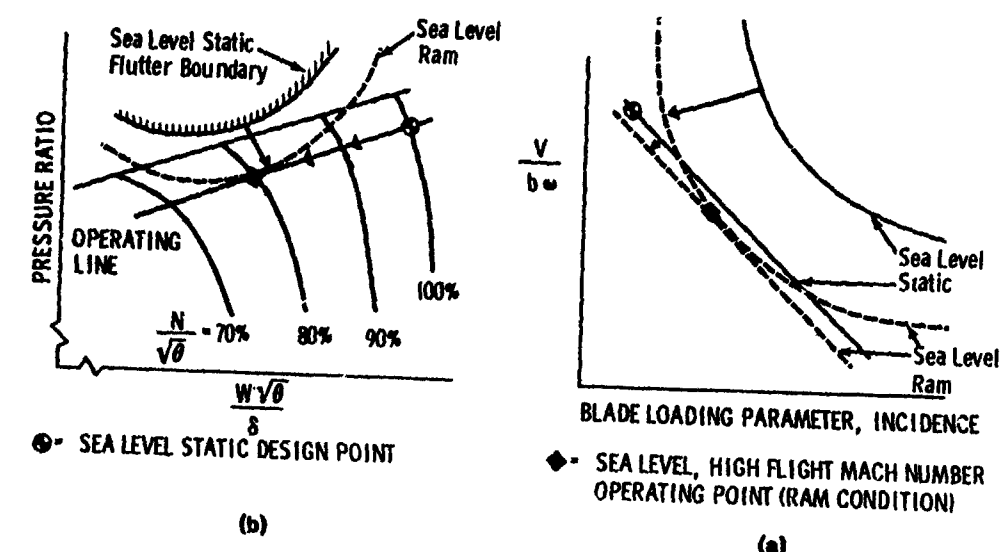


Figure 29. Consideration of Subsonic/Transonic Stall Flutter in Fan/Front Compressor Stages at Sea Level Ram Conditions.

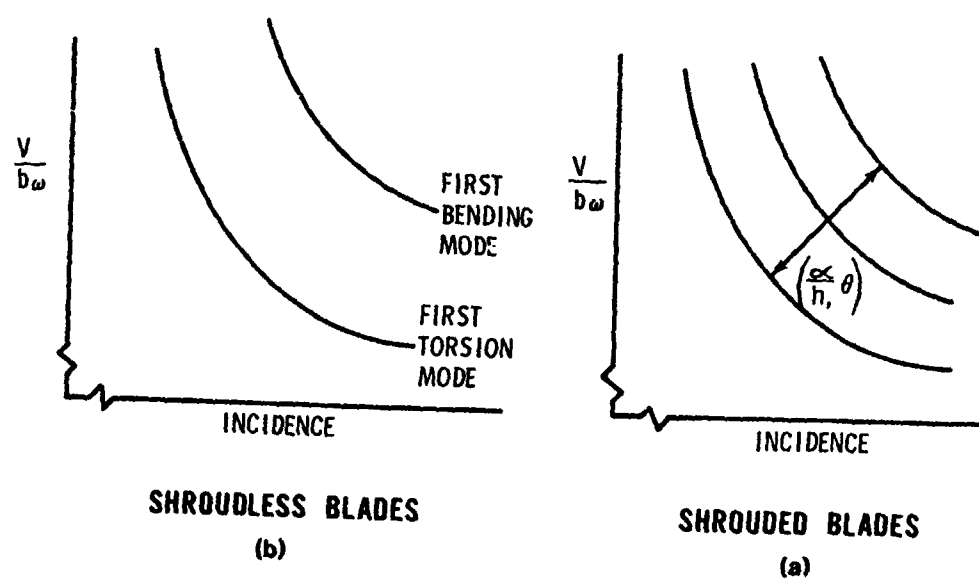


Figure 30. Effect of Mode Shape on Subsonic/Transonic Stall Flutter.

The simplest classical unstalled supersonic flutter design system consists of plotting available classical USF data on a plot of reduced velocity versus inlet Mach number and drawing a curve (flutter boundary) which best separates the flutter and no flutter data points (Figure 31). The flutter data points should be about this curve, while the no flutter data points should be below the line. The design system can be applied to new designs by calculating the parameters reduced velocity and Mach number for points along the compressor operating line and then plotting the operating line on the design system plot. No classical USF is predicted if the operating line is below the flutter boundary.

As in the case of subsonic/transonic stall flutter, increasing the product $b\omega$ is stabilizing for classical supersonic unstalled flutter. The effect of increasing $b\omega$ is to push the flutter boundary to higher operating speeds. This is illustrated in Figure 32. The slope of the "new" operating line on the design plot is inversely proportional to $b\omega$. For successful designs, the flutter boundary is beyond the highest expected operating speed.

Classical unstalled supersonic flutter is the one type of flutter for which a reasonably accurate analytical design system exists. This analytical design system parallels the ideal flutter design system. The existing analytical design system contains a blade-disk-shroud vibrational analysis, an unsteady, flat plate, cascade analysis, and an aerodynamic damping calculation. The result is the capability to calculate the aerodynamic damping for each mode (and nodal diameter if necessary) of a compressor blade/disk assembly. A typical plot of the resulting data is shown in Figure 22.

The effect on classical USF of lowering static density at constant static temperature is stabilizing since aerodynamic damping is proportional to blade inlet static density. This stabilizing effect

is shown on both the empirical and analytical design systems in Figure 33. In each case three points are shown: The original flutter point, the same operating point after the decrease in static density, and a new flutter free operating point at higher rotor speed.

Since reducing inlet static temperature at constant corrected rotor speed causes the mechanical rotor speed and, hence, blade inlet relative velocity to decrease, the effect of reducing inlet static temperature at constant static density is stabilizing for classical USF. The result of such a change is to move the flutter boundary to a higher speed. This is illustrated in Figure 34 on both empirical and analytical design system.

References for classical unstalled supersonic flutter are Snyder (1972, 1974), Mikolajczak (1975), Garrick (1946), Whitehead (1960), Smith (1971), Verdon (1973, 1977), Brix (1974), Caruthers (1976), Nagashima (1974), Goldstein (1975), Ni (1975), Fleeter (1976), Adamczyk (1979), and Halliwell (1976).

A third type of fan/compressor flutter, which has been identified, is A100 type supersonic flutter, Troha (1976). This was identified as a torsional mode flutter of a shroudless blade. The flutter boundary for this type of flutter is unlike the other types of flutter, indicating that the unsteady aerodynamics of this type of flutter are unique. Looking at Figure 21, a moderate pressure ratio at constant corrected speed is destabilizing, while at sufficiently higher pressure ratio the effect of the same change is stabilizing. However, though unique in boundary it is very similar to USF. The outer portion of the blade is supersonic. The stress boundary is steep. All blades vibrate at the same frequency and interblade phase angle. The reduced velocity/inlet Mach number empirical method also predicts this instability. Varying of $b\omega$, static pressure/density and inlet static temperature produces similar effects as those observed with USF.

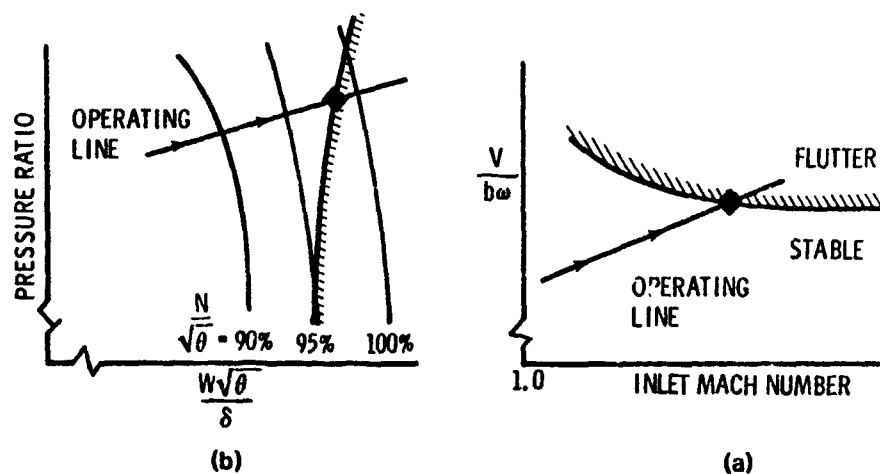


Figure 31. Classical Unstalled Supersonic Flutter Design System Using Reduced Velocity and Mach Number.

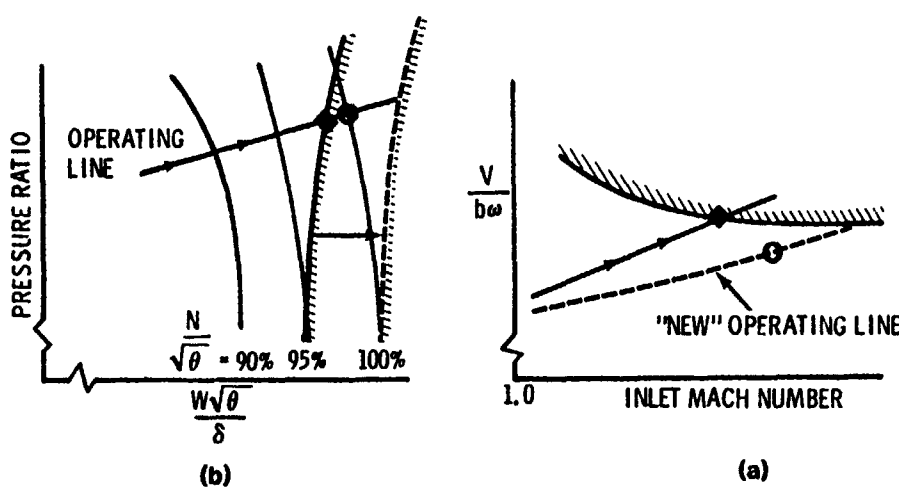
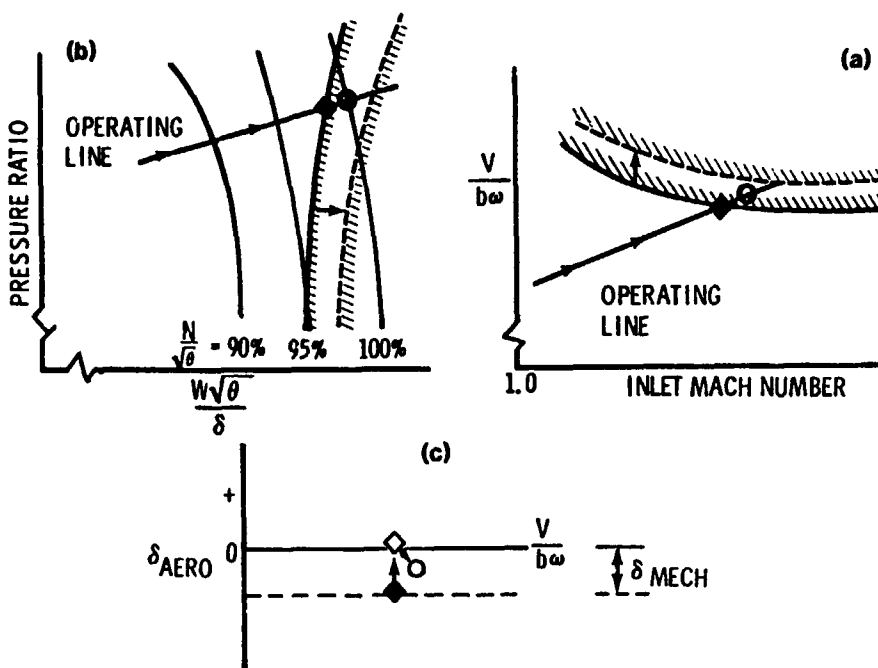
Figure 32. Stabilizing Effect of Increasing the Product $b\omega$.

Figure 33. Stabilizing Effect of Lowering Static Pressure/Density at Constant Static Temperature.

Choke flutter received its name from the close proximity of the flutter boundary and the choke operating region of the compressor. This boundary can be encountered during part speed operation, Figure 21. Blades are usually operating at negative incidences in the transonic flow regime. In this near choke condition, in-passage shocks with associated flow separation are thought to influence the aero-elastic characteristics and thus the blade stability. Recently, modal aerodynamic solution codes which analytically predict aerodynamic damping as in the ideal flutter design system and the USF analytical design system have been developed for choke flutter. The crucial element in these codes is the development of the transonic unsteady aerodynamic programs. Improvement in this area is presently underway and will benefit the designer in predicting the occurrence of choke flutter. Experimental data has been correlated much like S/TSF data as a function of reduced velocity and incidence. Reducing solidity has been found to increase stability due to increases in incidence. As with S/TSF lowering reduced velocity, static pressure/density and inlet static temperature are stabilizing effects. Choke flutter has been observed in both bending and torsional modes.

References for choke flutter are Carter (1953, 1957), Schneider (1980), and Jutras (1982).

The last type of flutter to be discussed will be supersonic stall flutter. The position of this flutter boundary on the compressor map is suggested by the title. This flutter is like unstalled supersonic flutter in that all blades vibrate at a common frequency. Experience indicates that

the mode is generally first bending. An analytical design approach which determines the unsteady aerodynamic force, aerodynamic damping, as a function of interblade phase angle has been developed for the designer by Adamczyk (1981). The authors use two dimensional actuator disk theory in which flow separation is represented through rotor loss and deviation-angle correlations. The analysis is for the fundamental mode bending of shroudless blades. Based on experimental data, Ruggieri (1974), blade stability is increased by increases in $b\omega$ and reduction in blade loading. The presence of strong shocks is indicated to have an effect on this type of flutter, Goldstein (1977). This effect is one of destabilizing for both bending and torsional motions and as such may be expected to lower the back pressure at which this flutter first occurs. Flow separation was observed to exist, Riffel (1980), for a cascade of airfoils representing the airfoils exhibiting flutter above 105% speed in Ruggieri (1974).

This concludes the discussion of forced vibration and flutter design methodology. Design principles have been presented to aid the designer of turbomachinery in understanding the mechanisms involved and in properly evaluating the crucial components of turbomachinery. Effective application of the design steps for both forced vibration and flutter are necessary to limit the occurrences of HCF failure in new turbine engine designs. Research is continuing at this time to define and model the unsteady flow fields and forces present during forced vibration and flutter. As knowledge is acquired, experimental and theoretical, and combined to develop better analytical predictions tools, the possibility of eliminating high cycle fatigue from turbine engines in design is increased and costs decreased.

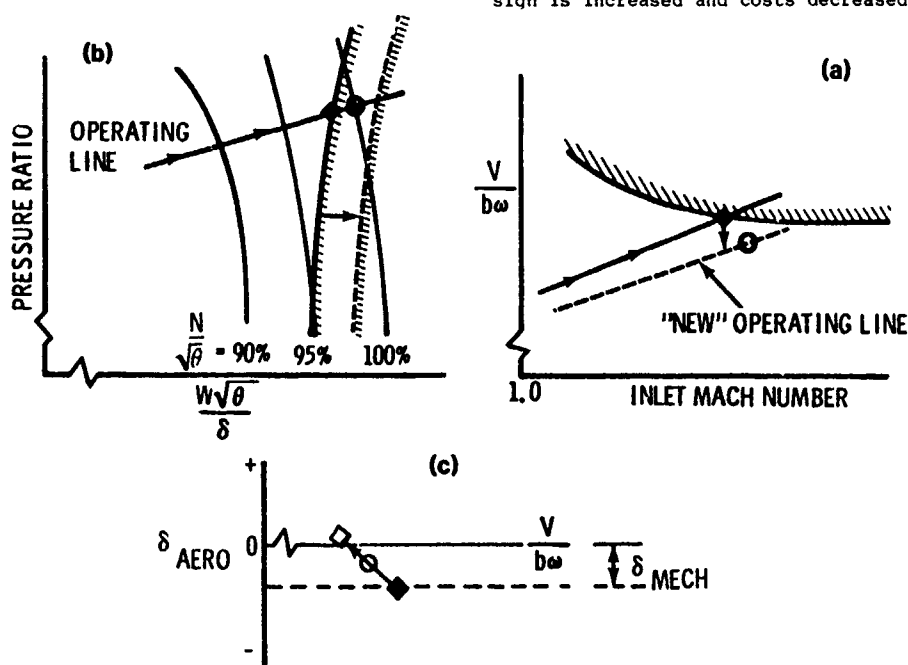


Figure 34. Stabilizing Effect of Reducing Inlet Static Pressure.

ADDENDUM TO PROGRAM LISTING FOR
UNSTEADY TWO-DIMENSIONAL LINEARIZED SUBSONIC FLOW IN CASCADES
VOLUME I, CHAPTER 3, PAGES 3-24 TO 3-30

MODIFICATION TO LINSUB

Rw

D. S. Whitehead

It has been found that program LINSUB (pp. 3-24 through 3-30 in Volume I) produces incorrect results in certain cases when the phase angle is not within the recommended range. This is due to the condition used to terminate the series, which terminates when one term of the series becomes small. In order to eliminate this behaviour, it is recommended that the program should be modified so that the series is terminated when two successive terms of the series become small. The modifications occur in subroutine DSWK (pp. 3-26, 3-27) and are shown in the following two extracts.

[Left Column, p. 3-271]

```

C ASSEMBLE MATRIX
C I=-M+1 IN PAPER) GIVES VORTEX POSITION
C J=(-L+1 IN PAPER) GIVES MATCHING POINT
C
30      CALL WAVE(IR,IW)
        IF(IV.EQ.1) GO TO 142
        DO 131 I=1,NP
        DO 131 J=1,NP
        IF(ICHECK(I,J).EQ.2) GO TO 131
          Replace .EQ.1 by .EQ.2.

```

[Right Column, p. 3-271]

```

C CHECK CONVERGENCE OF SERIES
C
      X=TERMR*TERMR+TERMI*TERMI
      Y=KR(I,J)*KR(I,J)+KI(I,J)*KI(I,J)
      IF((X/Y).LE.1.0E-10) GO TO 111
      ICHECK(I,J)=0
      GO TO 131
111   IF(ICHECK(I,J).EQ.1) GO TO 112
      ICHECK(I,J)=1
      GO TO 131
112   ICHECK(I,J)=2
      ICOUNT=ICOUNT+1

```

REFERENCES

- ADAMCZYK, J., and GOLDSTEIN, M.E. 1978 Unsteady Flow in a Supersonic Cascade with Subsonic Leading-Edge Locus. AIAA Journal, Vol. 16, No. 12, December 1978.
- ADAMCZYK, J., GOLDSTEIN, M. and HARTMAN, M. 1978 Supersonic Unstalled Flutter. NASA TM 79001, October 1978.
- ADAMCZYK, J., STEVENS, W., and JUTRAS, R. 1981 Supersonic Stall Flutter of High Speed Fans. ASME 81-GT-184.
- AFOLABI, H.D. 1982 Vibration of Mistuned Bladed Disc Assemblies. Ph. D. Thesis, Department of Mechanical Engineering, Imperial College.
- AFOLABI, H.D. 1986 Natural Frequencies of Cantilever Blades with Resilient Roots. Journal of Sound & Vibration, 110(3), pp. 429-441.
- ARMSTRONG, E.K. 1955 An Investigation into the Coupling between Blade and Disc Vibration. Ph.D. Thesis, Cambridge University.
- ARMSTRONG, E.K. 1967 Recent Blade Vibration Techniques. Trans. ASME Journal of Engineering for Power, Vol. 89, Series A, No. 3, July 1967, pp. 437-444.
- ARMSTRONG E.K. 1977 Novel Aspects of Signature Analysis in Aero Engines. Application of New Signature Analysis Technology Conference, Engineering Foundation, July 1977.
- ARMSTRONG, E.K. 1980 What Can Research Do for Aero Engine Vibration and Dynamics?. Paper - British Theoretical Mechanics Colloquium held in Cambridge 1980.
- ARMSTRONG, E.K., CHRISTIE, P.I., and HUNT, T.M. 1966a Vibration in Cylindrical Shafts. Paper 10 - Applied Mechanics Convention 1966, Proc. Inst. Mech. Engrs 1965-66, Vol. 180.
- ARMSTRONG, E.K., CROWCROFT, R.S., and HUNT, T.M. 1966b Fatigue Life of Compressor Blading. Paper 14 - Applied Mechanics Convention 1966, Proc. Inst. Mech. Engrs 1965-66, Vol. 180.
- ARMSTRONG, E.K. and STEVENSON, R.E. 1960 Some Practical Aspects of Compressor Blade Vibration. Journal Royal Aero. Soc., Vol. 64, No. 591, March 1960, pp. 117-130.
- ARMSTRONG, E.K. and WILLIAMS, D.D. 1965 Some Intake Flow Mal-Distribution Effects on Compressor Rotor Blade Vibration. Journal of Sound and Vibration, 1965, pp. 1-15.
- ARMSTRONG, P.J. and FREDERICK, C.O. 1966 A Mathematical Representation of the Multiaxial Bauschinger Effect. C.E.G.B., Report RD/B/N 731, 1966.
- ATASSI, H. and AKAI, F.J. 1978 Effect of Blade Loading and Thickness on the Aerodynamics of Oscillating Cascades. AIAA 16th Aerospace Science Meeting, Paper No. 77-227.
- BELINGER, V., BOLLETEN, U., and LOCHER, W.E. 1976 Effects of Shear Deformation, Rotary Inertia and Elasticity of Support on the Resonance Frequencies of Short Cantilever Beams. Trans. ASME, J. Eng. Power 98, pp. 79-97.
- BENDAT, J.S. and PIERSOLL, A.G. 1971 Random Data. John Wiley & Sons.
- BENDIKSEN, O.O. 1984 Flutter of Mistuned Turbomachinery Rotors. Trans. ASME, Journal of Engineering for Gas Turbines and Power, Vol. 106, No. 1, pp. 25-33.
- BENDIKSEN, O.O. and FRIEDMAN, P.P. 1981 Coupled Bending-Torsion Flutter in Cascades. AIAA Journal, Vol. 18, No. 2, pp. 194-201.
- BISHOP, R.E.D. and JOHNSON, D.C. 1960 The Mechanics of Vibration. Cambridge University Press.
- BISPLINGHOFF, R.L., ASHLEY, H., and HALFMAN, R.L. 1955 Aeroelasticity. Addison-Wesley Publishing Co., Reading, Mass.
- BISPLINGHOFF, R.L., and ASHLEY, H. 1962 Principles of Aeroelasticity. John Wiley and Sons, New York.
- BLACKWELL, B.D. 1958 Some Investigations in the Field of Blade Engineering. Journal of Royal Aeronautical Society, Vol. 62, pp. 633-646.
- BLEVINS, R.D. 1979 Formulas for Natural Frequency and Mode Shape. Van Nstrand, New York.
- BRIX, C.W. and PLATZER, M.F. 1974 Theoretical Investigation of Supersonic Flow Past Oscillating Cascades with Subsonic Leading-Edge Locus. AIAA Paper No. 74-14, Washington, D.C.
- BROOKER, M.J. and HALLIWELL, D.G. 1984 A Comparison of Measured and Predicted Unsteady Pressure on a Fan Blade in Unstalled Supersonic Flutter, presented at the Symposium on the Aeroelasticity of Turbomachines and Propellers, Cambridge University, UK, September 1984.
- BUI QUOC, T., DUBUC, J., BAZERGUE, A., and BIRON, J. 1971 J. Bas. Eng., Trans. ASME, pp. 691-698.
- BURDEKIN, F.M. 1981 Practical Aspects of Fracture Mechanics in Engineering Design. John Player Lecture, Proc. I. Mech. E., Vol. 195, No. 12.

- CAILLETAUD, G., POLICELLA, H., and GAUDIN, G. 1980 Mesure de deformation et d'endommagement par methode electrique. R. A., 1980-1.
- CAMPBELL, W. 1924 Protection of Steam Turbine Disc Wheels from Axial Vibration. ASME Paper No. 1920, May 26, 1924.
- CARDINALE V.M., BANKHEAD, H.R., and MCKAY, R.A. 1980 Experimental Verification of Turbo Blading Aeromechanics. AGARD Conference Proceedings, No. 293, AGARD Propulsion and Energetics Panel, Turin Italy, 29 September - 30 October 1980.
- CARNEGIE, W., DAWSON, B., and IHOMAS, J. 1966 Vibration Characteristics of Cantilever Blading. Proc. Inst. Mech. Engrs. 180 (31).
- CARRY, C. and STRUDEL, J.L. 1978 Apparent and Effective Creep Parameter in Single Crystals of a Nickel Base Super Alloy. Acta Metallurgica, Vol. 26, pp. 859-870.
- CARTA, F.O., 1966 A Parametric Study of Coupled Blade-Disk-^o and Flutter Instabilities in Turbojet Engine Rotors. United Aircraft Research Laboratories Report E7-1.
- CARTA, F.O. 1967 Coupled Blade-Disk-Shroud Flutter Instabilities in Turbojet Engine Rotors. ASME Journal of Engineering for Power 89 (ASME Paper 66-WA/GT-6), p. 419-426.
- CARTA, F.O., 1983 Unsteady Aerodynamics and Gapwise Periodicity of Oscillating Cascaded Airfoils. Trans. ASME, Journal of Engineering for Power, Vol. 105, July, pp. 565-574.
- CARTA, F.O. and ST. HILAIRE, A.O. 1980 Effect of Interblade Phase Angle and Incidence Angle on Cascade Pitching Stability. Trans. ASME Journal of Engineering for Power, Vol. 102, No. 2, pp. 391-396.
- CARTER, A.D.S. 1953 Some Preliminary Notes on the Flutter of Axial Compressor Blades. N.G.T.E. Memorandum No. M. 181, November 1953.
- CARTER, A.D.S. 1955 A Theoretical Investigation of the Factors Affecting Stalling Flutter of Compressor Blades. N.G.T.E., A.R.C. Technical Report N. R. 172, C.P. No. 265, April 1955.
- CARTER, A.D.S., KILPATRICK, D.A., MOSS, C.E., and RITCHIE, J. 1955 An Experimental Investigation of the Blade Vibratory Stresses in a Single-Stage Compressor. N.G.T.E., A.R.C., Technical Report No. 4. 174, C.P. No. 266, April 1955.
- CARTER, A.D.S. and KILPATRICK, D.A. 1957 Self-Excited Vibration of Axial-Flow Compressor Blades. Proceedings of the Institution of Mechanical Engineers, Vol. 171, pp. 245-281.
- CARUTHERS, J.E. 1976 Theoretical Analysis of Unsteady Supersonic Flow Around Harmonically Oscillating Turbofan Cascades. Ph.D. Thesis, Georgia Institute of Technology, September 1976.
- CARUTHERS, J.E. 1980 Aerodynamic Analysis of Cascaded Airfoils in Unsteady Rotational Flow. Symposium on Aeroelasticity in Turbomachines, Lausanne, Switzerland, September 1980.
- CHABOCHE, J.L. 1974 Revue Francaise de Mecanique 50-51. Annales de l'IIRTP, HS39, 1977.
- CHABOCHE, J.L. 1977 Viscoplastic Constitutive Equations for the Description of Cyclic and Anisotropic Behaviour of Metals, Bull. Acad. Pol. Sc., Serie Sc. et Tech., Vol. 25, n° 1.
- CHABOCHE, J.L. 1978 Description Thermodynamique et Phenomenologique de la Visco-plasticite Cyclique avec Endommagement. These Publication CNERA.
- CHABOCHE, J.L. and CAILLETAUD, G. 1979 Macroscopic Description of Microstructural Changes Induced by Varying Temperatures. Example of IN 100 Behaviour. ICM 3, Cambridge -T. P. CNERA n° pp. 79-112.
- CHABOCHE, J.L. and CAILLETAUD, G. 1984 Life Prediction at High Temperature under Multiaxial Loading, 63rd Specialists Meeting, AGARD/PEP, Lisse, 1984.
- CHABOCHE, J.L. and CULIE, J.P. 1980 On Turbine Blade Creep and Fatigue Analysis by Special Kinematic Assumptions. Int. Conf. on Eng. Aspects of Creep, Sheffield.
- CHABOCHE, J.L., POLICELLA, H. and KACZMAREK, H. 1978 Application of the SRP Method and Creep-Fatigue Approach to LCFHT Life Prediction of IN 100 Alloy. AGARD CP-243.
- CHABOCHE, J.H., POLICELLA, H. and SAVALLE, S. 1978 Application of the Continuous Damage Approach to the Prediction of High Temperature Low Cycle Fatigue. High Temperature Alloys for Gas Turbines, Liege, 1978.
- CHI, M.R. 1980 Unsteady Aerodynamics in Stalled Cascade and Stall Flutter Prediction. ASME Aerospace Science Meeting, Paper No. 80,c2/aero-1.
- CHI, M.R. and SRINIVASAN, A.V. 1984 Some Recent Advances in the Understanding and Prediction of Turbomachine Subsonic Stall Flutter. ASME Paper No. 84-GT-151.
- CHURCH, A.H., 1957 Mechanical Vibrations, John Wiley & Sons, Inc., New York, N.Y.
- CLOUGH, R. W. 1980 The Finite Element Method After Twenty Years: A Personal View. Computers & Structures, 12, pp. 361-370.
- COFFIN,JR.,L.F. 1954 A Study of the Effect of Cyclic Thermal Stresses in a Ductile Metal. Trans. ASME, 76.

- CRAWLEY, E.F. 1983 Aerodynamic Damping Measurements in a Transonic Compressor, Transactions ASME, Journal of Engineering for Power, Vol. 105, July 1983, pp. 575-584.
- CRAWLEY, E.F. and HALL, K.S. 1985 Optimization and Mechanisms of Mistuning in Cascades, ASME Journal of Engineering for Gas Turbines and Power, Vol. 107, No. 2, 1985, pp. 418-426.
- CULIE, J.P., CAILLETAUD, C., and LASALMONIE, A. 1982 Internal Stress in Viscoplasticity, Comparison Between Mechanical and Microscopic Approaches. Rech. Aeroesp.
- DANFORTH, C.E. 1967 Designing to Avoid Fatigue in Long Life Engineering, Society of Automotive Engineers Transactions, Vol. 75, Sec. 1, pp. 248-262.
- DANFORTH, C.E. 1974 Distortion Induced Vibration in Fan and Compressor Blades. AIAA Paper No. 74-232, 12th Aerospace Sciences Meeting, Washington, D.C., 30 January 1974.
- DANFORTH, C.E. 1975 Blade Vibration: Some Key Elements in Design Verification. J. Aircraft, Vol. 12, No. 4, April 1975, pp. 333-342.
- DOKAINISH, M.A. and RAWTANI, S. 1973 Vibration Analysis of Rotating Cantilever Plates. Int. J. for Num. Methods in Engg. 3(2), pp. 233-248.
- DUGUNDJI, J. and PUNDAS, D.J., 1984 Flutter - Forced Response of Mistuned Rotors Using Standing Wave Analysis, AIAA Journal, Vol. 22, No. 11, November 1984, pp. 1652-1661.
- DUVAUT, G. 1976 Analyse fonctionnelle - mecanique des milieux continus - homogeneisation. Th. and Appl. Mech., North Holland, Amsterdam, 1976.
- DYE, R.C.F. and HENRY, T.A. 1969 Vibration Amplitudes of Compressor Blades Resulting from Scatter in Natural Frequencies. Journal Eng. for Power, ASME 91, pp. 182-188.
- ECCLES, E.S. and SEYMOUR, D.G. 1962 Measuring Gas Turbine Blade Vibration. Engineering, London, England, March 1962.
- EDWARDS, J.W., ASHLEY, H., and BREAKWELL, J.V. 1979 Unsteady Aerodynamic Modeling for Arbitrary Motions, AIAA Journal, Vol. 17, No. 4, April 1979, pp. 365-374.
- E.S.D.U. 1983, Engineering Sciences Data Unit 1983, UK 251-259 Regent Street London W1R 7AD, USA Suite 200, 1495 Chain Bridge Road, McLean, VA 22101.
- EWINS, D.J. 1973 Vibration Characteristics of Bladed Disc Assemblies. Journal of Mechanical Eng. Sci. 15, 3, pp. 165-186.
- EWINS, D.J. 1974 Vibration Modes of Mistuned Bladed Disks. Journal of Engineering for Power, ASME Paper No. 75-GT-114, pp. 349-354.
- EWINS, D.J. and COTTNEY, D.J. 1975 On Predicting the Natural Frequencies of Shrouded Bladed Discs. ASME Paper 75-DET-113.
- EWINS, D. J. 1980 Bladed Disc Vibration - A Review of Techniques and Characteristics. Paper presented at Int. Conference on Recent Advances in Structural Dynamics, Southampton, p. 187-210.
- EWINS, D.J. and HAN, Z.S. 1983 Resonant Vibration Levels of a Mistuned Bladed Disc. ASME Monograph (Ewins, D.J. and Srinivasan, A.V., Editors).
- EWINS, D.J. and IMREGUN, M. 1983 Vibrations of Packeted Bladed Disc Assemblies. ASME Monograph (Ewins, D.J. and Srinivasan, A.V., Editors).
- FERRARIS, G. 1982 Provision du Comportement Dynamique des Ensembles Disque-aubes. These 3 cycle, Univ. de Lyon -INSA.
- FERRARIS, G., HENRY, R., and GAERINER, R. 1983 Determination des Characteristiques des Sections Droites Quelconques des Poutres: Application aux Aubes de Turbomachines. 6eme Congres Francais de Mecanique, Lyon, ALM.
- FERRARIS, G., HENRY, R., LALANNE, M., and TROMPETTE, P. 1983 Frequencies and Mode Shapes of Rotating Bladed Axisymmetric Structures. ASME Monograph Vibrations of Bladed Disk Assemblies, pp 1-10.
- FLEETER, S., NOVICK, A.S., RIFFEL, R.W. and CARUTHERS, J.E. An Experimental Determination of the Unsteady Aerodynamics in a Controlled Oscillating Cascade. ASME Paper 76-GT-17.
- FROST, N.E., MASH, K.J., and POOK, L.P. 1974 Metal Fatigue. Clarendon Press, Oxford.
- FUNG, Y.C. 1955 An Introduction to the Theory of Aeroelasticity. John Wiley and Sons, New York.
- GALLUS, H.E., LAMBERTZ, J., AND WALLMAN, T. 1979 Blade Row Interaction in an Axial Flow Subsonic Compressor Stage. ASME Paper No. 79-GT-92.
- GALLUS, H.E., GROLLIUS, H., AND LAMBERTZ, J. 1982 The Influence of Blade Number Ratio and Blade Row Spacing on Axial-Flow Compressor Stator Blade Dynamic Load and Stage Sound Pressure Level. Journal of Engineering for Power, Vol. 104, July 1982, pp. 633-641.

- GARRICK, I.S. and RUBINOW, S.I. 1946 Flutter and Oscillating Air Force Calculations for an Airfoil in Two-Dimensional Supersonic Flow. NACA Report 846.
- GERMAIN, P. 1973 Cours de Mecanique des milieux continus. Tome 1, Masson, Paris.
- GOLDSTEIN, M.E. 1975 Cascade with Subsonic Leading-Edge Locus. AIAA Journal, Vol. 13, No. 8, August 1975, pp. 1117-1118.
- GOLDSTEIN, M., BRAUN, W., ADAMCZYK, J. 1977 Unsteady Flow in a Supersonic Cascade with Strong In-Passage Shocks. J. Fluid Mech., 1977, Vol. 83, Part 3, pp. 569-604.
- GRAHAM, R.W. and COSTILOW, E.L. 1965 Compressor Stall and Blade Vibration. Chapter XI in Aerodynamic Design of Axial-Flow Compressors, NACA SP-36, 1965.
- GRiffin, J.H. and HOOSAC, T.M. 1983 Modal Development and Statistical Investigation of Turbine Blade Mistuning. ASME Monograph "Vibrations of Bladed Disc Assemblies" (Ewins, D.J. and Srinivasan, A.V., Editors).
- GUPTA, K.K. 1973 On a Combined Sturm Sequence and Inverse Iteration Technique for Eigenproblem Solution of Spinning Structures. International Journal for Numerical Methods in Engineering, Vol. 7, pp. 509-518.
- HALFMAN, R.L., JOHNSON, H.C., and HALEY, S.M. 1951 Evaluation of High Angle of Attack Aerodynamic - Derivative Data and Stall-Flutter Prediction Techniques, NACA TN 2533, November 1951.
- HALL, R.M. and ARMSTRONG, E.K. 1976 The Vibration Characteristics of an Assembly of Interlocking Shrouded Turbine Blades. ASME Winter Annual Meeting, Structural Dynamic Aspects of Bladed Disk Assemblies, New York, December 1976.
- HALLIWELL, D.G. 1975 Fan Supersonic Flutter: Prediction and Test Analysis. Aeronautical Research Council R. & I. No. 3789.
- HALLIWELL, D.G. 1978 The Effect of Intake Conditions on Supersonic Flutter in Turbo-Fan Engines. AGARD Conference, Proceedings No. 248, Stress, Vibration, Structural Integration, and Engine Integrity, P.E.P. Meeting, Cleveland, 23-28 October 1978.
- HALLIWELL, D.G. 1980 Effect of Intake Conditions on Supersonic Unstalled Flutter in Turbofan Engines. AIAA Journal of Aircraft, Vol. 17, No. 5, pp. 300-304.
- HALLIWELL, M.A. 1976 The Characteristics, Prediction, and Test Analysis of Supersonic Flutter in Turbofan Engines, Vibrations in Rotating Machinery Conf. C186/76, pp. 181-185, September 1976.
- HALPHEN, B., NGUYEN, Q.S. 1975 Sur les materiaux standards generalises. J. Mecanique, Vol. 14, n° 1, 1975, pp. 39-63.
- HENRY, R. 1973 Calcul de Coques Minces en Grandes Deformations par Elements Finis: Application Aux Aubes de Compresseurs en Rotation. These, Docteur-Ingenieur, Univ. de Lyon.
- HENRY, R. 1980 Calcul des Frequences et Modes des Structures Repetitives Circulaires. Journal de Mecanique Appliquee, Vol. 4, No. 1.
- HENRY, R. AND FERRARIS, G. 1984 Substructuring and Wave Propagation: an Efficient Technique for Impeller Dynamic Analysis. Journal of Engineering for Gas Turbine and Power, ASME, Vol. 106, No. 1.
- PENNY, R. and LALANNE, M. 1974 Vibration Analysis of Rotating Compressor Blades. Trans. ASME, J. Eng. Industry 96(3), pp. 1028-1035.
- HEYWOOD, R.B. 1962 Designing Against Fatigue. Chapman and Hall Ltd., London.
- HITCHINGS, D., EWINS, D.J., and SINGH, M.P. 1980 Dynamic Analysis of Turbine Blades. ASME Century 2 - Emerging Technology Conf., Advances in Computer Technology, Vol. 2.
- HUNT, T.M. 1982 Testing for Acceptable Life. Society of Environmental Engineers, London Symposium on Testing for Reliability, 13 December 1982.
- HUPPERT, M.C., CALVERT, H.F., and MEYER, A.J. 1954 Experimental Investigation of Rotating Stall and Blade Vibration in the Axial-Flow Compressor of a Turbojet Engine, NACA RM E54A08, April 26, 1954.
- IRRETTIER, H. and MARENHOLTZ, O. 1981 Eigenfrequencies and Mode Shapes of a Free-Standing Twisted, Tapered and Rotating Blade with Respect to an Elastically-Supported Root. ASME Paper 81-DET-125.
- IRWIN, G.R. 1957 Analysis of Stresses and Strains Near the End of a Crack Traversing a Plate. Journal of Applied Mechanics, Vol. 24, Trans. ASME, Vol. 79, 1957, p. 36J.
- JACOBSEN, L.S. 1938 Natural Frequencies of Uniform Cantilever Beams of Symmetrical Cross Section. J. Appl. Mech. 5.
- JAY, R.L., BURNS, D.W. 1983 Bladed Disk Response Study, Draft Final Report Number AFWAL-TR-83-2050 under Air Force Contract F33615-79-C-2045, July 1983.
- JEFFERS, J.D., MAY, A. and DESKIN, W.J. 1978 Evaluation of a Technique for Predicting Stall Flutter in Turbine Engines, NASA CR-135423.

- JEFFERS, J.D. and MEECE, C.E. 1975 F100 Fan Stall Flutter Problem Review and Solution. *J. Aircraft* 12, p. 350-357.
- JENNINGS, A. and CLINT, M. 1970 The Evaluation of Eigenvalues and Eigenvectors of Real Symmetric Matrices by Simultaneous Iteration. *The Computer Journal*, Vol. 13, No. 1, pp. 78-80.
- JIMBOH, K., AONO, H., and KAWASHIMA, T. 1977 An Automatic Processing System for Vibration Data Analysis of Gas Turbine Engines. Paper No. 55 of Tokyo Joint Gas Turbine Congress.
- JONES, D.I.G., HENDERSON, J.P. and ROGERS, L.C. 1979 Viscoelastic Damping in USAF Applications. AGARD Conference Proceedings No. 277, Damping Effects in Aerospace Structures, Williamsburg, VA, April 1979.
- JONES, D.I.G. and MUSZYNSKA, A. 1983 A Discrete Model of a Multiple Blade System with blade Slip. ASME Monograph "Vibrations of Bladed Disc Assemblies" (Ewins, D.J. and Srinivasan, A.V., eds.).
- JISTRAS, R., CHI, M., and FUST, R. 1982 Experimental Analysis of Blade Instability - - Fiber Data Correlation for Turbomachinery Blading. AFWAL-TR-82-2008, March 1982.
- KACHANOV, L.M., 1958 Izv. Akad. Nauk. SSR, Otd. Tech. Nauk. 8, 1958.
- KAZA, K.R.V. and KIELB, R.E. 1982 Flutter and Response of a Mistuned Cascade in Incompressible Flow. *AIAA Journal*, Vol. 20, No. 8, pp. 1120-1127.
- KAZA, K.R.V. and KIELB, R.E. 1984 Flutter of Turbofan Rotors with Mistuned Blades. *AIAA Journal*, Vol. 22, No. 1, pp. 1618-1625.
- KAZA, K.R.V. and KIELB, R.E. 1985 Vibration and Flutter of Mistuned Bladed-Disk Assemblies. *AIAA Journal of Propulsion and Power*, Vol. 1, No. 5, pp. 32-344.
- KAZA, K.R.V., MEHMED, O., NARAYANAN, G.V., and MURTHY, D.V. 1987a Analytical Flutter Investigation of a Composite Propfan Model. *AIAA Paper* 87-0738.
- KAZA, K.R.V., MEHMED, O., WILLIAMS, M., and MOSS, L.A. 1987b Analytical and Experimental Investigation of Mistuning in Propfan Flutter. *AIAA Paper* 87-0739.
- KELLY, D.A. and MORRISON, J.L.M. 1971 Effect of Specimen Size and Preparation on the Fatigue Strength of a Plain Carbon Steel Tested in Rotating Bending and in Torsion. *Proc. Inst. Mech. Engrs.*, Vol. 185, pp. 38-71.
- KIELB, R.E. and KAZA, K.R.V. 1983 Aeroelastic Characteristics of a Cascade of Mistuned Blades in Subsonic and Supersonic Flows. *Trans. ASME, Journal of Vibration, Acoustics, Stress, and Reliability in Design*, Vol. 105, October, pp. 425-433.
- KIELB, R.E. and KAZA, K.R.V. 1984 Effects of Structural Coupling on Mistuned Cascade Flutter and Response. *Trans ASME, Journal of Engineering for Gas Turbines and Power*, Vol. 106, January, pp. 17-24.
- KIELB, R.E., LEISSA, A.W., MACBAIN, J. C., CARNEY, K.S. 1985 Joint Resonance Effect on Vibration of Twisted Blades: Phase I - Final Results, NASA Ref. Publ. 1150.
- KIRKHOPE, J. and WILSON, G.J. 1976 A Finite Element Analysis for the Vibration Modes of a Bladed Disc. *Journal of Sound and Vibration* 49, 4, pp. 469-482.
- KOFF, B.L. 1978 Aircraft Engine Design Using Experimental Stress Analysis Techniques. AGARD Conference Proceedings No. 248, Stresses, Vibrations, Structural Integration, and Engine Integrity, P.E.P. 52 Meeting, Cleveland, 23-28 October 1978.
- KOMMERS, J.B. 1945 Proc. ASTM45, pp. 522-543.
- KREML, E. 1977 On Phenomenological Failure Laws for Metals Under Repeated and Sustained Loadings. Conf. on Environmental Degradation of Eng. Mat., Blacksburg, 1977.
- KREML, E., and WALKER, C.D. 1968 ASTM-STP 459.
- KURKOV, A.P. 1980 Flutter Spectral Measurements using Stationary Pressure Transducers. Measurement Methods in Rotating Components of Turbomachinery. ASME; also ASME Journal for Engineering for Power 103, No. 2, pp. 461-467.
- KURKOV, A.P. 1982 Measurement of Aerodynamic Work during Fan Flutter. NASA TM-82-652.
- KURKOV, A.P. and DICUS, J. 1978 Synthesis of Blade Flutter Vibratory Patterns using Stationary Transducers. ASME Paper 78-GT-160.
- LANE, F., 1957 Supersonic Flow Past an Oscillating Cascade with Supersonic Leading Edge Locus. *IAS Journal of the Aeronautical Sciences*, Vol. 24, January, pp. 65-66.
- LANE, F. and WANG, C.T. 1954 A Theoretical Investigation of the Flutter Characteristics of Compressor and Turbine Blade Systems, WADC Technical Report 54-449.
- LARSON, B. and STORAKERS, B. 1978 A State Variable Interpretation of Some Rate-Dependent Inelastics Properties. *J. of Eng. Mat. and Techn.*, Vol. 100, 1978, pp. 395-401.
- LEISSA, A. 1980 Vibrations of Turbine Engine Blades by Shell Analysis. *Shock & Vibration Digest* 12(11), pp. 3-10.

- LEISSA, A. 1981 Vibrational Aspects of Rotating Turbomachinery Blades. *Appl. Mech. Reviews* 34(5), pp. 629-635.
- LEISSA, A.W., MACBAIN, J.C., and KIELB, R.E. 1984 Vibrations of Twisted Cantilevered Plates. *J. Sound & Vib.*, Vol. 96, No. 2, pp. 158-173.
- LEMAITRE, J. 1971 Sur la determination des lois de comportement des materiaux elasto-viscoplastiques. ONERA, Publication n° 135, 1971.
- LEMAITRE, J. and CHABOCHE, J.L. 1975 A Nonlinear Model for Creep-Fatigue Damage Cumulation and Interaction. *Mech. of Viscoplastic Media and Bodies*, ed. J. HULT, Springer, Berlin, 1975, pp. 291-301.
- LEMAITRE, J. and DUFAILLY, J. 1977 Modelisation de l'endommagement plastique des metaux. 3eme Congres Francais de Mecanique, Grenoble.
- MACBAIN, J.C. 1975 Vibratory Behaviour of Twisted Cantilever Plates. *J. of Aircraft* 12(4), pp. 343-349.
- MANDEL, J. 1973 Equations constitutives et directeurs dans les milieux plastiques et viscoplastiques. *Int. J. Solids and Struct.*, Vol. 9, 1973, pp. 725.
- MANSON, S.S. 1954 Behaviour of Materials under Conditions of Thermal Stress. NACA TN 2933, 1954.
- MANSON, S.S. 1971 Metal Fatigue Damage - Mechanism, Detection, Avoidance, and Repair with Special Reference to Gas Turbine Components, ASTM Publication STP-495 (book).
- MANSON, S.S., NACHTIGALL, A., ENSIGN, C.R., and FRECHE, J. C. 1965 Trans. ASME, J. Eng. Ind., 87, 1, 1965, pp. 22-35.
- MEETHAM, G.W. 1981 The Development of Gas Turbine Materials, Edited by G.W. Meetham, Applied Science Publishers Ltd., London 1981 (book).
- MEHALIC, C.M., DICUS J., and KURKOV, A.P. 1977 Effect of Pressure and Temperature on the Subsonic Stall Flutter Region of a YF100 Engine. NASA TM-73785.
- Metal Improvement Company, 1980 Shot Peening Applications, 6th Edition, Copyright 1980.
- MIKOŁAJCZAK, A.A., ARNOLDI, R., STARGARDTER, H., and SNYDER, L.E. 1975 Advances in Fan and Compressor Blade Flutter Analysis and Prediction. *AIAA Journal of Aircraft*, Vol. 12, No. 4, April 1975. pp. 325-332.
- MINER, M.A. 1945 Cumulative Damage in Fatigue. *J. Appl. Mechanics*, Vol. 12, No. 3., pp. A159-A164, September 1945.
- MONTOYA, J.G. 1966 Coupled Bending and Torsional Vibrations in a Twisted Rotating Blade. *Brown Boveri Review* 53, No. 3, pp. 216-230.
- MOORE, H.F. and KOMMERS, J.B. 1927 The Fatigue of Metals, McGraw-Hill Book Company, Inc., 1927.
- MOTA SOARES, C.A. and PETYT, M. 1978 Finite Element Dynamic Analysis of Practical Bladed Discs. *Journal of Sound and Vibration* 61, 4, pp. 561-579.
- NAGASHIMA, T. and WHITEHEAD, D.S. 1974 Aerodynamic Forces and Moments for Vibrating Supersonic Cascade Blades. University of Cambridge, Department of Engineering Report CUED/A-Turbo/TR59.
- NAMBA, M., 1987 "Three-Dimensional Flows," AGARD Manual on Aerelasticity in Axial Flow Turbomachines, Vol. 1, AGARD-AG-298, pp. 4-1 through 4-29.
- NI, R.H. and SISTO, F. 1975 Numerical Computation of Nonstationary Aerodynamics of Flat Plate Cascades in Compressible Flow. ASME Paper No. 75-GT-5.
- ODQUIST, F.J. and HULT, J. 1962 Kriechfestigkeit Metallischer Werkstoffe. Springer-Verlag, 1962.
- OLSON, M.D. and BEARDEN, I.W. 1979 A Simple Flat Triangular Shell Element Revisited. *Int. J. Num. Methods in Eng.*, 14(1), pp. 51-68.
- PALMGREN, A. 1924 Die Lebensdauer von Kugellagern. *Z.V.D.I.*, 1924, Vol. 68, (Apr. No. 14), pp. 239.
- PARIS, P.C. and ERDOGAN, F. 1963 A Critical Analysis of Crack Propagation Laws. *Trans. ASME J. Basic Eng.*, Vol. PS, pp. 528-534.
- PARRY, J.F.W. and PEARSON, H. 1954 Cascade Flutter and Wake Excitation. *Journal of the Royal Aeronautical Society*, July 1954, pp. 505-508.
- PASSEY, R.D.C. 1976 Reliability of Compressor Aerofoils. *Prog. Aerospace Sci.*, 1976, Vol. 17, pp. 67-92, Pergamon Press, Great Britain.
- PEARSON, H. 1953 The Aerodynamics of Compressor Blade Vibration. Fourth Anglo-American Aeronautical Conference, London, 16-17 September 1953, pp. 127-162.
- PETERSON, M.R., ALDERSON, R.G., and STOCKTON, R.J. 1978 Three-Dimensional Finite Element Techniques for Gas Turbine Blade Life Prediction. AGARD Conference Proceeding No. 248, Stresses, Vibration, Structural Integration, and Engine Integrity, P.E.P. Meeting, Cleveland, 23-28 October 1978.

- PINES, S. 1958 An Elementary Explanation of the Flutter Mechanism. Proc. National Specialists Meeting on Dynamics and Aeroelasticity, Inst. of the Aeronautical Sciences, Ft. Worth, Texas, November 1958, pp. 52-58.
- POLICELLA, H. and CULIE, J.P. 1981 A Method for Predicting the Life Time of Turbine Blades. Fat. of Eng. Mat. and Struct., 4, n° 2, 1981, pp. 157-172.
- POPE, J.A. 1959 Metal Fatigue. Chapman and Hall, London, 1959.
- PRAGER, W. 1949 Recent Developments in the Mathematical Theory of Plasticity. J. Appl. Phys., Vol. 20, n° 3, 1949, pp. 235-241.
- RABOTNOV, Y.N. 1969 Creep Problems in Structural Members. North Holland Publ. Co.
- RABOTNOV, Y.N. 1969 Creep Rupture. Proc. XII Int. Cong. Appl. Mech., Stanford-Springer.
- RABY, H. 1970 Rotor Blade Vibration Observed from the Casing. Conference on Method of Transmitting Signals from Rotating Plant. Central Electricity Research Laboratories, Leatherhead, England, 25-26 June 1970.
- RAMAMURTI, V. and KIELB, R. 1984 Natural Frequencies of Twisted Rotating Plates. J. Sound & Vib. 97(3), pp. 429-449.
- RAO, J.S. 1973 Natural Frequencies of Turbine Blading - a Review. Shock & Vib. Digest 10), pp. 3-16.
- RAO, J.S. 1980 Turbomachine Blade Vibration. Shock & Vib. Digest 12(2), pp. 19-26.
- RIFTEL, R. and ROTHROCK, M. 1980 Experimental Determination of Unsteady Blade Element Aerodynamics in Cascades. NASA CR-165166, December 1980.
- ROWE, J.R. and MENDELSON, A. 1955 Experimental Investigation of Blade Flutter in Annular Cascade. NACA TN 3581, November 1955.
- RUGGERI, P.S. and BENSER, W.A. 1974 A Performance of a Highly Loaded Two-Stage Axial-Flow Fan. TM X-3076, August 1974.
- SAADA, A.S. 1974 Elasticity: Theory and Applications. (Chapter 10) Pergamon Press.
- SALAMA, A.M., PETYT, M., and MOTA SOARES, C.A. 1976 Dynamic Analysis of Bladed Discs by Wave Propagation and Matrix Difference Techniques. Struc. Dyn. Aspects Bladed Discs, ASME pp. 45-46.
- S'WALLE, S. and CULIE, J.P. 1978 Methodes de calcul associees aux lois de comportement et d'endommagement. I.A. n°, 1978-5, pp. 263-278.
- SCANLAN, R. H. and ROSENBAUM, R. 1951 Introduction to the Study of Aircraft Vibration and Flutter. The Macmillan Co., New York, 1951.
- SCHNEIDER, J.R. 1955 The Stress Problem of Vibrating Compressor Blades. Journal Appl. Mech., Vol. 22, No. 1, 1955, pp. 57-64.
- SCHNEIDER, P. 1980 Analysis of J35-21 Compressor Aerodynamic Flutter Data. NASA CR 159795, February 1980.
- SCHNITTGER, J.R. 1954 Single Degree of Freedom Flutter of Compressor Blades in Separated Flow. Journal Aero Sciences, Vol. 21, No. 1, January 1954, pp. 27-36.
- SHANNON, J.F. 1945 Vibration Problems in Gas Turbines, Centrifugal, and Axial-Flow Comp.ors. A.R.C. R&M No. 2226, 1945.
- SHORR, B.L. 1961 Vibration of retwisted Rods, Izvestiya Akademii Nauk, SR., OTN, Mekhanika i Mashinostroenie, 1961, Vol. 3, pp. 102-112.
- SIDOROFF, F. 1975 On the Formulation of Plasticity and Viscoplasticity with Internal Variables. Arch. Mech., Poland, Vol. 27, n° 5-6, 1975, pp. 807-819.
- SIPES, G. and WAISMAN, J. L. 1959 University of California, Engineering Extension Series, Edited by G. Sires and J.L. Waisman, Published 1959 McGraw-Hill Book Company, Inc.
- SISTO, F. 1952 Flutter of Airfoils in Cascade. Sc.D. Dissertation, Massachusetts Institute of Technology, Cambridge, Mass.
- SISTO, F. 1953 Stall Flutter in Cascades. Journal Aero. Sciences, Vol. 20, No. 9, September 1953, pp. 598-604.
- SISTO, F. 1967 Linearized Theory of Nonstationary Cascades at Fully Stalled or Supercavitated Conditions. ZAMP 47, Heft 8, 1967, pp. 531-542.
- SISTO, F. and PERUMAL, P.V. 1974 Lift and Moment Predictions for an Oscillating Airfoil with a Moving Separation Point. ASME Paper 74-GT-28, April 1974.
- SISTO, F. and NI, R., 1974 Research on the Flutter of Axial Turbomachine Blading. ONR Tech. Report ME-RT 74-008, Stevens Institute of Technology, Hoboken, N.J.

- SISTO, F. and NI, R.H. 1972 Quasi-Static Moment Measurements for Airfoils in an Annular Cascade. *Journal of Aircraft*, Vol. 9, No.4, April 1972.
- SMILG, B. and WASSERMAN, L.S. 1942 Application of Three-Dimensional Flutter Theory to Aircraft Structures. AAF Technical Report 4798, July.
- SMITH, S.N. 1971 Discrete Frequency and Sound Generation in Axial Flow Turbomachines. University of Cambridge Report CUED/A-Turbo/TR 29, 1971.
- SMITH, S.N. 1972 Discrete Frequency and Sound Generation in Axial Flow Turbomachines. ARC Reports and Memoranda No. 3709, March 1972.
- SNIDER, L.E. 1972 Supersonic Unstalled Torsional Flutter. *Aeroelasticity in Turbomachinery*, S. Fleeter, ed., Proceedings of Project SQUID. Workshop held at Detroit Diesel Allison, Indianapolis, June 1-2, 1972, Project SQUID, Office of Naval Research, pp. 164-195.
- SNIDER, L.E. and COMMERFORD, G.L. 1974 Supersonic Unstalled Flutter in Fan Rotors; Analytical and Experimental Results. *Journal of Engineering for Power*, TRANS. ASME, Series A, Vol. 96, No. 4, October 1974, pp. 379-386.
- SOKOLNIKOFF, I. 1956 Mathematical Theory of Elasticity. Chapter 4, McGraw-Hill.
- SRINIVASAN, A.V., 1980 Influences of Mistuning on Blade Torsional Flutter, NASA CR-165137, August 1980.
- SRINIVASAN, A.V., CUTTS, D.G., and SRIDHAR, S. 1981 Turbojet Engine Blade Damping. NASA CR-165406, July 1981.
- SRINIVASAN, A.V. and FABUNMI, J.A. 1984 Cascade Flutter Analysis of Cantilevered Blades, *Journal of Engineering for Gas Turbines and Power*, Transactions ASME, Vol. 106, January 1984, pp. 34-43.
- STARGARDTER, H. 1966 Dynamic Models of Vibrating Rotor Stages. ASME Paper 66-WA/GT-8.
- STARGARDTER, H. 1977 Optical Determination of Rotating Fan Blade Deflections. ASME Transactions - Engineering for Power, Vol. 99, No. 2, April 1977.
- STARGARDTER, H., PATENT 4080823, Vibration Measurement.
- STARGARDTER, H. 1979 Subsonic/Transonic Stall Flutter Study. NASA CR-165256, PWA 5517-31, June 1979.
- SZECHENYI, E., CAFARELLI, I., NOTIN, C., and GIRAUT, J.P. 1984 A Straight Cascade Wind-Tunnel Study of Fan Blade Flutter in Started Supersonic Flow, presented at the Symposium on the Aeroelasticity of Turbomachines and Propellers, Cambridge University, UK, September 1984.
- THEODORSEN, T. 1935 General Theory of Aerodynamic Instability and the Mechanism of Flutter. NACA Report 36.
- THOMAS, J. and BELEK, H.T. 1977 Free Vibrations of Blade Packets. JMEMS, IMechE, pp. 13-21.
- THOMPSON, W. T. 1981 Theory of Vibration with Applications. Prentice Hall.
- TIMOSHENKO, S. 1937 Vibration Problems in Engineering. 2nd Edition, 1937, D. Van Nostrand Company.
- TROHA, W. and SWAIN, K. 1976 Composite Inlays Increase Flutter Resistance of Turbine Engine Fan Blades. ASME Paper 76-FT-29.
- TROMPETTE, P. and LALANNE, M. 1974 Vibration Analysis of Rotating Turbine Blades. ASME Paper, 74-WA/DE-23.
- VERDON, J.M. 1973 The Unsteady Aerodynamics of a Finite Supersonic Cascade with Subsonic Axial Flow. *Journal of Applied Mechanics*, Vol. 95, TRANS ASME, Series E, Vol. 40, No. 3, September 1973, pp. 667-671.
- VERDON, J.M. 1977 Further Developments in the Aerodynamic Analysis of Unsteady Super-sonic Cascades, Part 1: The Unsteady Pressure Field, and Part 2: Aerodynamic Response Predictions. ASME Paper No. 77-GT-44 & 45.
- VERDON, J.M. and McCUNE, J.E. 1975 Unsteady Supersonic Cascade in Subsonic Axial Flow. AIAA Journal, Vol. 13, No. 2, pp. 193-201.
- VERDON, J.M. and CASPAR, J.R. 1982 Development of a Linear Aerodynamic Analysis for Unsteady Transonic Cascades. NASA CR-168038.
- WATERHOUSE, R.B. 1981 Fretting Fatigue. Edited by R. B. Waterhouse, Applied Science Publishers London.
- WHITEHEAD, D.S. 1960 Force and Moment Coefficients for Vibratory Aerofoils in Cascade. British Aeronautical Research Council, London R&M No. 3254.
- WHITEHEAD, D.S. 1966 Torsional Flutter of Unstalled Cascade Blades at Zero Deflection, ARC Reports and Memoranda No. 3429.
- WOODFORD, D.A. 1974 A Critical Assessment of the Life Fraction Rule, for Creep Rupture under Nonsteady Stress or Temperature. Int. Conf. on Creep Fatigue in Elevated Temperatures Applications, Philadelphia, 1973, Sheffield, 1974.

YATES, H.G. 1948 Vibration Diagnosis in Marine Geared Turbines. Trans. N.E. Coast Inst. Engrs. and Shipbuilders, Vol. 65, pp. 225-261, App I & II, pp. 245-249.

ZBIROHOWSKI-KOSCIA, K. 1967 Thin Walled Beam from Theory to Practice. Published 1967 by Crosby Lockwood and Son, Ltd., 26 Old Brompton Road, London SW7.

ZIENKIEWICZ, O. C. 1970 The Finite Element Method in Engineering Science. McGraw-Hill.

REPORT DOCUMENTATION PAGE							
1. Recipient's Reference	2. Originator's Reference	3. Further Reference	4. Security Classification of Document				
	AGARD-AG-298 Volume 2	ISBN 92-835-0467-4	UNCLASSIFIED				
5. Originator	Advisory Group for Aerospace Research and Development North Atlantic Treaty Organization 7 rue Ancelle, 92200 Neuilly sur Seine, France						
6. Title	AGARD MANUAL ON AEROELASTICITY IN AXIAL-FLOW TURBOMACHINES, VOLUME 2 - STRUCTURAL DYNAMICS AND AEROELASTICITY						
7. Presented at							
8. Author(s)/Editor(s)	Editors: M.F.Platzer and F.O.Carta		9. Date				
10. Author's/Editor's Address	See flyleaf.		11. Pages				
12. Distribution Statement	This document is distributed in accordance with AGARD policies and regulations, which are outlined on the Outside Back Covers of all AGARD publications.						
13. Keywords/Descriptors	<ul style="list-style-type: none"> › Reviewing Turbomachinery Structural dynamic analysis Aeroelasticity Metal fatigue <table style="margin-left: 20px;"> <tr><td>Flutter</td></tr> <tr><td>Blades</td></tr> <tr><td>Discs</td></tr> <tr><td>Rotors</td></tr> </table>			Flutter	Blades	Discs	Rotors
Flutter							
Blades							
Discs							
Rotors							
14. Abstract	<p>The first volume of this Manual reviewed the state of the art of unsteady turbomachinery aerodynamics as required for the study of aeroelasticity in axial turbomachines. This second volume aims to complete the review by presenting the state of the art of structural dynamics and of aeroelasticity.</p> <p>The eleven chapters in this second volume give an overview of the subject and reviews of the structural dynamics characteristics and analysis methods applicable to single blades and bladed assemblies.</p> <p>The blade fatigue problem and its assessment methods, and life-time prediction are considered. Aeroelastic topics covered include: the problem of blade-disc shroud aeroelastic coupling, formulations and solutions for tuned and mistuned rotors, and instrumentation on test procedures to perform a fan flutter test. The effect of stagnation temperature and pressure on flutter is demonstrated and currently available forced vibration and flutter design methodology is reviewed.</p> <p>This AGARDograph was prepared at the request of the Propulsion and Energetics Panel and of the Structures and Materials Panel of AGARD.</p>						

<p>AGARDograph No.298 Advisory Group for Aerospace Research and Development, NATO AGARD MANUAL ON AEROELASTICITY IN AXIAL-FLOW TURBOMACHINES, VOLUME 2 – STRUCTURAL DYNAMICS AND AERO-ELASTICITY Edited by M.F.Platzer and F.O.Carta Published June 1988 268 pages</p>	<p>AGARD-AG-298 Reviewing Turbomachinery Structural dynamic analysis Aeroelasticity Metal fatigue Flutter Blades Discs Rotors</p> <p>The first volume of this Manual reviewed the state of the art of unsteady turbomachinery aerodynamics as required for the study of aeroelasticity in axial turbomachines. This second volume aims to complete the review by presenting the state of the art of structural dynamics and of aeroelasticity.</p> <p>P.T.O.</p>	<p>AGARDograph No.298 Advisory Group for Aerospace Research and Development, NATO AGARD MANUAL ON AEROELASTICITY IN AXIAL-FLOW TURBOMACHINES, VOLUME 2 – STRUCTURAL DYNAMICS AND AERO-ELASTICITY Edited by M.F.Platzer and F.O.Carta Published June 1988 268 pages</p> <p>AGARD-AG-298 Reviewing Turbomachinery Structural dynamic analysis Aeroelasticity Metal fatigue Flutter Blades Discs Rotors</p> <p>The first volume of this Manual reviewed the state of the art of unsteady turbomachinery aerodynamics as required for the study of aeroelasticity in axial turbomachines. This second volume aims to complete the review by presenting the state of the art of structural dynamics and of aeroelasticity.</p> <p>P.T.O.</p>
--	---	--

<p>The eleven chapters in this second volume give an overview of the subject and reviews of the structural dynamics characteristics and analysis methods applicable to single blades and bladed assemblies.</p> <p>The blade fatigue problem and its assessment methods, and life-time prediction are considered. Aeroelastic topics covered include: the problem of blade-disc shroud aerelastic coupling, formulations and solutions for tuned and mistuned rotors, and instrumentation on test procedures to perform a fan flutter test. The effect of stagnation temperature and pressure on flutter is demonstrated and currently available forced vibration and flutter design methodology is reviewed.</p> <p>This AGARDograph was prepared at the request of the Propulsion and Energetics Panel and of the Structures and Materials Panel of AGARD.</p>	<p>ISBN 92-835-0467-4</p>	<p>The eleven chapters in this second volume give an overview of the subject and reviews of the structural dynamics characteristics and analysis methods applicable to single blades and bladed assemblies.</p> <p>The blade fatigue problem and its assessment methods, and life-time prediction are considered. Aeroelastic topics covered include: the problem of blade-disc shroud aerelastic coupling, formulations and solutions for tuned and mistuned rotors, and instrumentation on test procedures to perform a fan flutter test. The effect of stagnation temperature and pressure on flutter is demonstrated and currently available forced vibration and flutter design methodology is reviewed.</p> <p>This AGARDograph was prepared at the request of the Propulsion and Energetics Panel and of the Structures and Materials Panel of AGARD.</p>
		<p>ISBN 92-835-0467-4</p>

AGARD
 NATO OTAN
 7 rue Ancelle • 92200 NEUILLY-SUR-SEINE
 FRANCE
 Telephone (1)47.38.57.00 • Telex 610 176

**DISTRIBUTION OF UNCLASSIFIED
 AGARD PUBLICATIONS**

AGARD does NOT hold stocks of AGARD publications at the above address for general distribution. Initial distribution of AGARD publications is made to AGARD Member Nations through the following National Distribution Centres. Further copies are sometimes available from these Centres, but if not may be purchased in Microfiche or Photocopy form from the Purchase Agencies listed below.

NATIONAL DISTRIBUTION CENTRES

BELGIUM

Coordonnateur AGARD — VSL
 Etat-Major de la Force Aérienne
 Quartier Reine Elisabeth
 Rue d'Evere, 1140 Bruxelles

CANADA

Director Scientific Information Services
 Dept of National Defence
 Ottawa, Ontario K1A 0K2

DENMARK

Danish Defence Research Board
 Ved Idrætsparken 4
 2100 Copenhagen Ø

FRANCE

O.N.E.R.A. (Direction)
 29 Avenue de la Division Leclerc
 92320 Châtilion

GERMANY

Fachinformationszentrum Energie,
 Physik, Mathematik GmbH
 Karlsruhe
 D-7514 Eggenstein-Leopoldshafen 2

GREECE

Hellenic Air Force General Staff
 Aircraft Support Equipment Directorate
 Department of Research and Development
 Holargos, Athens, 15500

ICELAND

Director of Aviation
 c/o Flugrad
 Reykjavik

UNITED STATES

National Aeronautics and Space Administration (NASA)
 Langley Research Center
 M/S 180
 Hampton, Virginia 23665

ITALY

Aeronautica Militare
 Ufficio del Delegato Nazionale all'AGARD
 3 Piazzale Adenauer
 00144 Roma/EUR

LUXEMBOURG

See Belgium

NETHERLANDS

Netherlands Delegation to AGARD
 National Aerospace Laboratory, NLR
 P.O. Box 126
 2600 AC Delft

NORWAY

Norwegian Defence Research Establishment
 Attn: Biblioteket
 P.O. Box 25
 N-2007 Kjeller

PORTUGAL

Portuguese National Coordinator to AGARD
 Gabinete de Estudos e Programas
 CLAFA
 Base de Alfragide
 Alfragide
 2700 Amadora

TURKEY

Milli Savunma Bakanlığı (MSB)
 ARGE Daire Başkanlığı (ARGE)
 Ankara

UNITED KINGDOM

Defence Research Information Centre
 Kentigern House
 65 Brown Street
 Glasgow G2 8EX

PURCHASE AGENCIES

National Technical
 Information Service (NTIS)
 5285 Port Royal Road
 Springfield
 Virginia 22161, USA

ESA/Information & Technical Service
 European Space Agency
 10, rue Mario Nikis
 75015 Paris, France

The British Library
 Document Supply Division
 Boston Spa, Wetherby
 West Yorkshire LS23 7BQ
 England

Requests for microfiche or photocopies of AGARD documents should include the AGARD serial number, title, author or editor, and publication date. Requests to NTIS should include the NASA accession report number. Full bibliographical references and abstracts of AGARD publications are given in the following journals:

Scientific and Technical Aerospace Reports (STAR)
 published by NASA Scientific and Technical
 Information Branch
 NASA Headquarters (NIT-40)
 Washington D.C. 20546, USA

Government Reports Announcements (GRA)
 published by the National Technical
 Information Services, Springfield
 Virginia 22161, USA

Printed by Specialised Printing Services Limited
 40 Chigwell Lane, Loughton, Essex IG10 3TZ

ISBN 92-835-0467-4